THE PHYSICS AND CHEMISTRY OF SOLIDS

AN INTERNATIONAL JOURNAL

VOLUME 10 1959

Editor-in-Chief HARVEY BROOKS *Cambridge, Mass.*

Associate Editors
H. B. G. CASIMIR *Eindhoven*
G. J. DIENES *Brookhaven*
JACQUES FRIEDEL *Paris*
E. M. LIFSHITZ *Moscow*

Editorial Advisory Board

U.S.A.: E. N. ADAMS, Pittsburgh · D. ALPERT, Illinois · L. APKER, Schenectady · J. BARDEEN, Illinois · D. S. BILLINGTON, Oak Ridge · R. G. BRECKENRIDGE, Cleveland · LEO BREWER, Berkeley, Calif. · E. BURSTEIN, Penn. J. A. BURTON, New Jersey · N. CABRERA, Virginia · C. C. DANIELSON, Iowa · I. ESTERMANN, Washington, D.C. J. C. FISHER, Schenectady · F. HERMAN, Princeton · CONYERS HERRING, New Jersey · A. R. VON HIPPEL, Cambridge, Mass. · J. H. HOLLOMON, Schenectady · W. V. HOUSTON, Houston · H. B. HUNTINGTON, Troy · H. M. JAMES, Purdue · JOHN G. KIRKWOOD, Yale · C. KITTEL, Berkeley, Calif. · W. KOHN, Pittsburgh · J. A. KRUMHANSL, Cleveland · A. W. LAWSON, Chicago · H. W. LEVERENZ, Princeton · O. T. MARZKE, Pittsburgh · B. T. MATTHIAS, New Jersey · L. R. MAXWELL, Silver Spring · JOSEPH E. MAYER, Chicago · E. W. MONTROLL, Maryland · DAVID PINES, Princeton · H. REISS, New Jersey · J. R. REITZ, Cleveland · A. ROSE, Princeton · O. C. SIMPSON, Argonne R. SMOLUCHOWSKI, Pittsburgh · F. H. SPEDDING, Iowa · D. TURNBULL, Schenectady · J. H. VAN VLECK, Harvard B. E. WARREN, Cambridge, Mass. · Eugene P. WIGNER, Princeton · B. H. ZIMM, Schenectady.

Canada: R. E. BURGESS, Vancouver · D. K. C. MACDONALD, Ottawa.

United Kingdom: A. CHARLESBY, Shrivenham, Berks · W. J. DUNNING and F. C. FRANK, Bristol · H. K. HENISCH, Reading · H. JONES, London · J. W. MITCHELL, Bristol · A. B. PIPPARD, Cambridge · M. H. L. PRYCE, Bristol R. A. SMITH, Malvern · K. W. H. STEVENS, Nottingham · F. C. TOMPKINS, London.

France: E. F. BERTAUT, Grenoble · A. GUINIER, Paris · LOUIS NÉEL and LOUIS WEIL, Grenoble.

Germany: M. BORN, Bad Pyrmont · ULRICH DEHLINGER, Stuttgart · R. HILSCH and G. LEIBFRIED, Göttingen E. MOLLWO, Erlangen · H. PICK, Stuttgart · M. VON LAUE, Berlin · H. WELKER, Erlangen.

Italy: F. G. FUMI, Pavia.

Czechoslovakia: J. TAUC, Praha.

Japan: TOSHINOSUKE MUTO, Tokyo.

The Netherlands: A. MICHELS and G. W. RATHENAU, Amsterdam. *Sweden:* J. O. LINDE, Stockholm · PER-OLOV LÖWDIN, Uppsala.

Switzerland: G. BUSCH and P. SCHERRER, Zürich. *U.S.S.R.:* G. S. ZHDANOV, Moscow.

PERGAMON PRESS NEW YORK · LONDON · PARIS · LOS ANGELES

NOTES FOR CONTRIBUTORS

I. GENERAL

1. Submission of a paper to the *Journal of the Physics and Chemistry of Solids* will be taken to imply that it represents original research not previously published (except in the form of an abstract or preliminary report), that it is not being considered for publication elsewhere, and that if accepted, it will not be published elsewhere in the same form, in any language, without the consent of the editor-in-chief. It should deal with original research work in the field of the physics and chemistry of solids.

2. Papers should be submitted to the appropriate regional editor (all English-language papers to be sent to the U.S. editor).

3. Papers will be published as quickly as possible after acceptance, and, subject to space being available, should appear in the following issue, if this is due for publication not earlier than three months after the acceptance date. Short communications under the heading of "Letters to the Editors" will receive priority for publication, and will be published in the issue following receipt, if accepted not later than the beginning of the month preceding publication.

4. Fifty free reprints of each paper are supplied. Additional copies can be obtained at a reasonable cost if ordered when proofs are returned. A reprint order form will accompany first proofs.

II. SCRIPT REQUIREMENTS

1. Papers submitted should be concise and written in a readily understandable style. Scripts should be typed and double spaced and submitted in duplicate to facilitate refereeing.

It will be appreciated if authors clearly indicate any special characters used. An abstract, not exceeding 200 words, should be provided in the language of the paper. French and German papers should be submitted with English abstract and titles, but if this is not possible the abstract will be translated by the publishers. To conserve space, authors are requested to mark less important parts of the paper, such as details of experimental technique, methods, mathematical derivations, etc. for printing in small type. The technical description of methods should be given in detail only when such methods are new. Authors will receive proofs for correction when their papers are first set; page proofs will be sent only when the amount of alteration makes it advisable.

2. Illustrations should not be included in the typescript of the paper, and legends should be typed on a separate sheet. Line drawings which require redrawing should include all relevant details and clear instructions for the draughtsman. If figures are already well drawn it may be possible to reproduce them direct from the originals, or from good photo-prints if these can be provided. It is not possible to reproduce from prints with weak lines. Illustrations for reproduction should normally be about twice the final size required. Photographs should only be included where they are essential.

Tables and figures should be so constructed as to be intelligible without reference to the text. Every table and column should be provided with an explanatory heading. Units of measure must always be clearly indicated. The same data should not be published in both tables and figures. The following standard symbols should be used on line drawings since they are easily available to the printers: ○, ●, +, ×, □, ■, △, ▲, ◇, ◆, ▽, ▼.

4. References are indicated in the text by superior numbers in parentheses, and the full reference should be given in a list at the end of the paper in the following form:

1. HILL R., *J. Iron St. Inst.* **158**, 177 (1948).
2. PEARSON C., *The Extrusion of Metals*, Chapman and Hall, London (1944).

Abbreviations of journal titles should follow those given for *Physics Abstracts*. It is particularly requested that authors' initials, and appropriate volume and page numbers, should be given in every case.

Footnotes, as distinct from literature references should be indicated by the following symbols—*, †, ‡, ‡‡, commencing anew on each page; they should *not* be included in the numbered reference system.

5. Due to the international character of the journal no rigid rules concerning notation and spelling will be observed, but each paper should be consistent within itself as to symbols and units.

VOL
10
195

OL.
10
959

VOL.
10
1959

CONTENTS

NUMBER 1

A. W. Hornig, R. C. Rempel and H. E. Weaver: Electron paramagnetic resonance in single crystals of $BaTiO_3$ 1

A. Michels, J. van Eck, S. Machlup and C. A. Ten Seldam: Pressure-dependence of the resistivity of germanium 12

H. Sato, A. Arrott, and R. Kikuchi: Remarks on magnetically dilute systems 19

G. Shirane, S. J. Pickart, R. Nathans and Y. Ishikawa: Neutron-diffraction study of antiferromagnetic $FeTiO_3$ and its solid solutions with α-Fe_2O_3 35

John C. Fisher: Antiferromagnetic ground state 44

D. G. Thomas: Infrared absorption in zinc oxide crystals 47

F. Kettel: Die Wärmeleitfähigkeit von Germanium bei hohen Temperaturen 52

Hartmut Kallmann, Bernard Kramer and Peter Mark: Calculation of the photoconductivity from a.c. impedance changes induced in ZnS and ZnCdS phosphors 59

Letters to the Editors:

D. G. Martin: Dimensional changes in single crystals of synthetic sapphire after irradiation . . . 64

Notices 66

Contents Lists of Volume 7, Numbers 1–4 68

Papers to be published in future issues 76

NUMBERS 2/3

Taira Suzuki and Masao Doyama: Hardening induced by additive coloration in KCl 77

Junjiro Kanamori: Superexchange interaction and symmetry properties of electron orbitals 87

A. F. Forestieri and L. A. Girifalco: The effect of plastic deformation on self-diffusion in silver . . 99

J. L. Davis, G. E. Devlin, V. Jaccarino and A. L. Schawlow: Structure-sensitivity of the high-frequency NMR in powdered antiferromagnetic MnF_2 106

J. J. Hopfield: A theory of edge-emission phenomena in CdS, ZnS and ZnO 110

Edgar F. Westrum, Jr. and D. M. Grimes: Low-temperature heat capacities and thermodynamic properties of zinc ferrites–III Effect of copper substitution 120

A. Blandin et E. Daniel: Sur le déplacement de Knight dans les alliages 126

R. Nathans, C. G. Shull, G. Shirane and A. Andresen: The use of polarized neutrons in determining the magnetic scattering by iron and nickel 138

R. J. Weiss and A. F. Freeman: X-ray and neutron scattering from electrons in a crystalline field and the determination of outer electron configurations in iron and nickel 147

R. Guccione, M. P. Tosi and M. Asdente: Migration barriers for cations and anions in alkali halide crystals . 162

Issai Lefkowitz: Radiation-induced changes in the ferroelectric properties of some barium titanate-type materials 169

E. Daniel: Sur le déplacement de Knight des impuretés dans les métaux 174

M. A. Gilleo and D. W. Mitchell: The ferrimagnetism and crystal chemistry of substituted manganese–tin spinels 182

M. A. Gilleo and S. Geller: The interaction of magnetic ions in $Gd_3Mn_2Ge_2GaO_{12}$ and related garnets . 187

F. D. Rosi, B. Abeles and R. V. Jensen: Materials for thermoelectric refrigeration 191

S. H. Koenig and R. D. Brown III: Thermal oscillations in *n*-germanium at low temperature . . . 201

M. S. Abrahams, R. Braunstein and F. D. Rosi: Thermal, electrical and optical properties of (In,Ga)As alloys 204

K. Teegarden and R. Weeks: Trapped charge and the low-temperature luminescence of undoped KI . 211

G. J. Ogilvie and M. J. Ridge: The cathodic sputtering of silver 217

G. J. Ogilvie: The surface structure of silver crystals after argon-ion bombardment 222

M. L. Glasser: Symmetry properties of the wurtzite structure 229

Letters to the Editors:

D. W. G. Ballentyne: Crystal structure and electroluminescence in ZnS 242

S. J. Pickart and A. C. Turnock: Magnetic properties of solid solutions of Fe_3O_4 and $FeAl_2O_4$ . . 242

Papers to be published in future issues 244

NUMBER 4

JUN KONDO and JIRO YAMASHITA: Nuclear quadrupolar relaxation in ionic crystals 245

E. N. ADAMS and T. D. HOLSTEIN: Quantum theory of transverse galvanomagnetic phenomena . . . 254

PIERRE MOREL: Calcul semi-empirique de la température de transition des superconducteurs et de l'effet de la pression sur la transition 277

E. N. ADAMS and E. I. BLOUNT: Energy bands in the presence of an external force field—II Anomalous velocities. 286

H. M. C. SOSNOVSKY: The catalytic activity of silver crystals of various orientations after bombardment with positive ions 304

J. P. EVANS and P. G. MARDON: Some physical properties of neptunium metal—I A determination of the specific heat of α-neptunium 311

E. ANTONČÍK: Approximate formulation of the orthogonalized plane-wave method 314

I. KENDE, L. GUCZI and D. GÁL: Investigation of the interaction of alkyl iodide vapours with a carbon surface by kinetic and isotopic methods 321

L. GUCZI, I. KENDE and D. GÁL: Use of the differential isotope method for studying the interaction between vapours of alkyl iodide and surface of red phosphorus 326

Letters to the Editors:

RICHARD H. BUBE and WILLIAM H. MCCARROLL: Photoconductivity in indium sulfide powders and crystals. 333

K. F. HULME and JANET E. KEMP: The diffusion coefficient of zinc in indium antimonide. 335

M. GLICKSMAN and K. WEISER: Electrical properties of *p*-type InP 337

S. GELLER: On the boron–nitrogen donor–acceptor bond 340

E. F. HOCKINGS: The thermal conductivity of silver antimony telluride 341

B. T. MATTHIAS: Superconductivity of AuBe 342

H. L. SUCHAN, A. S. BALCHAN and H. G. DRICKAMER: The effect of pressure on the absorption edge of $BaTiO_3$ and TiO_2 343

Book Reviews:

"Optical properties of semiconductors, a semiconductor monograph", general editor C. A. HOGARTH (reviewed by WILLIAM PAUL) 345

"Growth and perfection of crystals" edited by R. H. DOREMUS, B. W. ROBERTS and DAVID TURNBULL (reviewed by W. BOAS) 346

Books Received 348

Errata 348

AUTHOR INDEX TO VOLUME 10

(B) denotes book review

ABELES, B. 191
ABRAHAMS, M. S. 204
ADAMS, E. N. 254, 286
ANDRESEN, A. 138
ANTONČÍK, E. 314
ARROTT, A. 19
ASDENTE, M. 162
BALCHAN, A. S. 343
BALLENTYNE, D. W. G. 242
BLANDIN, A. 126
BLOUNT, E. I. 286
BOAS, W. 346 (B)
BRAUNSTEIN, R. 204
BROWN, R. D. III 201
BUBE, R. H. 333
DANIEL, E. 126, 174
DAVIS, J. L. 106
DEVLIN, G. E. 106
DOYAMA, M. 77
DRICKAMER, H. G. 343
ECK, J. VAN 12
EVANS, J. P. 311
FISHER, J. C. 44
FORESTIERI, A. F. 99
FREEMAN, A. J. 147
GÁL, D. 321, 326
GELLER, S. 107, 340
GILLEO, M. A. 182, 187
GIRIFALCO, L. A. 99
GLASSER, M. L. 229
GLICKSMAN, M. 337
GRIMES, D. M. 120
GUCCIONE, R. 162
GUCZI, L. 321, 326
HOCKINGS, E. F. 341
HOLSTEIN, T. D. 254
HOPFIELD, J. J. 110
HORNIG, A. W. 1
HULME, K. F. 335
ISHIKAWA, Y. 35
JACCARINO, V. 106
JENSEN, R. V. 191
KALLMANN, H. 59
KANAMORI, J. 87
KEITEL, F. 52
KEMP, J. E. 335
KENDE, I. 321, 326
KIKUCHI, R. 19
KOENIG, S. H. 201
KONDO, J. 245
KRAMER, B. 59
LEFKOWITZ, I. 169
MACHLUP, S. 12
MARDON, P. G. 311
MARK, P. 59
MARTIN, D. G. 64
MATTHIAS, B. T. 342
MCCARROLL, W. H. 333
MICHELS, A. 12
MITCHELL, D. W. 182
MOREL, P. 277
NATHANS, R. 35, 138
OGILVIE, G. J. 217, 222
PAUL, W. 345 (B)
PICKART, S. J. 35, 242
REMPEL, R. C. 1
RIDGE, M. J. 217
ROSI, F. D. 191, 204
SATO, H. 19
SCHAWLOW, A. L. 106
SELDAM, C. A. TEN 12
SHIRANE, G. 35, 138
SHULL, C. G. 138
SOSNOVSKY, H. M. C. 304
SUCHAN, H. L. 343
SUZUKI, T. 77
TEEGARDEN, K. 211
THOMAS, D. G. 47
TOSI, M. P. 162
TURNOCK, A. C. 242
WEAVER, H. E. 1
WEEKS, R. 211
WEISER, K. 337
WEISS, R. J. 147
WESTRUM, E. F. JR. 120
YAMASHITA, J. 245

VOL
10
195

VOL.
10
959

VOL
10
1959

J. Phys. Chem. Solids Pergamon Press 1959. Vol. 10. pp. 1–11. Printed in Great Britain.

ELECTRON PARAMAGNETIC RESONANCE IN SINGLE CRYSTALS OF $BaTiO_3$

A. W. HORNIG

I.B.M. Research Laboratory, San Jose, California

R. C. REMPEL and H. E. WEAVER

Instrument Division, Varian Associates, Palo Alto, California

(*Received* 12 *June* 1958; *revised* 15 *October* 1958)

Abstract—The paramagnetic resonance of an impurity in single crystals of $BaTiO_3$ has been studied. The impurity ion has been identified as Fe^{3+} and is believed to be located at the titanium position in the unit cell. The zero field splittings for the Fe^{3+} ion in the tetragonal ferroelectric phase have been measured at room temperature and as a function of temperature through the Curie point. The values at room temperature are 11·7 and 4·9 kmc/s, respectively. The corresponding zero field splitting in the cubic phase is about 0·90 kmc. The effects of temperature variation on the resonant magnetic fields are discussed with special reference to the observation of a zero magnetic field transition at 9·5 kmc/s and at a temperature of 75°C.

1. INTRODUCTION

IT has been established[1] that single crystals of $BaTiO_3$* exhibit electron paramagnetic resonance (EPR) signals and that the spectrum consists of several components. A complete scan of the magnetic field over a range of values up to 8000 G at 9·5 kmc/s revealed many components whose relative positions and line widths depended strongly upon the orientation of the crystal axes in the external magnetic field.

It was assumed from the beginning[1] that the spectrum (see Fig. 1) stemmed from paramagnetic impurities, since a pure crystal contains no paramagnetic ions. It was the objective of this program to understand the spectrum observed, identify and locate the paramagnetic ion responsible for the spectrum, and correlate the EPR results with the known ferroelectric properties of $BaTiO_3$ single crystals.

As a result of this investigation the EPR spectrum is now generally understood. It can be described as stemming from the ferric ion (Fe^{3+}), which has a basic $^6S_{5/2}$ level, located at the titanium position. The facts which lead to this picture will be presented in detail in the ensuing sections.

2. SUMMARY OF PERTINENT EXPERIMENTS

The primary experiments included effects on the EPR spectrum due to: crystal orientation, temperature-dependence, frequency-dependence, and heating of the crystals in reducing and oxidizing atmospheres.

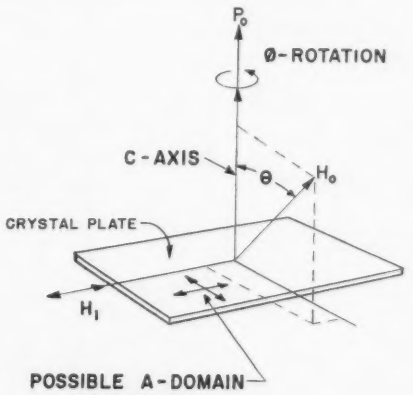

FIG. 2

* For a general description of ferroelectricity, see, for example, SHIRANE *et al.*[2a] and KANZIG.[2b]

In principle, polarization may occur along any one of the three principal crystal axes. In practice complete permanent polarization could be reliably obtained only in the direction normal to the surface of the plate (see Fig. 2). This direction is commonly called the *c*-direction and such plates are called *c*-plates. Domains which have their polarization parallel to the surface of the plate are commonly referred to as *a*-domains. Unless stated otherwise, *c*-plates were used in all experiments. It is worth while noting that crystals which appeared to have no *c*-domains when viewed between crossed-polaroids in fact possessed roughly two-thirds *c*-domains as revealed by paramagnetic resonance. The sum of resonance intensities from the three possible domain directions in these crystals agrees, within the experimental error, with that obtained when the crystal is completely polarized in the *c*-direction.

(a) *Rotation of the crystal*

(i) *θ-rotation* (see Fig. 2). In these measurements the crystal plate (typically 3 by 5 by 0·2 mm thick) was mounted on the narrow wall of the TE_{102} mode rectangular cavity midway between the median plane and the plane of the coupling

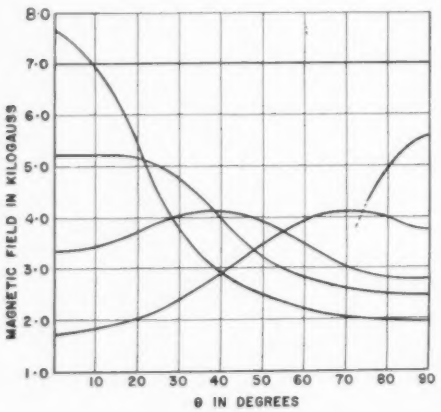

FIG. 3

iris, a region where the longitudinal r.f. magnetic field is a maximum. The resonant cavity was so oriented in the d.c. magnetic field, $\boldsymbol{H}_0$, that the value of θ could be varied without changing the angle between the r.f. field, $\boldsymbol{H}_1$ and $\boldsymbol{H}_0$. Changing the angle between $\boldsymbol{H}_1$ and $\boldsymbol{H}_0$ would alter the selection rules and affect the intensity of the various lines. Through rotation of the magnet, the angle θ could be continuously and reproducibly varied from 0° to 90°. Keeping the crystal fixed in the cavity during rotation experiments is a great advantage, for then the electrical properties of the cavity do not change during measurement.

A summary of the results at 9·5 kmc/s and at room temperature is given in Fig. 3. It may be observed from such a plot that the angular behavior of the various transitions does not follow a typical $3(g_{\|}/g)^2 \cos^2\theta - 1$ law[3] as would be expected if 9·5 kmc/s were large compared to the zero magnetic field splitting. The large separations of resonant magnetic fields at $\theta = 0°$ also support this conclusion.

One underlying fact is evident from the angular behavior, and that is that there are basically five relatively intense transitions, labelled 1 through 5 in Fig. 1, plus weaker higher-order ones. At particular values of θ some of the lines are not visible because of excessive line widths. This five-line pattern is even more clearly seen at 16·3 kmc/s, where the same rotation experiment was

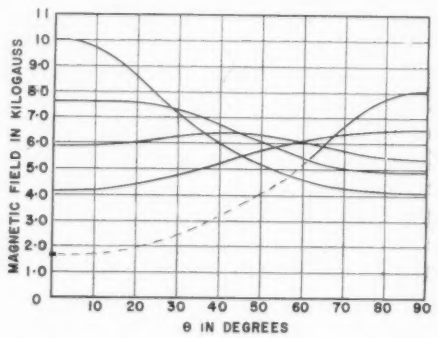

FIG. 4

performed (see Fig. 4). At this frequency the relative intensities of the higher-order terms were diminished as compared with their values at 9·5 kmc/s.

(ii) *φ-rotation with* $\theta = 90°$. When the crystal is rotated about $\boldsymbol{P}_0(\boldsymbol{P}_0 \perp \boldsymbol{H}_0)$, the positions of the transitions repeat with every 90° of rotation. This shows that the site containing the paramagnetic species has a four-fold axis of symmetry when the crystal is in the tetragonal phase.

VOL.
10
1959

OL.
10
959

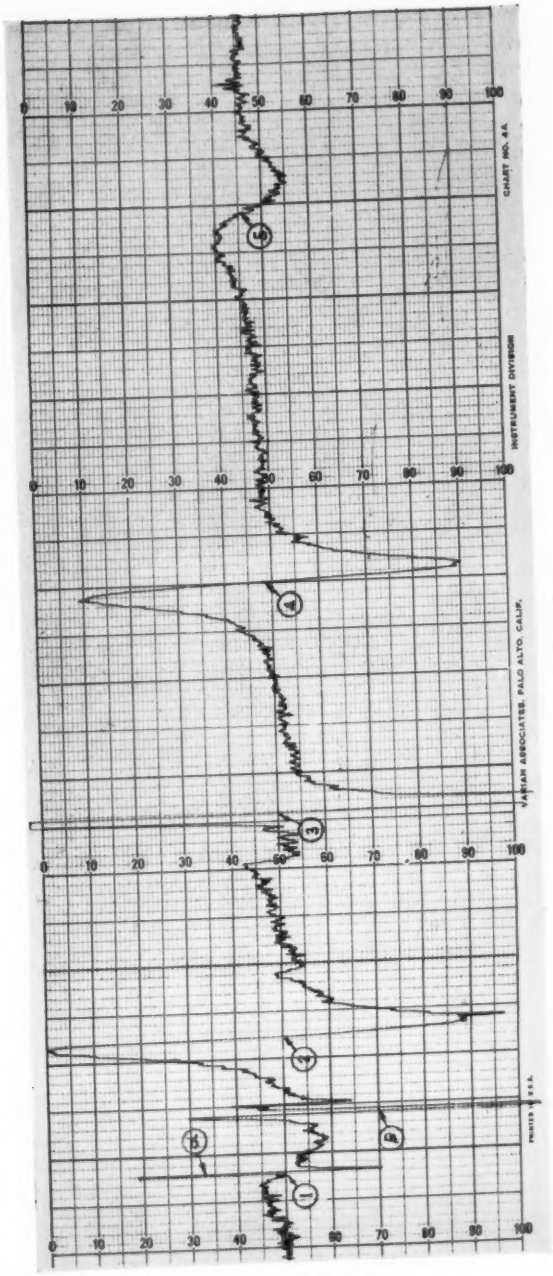

FIG. 1

[facing p. 2

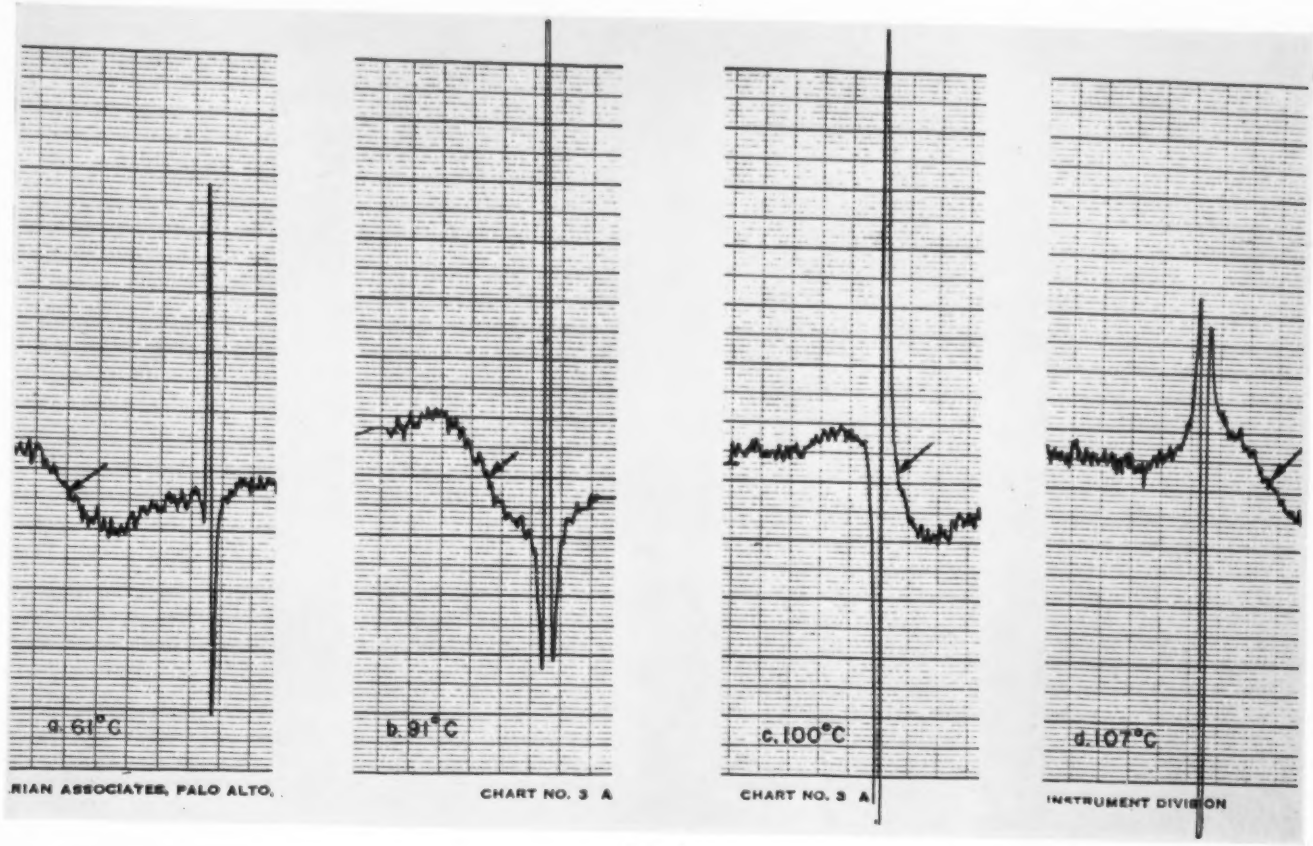

FIG. 9

VOL
10
195

(b) *Temperature-dependence in $BaTiO_3$*

Barium titanate exists in four phases.[2] Above 120°C it is cubic and non-ferroelectric. Between 120 and 0°C it is tetragonal with its axis of polarization along a cell edge. Between about 0 and −80° C it is orthorhombic with polarization along a cell face-diagonal. Below −80°C it is rhombohedral with its polarization along a cell body-diagonal.

The behavior of the resonant magnetic fields as the temperature is varied from room temperature to above the Curie point is plotted in Fig. 5. This large variation of crystal field splittings with such an easily varied experimental parameter is unusual. The variation of these splittings is connected with the temperature-dependence of the spontaneous polarization in the ferroelectric state of $BaTiO_3$.

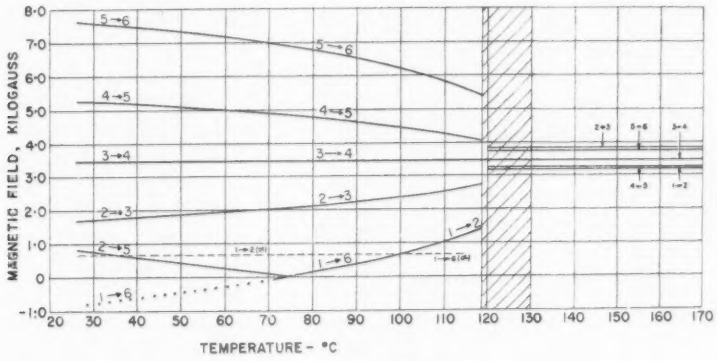

FIG. 5

Preliminary measurements revealed that resonances exist in the orthorhombic and rhombohedral phases. This paper, however, is concerned with measurements made either in the tetragonal phase or in the cubic phase.

(c) *Application of electric fields to the crystal at temperatures near the Curie point*

At temperatures near the Curie point the properties of $BaTiO_3$ are particularly interesting; for in this region the dielectric constant is very large and changes rapidly with temperature. The application of an electric field, coupled with the large dielectric constant ($\sim 10^4$), induces a large polarization and is known to alter significantly the temperature at which the ferroelectric transition occurs.[2] It was therefore worth while to study the effect of these characteristics on the paramagnetic resonance spectrum.

Accordingly, a thin crystal was electroded by sputtering copper on both surfaces to such a thickness that the surfaces were conducting, yet slightly transparent to light. The crystal was then mounted in a microwave resonant cavity in a manner similar to that described above. Electrical contact was established with the crystal in such a way that microwave losses were at a minimum. This arrangement permitted the application of electric fields and the observation of hysteresis loops.

The EPR signal intensity was very seriously affected by the large dielectric constant and high dielectric loss of the crystal near the Curie point. Also the rapid temperature variation of the dielectric properties of the crystal made the operation of the microwave bridge extremely temperature-sensitive. The combined effects made the EPR data taken near the Curie temperature at best fragmentary. However, a few points appear to be clear despite these difficulties. The tetragonal →cubic transition appears to be significantly discontinuous as measured by the EPR splittings. With the crystal held at a temperature 1° above the Curie point, the application of a large electric field, up to 18,000 V/cm, gave no observable tetragonal field splitting. Evidence that the d.c. electric field had indeed induced the ferroelectric state at this temperature was found in the existence

of hysteresis loops. The dielectric properties of the crystal at microwave frequencies were also found to change. A similar experiment was performed 1° below the Curie point in the hope that the tetragonal field splittings could be altered by the external electric field. No measurable effect was observed. A further attempt was made to observe such a shift by synchronously sweeping the voltage across the crystal at the phase detection frequency. A large bias existed on the output of the phase detector from synchronous dimensional and dielectric changes of the crystal at the sweep frequency. Instabilities in this bias from small temperature changes completely masked whatever paramagnetic effect may have been present.

(d) *Effects of oxidation and reduction on the EPR spectrum*

Heating the crystals for several minutes at temperatures above 1000°C in hydrogen produced crystals with a purple coloration and completely removed the paramagnetic spectrum. Subsequent heating in air restored the spectrum to its initial intensity. Experiments, after reduction at intermediate temperatures in hydrogen, indicated that the EPR lines decreased monotonically in intensity with increasing temperature. This effect might be accounted for by assuming that the hydrogen reduces Fe^{3+} to Fe^{2+}, which has a quite different basic level in octahedral symmetry and is not likely to be observed at room temperature.[4] Presumably the introduction of hydrogen may reduce the Ti^{4+} to Ti^{3+}, which is also paramagnetic. This ion should again not be observable at room temperature in the same symmetry.[4]

3. EQUIPMENT

(a) *Magnet*

A Varian V-4012-3B 12-in. magnet and associated power supply were employed for the majority of the experiments. This magnet has a $2\frac{5}{8}$ in. air gap and rotates about a vertical axis through a total angle of about 200°. Rotation experiments were carried out by rotating the magnet with the sample fixed in the resonant cavity.

(b) *Spectrometer*

Several microwave bridges and resonant cavities were used to cover a range of frequencies of 5–7·5, 8·5–11·0 and 16·3 kmc/s. For detection and display of the resonance, components of a standard Varian V-4500 EPR spectrometer were used.

4. THEORY

(a) *Origin of spectrum*

On the basis of the experimental data it is plausible to assume that the spectrum stems from a paramagnetic ion with a spin 5/2. From spectrochemical analysis the rare-earth, palladium and actinide groups are not present, with platinum the only member of the 5*d* group detected. Of the 3*d* group, copper, manganese and iron were found to be present.

Measurements on crystals grown in special palladium–gold and pure graphite* crucibles indicate the same general resonance pattern as before, although no platinum is present. This is regarded as conclusive evidence that platinum is not the source of the observed resonances.

A spin of 5/2 in the 3*d* group requires that the ion under consideration be in the $^6S_{5/2}$ state. In the crystalline field the six levels split into three Kramers doublets, of which two are degenerate in a field of cubic symmetry. The mechanism giving rise to these splittings is quite different from that in other 3*d* paramagnetic ions, all of which have a degenerate orbital state.

For non-*S*-state ions the crystalline electric field splits the degeneracy and in general leaves a single orbital level several hundred to several thousand wave numbers below any other orbital level. Admixing, via the spin-orbit interaction, of the higher orbital states to this lowest orbital singlet provides the mechanism for zero field splitting and departures of the *g*-value from 2. These effects appear in second order in the perturbation calculation.

For a $^6S_{5/2}$ ion there is no orbital degeneracy. Two mechanisms have been proposed which can contribute to the splittings. In the first, these splittings arise from a coupling, via the spin-orbit interaction and the crystalline electric fields, to excited *P* states.[3,5] It is found that for a cubic field it is necessary to go to the fourth or fifth order in the perturbation, depending on the particular *P* state, to obtain a non-vanishing result.

*The crystals grown in pure graphite crucibles were kindly furnished by H. H. WIEDER, Naval Ordnance Laboratory, Corona, California.

VOL. 10 1959

The tetragonal component of the field will, however, give a third order contribution in this perturbation calculation. In the second mechanism the splittings arise from the effect of crystalline-field-induced orbit distortion on the direct spin–spin interaction between electrons;[6] these splittings appear in second order in the perturbation calculation. The task of carrying out the calculation of splittings in terms of crystalline field parameters is quite involved. In a recent paper by WATANABE[7] these calculations have been carried out in detail for perturbations which couple to $3d^5$ excited states. It is hoped that in the future these results can be used to give information about local crystalline fields in ferroelectric $BaTiO_3$; this will, however, require a more detailed knowledge of these excited $3d^5$ states of the ferric ion than is currently available.

When a magnetic field is applied, six energy levels are created and, at frequencies greater than the zero field splittings, five strong $|\Delta m| = 1$ "allowed" transitions will occur. This is what is observed in the spectrum and is the strongest argument that the resonance is due to Fe^{3+}. Mn^{2+}, being also ${}^6S_{5/2}$, could give a five-line spectrum from purely crystalline field splittings; however, for manganese there would also be an additional six-line structure arising from a hyperfine interaction of the form $\boldsymbol{I} \cdot \boldsymbol{S}$, with $I = 5/2$. This is not observed in normal crystals. No other $3d$ transition-group ion could, under the same conditions, give this many strong lines. The five-line pattern is particularly evident in the data taken near the Curie point.

Iron, as an impurity, is found by spectrochemical analysis to be present in typical barium titanate crystals in amounts of the order of 0·04 mole per cent. The Fe^{3+} ion is believed to go into the normal Ti^{4+} lattice site to compensate for the charge deficiency arising from an oxygen deficiency in the crystal. Complete charge compensation would require two Fe^{3+} ions going into normal Ti^{4+} positions for every missing oxygen.

(b) *Theory of Fe^{3+}*

The energy levels of a ${}^6S_{5/2}$ Fe^{3+} ion in a tetragonal crystalline electric field and an external magnetic field are given by a spin-Hamiltonian of the form

$$\mathcal{H} = \beta \boldsymbol{H} \cdot \boldsymbol{g} \cdot \boldsymbol{S} + DS_z^2 + aS_z^4 + b(S_x^4 + S_y^4),$$

where z is the direction of the axis of tetragonality.* The tensor g has the principal values $g_{||}$ and $g_{\perp}$. The principal axis corresponding to the principal value $g_{||}$ lies in the direction of the axis of tetragonality. The principal axes corresponding to $g_{\perp}$ lie in the plane orthogonal to this tetragonal axis. D has its origin in the tetragonal component of the crystalline electric field; for a cubic field D will vanish and $a = b$. Except for the magnetic interaction, it may be argued on very general grounds that the spin-Hamiltonian must contain only even powers of S. For a total spin of 5/2 any term of sixth or higher power in the spin operators can be reduced by the commutation relations to terms in fourth and lower powers in these operators. This then is the most general form of the spin-Hamiltonian for a crystalline field of tetragonal symmetry.

The problem is now that of finding the energy levels of the spin-Hamiltonian and then comparing with experiment to determine the five parameters $g_{||}$, $g_{\perp}$, a, b and D. In matrix form the spin-Hamiltonian is:

$$\begin{bmatrix}
5p/2+\xi & \sqrt{5}q & 0 & 0 & 3\sqrt{5}b & 0 \\
\sqrt{5}q^* & 3b/2+\eta & \sqrt{8}q & 0 & 0 & 3\sqrt{5}b \\
0 & \sqrt{8}q^* & p/2+\zeta & 3q & 0 & 0 \\
0 & 0 & 3q^* & -p/2+\zeta & \sqrt{8}q & 0 \\
3\sqrt{5}b & 0 & 0 & \sqrt{8}q^* & -3p/2+\eta & \sqrt{5}q \\
0 & 3\sqrt{5}b & 0 & 0 & \sqrt{5}q^* & -5p/2+\xi
\end{bmatrix}$$

*This notation was chosen for simplicity. There appears to be no standard notation for the tetragonal field case. For the cubic field case $a = b$ corresponds to $a/6$ in references (3) and (4).

where

$$p = g_{\parallel}\beta H\cos\theta \qquad q = \tfrac{1}{2}g_{\perp}\beta H\sin\theta e^{-i\phi}$$
$$\xi = 25D/4+625a/16+65b/8$$
$$\eta = 9D/4+81a/16+241b/8$$
$$\zeta = D/4+a/16+401b/8.$$

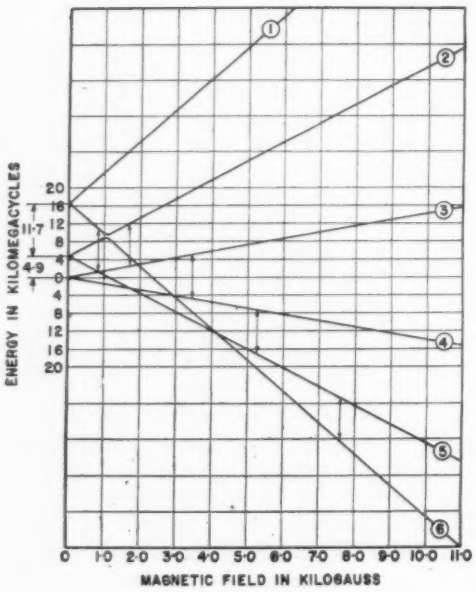

FIG. 6

The term $(S_x^4+S_y^4)$ mixes states differing by $|\Delta m| = 4$. The states may be written as:

$$\psi^1 = a^1_{5/2}|5/2)+a^1_{-3/2}|-3/2)$$
$$\psi^2 = a^2_{3/2}|3/2)+a^2_{-5/2}|-5/2)$$
$$\psi^3 = |1/2)$$
$$\psi^4 = |-1/2)$$
$$\psi^5 = a^5_{-3/2}|-3/2)+a^5_{5/2}|5/2)$$
$$\psi^6 = a^6_{-5/2}|-5/2)+a^6_{3/2}|3/2)$$

$$a^1_{5/2} = \frac{1}{\sqrt{1+(W^+)^2}} \qquad a^1_{-3/2} = \frac{-W^+}{\sqrt{1+(W^+)^2}}$$

$$a^2_{3/2} = \frac{1}{\sqrt{1+(W^-)^2}} \qquad a^2_{-5/2} = \frac{W^-}{\sqrt{1+(W^-)^2}}$$

$$a^5_{-3/2} = \frac{1}{\sqrt{1+(W^+)^2}} \qquad a^5_{5/2} = \frac{W^+}{\sqrt{1+(W^+)^2}}$$

$$a^6_{-5/2} = \frac{1}{\sqrt{1+(W^-)^2}} \qquad a^6_{3/2} = \frac{-W^-}{\sqrt{1+(W^-)^2}}$$

where

$$W^{\pm} = \frac{1}{3\sqrt{5b}}[\Delta\pm 2g_{\parallel}\beta H\mp\sqrt{(\Delta\pm 2g_{\parallel}\beta H)^2+45b^2}]$$

and

$$\Delta = 2D+17a-11b$$

To solve this eigenvalue problem for the general orientation of the crystal with respect to the magnetic field requires the solution of the sixth-order secular equation. However, for the special case $\theta = 0°$ the solution is particularly simple. The parameters of the spin-Hamiltonian are then evaluated by comparing theory and experimental data taken at this angle. The energy-level diagram at $\theta = 0°$ is presented in Fig. 6. The states are labelled 1 through 6. In the high-field limit, state 1 is $|+5/2)$, state 2 is $|+3/2)$,—and state 6 is $|-5/2)$.

Relative line intensities are given by the absolute square of the operator $\beta\boldsymbol{H}_1\cdot\boldsymbol{g}\cdot\boldsymbol{S}$ between states, where $\boldsymbol{H}_1$ is the r.f. magnetic field inducing the transitions. The $S_{\pm}$ operator will have matrix elements between states 1 and 2, 2 and 3, &c.; between states 1 and 4, 2 and 5, 3 and 6 (nominal $|\Delta m| = 3$); and between states 1 and 6 (nominal $|\Delta m| = 5$).* The S_z operator will have matrix

*The sign of the "g-value" will be reversed for transitions in which the raising operator $\mathbf{S}_+$ takes the state of higher energy into the one of lower energy.

elements between states 1 and 5, and 2 and 6 (nominal $|\Delta m| = 4$). Expressions for the intensities can be obtained, but need not be written out here.

The magnetic fields for the various transitions are given through

$$h\nu = g_{\parallel}\beta H_{12}+\sqrt{(\Delta+2g_{\parallel}\beta H_{12})^2+45b^2}-\sqrt{(\Delta-2g_{\parallel}\beta H_{12})^2+45b^2}$$
$$h\nu = -g_{\parallel}\beta H_{23}+2\Delta-12a-9b+\sqrt{(\Delta-2g_{\parallel}\beta H_{23})^2+45b^2}$$
$$h\nu = g_{\parallel}\beta H_{34}$$
$$h\nu = -g_{\parallel}\beta H_{45}-2\Delta+12a+9b+\sqrt{(\Delta+2g_{\parallel}\beta H_{45})^2+45b^2}$$
$$h\nu = g_{\parallel}\beta H_{56}+\sqrt{(\Delta-2g_{\parallel}\beta H_{56})^2+45b^2}-\sqrt{(\Delta+2g_{\parallel}\beta H_{56})^2+45b^2}$$
$$h\nu = g_{\parallel}\beta H_{14}+2\Delta-12a-9b+\sqrt{(\Delta+2g_{\parallel}\beta H_{14})^2+45b^2}$$
$$h\nu = -g_{\parallel}\beta H_{25}+\sqrt{(\Delta+2g_{\parallel}\beta H_{25})^2+45b^2}+\sqrt{(\Delta-2g_{\parallel}\beta H_{25})^2+45b^2}$$
$$h\nu = g_{\parallel}\beta H_{36}-2\Delta+12a+9b+\sqrt{(\Delta-2g_{\parallel}\beta H_{36})^2+45b^2}$$
$$h\nu = 2\sqrt{(\Delta+2g_{\parallel}\beta H_{15})^2+45b^2}$$
$$h\nu = 2\sqrt{(\Delta-2g_{\parallel}\beta H_{26})^2+45b^2}$$
$$h\nu = g_{\parallel}\beta H_{16}+\sqrt{(\Delta+2g_{\parallel}\beta H_{16})^2+45b^2}+\sqrt{(\Delta-2g_{\parallel}\beta H_{16})^2+45b^2}$$

It should be pointed out that it will not be possible to determine the absolute signs of a, b and D. Fig. 6 is drawn for $\Delta = 2D+17a-11b$ positive.

In zero magnetic field the splitting between the upper level (states 1 and 2) and the intermediate level (states 5 and 6) is $2\sqrt{\Delta^2+45b^2}$; the zero field splitting between the intermediate level and the lower level (states 3 and 4) is $2\Delta-12a-9b-\sqrt{\Delta^2+45b^2}$.

5. EVALUATION OF THE PARAMETERS OF THE SPIN HAMILTONIAN FROM DATA AT $\theta = 0°$

(a) *Room-temperature values*

For an S-state ion in a field of tetragonal symmetry there are altogether five parameters of the spin-Hamiltonian which have to be evaluated at each temperature.

(i) *g-tensor.* The transition 3–4 was found to occur at the same field as that for the free radical DPPH. This then gives

$$g_{\parallel} = 2{\cdot}003.$$

The value of $g_{\parallel}$ is essentially that of the free electron. Hence it may be concluded that the g-tensor is isotropic; this is to be expected since the energy difference between the excited states and ground state is so large. For the same reason the g-tensor is found to be independent of temperature.

(ii) Δ, a and b. Because of the rather large effect of the crystalline electric field relative to the Zeeman interaction at room temperature, it was rather difficult to identify positively the various transitions without a detailed knowledge of the energy-level diagram. This difficulty encountered at 9·5 kmc/s and lower frequencies is to a large degree removed at 16·3 kmc/s. This frequency is still not high enough to permit a perturbation calculation and hence a complete use of the experimentally measured angular behavior of the resonant lines. However, a good determination of Δ and a fair estimate of a and b are possible for a particular value, $\theta = 0°$.

Identifying the transitions under the assumption $\Delta > 0$, the resonant magnetic fields at 16·3 kmc/s are:

H_{12} = line too broad to permit reliable measurement
$H_{23} = 4{\cdot}14$ kG
$H_{34} = 5{\cdot}83$ kG ($g = 2{\cdot}00$)
$H_{45} = 7{\cdot}59$ kG
$H_{56} = 9{\cdot}97$ kG.

If it is now assumed that D is large compared with a and b, then Δ is the dominant term in the

expressions for the resonant magnetic fields at constant frequency. These expressions may be written approximately for $g_{\|}\beta H > (\Delta/2)$:

$$1\text{–}2: h\nu = g_{\|}\beta H_{12}+2\Delta-45b^2\Delta/[(g_{\|}\beta H_{12})^2-\Delta^2] \ldots$$
$$2\text{–}3: h\nu = g_{\|}\beta H_{23}+\Delta-12a-9b+45b^2/[4g_{\|}\beta H_{23}-2\Delta] \ldots$$
$$4\text{–}5: h\nu = g_{\|}\beta H_{45}-\Delta+12a+9b+45b^2/[4g_{\|}\beta H_{45}+2\Delta] \ldots$$
$$5\text{–}6: h\nu = g_{\|}\beta H_{56}-2\Delta+45b^2\Delta/[(g_{\|}\beta H_{56})^2-\Delta^2] \ldots$$

a and b have the least contribution to the 1–2 and 5–6 transitions.

Neglecting terms of order b^2, the data taken at 16·3 kmc/s yield for $|\Delta|$ and $(12a+9b)$ the following values:

$$|\Delta| = 0{\cdot}195 \pm 0{\cdot}004 \text{ cm}^{-1} (5{\cdot}85 \text{ kmc/s})$$

and

$$12a+9b = 0{\cdot}032 \pm 0{\cdot}007 \text{ cm}^{-1} (0{\cdot}95 \text{ kmc/s}),$$

with the same sign as Δ. It is important to note here that the evaluation of the parameters of the energy level diagram at 16·3 kmc/s, while not necessarily more accurate, was a necessary step, because the identification of the various transitions at this frequency could be unequivocally made. Once having established the nature of the energy-level diagram measurements could then be made at a convenient frequency. Accordingly, most measurements were subsequently performed at 9·5 kmc/s, because of the greater sensitivity of the spectrometer at this frequency. Consequently, values obtained for Δ and $(12a+9b)$ at 9·5 kmc/s (see (b) below) are considered more reliable. However, the room-temperature values obtained at 16·3 and 9·5 kmc/s agree within the experimental accuracy.

(b) *Temperature-dependence*

A striking feature of the observed paramagnetic resonance is the dependence of the splittings on temperature (see Fig. 5). Values of Δ versus temperature, as plotted in Fig. 7, are averages of the values determined from the lowest and highest field lines of Fig. 5 and are accurate to within $\pm 0{\cdot}12$ kmc/s.* Using the value of Δ at a given temperature in the expressions for the transitions 4–5 and 2–3, and keeping only the linear terms in

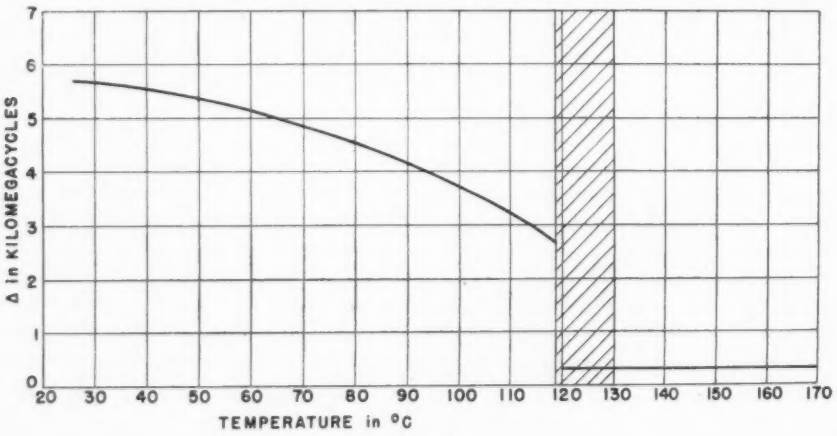

FIG. 7

*The parameter Δ is represented instead of D, since it can be determined with greater accuracy.

VOL. 10 1959

a and b, the term $(12a+9b)$ was found to be that quoted above and independent of temperature.

(c) *Cubic field splitting*

As pointed out in Section 2(c), because of dielectric effects experimentation is very difficult near the Curie point. Accordingly, Fig. 8, which

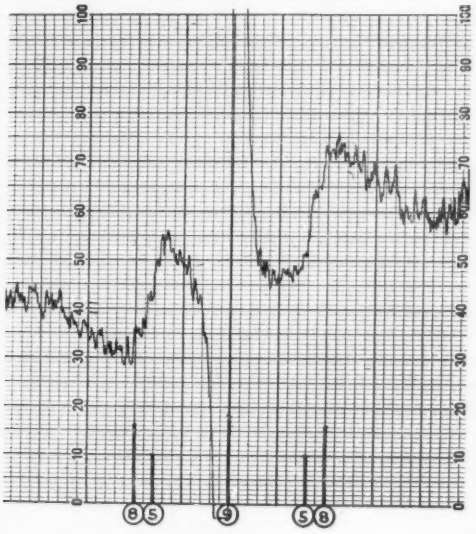

FIG. 8

shows the spectrum in the cubic phase, with magnetic field parallel to a cube edge, was made at 160°C. A central line and two satellites are to be observed. Each satellite consists of two unresolved lines whose positions are also indicated. As expected, each satellite has an intensity approximately 13/9 that of the central line. The angular behavior of these splittings is that expected for $S = 5/2$ in a cubic field.[8] The separation between the two outermost lines is about 540 G. This then gives in the cubic phase

$$|a| = 0{\cdot}0017 \pm 0{\cdot}0002 \text{ cm}^{-1} \ (0{\cdot}050 \text{ kmc/s})$$

In the tetragonal phase, if it is assumed $a \simeq b$, then $|a| = 0{\cdot}0015$ cm^{-1}. These two values are in essential agreement and represent no change in the cubic field term in traversing the phase transition.

(d) *Discussion*

The energy-level diagram at room temperature and at $\theta = 0°$, drawn to scale using the parameters obtained above, has been given in Fig. 6. The zero field splittings at room temperature are 0·390 cm^{-1} (11·7 kmc/s) and 0·163 cm^{-1} (4·9 kmc/s).

In the plot of resonant magnetic fields as a function of temperature of Fig. 5, the low-field line (labelled 1 in Fig. 1) is the most interesting. As the temperature rises this line first goes to zero magnetic field at 75°C and then rises. This feature can be explained in terms of the energy-level diagram and its change with temperature. At room temperature the microwave frequency is less than the upper zero-field splitting and the observed transition can be taken to be 2–5 with negative "g-value".* As the temperature rises this zero-field splitting drops and at 75°C becomes equal to the microwave frequency. For temperatures above 75°C the transition is 1–6 and rises in field with increasing temperature.

It has been observed that there is considerable variation between the widths of the various lines and that individual lines have widths which vary markedly with angle. The line widths of the principal transitions vary from a minimum of 7 G for the 3–4 transition at $\theta = 0°$ to a maximum of about 200 G for the 5–6 transition at the same angle. This variation of line width has an explanation in inhomogeneity broadening stemming from lattice defects. Because of these defects the individual paramagnetic ions see differing crystalline electric fields. This gives a distribution of values to the parameters Δ, a and b and can also introduce other terms in the spin-Hamiltonian arising from lack of complete tetragonal symmetry. Δ, through its dependence on D, has not only the greatest effect on line position but also the largest spread of values. Accordingly, the narrow lines are those which are to first order independent of Δ. At $\theta = 0°$ these are the 3–4 transition at all fields, the 1–2 transition for $2g_{\|}\beta H_{12} < \Delta$, the 5–6 transition for $2g_{\|}\beta H_{56} < \Delta$, the 2–5 transition for $2g_{\|}\beta H_{25} > \Delta$ and the 1–6 transition for $2g_{\|}\beta H_{16} > \Delta$. In the $\theta = 0°$ room-temperature curve of Fig. 1, weak narrow lines may be observed at fields of 670 and 1100 G. The line at 670 G, labelled α, is identified as the 1–2 transition and

*This line may equally well be considered to be the transition 1–6 at negative magnetic field; see the dotted line of Fig. 5.

that at 1100 G, labelled β, is identified as the 2–5 transition. Since these lines are independent of Δ, their position is also independent of temperature.

From a comparison of the relative intensities of the observed resonances stemming from a known amount of Mn^{2+} ions in water placed in the microwave cavity along with a $BaTiO_3$ crystal (oriented such that $\theta = 0°$), the concentration of the Fe^{3+} ion was found to be 0·01–0·04 mole per cent; about 10^{18} ions per gram of $BaTiO_3$.* This result is in agreement with that obtained from spectrochemical analysis of similar crystals.† It should be remarked that charge compensation by the Fe^{3+} ion does not imply that this ion goes into the oxygen-deficient cell. At the temperatures at which the crystals are grown, the iron is quite mobile until it is frozen into the lattice. The Fe^{3+} ions and the oxygen deficient sites should be randomly distributed throughout the crystal with little correlation between their positions.

One last point to be mentioned is the crossing over, at about 100°C, of the narrow line at 670 G designated as α in Figs. 1 and 5) and the strong low-field line (designated as 1 in Fig. 1). At temperatures well below 100°C, but above 75°C, the broad and narrow lines are identified as the transitions between energy levels, 1 and 6 and 1 and 2, respectively (see Figs. 5 and 6). At temperatures well above 100°C the corresponding lines are now the 1–2 and 1–6 transitions. It would be expected that as the cross-over temperature is approached, the broad line would narrow and the narrow line would broaden. This is verified, to some extent, by experiment.

Referring to Figs. 9*a*, *b*, *c* and *d*, an unusual effect may be observed in connection with the line cross-over. At temperatures at which the broad and narrow lines do not overlap, both are observed to be normal absorption lines; this is illustrated in Fig. 9*a*, at 61°C. In Fig. 9*b*, at 91°C, the narrow line is seen to be dispersive. In Fig. 9c, at 100°C, the narrow line is seen to be purely emissive. In Fig. 9d, at 107°C, the narrow line is seen to be again dispersive, with sign opposite to that of Fig. 9b. It may be noted that the narrow line is dispersive at the points of maximum dispersion of the broad line. With further increase in temperature the narrow line is observed to return to normal absorption when the lines no longer overlap. In effect, the narrow resonance goes through a complete 360° phase rotation as the broad line passes through it. It may be seen from the energy-level diagram that the line centers can never pass through each other; the 1–2 transition always occurs at higher magnetic field than the 1–6 transition. Their true behavior is obscured by the distribution of spin-Hamiltonian parameters.

A salient feature of this effect is that the two transitions have energy level 1 in common. Preliminary experiments show no measureable change in the anomalous shape of the narrow line as the r.f. magnetic field is reduced by a factor of ten. Further investigation of this effect is in progress.

Acknowledgements—The authors wish to express their appreciation of the co-operation received from Dr. D. R. YOUNG and Dr. S. TRIEBWASSER of I.B.M. Research Center, Poughkeepsie, New York, who were instrumental in supplying specially prepared $BaTiO_3$ single crystals.

The assistance received from Professor E. T. JAYNES, of Stanford University, which contributed materially to the success of this program, is hereby gratefully acknowledged.

*It is perhaps appropriate to mention at this point that because of the large variation in the line shape of the various transitions, relative intensities were obtained from numerical calculation of the first moment of each of the curves.

†All crystals thus far investigated have been grown from saturated solutions of $BaTiO_3$ in KF flux. Crystals obtained from highly purified $BaTiO_3$ powder and reagent grade KF have still sufficient iron impurity to account for the observed EPR spectrum.

REFERENCES

1. HORNIG A. W., JAYNES E. T., and WEAVER H. E., *Phys. Rev.* **96,** 1703 (1954).
   LOW W. and SHALTIEL D., *Phys. Rev. Letters* **1,** No. 2, 51 (1958); **1,** No. 8, 286 (1958).
   HORNIG A. W., REMPEL R. C., and WEAVER H. E., *Phys. Rev. Letters.* **1,** No. 8, 284 (1958).
2(a). SHIRANE G., JONA F., and PEPINSKY R., *Proc. Inst. Radio Engrs.* **43,** 1738 (1955).
 (b). KANZIG W., *Solid State Physics* (Edited by F. SEITZ and D. TURNBULL), Vol 4., pp. 5–180. Academic Press, New York (1957).
3. See for example, INGRAM D. J. E., *Spectroscopy of Radio and Microware Frequencies*, p. 152. Butterworths Scientific Publications, London (1955).

VOL
10
195

4. BLEANEY B. and STEVENS K. W. H., *Rep. Progr. Phys.* **16,** 108 (1953).
BOWERS K. D. and OWEN J., *Rep. Progr. Phys.* **18,** 304 (1955).
5. VAN VLECK J. H. and PENNEY W. G., *Phil. Mag.* **17,** 961 (1934).
6. ABRAGAM A. and PRYCE M. H. L., *Proc. Roy. Soc.* **A205,** 135 (1951).
7. WATANABE H., *Progr. Theor. Phys.* **18,** 405 (1957).
8. MATARRESE L. M. and KIKUCHI C., *J. Phys. Chem. Solids* **1,** 117 (1956).
LOW W., *Phys. Rev.* **105,** 793 (1957).

VOL.
10
1959

J. Phys. Chem. Solids Pergamon Press 1959. Vol. 10. pp. 12–18. Printed in Great Britain.

PRESSURE-DEPENDENCE OF THE RESISTIVITY OF GERMANIUM

A. MICHELS, J. VAN ECK, S. MACHLUP* and C. A. TEN SELDAM

158th publication of the Van der Waals Fund

Van der Waals-laboratorium, Gemeente Universiteit, Amsterdam, Netherlands

(*Received* 14 *August* 1957; *revised* 16 *October* 1958)

Abstract—The effect of hydrostatic pressure on the resistance of a *p*-type sample of germanium (specific resistivity about 80 Ω-cm at 293°K) has been investigated up to 2700 atm at temperatures between 125 and −150°C. The results in the intrinsic range indicate an increase in the energy gap of $5{\cdot}4 \times 10^{-6}$ eV/atm, in agreement with earlier experimental determinations. In the extrinsic region the resistivity decreases slightly with pressure, indicating an increase in hole mobility of 9 p.p.m./atm.

1. INTRODUCTION

VARIOUS authors have studied the pressure-dependence of the electrical properties of semiconductors.[1] To the knowledge of the present authors, only a few of these[1g,1,q,r,s,t] give data on *p*-type germanium. The measurements reported here, on a *p*-type germanium crystal of high specific resistivity, yield the temperature- and pressure-dependence of the hole mobility and of the forbidden energy gap. The latter is of interest in understanding the band structure, which again is related to the mobilities of electrons and holes.[2]

2. APPARATUS AND METHOD

The sample, a germanium single crystal 3 cm × 5·5 mm², with a specific resistivity of 80 Ω-cm at 293°K, kindly supplied by Philips Laboratories, was placed in a steel container which could be pressurized with gas; the pressure was measured with a pressure balance.[3]

The resistance was compared with a Diesselhorst compensator[4] against a known resistance. With each reading the temperature was determined by a platinum resistance wire and a second Diesselhorst compensator. The pressure was produced with an oil press and transmitted to the gas via a mercury seal. The pressure balance was connected to the oil side of the system.

In the range between 25 and 125°C the reservoir containing the germanium was immersed in a symetrically heated, continuously stirred oil bath. A mercury regulator controlled the heating current, keeping the temperature constant to better than 0·003°C.[5] The gas compressing the sample was nitrogen. While the temperature was kept constant, measurements were taken at 300-atm intervals up to 2700 atm, at both increasing and decreasing pressure; no hysteresis was found.

The experiments below room temperature (from 12·5 to −150°C) were all carried out in a cryostat filled with isopentane, the temperature of which was controlled to within 0·001°C by means of a platinum resistance thermometer described in a previous publication.[6] Helium was used as a transmitting gas. Readings were taken at 500-atm intervals up to 2500 atm; at each pressure the temperature was varied. As in the high-temperature range, no hysteresis was found. At very low temperatures (−150°C), the influence of various induction fields on the resistance measurements was noticeable. This was probably due to a rectifying effect at the germanium-to-metal contacts.

The pressure could be controlled to one part in 10^5. The temperature was read to 0·001°C. The relaxation time for re-establishing temperature equilibrium after pressure or temperature variations was of the order of minutes. All resistance measurements were reproducible to at least 0·1 per cent; in the high-temperature range they were better.

The resistivity is obtained from the measured resistance corrected for the change in crystal dimensions with pressure and temperature; published values[7] of the compressibility and linear expansion coefficients $\alpha = 1{\cdot}3 \times 10^{-6}$ cm²/kg; $\beta = 6{\cdot}1 \times 10^{-6}$/°C were used. For this correction no account need be taken of the change of these coefficients with temperature and pressure.

3. RESULTS

The resistance of the crystal has been measured between −150 and +125°C and at pressures up

* Now at Western Reserve University, Cleveland 6, Ohio, U.S.A.

Table 1. *The specific resistivity* ρ *(in* Ω*-cm) at various pressures and temperatures*

P (atm) \ t(°C)	125·65	99·25	74·89	49·48	24.70
1	1·308	2·849	6·546	17·98	58·55
300	1·338	2·921	6·720	18·53	60·45
600	1·370	2·995	6·902	19·08	62·35
900	1·402	3·070	7·092	19·65	64·27
1200	1·434	3·149	7·280	20·23	66·27
1500	1·467	3·227	7·483	20·83	68·21
1800	1·502	3·310	7·683	21·45	70·42
2100	1·537	3·392	7·890	22·07	72·62
2400	1·572	3·477	8·102	22·71	74·88
2700	1·607	3·566	8·319	23·37	77·17

VOL. 10 1959

to 2700 atm. The values of the resistivity ρ are given in Tables 1 and 2. Some of the results are plotted in Figs. 1–3.

For all temperatures below −50°C (Table 2), ρ falls slightly and linearly with increasing pressure (1·0 parts in 10^5 per atm). In the transition region (−25 to −5°C), where the conduction changes from extrinsic (p-type) to intrinsic, the sign of the pressure-dependence of the specific resistivity reverses (Fig. 2.).

If ln ρ is plotted as a function of the reciprocal absolute temperature, the isobar, represented in this way, shows a maximum. This maximum shifts to higher temperatures with increasing pressures; the isobars at 1 atm and 2500 atm, shown in Fig. 3, intersect at about −15°C.

Table 2. *The specific resistivity* ρ *(in* Ω*-cm) at various pressures and temperatures*

P (atm) \ t(°C)	12·5	0	−5	−10	−15	−20	−25
1	109·1	181·8	204·8	218·3	222·9	220·9	215·3
500	114·4	187·1	208·5	220·3	223·7	221·0	214·9
1000	119·8	192·0	211·9	222·2	224·3	220·9	214·4
1500	125·6	196·9	215·1	223·9	224·7	220·7	213·8
2000	131·4	201·3	217·8	224·8	234·6	219·9	212·8
2500	137·1	205·2	219·8	225·5	224·3	219·1	211·7

P (atm) \ t(°C)	−35	−50	−75	−100	−125	−150
1	199·2	172·4	130·2	94·09	64·79	42·32
500	198·5	171·6	129·6	93·65	64·49	42·05
1000	197·8	170·9	128·9	93·20	64·21	41·81
1500	196·9	170·1	128·3	92·73	63·89	41·62
2000	195·8	169·1	127·5	92·24	63·52	41·44
2500	194·7	168·0	126·8	91·68	63·18	41·22

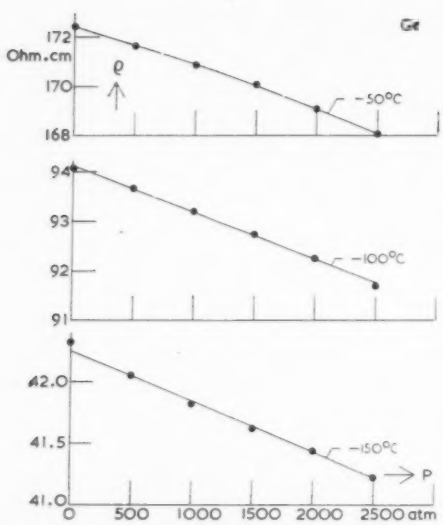

FIG. 1. Resistivity ρ versus pressure P at some of the lower temperatures (p-type conduction). The "relative slope" $(1/\rho)_{1\ \mathrm{atm}}(\partial\rho/\partial P)_T$, is the same for all isotherms in this range.

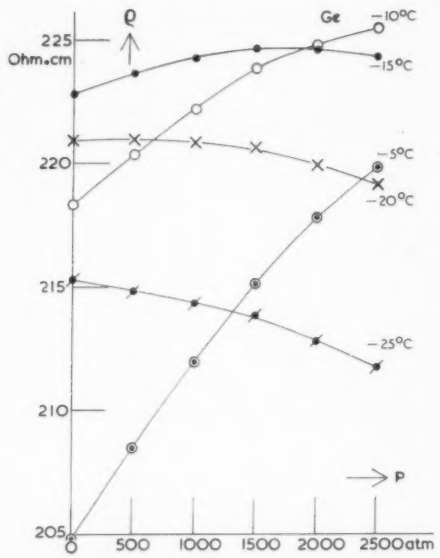

FIG. 2. Resistivity ρ versus pressure P at some temperatures in the region of transition from extrinsic (p-type) to intrinsic conduction, i.e. near the intersection of the isobars in Fig. 3.

4. ANALYSIS OF THE DATA

In the extrinsic range, where, for a p-type specimen, the contribution of the electrons to the conductivity can be neglected, the effect of pressure on the hole mobility can be calculated from the resistivity measurements (Fig. 1). In a similar way, PAUL and BROOKS[1f] determined the effect on the electron mobility for a n-type crystal.

From the measurements in the intrinsic region (above 50°C), the energy gap can be determined as a function of pressure and temperature; 1-atm values of the effective masses of electrons and holes, obtained from the literature, were used.

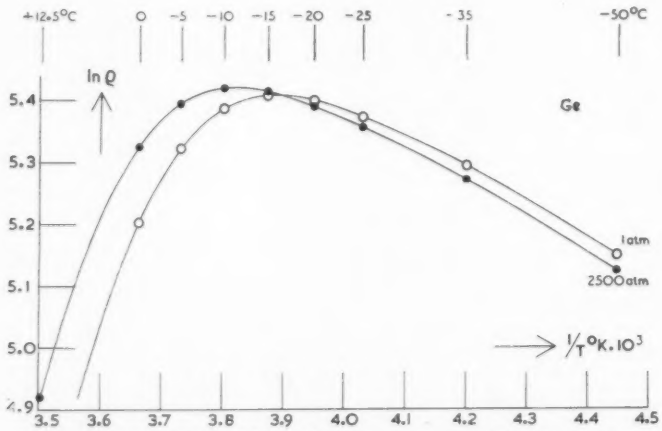

FIG. 3. ln ρ versus $1/T$ (T = absolute temperature) in the transition region at two pressures. The maximum shifts towards higher temperatures with increasing pressures.

(a) *The temperature-dependence of the hole mobility at 1 atm*

For very pure germanium, where scattering by lattice vibrations overshadows impurity scattering, the mobilities μ_n, μ_p (of electrons and holes, respectively) at 1 atm are reported in the literature.[8] For the extrinsic range (exhaustion region), they read (in cm^2/V):

$$\mu_n = 4{\cdot}90\times10^7 T^{-1{\cdot}66};\ \mu_p = 1{\cdot}05\times10^9 T^{-2{\cdot}33}, \quad (1)$$

where T = absolute temperature. The present measurements allow the verification of the temperature-dependence of μ_p for the present sample. In the temperature region covered, all acceptors and donors may be considered ionized, as can be concluded from an analysis analogous to the ones given by SHOCKLEY[2] (pp. 467–71); hence the difference between the concentrations of free holes and electrons,

$$p_0 = p - n, \quad (2)$$

being the excess concentration of acceptors over donors, $N_a - N_d$, is a constant of the crystal (except for the small thermal-expansion correction). The resistivity, ρ, is given by

$$1/\rho = e(n\mu_n + p\mu_p), \quad (3)$$

where e is the electron charge. For a p-conductor, in the extrinsic range (where n can be neglected in comparison to p), formula (3) reduces to:

$$\rho = 1/ep_0\mu_p. \quad (3a)$$

When the low-temperature data are plotted in the form of a log ρ versus log T graph, a straight line is obtained with a slope of $+2{\cdot}391$, on which the points lie with an accuracy of 0·4 per cent. The slight change of p_0 on thermal expansion can be represented by a log p_0 versus log T plot with a slope of $-3\beta T_0 \approx -0{\cdot}004$ (β is given in Section 2; $T_0 \approx 200°K$ is the centre of the temperature range considered). The resulting slope of log u_p versus log T is $= -2{\cdot}391 + 0{\cdot}004$ (cf. equation (3a)), giving:

$$\mu_p = \gamma T^{-2{\cdot}387}\,cm^2/V. \quad (1a)$$

For the determination of γ it is necessary to know the value of μ_p at one temperature only. For this, the data of PRINCE (cf. MORIN[8]) are used:

$$\mu_p = 1820\,cm^2/V \text{ at } T = 300°K,$$

under the assumption that the linear log μ_p versus log T relation can be extrapolated into the intrinsic region.* This procedure yields a value for γ of $1{\cdot}489\times10^9$.

Substitution of these values in formula (3a) gives:

$$p_0 = 0{\cdot}9793\times10^{13}/cm^3 \text{ at } 273°K.$$

In retrospect, it turns out that this value of p_0 is sufficiently small to be consistent with the assumption that practically all acceptors and donors are ionized; a much larger value of p_0 would invalidate this assumption.

(b) *Dependence of the mobility of holes on pressure*

For an understanding of the pressure effects on the resistance, it is advantageous to consider the phenomena in the extrinsic region. In fact, in the intrinsic region an influence can be expected on the mobilities of both electrons and holes, as well as on the numbers n and p (through a possible effect on the energy gap). On the other hand, in the extrinsic region, when all impurities are ionized, only μ_p can be expected to vary.

A correction must also be made for the change in specific volume, and therefore in p_0, by compression. This accounts for a decrease of ρ of $1{\cdot}3\times10^{-6}$ parts per atm increase of pressure. The remainder of the observed linear decrease of ρ with pressure, $1{\cdot}0\times10^{-5}$ parts per atm, must, therefore, be accounted for by an increase of the hole mobility,

$$(1/\mu_p)_{1\text{ atm}}(\partial\mu_p/\partial P)_T = 0{\cdot}9\times10^{-5}/\text{atm}.$$

This value is much larger than those reported elsewhere[11,t] for more strongly p-type specimens. No explanation of this discrepancy is here suggested.

(c) *The intrinsic region: calculation of the concentration product n_i^2*

The concentration product or "dissociation constant", defined as

$$n_i^2 = np, \quad (5)$$

* In this connection it may be noted that BASHIROV and TSIDIL'KOVSKIĬ,[14] from measurements of the Nernst–Ettinghausen effect in the intrinsic region, found μ_p to be proportional to about $T^{-2{\cdot}4}$.

can be expressed in terms of the resistivity (given by the experiment) by eliminating n and p from equations (2), (3) and (5):

$$n_i^2 = [e(\mu_n+\mu_p)\rho]^{-2}\times$$
$$\times\{1+e\rho_0(\mu_n-\mu_p)\rho-e^2\rho_0^2\mu_n\mu_p\rho^2\}. \quad (6)$$

At high temperatures the expression between curly brackets is effectively unity.

For the calculation of n_i^2 the values of the mobilities in the intrinsic region are needed. This necessitates an assumption regarding the pressure- and temperature-dependence of the mobilities in this region. In the same way as has already been accepted for μ_p, it will be assumed that the value of μ_n in the intrinsic region can be obtained by linear extrapolation of the log μ_n versus log T relation (cf. equation (1)) over a limited range into this region.

It was found that in the extrinsic range $(1/\mu_p)_{1\,\mathrm{atm}}\,(\partial\mu_p/\partial P)_T$ is independent of temperature. The validity of this relation is assumed to be extensible into the intrinsic region. A similar behaviour is ascribed to the pressure effect on the mobility of electrons, which is taken from the work of PAUL and BROOKS.[1m]*

$$(1/\mu_n)_{1\,\mathrm{atm}}(\partial\mu_n/\partial P)_T = -2\times10^{-6}/\mathrm{atm}$$

Under these assumptions the values for n_i^2 given in Table 3 were obtained.

(d) *Energy gap*

The width of the forbidden energy gap, E_g, is related to the concentration product n_i^2 by the equation:[10]

$$n_i^2 = 4(2\pi mkT/h^2)^3(m_nm_p/m^2)^{\frac{3}{2}}\exp(-E_g/kT) \quad (7)$$

or

$$E_g = kT\{\ln 4(2\pi mkT/h^2)^3+$$
$$+(3/2)\ln(m_nm_p/m^2)-2\ln n_i\}, \quad (7a)$$

where m is the electron mass, and m_n, m_p are the density-of-states effective masses of electrons and holes, respectively.

Information on m_n, m_p, is obtained from the literature. They are reported as results from microwave-transmission[11] and cyclotron-resonance[12] experiments at 1 atm, by proper averaging over all directions. Both experiments give a value for m_p/m of $0{\cdot}34\pm10$ per cent, independent of temperature. They also agree that the value of m_n/m is 0·55 at very low temperatures, but they disagree on the temperature-dependence of the latter. At any temperature in the range here reported, the uncertainty in m_n is about 20 per cent. This, however, does not have a disastrous effect on the accuracy of E_g. At 125°C an uncertainty of ±30 per cent in m_nm_p/m^2 contributes 0·015 eV to the uncertainty in the gap E_g, and $\pm3{\cdot}5\times10^{-5}$ eV/°K to that of $(\partial E_g/\partial T)_P$. An additional $\pm0{\cdot}003$ eV in E_g is contributed by the uncertainty in the mobility data.[8] These

Table 3. The concentration product, n_i^2 *(in* cm^{-6}*), at various pressures and temperatures*

P (atm) \ T(°K)	398·80	372·40	348·04	322·63
1	$2{\cdot}120\times10^{30}$	$3{\cdot}473\times10^{29}$	$5{\cdot}155\times10^{28}$	$5{\cdot}289\times10^{27}$
300	2·025	3·301	4·889	4·981
600	1·9300	3·139	4·633	4·699
900	1·8418	2·986	4·386	4·431
1200	1·7595	2·836	4·161	4·182
1500	1·6802	2·699	3·937	3·945
1800	1·6019	2·564	3·733	3·722
2100	1·5289	2·440	3·539	3·516
2400	1·4607	2·321	3·355	3·322
2700	1·3970	2·206	3·181	3·138

* In metals the change of mobility with pressure is controlled by the change of the elastic constants.[9]

VOL. 10 1959

Table 4. The energy gap E_g (in eV), at various pressures and temperatures

P (atm) \ T(°K)	398·80	372·40	348·04	322·63
1	0·6134	0·6243	0·6346	0·6452
300	0·6150	0·6259	0·6362	0·6469
600	0·6167	0·6275	0·6378	0·6485
900	0·6183	0·6292	0·6394	0·6502
1200	0·6199	0·6308	0·6410	0·6518
1500	0·6214	0·6324	0·6427	0·6534
1800	0·6231	0·6340	0·6443	0·6550
2100	0·6247	0·6356	0·6459	0·6566
2400	0·6262	0·6372	0·6475	0·6582
2700	0·6278	0·6389	0·6491	0·6598

uncertainties are an order of magnitude greater than those introduced by the measurements of resistance and temperature here reported (±0·0001 eV).

Assuming temperature-independent effective masses, the measurements at 1 atm show E_g to be a linear function of temperature with

$$(\partial E_g/\partial T)_P = -4{\cdot}19\times10^{-4}\ \text{eV/°K}\pm0{\cdot}9\ \text{per cent.}^*$$

This figure holds at all pressures, and may be compared with the value determined by means of the temperature shift of the infrared absorption edge,

$$(\partial E_g/\partial T)_{1\ \text{atm}} = -4{\cdot}4^{(13)}\ \text{or}\ -4{\cdot}5^{(15)}\times10^{-4}\ \text{eV/°K}.$$

If, however, the temperature coefficient of the electron effective mass as reported in[11b] is substituted, the resulting value of $(\partial E_g/\partial T)_P$ is numerically about 50 per cent smaller.

For the evaluation of the pressure effect on the energy gap, it is assumed that the influence of pressure on the effective masses can be neglected in comparison with that on the concentration product n_i^2 (cf. equation (7a)). The values of the energy gap E_g thus obtained are tabulated in Table 4 for different pressures along a series of isotherms; E_g is a linear function of pressure in the range investigated, with a pressure coefficient,

$$(\partial E_g/\partial P)_T = 5{\cdot}37\times10^{-6}\ \text{eV/atm}\pm0{\cdot}6\ \text{per cent}$$

independent of temperature up to the top of the measured range (125°C). This value agrees with that reported in ref. (1f); it does not agree with the results obtained from the pressure shift of the infrared absorption edge.[13]

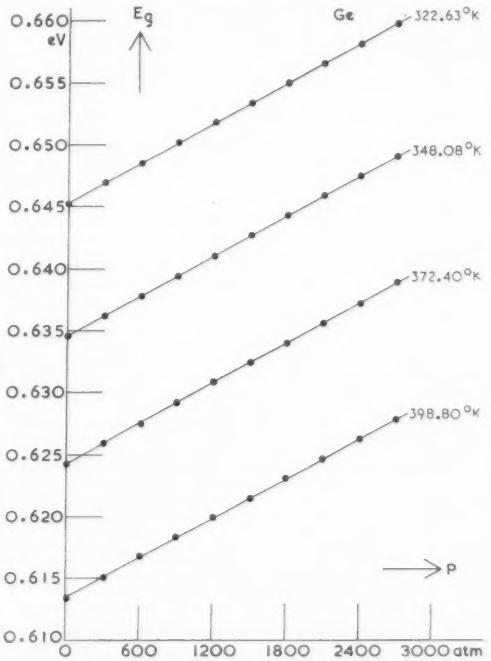

FIG. 4. Energy gap, E_g, versus pressure, P, at four temperatures in the intrinsic range, obtained numerically. They are straight lines and, within the limits of experimental accuracy, parallel.

* The uncertainty given here, as well as that in $(\partial E_g/\partial P)_T$ given below, does not take into account the above-mentioned uncertainties in the effective masses.

The values of E_g at 1 atm agree satisfactorily with the infrared absorption values (in eV) 0·64[15],* 0·65[16] at 300°K; 0·63[16] at 350°K.

5. DISCUSSION

The rather high resistivity (about 80 Ω-cm at 20°C) might suggest inhomogeneity of the sample. However, strong inhomogeneity, which would lead to tortuous current paths and therefore to abnormally low apparent mobilities (SHOCKLEY,[2] p. 288) presumably would cause such anomalous behaviour (versus T) as that observed in the high-purity p-silicon sample no. 1 (SHOCKLEY,[2] Fig. 11–7, p. 284). Since the present sample behaved quite normally in this respect, its inhomogeneity presumably is very slight; it is possible, however, that the discrepancy in the pressure-dependence of μ_p, noted earlier, is related to this inhomogeneity.

Furthermore, a specific resistivity ρ_p of 80 Ω-cm at 20°C for our p-type sample corresponds to the lower value ρ_n of about 64 Ω-cm† for an n-type sample with the same n_i^2 and the opposite value of p_0, because of the higher mobility of the electrons; this value does not seem exceedingly high.

REFERENCES

1. (a) BARDEEN J., *Phys. Rev.* **75,** 1777 (1949) (L) : Te.
   (b) MILLER P. H., Jr., and TAYLOR J., *Phys. Rev.* 76, 179 (1949) (A) : Ge.
   (c) TAYLOR J. H., *Phys. Rev.* **80,** 919 (1950) (L) : Ge.
   (d) HALL H. H., BARDEEN J., and PEARSON G. L., *Phys. Rev.* **84,** 129 (1951): Ge p–n junctions.
   (e) PAUL W., *Phys. Rev.* **90,** 336 (1953) (A): Ge.
   (f) PAUL W. and BROOKS H., *Phys. Rev.* **94,** 1128 (1954): Ge.
   (g) PAUL W., BENEDEK G. B., and BROOKS H., *Phys. Rev.* **94,** 1415 (1954) (A): Ge.
   (h) LONG D. and MILLER P. H., Jr., *Phys. Rev.* **98,** 1192 (1955) (A): InSb.
   (i) BENEDEK G. B., PAUL W., and BROOKS H., *Phys. Rev.* **98,** 1193 (1955) (A): Ge.
   (j) PAUL W. and PEARSON G. L., *Phys. Rev.* **98,** 1755 (1955): Si.
   (k) LONG D., *Phys. Rev.* **99,** 388 (1955): InSb.
   (l) KEYES R. W., *Phys. Rev.* **99,** 490 (1955): InSb.
   (m) BENEDEK G. B., PAUL W., and BROOKS H., *Phys. Rev.* **100,** 1129 (1955): Ge.
   (n) TAYLOR J., *Phys. Rev.* **100,** 1593 (1955): InAs.
   (o) BRIDGMAN P. W., *Proc. Amer. Acad. Arts Sci.* **72,** 157 (1938): Te.
   (p) BRIDGMAN P. W., *Proc. Amer. Acad. Arts Sci.* **79,** 125 (1951): Ge, Si, several compounds.
   (q) BRIDGMAN P. W., *Proc. Amer. Acad. Arts Sci.* **81,** 165 (1952): 72 substances incl. Ge.
   (r) BRIDGMAN P. W., *Proc. Amer. Acad. Arts Sci.* **82,** 71 (1953): Ge.
   (s) LONG D., *Phys. Rev.* **101,** 1256 (1956): Ge, InSb, InAs, GaSb, Te, Mg_2Sn.
   (t) SMITH A. C., *Bull. Amer. Phys. Soc.* **3,** 14 (1958) (A): Ge.
   (u) NATHAN M. I., PAUL W., and BROOKS H., *Bull. Amer. Phys. Soc.* **3,** 14 (1958) (A): Ge.
2. SHOCKLEY W., *Electrons and Holes in Semiconductors* §11.3b. D. Van Nostrand Co., New York (1950).
3. MICHELS A., *Ann. Phys. Lpz.* **73,** 577 (1924).
4. JAEGER W., *Elektrische Messtechnik* p. 321. J. A. Barth, Leipzig (1928).
5. MICHELS A. and MICHELS C., *Phil. Trans. Roy. Soc.* A**231,** 409 (1933).
6. MICHELS A., BLAISSE B., and HOOGSCHAGEN J., *Physica* **9,** 565 (1942).
7. CONWELL E., *Proc. Inst. Radio Engrs.* **40,** 1327 (1952)
8. MORIN J. F., *Phys. Rev.* **93,** 62 (1954).
9. LENSSEN M. H., Thesis, Amsterdam (1936).
10. SHOCKLEY W., *loc. cit.* §10.3. ref. 2.
11. (a) GOLDEY J. M. and BROWN S. C., *Phys. Rev.* **98,** 1192 (1955) (A).
    (b) ALTROY F. D. and FAN H. Y., *Phys. Rev.* **98,** 1561 (1955) (A).
12. DRESSELHAUS G., KIP A. F., and KITTEL C., *Phys. Rev.* **98,** 368 (1955). The theoretical interpretation of these experiments is reviewed in detail by BROOKS H., *Advances in Electronics and Electron Physics* Vol. 7, esp. pp. 99 and 120 (1955).
13. FAN H. Y., *Solid State Physics* (Edited by D. TURNBULL and F. SEITZ) Vol. 1 p. 307. Academic Press, New York (1955).
    FAN H. Y., SHEPHERD M. L., and SPITZER W., *Photoconductivity Conference* (Ed. R. G. BRECKENRIDGE *et al.*) p. 196. John Wiley and Sons, New York (1956).
    See also WARSCHAUER D. M., PAUL W., and BROOKS H., *Phys. Rev.* **98,** 1193 (1955) (A) and NEURINGER L. J., *Bull. Amer. Phys. Soc.* **2,** 134 (1957) (A), where explanations of the discrepancy between the electrical and optical results are proposed. An explanation depending upon a pressure-dependence of $\partial E_g/\partial T$ would seem to be precluded by the present measurements.
14. BASHIROV R. I. and TSIDIL'KOVSKIĬ I. M., *Zh. tekh. fiz.* **26,** 2195 (1956).
15. DASH W. C. and NEWMAN R., *Phys. Rev.* **99,** 1151 (1955).
16. MACFARLANE G. C. and ROBERTS V., *Phys. Rev.* **97,** 1714 (1955) (L).

* To the value such as 0·62 eV at 300°K in ref. (15), the energy of a certain phonon, estimated as 260°K = 0·022 eV,[16] has to be added for purposes of comparison.

† Calculated with the help of $1/\rho_n - 1/\rho_p = e(\mu_n - \mu_p)p_0$; $\mu_n - \mu_p \approx 2000$ cm²/V at 20°C; $|p_0| \approx 1{\cdot}0 \times 10^{13}$/cm³.

J. Phys. Chem. Solids Pergamon Press 1959. Vol. 10. pp. 19–34. Printed in Great Britain.

REMARKS ON MAGNETICALLY DILUTE SYSTEMS

H. SATO and A. ARROTT

Scientific Laboratory, Ford Motor Company, Dearborn, Michigan

and

R. KIKUCHI*

Wayne State University, Detroit, Michigan

(*Received* 7 *November* 1958)

VOL.
10
1959

Abstract—Because of the inadequacies of previous treatments of the magnetic properties of magnetically dilute systems when used to interpret experimental results, a re-examination of the problem starting from a simple model is made. The treatments of the problem discussed here, using an Ising model, show that a Curie or a Néel temperature does not appear until a finite concentration of magnetic atoms is obtained if the atomic distribution is random. This concentration depends on the co-ordination number of the lattice and on the range of interaction, but not on the strength of the interaction. The results given here for nearest-neighbor interactions describe the general behavior observed in magnetically dilute solutions. Such things as anomalously high values of "effective magnetic moments" per magnetic atom and its concentration-dependence, curvature in inverse susceptibility against temperature plots, and parasitic paramagnetism in the weakly ferromagnetic alloys, &c., are reasonably well explained. When the system has antiferromagnetic interactions, it is found that the inverse susceptibility shows a complicated temperature-dependence varying with concentration and that the existence of a maximum in the susceptibility does not necessarily mean the onset of antiferromagnetism. Special references are made to iron in gold and chromium and to manganese in copper.

1. INTRODUCTION

In the study of the origin of ferromagnetism or of antiferromagnetism, it is of fundamental importance to know the nature of the interaction between magnetic atoms and the value of the magnetic moment of such atoms. One of the most powerful tools for this purpose is the study of the magnetic properties of a magnetically dilute system, that is, a system in which a small fraction of magnetic atoms is added to a non-magnetic matrix. Since we can assume that only the magnetic atoms have magnetic moments in such a case, we can obtain the magnetic moment of magnetic atoms and their dependence upon the concentration from the measurement of the paramagnetic susceptibility. Also, from the behavior of the transition from paramagnetism to ferro- or antiferromagnetism and its dependence upon concentration, we can obtain information concerning the nature of the interaction between magnetic atoms. The dependence of the magnetic moment upon the concentration which we can obtain from such a system is also very instructive for the study of the band structure of transition elements. There seems to be a considerable difference in band structure between f.c.c. metals and b.c.c. metals which is reflected in the difference in the concentration-dependence of the magnetic moment of the added atoms.[1–3]

With such purposes in mind, the behavior of chromium-rich chromium–iron alloys has been investigated by the present authors[4] in connection with the transition from paramagnetism to ferromagnetism depending on the concentration. Also, the antiferromagnetic transition in extremely low-concentration copper–manganese alloys has attracted much interest concerning the nature of the interaction between manganese atoms.[5] In order

* Present address: Hughes Research Laboratories, Culver City, California.

to draw conclusions from measurements, we must have resort to a model of magnetism in some form or other. It appears that all magnetically dilute systems investigated so far, including a dilute solution of iron in gold and copper which will be referred to later, show very anomalous properties from the standpoints adopted in the past. It is useful therefore first to make clear whether or not such anomalies are common characteristics of magnetically dilute systems before drawing any conclusion from such measurements. Second, it should be mentioned that the molecular-field treatment, usually adopted to analyze such systems, is quite inappropriate even qualitatively in the case of magnetically dilute solutions. Therefore, great caution must be exercised in interpreting the molecular field constant obtained from such an analysis.

In order to make clear these situations, a highly idealized system is adopted and its magnetic properties are investigated statistical mechanically, carefully avoiding difficulties characteristic of a dilute solution arising from averaging processes.

2. A MODEL FOR A MAGNETICALLY DILUTE SYSTEM AND THE EXAMINATION OF STATISTICAL METHODS

In order to treat the problem quantitatively, we must set up a suitable model. Here we are interested in a system in which a fraction of the lattice points of a given crystal is occupied by magnetic atoms. We assume further an exchange interaction only between magnetic atoms which are nearest neighbors. This is, of course, a highly idealized system but not without justifications. In the case of ionic crystals, a localized model has been proved to be successful, and the present model is considered to hold well in such a case as a mixed ferrite with a small degree of inversion. In the case of alloys, a foreign atom is considered to behave rather independently because of the screening as long as the concentration is low.[6] Therefore the above assumption also well represents the case of a dilute alloy.

Earlier work on similar models indicates, however, that any finite concentration of magnetic atoms no matter how dilute produces a finite Curie temperature. Since the interaction exists only between nearest-neighboring magnetic atoms and since we can expect that only a very minor fraction of magnetic atoms is at the nearest-neighboring position in a dilute solution, it is quite unreasonable to expect the above conclusion that a co-operative phenomenon occurs in such a dilute solution. This conclusion is, however, the result of the averaging process characteristic of the approximation adopted. Special care is necessary to treat such a system. It should be mentioned that a rather good approximational method in the high-concentration case does not necessarily give a good result in the case of low concentration. Since this problem has not been treated properly and apparently a wrong conclusion has been drawn from past treatments, it is felt that it is worthwhile to show very briefly how such defects appear in the methods frequently adopted before appropriate methods are given.

3. SUMMARY OF PREVIOUS TREATMENTS

(a) *Molecular-field treatment: C–W method*

This is a method most frequently used for such a problem in analyzing the measured magnetic properties to obtain the value of magnetic moment, the strength of the interaction, etc. Although the degree of approximation is not good, the treatment is simple and clear cut, and generally it gives a reasonable result in understanding the qualitative nature of most of the problems.[7]

Let us assume that the magnetic atom A with a magnetic moment β is dissolved in the non-magnetic matrix B and let the concentration of A atoms be c. Further, let us assume a positive exchange interaction energy J between nearest-neighboring A atoms. Also let us assume that the distribution of A atoms is random. Then the result of calculation of this method (equivalent to the Bragg–Williams approximation in order–disorder problems) will be given as follows:

$$\Theta = \frac{c}{2} \cdot \frac{zJ}{k}$$

$$\frac{1}{\chi} = \frac{k}{c\beta^2}[T-\Theta] = \frac{kT}{c\beta^2} - \frac{zJ}{2\beta^2} \qquad (1)$$

Here Θ is the Curie point, z is the number of nearest neighbors (co-ordination number of the crystal), k is the Boltzmann constant, χ is the susceptibility per atom (not per magnetic atom), and T is the temperature of the system.

VOL. 10 1959

The main conclusions to be drawn are:

(1) The Curie point is proportional to the concentration of magnetic atoms.

(2) The $1/\chi$ versus T relation is linear and its inclination gives the magnetic moment of constituent magnetic atoms.

(3) The interaction constant between magnetic moments, which is represented by $\delta = zJ/2\beta^2$ in equations (1) in the expression of the inverse susceptibility, is independent of the concentration. The expression with $\delta = 0$ is known as Curie's law. Hereafter let us refer to this method as the C–W method (Curie–Weiss method) for the sake of simplicity.

Since the C–W method is applied so often, some of the conclusions from the method have become a kind of "common sense" of magnetism. However, the conclusion that the Curie point starts from the zero concentration is apparently unreasonable. The reason for this unreasonableness becomes apparent if we think of the nature of this approximation. For that purpose, let us adopt the method used by FOWLER and GUGGENHEIM or by TAKAGI[8] in interpreting the molecular-field treatment, because this is clearer from a statistical-mechanical point of view than the original molecular-field treatment. There, the number of pairs is taken to be proportional to the product of the probabilities of the respective states of atoms on the nearest-neighboring sublattices. Therefore, even if we start from the assumption of nearest-neighbor interaction, it is equivalent to taking into account both near and distant atoms with the same weight. Although this defect does not become serious in the case of high concentrations except near the Curie point, it becomes completely meaningless in the case of dilute solutions. No reliance should be placed upon the results calculated by the C–W method in this case. This is especially so if the system includes more than two kinds of interaction with different interaction ranges, because the range of the interaction is not properly taken into account. The copper–manganese system is supposed to be such a system.

(b) *A generalization of Bethe's method*

Since the molecular-field treatment is not applicable in the dilute solution, the next step might be an extension of BETHE's method to this problem, because the short-range interaction is reasonably taken into account in this method. There are several ways to generalize this method. However we would like to point out here that a method, which looks like rather a formal extension of BETHE's original idea and which is adopted by several authors,[9] fails to treat the problem.

BETHE's original treatment may be explained in the following way. A small group of sites, with a center site and its z neighbors, is taken out from the crystal lattice and a grand partition function for that system is built up. Considering that this small system represents the whole system, we determine the thermodynamical properties of the whole system from those of the small system with the condition that this system is in thermodynamical equilibrium with the rest of the system. A parameter which specifies the interaction of the neighboring atoms with the outside is determined by this condition and then the partition function can be calculated exactly in such a small system. The thermodynamical nature of the total system is thus determined. We call the above condition to determine the statistical parameter the consistency relation.

The generalization of this method to the present problem is then, in a way, straightforward. It is necessary to build up three kinds of grand partition functions for a system of $z+1$ atoms, f_A^+, f_A^-, and f_B. The suffix A or B indicates that the center atom is A or B and $+$ or $-$ means that the spin at the central A atom is up or down. The total grand partition function should be the sum of these three functions, and these functions can be calculated as an extension of the BETHE[10]–EASTOPE[11]–FIRGAU[12] method though very much complicated. These functions thus include two (or more) statistical parameters, one for the atomic distribution and one (or more) for the spin arrangement, which are to be determined using consistency relations. The first consistency relation requires that the probability of having an A atom or a B atom is the same for the central site and the neighboring site, because there is no long-range order. The second consistency relation (not necessarily only one) then inevitably requires that the average magnetic moment of the central site and that of the neighboring site is equal, because the probability of finding an A atom is the same for both sites. These procedures look like a literal generalization

of BETHE's method. However, the unreasonableness arises from the second-type consistency relation. Briefly speaking, the consistency relation concerning the magnetic arrangements, from its physical meaning, should be limited to only the spin arrangement of a magnetically homogeneous system, but in the above treatment, this is generalized to a case in which the model site and the outside have different atomic distributions. In other words, the grand partition function for the $z+1$ sites include all conceivable concentration fluctuations of A and B atoms with weighted probabilities. Then it is easily understood that, among possible concentration fluctuations taken in the system of $z+1$ atoms, unreasonable cases which are never realized as a whole system are included. For example, a case that both central and its z neighbors are occupied by A atoms can occur with a finite probability at any concentration of A atoms. However, all the lattice points of the crystal cannot be occupied by A atoms. The application of the consistency relations to such a system then gives a weighted mean of the magnetic properties of all homogeneous systems which are represented by the configurations of $z+1$ sites. For this reason, the Curie point starts from zero concentration in this manner of generalization. Although the error is not very serious in the case of high concentration, this defect becomes very important when the concentration is low. A generalization made to avoid this kind of difficulty is given later.

(c) *High-temperature expansion method*

As another method to obtain the Curie point and the paramagnetic susceptibility above the Curie point, a high-temperature expansion method such as OPECHOWSKI's is conceivable.[13] However, the application of this method to such a problem is also not reasonable. The expansion is given in terms of J/kT. In the usual case, the Curie point Θ is comparable to J/k and therefore, by choosing an appropriate form of expansion, we can get a reasonably accurate Curie point. However, in the case of low concentration, the Curie point of the system is low or disappears while J remains constant. Therefore a series in terms of J/kT does not converge for T near Θ. On the other hand, the extrapolation of the susceptibility calculated at temperatures high enough for convergence results in a finite Curie point. Therefore, this kind of method is only applicable to calculating the paramagnetic susceptibility at reasonably high temperature ranges.

4. GENERALIZATIONS OF BETHE'S METHOD APPLICABLE TO THE DILUTE SYSTEM

In principle, a BETHE-type treatment should give a reasonable result. However, a difficulty arises in a manner explained before. The "molecular field" which acts on the neighbor z atoms of $z+1$ sites depends not only upon the atomic configuration of $z+1$ sites, but also very sensitively upon the configuration outside, which is not properly taken into account but averaged in the previous method. In order to avoid this difficulty, two kinds of methods are conceivable. One way is to fix the system so that the atomic configuration of the $z+1$ sites is the same as that of the outside and then to apply the usual BETHE-type treatment. The other way is to abandon the original grand partition function type of treatment, but to start from a partition function of the whole system which then takes care of the all possible distributions of the system, both the $z+1$ sites and the outside at the same time. Although the first approach was found to have some defects and all of its results can also be deduced from the more general second approach, it is described, as well as the second approach, because it is simpler yet still gives a reasonable result as long as the interaction constant J is positive.

(a) *The first approach: A–C–N method*

Since we are treating the disordered state, we can assume a more or less uniform distribution of A atoms over the whole crystal, so that the average number of A atoms neighboring to one A atom would be cz. The interactions other than magnetic interaction between A–A pairs are neglected here as before, because we are interested only in the magnetic properties at reasonably low temperatures where practically no redistribution of atoms takes place. We then replace the system by an assembly of A atoms with the co-ordination number cz. This cannot be true in a rigorous sense, because there should be a local fluctuation in the number of nearest-neighboring A atoms. By adopting this version of the system, however, we can assume the model sites certainly represent the whole system and we can directly apply the BETHE method to calculate the magnetic properties. The same kind of method was adopted by TOMITA[14] in calculating

the co-operative nature of the rotation of the hydrogen molecules and by HECHT[15] for the discussion of liquid He^3–He^4 mixture. The application of the BETHE method is then straightforward, simply replacing the co-ordination number z by cz (from which is derived the name A–C–N method for averaged co-ordination number method). We can get for Θ and $1/\chi$ the following relations which should be compared with equations (1).

$$\Theta = \frac{J}{k}\Big/\ln\left(\frac{cz}{cz-2}\right)$$

$$\frac{1}{\chi} = \frac{kT}{c\beta^2}\left[1-\frac{cz}{2}(1-e^{-J/kT})\right]$$

$$= \frac{kT}{c\beta^2} - \frac{zJ}{2\beta^2}(1-e^{-J/kT})\frac{kT}{J}. \qquad (2)$$

The results from these equations are plotted in Figs. 1 and 2 along with the results for the C–W method described in equations (1) and the C–V method to be described below. For graphical purposes the value $z = 8$ is chosen; thus the body-centered cubic case is represented.

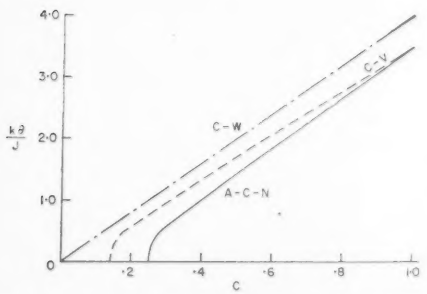

FIG. 1. Reduced transition temperatures (Curie or Néel points) as a function of concentration for the molecular-field treatment (C–W), for the averaged-co-ordination-number method, and for the cluster-variation theory.

The Curie point does not have a finite value unless the concentration is sufficient for cz to be greater than 2. Thus the appearance of ferromagnetism coincides with the concentration for which the number of magnetic atoms is just greater than sufficient to make a linear chain in the crystal on the average. This is in marked contrast to the C–W treatment.

The inverse susceptibility agrees with the C–W treatment in the first term which contains the concentration-dependence. The interaction term, however, agrees with the C–W treatment only in the high-temperature limit. For all compositions up to $cz = 2$ the inverse susceptibility starts at zero for $T = 0$ and with gradually increasing slope approaches the C–W behavior at high temperatures. In the very low concentration range, therefore, the system obeys approximately the Curie law $(1/\chi \sim T)$.

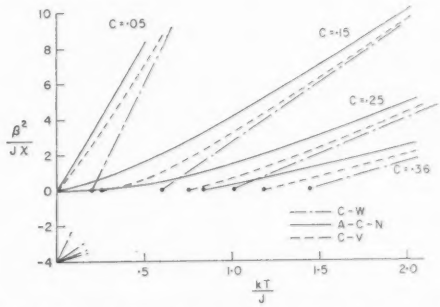

FIG. 2. The reduced inverse susceptibility per atom as a function of reduced temperature for several concentrations of magnetic atoms as calculated by the various methods for $z = 8$.

In terms of the high-temperature approach to the straight-line relation between $1/\chi$ and T, one defines the paramagnetic Curie point, Θ_p, as the temperature at which the extrapolation of this straight line shows $1/\chi$ going to zero. By definition this paramagnetic Curie point agrees with the C–W treatment at all compositions, but is different from the ferromagnetic or actual Curie point. Because the two treatments of the susceptibility approach agreement at sufficiently high temperatures, the two treatments approach agreement for the paramagnetic range of those compositions which possess high Curie points. Thus for cz somewhat greater than 4, the two treatments are qualitatively similar.

The behaviors shown are similar in many ways to experimental results for the chromium–iron system.[4] The important features of this treatment are:

(1) The ferromagnetic Curie point does not appear until a certain finite concentration is reached. This concentration does not depend on

the strength of the coupling, but only on its nature (the range of interaction) and its co-ordination number. The paramagnetic Curie point rises linearly with composition; this slope depends on the strength of the coupling.

(2) The $1/\chi$ versus T curves in the low concentration range start from zero $1/\chi$ and zero T with a slope which increases with increasing temperature. Thus the magnetic moment calculated from the slope of the curve at all but the high-temperature limit is overestimated.

(3) The interaction between magnetic moments is represented by a term which is independent of concentration but which is temperature-dependent. The temperature-dependence accounts for the difference with the C–W treatment. The lack of concentration-dependence may be a remaining defect of the treatment.

All of the above points show marked differences from the molecular-field treatment in the low concentration range. For this reason, analysis of experimental data by means of the "classical" methods based on the Curie–Weiss molecular-field treatment is of limited applicability for the magnetically dilute systems. It is therefore instructive to consider the behavior of several alloy systems from the point of view expressed by the A–C–N treatment.

First, these points of view suggest an important aspect about the nature of the interaction of small amounts of manganese in copper alloys. This system has a positive paramagnetic Curie point which rises with the concentration of manganese atoms. At the same time, this system also shows what appears to be an antiferromagnetic transition, the Néel temperature of which rises with manganese atoms. In view of the above conclusions, it is most probable that both a short-range ferromagnetic interaction (not necessarily a nearest-neighbor interaction) and a weak longer-range antiferromagnetic interaction[16] co-exist in the copper–manganese system. The short-range ferromagnetic interaction makes the paramagnetic Curie point of the system positive and increasing with the manganese content. However, the short-range nature of the interaction does not make the system ferromagnetic in the dilute case until some finite concentration is reached characteristic of the nature of the interaction. On the other hand, a co-existing weak longer-range antiferromagnetic interaction does not affect the property at high temperature much, except to make the paramagnetic Curie point a little bit lower. However, at low temperatures, this longer-range interaction could become effective and thus make the system antiferromagnetic. The Néel point then should also rise with the concentration of manganese atoms. On the other hand, the stronger short-range ferromagnetic interaction should make the system ferromagnetic when the concentration of manganese atoms reaches a certain amount. Actually, the ferromagnetism of this system was found at about 20 atomic per cent manganese by SCHEIL and WACHTEL.[4] This fact also supports the above assumption.

KAUFMANN *et al.*[17] have measured the properties of dilute solutions of iron and nickel in gold, of which we are mainly interested in the case of iron, since there seems to be some controversy both experimentally and theoretically in the case of nickel. The results are somewhat surprising from the viewpoint of the molecular-field treatment. Although these data still retain some of their mysteries, certain effects are more understandable from the viewpoint of the A–C–N treatment. The essential features of their results are the onset of ferromagnetism at a finite concentration of magnetic atoms, the concentration-dependence of the susceptibility in a stronger than linear manner, an anomalously high value and a concentration-dependence of the effective magnetic moment of magnetic atoms, etc. In the case of face-centered-cubic systems, $cz = 2$ occurs for $c = 0{\cdot}167$, which for iron–gold alloys is at 5·4 weight per cent iron. A re-analysis[18] of KAUFMANN's data shows the onset of ferromagnetism at approximately 4 weight per cent iron, rather than at less than 2 weight per cent as given in the original work. This compares with an observed 20 atomic per cent in the iron–chromium system, against 25 per cent predicted by the A–C–N treatment. While the confusion of curvature in magnetization versus field plots with the presence of ferromagnetism in separating the data leaves the interpretation of some of the data in doubt, it appears rather certain from the data that this system includes some negative interactions as well as positive. Thus there may well be similarities between explanations of behavior in iron–gold and manganese–copper systems.

VOL. 10 1959

The concentration-dependence of the susceptibility, which is stronger than linear in manner, is a result of mutual interaction between spins and can be interpreted by means of C–W method except for the fact that in the C–W method the Curie point appears. However, the non-appearance of the Curie point in the A–C–N method makes the temperature effect on the above behavior clearer. By expanding the susceptibility expression of equations (2) in J/kT, assuming that the temperature is reasonably high, we get

$$\chi = \frac{c\beta^2}{kT}\left(1+\frac{czJ}{2kT}\right) = \frac{c\beta^2}{kT}+\frac{c^2z\beta^2J}{2k^2T^2}. \qquad (3)$$

The increase in χ is, therefore, not proportional to the concentration of the magnetic atoms as in the Curie law, but is actually steeper. Also this increase should depend upon the temperature. The lower the temperature, the stronger is the concentration-dependence. It is clear that the predictions are

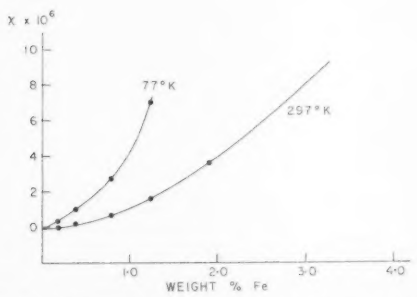

FIG. 3. The susceptibility data of KAUFMANN *et al.*[17] for iron in gold, showing composition- and temperature-dependence.

borne out experimentally (Fig. 3), although this effect is also understandable by means of C–W method.

One of the problems in interpreting the data has been the large values of the effective magnetic moment obtained from fitting the data with the Curie–Weiss law. With increasing concentration, the effective moment of the iron atoms appears to reach the value corresponding to $S = 5/2$ and still to be increasing. This effect is held to be the result of applying the molecular-field treatment to calculate the effective moments, that is, the slope of the inverse susceptibility versus temperature curve accurately reflects the moment of the magnetic carriers only if the temperature is sufficiently high. The effective magnetic moment is defined as:

$$\beta^2_{\text{eff}} \equiv \frac{k}{c}\cdot\frac{dT}{d(1/\chi)} = \beta^2\left(1+\frac{czJ^2}{4k^2T^2}\right), \qquad (4)$$

where the right-hand side is evaluated for the A–C–N method at moderately high temperatures. The second term does not appear in the Curie–Weiss model. Yet it is clearly appropriate in analyzing the data as shown for the results over the range of temperatures studied by KAUFMANN (see Fig. 4). Equation (4) shows the concentration-dependence of the effective magnetic moment and

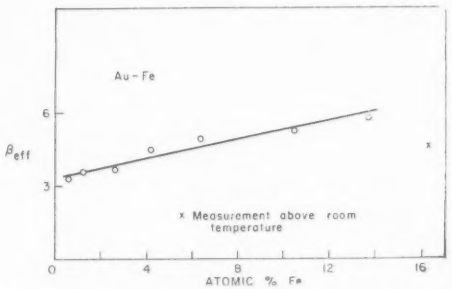

FIG. 4. Estimates of the effective magnetic moment of iron in gold from the data of KAUFMANN *et al.*[17]

the effect of the temperature of the measurement. In particular, it is important to realize that temperatures are to be considered high in relation to zJ/k rather than to the usually adopted Curie temperature, which can be zero for finite zJ/k. Note that a value of β_{eff} given by KAUFMANN evaluated over a higher temperature range shows the predicted decrease in β_{eff}. These results have tempted in the past an explanation in terms of electronic changes as a function of composition, but this result shows that to a first order such a mechanism is not necessary. The value of β_{eff} found in the limit of $c = 0$ should have some interpretable significance. This value corresponds closely to the moment sometimes ascribed to pure iron, namely $g = 2{\cdot}2$ and $S = 1$, which gives $\beta_{\text{eff}} = 3{\cdot}1$.

(b) *The second approach to the problem: C–V method*

The first approach treats the problem in which the fluctuation of the atomic distribution is fixed, as this allows us to apply BETHE's original idea that

the model sites actually represent the whole system. Although this approximation is a marked improvement over the C–W treatments, it includes defects because we neglected the fluctuation of the atomic distribution. The defect can be most easily visualized in Fig. 5. Suppose the black circles on

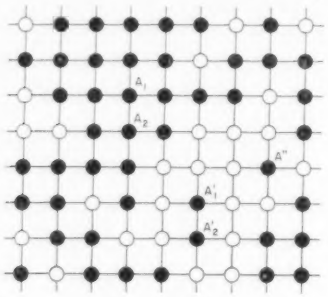

FIG. 5. Atom configurations in a random alloy.

the lattice points are the magnetic A atoms. Then the pair A_1'–A_2' in this distribution is not equivalent to the pair A_1–A_2, because A_1' and A_2' atoms are not surrounded by magnetic atoms, while A_1 and A_2 are. The first approach corresponds to the one in which we assume that these pairs are equivalent. In this sense, the constraint applied to the atoms is too strong in the first approach, especially at extremely low concentrations. Furthermore, an isolated A atom can exist (A'' in Fig. 5). In order to take into account the inequality of these pairs of atoms, we must adopt the second approach, and proceed to build up a partition function in which the distribution of the atoms in the whole system is taken into account. Among several methods on this line, which can be reduced to BETHE's approximation in the case $c = 1$, we selected the TAKAGI[19]–KIKUCHI[20] method (cluster-variation method) for its clarity in statistical nature. This method consists in the direct calculation of the entropy of the system when the numbers of different pairs of atoms are specified. (In the nearest-neighbor assumption, the energy of the system is then known). The idea is to count the number of possible arrangements of these pairs without any contradiction on the crystal lattice. Here we limit ourselves only to the approximation of arranging pairs. This method can be considered a generalization of BETHE's method as it gives the identical result as BETHE's when $c = 1$. Expressing the energy and the entropy in terms of parameters and then minimizing the free energy with respect to the parameters we can calculate the thermodynamical properties of the system. The details of the treatment are given in the Appendix and only the results are given here comparing with those of the first approach.

We neglect completely the interaction between atoms except for the magnetic interaction between A–A pairs because as before we are treating the system with "quenched-in" atomic distribution. The Curie point and the inverse susceptibility of the system are given with this approximation, assuming the completely random distribution of A atoms, as follows:

$$\Theta = \frac{J}{k} \Big/ \ln\left\{\frac{cz+(1-c)}{cz-(1+c)}\right\} \tag{5}$$

$$\frac{1}{\chi} = \frac{kT}{c\beta^2}\left[1 - \frac{cz(e^{J/kT}-1)}{(1+c)e^{J/kT}+(1-c)}\right]$$

$$= \frac{kT}{c\beta^2} - \frac{zJ}{2\beta^2}(1-e^{-J/kT})\frac{kT}{J}\left\{\frac{1+c}{2}+\frac{1-c}{2}e^{-J/kT}\right\}^{-1} \tag{6}$$

These expressions agree with equations (2) for $c = 1$. The appearance of ferromagnetism, however, is from $c = 1/(z-1)$. A plot of Θ versus c for $z = 8$ is shown in Fig. 1 as a dashed line. The susceptibility equation agrees with the A–C–N method in the limit $c = 1$, but gives not only a temperature-dependence to the variation of the interaction term but also a composition-dependence. In the limit of high temperature, the behavior is again as in the C–W treatment as δ goes to $zJ/2\beta^2$. Qualitatively, the behavior is much the same as in the A–C–N treatment already discussed (see Figs. 1 and 2). In comparing with the chromium–ion and gold–iron systems, we find for c_0, the composition at which ferromagnetism should appear, the following values:

	C–W	C–V	A–C–N	Expt
Fe–Cr	0	0·14	0·25	$\sim$ 0·20
Fe–Au	0	0·09	0·17	$\sim$ 0·14

The biggest qualitative difference of this approach from the previous one appears in the value

VOL. 10 1959

of the magnetic moment per magnetic atom as seen in the spontaneous magnetization at absolute zero. Since, in the previous approach, all magnetic atoms are treated as equivalent, all magnetic moments point in the same direction at the absolute zero of the temperature as long as the system is ferromagnetic. Therefore, the value of the spontaneous magnetic moment per magnetic atom does not change until the ferromagnetism vanishes. This is not necessarily so in the C–V approach, because of the existence of the isolated atoms A''. Because not all magnetic atoms link together in the case of the dilute solution, the spontaneous magnetization at $T = 0$ per magnetic atom decreases as the concentration decreases and vanishes continuously at the same concentration where the ferromagnetism vanishes. The magnetization at $T = 0$ per atom of the crystal, σ, is given by equations (A.16) and (A.20) in the Appendix. This behavior is shown in Fig. 6. One important

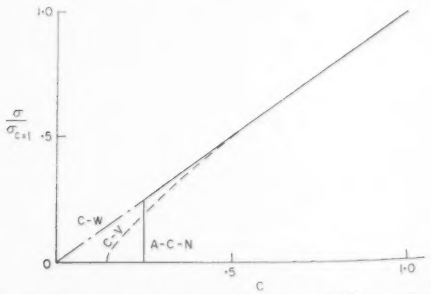

FIG. 6. Spontaneous magnetization at 0°K as a function of composition as calculated by three methods.

consequence of this lack of complete alignment of magnetic moment is the appearance of parasitic paramagnetism arising from the alignment of magnetic moments by the external field. It appears that this prediction is borne out experimentally in many systems.

5. THE SYSTEM WITH ANTIFERROMAGNETIC INTERACTION

For completeness of the discussion, it is necessary to discuss the model when the interaction is such as to favor antiparallel spin alignment. In this case, it is necessary to consider at least two sublattices in order to distinguish the case of antiferromagnetism. Although the treatment for antiferromagnetism becomes more complicated than for ferromagnetism, it turns out that, in the paramagnetic range, the treatment becomes equivalent except that the equation for the susceptibility is changed only by replacing J by $-J$ for the case of antiferromagnetic interaction. The appearance of antiferromagnetism, therefore, meets the same conditions as the appearance of ferromagnetism. Thus the Néel points start at a finite concentration and vary with concentration just as the Curie points as shown in Fig. 1.

The equations for the susceptibility in the paramagnetic temperature ranges may be summarized in the following in reduced notation where $\tau = kT/|J|$ and $\mathrm{X} = |J|\chi/\beta^2$.

For the C–W method

$$1/\mathrm{X} = \tau/c + z/2.$$

For the A–C–N method

$$1/\mathrm{X} = \tau/c + (z/2)\tau(1-e^{-1/\tau})e^{1/\tau}. \qquad (7)$$

For the C–V method

$$1/\mathrm{X} = \tau/c + \\ +(z/2)\tau(1-e^{-1/\tau})\left\{\frac{(1-c)}{2}+\frac{(1+c)}{2}e^{-1/\tau}\right\}^{-1}$$

As before, in the limit of high τ, all three methods agree and, in the limit of $c = 1$, the A–C–N and C–V methods agree.

A big difference between the A–C–N and C–V approach, however, appears at low temperatures. The A–C–N method always gives $1/\chi$ going to infinity with decreasing temperature even if no long-range order of spins exists. This is because of the assumption adopted in the method that all atoms are equivalent and thus have antiferromagnetic interaction with each other however small is the concentration. The C–V method, on the other hand, because of the existence of magnetically isolated atoms, has magnetic moments free to align at absolute zero. Thus the C–V method for all concentrations except $c = 1$ has $1/\chi$ going to zero with decreasing temperature. These statements concerning the susceptibility also hold for the antiferromagnetic compositions if we concern ourselves with the susceptibility parallel to the antiferromagnetic easy direction. The parallel susceptibility has been evaluated for the C–V method as equations (A.32) and (A.33) in the

Appendix. Because of the serious defect of the A–C–N method in the case of antiferromagnetism, the application of this method in this case is not appropriate. However, since this method still has a meaning when the fluctuation is limited, further comparison of the results of this method with those of C–V method is rationalized.

The A–C–N method for calculating the parallel susceptibility in the antiferromagnetic state gives properties which are similar to those of the usual treatment of antiferromagnetism.[21] Thus the parallel susceptibility goes to zero as the sublattice magnetizations saturate on going to absolute zero of temperature. In the C–V method, however, these sublattices do not saturate except in the limit $c = 1$, where there are no magnetically isolated atoms.

In view of the above results, two important points should be made concerning the system with antiferromagnetic interaction. One is that a maximum of the susceptibility does not always mean the onset of antiferromagnetism. The other is that the onset of antiferromagnetism in the dilute alloy range seems to be a very difficult thing to determine from susceptibility measurements. These points need some further discussion with some numerical results.

In the A–C–N method, the susceptibility can have a broad maximum due to the increase in the short-range order of spins even if there is no co-operative transition to antiferromagnetism. If a co-operative transition to long-range order begins (Néel point), a sharp peak should be observed as usual. The temperature of this broad maximum in the susceptibility depends on cz, and so does the Néel temperature. If $cz < 3{\cdot}6$, the broad maximum occurs above the Néel point and if $cz < 2$, the maximum still occurs even though there is no Néel point. For $cz > 3{\cdot}6$, on the other hand, the Néel point appears above the temperature of the broad maximum and only a sharp peak is found. Since the A–C–N method is applicable when the concentration fluctuation is limited, the cases $cz = 2$ and $cz = 3$ can have more exact physical meaning if the distribution of magnetic atoms is such that the number of nearest neighbors is always 2 or 3 everywhere and no other fluctuation exists. In such a system, therefore, antiferromagnetism is not to be inferred from a maximum in the susceptibility.

In the C–V treatment, the condition for a broad maximum to occur above the Néel point is that $z < 4$. For the case $z = 2$, where no Néel point occurs, a maximum in χ is found if $c > 0{\cdot}8$. For the case $z = 3$, the Néel point lies at a lower temperature than the maximum for $c > 0{\cdot}7$. Since in

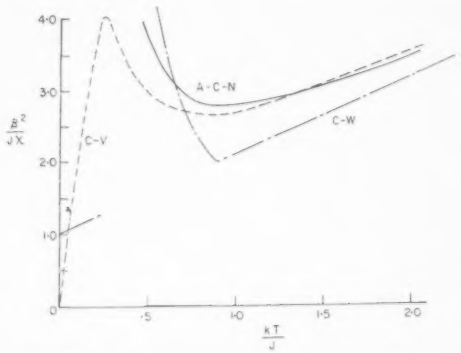

FIG. 7. Reduced inverse susceptibility as a function of reduced temperature for the "not quite complete linear chain"; ($z = 2$, $c = 0{\cdot}9$).

the case of the C–V method the susceptibility should go to infinity at the absolute zero of the temperature (except the case $c = 1$), the susceptibility may go through a minimum as well as a

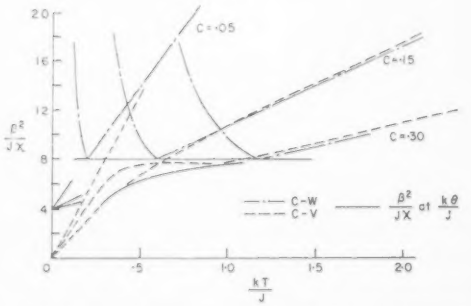

FIG. 8. Reduced inverse susceptibility as a function of reduced temperature for several compositions. The solid line represents the susceptibility at the Néel point as a function of the Néel temperatures of the compositions ranging from $c = 0{\cdot}15$ to $c = 0{\cdot}32$.

maximum. As an example, the almost complete linear chain ($z = 2$, $c = 0{\cdot}9$) is illustrated for the three methods in Fig. 7. The existence of the fluctuations, however, makes it so that no minimum

occurs in the dilute alloy range for the usual larger co-ordination numbers, like $z = 8$, unless there is an onset of antiferromagnetism. This minimum due to the onset of antiferromagnetism, however, is very difficult to detect, contrary to the usual expectation, unless the composition is sufficient to raise the Néel point to a reasonable fraction of zJ/k. This is shown in Fig. 8, where the susceptibility is plotted against the reduced temperature for $z = 8$ and several values of c. The break in the curve for $c = 0{\cdot}15$ is not discernible on the scale used. Because of this fact, the susceptibility does not seem to provide a good criterion concerning the onset of antiferromagnetism in the case of a magnetically dilute solution. As the degree of approximation of the Ising model seems to be even worse in the case of antiferromagnetism than the ferromagnetism, further detailed discussion of the problem is, therefore, unwarranted.

VOL. 10 1959

6. SPECIFIC HEAT OF THE SYSTEM

The specific heat of the magnetically dilute system is as important as the magnetic properties in analyzing such a system. The results are given by differentiating with respect to temperature the energies given by equation (A.35) in the paramagnetic state and equation (A.36) for the co-operative state whether it be in the ferromagnetic or the antiferromagnetic state. The paramagnetic state gives a specific heat due to spin orientation which is of the Schottky type. The maximum in the Schottky-type curve occurs at a temperature depending only on the strength of the interaction and not on the composition or co-ordination number.

The co-operative states give sharply increasing specific heats with increasing temperature accompanied by discontinuities to the paramagnetic values at the transition temperatures. Thus depending on whether the co-operative transition temperature lies above the Schottky-type maximum ($\tau = 0{\cdot}8$ in the above calculation) or not, there will be one or two peaks (a sharp peak below a broad maximum) in the specific heat. If there is no co-operative transition, there will be only the Schottky-type anomally, and if the co-operative transition lies above $\tau = 0{\cdot}8$ there will be only the sharp co-operative specific-heat peak. As susceptibility does not provide a good criterion concerning the onset of antiferromagnetism in this case, the analysis of specific-heat data is especially important.

As a final remark on the copper–manganese system, it may be significant to mention that the specific heat of the system in the dilute alloy range appears to be a Schottky type rather than a co-operative type.[22] This might be an indication that the existence of the minimum in the $1/\chi$ versus T curve in this alloy system is not associated with the formation of antiferromagnetic long-range order. But in view of the previously mentioned hypothesis of a long-range antiferromagnetic interaction in this system, it is clear that the results based on the above models do not apply to the antiferromagnetic interaction in this system, even though it appears they may apply to the ferromagnetic shorter-range interactions.

7. SUMMARY

An attempt has been made to provide a "common sense" for the discussion of the magnetic properties of magnetically dilute systems. The model chosen for this purpose is essentially the Ising model. The statistical treatments discussed here show why the "molecular-field treatment" is not applicable even qualitatively in the discussion of a magnetically dilute system. The main conclusions obtained are:

(1) Co-operative phenomena do not occur until a finite concentration of magnetic atoms is obtained if the atomic arrangement is random. This concentration depends on the range of interaction and its co-ordination number, but not on the strength or sign of the interaction.

(2) The temperature-dependence of the inverse susceptibility is not linear except in the limit of high temperatures; the magnetic moments calculated from the slope are thus generally overestimated and the strengths of the interaction between moments is not readily calculable from low-temperature data. Here the temperatures are to be considered high in relation to the strength of the interaction zJ/k rather than to the Curie temperature as usually assumed.

The Curie–Weiss law for an alloy system

$$1/\chi = kT/c\beta^2 - \delta$$

is retained except that δ, the interaction parameter, is no longer constant but depends on temperature

and on the concentration of magnetic atoms. The degree to which the effective moment calculated from the susceptibility data at finite temperatures is overestimated increases with the concentration of magnetic atoms.

(3) With negative interactions the appearance of antiferromagnetism is sometimes difficult to determine from susceptibility measurements. A maximum in susceptibility does not necessarily imply the long-range order of spins on the one hand, and on the other the onset of antiferromagnetism in the dilute system can be accompanied by almost negligible effects on the susceptibility/temperature relation.

(4) The existence of "magnetically isolated atoms" causes a parasitic paramagnetism in the case of ferromagnets and a decrease of the inverse susceptibility to zero at the absolute zero temperature in the case of antiferromagnetic interactions.

(5) In the low concentration range where no co-operative phenomena occur, a broad Schottky-type anomaly in the specific-heat curve would be observed which is in contrast to the appearance of a sharp λ-type curve when the co-operative phenomena appear.

The alloy systems of iron in gold and in chromium and of manganese in copper have been discussed in the light of these conclusions.

Table A.1

Configuration of a pair		*Probability parameter*	*Energy*
A^+	A^+	x_1	$-J/2+\epsilon_{AA}$
A^+	A^-	x_2	$J/2+\epsilon_{AA}$
A^-	A^+	x_3	$J/2+\epsilon_{AA}$
A^-	A^-	x_4	$-J/2+\epsilon_{AA}$
B	A^+	x_5	ϵ_{AB}
A^+	B	x_6	ϵ_{AB}
A^-	B	x_7	ϵ_{AB}
B	A^-	x_8	ϵ_{AB}
B	B	x_9	ϵ_{BB}

APPENDIX

The alloy considered here has two species of atoms, A and B. Only the A atoms are magnetic and these take spin directions designated by A^+ or A^-. The probability that any lattice point is an A^+, A^-, or B atom is given by y_1, y_2, or y_3 respectively. The probability that any neighboring pair of atoms has a given configuration is shown in Table A.1, along with the energies associated with the pair configuration.

It is clear from symmetry that $x_2 = x_3$, $x_5 = x_6$, and $x_7 = x_8$ when no distinction is necessary between the left- and right-hand columns of A's and B's. The ϵ_{AA}, ϵ_{AB}, and ϵ_{BB} are the energies due to atomic interactions excepting the exchange interaction between magnetic spins, and the J is the energy due to the exchange interaction. The probability parameters, of course, meet the requirements

$$\sum_{i=1}^{9} x_i = 1 \text{ and } \sum_{i=1}^{3} y_i = 1.$$

In addition, the following quantities are useful:

$$\left.\begin{aligned} n_A &= y_1+y_2 = x_1+x_2+x_3+x_4+x_6+x_7 \\ n_B &= y_3 = x_5+x_8+x_9 \\ n_{AA} &= x_1+x_2+x_3+x_4 \\ n_{AB} &= x_6+x_7 \\ n_{BA} &= x_5+x_8 \\ n_{BB} &= x_9. \end{aligned}\right\} \quad (A.1)$$

Here, for instance, n_A is the probability of finding an A atom on a lattice point and n_{AB} is that of finding an A–B configuration on a pair of neighboring sites. As the composition of any alloy is fixed, n_A and n_B are given. If one assumes that the system has been quenched from a certain temperature and that the atoms cannot migrate at the temperature of observation, as assumed in the text, the atomic configuration of the crystal is frozen in. This means that the values of n_{AA}, n_{AB}, n_{BA}, and n_{BB} are fixed and only the spin configuration changes with temperature. As an example, consider the case where the crystal has been quenched from a very high temperature. This leads to a random arrangement, hence:

$$\left.\begin{aligned} n_{AA} &= c^2 \\ n_{AB} &= n_{BA} = c(1-c) \\ n_{BB} &= (1-c)^2 \end{aligned}\right\} \quad (A.2)$$

where $c = n_A$ is the concentration of magnetic atoms.

The energy per atom of the alloy system is then given by

$$E/N = zJ\left(\frac{x_2+x_3}{2} - \frac{n_{AA}}{4}\right)+\frac{z}{2}\{\epsilon_{AA}n_{AA}+\epsilon_{AB}(n_{AB}+n_{BA})+\epsilon_{BB}n_{BB}\}-(y_1-y_2)\beta H \quad (A.3)$$

where z is the number of nearest neighbors, β is the magnetic moment of a single A atom, and H is the external magnetic field. The entropy can be obtained from the general formula for the pair approximation of the C–V method[16]

$$S/N = k(z-1)\sum_{i=1}^{3} y_i \ln y_i - \frac{kz}{2}\sum_{i=1}^{9} x_i \ln x_i. \tag{A.4}$$

The Helmholtz free energy, $F = E-TS$, is then minimized with respect to the independent parameters in order to determine the equilibrium state. If there is no division of the lattice into sublattices either from atomic ordering or antiferromagnetic spin ordering, the conditions $x_2 = x_3$, $x_5 = x_6$, and $x_7 = x_8$ hold. The three y_i's are given directly by the six x_i's. The six x_i's satisfy $\sum_{i=1}^{9} x_i = 1$, leaving five variables. The atomic distribution is specified if we specify n_{AA} and n_{AB}. Thus there are three independent variables. These are chosen so that

$$\eta \equiv (x_2+x_3)/2 = x_2 \tag{A.5}$$

gives the variation of the energy and

$$2\beta\xi_1 \equiv (y_1-y_2)\beta \tag{A.6}$$

gives the magnetization per atom. The third parameter

$$2\xi_4 \equiv x_6-x_7 \tag{A.7}$$

gives the relative abundance of + spins over − spins of A atoms which are neighboring to B atoms. Minimizing the free energy with respect to η, ξ_1, and ξ_4 gives

$$\left.\begin{aligned} x_1x_4 &= x_2^2\, e^{2J/kT} \\ (x_1/x_4)^{z/2} &= (y_1/y_2)^{z-1}\, e^{2\beta H/kT} \\ (x_1/x_4) &= (x_6/x_7)^2 \end{aligned}\right\} \tag{A.8}$$

These equations are solved by algebraic transformations. The results are given in the following cases.

I. *The paramagnetic state.* When the external field is zero, there is no long-range spin order, so that $\xi_1 = \xi_4 = 0$ and the energy parameter is given by

$$\eta = \frac{n_{AA}/2}{e^{J/kT}+1}. \tag{A.9}$$

The inverse paramagnetic susceptibility per atom defined as

$$\frac{1}{\chi} = \lim_{H\to 0}\frac{H}{2\beta\xi_1} \tag{A.10}$$

is found by expansion of equations (A.8) in powers of ξ_1 and ξ_4. Thus

$$\frac{1}{\chi} = \frac{kT}{\beta^2}\cdot\frac{n_A-(z-1)(n_{AA}-4\eta)}{n_A(n_A+n_{AA}-4\eta)} \tag{A.11}$$

which, under the conditions of random atomic distribution, equations (A.2), becomes

$$\frac{1}{\chi} = \frac{kT}{c\beta^2}\left[1-\frac{cz(e^{J/kT}-1)}{(1+c)e^{J/kT}+(1-c)}\right]. \tag{A.12}$$

II. *The Curie temperature.* The transition to ferromagnetism can be found by setting $1/\chi = 0$ in equation (A.11). Thus:

$$e^{J/k\Theta} = \frac{(z-1)n_{AA}+n_A}{(z-1)n_{AA}-n_A} \tag{A.13}$$

which under the conditions (A.2) becomes

$$\frac{k\Theta}{J} = \left\{\ln\frac{(z-1)c+1}{(z-1)c-1}\right\}^{-1} \tag{A.14}$$

III. *The ferromagnetic state.* The spontaneous magnetization is conveniently expressed in terms of a parameter t defined by

$$t = \frac{1}{z}\tanh^{-1}\frac{2\xi_1}{n_A}, \tag{A.15}$$

where $2\xi_1/n_A$ is the relative magnetization of the A atoms. Thus the spontaneous magnetization per atom of the crystal σ is given by

$$\sigma = 2\beta\xi_1 = n_A\beta\tanh zt. \tag{A.16}$$

In terms of t, the parameters ξ_4 and η are given by

$$\eta = \frac{n_{AA}/2}{1+e^{J/kT}\cosh 2(z-1)t} \tag{A.17}$$

$$\xi_4 = (n_{AB}/2)\tanh(z-1)t \tag{A.18}$$

where t must satisfy the relation

$$e^{J/kT} = \frac{n_A\tanh zt - n_{AB}\tanh(z-1)t}{\cosh 2(z-1)t\{n_{AA}\tanh 2(z-1)t - n_A\tanh zt + n_{AB}\tanh(z-1)t\}}. \tag{A.19}$$

Note that t does not in general go to infinity as the temperature approaches absolute zero. Thus the magnetization does not saturate in general. For the conditions (A.2) we can write at absolute zero

$$c = \frac{\sinh t \cosh 2(z-1)t}{\sinh(z-1)t \cosh zt}. \qquad \text{(A.20)}$$

The spontaneous magnetization at absolute zero is then obtained by eliminating t from equations (A.16) and (A.20).

IV. *Antiferromagnetism.* To treat antiferromagnetism, consider the simple case of two sublattices. In this case Table A.1 is unchanged except that the left-hand column of the pair configurations represents one sublattice and the right-hand column represents the other sublattice. The value of J is negative. The probabilities of a point are changed to consider y_1, y_2, y_3 as the probabilities of finding an A^+, A^-, or B atom on sublattice I and y_4, y_5, y_6 as the probabilities of finding an A^+, A^-, or B atom on sublattice II.

$$\sum_{i=1}^{3} y_i = \sum_{i=4}^{6} y_i = 1 \qquad \text{(A.21)}$$

The six y_i's are given in terms of the nine x_i's. The conditions $\sum_{i=1}^{9} x_i = 1$ and the symmetry condition $n_{AB} = n_{BA}$ determine two relations between these nine. In addition the specification of the distribution by n_{AA} and n_{AB} reduces the number of independent variables by two more, leaving five independent variables. These are taken as:

$$\eta = (x_2+x_3)/2 \qquad \text{(A.22)}$$

which again is the energy parameter;

$$2\beta\xi_1 = \tfrac{1}{2}(y_1+y_4-y_2-y_5)\beta \qquad \text{(A.23)}$$

gives the magnetization of the total crystal per atom;

$$2\beta\xi_2 = \tfrac{1}{2}(y_1-y_2+y_5-y_4)\beta \qquad \text{(A.24)}$$

gives the difference in magnetization between the two sublattices;

$$4\xi_4 = (x_6+x_5-x_7-x_8) \qquad \text{(A.25)}$$

gives the relative abundance of $+$ spins over $-$ spins of all A atoms which are neighboring to B atoms; and

$$4\xi_5 = (x_5-x_8)+(x_7-x_6) \qquad \text{(A.26)}$$

gives the difference of the same quantity but for the A atoms in each sublattice. The free energy is given by

$$\left.\begin{aligned} F/N = {} & zJ\eta - \frac{zJ}{4}n_{AA} \\ & + \frac{z}{2}n_{AA}\epsilon_{AA} + z\epsilon_{AB}\epsilon_{AB} + \frac{z}{2}n_{BB}\epsilon_{BB} \\ & - 2\beta H\xi + \frac{z}{2}kT \sum_{i=1}^{9} x_i \ln x_i \\ & - \frac{z-1}{2}kT \sum_{i=1}^{6} y_i \ln y_i, \end{aligned}\right\} \qquad \text{(A.27)}$$

where the two in the denominator of the last term appears because

$$\sum_{i=1}^{6} y_i = 2.$$

Minimizing the free energy gives

$$\left.\begin{aligned} x_1x_4 &= x_2x_3\, e^{2J/kT} \\ (x_1/x_4)^{z/2} &= (y_1/y_2 \cdot y_4/y_5)^{(z-1)/2}\, e^{2\beta H/kT} \\ x_1/x_4 &= x_6/x_7 \cdot x_5/x_8 \\ (x_2/x_3)^{z/2} &= (y_1/y_2 \cdot y_5/y_4)^{(z-1)/2} \\ x_2/x_3 &= x_5/x_8 \cdot x_7/x_6. \end{aligned}\right\} \qquad \text{(A.28)}$$

In the paramagnetic state, there is no distinction between the sublattices and the above equations are identical to equations (A.8). The energy parameter and the susceptibility are given by equations (A.9) and (A.12) with negative value of J.

V. *The Néel point.* The Curie point can be found from these equations by expanding in powers of the long-range-order parameters ξ_1 and ξ_4, setting $\xi_2 = \xi_5 = 0$. The Curie point is determined by requiring a solution for the homogeneous equation in the first powers of ξ_1 and ξ_4. This result, of course, agrees with that found before by setting $1/\chi = 0$ in the expression for the paramagnetic susceptibility. The Néel point is similarly found by expanding equations (A.28) in powers of the long-range-order parameters ξ_2 and ξ_5, setting $\xi_1 = \xi_4 = 0$. It is clear from symmetry that these equations lead to identical relations for the Néel and Curie points where J is negative for the one case and positive for the other.

VI. *Antiferromagnetic state.* In the absence of an applied field $\xi_1 = \xi_4 = 0$, as the crystal as a whole has no net moment. The sublattices however are magnetized, each sublattice behaving as the whole crystal does in the ferromagnetic case.

Thus ξ_2, ξ_5, and η are defined in terms of t as before

$$2\xi_2 = n_A \tanh zt \tag{A.29}$$

$$2\xi_5 = n_{AB} \tanh(z-1)t \tag{A.30}$$

$$\eta = \frac{n_{AA}/2}{1+e^{J/kT} \operatorname{sech} 2(z-1)t,} \tag{A.31}$$

where t satisfies the equation

$$e^{-J/kT} = \frac{n_A \tanh zt - n_{AB} \tanh(z-1)t}{\cosh 2(z-1)t\{n_{AA} \tanh 2(z-1)t - n_A \tanh zt + n_{AB} \tanh(z-1)t\}}. \tag{A.32}$$

The initial susceptibility in a direction parallel to the spin alignment can be calculated from equations (A.28), using for ξ_2, ξ_5, and η the values at $H = 0$, expanding in powers of ξ_1 and ξ_4, and calculating

$$\frac{1}{\chi} = \lim_{H \to 0} \frac{H}{2\xi_1 \beta}.$$

The result is

$$\frac{1}{\chi} = \frac{kT}{c\beta^2} \cdot \cosh zt \left\{ \frac{z}{2} \cdot \frac{\sinh 2(z-1)t}{\sinh(z-2)t} - (z-1)\cosh zt \right\} \tag{A.33}$$

where use has been made of equations (A.2) and t is given by equation (A.32).

VII. *The specific heat.* The magnetic part of the energy is given by

$$\frac{E_m}{N} = \frac{zJ}{4}(4\eta - n_{AA}), \tag{A.34}$$

where η is given by equation (A.9) in the paramagnetic state, and by equations (A.17) and (A.31) for the ferromagnetic and antiferromagnetic states, respectively. The energy does not depend on the sign of J. For the paramagnetic state

$$\frac{E_m}{N} = -\frac{zJn_{AA}}{4} \left\{ \frac{1-e^{-J/kT}}{1+e^{-J/kT}} \right\} \tag{A.35}$$

and for either the ferromagnetic or antiferromagnetic state

$$\frac{E_m}{N} = -\frac{z|J|n_{AA}}{4} \left\{ \frac{1-e^{-|J|/kT} \operatorname{sech} 2(z-1)t}{1+e^{-|J|/kT} \operatorname{sech} 2(z-1)t} \right\}. \tag{A.36}$$

Then the magnetic contribution to the specific heat in the paramagnetic state is

$$\frac{C_m}{kN} = \frac{1}{kN} \cdot \frac{dE_m}{dT} = \frac{zn_{AA}}{2} \left(\frac{J}{kT} \right)^2 \frac{e^{-J/kT}}{(1+e^{-J/kT})^2}. \tag{A.37}$$

The specific heat from the co-operative transition is found by combining equations (A.36) and (A.32).

REFERENCES

1. Weiss R. J. and De Marco J. J., *Rev. Mod. Phys.* **30,** 50 (1958).
2. Mott N. F. and Stevens K. W. H., *Phil. Mag.* **2,** 1364 (1957).
3. Lomer W. M. and Marshall W., *Phil. Mag.* **3,** 185 (1958).
4. Arrott A. and Sato H., *Bull. Amer. Phys. Soc.* **3,** 42 (1958).
5. Owen J., Browne M. E., Arp V., and Kip A. F., *J. Phys. Chem. Solids* **2,** 85 (1957).
   Pratt G. W. Jr., *Phys. Rev.* **106,** 53 (1957); **108,** 1233 (1957).
   Schmitt R. W. and Jacobs I. S., *J. Phys. Chem. Solids* **3,** 324 (1957).
   Scheil E. and Wachtel E., *Z. Metallk.* **48,** 571 (1957).
   Yosida K., *Phys. Rev.* **106,** 893 (1957).
   Hart E. W., *Phys. Rev.* **106,** 467 (1957).
6. See, for example, Friedel J., *Advances in Phys.* **3,** 446 (1954).
7. See, for example, Néel L., *Ann. Phys., Paris* **5,** 23 (1936).
8. Fowler R. H. and Guggenheim E. A., *Statistical Thermodynamics*, p. 563. Cambridge University Press (1939).
   Takagi Y., *Proc. Phys.-Math. Soc. Japan* **23,** 553 (1941).
9. Muto T., Eguchi T., and Shibuya M., *J. Phys. Soc. Japan* **3,** 277, 284 (1948).
   Sato H., *Proc. Pittsburgh Conference on Magnetism and Magnetic Materials*, p. 119. American Institute of Electrical Engineers (1955).
10. Bethe H. A., *Proc. Roy. Soc.* A**150,** 89 (1935).
11. Easthope C. E., *Proc. Camb. Phil. Soc.* **33,** 502 (1937).

12. FIRGAU V., *Ann. Phys., Lzg.* **40,** 295 (1941).
13. BEHRINGER R. E., *J. Chem. Phys.* **26,** 1504 (1956).
14. TOMITA K., *Proc. Phys. Soc.* **A68,** 214 (1955).
15. HECHT C. Private communication; to be published in *Physica.*
16. YOSIDA K., *Phys. Rev.* **106,** 893 (1957).
17. KAUFMANN A. R., PAN S. T., and CLARK J. R., *Rev. Mod. Phys.* **17,** 87 (1945).
18. ARROTT A., *Phys. Rev.* **108,** 1394 (1957).
19. TAKAGI Y., *Proc. Phys.-Math. Soc. Japan* **23,** 44 (1941).
20. KIKUCHI R., *Phys. Rev.* **81,** 988 (1951).
KURATA M., KIKUCHI R., and WATARI T., *J. Chem. Phys.* **21,** 434 (1953).
21. TAKAGI Y., *Proc. Phys.-Math. Soc. Japan* **24,** 333 (1942).
LI Y. Y., *Phys. Rev.* 84, 721 (1951).
22. ZIMMERMAN J. E., Private communication; see also *Bull. Amer. Phys. Soc.* **3,** 124 (1958).

VOL
10
195

J. Phys. Chem. Solids Pergamon Press 1959. Vol. 10. pp. 35–43. Printed in Great Britain.

NEUTRON-DIFFRACTION STUDY OF ANTIFERROMAGNETIC $FeTiO_3$ AND ITS SOLID SOLUTIONS WITH α-Fe_2O_3*

G. SHIRANE

Westinghouse Research Laboratories, Pittsburgh, Pennsylvania

S. J. PICKART

Naval Ordnance Laboratory, White Oak, Maryland, and Brookhaven National Laboratory, Upton, New York

R. NATHANS

Pennsylvania State University, University Park, Pennsylvania, and Brookhaven National Laboratory, Upton New York

and

Y. ISHIKAWA

University of Tokyo, Tokyo, Japan

(*Received* 19 *November* 1958)

Abstract—While $FeTiO_3$ and α-Fe_2O_3 are both antiferromagnetic, some solid solutions of the two possess strong magnetic moments which are believed to be related to an ordering of the Fe and Ti atoms. Neutron powder patterns confirm the X-ray picture of $FeTiO_3$ as alternating layers of Fe and Ti along the [111] axis of the rhombohedral cell with intervening oxygen layers, and provide more accurate oxygen parameters. Data taken below the Néel point of 68°K suggest a model for the spin structure in which Fe^{2+} moments are ferromagnetically coupled within a (111) sheet and directed perpendicular to it. Studies on the solid solutions connect the presence of the spontaneous moment with ordering of the Ti and Fe atoms, and show that the spin arrangement in most of these compositions is of the α-Fe_2O_3 type with spins ferromagnetically coupled and lying within (111) sheets. The fact that no long-range ordered spin structure is observed down to 4·2°K for the sample containing 12 per cent hematite can be explained on the basis of an inhomogeneous magnetic structure.

1. INTRODUCTION

In recent years the magnetic properties of the $FeTiO_3$–α-Fe_2O_3 system have received considerable attention because of their importance in rock magnetism.[1–3] Though both the end members of this system are antiferromagnetic, strong magnetization was observed in some compositions on the $FeTiO_3$ side, and its existence was regarded as an important factor in determining the characteristics of the remanent magnetism in various rocks. A study of spin arrangement in this system by neutron diffraction seemed to be of special interest not only for its bearing on rock magnetism, but also for an understanding of magnetic interactions in this type of structure.

Both ilmenite, $FeTiO_3$, and hematite, α-Fe_2O_3, have the rhombohedral structure. α-Fe_2O_3 can be visualized as consisting of layers of Fe atoms in the (111) planes with oxygen layers between them. This is illustrated in Fig. 1, in which the cations *A* and *B* form alternate layers. It should be noticed that these cations are lying slightly above and below the plane of the layer, as shown schematically in Fig. 1(b). The structure of $FeTiO_3$ can be derived from that of α-Fe_2O_3 by replacing every other layer of Fe atoms by a layer of Ti atoms.

* This work was carried out in part at Brookhaven National Laboratory under the auspices of the Atomic Energy Commission and the National Security Agency.

Hematite exhibits a feeble ferromagnetism in addition to the fundamental antiferromagnetism below its Néel point of 950°K. An additional magnetic phase transition at 260°K was believed by NÉEL[4] to be a change of spin direction, which lies in the (111) plane above the transition temperature and along the [111] direction below it. This spin reorientation was confirmed by a neutron-diffraction study of SHULL *et al.*[5] who showed also that the spins are parallel within a given (111) plane and antiparallel between the adjacent planes. This structure may be written schematically as $(+\mathrm{Fe})_A(-\mathrm{Fe})_B(+\mathrm{Fe})_A$----, where A and B represent the different layers shown in Fig. 1.

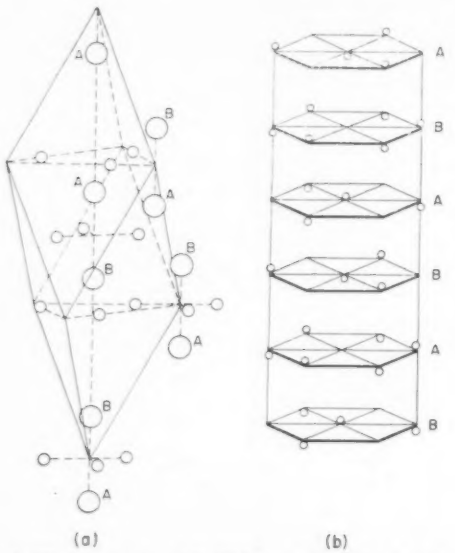

FIG. 1. The structure of $FeTiO_3$ and α-Fe_2O_3, showing (a) the rhombohedral and (b) the hexagonal unit cell. Circle A represents Fe, and B represents Fe in α-Fe_2O_3 and Ti in $FeTiO_3$. In ordered $FeTiO_3$–α-Fe_2O_3 solid solutions, A represents Fe and B represents Fe and Ti. Small circles in (a) are oxygens, which are omitted in (b).

The magnetic properties of ilmenite single crystals have recently been investigated by BIZETTE and TSAI.[6] Their measurements showed that $FeTiO_3$ is antiferromagnetic below a Néel temperature of 68°K and that the spin direction lies along [111]. Two models, which are shown in Fig. 4, have been proposed[3] for the spin arrangement. In one of these models (Fig. 4(c)) the spins are antiferromagnetically coupled within each layer; in the other (Fig. 4(a)) the spins are parallel to each other within a plane, but adjacent planes are antiparallel.

Finally, detailed studies of the magnetic properties of the solid solutions of these materials have been made by several investigators, working with both natural and synthesized compounds.[1,7,8] The Néel temperature of the system decreases almost linearly from 950°K for Fe_2O_3 to 68°K for $FeTiO_3$. Strong ferromagnetic moments were observed in the compositions on the $FeTiO_3$ side (see Fig. 2), and it was suggested that these moments result from a ferrimagnetic spin structure caused by ordering of the Fe and Ti atoms.

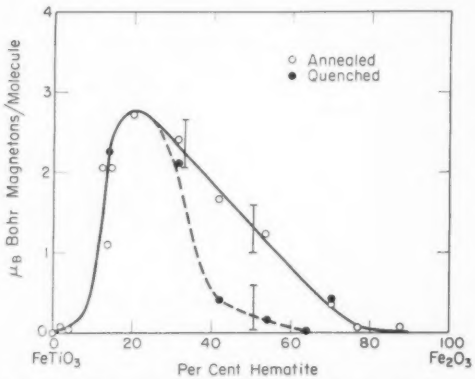

FIG. 2. The saturation moment of $(1-x)$ $FeTiO_3$–(x) Fe_2O_3 as measured by BOZORTH *et al.*[8] The moments estimated on the basis of the ordering parameter S, given by the neutron-diffraction data, are marked by vertical lines.

Additional evidence of this ordering is found in the fact that the magnetic moment of quenched samples was well below that of annealed samples near the composition 50 $FeTiO_3$–50 Fe_2O_3.[7–9]

The neutron measurements were carried out on synthesized powder specimens. Sample preparation consisted of placing the appropriate mixture of $FeTiO_3$ and α-Fe_2O_3 in an evacuated quartz tube (10^{-3} mm Hg) and quenching from 1200°C. Samples were maintained at this high temperature for at least 12 hr before quenching. Further details of the preparation and also the magnetic and electrical properties of the samples can be found in references (7) and (10). In addition to the end members, four solid solutions of varying compositions were prepared for the diffraction studies.

Their chemical composition is known to be within ±2 per cent of the quoted values.

The actual sample of $FeTiO_3$ used had a Néel point of 55°K (from susceptibility measurements), which is somewhat lower than the 68°K reported for the natural crystal. In addition, the prepared sample had a slightly lower resistivity than that found in pure ilmenite,[10] where the observation of a high resistivity indicates the presence of iron in the form of Fe^{2+} and titanium as Ti^{4+}. Chemical analysis of the neutron sample showed it to contain a small amount of hematite (1·5 per cent). While it is not known definitely whether this α-Fe_2O_3 formed a solid solution, the persistence of a rather high resistivity suggests that the amount of Fe^{3+} and Ti^{3+}, if they are at all present, must be quite small. Consequently, in the calculations for $FeTiO_3$ the stoichiometric formula was used, along with the assumption of divalent iron and tetravalent titanium.

2. STRUCTURE OF $FeTiO_3$

The rhombohedral unit cell of $FeTiO_3$ contains two molecular units and the atomic positions can be described by the five parameters given in Table 1. (The parameters for α-Fe_2O_3 are shown in the same table for comparison.) The parameters for $FeTiO_3$ were determined by BARTH and POSNJAK,[11] using natural crystals. The ordering of Fe and Ti required by the space-group was clearly established by the difference in intensities of (210) and (120), which should be equal if Fe and Ti are distributed at random.

However, the small difference in scattering factors of Fe and Ti for X-rays made it difficult to determine whether Fe and Ti are perfectly ordered or not. Neutron intensities, on the other hand, are quite sensitive to this ordering, because of the negative scattering amplitude of Ti ($b = -0{\cdot}38\times10^{-12}$ cm) compared with that of Fe ($b = +0{\cdot}96\times10^{-12}$ cm). Obviously, this situation is considerably more favorable than the X-ray case, even though the powder technique is used for the neutron data.

It should be noted that the oxygen parameters given for $FeTiO_3$ satisfy the requirements of the higher symmetry of $R\bar{3}C$, that is, $y = (\frac{1}{2})-x$ and $z = \frac{1}{4}$, though these are not necessary for $R\bar{3}$.

Table 1. Structural parameters of $FeTiO_3$ and α-Fe_2O_3

The origin is chosen according to BARTH and POSNJAK[11] and differs from other choices,[5,15] including Fig. 1(a), by $(\frac{1}{4}, \frac{1}{4}, \frac{1}{4})$. Improved oxygen parameters obtained by the present work are given in parentheses.

$FeTiO_3$	α-Fe_2O_3
$R\bar{3}$ (C_{3i}^2)	$R\bar{3}C$ (D_{3d}^6)
$a = 5{\cdot}538$ Å $\alpha = 54°41'$	$a = 5{\cdot}424$ Å $\alpha = 55°17'$
2 Fe $\pm(u_1, u_1, u_1)$	4 Fe $\pm(u, u, u)$
2 Ti $\pm(u_2, u_2, u_2)$	$\pm(\frac{1}{2}+u, \frac{1}{2}+u, \frac{1}{2}+u)$
6 O $\pm(x, y, z)$	6 O $\pm(x, \frac{1}{2}-x, \frac{1}{4})$
$u_1 = 0{\cdot}358$	$u = 0{\cdot}355$
$u_2 = 0{\cdot}142$	
$x = 0{\cdot}555$	$x = 0{\cdot}542$ (0·550)
$y = -0{\cdot}055$ (−0·040)	
$z = 0{\cdot}250$ (0·235)	

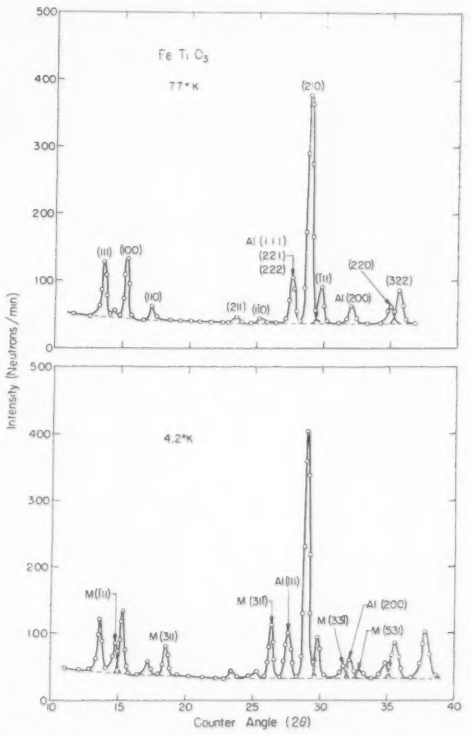

FIG. 3. Neutron-diffraction patterns of $FeTiO_3$ taken above and below the Néel point. The wavelength $\lambda = 1{\cdot}12$ Å.

Table 2. Calculated and observed integrated intensities for $FeTiO_3$, relative to (210)

The data are taken at 4·2°K with a cylindrical sample. Magnetic intensities are calculated by using the scattering amplitude shown in Fig. 5(a).

hkl	Calculated intensities		Observed intensities
	(*a*) $S = 1{\cdot}0$, $x = 0{\cdot}555$, $y = -0{\cdot}055$, $z = 0{\cdot}250$	(*b*) $S = 0{\cdot}95$, $x = 0{\cdot}555$, $y = -0{\cdot}040$, $z = 0{\cdot}235$	
Nuclear			
(111)	231	211	190
(100)	274	218	195
(110)	28	45	44
(211)	19	16	18
(1$\bar{1}$0)	10	10	12
(210)(120)	800	800	800
($\bar{1}$11)	75	112	130
(200)	4	9	< 10
(220)	56	77	64
(322)	135	145	158
Magnetic (double cell)			
(111)		0	< 5
($\bar{1}$11)		73	68
(311)		88	87
(333)		0	< 5
(331)		0	< 5
(31$\bar{1}$)		157	162
(33$\bar{1}$)		29	25
(531)		33	36

Considering the fact that $u_2 = (\frac{1}{2}) - u_1$, which is again the requirement for $R\bar{3}C$, these oxygen parameters imply that Fe and Ti occupy crystallographically equivalent positions and are at the same distance from the surrounding oxygens. Since the ionic radius of Fe^{2+}(0·83 Å) is not identical with that of Ti^{4+}(0·64 Å), different bond distances might have been expected. For this reason, it appeared likely that the oxygen parameters could be improved, although the metal positions have been quite well determined by X-rays. Neutron diffraction can give more accurate oxygen parameters because the scattering amplitude of oxygen ($0{\cdot}58 \times$ $\times 10^{-12}$ cm) is of the same order of magnitude as those of Fe and Ti. A refinement of the crystal structure was carried out in this direction, together with a determination of the magnetic spin arrangement below the Néel point.

Powder data taken on the ilmenite sample at 77 and 4·2°K are plotted in Fig. 3; the nuclear intensities of both runs agree satisfactorily. Calculations were first made from the parameters given by BARTH and POSNJAK,[11] which gave a reasonably good agreement with the observed nuclear intensities (see Table 2(a)). However, a careful comparison of observed and calculated values revealed a systematic difference which suggested that the ordering of Fe and Ti may not be complete. It was also clear at this stage that there was little room for improvement of the metal parameters u_1 and u_2. An attempt was made to improve the agreement between calculated and observed intensities by introducing three oxygen parameters and adjusting S, the ordering parameter. S is defined as the fraction of Ti at $\pm$ (u_2, u_2, u_2), which correspond to the B layer in Fig. 1, and ranges from unity for complete order to one-half for complete disorder. Systematic study led to the following parameters for the best fit:

$S = 0{\cdot}95 \quad x = 0{\cdot}555 \quad y = -0{\cdot}040 \quad z = 0{\cdot}235.$

According to the Goldschmidt radii, the Fe–O and Ti–O distances should be 2·15 and 1·96 Å respectively. The new oxygen parameters give Fe–O distances of 2·15 and 2·03 Å and Ti–O distances of 2·14 and 1·92 Å, and therefore result in more reasonable bond distances than the previous ones. It should be stressed, however, that the small number of reflections available for a determination of the parameters leaves some uncertainty in the final values.

The powder data taken below the Néel temperatures show several lines of magnetic origin in addition to the nuclear scattering (see Fig. 3). Indexing of these lines requires a doubling of the rhombohedral unit cell, and all of the observed lines can be indexed with h, k, and l all odd. Furthermore, no magnetic reflection was observed at (111) of the new unit cell, which implies that the spin direction is along [111], in agreement with the magnetic measurements by BIZETTE and TSAI.[6]

As can be seen in Fig. 1, the arrangement of the metal atoms in $FeTiO_3$ and α-Fe_2O_3 is such that it can be conveniently represented by a hexagonal lattice. Using such a cell for the magnetic structure and transposing the indices to the new representation, one finds that the hexagonal lattice must be doubled only along the main axis and not in the basal plane. The new hexagonal unit cell dimensions are:

$$a = 5{\cdot}09\ \text{Å} \qquad c = 28{\cdot}16\ \text{Å}.$$

The magnetic unit cell then contains 12 Fe atoms distributed in six layers. Among the several possible spin configurations, only the three models shown in Fig. 4(a)–(c) have plausible arrangements. These three are those obtained by considering three possible sequences of sign along the hexagonal axis, i.e. $(+\,-\,-\,+)$, $(+\,+\,-\,-)$, and $(+\,-\,+\,-)$. The spins in model (a) are coupled ferromagnetically within the same layer. On the other hand, the models (b) and (c) have antiparallel spin arrangements within the same layer. The models (a) and (c) correspond to the two models previously proposed, while the model (b) has not yet been considered.

Model (c) can be immediately excluded because it disagrees with the observed doubling of the unit cell. The intensities calculated on the basis of model (b) show poor agreement with the observed values, but satisfactory agreement is obtained with

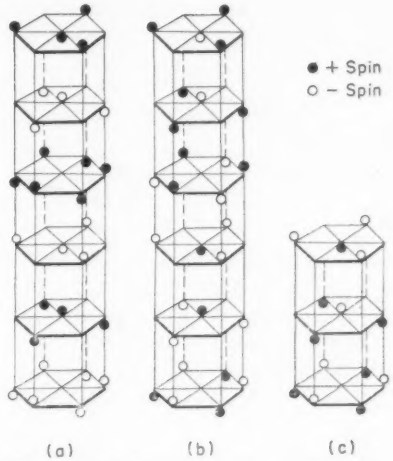

FIG. 4. Three possible magnetic structures for ilmenite, $FeTiO_3$. The Ti layer is omitted (see Fig. 1).

model (a). The calculated intensities are systematically smaller than the observed values, but this discrepancy can be removed by the assumption of orbital contribution to the magnetic moment of Fe^{2+}, as was observed in both FeO[5] and FeF_2.[12] The effect of an orbital contribution is not only to raise the moment value of Fe^{2+}, but to produce a magnetic form factor which falls off less rapidly with Bragg angle than that of Fe^{3+}, which was used

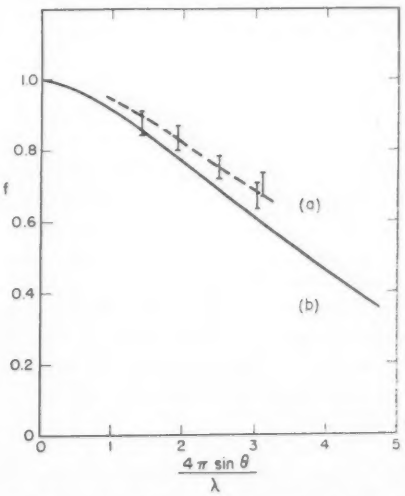

FIG. 5. The magnetic scattering amplitude of (a) Fe^{2+} in $FeTiO_3$, normalized to a value $1{\cdot}08 \times 10^{-12}$ cm and (b) Fe^{3+} in $MgFe_2O_4$,[13] normalized to $1{\cdot}26 \times 10^{-12}$ cm.

in the calculations. Fig. 5 is a plot of the observed magnetic scattering amplitude as a function of $\sin\theta/\lambda$, together with the normalized values for Fe^{3+} obtained by CORLISS *et al.*,[13] in their measurements on $MgFe_2O_4$. The observed and calculated intensities are compared in Table 2, where the magnetic component was calculated by using the amplitude of Fe^{2+} shown by the broken line in Fig. 5.

It should be borne in mind that the lack of complete ordering of the Fe and Ti atoms requires the partial occupation of the Ti layer by Fe, which may have an important bearing on the magnetic ordering of the spins. Although the neutron data can in principle give the average moment on the Ti layer, its contribution to the total magnetic intensity for this small amount of disorder is too small to be evaluated quantitatively.

3. STRUCTURE OF $(1-x)$ $FeTiO_3$–(x) Fe_2O_3

In the solid solutions the two questions that must be answered are the nature of the magnetic spin arrangement and the dependence of the Fe–Ti ordering, or the quantity S, on composition and heat treatment. Four compositions of the solid-solution system $(1-x)$ $FeTiO_3$–(x) Fe_2O_3, with $x = 0{\cdot}12$, $0{\cdot}33$, $0{\cdot}50$ and $0{\cdot}70$, were studied. In addition, a sample of pure α-Fe_2O_3 was investigated in order to verify the spin structure previously reported by SHULL *et al.*[5] The data, taken with somewhat improved resolution, are satisfied by their model. In giving a spin arrangement in α-Fe_2O_3, one should note that the neutron powder data are independent of any specific direction for the spin within the (111) planes. The best agreement for the nuclear intensities was obtained by adjusting the oxygen parameter to 0·550 from the reported value of 0·542.[14]

Room-temperature patterns were taken on all four mixed compounds. In addition, the sample with $x = 0{\cdot}12$ was run at liquid-helium temperature, since the magnetic transition of this compound is below room temperature. In no case was there any evidence of superlattice reflections as found in $FeTiO_3$.

For the sample of composition $x = 0{\cdot}12$, no significant difference could be noted between the room-temperature data and that taken at 4·2°K, although the latter temperature is far below the quoted value of 170°K for the onset of ferromagnetic ordering.[7] The single exception was the presence of broad "humps" in the diffraction pattern near the positions of the (100) and (210) reflections, which are characteristic of short-range ordering (see Fig. 6). The absence of superlattice

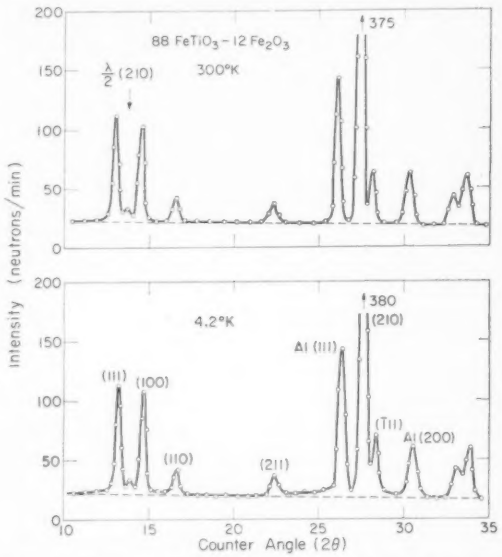

FIG. 6. Neutron-diffraction patterns of 88 $FeTiO_3$–12 Fe_2O_3 at 300 and 4·2°K. $\lambda = 1{\cdot}05$ Å.

reflections and the ordering of Fe and Ti known from the room-temperature data allow only model (c) in Fig. 4, but in that case there would be an appreciable magnetic contribution to the observed intensities for any possible direction of the spin. It may be concluded, therefore, that there is no long-range magnetic order in this compound, at least down to 4·2°K. A discussion of this result, which is somewhat surprising in view of the known ferromagnetic moment, will be deferred until the next section. In order to establish this behavior as not characteristic of the particular sample, a similar composition with $x = 0{\cdot}10$ provided by Dr. R. M. BOZORTH, of the Bell Telephone Laboratories, was also investigated at 77°K and it showed identical results.

The analysis of the compounds for $x > 0{\cdot}33$ is complicated by the large number of parameters to be determined from the relatively few observable lines. Since the data were taken below the Curie temperature, the degree of magnetic saturation

VOL. 10 1959

(σ_{RT}/σ_0) becomes an unknown, as well as S, the ordering parameter. Moreover, the results on $FeTiO_3$ raise the possibility of three oxygen parameters instead of one as in hematite. The data were analyzed in the following manner. Since the magnetic intensities were of the same nature as those found in α-Fe_2O_3 with no additional lines present, a model for the spin arrangement similar to that in hematite was adopted, that is, spins ferromagnetically coupled and lying within the (111) planes with adjacent planes antiparallel. The positional parameters of $FeTiO_3$ were used for compositions with $x < 0{\cdot}5$ and those of α-Fe_2O_3 for $x > 0{\cdot}5$. The

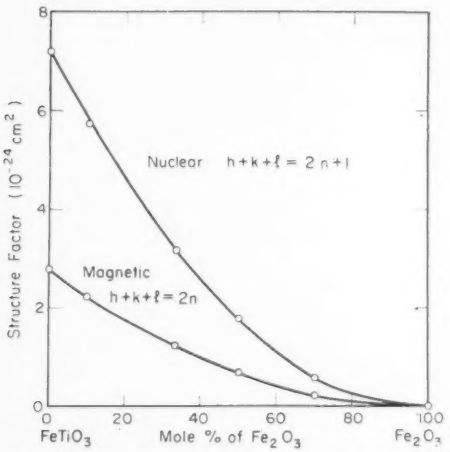

FIG. 7. Nuclear and magnetic structure factors as a function of composition for the perfectly ordered case (per two molecular units). The magnetic structure factors are calculated for $q^2 = 1$ and $f^2 = 0{\cdot}6$ ($\sin\theta/\lambda = 0{\cdot}25$).

order parameter S and the degree of saturation (σ_{RT}/σ_0) were then adjusted to secure the best agreement.

The intensities of the group of reflections with $h+k+l = 2n+1$ are proportional to $(b_A - b_B)^2$, where subscripts A and B refer to the layers shown in Fig. 1 and b_A is the sum of the nuclear scattering amplitude of atoms on the A layer. These intensities are very sensitive to the degree of order, but their absolute value for $S = 1$ decreases rapidly with increasing concentration of α-Fe_2O_3, as shown in Fig. 7. The value of the order parameter giving the best fit for the nuclear intensities in the $x = 0{\cdot}12$ and $0{\cdot}33$ compounds is $S = 0{\cdot}9$. For $x = 0{\cdot}50$, where the accuracy is less, S is found to lie between 0·5 (value for complete disorder) and 0·65. For the composition $x = 0{\cdot}70$ no estimate of the degree of order can be made, but it seems reasonable to assume that it is not greater than for $x = 0{\cdot}50$. It can be summarized that the ordering of Fe and Ti in quenched samples develops only when the concentration of $FeTiO_3$ in the solid solutions exceeds 50 per cent.

As mentioned earlier, the saturation moments of compositions near $x = 0{\cdot}50$ are strongly affected by heat treatment. It was assumed that this was related to an increased ordering of Fe and Ti ions brought about by the annealing. This point was directly tested by neutron diffraction with samples of composition $x = 0{\cdot}50$. After the diffraction data were collected with the quenched sample, the same sample was annealed by cooling slowly (10°/hr)

Table 3. *Calculated and observed integrated intensities for quenched and annealed sample of* 50 *$FeTiO_3$*–50 *Fe_2O_3*

The data are taken at 300°K.

(a) Quenched. Calculated with $S = 0{\cdot}50$ (disorder), $u = 0{\cdot}356$, $x = 0{\cdot}553$, $y = -0{\cdot}053$, $z = 0{\cdot}250$

hkl	Calculated intensities			Observed intensities
	Nuclear	Magnetic	Total	
(111)	0	321	321	321
(100)	0	190	190	176
(110)	132	0	132	125
(211)	250	0	250	234
(1$\bar{1}$0)	46	0	46	35
(210)	837	146	983	1038
($\bar{1}$11)	0	28	28	32

(b) Annealed. Calculated with $S = 0{\cdot}85$, $u = 0{\cdot}356$, $x = 0{\cdot}553$, $y = -0{\cdot}043$, $z = 0{\cdot}240$

hkl	Calculated intensities			Observed intensities
	Nuclear	Magnetic	Total	
(111)	54	321	375	400
(100)	43	190	233	262
(110)	159	2	161	150
(211)	220	7	227	229
(1$\bar{1}$0)	46	4	50	58
(210)	886	146	1032	971
($\bar{1}$11)	35	28	63	66

from 800°C to room temperature.[9] As a result of this heat treatment, the saturation moment at room temperature increased from 4 to 22 e.m.u./g (0·6μ_B per molecule), but no change in lattice constants was observed.

The neutron-diffraction intensities taken with this annealed sample are compared in Table 3 with the data on the same sample in the quenched state. A definite increase in intensity was observed in (100) and ($\bar{1}$11) and, to a lesser extent, in (111). These differences can be accounted for qualitatively by assuming an increased order of Fe and Ti, but better agreement can be obtained if the oxygen parameters are changed from the α-Fe_2O_3 type to the $FeTiO_3$ type, as shown in the table. This result is reasonable, since one might expect the ordering of Fe and Ti to be accompanied by a rearrangement of oxygen positions. Though the increased order ($S = 0{\cdot}85$) and associated change of oxygen parameters are definitely established, the final value of parameters must be taken with some reserve because of the small number of lines available for analysis.

With regard to the magnetic structure, one finds that the magnetic reflections can be divided into two groups:

$$F^2 \sim (p_A - p_B)^2 \text{ for } h+k+l = 2n+1,$$

$$F^2 \sim (p_A + p_B)^2 \text{ for } h+k+l = 2n,$$

where suffixes A and B refer to A and B layers. In the first case, since the spin direction in the B layer is opposite to that of the A layer, $(p_A - p_B)^2 = (|p_A| + |p_B|)^2$, and there arises a large contribution to the intensity which can be established without any difficulty. These reflections, however, do not provide information on how the spins are distributed between A and B layers, and equal intensities are obtained as long as they are parallel within the same layer and the total moment is the same.

The second group of lines with $h+k+l = 2n$ should show how the spins are distributed in A and B layers. However, the intensities of this group are not very strong, as can be seen in Fig. 7, where the most favorable case with $q^2 = 1$ is taken. Moreover, the trigonometric part of the structure factor is not very large for reflections observed in the forward direction (see Table 3(b)). Therefore, it is not possible to draw any conclusion from these lines for compositions with $x \geqslant 0{\cdot}33$. However, the distribution of Ti and Fe atoms in the two layers has already been determined by the nuclear scattering, so that the only remaining ambiguity is how Fe^{3+} and Fe^{2+} are distributed between the two layers.

4. DISCUSSION

In summary, there are in the $FeTiO_3$–α-Fe_2O_3 series two distinct magnetic structures. One of these is that observed in ilmenite and is shown as model (a) in Fig. 4; the other, a modified form of the hematite structure, can be easily visualized from Fig. 1. In this structure one of the layers is occupied mostly by Fe atoms and the other by Ti and Fe atoms; the spins are parallel within the layer and adjacent layers are antiparallel. The amount of order developed between Ti and Fe atoms depends on the fraction of hematite in the sample and, for certain concentrations, on the heat treatment.

Because of the small amount of disorder found in $FeTiO_3$, it is difficult to say very much concerning the type of interactions responsible for the ordering scheme. Li's suggestion[15] that magnetic Ti^{3+} ions in the layer separating the Fe^{2+} are needed to propagate the order would seem to be ruled out, since it predicts a magnetic lattice unlike the one observed. The possible role of the Fe on the Ti layer is unknown, however, and the question also arises as to whether the ordering is stabilized by the slight impurity of hematite present in the sample. These points are best discussed in relation to the phenomena observed in the compound containing 12 per cent hematite.

In spite of the fact that the sample with $x = 0{\cdot}12$ had a measured moment of about 1μ_B/molecule, the neutron data for this composition indicated no long-range magnetic order far below the ferromagnetic Curie point. The explanation for this apparent inconsistency may be sought in the magnetic structure of $FeTiO_3$. The required doubling of the unit cell means that an antiferromagnetic coupling must exist between two widely separated iron layers (at least 4·0 Å apart). If a small amount of Fe on the intervening Ti layer is the means by which the over-all antiferromagnetic order is propagated, one would not expect the addition of slightly more Fe to cause the observed destruction of the long-range order. Rather, if a weak superexchange coupling between the Fe^{2+} ions on

VOL. 10 1959

alternate layers is responsible for the antiferromagnetism, then the introduction of a certain amount of Fe^{3+} on the intermediate Ti layer may quite conceivably alter the Néel point. The much stronger interaction between the Fe^{2+}–Fe^{3+} on adjacent layers will tend to define the spin configuration in the immediate vicinity of an Fe^{3+} ion, thus effectively lowering the number of magnetic neighbors (and the transition temperature) of the $FeTiO_3$ type of ordering. Upon further substitution of Fe^{3+}, a point will be reached where the coupling between neighboring layers is able to produce a short-range order, forming ferrimagnetic clusters which are not sufficient in extent to produce coherent diffraction peaks but can result in an observable over-all moment. Evidence for these clusters is found in the broad "humps" in the low-temperature pattern for $x = 0{\cdot}12$, which occur near the Bragg angles where strong magnetic reflections are observed for the ordered ferrimagnetic structures. This explanation accounts for the initial lowering of the Néel point, for the minimum addition of hematite required before a magnetic moment is observed (nearly 5 per cent according to the magnetic data), and for the subsequent increase in the saturation moment and Curie point with the addition of more iron. The picture of local fluctuations in the magnetic structure has already been used by NÉEL[16] and by GRIMES *et al.*,[17] to explain the magnetic moments and specific heats of solutions of an antiferromagnetic and a ferrimagnetic ferrite.

The distribution in the solid solutions of the Fe^{2+} and Fe^{3+} atoms between the different layers remains unsolved. However, assuming that both valence states are positioned at random on the two layers, and using the neutron values for the ordering parameter S, one can calculate the expected moment. If the Fe^{2+} ions are assumed to be confined to the A layers, the calculated moments become smaller by approximately 10 per cent. The results are compared with the saturation moments measured by BOZORTH *et al.*[8] in Fig. 2. In both cases, the calculated and experimental points agree within the uncertainty of the measurement of S.

Finally, it should be mentioned that the values of σ_{RT}/σ_0 found from the neutron data are in disagreement with those calculated from the magnetic measurements. For the compositions with $x = 0{\cdot}33$ and $0{\cdot}50$, σ_{RT}/σ_0 was found to be $0{\cdot}4$ and $0{\cdot}75$, respectively, while the curves of saturation magnetization versus temperature[7] are nearly linear and yield values of $0{\cdot}3$ and $0{\cdot}5$. The neutron values are more typical of a Brillouin function than the magnetization data. Since the quantity measured by neutron diffraction is $|\sigma_A|+|\sigma_B|$ and the magnetic moment depends on $|\sigma_A|-|\sigma_B|$, a difference in the temperature-dependences of σ_A and σ_B could explain the observed discrepancy. Further study of the temperature-dependence of the magnetic intensities may be desirable to confirm this point.

Acknowledgements—The authors wish to thank Dr. R. M. BOZORTH, of the Bell Telephone Laboratories, for supplying the sample for comparison, and Dr. J. S. KASPER, of the General Electric Research Laboratory, for discussion concerning the parameters found in his unpublished work on the α-Fe_2O_3–Cr_2O_3 system.

REFERENCES

1. NAGATA T., AKIMOTO S., and UYEDA S., *J. Geomagn. Geoelect., Kyoto* **5,** 168 (1953).
   NAGATA T. and AKIMOTO S., *Geofis. Pura Appl., Milano* **34,** 36 (1956).
2. NÉEL L., *Advances in Phys.* **4,** 191 (1955).
3. NICHOLLS G. D., *Advances in Phys.* **4,** 139 (1955).
4. NÉEL L., *Rev. Mod. Phys.* **25,** 58 (1953).
5. SHULL C. G., STRAUSER W. A., and WOLLAN E. O., *Phys. Rev.* **83,** 333 (1951).
6. BIZETTE H. and TSAI B., *C.R. Acad. Sci., Paris* **242,** 2124 (1956).
7. ISHIKAWA Y. and AKIMOTO S., *J. Phys. Soc. Japan* **12,** 834, 1083 (1957).
8. BOZORTH R. M., WALSH D. E., and WILLIAMS A. J., *Phys. Rev.* **108,** 157 (1957).
9. ISHIKAWA Y., *J. Phys. Soc. Japan* **13,** 828 (1958).
10. ISHIKAWA Y., *J. Phys. Soc. Japan* **13,** 37 (1958).
11. BARTH F. W. and POSNJAK E., *Z. Krist.* **88,** 265 (1934).
12. ERICKSON R. A., *Phys. Rev.* **90,** 779 (1953).
13. CORLISS L. M., HASTINGS J. M., and BROCKMAN F. G., *Phys. Rev.* **90,** 1013 (1953).
14. WYCKOFF R. W. G., *Crystal Structures* Vol. I. Interscience Publishers, New York (1948).
15. LI Y. Y., *Phys. Rev.* **102,** 1015 (1956).
16. NÉEL L., *C.R. Acad. Sci., Paris* **230,** 375 (1950).
17. GRIMES D. M., LEGVOLD S., and WESTRUM E. F., Jr., *Phys. Rev.* **106,** 866 (1957).

J. Phys. Chem. Solids Pergamon Press 1959. Vol. 10. pp. 44–46. Printed in Great Britain.

ANTIFERROMAGNETIC GROUND STATE

JOHN C. FISHER

General Electric Research Laboratory, Schenectady, New York

(*Received* 8 *December* 1958)

Abstract—The ground-state wave function for an antiferromagnetic spin array, corresponding to the Hamiltonian $H = J\Sigma$ (neighbors) $S_i \cdot S_j$, has been approximated by a simple linear combination of those basis vectors that can be derived from the idealized Néel ground state by transferring a few spin deviations between neighboring spins. The resulting wave function is very nearly an eigenfunction of H, the corresponding energy is $\lambda_0 = -[1+(2ZS-1)^{-1}]\,JZNS^2/2$, and the fractional spin alignment is $\theta = 1-ZS/(2ZS-1)^2$. The energy is very close to that given by the spin-wave approximation, but the fractional spin alignment lies about halfway between the spin-wave value and unity.

VOL.
10
1959

THEORETICAL investigations of antiferromagnetism usually are based upon a model in which spins S are placed in a periodic array and are assumed to interact through a Hamiltonian of the form

$$H = J\,\Sigma\,(\text{neighbors})\boldsymbol{S}_i \cdot \boldsymbol{S}_j$$

where the sum runs over all nearest-neighbor pairs. The simplest periodic arrays are those that can be divided into two equivalent sublattices, each spin on one sublattice having as neighbors Z spins on the other. The linear chain, square net, simple cubic, and body-centered cubic arrays are examples with $Z = 2$, 4, 6 and 8 respectively. ANDERSON[1] has shown that the ground-state energy of such a ferromagnet must lie between $-JZS^2/2$ and $-(1+1/ZS)JZS^2/2$ per spin, a range of only 5 per cent for MnF_2, where $Z = 8$, $S = 5/2$. The upper bound $-JZS^2/2$ corresponds to the wave function $|\text{Néel}\rangle$ in which $S_z = +S$ for all spins on one sublattice, and $S_z = -S$ for all spins on the other. It is not an eigenfunction of H.

By a spin-wave treatment, ANDERSON[2] has shown that for two- and three-dimensional arrays of spins, the ground-state wave function resembles $|\text{Néel}\rangle$ in that long-range order exists with $\langle S_z\rangle_{\text{av}} = +\alpha S$ for the average spin component on one sublattice and $\langle S_z\rangle_{\text{av}} = -\alpha S$ on the other, with $\alpha \approx (1-1/2ZS)$. (There is no long-range order in the linear chain, either in the spin-wave approximation or in the exact ground-state wave function.[2–4] There is little doubt that the spin-wave treatment gives a good approximation to the ground-state energy of an antiferromagnet, but it is likely that the average spin component on a sublattice is known with less precision. My purpose here is to check the results of the spin-wave treatment by another method, and in particular to try to improve the estimate of the average spin component on a sublattice.

Each spin can be represented by a vector with $2S+1$ components, corresponding to $n = S+ -S_z = 0, 1, 2, \ldots, 2S$; and being a linear combination of the single-spin basis vectors $|0\rangle$, $|1\rangle$, ..., $|n\rangle$, ..., $|2S\rangle$ labelled by the spin-deviation quantum number, n. The basis vectors for a set of N spins can be constructed by taking the direct product of one single-spin basis vector for each spin. There are $(2S+1)^N$ such N-spin basis vectors in all. They can be classified as follows:

Class 0: The vector $|\text{Néel}\rangle$ where for all spins $n = 0$ on one sublattice, $n = 2S$ on the other.

Class 1: All the vectors that can be derived from class 0 by transferring a spin deviation from one site to a neighboring site.

Class 2: All the new vectors that can be derived from class 1 by transferring a spin deviation between neighboring sites.

. . .

Class m: All the new vectors that can be derived from class m–1 by transferring a spin deviation between neighboring sites.

Now consider a trial wave function made up of all the vectors from classes m in the range $a \leqslant m \leqslant b$ with all vectors in a given class having the common coefficient C_m. If a, b, and the C_m are treated as variational parameters, a fairly good approximation to the ground-state wave function should be obtained. In fact, the zero'th order choice of the single vector $|\text{Néel}\rangle$ in class 0 already gives a reasonable approximation to the ground-state energy.

Symbolically, the trial function is

$$|N\rangle = \sum_{m=a}^{b} (-1)^m C_m \sum_{i=1}^{n_m} |N_{mi}\rangle,$$

n_m being the number of basis vectors $|N_{mi}\rangle$ in the class m. The square of the length of $|N\rangle$ is

$$\langle N|N\rangle = \sum_{m=a}^{b} C_m{}^2 n_m.$$

It is reasonable to expect that each class of basis vectors in the optimum range $a \leqslant m \leqslant b$ will contribute essentially equally to $\langle N|N\rangle$, and that vectors belonging to classes well beyond these limits will contribute relatively little. In line with this expectation, the C_m's are removed from consideration as variational parameters by fixing them to satisfy the relationship

$$C_m{}^2 n_m (b-a) = 1.$$

This choice of C_m normalizes $|N\rangle$ and gives each class of vectors the same weight. The only remaining parameters are the class bounds a and b.

The Hamiltonian operator can be rewritten

$$\boldsymbol{H} = J \,\Sigma\,(\text{neighbors})[\tfrac{1}{2}(\boldsymbol{S}_i{}^+\boldsymbol{S}_j{}^- + \boldsymbol{S}_i{}^-\boldsymbol{S}_j{}^+) + \boldsymbol{S}_{iz}\boldsymbol{S}_{jz}]$$

where

$$\boldsymbol{S}_i{}^+ = \boldsymbol{S}_{ix} + i\boldsymbol{S}_{iy},\ \boldsymbol{S}_i{}^- = \boldsymbol{S}_{ix} - i\boldsymbol{S}_{iy}.$$

In a representation in which the spin-deviation operator $\boldsymbol{n}_i$ is diagonal, the non-vanishing matrix elements of $\mathbf{S}_i{}^+$, $\mathbf{S}_i{}^-$, $\mathbf{S}_{iz}$ are

$$\langle n_i|\boldsymbol{S}_i{}^+|n_i+1\rangle = (n_i+1)^{\frac{1}{2}}(2S-n_i)^{\frac{1}{2}}$$
$$\langle n_i+1|\boldsymbol{S}_i{}^-|n_i\rangle = (n_i+1)^{\frac{1}{2}}(2S-n_i)^{\frac{1}{2}}$$
$$\langle n_i|\boldsymbol{S}_{iz}|n_i\rangle = S-n_i.$$

The N-spin matrices for $\boldsymbol{S}_i{}^+$, $\boldsymbol{S}_i{}^-$, $\boldsymbol{S}_{iz}$ have this form with respect to n_i, but they are diagonal with respect to the n_j for other spins: they are direct products of the above matrices and $N-1$ unit matrices.

When $\boldsymbol{H}$ operates upon a many-spin basis vector, each $\boldsymbol{S}_i{}^-\boldsymbol{S}_j{}^+$ transfers a spin deviation from spin j to spin i, or multiplies by zero if $n_i = 2S$ or $n_j = 0$. Consider the result of operating with $\boldsymbol{H}$ upon a vector in the class m, with $m \ll ZN/2$, so that interference between transfers can be neglected:

(a) Each of the m spin deviations that have been transferred between neighbors can be transferred back. By this process the action of $\boldsymbol{H}$ generates m vectors of class $m-1$, each multiplied by JS.

(b) A new spin deviation can be transferred between each of $ZN/2$ possible pairs, generating $ZN/2$ vectors of class $m+1$, each multiplied by JS.

(c) For pairs of neighbors neither of which has participated in a spin-deviation transfer, the $\boldsymbol{S}_{iz}\boldsymbol{S}_{jz}$ portion of $\boldsymbol{H}$ multiplies the vector under consideration by the factor $-JS^2$. $[ZN/2-(2Z+-1)m]$ such pairs together contribute the factor $-[ZN/2-(2Z-1)m]JS^2$. The approximately m pairs of neighbors between which a spin deviation has been transferred contribute the factor $-mJ(S-1)^2$. The approximately $(2Z-2)m$ pairs of which one has and the other has not transferred a spin deviation contribute the factor $-(2Z+-2)mJS(S-1)$. The overall factor is the sum of these three, $-JZNS^2/2+J(2ZS-1)m$.

When $\boldsymbol{H}$ acts upon the sum of all the vectors in class m, the result is the sum of three terms, one related to each of the above paragraphs (a)–(c). Paragraph (a) shows that each of the n_m vectors produces m vectors of class $m-1$, a total of mn_m vectors. Class $m-1$ contains n_{m-1} vectors, so that each is reproduced mn_m/n_{m-1} times. Each of these times it is multiplied by JS, so that each $|N_{m-1,\,i}\rangle$ is multiplied by $JSmn_m/n_{m-1}$ in total. Similarly, each $|N_{mi}\rangle$ is multiplied by $[-JZNS^2/2+ +J(2ZS-1)m]$ and each $|N_{m+1,\,i}\rangle$ by $JSZNn_m/2n_{m+1}$. Symbolically,

$$\boldsymbol{H}\sum_{i=1}^{n_m}|N_{mi}\rangle = [JSmn_m/n_{m-1}]\sum_{i=1}^{n_{m-1}}|N_{m-1,\,i}\rangle +$$
$$+[-JZNS^2/2+J(2ZS-1)m]\sum_{i=1}^{n_m}|N_{mi}\rangle +$$

$$+[JSZNn_m/2n_{m+1}]\sum_{i=1}^{n_{m+1}}|N_{m+1,i}\rangle.$$

Multiplying both sides of this expression by $(-1)^m C_m$ and summing over m, the result is:

$$H|N\rangle=\sum_{m=a}^{b}(-1)^m C_m\sum_{i=1}^{n_m}H|N_{mi}\rangle$$

$$=\sum_{m=a}^{b}(-1)^m C_m\lambda_m\sum_{i=1}^{n_m}|N_{mi}\rangle$$

where

$$\lambda_m=-JSmC_{m+1}n_{m+1}/C_m n_m-JZNS^2/2+$$
$$+J(2ZS-1)m-JSZNC_{m-1}n_{m-1}/2C_m n_m,$$

save for the vectors in classes a and b which are incorrectly counted. However, since $|N\rangle$ contains many classes with equal weight, an incorrect count for two of them can be neglected.

When m is small, the number of vectors in class m is $n_m=(ZN/2)!/(ZN/2-m)!m!$, since each of m transfers of a spin deviation can occur between any of $ZN/2$ pairs. The corresponding ratio of n_{m-1} to n_m is $ZN/2m$. This fact, together with the normalization condition $C_m^2 n_m(b-a)=1$, can be used to simplify the expression for λ_m:

$$\lambda_m=-JZNS^2/2+J(2ZS-1)m-JS(2ZNm)^{\frac{1}{2}}.$$

If λ_m were independent of m, it could be factored out of the sum in the expression for $H|N\rangle$, giving

$$H|N\rangle=\lambda|N\rangle.$$

When $d\lambda_m/dm=0$, this condition is fulfilled, $|N\rangle$ approximates the ground-state wave function of H, and λ approximates the ground-state energy. The class bounds a and b have disappeared as variational parameters, it being required only that they contain the values of m for which $d\lambda_m/dm\approx 0$.

The value of m that minimizes λ_m is

$$m/N=ZS^2/2(2ZS-1)^2,$$

and the corresponding ground-state energy is

$$\lambda_0=-[1+(2ZS-1)^{-1}]JZNS^2/2.$$

The total z-component of spin on a sublattice is $S_{z\text{ total}}=(N/2)[S(1-2m/N)+(S-1)2m/N]$, and the fractional alignment θ is $S_{z\text{ total}}/(NS/2)$,

$$\theta=1-ZS/(2ZS-1)^2.$$

WALKER[5] has obtained identical expressions for λ_0 and θ by second-order perturbation theory, starting from the Néel ground state and treating the $J\Sigma$ (neighbors) $(\mathbf{S}_{xi}\mathbf{S}_{xj}+\mathbf{S}_{yi}\mathbf{S}_{yj})$ part of the Hamiltonian as the perturbation. The perturbation method is simpler, but does not reveal so closely the nature of the ground state.

For MnF_2, where $z=8$, $S=5/2$, these values are

$$m/N=0{\cdot}0164,$$
$$\lambda_0=-1{\cdot}026\,JZNS^2/2,$$
$$\theta=0{\cdot}987.$$

The agreement with ANDERSON's values for the energy is not bad. He gives factors 1·025 and 1·039, which are to be compared with the factor 1·026 obtained here. The agreement is not so good with respect to the fractional alignment of spin, where ANDERSON gets 0·969 in comparison with 0·987 here. On the other hand the agreement with experiment is improved as shown by JACCARINO's[6] experimental result $0{\cdot}98\leqslant\theta\leqslant 1{\cdot}03$, where the limits on θ are the extreme values of the experimental uncertainty.

The expressions for m/N, λ_0, and θ were derived by assuming long-range order in advance, so they cannot apply to the linear chain. The method depends also upon the smallness of m/N, which is essentially the smallness of $1/2Z$. This quantity appears to be sufficiently small for $Z\geqslant 6$ to make the expressions for λ_0 and θ reliable for three-dimensional spin arrays.

Acknowledgements—I wish to thank W. A. HARRISON, E. W. HART, V. HEINE, and T. O. WOODRUFF for valuable discussion.

REFERENCES

1. ANDERSON P. W., *Phys. Rev.* **83,** 1260 (1951).
2. ANDERSON P. W., *Phys. Rev.* **86,** 694 (1952).
3. BETHE H. A., *Z. Phys.* **21,** 205 (1931).
4. HULTHÉN L., *Ark. Mat. Astr. Fys.* **26A,** No. 1 (1938).
5. WALKER L. R. Private communication.
6. JACCARINO V. Private communication.

J. Phys. Chem. Solids Pergamon Press 1959. Vol. 10. pp. 47–51. Printed in Great Britain.

INFRARED ABSORPTION IN ZINC OXIDE CRYSTALS

D. G. THOMAS

Bell Telephone Laboratories, Inc., Murray Hill, New Jersey

(*Received* 6 *November* 1958)

VOL. 10 1959

Abstract—Optical absorption in the 1–12 μ region has been observed in single crystals of ZnO at 300 and 78°K. Lattice bands are observed at 10·1 and 11·5 μ at 300°K. It is likely that impurities also cause some absorption. Strong absorption can arise from the presence of free electrons, and by using crystals doped with lithium or indium this absorption has been measured as a function of electron concentration and wavelength. At constant wavelength the absorption is proportional to the electron concentration, and for $\lambda < 6$ μ at constant electron concentration, the absorption varies as λ^3.

1. INTRODUCTION

PURE zinc oxide is transparent in the visible region. Intrinsic ionization of the lattice occurs in the near ultraviolet region. This paper reports absorption of light in single crystals of ZnO in the 1–12 μ region of the spectrum, which will be shown to be caused by free carriers, lattice vibration bands, and probably by photo-ionization of impurities. TOLKSDORF[1] has observed absorption in the 2–22 μ region, using powdered ZnO. Her results were interpreted on the basis of an analysis of the possible vibration modes of the lattice. However it is now felt that other absorption mechanisms should have been considered.

2. EXPERIMENTAL

Optical transmission measurements were made on single crystals of ZnO. One crystal was obtained from commercial sources and was optically polished on two sides, but most measurements were made with crystals in the form of thin ribbons, grown in these laboratories. In these the use of a polarizing microscope shows that the six-fold C axis lies in the plane of the ribbon and at an angle of about 5° to the length of the ribbon. Unpolarized light was used, since a few experiments with polarized light showed that any anisotropy in the absorption coefficient amounted to less than 5 per cent. The ribbons were about 3×10^{-2} cm across, 1 cm long, and 5×10^{-3} cm thick. The thickness was measured directly with a microscope and was uniform over the crystal to within about 20 per cent, the average values being taken for the crystals used. The ribbons were not polished, as their surfaces were almost optically perfect when grown.

Transmission at normal incidence was measured by the crystal-in–crystal-out technique in conjunction with a Perkin–Elmer double monochromator equipped with a NaCl prism and a thermocouple as a detector. Slits of 0·5 mm were generally used, giving a resolution better than 0·13 μ. An image of the slit was focussed onto the crystal outside the monochromator. The radiation transmitted by the crystal was then focussed onto the thermocouple. The crystal was mounted on a holder illustrated in Fig. 1. There are two slots which open and close together as an adjusting screw is turned. A mask covers the two slots and over one slot on this mask the crystal is mounted. This holder is mounted so that it can be slid between two stops which are adjusted so that either the crystal slot or the blank slot is in the beam. The slots were of almost identical size, and slight differences were allowed for by measuring the beam intensity through the two slots when neither was covered with a crystal. The adjusting screw allowed the maximum area of the crystal to be exposed. The different masks allowed different crystal lengths to be exposed; either 6- or 8-mm lengths were employed. For measurements near 78°K a metal Dewar with NaCl windows was used. The crystal was stuck to a metal mask which was in contact with copper at 78°K. A radiation shield

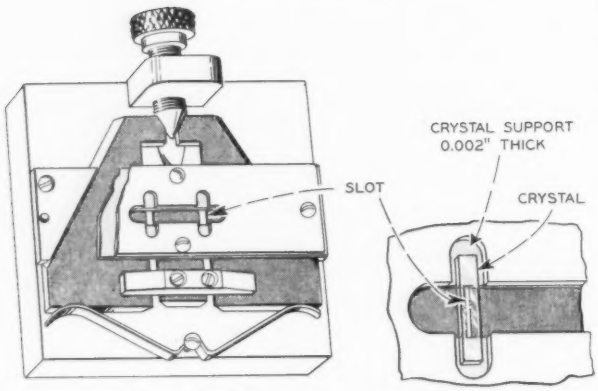

FIG. 1. Crystal holder used at 300°K.

with two holes for the light beam surrounded the crystal. A crystal was first observed at room temperature, then put in the Dewar and the transmission remeasured at the same temperature. In this way the system was calibrated and absolute transmission measurements made. Because this method is somewhat indirect, the results are not as precise as those taken at room temperature.

The absorption coefficient, α, was determined from the transmission data as follows. FAN[2] gives:

$$T = \frac{I}{I_0} = \frac{(1-R)^2}{e^{\alpha x} - R^2 e^{-\alpha x}} \qquad (1)$$

for $\alpha < 10^3\ \text{cm}^{-1}$. Here T is the transmission, I_0 the intensity of the incident beam, I that of the transmitted beam, R the reflectivity from one surface, and x the crystal thickness. This equation allows for reflection from the front and back crystal surfaces as well as for absorption. The reflectivity is given by:

$$R = \frac{(n-1)^2 + k^2}{(n+1)^2 + k^2}, \qquad (2)$$

where n is the refractive index and k the extinction coefficient. For $\alpha < 10^3\ \text{cm}^{-1}$, $k^2 < 1$ and so, in the wavelength region considered, is negligible in equation (2). MOLLWO[3] has determined the refractive index of ZnO as a function of wavelength by using a crystal as a prism and determining the angle of minimum deviation. In the region of interest it is 2·0, and is not altered by the absorption for $\alpha < 10^3\ \text{cm}^{-1}$.

Hence by using equation (1), α may be determined for any T value. It was found useful to calculate a graph of T versus αx. If $\alpha = 0$ there are only reflectivity losses and $T = 0{\cdot}80$. The observed T values in the visible spectral region fell within about 5 per cent of this value, indicating quite high perfection of the surfaces.

The crystals as grown have, at room temperature, electron concentrations in the range 10^{16}–10^{17}/cc. This may be reduced several orders of magnitude by coating the crystal with a dilute solution of LiOH and heating in air for 1 hr near 800°C. The lithium diffuses into the crystal and in substitutional sites becomes an electron acceptor. The electron concentration is increased by diffusing in indium by the technique already described.[4] Equilibrium was achieved at any particular doping temperature, so that the electron concentration was the same throughout the crystal. The optical quality of the crystal surfaces remained almost unchanged before and after doping providing that sufficiently dilute solutions of the doping agents were used.

The conductivity and Hall effect of the crystals were measured at room temperature in a holder in which two wires pressed against the opposite edges of the crystal and formed Hall contacts while current passed along the crystal. A calibrated permanent magnet and a Kintel microvoltmeter were used for observation of the Hall effect. The electron concentration n was derived from the relation:

$$R_H = \frac{3\pi}{8}\frac{1}{ne} \qquad (3)$$

where R_H is the Hall coefficient and e the electron charge. However, it is by no means certain that the factor $3\pi/8$ is applicable over the whole range studied, as the scattering mechanism may not remain constant.

3. RESULTS

(a) *Room temperature*

Most results were obtained at room temperature with the crystals surrounded by air. A lithium-doped crystal virtually free of conduction electrons showed no absorption between the intrinsic absorption near 0·4 μ and lattice absorption bands in the infrared with peaks at 10·1 and 11·5 μ as shown by crystal 3 in Fig. 2. These lattice bands

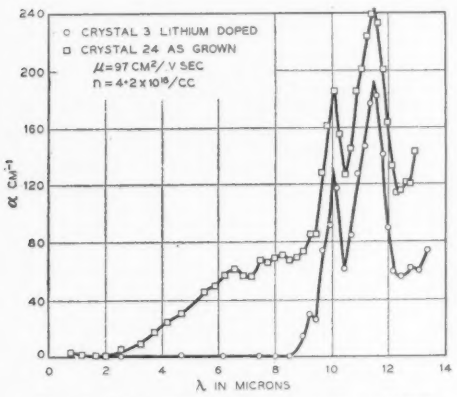

FIG. 2. Absorption in ZnO crystals at 300°K.

were observed in all crystals in which they were not masked by free-carrier absorption. At longer wavelengths much stronger lattice absorption occurs.[5] Fig. 2 also shows the results for crystal 24, which was undoped. Absorption is appreciable and increasing beyond 2 μ, but there are small maxima and minima before the lattice bands are reached.

Fig. 3 shows the results obtained with four crystals doped to different electron concentrations with indium. The logarithm of the absorption coefficient is plotted against the logarithm of the wavelength, and it can be seen that over an appreciable range α varies approximately as λ^3, the maxima and minima no longer being present. The slopes of the straight lines are indicated in the figure. The irregularities at the small α values arise

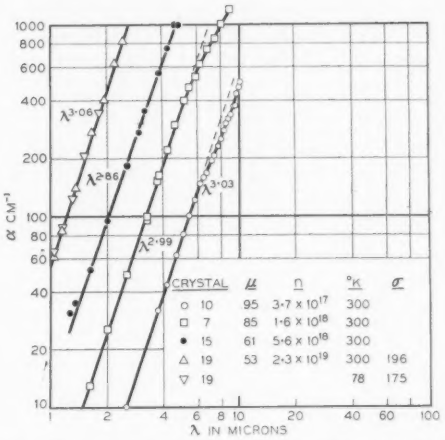

FIG. 3. Free carrier absorption in ZnO for crystals with different electron concentrations. The wavelength-dependence of the absorption is indicated for the linear sections. Notice that crystal 19 was observed at 78°K as well as at 300°K.

from experimental inaccuracies. Lattice absorption can be detected in crystal 10 near 9 μ, but it could not cause the deviation from a straight line which begins near 6 μ. Absorption in crystal 7 containing more electrons could only be followed to 9 μ, and it too showed a deviation from linear behavior near 6 μ. Crystals 15 and 19 could only be observed in the linear region.

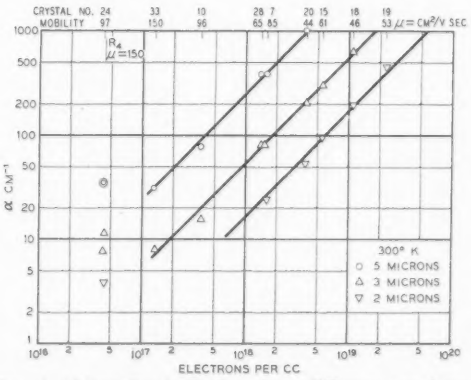
CRYSTAL NO. 24 33 10 28 7 20 15 18 19
MOBILITY 97 150 96 65 85 44 61 46 53 μ = CM²/V SEC
R4 μ=150
α CM⁻¹
300° K
○ 5 MICRONS
△ 3 MICRONS
▽ 2 MICRONS
ELECTRONS PER CC

FIG. 4. Absorption in ZnO at three different wavelengths as a function of electron concentration. The lines drawn have slopes of 45°. Notice the deviation from the lines at low electron concentration. All crystals were doped to equilibrium values with indium except crystals 24 and R4, which were used as-grown. Crystals 20 and 28 contain precipitated indium (see reference 4).

In Fig. 4 the logarithm of α at various wavelengths is plotted against the logarithm of the electron concentration, for several crystals. The electron mobility of the crystals is also tabulated. The lines drawn all have a slope of 45°, which is expected if α is proportional to n. Most of the points fall near these lines except at low electron concentrations, where the absorption is higher than expected. It is, however, in this region where irregularities show in the curves and the λ^3 relation is not obeyed.

(b) *Low temperature*

Crystal 19 was studied near 78°K with results shown in Fig. 3. The behavior is almost identical

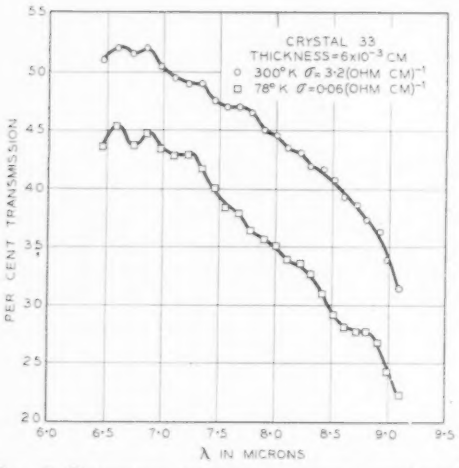

FIG. 5. Percentage transmission versus wavelength at 300 and 78°K. Crystal No. 33, undoped.

to that at room temperature. At this high electron concentration the conductivity is practically independent of temperature ($\sigma_{300°K} = 185(\Omega\ \text{cm})^{-1}$; $\sigma_{78°K} = 175(\Omega\ \text{cm})^{-1}$) because the shallow donor states merge into the conduction band, and the mobility does not change as the temperature is lowered.

Fig. 5 illustrates the behavior of an undoped crystal at room temperature and at 78°K. Because the absolute accuracy at 78°K is not very high, the percentage transmission is plotted against wavelength over part of the observed wavelength interval. At 300°K the conductivity is 3·2 $(\Omega\ \text{cm})^{-1}$ and at 78°K 0·06 $(\Omega\ \text{cm})^{-1}$, so that cooling lowered the electron concentration by nearly a factor of 100. However the absorption is stronger at low than at high temperature. Clearly, therefore, there is another mechanism of absorption besides that provided by free carriers. Probably this consists of excitation of electrons from states within a few tenths of an electron volt from the conduction band. There may be a variety of such states arising from various imperfections in the crystal. This explanation is in accord with the presence of irregularities in the absorption, which become somewhat more marked at low temperatures. However, further work is necessary to confirm this view. The irregularities cannot be explained in terms of interference effects. It may be pointed out that absorption due to excitation of bound electrons which is stronger than that due to free electrons has been observed before in n-type silicon.[6]

4. DISCUSSION

In the wavelength range examined, two lattice bands were observed as noted above. These are probably subsidiary bands of the main *restrahlen* peak near 24 μ.[5] The irregularities in the absorption of crystals containing 10^{16}–10^{17} electrons/cm^3 are not due to lattice bands, but are probably due to excitation of electrons out of bound states. If the crystal is doped with lithium, no absorption occurs, as shown in Fig. 2. Lithium introduces a level probably below the center of the gap[7] and so removes electrons not only from the conduction band but also from states near it. Excitation from lithium states to the conduction band has not yet been observed.

It may be concluded that the absorption observed in crystals with an electron concentration greater than about 5×10^{17}/cm^3 is to be ascribed to free electrons. At lower electron concentrations lattice bands or bound states play a prominent role in the absorption. The characteristics of the free-carrier absorption in the range studied may be summarized as follows:

(*a*) The absorption coefficient, α, varies approximately as λ^3 for wavelengths shorter than about 5 μ; at longer wavelengths the dependence becomes less steep.

(*b*) At a fixed wavelength α varies directly with the electron concentration.

(*c*) Although the Hall mobility values show considerable variation among the doped crystals

there is no apparent correlation of this variation with the α values.

ARNETH,[8] in a recent paper concerned with infrared absorption in ZnO, has reported that at 4 μ the absorption varies linearly with conductivity, in approximate agreement with conclusion (*b*) above. Lattice absorption peaks at 10·1 and 11·5 μ were also observed.

The electric field of electromagnetic radiation causes free electrons to accelerate. Absorption occurs when energy is lost by collisions between the electrons and irregularities in the host lattice. If the frequency of the oscillating electric vector, $\omega/2\pi$, is greater than $1/\tau$, the reciprocal of the relaxation time for electron collisions, then the loss of energy becomes less efficient with increasing frequency, and so α will decrease with increasing frequency.

FAN[2] has given an account of free carrier absorption. If $(\omega\tau)^2 > 1$ and if the electrons are scattered by ionized impurity centers, α is expected to vary as $\lambda^{3\cdot5}$, whereas if lattice vibrations predominate in the scattering, α should vary as $\lambda^{1\cdot5}$. In ZnO for $\lambda < 6\ \mu$ a λ^3 relation is obeyed, which is suggestive of impurity scattering, and at the impurity concentrations used previous work[4] has shown that impurities do affect the Hall mobility. However, the impurity-scattering theory is clearly not adequate, for if it were, α at a fixed wavelength should depend on n^2, where n is the electron concentration, since for every electron there is an ionized impurity center. Further theoretical work is necessary to account for the results, and this may take into account the screening of the scattering centers by the free electrons.

If $(\omega\tau)^2$ is not greater than unity, different relations are expected. τ may be estimated from the mobility by using the expression:[9]

$$\mu = \frac{e\tau}{m^*300}\ \text{cm}^2/\text{V sec}$$

where m^* is the effective electron mass. Using the approximate values $\mu = 100\ \text{cm}^2/\text{V sec}$ and $m^* \approx 0{\cdot}07m$,[5] we find $\tau \approx 4\times10^{-15}$ sec. The applicability of this relaxation time obtained from d.c. measurements of mobility may be questioned when frequencies greater than the *restrahlen* frequency are employed; nevertheless it is interesting to note that, if this figure is accepted, at 6 μ $\omega\tau \approx 1{\cdot}2$. It is perhaps not surprising, therefore, that in this region the wavelength-dependence of α changes.

Acknowledgements—Thanks are due to E. A. SADOWSKI for doping the crystals and measuring the Hall effect. The author benefited from conversations with R. J. COLLINS.

REFERENCES

1. TOLKSDORF S., *Z. phys. Chem.* **132,** 161 (1928).
2. FAN H. Y., *Rep. Progr. Phys.* **19,** 107 (1956).
3. MOLLWO E., *Reichsber. Phys.* **1,** 1 (1944).
4. THOMAS D. G., *J. Phys. Chem. Solids* **9,** 31 (1959).
5. COLLINS R. J. To be published.
6. SPITZER W. G. and FAN H. Y., *Phys. Rev.* **108,** 268 (1957).
7. LANDER J. J. To be published.
8. ARNETH R., *Naturwissenschaften* **45,** 282 (1958); see also BOGNER G. and MOLLWO E., *J. Phys. Chem. Solids* **6,** 136 (1958).
9. SHOCKLEY W., *Electrons and Holes in Semiconductors*. D. Van Nostrand, New York (1950).

J. Phys. Chem. Solids Pergamon Press 1959. Vol. 10. pp. 52–58. Printed in Great Britain.

DIE WÄRMELEITFÄHIGKEIT VON GERMANIUM BEI HOHEN TEMPERATUREN

F. KETTEL

Allgemeine Deutsche Philips Industrie G.m.b.H., Zentrallaboratorium Aachen

(*Received* 1 *July* 1958; *in revised form* 20 *November* 1958)

Zusammenfassung — Es wird über Messungen der Wärmeleitfähigkeit an eigenleitenden und stark *p*-leitenden Germaniumeinkristallen berichtet. Die für die theoretische Diskussion des elektronischen Anteils der Wärmeleitfähigkeit benötigten Werte für die Breite der verbotenen Zone und ihre Temperaturabhängigkeit sowie für die Beweglichkeiten werden Messungen anderer Autoren entnommen und durch Vergleich mit eigenen Messungen der Thermokraft und der elektrischen Leitfähigkeit bestätigt. Die gemessenen Werte des elektronischen Anteils der Wärmeleitfähigkeit liegen sowohl für eigenleitendes wie für *p*-leitendes Material um einen Faktor 4 höher, als die Theorie ergibt.

Abstract—An account is given of thermal conductivity measurements on germanium monocrystals, both intrinsic and with high hole-conductivity. The author took mobility values, and values for the width of the forbidden zone and its dependence on temperature—all necessary for theoretical discussion of the electronic component of thermal conductivity—from the measurements of other authors, and confirmed them by comparison with his own measurements of thermoelectric force and electrical conductivity. The measured values of the electronic component of thermal conductivity, of both intrinsic and hole-conductive germanium, are about 4 times as high as those determined theoretically.

1. EINLEITUNG

Bei hinreichend hohen Temperaturen kann bei Halbleitern der elektronische Anteil der Wärmeleitfähigkeit λ_e von der gleichen Grössenordnung sein wie der Gitteranteil λ_g. Für λ_g kann man einen Temperaturverlauf

$$\lambda_g = A/T$$

ansetzen und die Konstante A aus Messwerten in einem Temperaturbereich mit genügend kleinem elektronischen Beitrag bestimmen. Ist der Beitrag zur Wärmeleitfähigkeit infolge Wärmestrahlung genügend klein und ist der Beitrag zum Wärmewiderstand infolge Streuung von Phononen an freien Ladungsträgern genügend klein gegen alle anderen Phononenstreuprozesse, so kann die gesamte Wärmeleitfähigkeit als Summe der beiden Anteile λ_e und λ_g angesetzt, und der elektronische Beitrag bestimmt werden.

Für einen nicht entarteten Halbleiter bei thermischer Streuung der Ladungsträger errechnet man für λ_e[1]

$$\lambda_e = 2\left(\frac{k}{e}\right)^2 \sigma T\left[1+\frac{\sigma_n \cdot \sigma_p}{2\sigma^2}\left(\frac{\Delta E}{kT}+4\right)^2\right] \qquad (1)$$

mit ΔE = Breite der verbotenen Zone
$\sigma = \sigma_n + \sigma_p$ = elektrische Leitfähigkeit.

Das zweite Glied in der Klammer, das eine starke Erhöhung des elektronischen Anteils gegenüber dem Wiedemann-Franzschen Gesetz verursacht, rührt her von einem Diffusionsstrom der Elektron-Loch-Paare, der die Paarbildungsenergie transportiert. Goldsmid[2] fand bei Bi_2Te_3 Übereinstimmung des gemessenen elektronischen Anteils mit der Theorie, während Busch und Schneider[3] an InSb sehr viel höhere Werte fanden. Von Joffe[4] wurde über Messungen an mehreren Halbleitern berichtet, wobei nur bei Halbleitern mit kleiner Breite der verbotenen Zone Übereinstimmung gefunden wurde, dagegen höhere experimentelle Werte bei Halbleitern mit grösserem Bandabstand.

Die vorliegenden Messungen wurden an eigen-

leitenden und p-leitenden Germanium-Einkristallen vorgenommen.

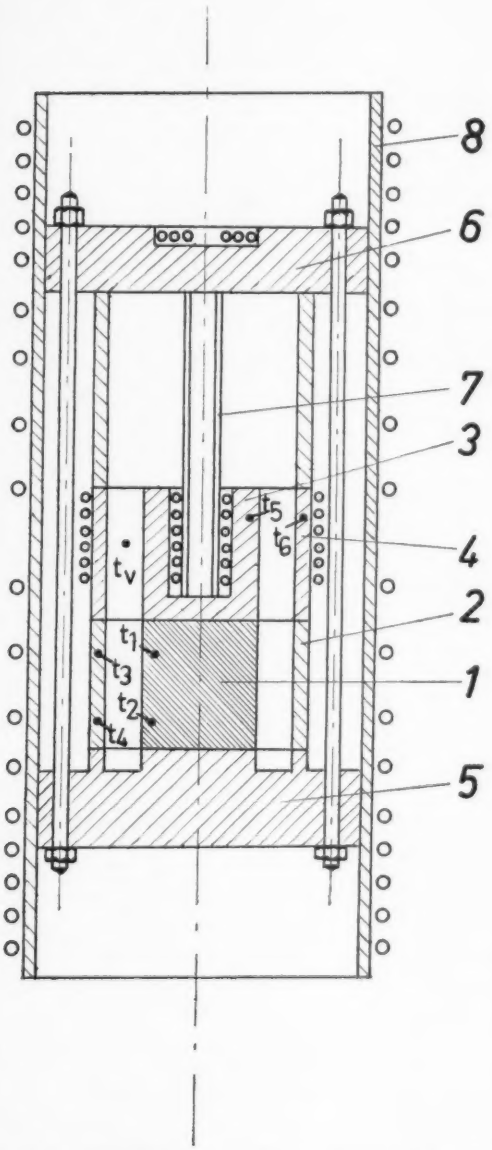

BILD 1. Messanordnung. (1) Germanium-Probe, (2) Schutzring, (3) Heizkörper, (4) Schutzheizung, (5) Wärmesenke, (6) Obere Abdeckplatte mit Heizung, (7) Keramisches Halterohr, (8) Ofen. t_1 bis t_6 Thermoelemente, t_v Vergleichsthermoelement.

2. MESSANORDNUNG

Die Messung der Wärmeleitfahigkeit erfolgte durch Bestimmung der Energiestromdichte und einer Temperaturdifferenz bei stationärem Zustand. Den Aufbau der Messeinrichtung zeigt Bild 1.

Als Wärmequelle diente eine elektrisch geheizte Spirale in einem Silberblock. Die Leistung wurde durch Strom und Spannungsmessung bestimmt. Die Germaniumprobe von 18 mm ϕ und 20 mm Länge war mit Graphit als Zwischenschichten zwischen Heizkörper und einer Silber-Kühlplatte gespannt. Die Thermoelemente, Nickel–Nickelchrom, waren mit ihren Silberlötperlen in 0,5 mm Bohrungen ca. 3 mm tief in die Probe eingesetzt und wurden durch Erwärmen auf 720°C in die Germaniumprobe einlegiert. Dadurch war guter elektrischer und thermischer Kontakt zwischen Probe und Thermoelement gewährleistet.

Probe und Heizkörper waren bis zur Höhe der Probe von einem Stahlring und bis zur Höhe des Heizkörpers mit einem geheizten Kupferring umgeben, dessen Heizung so eingestellt wurde, dass der Temperaturverlauf längs Heizkörper und Probe ($t_5-t_1-t_2$) auf $\pm 1{,}0$°C mit dem Temperaturverlauf in dieser Schutzhülle ($t_6-t_3-t_4$) übereinstimmte. Thermoelemente und Heizleitungen wurden durch die obere Abdeckplatte aus Kupfer geführt, die ebenfalls beheizt wurde, um den Temperaturabfall längs der Zuleitungen möglichst niedrig zu halten.

Die Anordnung war von einem Rohrofen umgeben und stand auf einem Porzellanring in einem Vakuumgefäss, dessen Druck auf 2×10^{-4} bis 4×10^{-4} mm Hg gehalten wurde.

Die Temperaturen der einzelnen Messstellen wurden gegen ein Vergleichselement (t_v) gemessen, das isoliert in der Nähe des Heizkörpers angebracht war. Die Heizleistung wurde so gewählt, dass eine Temperaturdifferenz von höchstens 2°C über der Messstrecke (t_1-t_2) von 10 mm auftrat.

Die Thermospannung Nickel-Germanium wurde zwischen den Nickel-Schenkeln der beiden Thermoelemente der Probe gemessen. Über die Thermoelemente im Heizkörper und Schutzring (t_5, t_4) konnte ferner ein Strom von etwa 100 mA zugeführt werden und dadurch unter Berücksichtigung der vorher gemessenen Thermospannung auch die elektrische Leitfähigkeit gemessen werden.

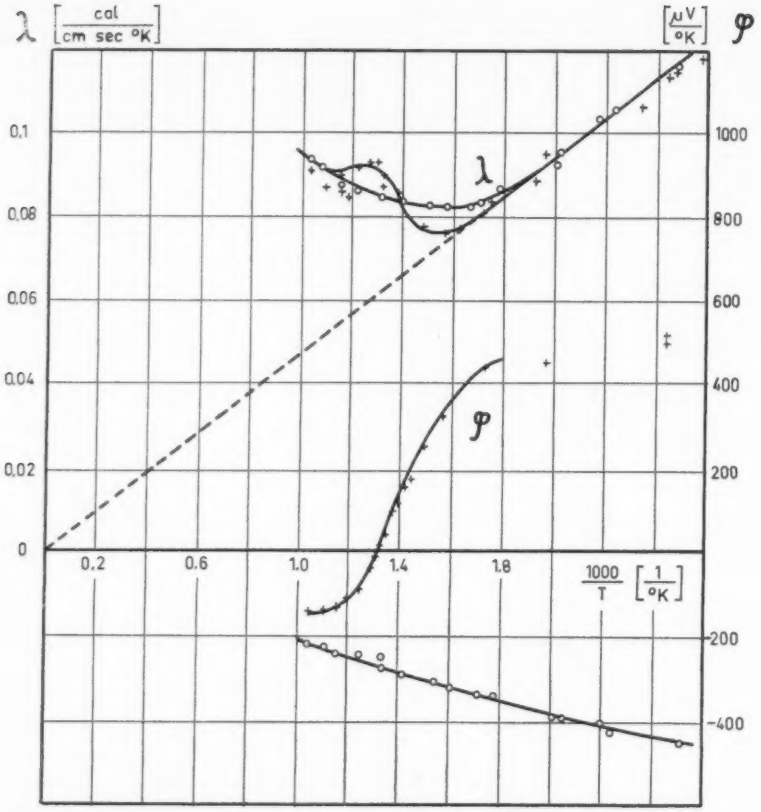

BILD 2. Wärmeleitfähigkeit und Thermokraft. 0 – 0 – 0 eigenleitend, + – + – + p-leitend, $n_s = 1{,}1 \times 10^{18}$ cm^{-3}.

3. MESSERGEBNISSE UND DISKUSSION

In Bild 2 sind die Wärmeleitfähigkeit und die Thermokraft der eigenleitenden und p-leitenden Probe über $1/T$ aufgetragen.

Die Wärmeleitfähigkeit geht bei tiefen Temperaturen, wo die Gitterleitung überwiegt, mit $1/T$. Die Messwerte liegen etwa 8% höher als von McCARTHY und BALLARD[5] bei 298°K und 368°K gemessen wurde, schliessen sich aber besser noch dem von DEVIATKOVA und SMIRNOV[6] von sehr tiefen Temperaturen bis 300°K gemessenen Verlauf an.

Von etwa 550°K ab macht sich bei der eigenleitenden Probe der elektronische Beitrag zur Wärmeleitung bemerkbar als Abweichung der Messwerte von dem nach hohen Temperaturen extrapolierten $1/T$ — Verlauf. Von den beiden Gliedern in Gleichung (1) überwiegt bei Eigenleitung der Anteil des Diffusionsstromes den Wiedemann–Franzschen Anteil um einen Faktor von 30 bei 500°K bis 6, 5 bei 1000°K. Bei der p-leitenden Probe ist der Beitrag des Diffusionsstromes zur elektronischen Wärmeleitung zunächst noch sehr klein wegen des Faktors $(\sigma_n \cdot \sigma_p / 2\sigma^2)$ in Gleichung (1). Der Anteil nach dem Wiedemann–Franzschen Gesetz ist zwar grösser als bei der eigenleitenden Probe, da die elektrische Leitfähigkeit grösser ist, bleibt aber klein gegen die Gitterleitfähigkeit und fällt im Gebiet der Störstellenerschöpfung mit steigender Temperatur ab. Überschreitet man bei höheren Temperaturen die Temperatur des Minimums der elektrischen Leitfähigkeit (Bild 3) so macht sich auch bei der p-leitenden Probe der elektronische

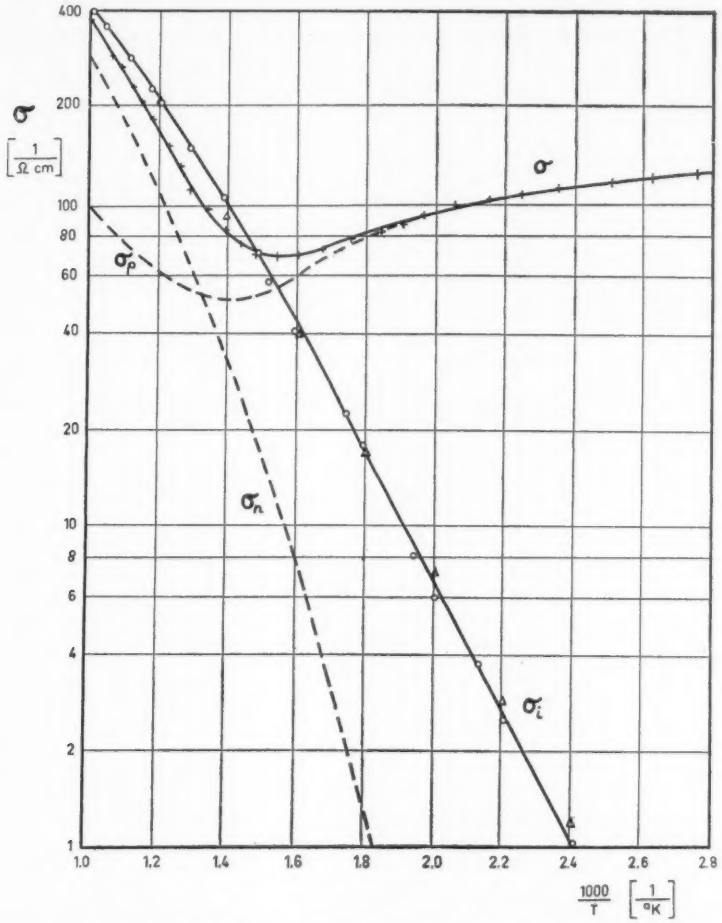

BILD 3. Elektrische Leitfähigkeit. 0 – 0 – 0 eigenleitend, + – + – + p-leitend, $n_s = 1{,}1 \times 10^{18}$ cm^{-3}, Δ-Werte nach MORIN und MAITA.[7]

Beitrag zur Wärmeleitfähigkeit bemerkbar und dann überwiegt auch wieder der Anteil des Diffusionsstromes den Anteil nach dem Wiedemann-Franzschen Gesetz. Der Faktor $(\sigma_n \cdot \sigma_p/2\sigma^2)$ nimmt für p-Leitung einen Maximalwert von 1/8 an, wenn $\sigma_n = \sigma_p$) ist.

Für die vorliegende p-leitende Probe ist diese Bedingung bei $1000/T = 1{,}3$ (1/°K) erfüllt. Für eigenleitendes Material kann der Faktor 1/8 nur erreicht werden, wenn Elektronen- und Löcherbeweglichkeit gleich sind. Bei Germanium mit $\mu_n/\mu_p \approx 3$ ist der Faktor für Eigenleitung kleiner als 1/10. Die Wärmeleitfähigkeit der p-leitenden Probe übersteigt deshalb den Wert des eigenleitenden Materials.

Für den Vergleich des aus den Messungen bestimmten elektronischen Beitrages zur Wärmeleitfähigkeit mit Gleichung (1) werden neben der elektrischen Leitfähigkeit, die gleichzeitig gemessen wurde (Bild 3), noch die Breite der verbotenen Zone und die Beweglichkeiten benötigt.

Für die Aktivierungsenergie wird aus elektrischen und Hall-Effekt-Messungen angegeben[7]

$$\Delta E = 0{,}785 - 3{,}5 \times 10^{-4} T - 4{,}61 \times 10^{-10} n_i^{\frac{1}{3}} T^{-\frac{1}{3}} \text{ eV}$$

in guter Übereinstimmung mit optisch gemessenen

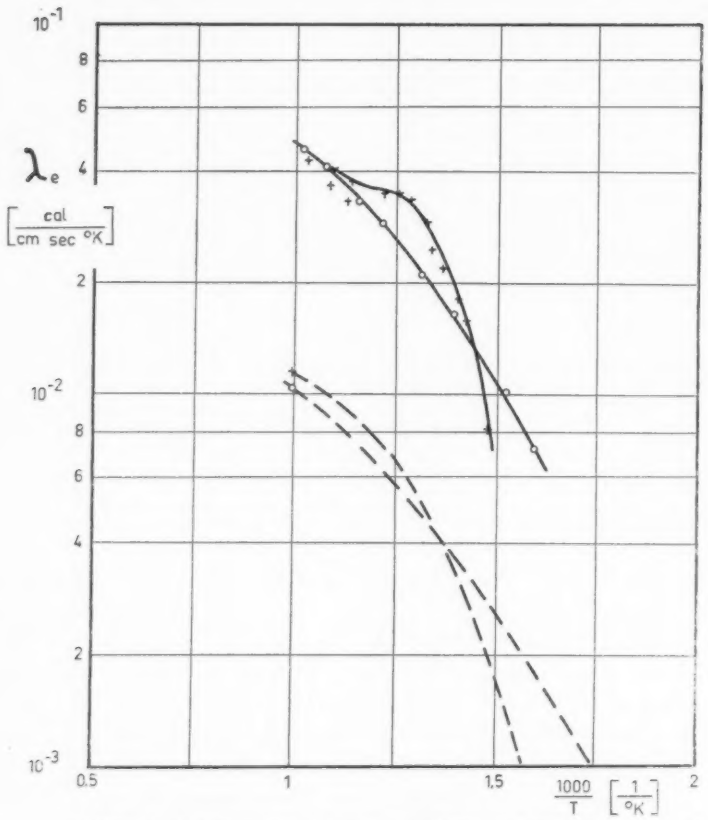

BILD 4. Elektronischer Anteil der Wärmeleitfähigkeit. 0 – 0 – 0 eigenleitend, + – + – + p-leitend, $n_s = 1{,}1 \times 10^{18}$ cm^{-3}, – – – – – theoretischer Verlauf.

Werten.[8] Für die Beweglichkeiten μ_n und μ_p finden MORIN und MAITA,[7] deren Messwerte der elektrischen Leitfähigkeit bei Eigenleitung mit den vorliegenden Messungen (Bild 3) sehr gut übereinstimmen, bis etwa 500°K einen Verlauf

$$\mu_n = 4{,}90 \times 10^7\ T^{-1{,}66}\ \text{cm}^2\ \text{V}^{-1}\ \text{sec}^{-1}$$

$$\mu_p = 1{,}07 \times 10^9\ T^{-2{,}66}\ \text{cm}^2\ \text{V}^{-1}\ \text{sec}^{-1}$$

Bei höheren Temperaturen berücksichtigen sie eine gegenseitige Streuung von Elektronen und Löchern, die zu einer Erniedrigung der Beweglichkeiten führt, wobei besonders die Elektronenbeweglichkeit einen stärkeren Abfall mit steigender Temperatur zeigt.

Der Faktor $(\sigma_n \cdot \sigma_p / 2\sigma^2)$ in Gleichung (1) kann für Eigenleitung $(n = p = n_i)$ geschrieben werden

$$\frac{b}{2(b+1)^2} \qquad b = \mu_n/\mu_p$$

Es wird also nur das Beweglichkeitsverhältnis benötigt.

Für die p-leitende Probe erhält man den Faktor $(\sigma_n \cdot \sigma_p / 2\sigma^2)$ über die Dichten der Elektronen und Löcher. Dazu wird zunächst aus der gemessenen elektrischen Leitfähigkeit im Bereich der Störstellenerschöpfung, $1000/T \approx 1{,}9$ bis $1{,}7$ in Bild 3, mit der angenommenen Beweglichkeit μ_p die Störstellendichte als konstanter Wert des Quotienten $n_s = (\sigma_{\text{mess}}/e\mu_p) = 1{,}1 \times 10^{18}$ per cm^3

VOL. 10 1959

bestimmt. Mit diesem Wert und der Eigenleitungsdichte

$$n_i = \frac{\sigma_{i\,\mathrm{mess}}}{e(\mu_n+\mu_p)}$$

wird mit Hilfe der Neutralitätsbedingung $p = n_s+n$ und der Bedingung $p \cdot n = n_i^2$ die Elektronen — und Löcherdichte errechnet. Die dann folgenden Kurven für σ_n und σ_p sind in Bild 3 gestrichelt gezeichnet. Rechnet man mit den angegebenen Werten für ΔE, μ_n, μ_p, σ_n, σ_p die Thermokraft, so erhält man gute Übereinstimmung mit den Messwerten, sowohl für die p-leitende Probe im Bereich $1000/T = 1{,}9$ bis $1{,}0$ als auch für die eigenleitende Probe. Die effektiven Massen der Elektronen und Löcher wurden dabei entsprechend Messungen anderer Autoren gleichgesetzt.[8]

Der elektronische Beitrag zur Wärmeleitung nach den Messungen sowie nach Gleichung (1) gerechnet zeigt Bild 4. Die gemessenen Werte liegen etwa 4-mal höher als der theoretische Verlauf für beide Proben.

Der Beitrag der Wärmestrahlung zur gemessenen Leitfähigkeit ist zu klein, um die Abweichung der Messungen zu erklären.

Für den Anteil der Strahlung an der Wärmeleitfähigkeit kann man setzen[4,10,11]

$$\lambda_R = \frac{16}{3}\frac{\sigma\epsilon}{\bar{x}}T^3$$

mit $\sigma =$ Stefan-Boltzmann-Konstante $= 1{,}37\times$ $\times 10^{-12}$ cal cm^{-2} sec^{-1} °K^{-4}

$\epsilon =$ Dielektrizitätskonstante

und $\bar{x} =$ Mittelwert der Absorptionskonstanten aus der Mittelwertbildung

$$\frac{1}{\bar{x}} = \frac{\int_0^\infty \frac{1}{x_\nu}\frac{\partial P_\nu}{\partial T}\,d\nu}{\int_0^\infty \frac{\partial P_\nu}{\partial T}\,d\nu}$$

mit P_ν als Plancksche Verteilung.

Die Absorptionskonstante infolge Absorption durch freie Ladungsträger ist proportional der Trägerzahl und dem Quadrat der Wellenlänge. Jaumann und Kessler[9] finden für eine Wellenlänge von $2{,}4\mu$ einen Temperaturverlauf der Absorptionskonstanten

$$x = C \cdot T^{2,9} \exp[-(\Delta E/2kT)],$$

$$\Delta E = \text{Bandbreite}$$

Für 1000°K entnimmt man ihren Messungen einen Wert $x = 1000$ cm^{-1}. Bei Proportionalität mit dem Quadrat der Wellenlänge errechnet man nach der angegebenen Mittelwertbildung einen mittleren Absorptionskoeffizienten von $\bar{x} = 78{,}5$ cm^{-1}.

Mit $\epsilon = 16$ wird dann

$$\lambda_R = 1{,}4\times 10^{-3} \text{ cal cm}^{-1} \text{ sec}^{-1} \text{ °K}$$

Das sind 3% des gemessenen elektronischen Anteils der Wärmeleitfähigkeit.

Von Joffe[4] und Deviatkova[12] wurde zur Erklärung einer an PbTe gemessenen ähnlich starken Abweichung ein zusätzlicher Transport von Energie durch Excitonen verantwortlich gemacht. Ein Diffusionsstrom der Excitonen im Temperaturgefälle transportiert ebenfalls die Bildungsenergie der Excitonen ΔE_{exc}. Für diesen Anteil soll gelten

$$\lambda_{\mathrm{exc}} = kD_{\mathrm{exc}}n_{\mathrm{exc}}\left[\left(\frac{\Delta E_{\mathrm{exc}}}{kT}+2\right)^2+2\right]$$

wobei D_{exc} der Diffusionskoeffizient der Excitonen ist und n_{exc} ihre Dichte, die mit $\exp-(\Delta E_{\mathrm{exc}}/kT)$ geht.

Der Anstieg des elektronischen Beitrages zur Wärmeleitung mit der Temperatur ist im wesentlichen durch den Verlauf $\sigma \sim \exp-(\Delta E/2kT)$ gegeben. Bei einem Energietransport durch Excitonen ist der Anstieg durch $n_{\mathrm{exc}} \sim$ $\sim \exp-(\Delta E_{\mathrm{exc}}/kT)$ bestimmt. Wollte man den Unterschied zwischen Theorie und Messung nach Bild 4 durch einen Excitonenbeitrag erklären, so müsste $\Delta E_{\mathrm{exc}} \approx (\Delta E/2)$ sein, was unwahrscheinlich ist. Ein Excitonenbeitrag sollte ferner unabhängig vom Leitungstyp sein und als additives Glied für beide Proben eingehen. Dann dürfte der Unterschied zwischen eigenleitendem und p-Typ-Material nicht so stark sein, wie ihn die vorliegenden Messungen zeigen.

LITERATUR

1. Madelung O., *Handbuch der Physik*. Bd. XX. Springer, Berlin (1957).

2. GOLDSMID H. J., *Proc. Phys. Soc.* B**69,** 851 (1956).
3. BUSCH G. und SCHNEIDER M., *Physica* **20,** 1084 (1954).
4. JOFFE A. F., *Canad. J. Phys.* **31,** 1342 (1956).
5. MCCARTHY K. A. und BALLARD S. S., *Phys. Rev.* **99,** 1104 (1955).
6. DEVIATKOVA E. D. und SMIRNOV I. A., *Zh. tekh. fiz., Moscow* **27,** 1944 (1957).
7. MORIN F. J. und MAITA J. P., *Phys. Rev.* **94,** 1525 (1954).
8. JOHNSON V. A. und LARK-KOROVITZ K., *Phys. Rev.* **92,** 226 (1953); GEBALLE T. H., HULL G. W., *Phys. Rev.* **94,** 1134 (1954).
9. MCFARLANE G. G. und ROBERTS V., *Phys. Rev.* **97,** 1714 (1955).
   JAUMANN J. und KESSLER R., *Z. Naturf.* **11a,** 387 (1956).
10. ROSSELAND S., *Astrophysik,* Springer, Berlin (1931).
11. GENZEL L., *Z. Phys.* **135,** 177 (1953).
12. DEVIATKOVA E. D., *Zh. tekh. fiz., Moscow,* **27,** 461 (1957).

VOL.
10
1959

J. Phys. Chem. Solids Pergamon Press 1959. Vol. 10. pp. 59–63. Printed in Great Britain.

CALCULATION OF THE PHOTOCONDUCTIVITY FROM A.C. IMPEDANCE CHANGES INDUCED IN ZnS AND ZnCdS PHOSPHORS*

HARTMUT KALLMANN
Department of Physics, New York University, Washington Square, New York, New York

BERNARD KRAMER
Department of Physics, New York University, Washington Square, New York, New York, and Physics Department, Hunter College, Bronx, New York

and

PETER MARK†
Department of Physics, New York University, Washington Square, New York, New York

(*Received* 10 *November* 1958; *in revised form* 8 *December* 1958)

Abstract—To determine the true induced conductivity of ZnCdS-type phosphors, a.c. impedance measurements are required so that the barrier effects of the grains and electrodes can be eliminated.

Five phosphors have been investigated, and from the capacitance change and the dissipation factor determined at various frequencies and intensities the conductivity of the sample was obtained for homogeneous excitation. For non-homogeneous excitation the actual conductivity cannot be as easily determined, but the dependence of the conductivity on excitation can be determined. A comparison of theoretical and experimental results is given for the samples investigated.

1. INTRODUCTION

THE identification of the a.c. impedance changes induced by light and particle radiation in specially activated ZnS and ZnCdS phosphors in powder form with changes of the photoconductivity has made it possible to study the photoconductivity of substances which cannot readily be prepared in the form of single crystals sufficiently large to allow electrodes to be attached.[1–5] This is especially important for the ZnCdS phosphors, which are not readily obtainable as single large crystals. So far, only a qualitative relationship between the change in the capacitance and dissipation factor of the powdered phosphor samples and the change in the actual photoconductivity has been discussed.[1,2,4]

It is the purpose of this paper to present an extension of this a.c. impedance theory which allows the photoconductivity and the conduction-band electron density to be computed directly from the a.c. impedance measurements and to illustrate the theory with some experimental results.

2. BASIC EQUATIONS

The simple layer model of a photoconductor in powder form discussed in a previous paper[1] leads to the following equations (in M.K.S. units) for the fractional series capacitance change ($\Delta C/C_0$) and the dissipation factor (D) under the assumption of uniform excitation:

$$\Delta C/C_0 = d_2/[(d_1+d_2)(\epsilon\omega/\sigma)^2+d_1) \qquad (1)$$

$$D = d_2/\{d_1[(\omega\epsilon/\sigma)(1+d_2/d_1)+\sigma/\epsilon\omega]\} \qquad (2)$$

C_0 is the dark capitance, d_2 and d_1 represent the

* This work was supported by the Signal Corps Engineering Laboratories, Evans Signal Laboratory, Belmar, New Jersey.

† Now with Polaroid Corporation, Research Division, Cambridge 39, Massachusetts.

thicknesses of the radiation sensitive and insensitive layers respectively, ω is the angular frequency of the bridge oscillator, ϵ is the dielectric constant,* and σ is the photoconductivity (assuming $\sigma_{dark} = 0$). For small values of σ,

$$D \simeq (\sigma/\omega\epsilon)[d_2/(d_1+d_2)] \tag{3}$$

while for large σ,

$$D \simeq (d_1/d_2)(\epsilon\omega/\sigma) \tag{4}$$

showing that D is small under both very strong and very weak excitation. The maximum D value is given by

$$D_{max} = (d_2/2d_1)[d_1/(d_1+d_2)]^{\frac{1}{2}} \tag{5}$$

and occurs at an intensity of excitation lying between the above mentioned extremes. The saturation value of the capacitance change (further increase of intensity does not increase the capacitance) is given by

$$(\Delta C/C_0)_{sat} = d_1/d_2 \tag{6}$$

and the $\Delta C/C_0$ value associated with the D_{max} is

$$(\Delta C/C_0)_{D^{max}} = d_1/2d_2. \tag{7}$$

Using equation (6), equation (5) may be written as

$$D_{max} = (\tfrac{1}{2})(\Delta C/C_0)_{sat}(C_0/C_s)^{\frac{1}{2}}, \tag{5a}$$

where C_s is the saturation capacitance obtained at strong exciting intensities. The derivation of these equations can be found in the Appendix of Reference (1), and their validity is illustrated by an examination of Figs. 1, 4, 5, 6 and 7 of the same paper. The dependence of the conductivity on the exciting intensity is of the form

$$\sigma = \gamma I^n \tag{8}$$

where the exponent n is generally considered to lie between $\frac{1}{2}$ and 1, depending on the intensity of the exciting radiation.[1,6]

One goal of the a.c. impedance theory of photoconductors is the actual calculation of the photoconductivity, σ, of equations (1) and (2). Then one can calculate the exponent of equation (8) as well as n_c, the density of electron in the conduction band, using the relation

$$\sigma = n_c e \mu \tag{9}$$

where μ is the mobility (~ 100 cm^2 V^{-1} sec^{-1}) of the conduction electrons and e is the electronic charge.

Equations (1) and (2) (which deal with uniform excitation only) are readily solved simultaneously for the unknown σ. The result is that

$$\sigma = \omega\epsilon(\Delta C/C_0)(1/D) \tag{10}$$

so that

$$n_c = (\omega\epsilon/\mu e)(\Delta C/C_0)(1/D). \tag{11}$$

Equations (10) and (11), then, present relations for the photoconductivity and the conduction-band electron density in terms of the mobility and quantities which are directly obtained from the a.c. impedance measurements. With the aid of these two equations, both σ and n_c can be obtained as a function of the exciting intensity.

3. RESULTS AND CALCULATIONS

The measuring system used to obtain the effective series capacitance and dissipation factor of the samples was a General Radio 716-capacitance bridge (Schering type) with an oscilloscope used as a detector.[2] The method of sample preparation has already been described for the case of excitation by light.[5] When beta particles were used for excitation, a slight variation was necessary in the sample preparation, since the beta particles could not penetrate the Nesa conducting glass slide. For this case, a thin aluminum foil 0·2 mg/cm^2 was placed over the powder (which had been deposited on a Nesa plate) and a microscope slide cover slip about 0·2 mm was placed on top of the foil. This was then pressed together with a clamp and sealed outside at the edge with an epoxy resin. The beta particles were obtained from a 10-mc ^{90}Sr–^{90}Y source. It was mounted so that its distance from the sample could be varied, thereby changing the intensity. Its closest position from the sample was 0·25 in. Infrared radiation of wavelength greater than 0·72 μ (through a Corning 7–56 filter) and 1 mW/cm^2 intensity and a 60-c/s a.c. field of 10,000 V/cm were used to quench the phosphors.

* Here we assume the dielectric constant is the same throughout the sample. If the dielectric constant of the material (for instance air) is not the same as that of the radiation sensitive material, d must be replaced by the actual thickness of the layer divided by the dielectric constant and ϵ must be replaced by $K_1\epsilon_0$ or $K_2\epsilon_0$, depending on which layer is being considered.

Table 1.*

1	2	3	4	5	6	7	8
Phosphor	Frequency (kcs)	Intensity	$\Delta C/C_0$(%)	D	$\sigma(\Omega\text{-m})^{-1}$	$n_c(\text{cm}^{-3})$	$n_c(\text{cm}^{-3})$ (calculated)
LG	1	$0{\cdot}007\ I_{max}$	32·4	0·18	$5{\cdot}2\times10^{-7}$	$3{\cdot}2\times10^{8}$	3×10^{9}
	10	$0{\cdot}2\ I_{max}$	30·5	0·19	46×10^{-7}	29×10^{8}	—
L	80	$0{\cdot}1\ \mu\text{W/cm}^2$	30·5	0·11	$6{\cdot}5\times10^{-5}$	$4{\cdot}1\times10^{+10}$	3×10^{9}
	800	$5{\cdot}0\ \mu\text{W/cm}^2$	29·7	0·13	50×10^{-5}	$31\times10^{+10}$	—
Sylvania	0·1	$3\times10^{-3}\ \mu\text{W/cm}^2$	11	0·027	$0{\cdot}11\times10^{-6}$	$7{\cdot}0\times10^{7}$	3×10^{7}
	10	$0{\cdot}25\ \mu\text{W/cm}^2$	6·8	0·028	$6{\cdot}8\times10^{-6}$	42×10^{8}	—
O	0·1	$4\times10^{-3}\ \mu\text{W/cm}^2$	14·7	0·017	$2{\cdot}5\times10^{-7}$	$1{\cdot}5\times10^{8}$	6×10^{8}
	10	$10^{-1}\ \mu\text{W/cm}^2$	11·8	0·011	$3{\cdot}1\times10^{-5}$	$1{\cdot}9\times10^{10}$	—
N	1	$4\times10^{-4}\ \mu\text{W/cm}^2$	17	0·27	$1{\cdot}8\times10^{-6}$	$1{\cdot}1\times10^{9}$	2×10^{8}
	10	$0{\cdot}2\ \mu\text{W/cm}^2$	27	0·27	$3{\cdot}6\times10^{-5}$	$2{\cdot}2\times10^{10}$	—

* We want to thank Dr. A. PERLMUTTER for use of some of his data which comprise part of this table.

The best experimental results are obtained in the region where D is a maximum, since the values of D are most accurate here and the capacitance change at this point is already appreciable (half its final value). Table 1 gives the data obtained with phosphors at various frequencies and intensities.

These data were taken as follows: at any one frequency the intensity of excitation was varied until the dissipation factor was a maximum. The measuring frequency was then changed, and the intensity again varied until the dissipation factor was again a maximum. That this is not exactly the case for every sample is mainly due to experimental difficulties.

All the samples except LG were excited by ultraviolet light (3660 Å) of an intensity given in Column 3. The LG phosphor which shows a very poor response to ultraviolet was excited by the β-source and I_{max} is the intensity when the source is $\frac{1}{4}$ in. from the sample. This would correspond to approximately 10^{13} electrons excited per unit volume per second in the sample.

The maximum value of D and the corresponding value of $\Delta C/C_0$ per cent so obtained (Columns 4 and 5) should be independent of both frequency and intensity (equations (5) and (7)). As can be seen from the table, this is approximately true for each phosphor.* The discrepencies may be due to experimental difficulties. The conductivity and the number of electrons in the conduction band can now be calculated (see Columns 6 and 7 of Table 1) and should be proportional to the exciting intensity in the range where the traps are saturated ($n_t \simeq n_0$) and proportional to the square root of the intensity when $n_t < n_0$.[6] These ratios of intensity increase and conduction density increase are given in Table 2.

Table 2.

Phosphor	Increase in intensity	Increase in n_c	n
LG	30	10	0·68
L	50	7	0·50
Sylvania	80	60	0·94
O	25	130	1·5
N	500	20	0·48

* Further verification of the fact that the D_{max} value is not dependent on frequency is provided by the data presented in the Ph.D. theses of A. PERLMUTTER (N.Y.U. 1955) and P. MARK (N.Y.U. 1958).

In column 8 of Table 1 are finally shown the theoretical values obtained using the following equations:

$$n_c = \alpha I/\beta^* n_0$$

$$n_c = [\alpha I\delta/\beta^*\beta' n_0]^{\frac{1}{2}}.$$

These are equations (13) and (15) of a previous paper.[6] The first equation is for traps saturated; the second when the traps are far from saturated. The values entering into these equations are given below:

αI—The number of electrons excited per second per cm^3.

β^*—The light-emission term is $\beta^* n_c n_t$ ($n_t \sim$ ionized activators). From decay-time measurements and theoretical calculations $\beta^* \sim 10^{-11}$ cm^3 sec^{-1}.

n_0—The total number of "deep" traps. This number can be obtained from fluorescent-rise curve measurements; it varies between 10^{14} and 10^{16} cm^{-3}; we use the value 10^{15} cm^{-3}.

β'—The trapping of conduction electrons is given by $\beta' n_c(n_0 - n_t)$. Assuming the trap is of atomic dimensions, and the velocity of the conduction electron is due to thermal energy, we get $\beta' \sim 10^{-7}$ cm^3 sec^{-1}.

δ—The release of electrons from traps may be written as $(se^{-E_t/kT} \cdot n_t)$. The "deep" traps range in energy depth from perhaps 1 to $\frac{1}{10}$ eV; this may be in discrete or continuous levels. We assume that $E_t \sim 0{\cdot}5$ eV, and this gives $\delta \sim 10^3$ sec^{-1}, using $s \sim 10^{12}$ sec^{-1}. It should be noted that the ratio $\delta/\beta' = (2\pi mkT/h^2)^{\frac{3}{2}} e^{-E_t/kT}$.

Comparing columns 7 and 8 one finds that for two of the phosphors (Sylvania, Powder 0) the calculated values agree rather well with the experimental values. For the other materials the differences between experimental and theoretical values are larger. This is to be expected, since certainly not all the phosphors have the characteristic constants given above.

4. THE CASE OF INHOMOGENEOUS EXCITATION

Up to now we have used equations assuming that the phosphor was uniformly excited. But even when non-uniform excitation occurs, valuable information regarding the relationship between n_c and the intensity can be obtained. Although in this case it is difficult to solve for $\sigma(x)$, the capacitance and dissipation factors depend (for a given type of illumination and for given d_1 and d_2) only on $\gamma I_0^n/\omega\epsilon$, as in the case of uniform excitation time where I_0 is the incident intensity. This follows from equations A(10) and A(11) of the previous paper[6] if $\sigma(x) = \gamma I^n(x)$. We also assume that n is approximately the same throughout the sample.

If the intensity is changed, n_c and therefore $\sigma(x)$ are changed, and so are $\Delta C/C_0$ and D. One can now change ω until the original $\Delta C/C_0$ and D are obtained again. If ω changes from ω_1 to ω_2 to reobtain the original $\Delta C/C_0$ and D values, then

$$\omega_1/\omega_2 = (I_{01}/I_{02})^n. \qquad (12)$$

The right-hand term follows from equation (8) if n shows no considerable change between I_1 and I_2. Repeating this operation until a large intensity and frequency range is covered, the variation of n over a large range of intensity can be obtained, since both ω and I are known. Thus an evaluation of n can also be obtained for non-homogeneous excitation.

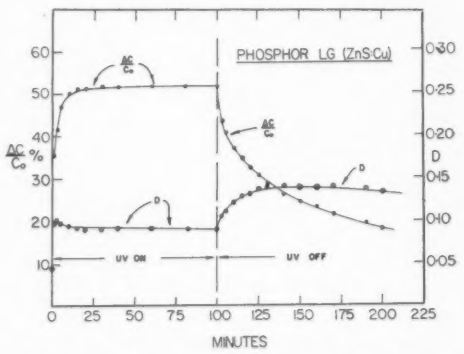

FIG. 1. Change of $\Delta C/C_0$ and D during the build-up and decay of photoconductivity under u.v. excitation.

The importance of the effect of the non-homogeneous excitation can be seen in the rise and decay measurements by considering the dissipation factor. Using an intensity such that the equilibrium D value of the phosphor is greater than the maximum value, it is evident that during the rise curve the D value will first reach a maximum and then fall to its equilibrium value, while during the decay it should retrace its values if the excitation is

homogeneous. In Fig. 1 is shown the D value for Phosphor LG during the rise and decay when illuminated with 10 μW/cm^2 of ultraviolet (3650 Å) The value of D_{max} is seen to be different, depending on whether we are in the rise or decay region. A similar behavior is found with other phosphors. On the other hand, the rise and decay of the same phosphor during β-excitation exhibits very little difference in the value of D_{max}, as shown in Fig. 2.

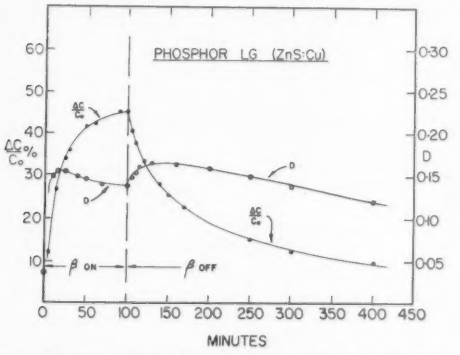

FIG. 2. Change of $\Delta C/C_0$ and D during the build-up and decay of photoconductivity under β-excitation.

This difference between the D_{max} values obtained during the rise and those obtained during the decay of photoconductivity is attributed to the non-homogeneity of excitation. Two effects contribute to this difference. If the phosphor is non-homogeneously excited, its D_{max} value will be smaller than for a homogeneously excited sample, since the impedance measurements are bulk measurements which include the entire sample thickness. This can be seen from formula (A8) of a previous paper.[1] This inhomogeneity is increased during the rise period because the phosphor layers closest to the illuminated electrode reach their equilibrium states earlier than the interior layers. This evidently increases the inhomogeneity during the rise period.

When the excitation is switched off, the initial decay of the strongly excited layers is faster than that of the interior layers. This tends to reduce the excitation gradient and thus the entire sample approaches a state of uniform excitation, accounting for the higher D_{max} observed during the decay.

These ideas are borne out by the experiment with β-excitation, where the sample is much more homogeneously excited. Indeed, in this case the value of D_{max} is almost the same during the rise as during the decay and is equal to the equilibrium D_{max} obtained by varying the intensity. The $\Delta C/C_0$ per cent values are also given in these two figures to show the monotonic change of the capacitance with conductivity.

5. SUMMARY

From equations (1) and (2), one can determine equation (10) and (11), which describe the photoconductivity and the conduction band electron density when the phosphor is in the state of uniform excitation. By varying the oscillator frequency and the intensity of excitation, the conductivity and the conduction-band electron density can be calculated. This procedure can be used to determine the dependence of the conductivity on intensity for non-uniform excitation as well.

These experiments demonstrate the correctness of the conductivity theory of the a.c. impedance changes observed with these phosphors under excitation. Experiments at low temperatures further confirm this. There the number of electrons remaining trapped after excitation is about 100 times larger than at room temperature. However, the $\Delta C/C_0$ and D values drop very sharply after excitation although the phosphor is still filled with trapped electrons.

Thus the idea that trapped electrons appreciably affect the a.c. impedance changes[7] should be abandoned.

REFERENCES

1. KALLMANN H., KRAMER B., and PERLMUTTER A., *Phys. Rev.* **89,** 700 (1953).
2. KALLMANN H., KRAMER B., and PERLMUTTER A., *Phys. Rev.* **99,** 391 (1955).
3. GARLICK C. F., *Handbuch der Physik* Vol. 19, p. 391. Springer-Verlag, Berlin (1956).
4. KALLMANN H. and MARK P., *Phys. Rev.* **105,** 1445 (1957).
5. KALLMANN H., KRAMER B., and MARK P., *Phys. Rev.* **109,** 721 (1958).
6. KALLMANN H. and KRAMER B., *Phys. Rev.* **87,** 91 (1952).
7. GARLICK G. F. G. and GIBSON A. F., *Proc. Roy. Soc.* A**188,** 485 (1947).
   ROUX J., "La Luminescence des Corps Cristallins Anorganiques" Paris 1956.
   KRONENBERGER S and ACCARDO C., *Phys. Rev.* **101,** 989 (1955).

Dimensional changes in single crystals of synthetic sapphire after irradiation

(*Received* 1 *December* 1958)

DIMENSIONAL changes along the principal axes of single crystals of synthetic sapphire have been measured after irradiation at 30°C and subsequent annealing.

The crystals, supplied by the Salford Electrical Instruments Ltd., measured $\frac{1}{2}\times\frac{1}{2}\times\frac{1}{4}$ in; the two large faces were ground and lapped parallel, to an accuracy of 1 μ in., and were either perpendicular to, or in the plane of, the *c*-axis. The distance between the faces in all specimens was equal to within 100 μ in.

Spectrographic analysis of the material gave: Si 0·3, Cr 0·05, Cu 0·05, Ni 0·01, and Mn 0·005 weight per cent. The following elements were not detected (detection limits are as stated):

Per cent	
0·002	Ca, Li, Na
0·005	Ag, Be, Cd, Fe, Mg
0·01	B, Co, Ti
0·02	Ba, K, Sr
0·05	Au, Ge, Mo, Pb, Sn
0·1	As, Sb, V
0·5	Bi, In, P, Pd, W
1	Tl, Zn, Cs, Rb.

The changes in length were measured on a calibrated mechanical comparator (magnification 4500) in a temperature-controlled room, unirradiated crystals being used as standards. The accuracy attainable was about 5 p.p.m.

The following photon and electron irradiations were performed:

(*a*) A 1·3-MeV γ-ray irradiation, dose $1{\cdot}5\times10^6$r.

(*b*) A 1·3-MeV γ-ray irradiation, dose 4×10^6r, performed at −196°C.

(*c*) An X-ray irradiation, the tube running at 50 kV and 80 mA for 5 hr, with a Cu target.

(*d*) A 1-MeV electron irradiation, dose 2×10^{18} electrons/cm^2.

None of the above irradiations caused any measurable change in the physical dimensions, although they all produced a very pale yellow colour in the previously colourless crystal. This probably indicates that for doses given the concentration of displaced ions present is smaller than about 10^{-5}.

All subsequent irradiations were performed in the Harwell reactor Bepo, inside a hollow uranium cylinder, cooled to 30°C. The thermal neutron flux was measured by cobalt foils. Measurements have shown that the ratio of fission neutrons (responsible for radiation effects) to thermal neutrons is nearly unity in the irradiation position used.

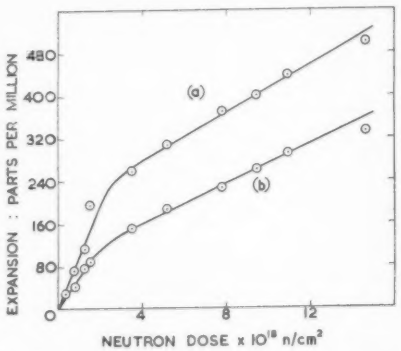

FIG. 1. The fractional increase in length (a) parallel and (b) perpendicular to the *c*-axis as a function of neutron dose.

The expansion along the two principal axes as a function of slow neutron dose is illustrated in Fig. 1. The results for the two directions lie approximately upon two straight lines with different slopes. Up to 2×10^{18} neutrons cm^{-2} the expansion rates parallel and perpendicular to the *c*-axis are 100 and 61 p.p.m./10^{18} neutrons cm^{-2} respectively; above 4×10^{18} neutrons cm^{-2} they are 23 and 19 p.p.m./10^{18} neutrons cm^{-2}. Above $1{\cdot}2\times10^{19}$ neutrons cm^{-2} there is unconfirmed evidence of a second change in slope of the two lines.

After undergoing a dose of $1{\cdot}46\times10^{19}$ neutrons cm^{-2}, the specimens were annealed at successively higher temperatures, each for 60 min, and the recovery of expansion in the two principal directions was observed. The resulting curves (Fig. 2) reveal two annealing stages, with maximum annealing rates at 300 and 550°C.

Neutron irradiation produced a dark-brown

coloration in the crystals, which was different from the colours observed after γ-ray, electron, or X-ray irradiation. Differences in the colour centres introduced after neutron and γ-ray irradiation have also been observed in the far ultraviolet by LEVY

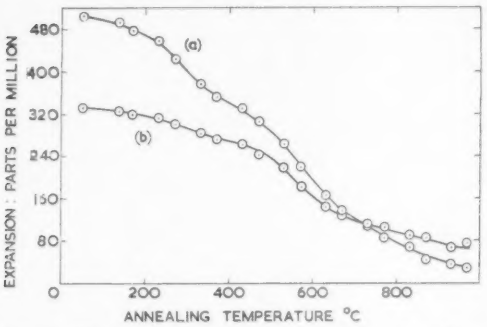

FIG. 2. The recovery of expansion, after annealing at successively higher temperatures for 60 min (*a*) parallel and (*b*) perpendicular to the *c*-axis.

and DIENES.[1] The coloration begins to change after annealing at about 350°C; by 450°C it becomes a very dark green and then turns more yellow and paler at higher temperatures until by 900°C it has practically disappeared.

If we use arguments presented earlier[2] to calculate the concentration of displaced ions from the expansions observed after neutron irradiation, the result is of the order of 50 times less than theoretical estimates.[3] This order of discrepancy seems to be quite usual in the study of radiation-damage phenomena in many materials.

ANTAL and GOLAND[4] have recently made two measurements of density changes after neutron irradiation and observed colour changes after annealing which are in agreement with the results presented here. Also, from a long-wavelength neutron-transmission experiment, they concluded that the concentration of defects observed was about 40 times less than theoretical estimates.

Interpretation of these results in terms of specific defects is difficult in view of our ignorance of the binding forces in various directions. If centres of pressure are produced by irradiation (for example, interstitial ions), then it would appear that a preferential expansion occurs along the *c*-axis. Perhaps the change in slope in Fig. 1 and the point of inflexion in Fig. 2 indicate respectively the production and annihilation of two different sorts of defects, one of which saturates at about 4×10^{18} neutrons cm^{-2}.

Atomic Energy Research Establishment, Harwell, Berks. D. G. MARTIN

REFERENCES

1. LEVY P. W. and DIENES G. J., *Report of Bristol Conference on Defects in Crystalline Solids* p. 256 (1955).
2. ADAM J. and MARTIN D. G., *Phil. Mag.* **3,** 1329 (1958).
3. KINCHIN G. H. and PEASE R. S., *Rep. Progr. Phys.* **18,** 1 (1955).
4. ANTAL J. J. and GOLAND A. N., *Phys. Rev.* **112,** 103 (1958).

NOTICES

INTERNATIONAL CONFERENCE ON SEMICONDUCTOR PHYSICS

In Prague 1960

The Czechoslovak Academy of Sciences is organizing an *International Conference on Semiconductor Physics* which will be held in Prague from 29th August to 2nd September 1960 under the auspices of the International Union for Pure and Applied Physics. This will continue the series of Conferences held in Reading 1950, Amsterdam 1954, Garmisch-Partenkirchen 1956, and Rochester 1958.

The Secretary of the Organizing Committee is Dr. MILOŠ MATYÀŠ, Institute of Technical Physics, Prague 5, Cukrovarnická 10, Czechoslovakia.

VOL.
10
1959

SOLID STATE PHYSICS U.S.S.R.

Editor-in-chief: A. F. IOFFE

Pergamon Press is pleased to announce that arrangements have been made for the translation and publication in the English language of the above-named Soviet journal, in the interests of making Russian work in this important field of physics easily and more widely known to non-Russian-speaking scientists throughout the world.

The English edition of this periodical will appear bi-monthly. The Table of Contents of Volume 1, No. 1 is as follows:

Editor: A. F. IOFFE (Academician)

Deputy Editor: V. M. TUCHKEVICH

Editorial Board: A. I. ANSEL'M, N. N. DAVIDENKOV, B. V. DERYAGIN, L. N. DOBRETSOV, V. P. ZHUSE, S. N. ZHURKOV, A. F. IOFFE, M. I. KORNFEL'D, L. I. KOROVIN, I. M. LIFSHITS, G. A. SMOLENSKII, V. M. TUCHKEVICH.

Contents: VOLUME 1, NO. 1, 1959

G. M. GURO: Characteristic times of the electronic stationary processes in semiconductors.

I. V. BOIKO: The theory of the field effect.

V. B. FIKS: The mechanism of ion mobility in metals.

A. A. GRINBER: Calculation of transient processes in crystal triodes.

Iu. A. FIRSOV: Cyclotron resonance in semiconductors with complex equipotential surfaces.

I. N. FRANTSEVICH, D. F. KALINOVICH, I. I. KOVENSKII and M. D. SMOLIN: Some quantitative correlations of the process of donor-acceptor interaction in metal alloys.

G. L. BIR: Influence of surface recombination on photoconductivity of semiconductors.

LI-CHZHI-TSIAN': Dependence of induced conductivity from electron energy in the layers of CdS and CdSe when bombarded by slow electrons.

LI-CHZHI-TSIAN': Investigation of intercrystal energy barriers in the thin layers of CdS by means of slow electron bombardment.

I. D. KONOZENKO and V. I. UST'IANOV: Crystal CdS receivers of gamma radiation.

A. I. LIKHTER and T. S. D'IAKONOVA: Measurement of Hall effect dependence in *n*-Ge from pressure at about 10,000 kg/cm^2.

P. T. KOZYREV: Dependence of conductivity of Se from pressure at about 30,000 atm (Part 1).

P. T. KOZYREV: Deoxidized Se and its conductivity dependence on pressure (Part 2).

K. P. ZUEV: Conductivity of Cu_2O when stabilized in the atmosphere (1020–1070°C)—I.

K. P. ZUEV: Conductivity of Cu_2O in its dissociation (1070–1250°C)—II.

L. D. DUDKIN and N. Kh. ABRIKOSOV: Alloying of the semiconductor compound $CoSb_3$.

Short notes

S. V. AIRAPETIANTS and M. S. BRESLER: Measurement of the conductivity anisotropy of semiconductors by means of four probes.

G. E. PIKUS and G. L. BIR: Influence of deformation on energy spectrum and electrical properties of *p*-germanium and *p*-silicon.

A. F. IOFFE: Two mechanisms of free charge movement.

A. F. IOFFE: Two mechanisms of heat conduction.

E. F. GROSS and I. PASTRNIAK: The fine structure of the spectral photosensitivity curve of Cu_2O crystals.

Letters to the Editor

G. A. SMOLENSKII, A. I. AGRANOVSKAIA, and S. N. POPOV: The mechanism of solid solution polarizat'on of $Pb_3NiNb_2O_9$–$Pb_3MgNb_2O_3$.

G. A. SMOLENSKII, V. A. ISUPOV, and A. I. AGRANOVSKAIA: New group of Seignette-electric substances (with complex structure).

G. A. SMOLENSKII, V. A. ISUPOV, and A. I. AGRANOVSKAIA: New Seignette-electric substances of complex composition type $A_2^{2+}(B_I^{3+}B_{II}^{5+})O_{61}$.

G. A. KUROV: Once again on thin layers structure obtained by evaporation of InSb in vacuum.

A. F. GORODETSKII, V. G. MEL'NIK and I. G. MEL'NIK: Method of Ohm-contact production with Si.

For subscription rates and sample copies please write to Pergamon Press at 4 and 5 Fitzroy Square, London W.1, 122 East 55th Street, New York 22, N.Y. or 24 rue des Ecoles, Paris V^e.

CONTENTS LISTS OF VOLUME 7, NOS. 1–4

Volume 7 No. 1

page

W. D. JOHNSTON, R. R. HEIKES et D. SESTRICH:
La préparation, la cristallographie et les propriétés magnétiques du système $Li_xCo_{(1-x)}O$. 1

R. T. BATE et C. V. HEER:
Quelques propriétés optiques et magnétiques de LiF irradié 14

PIERRE BRISSONNEAU:
Contribution à l'étude quantitative du trainage magnétique de diffusion du carbone dans le fer α 22

JAMES C. PHILLIPS:
Termes d'échange dans le formalisme de la masse effective 52

ULRICH GONSER et BOUDEWYN OKKERSE:
Le problème des changements de phase induits par irradiation 55

G. A. ALERS et J. R. NEIGHBOURS:
Les constantes élastiques du zinc entre 4,2 et 670°K 58

E. MOOSER et W. B. PEARSON:
La structure cristalline et les propriétés des éléments des groupes V B à VII B et de composés formés entre eux 65

R. F. WALLIS et H. J. BOWLDEN:
Théorie du spectre de photo-ionisation d'impureté des semi-conducteurs dans les champs magnétiques 78

C. R. VASSEL:
L'effet des éléments de la première longue période sur la résistivité du cuivre et de l'aluminium. 90

Lettres aux éditeurs:

NILS BÄCKLUND:
Résistance électrique de quelques alliages de métaux nobles aux températures de l'hélium liquide 94

T. J. ROWLAND:
Résonance magnétique nucléaire de Pt^{195} dans la platine métallique 95

B. T. MATTHIAS et W. H. ZACHARIASEN:
Supracondictivité du nitrure de rhénium 98

Volume 7 Nos. 2/3

M. YA AZBEL:
La théorie quantique de l'impédance de surface d'un métal à haute fréquence . . . 105

KURT WEISER:
Calcul théorique des coefficients de distribution d'impuretés dans le germanium et le silicium 118

MANUEL CARDONA et WILLIAM PAUL:
Un effet photoélectromagnétique quadratique dans le germanium 127

KATHERINE WOLFSTIRN et C. S. FULLER:
Comparaison des concentrations de trous et de radio-cuivre dans le germanium . . 141

VOL
10
195

page

N. T. MELAMED:
Transfert d'énergie dans les composés phosphorescents ZnS:Cu:Cl 146

G. MEIJER:
Fluorescence infrarouge des sulfures de zinc phosphorescents activés au cuivre . . 153

W. MARSHALL:
L'antiferromagnétisme de $CuCl_2$, $2H_2O$ 159

MAURICE GOLDMAN:
Résonance nucléaire des protons dans l'acide trichloracétique 165

CLIFFORD C. KLICK et W. DALE COMPTON:
Emission luminescente de KCl : Tl aux basses températures 170

H. A. KLASENS:
Variation de le photoconductibilité et de la luminescence des photoconducteurs avec l'intensité dans l'état stationnaire. 175

A. M. CLOGSTON:
Structure de l'état métastable de Mn^{++} et Fe^{+++} 201

T. E. SLYKHOUSE et H. G. DRICKAMER:
L'influence de la pression sur l'absorption de bord dans les halogénures d'argent . . 207

T. E. SLYKHOUSE et H. G. DRICKAMER:
L'influence de la pression sur la limite d'absorption optique du germanium et du silicium. 210

D. F. C. MORRIS:
L'instabilité de quelques dihalogénures de cuivre et d'argent. 214

J. F. LAURENT et J. BÉNARD:
Autodiffusion des ions dans les halogénures alcalins polycristallins 218

T. C. HARMAN, M. J. LOGAN et H. L. GOERING:
Préparation et propriétés électriques du tellurure de mercure. 228

H. J. HROSTOWSKI et R. H. KAISER:
Spectre d'absorption du silicium "dopé" à l'arsenic 236

J. H. WERNICK, S. GELLER et K. E. BENSON:
Constitution du système $AgSbSe_2$–$AgSbTe_2$–$AgBiSe_2$–$AgBiTe_2$ 240

R. J. WEISS et K. J. TAUER:
Thermodynamique du système Au–Pt 249

J. KORRINGA:
Théorie de la dispersion pseudo-périodique pour des électrons dans un réseau aléatoire avec applications à la structure électronique des alliages 252

B. S. CHANDRASEKHAR et J. K. HULM:
La résistivité électrique et la supraconductibilité de quelques alliages et composés d'uranium 259

JOHN RAYNE:
Chaleur spécifique d'alliages dilués magnésium-aluminium au-dessous de 4,2°K . . 268

Lettres aux éditeurs:

T. E. SLYKHOUSE et H. G. DRICKAMER:
L'influence de la pression sur la limite d'absorption du soufre. 275

L. E. ORGEL:
Distorsions de réseau dues au mélange *s–d* 276

page

Lettres aux éditeurs:—*continué*

F. A. KRÖGER:

Sur la relation entre la non-stoechiométrie et la formation des centres donneurs et accepteurs dans les composés 277

Revue du livre:

"The Calculation of Atomic Structures", par D. R. HARTREE (revu par PER-OLOV LÖWDIN) 279

Volume 7 No. 4

EIJI HIRAHARA et MIYUKI MURAKAMI:

Anisotropies électrique et magnétiques des monocristaux de sulfure de fer . . . 281

G. J. DIENES:

La variation avec la température du module élastique de la silice vitreuse . . . 290

O. G. FOLBERTH:

La pression de vapeur d'équilibre des composés InAs, GaAs, InP et GaP au point de fusion 295

ALVIN J. COHEN et HERBERT L. SMITH:

Absorption ultraviolette et infrarouge de GeO_2 fondu 301

M. S. WECHSLER et R. H. KERNOHAN:

Effets de l'irradiation aux neutrons sur les alliages cuivre–aluminium 307

GEORGE WEISS et ALEXEI MARADUDIN:

Propriétés thermodynamiques d'un réseau désordonné 327

P–G. DE GENNES:

Sur la relaxation nucléaire dans les cristaux ioniques 345

D. G. WICKHAM et W. J. CROFT:

Propriétés cristallographiques et magnétiques de plusieurs spinelles contenant du manganèse trivalent. 351

Lettre aux éditeurs:

ALVIN J. COHEN et EDWIN S. HODGE:

Spécificité zonale et non-spécificité de certaines impuretés pendant la croissance du quartz synthétique 361

Volume 7 No. 1

В. Д. Джонстон, Р. Р. Хейкес и Д. Сестрич:

Приготовление, кристаллографические и магнитные свойства системы $Li_xCo_{(1-x)}O$ 1

Р. Т. Бейт и К. Хеер:

Некоторые оптические и магнитные свойства облученного LiF . . . 14

П. Бриссоно:

К количественному исследованию эффектов магнитного последействия при диффузии углерода в α-железе 22

Дж. Филлипс:

Обменные члены в формализме эффективных масс 52

У. Гонзер и Б. Оккерсе:

Вопрос о фазовых переходах, индуцированных облучением 55

page

Г. Алерс и Дж. Нейбурс:
Упругие постоянные цинка при температурах от 4,2 до 670°К . . . 58

Е. Музер и В. Пирсон:
Кристаллическая структура и свойства элементов групп от VB до VIIB и их взаимных соединений 65

Р. Ф. Валлис и Г. Боулден:
Теория спектра примесной фото-ионизации полупроводников в магнитном поле . 78

К. Р. Вассель:
Влияние элементов первого длинного периода на сопротивление меди и алюминия 90

Письма в Редакцию:

Нилс Бэклунд:
Электрическое сопротивление некоторых сплавов ценных металлов при температуре жидкого гелия 94

А. Т. Дж. Роуланд:
Ядерный магнитный резонанс Pt^{195} в платине металле 95

В. Т. Маттиас и В. Х. Захариасен:
Сверхпроводимость азотистого рения 98

VOL. 10 1959

Volume 7 Nos. 2/3

М. Я. Азбель:
Квантовая теория высокочастотного поверхностного импеданса металлов . . 105

К. Вейсер:
Теоретическое вычисление коэффициентов распределения примесей в германии и кремнии 118

М. Кардона и В. Поль:
Квадратичный фотоэлектромагнитный эффект в германии 127

К. Волфштирн и К. Фуллер:
Сравнение концентраций ^{67}Cu и дырок в германии 141

Н. Т. Меламед:
Перенос энергии в ZnS.Cu.Cl- фосфорах 146

Г. Мейер:
Инфракрасная флюоресценция в активированных медью цинк-сульфидных фосфорах 153

В. Маршалл:
Антиферромагнетизм $CuCl_2.2H_2O$ 159

М. Гольдман:
Ядерный резонанс на протонах в трихлоруксусной кислоте 165

К. Клик и В. Д. Комптон:
Поляризованная люминесценция KCl–Tl при низких температурах . . . 170

Г. А. Клазенс:
Зависимость от интенсивности фотопроводимости и люминесценции фотопроводников в стационарном состоянии 175

А. М. Клогстон:
Структура метастабильного состояния Mn^{++} и Fe^{+++} 201

page

Т. Е. Сликхауз и Г. Дрикамер:
Влияние давления на границу поглощения в галогенидах серебра . . . 207

Т. Е. Сликхауз и Г. Дрикамер:
Влияние давления на оптическую границу поглощения в германии и кремнии . 210

Д. Ф. Моррис:
Неустойчивость некоторых дигалидов меди и серебра 214

Дж. Лоран и Ж. Бенар:
Автодиффузия ионов в поликристаллических галогенидах щелочных металлов . 218

Т. Гарман, М. Логан и Г. Геринг:
Приготовление и электрические свойства теллурида ртути 228

В. Генри Дж. Хростовский и Р. Г. Кайзер:
Абсорбционный спектр кремния, обработанного мышьяком 236

Дж. Верник, С. Геллер и К. Е. Бенсон:
Фазовая диаграмма системы $AgSbSe_2$–$AgSbTe_2$–$AgBiSe_2$–$AgBiTe_2$ . . . 240

Р. Вейсс и К. Тауер:
Термодинамика системы Au–Pt 249

Дж. Корринга:
Псевдо-периодическая теория дисперсии для электронов в произвольной решетке и ее применение к электронной структуре сплавов 252

Б. С. Чандрасскар и Дж. Хелм:
Электрическое сопротивление и сверхпроводимость некоторых сплавов и соединений урана 259

Дж. Райн:
Теплоемкость слабых твердых растворов алюминия в магнии при температурах ниже 4,2°К 268

Письма в Редакцию:

Т. Е. Слайкхаус и Г. Г. Дрикамер:
Влияние давления на абсорбционный край серы 275

Л. Е. Оргел:
Искажения решетки при смешивании *d–s* 276

Ф. А. Крогер:
О взаимоотношении между нестойхиометрией и образованием донорных и акцепторных центров в соединениях 277

Рецензия:
«К расчету атомных структур» Д. Р. Хартри (рецензент: Пер-Олов Лаудин) . 279

Volume 7 No. 4

Е. Хирахара и М. Мураками:
Магнитная и электрическая анизотропия монокристаллов сульфида железа . 281

Г. Динес:
Температурная зависимость упругих модулей стекловидного кварца . . 290

О. Г. Фольберт:
Равновесная упругость пара соединений InAs, GaAs, InPnGaP в точке плавления . 295

А. Коен и Г. Смит:
Ультрафиолетовое и инфракрасное поглощение в плавленном германии . . 301

page

М. С. Векслер и Р. Керноган:
Влияние нейтронного облучения на медно-аллюминиевые сплавы . . . 307

Дж. Вейсс и А. Марадудин:
Термодинамические свойства неупорядоченной решетки 327

П. де Геннес:
О ядерной релаксации в ионных кристаллах 345

Д. Викхам и В. Крофт:
Кристаллографические и магнитные свойства некоторых шпинелей, содержащих трехвалентный марганец 351

Письмо в редакцию:

Алвин Дж. Коэн и Эдвин С. Ходж:
Зональная специфичность и неспецифичность известных примесей во время выращивания синтетического α-кварца 361

OL.
10
959

Volume 7 No. 1

W. D. Johnston, R. R. Heikes und D. Sestrich:
Herstellung, Kristallographie und die magnetischen Eigenschaften des Systems- $Li_xCo_{1-x}O$ 1

R. T. Bate und C. V. Heer:
Einige optische und magnetische Eigenschaften von bestrahltem LiF 14

Pierre Brissonneau:
Ein Beitrag zum quantitativenStud ium der magnetischen Diffusionsnachwirkung des Kohlenstoffs in α-Eisen 22

James C. Phillips:
Austauschglieder im Formalismus der effektiven Masse 52

Ulrich Gonser und Boudewyn Okkerse:
Die Frage der durch Bestrahlung hervorgerufenen Phasenumwandlungen . . . 55

G. A. Alers und J. R. Neighbours:
Die elastischen Konstanten von Zink zwischen 4·2° und 670°K 58

E. Mooser und W. B. Pearson:
Die Kristallstruktur und die Eigenschaften der Elemente von Gruppe VB bis VIIB und der zwischen ihnen gebildeten Verbindungen 65

R. F. Wallis und H. J. Bowldenz:
Die Theorie des Photoionisationsspektrums der Verunreinigungen von Halbleitern in magnetischen Feldern 78

C. R. Vassel:
Der Einfluss der Elemente der ersten langen Periode auf den widerstand von Kupfer und Aluminium 90

Briefe an die Herausgeber:

Nils Bäcklund:
Der elektrische Widerstand einiger Edelmetallegierungen bei der Temperatur des flüssigen Heliums 94

T. J. Rowland:
Kernmagnetische Resonanz des Pt^{195} vin metallischem Platin 95

Briefe an die Herausgeber:—*fortsetzung* *page*

B. T. MATTHIAS und W. H. ZACHARIASEN:
Die Supraleitfähigkeit von Rheniumnitrid 98

Volume 7 Nos. 2/3

M. YA. AZBEL:
Die Quantentheorie der Oberflächenimpedanz für Metalle bei hohen Frequenzen . . 105

KURT WEISER:
Theoretische Berechnung des Verteilungskoeffizienten von Verunreinigungen in Germanium und Silizium 118

MANUEL CARDONA und WILLIAM PAUL:
Ein quadratischer photoelektromagnetischer Effekt in Germanium 127

KATHERINE WOLFSTIRN und C. S. FULLER:
Vergleich zwischen den Konzentrationen des radioaktiven Kupfers und den Leerstellen in Germanium 141

N. T. MELAMED:
Energieaustausch in ZnS:Cu:Cl-Phosphoren 146

G. MEIJER:
Infrarote Fluoreszenz von Zinksulfidphosphoren, die mit Kupfer aktiviert wurden . . 153

W. MARSHALL:
Der Antiferromagnetismus von $CuCl_2 \cdot 2H_2O$ 159

MAURICE GOLDMAN:
Nukleare Resonanz der Protonen in Trichloressigsäure 165

CLIFFORD C. KLICK und W. DALE COMPTON:
Polarisierte Luminiszenz von KCl:Tl bei tiefen Temperaturen 170

H. A. KLASENS:
Die Intensitätsabhängigkeit der Photoleitung und der Luminiszenz bei Photoleitern im stationären Zustand 175

A. M. CLOYSTON:
Die Struktur des metastabilen Zustandes von Mn^{++} und Fe^{+++} 201

T. E. SLYKHOUSE und H. G. DRICKAMER:
Die Druckabhängigkeit der Absorptionskante bei Silberhalogeniden 207

T. E. SLYKHOUSE und H. G. DRICKAMER:
Die Druckabhangigkeit der optischen Absorptionskante von Germanium und Silizium . 210

D. F. C. MORRIS:
Die Instabilität einiger Dihalogenide von Kupfer und Silber 214

J. F. LAURENT und J. BÉNARD:
Selbstdiffusion der Ionen in polykristallinen Alkalihalogeniden 218

T. C. HARMAN, M. J. LOGAN und H. L. GOERING:
Herstellung und elektrische Eigenschaften des Quecksilbertellurids 228

HENRY J. HROSTOWSKI und R. H. KAISER:
Das Absorptionsspektrum von arsendotiertem Silizium 236

J. H. WERNICK, S. GELLER und K. E. BENSON:
Die Konstitution des Systems $AgSbSe$–$AgSbTe_2$–$AgBiSe_2$–$AgBiTe_2$ 240

VOL.
10
195

VOL. 10 1959

page

R. J. Weiss und K. J. Tauer:
Die Thermodynamik des Systems Au–Pt 249

J. Korringa:
Eine Dispersionstheorie für Elektronen in einem ungeordneten Gitter mit Anwendungen auf die Elektronenstrukturen der Legierungen 252

B. S. Chandrasekhar und J. K. Hulm:
Der elektrische Widerstand und die Supraleitfähigkeit einiger Legierungen und Verbindungen des Urans 259

John Rayne:
Wärmekapazität von verdünnten Magnesium-Aluminium-Legierungen unterhalb 4,2°K . 268

Briefe an die Herausgeber:

T. E. Slykhouse und H. G. Drickamer:
Die Druckabhängigkeit der Absorptionskante von Schwefel 275

L. E. Orgel:
Gitterverzerrungen infolge Überlappung der *d*–*s*–Zustände 276

F. A. Kröger:
Über die Beziehung zwischen nicht stöchiometrischen Zusammensetzung und der Bildung von Donator- und Akzeptorzentren in Verbindungen 277

Buchbesprechung:
"The Calculation of Atomic Structures," von D. R. Hartree (besprochen von Per-Olov Löwdin) 279

Volume 7 No. 4

Eiji Hirakara und Miyuki Murakami:
Magnetische und elektrische Anisotropien von Einkristallen des Eisensulfids . . . 281

G. J. Dienes:
Die Temperaturabhängigkeit der Elastizitätsmoduln bei Silikatgläsern 290

O. G. Folberth:
Zur Frage des Damfdrucks der Verbindungen InAs, GaAs, InP und GaP . . . 295

Alvin J. Cohen und Herbert L. Smith:
Absorption im Ultraviolett und Infraroten bei flüssigem Germanium 301

M. S. Wechsler und R. H. Kernohan:
Der Einfluss einer Neutronenbestrahlung auf Kupfer–Aluminium-Legierungen. . . 307

Georg Weiss und Alexei Maradudin:
Thermodynamische Eigenschaften eines ungeordneten Gitters 327

P–G. de Gennes:
Über die Kernrelaxation in Ionenkristallen 345

D. G. Wickham und W. J. Croft:
Kristallographische und magnetische Eigenschaften verschiedener Spinelle die 3-wertiges Mangan enthalten 351

Briefe an die Herausgeber:

Alvin J. Cohen und Edwin S. Hodge:
Zonenartige Besonderheiten gewisser Verunreinigungen während des Wachstums synthetischen α-Quarzes 361

PAPERS TO BE PUBLISHED IN FUTURE ISSUES

TAIRA SUZUKI and MASAO DOYAMA: Hardening induced by additive coloration in KCl.

JUNJIRO KANAMORI: Super exchange interaction and symmetry properties of electron orbitals.

JUN KONDO and JIRO YAMASHITA: Nuclear quadrupolar relaxation in ionic crystals.

A. F. FORESTIERI and L. A. GIRIFALCO: The effect of plastic deformation on self-diffusion in silver.

J. L. DAVIS, G. E. DEVLIN, V. JACCARINO and A. C. SCHAWLOW: Structure sensitivity of the high-frequency NMR in powdered antiferromagnetic MnF.

J. J. HOPFIELD: A theory of edge emission phenomena in CdS, ZnS and ZnO.

EDGAR F. WESTRUM, Jr. and D. M. GRIMES: Low temperature heat capacities and thermodynamic properties of zinc ferrites—III Effect of copper substitution.

R. J. WEISS and A. F. FREEMAN: X-ray and neutron scattering from electrons in a crystalline field and the determination of outer electron configurations in Fe and Ni.

A. BLANDIN and E. DANIEL: Sur le déplacement de Knight dans les alliages.

R. NATHANS, C. G. SHULL, G. SHIRANE and A. ANDRESEN: The use of polarized neutrons in determining the magnetic scattering by iron and nickel.

E. N. ADAMS and T. D. HOLSTEIN: Quantum theory of transverse galvanomagnetic phenomena.

R. GUCCIONE, M. P. TOSI and M. ASDENTE: Migration barriers for cations and anions in alkali halide crystals.

ISSAI LEFKOWITZ: Radiation induced changes in the ferroelectric properties of some barium titanate type materials.

E. DANIEL: Sur le déplacement de Knight des impuretés dans les métaux.

M. A. GILLEO and S. GELLER: The interaction of magnetic ions in $Gd_3Mn_2Ge_2GaO_{12}$ and related garnets.

M. A. GILLEO and D. W. MITCHELL: The ferrimagnetism and crystal chemistry of substituted manganese–tin spinels.

PIERRE MOREL: Calcul semi-empirique de la témperature de transition des superconducteurs et de l'effet de la pression sur la transition.

F. D. ROSI, B. ABELES and R. V. JENSEN: Materials for thermoelectric refrigeration.

S. H. KOENIG and R. D. BROWN: Thermal oscillations in *n*-Ge at low temperatures.

M. S. ABRAHAMS, R. BRAUNSTEIN and F. D. ROSI: Thermal, electrical and optical properties of (In,Ga)As alloys.

E. N. ADAMS and E. I. BLOUNT: Energy bands in the presence of an external force field—II Anomalous velocities.

K. TEEGARDEN and R. WEEKS: Trapped charge and the low temperature luminescence of undoped KI.

G. J. OGILVIE and M. J. RIDGE: The cathodic sputtering of silver.

G. J. OGILVIE: The surface structure of silver crystals after argon ion bombardment.

H. M. C. SOSNOVSKY: The catalytic activity of silver crystals of various orientations after bombardment with positive ions.

J. P. EVANS and P. G. MARDON: Some physical properties of neptunium metal—I A determination of the specific heat of α-neptunium.

E. ANTONČIK: Approximate formulation of the orthoganalized plain-wave method.

I. KENDE, L. GUCZI and D. GÁL: Investigation of the interaction of alkyl iodide vapours with a carbon surface by kinetic and isotopic methods.

L. GUCZI, I. KENDE, and D. GÀL: Use of the differential isotope method for studying the interaction between vapours of alkyl iodide and surface.

I S. JACOBS: Evidence for triangular moment arrangements in $Mo.Mn_2O_3$.

TED G. BERLINCOURT: Hall effect, resistivity and superconductivity of some metastable uranium rich alloys.

P. ZWIETERING, H. L. T. KOKS and C. V. HEERDEN: Quantitative aspects of the changes in the electric conductivity of metals due to chemisorption.

J. Phys. Chem. Solids Pergamon Press 1959. Vol. 10. pp. 77–86.

HARDENING INDUCED BY ADDITIVE COLORATION IN KCl*

TAIRA SUZUKI† and MASAO DOYAMA

Department of Physics, University of Illinois, Urbana, Illinois

(*Received* 12 *December* 1958)

Abstract—The critical shear stress of KCl crystals has been measured as a function of the number of F-centers (n_F) in the range of 0–10^{18} cm^{-1} introduced by additive coloration. The introduction of the F-centers gives a marked increase of critical shear stress σ_C as $\Delta\sigma_C = (3{\cdot}1 - 0{\cdot}22\ T^{\frac{1}{2}})10^{-16} n_F$ g/mm^2, where T is the measuring temperature in °K. If the colored crystals are held in the dark below room temperature, even at nitrogen temperature, the critical shear stress increases with time until a saturation level is reached which depends upon n_F and the aging temperature. The irradiation of the F-light enhances the rate of the process greatly. The hardening due to aging is a reversible function of the aging temperature. The effect of the coagulation of F-centers on the mechanical properties has also been studied.

As the aging proceeds at nitrogen temperature, the absorption curve on the shorter-wavelength side of the F-band produces a broadening and a peak at 2·78 eV. Although cold working before aging does not produce a large effect, deformation at the coloration temperature after coloration gives rise to extensive effects on the broadening of the F-band in the above region, while no indication of the growth of complex centers is observed. A qualitative discussion of the present phenomena is given. This is based on the electronic process associated with the clustering of point defects, including the F-centers, in the vicinity of the dislocations.

1. INTRODUCTION

STUDIES of the mechanical effects of color centers in alkali halides have been concerned hitherto with the color centers introduced by X-rays or ultraviolet light. Very few investigations have been carried out on additively colored crystals. It has been shown that X-ray irradiation increases the yield stress of rock-salt above the breaking strength of unirradiated crystals.[1,2] Recently, GORDON and NOWICK[3] studied the elastic modulus and internal friction of NaCl crystals irradiated by X-rays. They found an increase in the modulus and a decrease in the internal friction. These hardening effects are permanent; they are not reversed by optical bleaching. GORDON and NOWICK thus propose, following FRANKL[4] and SEITZ[5], that the hardening is due to the pinning of the dislocations by the positive-ion vacancies which are released from pairs of vacancies, leaving behind the F-centers. The F-centers have been considered to have little effect on the hardening.

The ions surrounding an F-center are normally assumed to be nearly in their normal positions, since the electron should have almost the same electrostatic effect as the missing halogen ion. However, GOURARY and ADRIAN[6] have recently calculated the displacement of the neighboring alkali ions into the F-center and have found that the shift cannot be neglected in comparison with the corresponding displacement due to the positive- or negative-ion vacancy. However, since the results of calculation are strongly dependent upon the type of wave function used, it is not yet conclusive. It is of interest, therefore, to carry out experiments on the effects of the F-centers on mechanical and optical properties. A shift in the peak and a broadening of the F-band are to be expected when the F-centers concentrate in the vicinity of the

* Supported by the Office of Naval Research.

† On leave from the Research Institute for Iron, Steel, and Other Metals, Tohoku University, Sendai, Japan. Address will change after August of 1959 to the Institute for Solid State Physics, Tokyo University, Tokyo, Japan.

dislocations.[7] On the other hand, if the line charge of the dislocations is altered by additive coloration, effects on the mechanical properties are to be expected on the basis of reasoning similar to that used by ESHELBY *et al.*[8] recently. It is desirable to distinguish the mechanisms from each other on the basis of experimental results.

When the colored crystals are held in the dark or are irradiated with *F*-light above room temperature, the *F*-centers agglomerate into the complex centers. Since such a process can be followed to some extent quantitatively by optical methods, a study of the effects of irradiation upon the mechanical properties will throw light on problems such as precipitation-, radiation- and quench-hardening in crystals, where the processes can be followed less directly.

2. EXPERIMENTAL PROCEDURE

The KCl crystals used in the present work were supplied by the Harshaw Chemical Company. The potassium metal of 99·9 per cent purity was first distilled by heating at 300°C in a Pyrex tube connected to the evacuating system. The distillation was done in three steps. After the final distillation, a crystal block $\frac{1}{4}\times\frac{1}{2}\times 1$ in, bounded by (100) cleavage surfaces, was inserted into the tube, which was separated from the metal by a constriction in the tube. The whole system was evacuated to 2×10^{-6} mm Hg and sealed off. The sealed tube was 20 mm in internal diameter and 20 cm in length. The tube was wrapped in aluminum foil and inserted into a controlled furnace supported horizontally. The coloration was carried out at 550°C except in special cases. The potassium metal was maintained at a certain temperature around 350°C, depending upon the desired concentration of *F*-centers. Later, however, we obtained the desired concentration of *F*-centers by controlling the amount of the metal and the length of annealing time. In the latter case the whole system was maintained at 550°C for about 30 hr. The wrapped tube was quenched onto the copper plate at room temperature. This procedure was chosen so that there would be no significant thermal strain. The crystals thus obtained were checked for such strains by inspecting a thin section of the crystals with a polarizing microscope.

The Beckman spectrophotometer Model-DU was used for measuring the absorption spectrum from 300 to 1300 mμ. The optical specimens were cleaved from three parts of the whole block of the colored crystal at different depths from the surface. The crystals to be used were colored homogeneously with a variation of less than about 5 per cent in the density of *F*-centers. For the determination of the number of *F*-centers per unit volume, n_F, we employed the Smakula equation: $n_F = AK_{\max}H\ \mathrm{cm}^{-3}$, where $A = 1{\cdot}31\times 10^{16}$ (eV cm^2)$^{-1}$ at 20°C, $K_{\max}$ is the absorption coefficient for the band maximum in cm^{-1} and H is the half-width of the band in eV. The apparatus for the compression tests was the same as that previously used by one of the present authors.[9] The size of the specimen for the mechanical test was about $\frac{1}{8}\times\frac{1}{8}\times\frac{1}{2}$ in. The surfaces were prepared by cleavage followed by gentle polishing with a wet silk-cloth.

The optical-absorption measurements were all made at room temperature. For the annealing and the measurements of stress/strain curves at low temperatures, liquid nitrogen and a mixture of dry ice and ethyl alcohol were used. The *F*-light irradiation was made by using a mercury lamp with Kodak filter No. 61. Weighing the specimen crystal showed that the effects of alcohol upon the surfaces during the measurements of critical shear stress at the temperature concerned were very small.

3. RESULTS

(a) *Critical Shear Stress versus* n_F

As a general approach to the problems concerning the mechanical effects of *F*-centers introduced additively into KCl crystals, we first measured the critical shear stress as a function of the concentration of *F*-centers. The results are shown in Fig. 1. The specimen crystals were held in the dark at room temperature for at least 1 day after quenching, and the critical shear stress σ_C was measured in the dark at the same temperature. Some of the crystals were quickly brought to 77 and 423°K and the effects of temperature of measurement were studied.

No change in σ_C was observed until n_F becomes about 10^{16} cm^{-3}. Above this critical concentration the critical shear stress starts to increase as follows:

$$\sigma_C - \sigma'_C = An_F, \qquad (1)$$

where $A = (3{\cdot}1-0{\cdot}22\ T^{\frac{1}{2}})\ 10^{-16}$ g/mm^2 and

$\sigma'_C = 99 - 3{\cdot}87\ T^{\frac{1}{2}}$ g/mm². The equation for σ'_C is simply the expression for the critical shear stress of an uncolored crystal. It is to be noted that both $(\sigma_C - \sigma'_C)$ and σ'_C could be expressed as linear

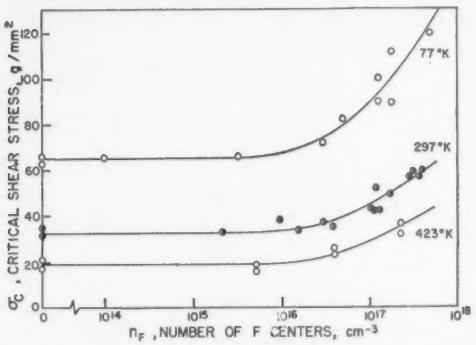

FIG. 1. Critical shear stress of additively colored crystals plotted against the concentration of *F*-centers. Crystals were kept in the dark for a few days at room temperature and then the critical shear stress was measured in the dark at 77, 297 and 423°K.

functions of temperature within the limits of experimental error. To determine the exact form of the temperature-dependence, it is necessary to carry out experiments at liquid-helium temperature.

The critical concentration of n_F probably is a result of the presence of other imperfections such as positive- and negative-ion vacancies, and metallic impurities in the surrounding of the dislocations. We have attempted to check the effect due to the vacancies by varying the quenching temperature in the range from 630 to 450°C. Each crystal was colored additively at a temperature in that range and then quenched, but no appreciable effect was found. The present crystals from Harshaw contain some multivalent impurities, of the order of 10^{17} or less per unit volume.[10] If these impurities are really important, the mechanical effects of *F*-centers will be masked in the case of impure crystals.

WESTERVELT[11] found no effect on surface hardness of additively colored KCl with $n_F = 10^{17}$ cm^{-3}. The surface hardness measured by an indentation method, however, may not be adequate for the present purpose for the following reason. The hardness thus obtained depends upon the form of the stress/strain curve. The stress/strain curve of a colored crystal shows a higher yield stress and a smaller rate of hardening than that of an uncolored crystal. Therefore, it may fail to reveal the effect concerned here. In Table 1 we show the results for the surface hardness obtained by varying the indentation load from 100 to 25 g. By this procedure it is possible to extrapolate the hardness to the value at zero load so as to obtain the yield stress. It is clearly seen in Table 1 that the *F*-centers introduced additively give rise to an appreciable effect.

Table 1. *Effect of additive coloration on surface hardness**

Indentation load (g)	25	50	100
Uncolored	9·33	9·27	8·94
Colored ($n_F = 10^{17}$ cm^{-3})	9·89	9·61	9·27

* The specimen crystals were all quenched from 550°C and held in the dark at room temperature for at least 1 day. The surfaces to be examined were prepared by cleavage followed by gentle polishing with a wet cloth. The numbers are diamond pyramid hardness numbers determined by a Tukon tester.

(b) *Age-hardening Below Room Temperature*

When quenched crystals were held in the dark at room temperature, the critical shear stress was found to increase with time. For this reason the observations illustrated in Fig. 1 were made on crystals which were held for 1 or 2 days after quenching, where σ_C was almost saturated. Other curves show the effects in more detail. The three

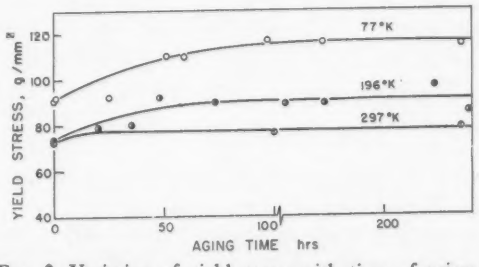

FIG. 2. Variation of yield stress with time of aging at 77°K ($n_F = 1{\cdot}64 \times 10^{17}$ cm^{-3}), 196°K ($n_F = 1{\cdot}19 \times 10^{17}$ cm^{-3}), and 297°K ($n_F = 1{\cdot}15 \times 10^{17}$ cm^{-3}). Crystals were held in the dark at each temperature before the measurements at room temperature were made.

curves in Fig. 2 were taken for the crystals held in the dark after quenching at 77, 196, and 297°K, respectively. All measurements, however, were made at room temperature in the dark in a short time. Although the rate of increase of yield stress with time does not indicate a large dependence upon aging temperature, the amount of the change increases remarkably with decreasing temperature. On the assumption that the process requires thermal activation, we have attempted to determine the activation energy from similar curves, as shown in Fig. 2. Although we are not certain that the activation energy thus obtained gives an exact value, because of the difficulty in obtaining smooth curves in the early stage of aging, it proved to be of the order of 0·1 eV or less.

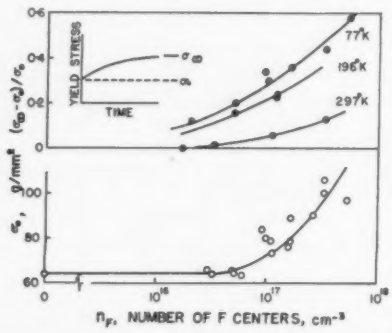

FIG. 3. Yield stress immediately after quenching σ_0, and the ratio of total change of yield stress to σ_0 plotted against concentration of *F*-centers. Aging temperatures are indicated.

In Fig. 3 we plot the initial yield stress σ_0, measured at room temperature, which is equal to $2\sigma_C$ at $t = 0$, and the ratio of the final increase of yield stress to the initial yield stress $(\sigma_\infty - \sigma_0)/\sigma_0$ as a function of n_F. It can be expressed as follows:

$$\left.\begin{aligned} \sigma_0 - 2\sigma'_C &= 1{\cdot}0\times10^{-16} n_F \\ \text{and} \qquad \sigma_\infty - \sigma_0 &= c n_F, \end{aligned}\right\} \quad (2)$$

where c is $2{\cdot}1\times10^{-16}$ at 77°K, $1{\cdot}65\times10^{-16}$ at 196°K, and $0{\cdot}4\times10^{-16}$ at 297°K.

The effects of aging are surprisingly large; $\sigma_\infty/\sigma_0 = 1{\cdot}6$ at 77°K for $n_F = 5\times10^{17}$ cm^{-3}. Fig. 4 illustrates the relation between σ_∞/σ_0 and aging temperature for certain values of n_F. The ratio σ_∞/σ_0 decreases with increasing temperature and the effects of aging vanish rapidly at $T_C = 325$°K. There seems to be a tendency for saturation to occur at very low temperature. Fig. 5 illustrates the variation of yield stress with time for a cyclic change of aging temperature from 77 to 297°K. Age-hardening is completely reversible against aging temperature below room temperature.

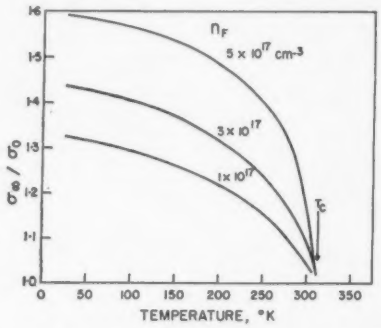

FIG. 4. σ_∞/σ_0 vs. aging temperature. Measurements were made at room temperature.

It is interesting to note that the phenomenon shown in Fig. 5 is very similar to the phenomenon called *Rückbildung* in age-hardening alloys such as aluminum–copper alloys. The latter is believed to

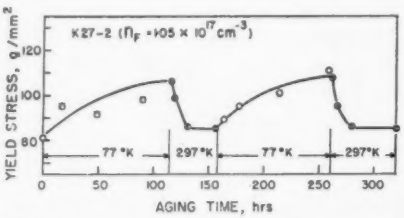

FIG. 5. Variation of yield stress with a cyclic change of aging temperature. Measurements were made at room temperature; $n_F = 1{\cdot}05\times10^{17}$ cm^{-3}.

be due to the re-solution of copper atoms by atomic diffusion from the Guinier–Preston zones in the aluminum matrix. In the present case, however, the diffusion of imperfections does not appear to play a primary role for the following reasons: First, the temperature-dependence of the present phenomenon is too small to be explained by the diffusion of any imperfection. One may expect a certain reduction of the activation energy for the motion of the imperfection if it moves in the close vicinity of the dislocation line. However, there are

other factors which support the view that the ionic diffusion is not a major process in the present case. We have observed (1) no strain-hardening, (2) no coagulation of the *F*-centers and (3) a remarkable acceleration in aging on irradiation by light. After the colored crystals had been strained in compression at room temperature by 0·5–10 per cent, they were kept in the dark at 77°K. No appreciable further hardening was observed even after one month. If diffusion occurs in the lattice the fresh dislocations introduced by deformation will be surrounded by imperfections after a sufficient aging time. Moreover no evidence of the coagulation of the *F*-centers has been observed in the foregoing case.

If the colored crystals were held under the *F*-light at 77°K after quenching, the rate of the reaction which results in the additional hardening was enhanced by a factor of ten. The final state of hardness is almost the same as that obtained in the dark. Table 2 gives some examples.

(c) *Optical Effects Associated With the Hardening of Colored Crystals*

In the following, we will describe the optical effects which accompany the hardening of the crystals. The specimen crystals were deformed by 4·4 per cent at room temperature and then held at 77°K. No significant change was observed in the absorption spectrum on the long-wavelength side of the *F*-band. On the short-wavelength side, however, a small peak, at 2·78 eV in photon energy, became noticeable. This is interesting, because it apparently corresponds to the *K*-band, which was first found by KLEINSCHROD[12] and studied later by DUERIG and MARKHAM[10]. The *K*-band is not yet completely understood. It seems necessary to carry out further experiments before any conclusion can be reached.

There are two points to be noted in the above experiment. First, the procedure for introducing dislocations may not be adequate to give pronounced optical effects. This is because no

Table 2. The effect of irradiation of light on the yield stress of colored crystals

Crystal No.	n_F (cm^{-3})	Temperature (°K)	Unirradiated (kept in dark) (hr)	Irradiated (hr)	Yield stress* (g/mm^2)
K 40–0	$9·3 \times 10^{16}$	77	0	– – –	84
a			24	– – –	87·9
c			24	– – –	86·4
1			– – –	*F*-light, 24	115·1
2			– – –	*F*-light, 24	117·2
3			– – –	*F*-light, 36	113
4			– – –	*F*-light, 36	121
5			240	– – –	113
K 42–0	$3·3 \times 10^{17}$	77	0	– – –	100·5
a			10	– – –	108
b			10	– – –	107·3
1			– – –	White light, 10	141·8
2			– – –	White light, 10	142·5–145·6
3			One month	– – –	144
K 43–0	$3·4 \times 10^{17}$	300	0	– – –	106·3
c			12	– – –	94·1–111
d			12	– – –	104·6–110·9
2			– – –	*F*-light, 12	111·2–118
f			44	– – –	113·5
4			– – –	*F*-light, 44†	109·9–115·5

* Yield stress was measured at room temperature in the dark.

† The effect of longer periods of irradiation will be described later.

appreciable diffusion which can build up the atmosphere of F-centers around the new dislocations takes place at 77°K. If this is true, the introduction of dislocations sufficient to render the effects observable must be effected at elevated temperatures. Therefore we adopted the following procedures: Crystals were first additively colored at 550°C and then deformed in the dark at the same temperature. To preserve as many dislocations as possible and to avoid the agglomeration of F-centers, the crystals were again quenched to room temperature immediately after the deformation. The results shown in Fig. 6 were obtained on crystals held at

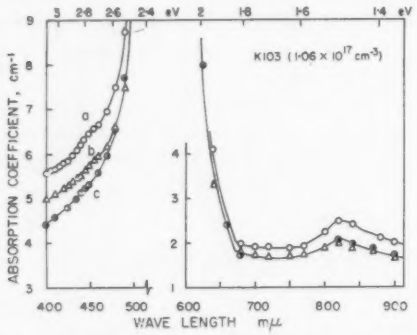

FIG. 6. Absorption spectrum of crystals deformed at 550°C by 10 per cent strain after additive coloration ($n_F = 1{\cdot}06 \times 10^{17}$ cm^{-3}) and held at 77°K for: (*a*) 17 hr under F-light, (*b*) 20 days in the dark and (*c*) 17 hr in the dark.

77°K after quenching: (*a*) under the F-light for 17 hr, (*b*) in the dark for 20 days and (*c*) in the dark for 17 hr. These crystals were cleaved before aging from a single block of the deformed crystal. There is a pronounced growth of the tail of the F-band with aging time in the range 400–500 mμ. The M-band at 820 mμ was observed from the beginning, but no appreciable growth of the band was detected. Although curve (*a*) shows a higher background, we believe that this is due to some accidental error such as, for instance, surface contamination. Thus one is led to conclude that the pronounced broadening on the high-energy side of the F-band occurs during aging, although no appreciable coagulation of the F-centers takes place.

(d) *Coagulation of F-centers and Hardening of Crystals*

It will be of special interest to study the effect on hardening induced by the coagulation of F-centers. In crystals containing essentially only F-centers, the electrons are released by irradiation with F-light above room temperature. These electrons are captured by various kinds of traps to form new F-, M-, R-, N- and more complex centers. Fig. 7 illustrates the irradiation effects of

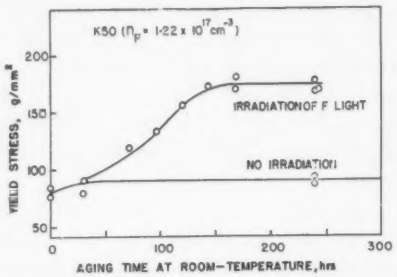

FIG. 7. Effect of irradiation with F-light on age-hardening at room temperature ($n_F = 1{\cdot}22 \times 10^{17}$ cm^{-3}). The upper curve corresponds to the irradiated crystal and the lower curve to the unirradiated crystal.

F-light on the yield stress at room temperature. The yield stress increased to a value twice as large as the initial value by the irradiation. It is concluded that the hardening produced additional to that generated by aging the same crystal in the dark is associated with the formation of complex centers.

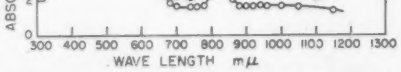

FIG. 8. Growth of complex centers by irradiation with F-light at room temperature: (*a*) after 151 hr under the light, (*b*) 124 hr in the dark and (*c*) 3 hr in the dark. The initial concentration of F-centers was $2{\cdot}50 \times 10^{17}$ cm^{-3}.

Fig. 8 gives the absorption curves of the crystals aged for (*a*) 151 hr under F-light, (*b*) 124 hr in the dark and (*c*) 3 hr in the dark. The initial concentration of F-centers, namely $2{\cdot}50 \times 10^{17}$ cm^{-3},

decreased to $0{\cdot}93\times10^{17}$ cm^{-3} after 151 hr under F-light. The F-centers were transferred to the complex centers. The concentration of F-centers after 124 hr in the dark is $2{\cdot}36\times10^{17}$ cm^{-3}, which is practically the same as the initial value. The hardening of the irradiated crystal increases slowly at the beginning of aging. It is known, however, that bleaching takes place very rapidly at the start. According to UETA and KÄNZIG[13], the formation of M-centers is predominant in this stage. One is led to conclude, therefore, that the M-centers produce less distortion in the neighboring lattice. In fact, this conclusion is supported by the theoretical prediction made by GOURARY and LUKE[14]. Curve (c) in Fig. 8 shows a higher background than (b). This contradiction may be due to the same cause as is operative in the case of (a) in Fig. 6.

The dependence of yield stress upon temperature of measurement provides a critical test of the hardening mechanism. Curve (a) in Fig. 9 was

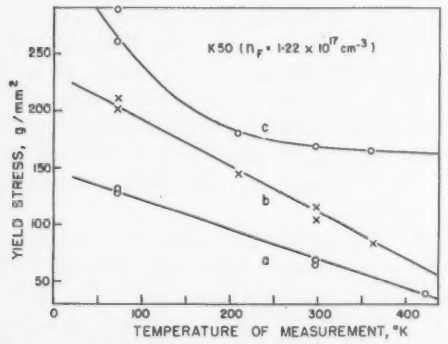

FIG. 9. Dependence of yield stress upon measuring temperature: (a) uncolored, (b) aged in the dark for 240 hr at room temperature, and (c) irradiated by F-light for 240 hr at room temperature. The initial concentration of F-centers was $1{\cdot}22\times10^{17}$ cm^{-3}.

taken from uncolored crystals, which were otherwise similarly treated. Curve (b) in the same figure was taken from colored crystals held in the dark at room temperature for 240 hr. Both curves are proportional to $T^{\frac{1}{2}}$ within the range of temperature investigated, as already described. The slopes of the curves were found to increase with increasing n_F and to depend on the aging temperature. If the crystals were irradiated until the complex centers formed, the character of the dependence changed completely. Curve (c) was obtained on crystals held under the light for 240 hr at room temperature. The initial concentration of the F-centers of all crystals is $1{\cdot}22\times10^{17}$ cm^{-3}, while the uncolored crystals were cut from the same block as the colored crystal before annealing. Curve (c) gives $\sigma_C = 73\exp(44{\cdot}9/T)$ g/mm^2. The proportionality factor is sensitive to n_F, while the exponent is not. The temperature-dependence of the yield stress for uncolored crystals appears to be in good qualitative agreement with the results for NaCl crystals obtained by STEPANOV and MILKAMANOVICH[15].

4. DISCUSSION OF RESULTS

First we will discuss the mechanism of hardening induced by additive coloration on the basis of the experimental results described in the preceding section. The crystals concerned contain essentially only F-centers, as was confirmed by optical measurements. The possible mechanisms are as follows:

(1) Solution-hardening due to the F-centers, in which the F-centers are considered as the dispersed centers of dilatation.

(2) An increase of the number of dislocations by additive coloration followed by rapid cooling.[16]

(3) Dislocation-jogs formed during the coloration, as suggested by PRATT[17], which set up the resistance to the slip motion of the dislocations.

(4) Elastic interaction between the dislocation and the F-center.

(5) The formation of the Debye–Hückel cloud of negative charge around the dislocation,[8,18] which is supposed to be positively charged and locked by a Coulomb force.

The basic hardening, such as that illustrated by a plot of σ_0 versus n_F in Fig. 3, might be explained by any of the above mechanisms as far as a qualitative understanding is concerned. We have not tried to determine the origin of each contribution. However, if the time- and temperature-dependent feature of the hardening is considered a mechanism such as (1), (2) or (3) will hardly explain it satisfactorily. The most difficult feature to understand is the reversibility of hardening with aging temperature, shown in Fig. 5. Two mechanisms, (4) and (5), remain to be discussed.

(a) *The Cottrell Interaction of F-centers With Dislocations*

According to GOURARY and ADRIAN[6], the displacement δ_F of the neighboring alkali ion into the F-center is found to be $\delta_F = 0{\cdot}0058$ to $0{\cdot}030$ in NaCl in units of the lattice parameter a. The elastic interaction energy U_F of the F-center with an edge dislocation is obtained by inserting δ_F into the Cottrell-Bilby formula $U = 4\mu b \delta r_0^3 (\sin\theta)/r$. In this formula, μ is the rigidity modulus, b the Burgers vector and r_0 the interatomic distance. The position of the F-center is given by the parameters (r, θ) measured from the center of the dislocation in the plane of normal to the dislocation axis. The interaction energy $U_{[+]}$ of a positive-ion vacancy with the edge dislocation is given, for comparison, by using the estimate of BASSANI and THOMSON[18], namely $\delta_{[+]} = -0{\cdot}0115$ in NaCl. After simple calculations, one obtains

$$2{\cdot}6U_{[+]} \geqslant U_F \geqslant 0{\cdot}5U_{[+]}.$$

In the present situation of the theory concerning δ_F, it is clear that mechanism (4) cannot be ignored relative to mechanism (5).

In quenched crystals, many F-centers will remain in the expanded region around the dislocation. If the F-centers release their electrons, the negative-ion vacancies are left behind. As a result they can increase the locking force of the dislocation. This will give rise to the age-hardening phenomena and the reversibility of hardening as a function of aging temperature. The electrons released will be captured by the neighboring traps, such as the F-centers or the negative-ion vacancies in the compressed region around the dislocation, or by the incipient vacancies at dislocation jogs. A similar result could be attained by short-range diffusion of the F-centers and the negative-ion vacancies across the slip plane. The effect of irradiation of light upon aging speed (Table 2) shows, however, that the diffusion of the imperfections is not a primary process in the present phenomena, since irradiation presumably leads only to electron transfer. The temperature-dependence of age-hardening in the dark suggests that in general the electrons need not be ejected to the conduction band before being captured by the traps mentioned above. In such a case, electron tunnelling appears to be most conceivable.

In the case of aging in the dark, the electron in the ground state of the F-center in the expanded region is transferred. In the case of the irradiation with F-light, the electron is raised to the first excited state before being transferred by the electron tunnelling. The electron in the excited state will be able to tunnel readily from the F-center to another trapping center. According to DEXTER[7], who assumed pure tunnelling without energy dissipation, the rate of the capture at a distance of 30 Å is once in a few hours for the electron in the ground state. This is of the right order of magnitude, in agreement with the present observations.

Consider the perturbation of the F-band energy due to the strain around an edge dislocation. We obtain an expression for the energy $E(r, \theta)$ by expanding in a Taylor series in terms of the density change, which is known as a function of the position. Using experimental data, we obtain[7]

$$E(r, \theta) = 2{\cdot}29 + 0{\cdot}92(\sin\theta/r)\ \text{eV}$$

where r is measured in Å. Thus an F-center 5 Å from the dislocation may have its peak shifted by about $\pm 0{\cdot}2$ eV. Therefore, one may conclude that the peak we observe at 2·78 eV cannot be explained by the pressure effect alone. It will need further study to draw a final conclusion concerning the broadening and the appearance of the peak at 2·78 eV as observed in deformed, additively colored crystals.

It seems difficult to explain even the qualitative features of the saturation hardening when plotted against aging temperature as shown in Fig. 4 on the basis of the present mechanism. The rapid rise of σ_∞ below T_C cannot be understood in terms of the Cottrell interaction of the F-centers and the electron transfer by pure tunnelling.

(b) *Charged Dislocations and Hardening of Additively Colored Crystals*

According to ESHELBY *et al.*[8] the shear stress required to pull the dislocation away from the surrounding Debye cloud is

$$\sigma_{\max} = 0{\cdot}80q^2\kappa/\epsilon b. \qquad (3)$$

In this formula q is the line charge of the dislocation, ϵ is the static dielectric constant, b is the Burgers vector, and κ^{-1} is the Debye radius. κ is given by

$$\kappa^2 = 8\pi e^2 N\alpha/\epsilon kT, \qquad (4)$$

where e is the electron charge, N is the number of cation (or anion) sites and

$$\alpha = \exp\{-\tfrac{1}{2}(g_+ + g_-)/kT\},$$

where g_+ and g_- are the free energies of formation of anion and cation vacancies, respectively. As the investigators discussed, the dislocations in uncolored crystals are expected to be positively charged for the reason that metal-ion vacancies are formed more easily than chlorine-ion vacancies. Although we can expect that dislocations in additively colored crystals also are positively charged, there remains the problem of whether q is influenced by the concentration of F-centers or not. If the hardening of colored crystals seen in Figs. 3 and 4 is explained on the basis of equation (3), q must increase with n_F. One possibility for such an increase is given by a tendency of a small fraction of the F-centers to form the complex-centers such as M- or R-centers. The net negative charge in the volume surrounding the dislocation will increase in proportion to such events. According to SEITZ's model,[5] the R_1-center is composed of one F-center and one negative-ion vacancy; the M-center is formed by one F-center and a pair of positive- and negative-ion vacancies. Corresponding to the increase of the net negative charge in the crystal, q will increase to reduce the electrostatic energy. Since the probability of the formation of such complex centers increases with the concentration of the F-centers, q will be an increasing function of n_F. Taking Δq as the increase of the positive charge on the dislocation, we simply assume that Δq is proportional to n_F. One then obtains from equation (3)

$$\Delta\sigma_C = 2\Delta q \cdot q_0 A,$$

where A is a constant independent of q_0. It is assumed that $\Delta q_0^2 < 1$. As a result, one obtains the relation that $\Delta\sigma_C/\sigma_0$ is proportional to n_F and that $\Delta\sigma_C$ depends on the coloration temperature through q_0, which is the line charge to be expected when no color centers are introduced.

The phenomena of age-hardening of colored crystals may be explained in terms of the temperature-dependence of κ, according to the present theory. Inserting equation (2) into equation (1), one obtains

$$\sigma_{\max} = Bq^3/bT^{\frac{1}{2}}, \qquad (5)$$

where

$$B = Pk^{\frac{1}{2}}(N\alpha/\epsilon^3)^{\frac{1}{2}}.$$

In this equation, P is a factor determined by the detailed process governing the change of the Debye radius. The Debye cloud may change its radius by the diffusion of ion-vacancies or by electron tunnelling. As far as pure tunnelling is assumed, P is equal to 4·0, as in the case of the ionic diffusion.

As is seen from equation (5), the curves illustrated in Fig. 4 might not be expected on the basis of the present interpretation. However, it is possible that P depends on temperature in the case of electron tunnelling with radiation. We cannot draw any definite conclusion, therefore, until a detailed knowledge of P is obtained.

(c) *Temperature-Dependence of Yield Stress and Effects of Coagulation of F-Centers*

The temperature-dependence of the yield stress of colored crystals shown in Fig. 9 cannot be caused by the change of κ, for the crystals aged at room temperature were brought to each measuring temperature so quickly that no appreciable structural change occurs. Thus the temperature-dependence of yield stress concerned should be given by a mechanism whereby the dislocations surmount the barrier caused by the electrostatic potential due to the Debye cloud. Since κ^{-1} is taken to be at least of the order of ten angstroms, the potential wiil form a relatively broad barrier. Moreover, since the charge on the dislocation is conceived to be associated with multivalent impurities, negative-ion vacancies in the dislocation core, or jogs, which are separated from each other by a certain distance, the shear stress required possibly is a slowly varying function of temperature. For a simple example we may assume a kind of dislocation pinning. Take the mean separation distance to be l and assume $U = cs^2\kappa$ is the energy required by the dislocation to overcome the barrier. Here c is a constant and s is the effective charge on the dislocation at the pinning point. If we assume the uniform distribution of the charge s, it follows that $q = s/l$. The critical shear stress then is given by*

$$\sigma_C = (cs^2\kappa - \beta kT)/lbd, \qquad (6)$$

* In deriving equation (3), the dislocation is considered as a rigid line, but not in this case.

where β is a constant of the order of ten and d relates to the width of the barrer. [19] One can obtain the following results by assuming $d = 10b$ from curves (a) and (b) in Fig. 9:*

(a) Uncolored crystals; $l = 4{\cdot}5 \times 10^{-6}$ cm and $U = 0{\cdot}47$ eV.

(b) Colored crystals, $n_F = 1{\cdot}22 \times 10^{17}$ cm^{-3}; $l = 2{\cdot}0 \times 10^{-6}$ cm and $U = 0{\cdot}34$ eV.

It is important to note that the activation energy U is almost equal to the binding energy of the divalent impurity or the negative-ion vacancy in the core of the dislocation estimated by BASSANI and THOMSON[18]; they estimate that the binding energy of the positive-ion vacancy is 0·4 eV in NaCl. This provides quantitative evidence that the present mechanism plays an important role in the phenomena concerned. They also calculated the average distance between such imperfections in the dislocation core in NaCl and obtained values of the same order as the values of l obtained here.

The activation energy is found to be smaller in the colored crystals than in the uncolored crystals. This may be understood, if the effective charge at the pinning point, which is newly introduced by additive coloration, is less than that in the uncolored crystal. This is quite reasonable because Δq or s/l is thought to be introduced by the formation of complex centers at a distance relatively close to the dislocation. Moreover, s is not large compared with q_0/l_0, where the suffix 0 relates to the uncolored crystal.

Finally, we would like to mention the effects of agglomeration of the F-centers by irradiation with light at room temperature. The process increases the critical shear stress as shown in Fig. 7. The most significant change in the nature of hardening by the irradiation is found in the temperature-dependence of the critical shear stress. As seen in Fig. 9, the yield stress is proportional to $1/T$, being completely different from that before the irradiation. This may be understood either by taking account of the formation of the Cottrell atmosphere or by considering the effects of the complex centers formed in the lattice. With regard to the latter, it is interesting to note a recent experiment on the hardening of LiF crystals irradiated by neutron carried out by GILMAN and JOHNSTON[20]. A heavy bombardment of 10^{15} nvt induces clusters of point defects which are revealed by fine etching technique. They have concluded that radiation hardening of their crystals was mainly due to clusters of point defects.

In the above discussion we have been led to the opinion that there seems to be a slight advantage of mechanism (5) relative to (4) for understanding the present phenomena, but we cannot be definite.

* Curves (a) and (b) can be expressed in terms of linear functions of temperature, as already remarked.

Acknowledgements—The present authors wish to thank Professor F. SEITZ and PROFESSOR J. S. KOEHLER deeply for discussions and advice. They have also had a good opportunity to discuss the subject with Dr. R. THOMSON at the University of Illinois, Dr. B. S. GOURARY at the Johns Hopkins University, Dr. J. D. ESHELBY at Birmingham University and Professor H. KAWAMURA at Osaka City University, Japan.

REFERENCES

1. KUZNETSOV V. D. and SEMENTSOV V. A., *Zh. Eksper. Teor. Fiz.* **2,** 199 (1932).
2. PODASHEVSKY M. N., *Phys. Z. Sowjet.* **8,** 81 (1935).
3. GORDON R. B. and NOWICK A. S., *Acta Met.* **4,** 514 (1956).
4. FRANKL D. R. and READ T. A., *Phys. Rev.* **89,** 663 (1953).
5. SEITZ F., *Rev. Mod. Phys.* **26,** 7 (1954).
6. GOURARY B. S. and ADRIAN F. J., *Phys. Rev.* **105,** 1180 (1957).
7. DEXTER D., *Phys. Rev.* **93,** 985 (1954).
8. ESHELBY J. D., NEWEY C. W. A. and PRATT P. L., *Phil. Mag.* **3,** 75 (1958).
9. SUZUKI T., *Reports of a Conference on Dislocations and Mechanical Properties of Crystals*, p. 215. John Wiley and Sons, Inc., New York (1957).
10. DUERIG W. H. and MARKHAM J. J., *Phys. Rev.* **88,** 1043 (1952).
11. WESTERVELT D. R., *Acta Met.* **1,** 755 (1953).
12. KLEINSCHROD F. G., *Ann Phys.* (*Leipzig*) **27,** 97 (1936).
13. UETA M. and KÄNZIG W., *Phys. Rev.* **97,** 1591 (1955)
14. GOURARY B. S. and LUKE P. J., *Phys. Rev.* **107,** 960 (1957).
15. STEPANOV A. V. and MILKAMANOVICH E. A., *Zh. Eksper. Teor. Fiz.* **18,** 769 (1948).
16. JOHNSTON W. G., *Reports of a Conference on Dislocations and Mechanical Properties of Crystals*, p. 52. John Wiley and Sons, Inc., New York (1957).
17. PRATT P. L., *Reports of a Conference on Defects in Crystalline Solids*, p. 402. Physical Society, London (1955).
18. BASSANI F. and THOMSON R., *Phys. Rev.* **102,** 1264 (1956).
19. SEEGER, A., *Z. Naturforsch.* **9a,** 870 (1954).
20. GILMAN J. J. and JOHNSTON W. G., *J. Appl. Phys.* **29,** 877 (1958).

J. Phys. Chem. Solids Pergamon Press 1959. Vol. 10. pp. 87–98.

SUPEREXCHANGE INTERACTION AND SYMMETRY PROPERTIES OF ELECTRON ORBITALS

JUNJIRO KANAMORI*

Department of Physics, Osaka University, Osaka, Japan

(*Received* 31 *May* 1958; *revised* 6 *November* 1958)

Abstract—The relation between the symmetry of electron orbitals and superexchange interaction is discussed. It is shown that the sign of the superexchange interaction is closely connected with the cation orbital state, when the cation is subject to the crystalline field arising from octahedrally or tetrahedrally surrounding anions. In some cases, the sign of the superexchange interaction is definitely determined from the symmetry relations. The cases in which each cation is subject to an octahedral cubic field and the lines connecting the interacting cations to the intervening anion make an angle of either 180° or 90° are discussed in particular. Our discussion of the 180° case is applicable to crystals of the perovskite type and NaCl type and that of the 90° case to anhydrous chlorides. In the case where each cation is subject to a tetrahedral cubic field, there is a definite relation between the symmetry of the cation electron orbitals and superexchange interaction, if only the *s*-orbital of anion participates in the superexchange interaction. TiH_2 is an example of this case. The interaction between nearest-neighbor cations in the crystal of the NaCl type is also discussed.

1. INTRODUCTION

In 1950 ANDERSON[1] formulated KRAMERS' idea[2] of the superexchange interaction in magnetic compounds and showed that KRAMERS' mechanism gives rise to an antiferromagnetic interaction between cations with a more-than-half-filled *d*-shell and a ferromagnetic interaction between cations with a less-than-half-filled *d*-shell. His conclusion for the less-than-half-filled *d*-shell is, however, not always supported experimentally, though it proved to be valid in a few compounds such as CrTe, CrO_2, etc., which are ferromagnetic. In the meanwhile, various other mechanisms which give rise to antiferromagnetic interaction even in the less-than-half case have been proposed by SLATER[3], GOODENOUGH and LOEB[4], GOODENOUGH[5], and ANDERSON and HASEGAWA[6]. The present paper will show that more attention has to be paid to the symmetry relation between the occupied *d*-orbitals of the cation and the *p*- or *s*-orbitals of the anion before it is possible to conclude whether the superexchange mechanism gives rise to ferromagnetic or antiferromagnetic interaction. In certain cases it can be shown that the sign of the superexchange interaction is so closely connected with the orbital state of the cation that it does not depend on any specific mechanism conceivable.

In the crystal the orbital of the cation and that of the anions overlap each other considerably, so that we cannot generally consider them to be orthogonal to each other, except when they have certain different symmetry properties. In the case in which each cation is surrounded octahedrally or tetrahedrally by anions, there exist definite orthogonality relations between the occupied *d*-orbitals of the cation and the occupied orbitals of the anion through their different angular dependences. These orthogonalities determine, in the first place, the pair of the *d*-orbital and anion orbital forming a partial covalent bond and, in the second place, the sign of the exchange integral between the occupied *d*-orbital and anion orbital. As an illustrative example of the discussions in the following sections, we shall here present the case of $CaMnO_3$.

$CaMnO_3$ is an antiferromagnet having the crystal structure of the perovskite type.[7] Each Mn^{4+} is surrounded octahedrally by O^{2-}, and each O^{2-} is situated at the center of each line connecting two nearest-neighbor Mn^{4+}. Each Mn^{4+} is subject

* Now at the Institute for the Study of Metals, University of Chicago, Chicago 37, Ill., on leave from Osaka University.

to a crystalline field of cubic symmetry, in which the lowest state of the free Mn^{4+}, ^4F, is split into three sublevels. The lowest of these sublevels is non-degenerate, with such an electronic configuration that three $3d\epsilon$-orbitals, $d(xy)$, $d(yz)$, and $d(zx)$, are singly occupied, where yz, etc., represent the angular dependences of the d-orbitals and the coördinates refer to the cubic principal axes. It is usually understood that in the octahedral cubic field the $d\epsilon$-level, whose wave functions are $d(xy)$, $d(yz)$ and $d(zx)$, lies lower than the $d\gamma$-level whose wave functions are $d(x^2-y^2)$ and $d(2z^2-x^2-y^2)$. Now, let the anion orbital which partakes in the superexchange mechanism be the p-orbital whose axis points to one of the Mn^{4+} ($p\sigma$-orbital). This $p\sigma$-orbital does not change its sign when the coördinate axes are rotated about the line connecting these two ions, whereas the occupied $d\epsilon$-orbitals of Mn^{4+} do change their sign (see Fig. 1). Therefore the $p\sigma$-orbital is orthogonal

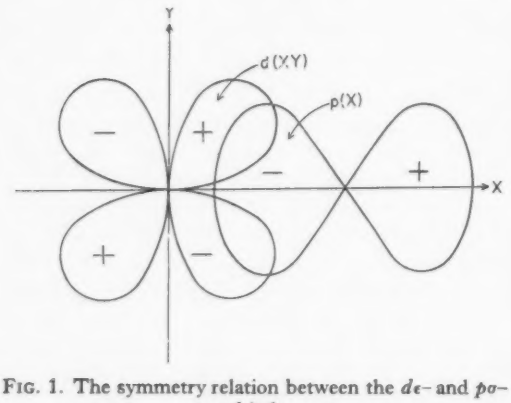

FIG. 1. The symmetry relation between the $d\epsilon$- and $p\sigma$-orbitals.

to the $d\epsilon$-orbitals. As for the $d\gamma$-orbitals, which are unoccupied, we can construct an appropriate linear combination of them in such a way that it does not change their sign under the same rotation; for instance, $d(2x^2-y^2-z^2)$ does not change sign by rotating the coördinate axes about the x-axis. Therefore, a partial covalent bond involving the $p\sigma$-orbital can be formed with the $d\gamma$-orbital, i.e. electron transfer from $p\sigma$ can take place to the $d\gamma$-orbital, but not to the $d\epsilon$-orbitals. Furthermore, the exchange integrals between $p\sigma$ and the occupied $d\epsilon$'s are positive (ferromagnetic), as they are mutually orthogonal. ANDERSON's mechanism is described in the scheme of perturbation theory by virtual processes in which an electron is first transferred from the $p\sigma$-orbital to one of the neighboring Mn^{4+} and then the unpaired spin left on O^{2-} couples with the spin of the other neighboring Mn^{4+} through exchange interaction. It follows from the above consideration that the transfer occurs to the unoccupied $d\gamma$ and, since the exchange interaction within Mn^{4+} favors parallel spins, the unpaired spin left on O^{2-} is antiparallel to the spin of that Mn^{4+}, and this unpaired spin couples ferromagnetically with the spin of the other Mn^{4+}. The resultant superexchange interaction is antiferromagnetic.

Other mechanisms, such as those proposed by SLATER[3], GOODENOUGH[5],* and ANDERSON and HASEGAWA[6] also give rise to antiferromagnetic interaction. SLATER's mechanism takes into account the polarization of the electron cloud of the anion through the exchange interaction with the cations. If the spins of the interacting cations are antiparallel to each other, the electrons with + spin and − spin polarize in opposite directions to lower the exchange energy with the cations. If the spins of the interacting cations are parallel, such polarizations cannot occur. In the present case, the polarization occurs through a mixing of the $3s$-orbital with the $2p\sigma$-orbital.† Since these orbitals are orthogonal to the occupied $d\epsilon$, the electron with + spin is pulled toward the cation with + spin and the electron with − spin toward the cation with − spin.

GOODENOUGH's mechanism takes into account the simultaneous partial bond formation of the anion with the cations on both side. If the spins of the cations are antiparallel to each other, the electron in $p\sigma$ with + spin forms the partial bond with the cation with + spin and the electron with − spin with the cation with − spin, while if the spins of the cations are parallel, such a bond formation cannot occur. ANDERSON and HASEGAWA have considered such virtual processes in which an electron is first transferred from the $p\sigma$-orbital to

* GOODENOUGH[5] discussed in detail the mechanism which was proposed by himself and LOEB[4]. In the following, we call it GOODENOUGH's mechanism.

† The mixing of an unoccupied $d\gamma$- into the $p\sigma$-orbital is also conceivable. However, this mechanism is essentially the same as GOODENOUGH's mechanism.

one of the neighboring Mn^{4+} and then two electrons are transferred simultaneously, one from the cation back to the $p\sigma$ and another from the $p\sigma$ to another Mn^{4+} and finally the electron is back to the $p\sigma$. This can be regarded as a kind of simultaneous formation of two partial bonds similar to that considered by GOODENOUGH, and therefore gives rise to the same sign of the superexchange interaction as in GOODENOUGH's mechanism.

Thus, it can be concluded that all the mechanisms of the superexchange interaction hitherto proposed give rise to antiferromagnetic interaction in $CaMnO_3$.

In the present paper various cases are investigated from a point of view similar to that presented above. In some cases we shall be able to determine the sign of the superexchange interaction merely by investigating the symmetry relations among the electron orbitals. Also, we shall be able to obtain some insight into the nature of the partial covalent bond by comparing the results of our qualitative discussion with the experimental results.

Recently YAMASHITA and KONDO[8] have formulated a theory of the superexchange interaction which takes rigorously into account the effect of the nonorthogonality among the electron orbitals. They show that the nonorthogonality itself can produce superexchange interaction without any configuration mixing, in other words, without any electron transfer. They also show that there are several combined effects of nonorthogonality and electron transfer. These arise because, if a *d*-orbital and a *p*-orbital are nonorthogonal to each other, the Pauli principle will produce effective deformations of these orbitals. In the conventional Heitler–London model, on which our following discussion is based, these effects are nothing other than that the exchange integral between nonorthogonal orbitals is negative or, in other words, that parallel spins in nonorthogonal orbitals repel each other.* Since the gist of the present theory is the consideration of the symmetry relations among the electron orbitals, the result will be valid even when nonorthogonality is taken into account.

In order to simplify the following discussion, we shall define here the sign of the partial covalent bond in ANDERSON's mechanism. If the transfer of an electron with spin parallel to the spin of the bonding cation is favored, that is, if the unpaired spin left on the anion is favored when it is antiparallel, we define the sign of the bond to be −. If, in SLATER's mechanism, the electron cloud with spin parallel to the spin of the cation is pulled towards the latter, the sign of the polarization is −. Conversely, if the partial covalent bond or the polarization produces unpaired spin on the anion parallel to the spin of the cation, the bond or the polarization is +. By so defining the sign, the sign of the superexchange interaction is determined in the following way. In ANDERSON's mechanism, the sign of the superexchange interaction is the product of the sign of the bond and the sign of the exchange integral between anion and cation; in $CaMnO_3$, the bond is − and the exchange integral is +, so that the resultant is −. In GOODENOUGH's or SLATER's mechanism the sign of the superexchange interaction is the product of the signs of the two simultaneous bonds or polarizations multiplied further by − sign which arises from the Pauli principle within the intervening anion orbital.

In Section 2 we shall discuss the case in which each cation is surrounded octahedrally by anions and the lines connecting the interacting cations to the intervening anion make an angle of 180° (180° case). This case includes the crystals of the perovskite type, NaCl type and ReO_3 type. In Section 3 will be discussed the case in which each cation is again surrounded octahedrally by anions, but the lines connecting the interacting cations to the intervening anion make an angle of 90° (90° case); it is applicable to anhydrous chlorides. The interaction between the nearest-neighbor cations in the NaCl-type crystal, which also belongs to this case, will be discussed in Section 5. Section 4 will treat the case where each cation is surrounded tetrahedrally by anions, the typical example of such a case being the interaction in TiH_2.

2. SUPEREXCHANGE INTERACTION BETWEEN CATIONS IN OCTAHEDRAL SITES: THE 180° CASE

The electronic configuration of the lowest orbital state of the cation which is subject to an octahedral cubic field is the following:[9] $d\epsilon^1$ for Ti^{3+}; $d\epsilon^3$ for

* The effect of nonorthogonality can be interpreted also as an effective electron transfer from anion to cation in some cases.[8]

V^{2+}, Cr^{3+} and Mn^{4+}; $d\gamma^1 d\epsilon^3$ for Cr^{2+} and Mn^{3+}; $d\epsilon^3 d\gamma^2$ for Mn^{2+} and Fe^{3+}; $(d\epsilon^2)d\epsilon^2 d\gamma^2$ for Fe^{2+}; $(d\epsilon^6)d\gamma^2$ for Ni^{2+}; $(d\epsilon^6)(d\gamma^2)d\gamma^1$ for Cu^{2+}; those in parentheses indicate paired electrons. The configuration of the ions of d^2 and d^7, such as Ti^{2+} and Co^{2+}, cannot be represented by a single one-electron configuration, because the Coulomb interaction between the electrons causes a configuration mixing. However, in Ti^{2+} the configuration $d\epsilon^2$ and in Co^{2+} the configuration $(d\epsilon^4)d\epsilon^1 d\gamma^2$ amount to $80 \sim 90$ per cent in their respective total wave functions.

Besides the $p\sigma$-orbital of the anion, the $p\pi$-orbitals and s-orbital can take part in the superexchange interaction. The $p\pi$-orbitals, whose axis is perpendicular to the line connecting the anion and cation, are orthogonal to the $d\gamma$-orbitals (see Fig. 2), but nonorthogonal to one of the $d\epsilon$-orbitals, and therefore can form a partial covalent

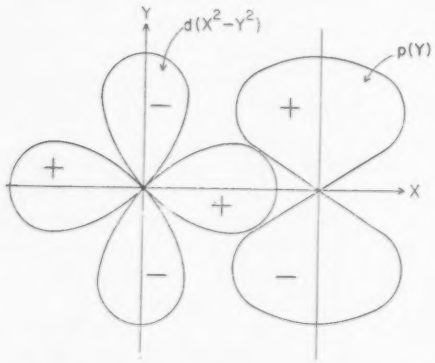

FIG. 2. The symmetry relation between the $d\gamma$ and $p\pi$ orbitals.

bond with the latter. (For instance, $p(x)$ of the anion on the z-axis can form a bond with $d(zx)$.) However, this $d\epsilon$–$p\pi$ bond should be weaker than the $d\gamma$–$p\sigma$ bond owing to a smaller overlap. The $d\gamma$–s bond has the same symmetry property as the $d\gamma$–$p\sigma$ bond, and therefore we shall confine ourselves in the following to the $d\gamma$–$p\sigma$ bond. In fact, we have no mean of clearly distinguishing between them, because an electron transfer can generally occur from an s–p hybridized orbital. Furthermore, the $4s$ and $4p\sigma$ cation orbitals can mix to $d\gamma$ and $4p\pi$ to $d\epsilon$. We can disregard all these mixings in the following discussion without affecting any qualitative conclusion. We shall consider the superexchange interaction between cations of different kinds as well as cations of the same kind.

(a) *Interaction between the cations of* $d\epsilon^3$

$CaMnO_3$ and $LaCrO_3$[10] belong to this case; they are known to exhibit antiferromagnetism. The superexchange interaction via the $2p\sigma$-orbital was discussed in Section 1. The sign of the $d\epsilon$–$p\pi$ bond is + according to the definition of Section 1, since all the $d\epsilon$'s are occupied. The average exchange integral between the $p\pi$ and $d\epsilon$'s may be negative, because a $p\pi$ has the largest overlap with a $d\epsilon$ which is nonorthogonal to it, and moreover the exchange integral between them is considered to be negative. Thus ANDERSON's mechanism via the $p\pi$-orbital gives rise to antiferromagnetic interaction. It can readily be seen that all the other mechanisms also give rise to antiferromagnetic interaction. So, together with the consideration given in Section 1, we can conclude that all the conceivable mechanisms give rise to antiferromagnetic interaction between ions Mn^{4+} or Cr^{3+}.

(b) *Interaction between the cations of* $(d\epsilon^6)d\gamma^2$

This is a typical more-than-half-filled case to which NiO[11] belongs. Only the $d\gamma$–$p\sigma$ bond can take part in the superexchange interaction. The sign of this bond is +, while the average exchange integral between $p\sigma$ and $d\gamma$'s is negative. Thus ANDERSON's mechanism gives rise to antiferromagnetic interaction. Other mechanisms also give rise to antiferromagnetic interaction.

(c) *Interaction between the cations of* $d\epsilon^3 d\gamma^2$

$LaFeO_3$[10] and MnO[11] belong to this case; they are both antiferromagnetic. In this case, the superexchange interaction via the $p\sigma$-orbital is antiferromagnetic for all conceivable mechanisms. The $d\epsilon$–$p\pi$ bonds can also take part in the superexchange interaction, but there is an ambiguity in the sign of the average exchange integral between $p\pi$ and $3d$'s. The exchange integral between nonorthogonal $p\pi$ and $d\epsilon$ will be negative, but other $p\pi$–$d\epsilon$ exchange integrals, as well as $p\pi$–$d\gamma$ exchange integrals, are positive. Thus the sign of the superexchange interaction arising from ANDERSON's mechanism via $p\pi$ is uncertain. Other mechanisms give rise to antiferromagnetic interaction. However, since the $d\gamma$–$p\sigma$ bond is stronger than

VOL. 10 1959

the $d\epsilon$–$p\pi$ bond, the total superexchange interaction will nevertheless be antiferromagnetic.

(d) *Interaction between* $Ni^{2+}((d\epsilon^6)d\gamma^2)$ *and* $V^{2+}(d\epsilon^3)$

Though there is no observation for this case, we expect here a ferromagnetic interaction. We shall attach a prime to the 3*d*-orbitals of V^{2+} and take O^{2-} as the intervening anion. In Table 1 are listed

Table 1. *The* 180° *interaction between* Ni^{2+} *and* V^{2+}

$d\gamma$–$p\sigma$ bond	$J(p\sigma$–$V^{2+})$	A
+	+	+
$d\gamma'$–$p\sigma$ bond	$J(p\sigma$–$Ni^{2+})$	A
−	−	+
G and A-H	S	
+	+	
$d\epsilon'$–$p\pi$ bond	$J(p\pi$–$Ni^{2+})$	A
+	+	+

A = ANDERSON's mechanism, G = GOODENOUGH's mechanism, A–H = ANDERSON and HASEGAWA's mechanism, S = SLATER's mechanism, $J(p\sigma$–$V^{2+})$ is the average exchange integral between $p\sigma$ and V^{2+}.

the sign of the bond, the sign of the average exchange integral between cation and anion, the sign of the polarizations in SLATER's mechanism, and finally the sign of the resultant superexchange interaction in each mechanism. The sign of the resultant superexchange interaction can be obtained by multiplying the signs in the same row for ANDERSON's mechanism, by multiplying the signs in the upper part of the same column and then attaching − for GOODENOUGH's, ANDERSON and HASEGAWA's and SLATER's mechanisms. In SLATER's mechanism, the signs of the exchange polarizations are just the reverse of those of *J*'s in the upper part of the same column. As shown in Table 1, all the mechanisms give rise to ferromagnetic interaction.

(e) *Interaction between* $Fe^{3+}(d\epsilon^3d\gamma^2)$ and $Cr^{3+}(d\epsilon^3)$

This case occurs in mixed crystals, such as $LaCr_xFe_{1-x}O_3$. It is known[12] that the paramagnetic Curie temperature, Θ, defined by $\chi = C/(T+\Theta)$, is smaller in this mixed crystal than in either $LaFeO_3$ or $LaCrO_3$. This suggests that the interaction between Fe^{3+} and Cr^{3+} is ferromagnetic.

As for the superexchange interaction via $p\sigma$, we can draw the same conclusion as that which we reached in case (d); it is ferromagnetic. The sign of the $d\epsilon$–$p\pi$ bond is positive for both the cations, while the average exchange integral between $p\pi$ and Cr^{3+} is negative and that between $p\pi$ and Fe^{3+} is uncertain. Thus GOODENOUGH's and ANDERSON and HASEGAWA's mechanisms via $p\pi$ give rise to antiferromagnetic interaction, while the sign in ANDERSON's mechanism is uncertain. The ferromagnetic interaction between Fe^{3+} and Cr^{3+} may be explained by considering that the $p\sigma$–$d\gamma$ bonds are more effective than the $d\epsilon$–$p\pi$ bonds.

(f) *Interaction between the cations of* $d\gamma^1d\epsilon^3$

This case, as well as that in which $Cu^{2+}((d\epsilon^6)\times$ $\times(d\gamma^2)d\gamma^1)$ is involved, is complicated because the lowest level in the cubic field is doubly degenerate. GOODENOUGH[5] discussed in detail the case of $LaMnO_3$, in which he considered that each Mn^{3+} forms a square covalent bond with the four surrounding O^{2-} and the plane of this square bond alternates between being parallel to the *zx*-plane and parallel to the *yz*-plane when one goes along any one of the cubic axes.

The square bond in the *zx*- (or *yz*-) plane can be formed by constructing the hybridized orbitals from $d(z^2-x^2)$(or $d(y^2-z^2)$) and 4*s*, 4*p*(*z*), and 4*p*(*x*)(or 4*p*(*y*)). The four 3*d*-electrons occupy the remaining four 3*d*-orbitals. Along the *z*-direction, the intervening O^{2-} forms simultaneous bonds with the cations on both its side, and therefore GOODENOUGH's mechanism gives rise to antiferromagnetic interaction. In the *x*- or *y*-direction, the intervening O^{2-} forms a covalent bond with only one cation; therefore GOODENOUGH assumed that in these directions ANDERSON's mechanism would give rise to ferromagnetic interaction. This assumption does not conflict with our own picture: the sign of the covalent bond, say in the *x*-direction, is − and the exchange integral between $p\sigma$ and the non-bonding cation is negative, because the singly occupied $d\gamma$ of this cation has the largest density in the *x*-direction.

(g) *Interaction in* FeO *and* CoO[13]

In the above cases (a)–(f), interactions involving $Fe^{2+}(d^6)$ and $Co^{2+}(d^7)$ have not been included. In the lowest orbital state of Fe^{2+}, only one of the three $d\epsilon$ is doubly occupied and in that of Co^{2+} approximately two of the three $d\epsilon$ are doubly occupied. These lowest states are triply degenerate. If the $p\sigma$–$d\gamma$ bond only is considered in these cases, one will come to the same conclusion as that of the case of Ni^{2+}. However, the existence of a $p\pi$–$d\epsilon$ bond makes the situation somewhat complicated. Also, compared with $LaMnO_3$, in which the lowest state of Mn^{3+} is doubly degenerate and hence the Jahn–Teller effect determines its orbital state as implied by GOODENOUGH's theory, the present case is different in that the $d\epsilon$–$p\pi$ bond is weaker than the $d\gamma$–$p\sigma$ bond and that there is a strong spin-orbit coupling which was absent in $LaMnO_3$. In FeO, the spins orient to the [111] direction in the antiferromagnetic state, and the spin-orbit coupling determines the orbital state in such a way that the orbital electronic current produces a magnetic field which points in the direction of the spin, i.e. the wave function of an electron outside the half-filled d-shell is a linear combination of the three $d\epsilon$-orbitals: $d(zx)+\exp(4\pi i/3)\,d(xy)+\exp(2\pi i/3)+$ $+d(yz)$. Thus the extra one electron occupies the three $d\epsilon$'s equally. Consequently, there is no difference among the superexchange interactions along the x-, y- and z-directions.

In CoO, the spins orient approximately to [001], and the spin-orbit coupling energy determines the orbital of the only unpaired $d\epsilon$-electron approximately as $1/\sqrt{2}(d(zx)+id(yz))$. Therefore the electrons of the two $p\pi$-orbitals of the O^{2-} can be transferred into the cation which is next to this O^{2-} in the z-direction, while in the x- or y-direction the transfer into the cation can occur only from one of the two $p\pi$ orbitals. Thus one expects a difference between the superexchange interaction in the z-direction and that in the x- or y-direction. In the paramagnetic state of FeO and CoO, the three $d\epsilon$ are occupied with equal probability, and there can be no anisotropy of the superexchange interaction. The same situation will occur in the case in which Ti^{2+}, V^{3+}, and Ti^{3+} are involved.

To conclude the above discussion for the 180° case, we may say that we expect generally antiferromagnetic interaction between cations of the same kind, except in the case of cations of d^4, in which case the sign of the superexchange interaction depends on the direction of the line of superexchange, and ferromagnetic interaction between a cation with more-than-half-filled d-shell and a cation with less-than-half-filled d-shell. Table 2 summarizes the discussion of this section.

3. SUPEREXCHANGE INTERACTION BETWEEN CATIONS IN OCTAHEDRAL SITES: THE 90° CASE

In this section we treat the case in which the two lines connecting the interacting cations to the intervening anion are at right angles and the cations are in an octahedral cubic field. Interactions within the same layer of a crystal of layer structure, such as the anhydrous chlorides of the iron-group elements, belong to the present type. Interactions between nearest-neighbor cations in crystals of the NaCl type are also of the same type, but we defer consideration of them to Section 5.

In the anhydrous chlorides of the iron-group elements, the anions form a cubic close-packed structure whose [111] axis coincides with the trigonal axis of the whole crystal, and the cations occupy the alternate (111) interstitial planes, forming a set of two-dimensional triangular lattices in the case of dichlorides and of honeycomb lattices in the case of the trichlorides. Strictly speaking, the cations are subject to a crystalline field of trigonal symmetry, but the six anions adjoining each cation form an almost regular octahedron, and the octahedral cubic field arising from them determines the main orbital configuration of the cation.

It is known experimentally that $FeCl_2$, $CoCl_2$, and $NiCl_2$ are antiferromagnets whose spin structure is such that the spins within each layer are all parallel and the spins of the neighboring layers antiparallel.[14] This structure itself suggests that cations in the same layer interact ferromagnetically with each other and cations in the adjacent layers interact antiferromagnetically. The magnetic properties of these compounds are well explained by assuming that the intra-layer ferromagnetic interaction is much stronger than the inter-layer antiferromagnetic interaction. We list their Néel temperature T_N and paramagnetic Curie temperature Θ in Table 3. It can be considered that both T_N and Θ are determined mainly by the

Table 2. The 180° interaction between cations in octahedral sites

Number of 3*d*-electrons of interacting cations	Species of interacting cations	Relevant bond and mechanism	Resultant superexchange interaction	Total superexchange interaction
d^3–d^3	Mn^{4+}–Mn^{4+} Cr^{3+}–Cr^{3+}	σ-bond and π-bond A, G, A–H, S	Antiferro.	Antiferro.
d^8–d^8	Ni^{2+}–Ni^{2+}	σ-bond A, G, A–H, S	Antiferro.	Antiferro.
d^5–d^5	Mn^{2+}–Mn^{2+} Fe^{3+}–Fe^{3+}	σ-bond A, G, A–H, S π-bond G, A–H, S π-bond A	Antiferro. Antiferro. (weak) Uncertain (weak)	Antiferro.
d^8–d^3	Ni^{2+}–V^{2+}	σ-bond and π-bond A, G, A–H, S	Ferro.	Ferro.
d^5–d^3	Fe^{3+}–Cr^{3+}	σ-bond A, G, A–H, S π-bond G, A–H π-bond A, S	Ferro. Antiferro. (weak) Uncertain (weak)	Ferro.
d^4–d^4	Mn^{3+}–Mn^{3+}	*		
d^6–d^6	FeO	σ-bond A, G, A–H, S π-bond	Antiferro. Uncertain (weak)	Antiferro.
d^7–d^7	CoO	σ-bond A, G, A–H, S π-bond	Antiferro. †	Antiferro.

* Depends on the direction of the line of superexchange.

† Weak, but dependent on the direction of the line of superexchange.

A = ANDERSON's mechanism, G = GOODENOUGH's mechanism, A–H = ANDERSON and HASEGAWA's mechanism, S = SLATER's mechanism.

intra-layer ferromagnetic interaction, except for a certain modification in the case of $FeCl_2$. The properties of $FeCl_2$ will be discussed elsewhere[15] in detail, but here it is noted that the large anisotropy energy in the case of $FeCl_2$ enhances its T_N twice (or more) as much as the value that one would expect if it were absent; also, it can be shown that Θ is affected considerably by the anisotropy energy. Thus, although $FeCl_2$ and $CoCl_2$ have approximately the same value of T_N, the ferromagnetic intra-layer interaction in the former is actually smaller than in the latter. In $MnCl_2$[14,16] and $FeCl_3$,[16] the cations in the same layer do not appear to interact ferromagnetically. From these facts, we can infer that the intra-layer ferromagnetic interaction decreases with decreasing number of 3*d*-electrons.

Mn–, Fe–, Co– and Ni–TiO_3 have the same crystal structure, which is similar to that of anhydrous chlorides. They become antiferromagnetic at low temperatures. In $FeTiO_3$ the ferrous ions form an antiferromagnetic structure which is the

Table 3. T_N and Θ of anhydrous chlorides[16]

Substance	T_N(°K)	$\Theta(\chi=C/(T-\Theta))$(°K)
VCl_2	?	−565
$CrCl_3$	16·8	27·0
$CrCl_2$	40	−149
$MnCl_2$	~ 2	− 3·3
$FeCl_3$	?	− 11·5
$FeCl_2$	23·5	48·0 or 20·4*
$CoCl_2$	24·9	38·1
$NiCl_2$	49·6	68·2

* WOLTIJER H. R. and WIERSMA E. C., *Proc. Roy. Acad. Amsterdam* **32,** 736 (1929).

same as that in $FeCl_2$, according to an observation made by neutron diffraction.[17] From magnetic measurements ISHIKAWA and AKIMOTO[18] have inferred that in Co–, Ni– and Fe–TiO_3 the exchange interaction within each layer may be ferromagnetic, but antiferromagnetic in $MnTiO_3$. Thus this titanate series resembles the anhydrous chlorides. However, since there are no available data for their T_N values, except that of $FeTiO_3$ ($T_N = 68$°K),[19] and since their anion octahedra are considerably deformed, we shall not consider them further but will rather confine ourselves to the anhydrous chlorides in the following. We shall include those anhydrous chlorides whose cations have a less-than-half-filled *d*-shell, such as $CrCl_3$, $CrCl_2$ and VCl_2. Among them, $CrCl_3$ is ferromagnetic,[16] but the other two seem to be antiferromagnetic, though this is not yet certain.

We define the $p\sigma$-orbital as the *p*-orbital which points to the cation situated to the left of the anion in Fig. 3 and the $p\sigma'$-orbital as the *p*-orbital which points to the cation situated to the right. We attach correspondingly a prime to the *d*-orbitals of the cation to the right. The $p\pi$-orbital is the one which is perpendicular to the plane containing the anion and the interacting cations.

(a) *The* 90° *interaction between* Ni^{2+} *ions*

In this case $p\sigma$ forms a partial covalent with $d\gamma$ of the cation on the left hand and the $p\sigma'$ with the $d\gamma'$ of the cation on the right hand. The sign is + for these bonds, that is, the unpaired spin produced on the anion is parallel to the spin of the cation. Since $p\sigma$ is orthogonal to $d\gamma'$ and $p\sigma'$ is orthogonal to $d\gamma$, the exchange interaction between the unpaired spin on the anion and that of the cation is ferromagnetic. Thus ANDERSON's mechanism gives rise to ferromagnetic interaction. On the other hand, ANDERSON mechanism via the 3*s*-orbital of Cl^- give rise to antiferromagnetic interaction.

Other mechanisms, such as GOODENOUGH's mechanism in 180° case, cannot produce superexchange interaction unless they are modified. If we treat them in the perturbation scheme, the superexchange interaction will be obtained in a higher order than in the 180° case. The higher-order mechanism which would correspond to GOODENOUGH's mechanism is such that two partial covalent bonds, $p\sigma$–$d\gamma$ and $p\sigma'$–$d\gamma'$, are simultaneously formed and the unpaired spins produced on $p\sigma$ and $p\sigma'$ interact with each other. Since $p\sigma$ and $p\sigma'$ are orthogonal to each other, the exchange interaction between them is ferromagnetic, and this mechanism gives rise to a ferromagnetic interaction.

What corresponds to SLATER's mechanism is more complicated. The $p\sigma$ electrons whose spin is parallel to the spin of the cation on the left hand mixes with the 4*s*-orbital of the anion through exchange repulsion, and since this 4*s*-orbital is non-orthogonal to the $d\gamma'$-orbital of the cation on the right hand, this mixing will increase the exchange energy between the unpaired spin in 4*s* and the spin in $d\gamma'$ if they are parallel. Thus it gives rise to antiferromagnetic interaction. Another possibility is that the simultaneous exchange polarization of $p\sigma$ and $p\sigma'$ occurs, and the Pauli principle works in

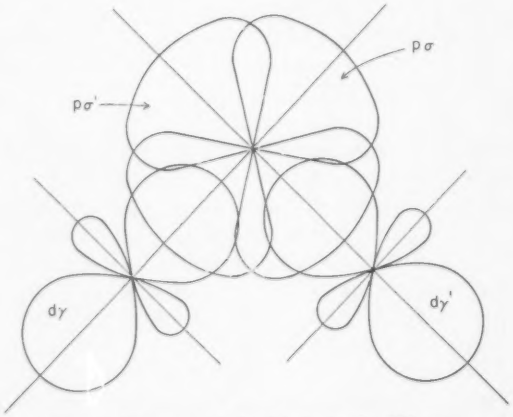

FIG. 3. The *p*- and *d*-orbitals in the 90° case.

the 4*s*-orbital favoring antiparallel spins of the cations. However, if we take into account the trigonality of crystal, there is another mechanism which will give rise to ferromagnetic interaction. The *p*-level of the anion is split in the trigonal field into two, one with the orbital $(1/\sqrt{3})(p(x)+p(y)+p(z))$ and the other with $(1/\sqrt{2})(p(x)-p(y))$ and $(1/\sqrt{6})(2p(z)-p(x)-p(y))$, the coördinates referring to the coördinate axes parallel to the lines connecting the anion to the three neighboring cations. In the anhydrous chlorides, there is a potential gradient at the site of the anion, which will polarize the electron cloud towards the cations. This polarization takes place through the mixing of the 4*s*-orbital with the singlet orbital, $(1/\sqrt{3})(p(x)+p(y)+p(z))$. Thus the singlet orbital will have a larger overlap with the electron clouds of the cations. This makes the exchange polarization of the singlet orbital more effective than that of the doublet orbitals. If the spins of the three cations are all parallel, the energy due to the exchange polarization would be the lowest, since the singlet orbital overlaps them equally.

We cannot determine without quantitative calculations which one of the above mechanisms is the most effective. However, as will be discussed below in (b), the decreasing ferromagnetic interaction with decreasing number of the 3*d*-electrons indicates that ANDERSON's mechanism is the most effective. It is, however, not excluded that the ferromagnetic interaction is a result of the cancellation of the various effects.

(b) *The* 90° *interaction between* Mn^{2+} *or* Fe^{3+}

In this case, the $d\epsilon$-orbitals can take part in the superexchange interaction. In ANDERSON's mechanism, the exchange interaction between the unpaired spin in $p\sigma$ and the cation on the right hand will be smaller than that in Ni^{2+}, or even reversed in sign, as $p\sigma$ is nonorthogonal to the $d\epsilon'$-orbitals which are now singly occupied. Also $p\sigma$ can form a partial covalent bond with $d\epsilon'$; ANDERSON's mechanism via this bond gives rise to antiferromagnetic interaction, since the exchange integral between $p\sigma$ and $d\gamma$ is definitely negative. As GOODENOUGH's mechanism, other than that discussed in the case of Ni^{2+}, there is such a one that simultaneous bonds are formed between $p\sigma$ and $d\gamma$ on the left, and $d\epsilon'$ on the right; this gives rise to antiferromagnetic interaction. Also $p\pi$ can form partial covalent bonds with $d\epsilon$ and $d\epsilon'$ and participate in the superexchange interaction, which is also antiferromagnetic.

Thus, if any of the $p\sigma$–$d\gamma'$, $p\pi$–$d\epsilon$, and $p\pi$–$d\epsilon'$ bonds are important in ANDERSON's and GOODENOUGH's mechanisms, the antiferromagnetic interaction due to them will partly cancel the ferromagnetic interaction arising from the $p\sigma$–$d\gamma$ or $p\sigma'$–$d\gamma'$ bond, and therefore the total superexchange interaction will decrease with decreasing number of 3*d*-electrons. On the other hand, if only $p\sigma$–$d\gamma$ and $p\sigma'$–$d\gamma'$ are important, ANDERSON's mechanism should be most effective, and since the exchange integral decreases with increasing number of unpaired electrons in $d\epsilon'$ and $d\epsilon$, the superexchange interaction here again decreases.

In SLATER's mechanism, the exchange polarization will be smaller compared with that in Ni^{2+}, since there are unpaired spins in the $d\epsilon$-orbitals and they pull the 4*s*-electron with parallel spin, whereas the spin in the $d\gamma$-orbital repels it.

(c) *The* 90° *interaction between* Cr^{3+}

First we investigate the interaction which involves $p\sigma$–$d\gamma$ and/or $p\sigma'$–$d\gamma'$. The sign of these bonds is negative. The exchange interaction between $p\sigma$ and the occupied $d\epsilon'$ is negative, since $p\sigma$ is nonorthogonal to $d\epsilon'$. Thus ANDERSON's mechanism gives rise to ferromagnetic interaction. GOODENOUGH's mechanism, in which both $p\sigma$–$d\gamma$ and $p\sigma'$–$d\gamma'$ are simultaneously formed, also gives rise to ferromagnetic interaction. SLATER's mechanism also gives rise to ferromagnetic interaction, since the occupied $d\epsilon$'s are orthogonal to the 4*s*-orbital of the anion.

If $p\sigma$–$d\epsilon'$ or $p\sigma'$–$d\epsilon$ is considered, ANDERSON's mechanism pertaining to it gives rise to ferromagnetic interaction, since the sign of these bonds is positive and the exchange integral between $p\sigma$ and $d\epsilon$ or $p\sigma'$ and $d\epsilon'$ is positive. Simultaneous bond formation of $p\sigma$–$d\gamma$ and $p\sigma$–$d\epsilon'$ gives rise also to ferromagnetic interaction, since the sign of the former is $-$ and the sign of the latter is $+$. Antiferromagnetic interactions can be obtained only if $p\pi$–$d\epsilon$ and 3*s*–$d\gamma$ are considered; however, since in our discussion of the anhydrous chlorides we could do without these bonds, it appears that they make little contribution to the superexchange interaction.

$CrCl_2$ and VCl_3 are suspected to be antiferromagnets. In the former the Jahn–Teller effect, such as occurs in $LaMnO_3$, will play an important role in the superexchange interaction, since there is a doubly degenerate lowest orbital state. We shall not enter into the details of this case. As for VCl_2, we might expect ferromagnetism, since V^{2+} is isoelectronic with Cr^{3+}. However, a very large negative paramagnetic Curie temperature is observed, for which we have no explanation.

(d) *The 90° interaction between* Ni^{2+} *and* V^{2+}

Contrary to the 180° case, we expect antiferromagnetic interaction between a cation with a less-than-half-filled d-shell and a cation with a more-than-half-filled d-shell in the 90° case. Here we shall discuss only the case of Ni^{2+}–V^{2+}. In Table 4 the signs of the bonds, the exchange integrals and the resultant superexchange interaction in ANDERSON's mechanism are listed. Attaching a prime to the $3d$-orbitals of V^{2+}, we see that ANDERSON's mechanism gives rise to antiferromagnetic interaction. By a similar consideration it can be shown that GOODENOUGH's mechanism gives rise to antiferromagnetic interaction. For SLATER's mechanism, it is hard to conclude the sign definitely. We may assume that ANDERSON's mechanism is most effective and the superexchange interaction is antiferromagnetic. Table 5 summarizes the discussion of this section.

Table 4. The 90° interaction between Ni^{2+} *and* V^{2+}

$p\sigma$–$d\gamma$ bond	$J(p\sigma$–$V^{2+})$	A
+	−	−
$p\sigma'$–$d\gamma'$ bond	$J(p\sigma'$–$Ni^{2+})$	A
−	+	−
$p\sigma$–$d\epsilon'$ bond	$J(p\sigma$–$Ni^{2+})$	A
+ •	−	−

A = ANDERSON's mechanism.

Table 5. The 90° interaction between cations in octahedral sites

Number of $3d$-electrons of interacting cations	Species of interacting cations	Relevant bond and mechanism	Resultant superexchange interaction	Total superexchange interaction
d^8–d^8	Ni^{2+}–Ni^{2+}	$p\sigma$–$d\gamma$ bond A, G S s–$d\gamma$ bond A, G, A-H, S	Ferro. Uncertain Antiferro.	Ferro.
d^5–d^5	Mn^{2+}–Mn^{2+} Fe^{3+}–Fe^{3+}		Uncertain	*
d^3–d^3	Cr^{3+}–Cr^{3+}	$p\sigma$–$d\gamma$ and $p\sigma$–$d\epsilon'$ A, G, A-H, S $p\pi$–$d\epsilon$ and s–$d\gamma$ A, G, A-H, S	Ferro. Antiferro. (weak)	Ferro.
d^8–d^3	Ni^{2+}–V^{2+}	$p\sigma$–$d\gamma$ and $p\sigma$–$d\epsilon'$ A, G, A-H S $p\pi$–$d\epsilon'$ and s–$d\gamma$, s–$d\gamma'$ A, G, A-H	Antiferro. Uncertain (weak) Ferro. (weak)	Antiferro.

* Tendency towards antiferromagnetic interaction with decreasing number of $3d$-electrons.

4. SUPEREXCHANGE INTERACTION BETWEEN CATIONS IN TETRAHEDRAL SITES

The discussion in this section applies to crystals of the ZnS type, such as β-MnS, and crystals of the CaF_2 type, such as TiH_2.[20] The orbital level splitting of the cation in a tetrahedral cubic field is such that the $d\gamma$-level lies lower than the $d\epsilon$-level. Therefore, the electronic configuration of Ti^{2+} is $d\gamma^2$ and that of Co^{2+} $(d\gamma^4)d\epsilon^3$. The cubic axes and the positions of the surrounding anions are shown in Fig. 4.

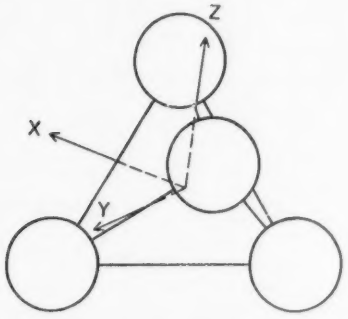

FIG. 4. The cubic axes and the positions of the surrounding anions in the tetrahedral case.

The symmetry relations among the orbitals are such that the $p\sigma$- and s-orbitals of the anion are orthogonal to the $d\gamma$-orbital and nonorthogonal to an appropriate linear combination of the $d\epsilon$-orbitals. For $d(x^2-y^2)$, this orthogonality is easily understood, since if we rotate the coördinate axes about the line connecting the anion to the cation, $d(x^2-y^2)$ changes its sign, while the wave functions of $p\sigma$ and s do not change sign. As for $d(2z^2-x^2-y^2)$, we can write it as a linear combination of $d(z^2-x^2)$ and $d(y^2-z^2)$, both of which are orthogonal to $p\sigma$ and s.

Unfortunately, however, we cannot give in this case such a simple qualitative discussion as in the octahedral case if the p-orbitals of the anion take part in the superexchange interaction. This is because the $p\sigma$-orbital referred to one cation has no definite symmetry relation with another cation. In a particular crystal of TiH_2, in which only the s-orbital takes part in the superexchange interaction, the situation is simple, and we can determine the sign of the superexchange interaction.

TiH_2 has a crystal structure of the CaF_2 type,[21] in which each Ti^{2+} is situated at the body-center site of the cube made of eight H^-. Since the two $3d$-electrons of Ti^{2+} occupy the $d\gamma$-orbitals, the s-orbital of H^- is orthogonal to the occupied cation orbitals. Thus this case resembles that previously discussed for $CaMnO_3$ except that s replaces $p\sigma$. The discussion proceeds similarly, therefore, and we can conclude that all the mechanisms give rise to antiferromagnetic interaction in TiH_2. In actuality TiH_2 is an antiferromagnet.[20]

The interaction between Ti^{2+} and Co^{2+} in the mixed crystal, $Ti_{1-x}Co_xH_2$, is ferromagnetic, since in Co^{2+} the unpaired electrons occupy the three $d\epsilon$-orbitals which are nonorthogonal to the s-orbital of H^-, and therefore the interaction between Ti^{2+} and Co^{2+} corresponds to that between Ni^{2+} and V^{2+} in octahedral sites. Furthermore, we can expect that the interaction between Ti^{2+} and a cation with a more-than-half-filled d-shell is always ferromagnetic in hydrides (see the discussion of Cr^{3+}–Fe^{3+} interaction in the octahedral case).

5. FURTHER DISCUSSION

In Section 3, the sign of the superexchange interaction within a layer in the anhydrous chlorides was discussed qualitatively. Another example of the 90° case is the exchange interaction between the nearest-neighbor cations in a crystal of the NaCl type. We list in Table 6 the experimental values of T_N and Θ of these crystals. As each cation is surrounded by an equal number of + and − spins, T_N is determined by the 180° interaction between the next-nearest neighbors, while the paramagnetic Curie temperature Θ is determined by the total exchange interactions including both

Table 6. T_N and Θ of crystals of the NaCl *type*[11,22,23]

Substance	T_N(°K)	$\Theta(\chi = C/(T+\Theta))$(°K)
MnO	122	610
α-MnS	165[a], 154[b]	528[a], 300[b]
CoO	293	280
NiO	540	2000

a—Ref. (11), b—Ref. (23).

the 180° and 90° interactions. Thus in MnO and α-MnS, for which $\Theta > T_N$, the 90° interaction is antiferromagnetic. For CoO, the present author has shown previously[13] that the value of Θ is strongly influenced by spin-orbit coupling which acts through the residual orbital angular momentum and that the 90° interaction is still antiferromagnetic. The magnitude of the 90° interaction in CoO was found to be about the same as in MnO For FeO there are no reliable experimental data In NiO, SINGER[22] obtained a very high Θ, but the measurements were not extended to temperatures high enough to eliminate the short-range effect. Thus, at present we cannot derive from experimental data any definite correlation between the magnitude of the 90° interaction with the number of 3*d*-electrons. The absolute magnitude of this interaction is very large as compared with the corresponding interaction in anhydrous chlorides. Comparing α-MnS with MnO, we find that Θ of MnO is larger than that of α-MnS, while the values of T_N are in the reversed relation.* This is also hard to understand, since the superexchange interaction is expected to increase with the decrease of the electronegativity of the intervening anion.

Possible mechanisms which might give rise to the large difference of the 90° interaction in monoxides and anhydrous chlorides would be the following. One is the direct interaction between the cations, which will depend on the distance between the cations; the distance is larger in anhydrous chlorides than in oxides. Electron transfer between the cations is also conceivable. This is the mixing of the excited configuration M^{+}–M^{3+} into the ground configuration M^{2+}–M^{2+}. If the spins of the cations are antiparallel to each other, the unpaired electrons can move from a cation to another, while if they are parallel, this cannot occur. Thus this will give rise to antiferromagnetic interaction. The excitation energy required for this process is about 10 eV in monoxides. With a transfer integral of the order of 1000 cm^{-1}, this mechanism gives the interaction of the right order. A clue to this problem might be obtained, if the electron transfer process in magnetitie should be theoretically investigated. Difference in the contribution from the *s*-orbitals may also be conceivable. The trigonality of the crystal of anhydrous chlorides discussed in Section 3 would be another cause of the difference.

* According to LINDSAY and BANEWICZ's measurement,[23] the susceptibility of α-MnS does not follow the Curie–Weiss law even in the temperature range above room temperature. They estimated the value of Θ at the high temperature limit from the Ising–Bethe approximation (see Table 6).

Acknowledgement—The author would like to express his sincere thanks to Professor NAGAMIYA for valuable discussions and to Professor STOUT for helpful comments on the manuscript.

REFERENCES

1. ANDERSON P. W., *Phys. Rev.* **79,** 350 (1950).
2. KRAMERS H., *Physica* **1,** 182 (1934).
3. SLATER J. C., *Quart. Progr. Rep. M.I.T.* July 15,1; Oct. 15,1 (1953).
4. GOODENOUGH J. B. and LOEB A. L., *Phys. Rev.* **98,** 391 (1955).
5. GOODENOUGH J. B., *Phys. Rev.* **100,** 564 (1955).
6. See NAGAMIYA T., YOSIDA K. and KUBO R., *Advances in Phys.* **4,** 1 (1955).
7. WOLLAN E. Q. and KOEHLER W. C., *Phys. Rev.* **100,** 545 (1955).
8. YAMASHITA J. and KONDO J., *Phys. Rev.* **109,** 730 (1958).
9. See, for example, BLEANEY B. and STEVENS K. W. H., *Rep. Progr. Phys.* **16,** 108 (1953).
10. KOEHLER W. C. and WOLLAN E. Q., *J. Phys. Chem. Solids* **2,** 100 (1957).
11. See ref. 6, part I.
12. TSUBOKAWA I. Private communication.
13. KANAMORI J., *Progr. Theor. Phys.* **17,** 177, 197 (1957).
14. KOEHLER W. C., WILKINSON M. K., CABLE J. W. and WOLLAN E. Q., *Colloque Internat. de Magnetisme de Grenoble* (1958).
15. KANAMORI J. To be published in *Progr. Theor. Phys.* See also NAGAMIYA T., *Colloque Internat. de Magnétisme de Grenoble* (1958).
16. STARR C., BITTER F. and KAUFMANN A. R., *Phys. Rev.* **58,** 977 (1940).
17. SHIRANE G. Unpublished work.
18. ISHIKAWA I. and AKIMOTO, S. Private communication.
    NAGAMIYA T., *Colloque Internat. Magnetisme de Grenoble* (1958).
19. BIZETTE H. and TSAI B., *C.R. Acad. Sci.* (*Paris*) **242,** 2124 (1956).
20. WOHLFARTH E. P., *Acta Met.* **4,** 225 (1956).
21. SIDHU S. S., HEATON L. and ZAUBERIS D. D., *Acta Cryst.* **9,** 607 (1956).
22. SINGER J. R., *Phys. Rev.* **104,** 929 (1956).
23. LINDSAY R. and BANEWICZ J. J., *Phys. Rev.* **110,** 634 (1958).

J. Phys. Chem. Solids Pergamon Press 1959. Vol. 10. pp. 99–105.

THE EFFECT OF PLASTIC DEFORMATION ON SELF-DIFFUSION IN SILVER

A. F. FORESTIERI and L. A. GIRIFALCO

Lewis Research Center, National Aeronautics and Space Administration, Cleveland, Ohio

(*Received in revised form* 21 *October* 1958)

Abstract—The self-diffusion coefficient of silver undergoing plastic compressive deformation was measured over temperatures ranging from 810 to 1172°K and at strain rates from 0·00075 to 0·006 hr^{-1}. At all temperatures it was found that the diffusion coefficient is proportional to the strain rate. The results were interpreted on the basis of a model in which two vacancy-production mechanisms and two vacancy-annealing mechanisms are assumed to be operative. At low temperatures, vacancy production is assumed to occur by a geometric, temperature-independent process, and the annealing mechanism is assumed to be the migration of vacancies to fixed sinks. At high temperatures, it is suggested that vacancies are formed by a thermally activated process and that they anneal by combining with a highly mobile defect. Energetic considerations lead to the conclusion that this mobile defect is probably a divacancy.

1. INTRODUCTION

THEORY and experiment both indicate[1–4] that, for simple types of deformation such as compression and shear, the rate at which vacancies are produced by plastic strain is proportional to the strain rate, so that during plastic flow the vacancy concentration in solids is raised above the thermodynamic equilibrium value. The vacancy concentration will have a tendency to approach the thermodynamic equilibrium value by a process in which the excess vacancies disappear by migrating to vacancy sinks, such as dislocations, grain boundaries and voids, or by combining with point defects such as divacancies and interstitials. If the strain rate is constant, a steady-state concentration of vacancies is eventually attained as a result of the balance between the production and annealing rates.

Recently, a simple theoretical framework has been advanced[5] which relates the diffusion coefficient of a substance that diffuses by a vacancy mechanism to the strain rate, the production rate of the vacancies and the annealing rate. A completely analogous theory is applicable for methods of introducing vacancies other than by plastic flow; for example, the case of radiation-enhanced diffusion considered in detail by DIENES and DAMASK[6].

The experiments of BUFFINGTON and COHEN[2] and UJIIYE *et al.*[7] on the self-diffusion of iron during compressive strain show that the self-diffusion rate is indeed increased linearly with strain rate by plastic deformation, but unfortunately there are not sufficient data available to enable an analysis of the production and annealing mechanisms to be made.

The purpose of this paper is to present the results of an experimental study of the effect of compressive deformation on the self-diffusion coefficient of silver. The strain rates were varied from 0·00075 to 0·006 hr^{-1}, and the temperature range covered was from 810 to 1172°K. The experimental results and their implications concerning the mechanism of vacancy production and destruction are discussed in terms of the theory of enhanced diffusion during plastic deformation.[5]

2. THEORETICAL

It is generally accepted that diffusion in solids takes place by the motion of defects in the crystal. If a number of defects contribute to diffusion, then the self-diffusion coefficients in an unstrained crystal is given by:

$$D_u = \sum_k D_k n_k, \qquad (1)$$

where D_k is the diffusion constant for the motion of the k^{th} type of defect and n_k is the atomic fraction of the k^{th} type of defect.

In equation (1) it is assumed that the contribution to the diffusion coefficient arising from the cross terms resulting from the interactions between the various types of imperfections can be neglected. The contribution of each type of defect to the diffusion coefficient is determined by the energy of formation and the energy of migration of the defect. According to the best available estimates, these energies are such that only vacancies and divacancies contribute significantly to the self-diffusion coefficient in face-centered metals. Therefore, equation (1) may be written as

$$D_u = D_v n_v + D_{v_2} n_{v_2}, \tag{2}$$

where D_v is the diffusion coefficient for vacancies, D_{v_2} is the diffusion coefficient for divacancies, n_v is the atomic fraction of vacancies and n_{v_2} is the atomic fraction of divacancies.

If it is assumed that the predominant effect of plastic flow on the diffusion coefficient is to increase the vacancy concentration above its thermodynamic equilibrium value, then in the system undergoing plastic deformation, the diffusion coefficient is:

$$D_s = D_v(n_v + n_x) + D_{v_2} n_{v_2}, \tag{3}$$

where n_x is the excess atomic fraction of vacancies introduced by plastic flow.

If the production rate of vacancies is proportional to the strain rate and the annealing rate of vacancies is proportional to the excess vacancy concentration, then the differential equation governing the vacancy concentration is:

$$\frac{dn_x}{dt} = K_1\dot{\epsilon} - K_2 n_x, \tag{4}$$

where t is the time, $\dot{\epsilon}$ is the strain rate and K_1 and K_2 are constants. K_1 and K_2 may depend on temperature, but not on strain.

It will be assumed that the build-up time of excess vacancies according to equation (4) is small compared to the time of the diffusion experiment, so that the steady-state solution of equation (4) may be used.

$$n_x = \frac{K_1\dot{\epsilon}}{K_2}. \tag{5}$$

Substituting equation (5) into equation (3) and combining with equation (2) gives:

$$D_s - D_u = D_v \frac{K_1\dot{\epsilon}}{K_2}. \tag{6}$$

Equation (6) will be assumed valid for all the experiments described in this paper.

The constants K_1 and K_2 may be evaluated as functions of temperature, if the mechanisms of vacancy production and annealing are known. If the production mechanism is a purely geometric one as discussed by SEITZ[3], then K_1 is a constant independent of temperature. If, however, the production rate depends on a thermally activated process, then K_1 is proportional to the Boltzmann factor of an activation energy. Thus, if both mechanisms are operating simultaneously, K_1 is given by:[5]

$$K_1 = C_1 + C_2 \exp(-E^*/kT), \tag{7}$$

where C_1 and C_2 are constants independent of temperature, E^* is an energy of activation for the production of vacancies by moving dislocations, k is Boltzmann's constant and T is the absolute temperature.

The excess vacancies may anneal out of the crystal in two ways: by migration to fixed vacancy sinks, such as dislocations and grain boundaries, or by combining with a mobile defect that effectively traps the vacancy. For migration to a fixed sink, K_2 is proportional to the vacancy diffusion coefficient and the concentration of sinks; for vacancy combination with a highly mobile defect, K_2 is proportional to the defect concentration and to its diffusion coefficient. Two defects present in crystals may be effective in combining with vacancies. These are interstitials and divacancies. The formation energy of interstitials is so high[9] that they would not be expected to contribute significantly to the annealing of vacancies. Recent calculations of the energetics of vacancy clusters, however, indicate that the energy of formation of a divacancy is about 1·7 eV and the energy of migration is about 0·2 eV in face-centered crystals.[11] Furthermore, it has been shown that the trivacancy formed by the combination of a vacancy with a divacancy is quite stable and immobile.[11] It is evident, therefore, that divacancies can act as effective traps for vacancies. Thus,

assuming that both fixed sinks and divacancies can act as vacancy traps, K_2 is given by:[5,6]

$$K_2 = afD_v + \frac{D_{v_2} n_{v_2}}{\lambda^2}, \tag{8}$$

where f is the atomic fraction of fixed vacancy sinks, a is a constant depending on the geometric character of the sink and λ is the jump distance for the motion of a divacancy. The diffusion coefficients are given by

$$D_v = A \exp(-E_v^m/k/T) \tag{9}$$

$$D_{v_2} = B \exp(-E_{v_2}^m/kT), \tag{10}$$

where E_v^m is the energy of activation for the migration of a vacancy, $E_{v_2}^m$ is the energy of activation for the migration of a divacancy and A and B are constants. If plastic flow does not alter the thermodynamic equilibrium concentration of the divacancies, then

$$n_{v_2} = C \exp(-E_{v_2}^f/kT), \tag{11}$$

where C is a constant and $E_{v_2}^f$ is the energy of formation of a divacancy. Using equations (9), (10) and (11), equation (4) may therefore be written as

$$K_2 = p \exp(-E_v^m/kT) + q \exp[-(E_{v_2}^m + E_{v_2}^f)/kT] \tag{12}$$

where p and q are constants independent of temperature.

In using equation (11), it is assumed that the crystal maintains a thermodynamic equilibrium concentration of divacancies even though they are combining with vacancies, that is, the time required to restore a displacement of the equilibrium is taken to be small compared to the lifetime of a vacancy.

The general expression for $(D_s - D_u)$ as a function of temperature when both production mechanisms and both annealing mechanisms are operating is obtained by combining equations (6), (7) and (12):

$$(D_s - D_u) = \frac{A[C_1 + C_2 e^{-E^*/kT}]\dot{\epsilon}}{p + q e^{-(E_{v_2}^f + E_{v_2}^m - E_v^m)/kT}} = \frac{AC_2\dot{\epsilon}}{q} \frac{\left(\frac{C_1}{C_2} + e^{-E^*/kT}\right)}{\left(\frac{p}{q} + e^{-\Delta E/kT}\right)}, \tag{13}$$

where

$$\Delta E = (E_{v_2}^f + E_{v_2}^m - E_v^m).$$

The temperature-dependence of $(D_s - D_u)$ affords an excellent criterion for deciding on the mechanisms of production and anneal occurring in the crystal. If both production and both annealing mechanisms are not operating simultaneously, equation (13) reduces to a number of special cases depending on which mechanisms predominate. Each of these special cases yields a different functional dependence of $(D_s - D_u)$ on temperature.

In the limit of low temperatures, equation (13) reduces to

$$(D_s - D_u) = \frac{AC_1\dot{\epsilon}}{p}, \text{ (low } T) \tag{14}$$

so that at low temperatures, vacancies are produced by a geometric mechanism and anneal by migrating to sinks. In the limit of high temperatures, provided that C_2/C_1 and q/p are both considerably greater than unity,

$$(D_s - D_u) = \frac{AC_2\dot{\epsilon}}{q} \exp[(\Delta E - E^*)/kT] \text{ (high } T) \tag{15}$$

so that at high temperatures, vacancies are produced by a thermally activated mechanism and anneal by combining with divacancies. Thus, a plot of $\log (D_s - D_u)$ against $1/T$ gives a constant value at high $1/T$ and is linear at low $1/T$ with a positive slope given by $(\Delta E - E^*)/k$. Taking logarithms of equation (13) and differentiating with respect to $1/T$ shows that the curve of $\log(D_s - D_u)$ against $1/T$ has a maximum at a temperature T_x given by

$$\Delta E\left(\frac{C_1}{C_2} e^{E^*/kT_x} + 1\right) = E\left(\frac{p}{q} e^{\Delta E/kT_x} + 1\right) \tag{16}$$

and an inflection point at T_F given by

$$(E^*)^2 \frac{\frac{C_1}{C_2} e^{E^*/kT_F}}{\left(\frac{C_1}{C_2} e^{E/kT_F} + 1\right)^2} = (\Delta E)^2 \frac{\frac{p}{q} e^{\Delta E/kT_F}}{\left(\frac{p}{q} e^{\Delta E/kT_F} + 1\right)^2}. \tag{17}$$

In view of the above discussion, an analysis of the variation of the diffusion coefficient with temperature at a constant strain rate should elucidate the mechanism of vacancy production and annealing during plastic flow.

3. EXPERIMENTAL

The specimens used in these experiments were prepared from 0·25-in.-dia. rods of 99·99 per cent pure silver. A thin layer (approx. 0·0001 in) of silver was electroplated onto one end of a $\frac{1}{2}$-in-long specimen from a $AgNO_3$–NaI solution having a ^{110}Ag to total silver ratio of 10^{-8}. An unplated specimen was placed on top of the plated end and the pair was compressed at a constant strain rate. The strain rates employed were 0·00075, 0·0015, 0·003, and 0·006 hr^{-1}. In every test, the specimens were deformed to a total strain of 10 per cent. The temperatures ranged from 810 to 1172°K and were controlled to ±0·5°K.

After the diffusion anneal, the specimens were mounted in bakelite and ground normal to the diffusion direction. This exposed the central plane without smearing the active region into the inactive one.

Autoradiographs were obtained by tightly fastening two layers of DuPont Dosimeter Film No. 510 to the ground face of the specimen and exposing for ten days. The blackening of the film adjacent to the specimen was due to beta radiation from the surface, to gamma radiation from the surface and to gamma radiation scattered from the specimen interior. Because of the short range of beta rays, the darkening of the outermost film was due only to the gamma radiation. Subtracting a densitometer trace of the outermost film from a trace for the innermost film gave a plot of the difference in film density versus the distance from the original radioactive plate. The diffusion coefficient was calculated from a plot of the log of this film density difference versus the square of the distance. This method was checked by a determination of the variation of the diffusion coefficient with temperature in the absence of strain. The data thus obtained were in good agreement with the literature values.

In all cases, the distances used in the strained specimen were corrected for thermal expansion and for the reduction in length of the specimen during compression.

4. RESULTS AND DISCUSSION

The results of the self-diffusion experiments in unstrained and strained silver are summarized in Tables 1 and 2 and shown graphically in Figs. 1–3. The diffusion coefficient in unstrained silver can be represented as a function of temperature by the equation:

Table 1

Temperature, (°K)	D_u (cm^2/sec) $\times 10^{-10}$
1037·5	2·25
1059·7	3·47
1080·3	5·63
1088·6	6·64
1091·4	6·72
1097·5	7·01
1118·1	12·00
1144·2	19·00
1163·6	24·42
1166·4	27·15

$$D_u = 1{\cdot}378 \exp(-46{,}450/RT) \text{ cm}^2 \text{ sec}^{-1}$$

which is in good agreement with the results of HOFFMAN and TURNBULL[8], who give

$$D_u = 0{\cdot}895 \exp(-45{,}950/RT) \text{ cm}^2 \text{ sec}^{-1}.$$

Fig. 1 shows that the diffusion coefficient is a

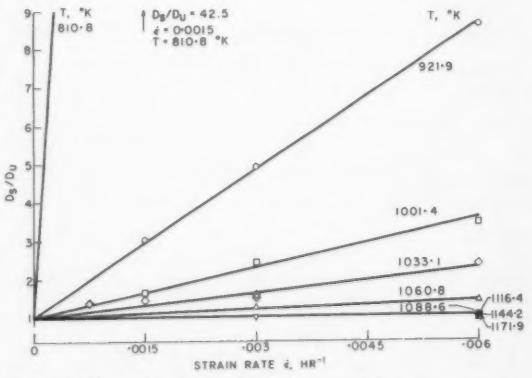

FIG. 1. The ratio of the diffusion coefficient in strained silver to the diffusion coefficient in unstrained silver versus the strain rate at various strain rates and temperatures.

Table 2

Temperature (°K)	D_s(cm²/sec)			
	$\dot{\epsilon} = 0{\cdot}006$ hr^{-1}	$\dot{\epsilon} = 0{\cdot}003$ hr^{-1}	$\dot{\epsilon} = 0{\cdot}0015$ hr^{-1}	$\dot{\epsilon} = 0{\cdot}00075$ hr^{-1}
	$\times 10^{-10}$	$\times 10^{-10}$	$\times 10^{-10}$	$\times 10^{-10}$
810·8	0·743*	0·374*	0·189	
921·9	1·176	0·672	0·411	
1001·4	3·42	2·43	1·657	
1033·1	4·73	3·22	2·96	2·83
1033·1		3·06		2·77
1060·8	5·15	4·60		
1088·6	6·72	6·40		
1116·4	10·85			
1144·2	18·1			
1171·9	29·0			

* Extrapolated.

linear function of strain rate for all the temperatures at which experiments were performed. This is in agreement with equation (6) and provides evidence for the validity of the theoretical model.

Fig. 2 is a plot of $\log(D_s - D_u)$ against the reciprocal absolute temperature for three different strain rates. The curves were calculated by fitting equation (13) to the data subject to the conditions given by equations (14), (15) and (16). The experimental data were not sufficient to define the inflection point, T_F, so that equation (17) was not used. The values of the parameters in equation (13) which gave the best fit to the experimental points are:

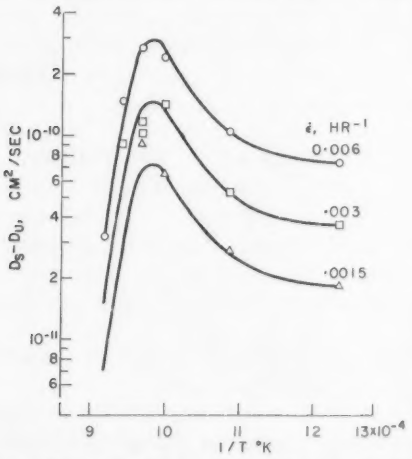

FIG. 2. The logarithm of the difference in diffusion coefficients in strained and unstrained silver versus the reciprocal absolute temperature for various strain rates.

$$\frac{AC_2}{q} = 7{\cdot}16 \times 10^{-30} \text{ cm}^2$$

$$\frac{C_1}{C_2} = 2{\cdot}39 \times 10^{-10} \frac{\dot{p}}{q} = 3{\cdot}92 \times 10^{-35}$$

$$E^* = 1{\cdot}83 \text{ eV} \quad \Delta E = 7{\cdot}13 \text{ eV}.$$

The sensitivity of the shape of the curves of $\log(D_s - D_u)$ against $1/T$ to changes in the parameters listed above, and the inaccuracies in the experimental data are such that E^* is known with an accuracy of $\pm 0{\cdot}2$ eV and ΔE is known with an accuracy of ± 5 eV. The value of ΔE is not known with sufficient accuracy to enable any conclusions to be drawn concerning its theoretical significance on the basis of the experimental data alone. However, E^* is known fairly accurately and can be interpreted in terms of the vacancy-production mechanism.

The value of $E^* = 1{\cdot}8 \pm 0{\cdot}2$ eV is very close to the activation energy for self-diffusion in silver. This suggests that vacancies can be produced by the thermally activated perpendicular motion of edge dislocations as proposed by MOTT[10]. Fig. 3 shows the usual log D versus $1/T$ plot for the various strain rates. The curves were calculated from equation (13). The apparent activation energy is considerably reduced and the diffusion coefficient

is increased by strain. At high temperatures, the strain has very little effect on diffusion.

The experimental data are thus seen to be consistent with the physical model leading to equation

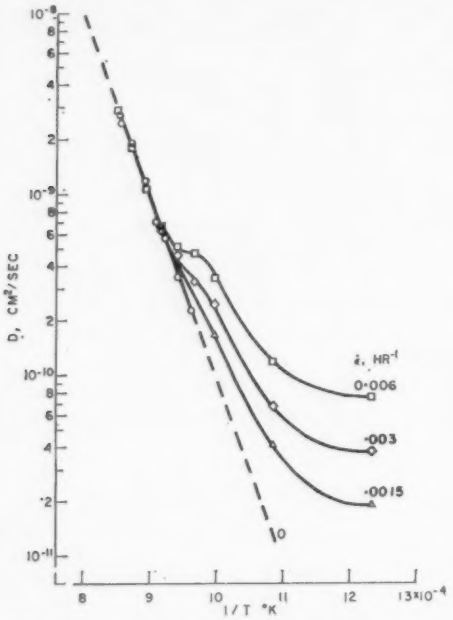

FIG. 3. The logarithm of the diffusion coefficient of silver versus the reciprocal absolute temperature for various strain rates.

(13), in which both production and both annealing mechanisms are operative.

It should be noted that the equations used in this analysis contain the assumption that the number of vacancy sinks is constant during the deformation. However, the dislocation density undoubtedly increases with increasing strain. It is difficult to decide, on the basis of the present data, whether or not such a dislocation density increase appreciably affects the results.

An objection may be raised to the annealing mechanisms involving the combination of vacancies and divacancies on the grounds that there is no direct evidence of any contribution to self-diffusion by divacancies. In fact, Arrhenius plots of the self-diffusion coefficients are quite linear, indicating that only one diffusion mechanism is important rather than two mechanisms as assumed in equation (2). However, recent calculations[11] of the energy of formation and motion of vacancies, divacancies and trivacancies suggest that the activation energy for diffusion by a divacancy mechanism is very close to that for diffusion by a vacancy mechanism in face-centered systems. An Arrhenius plot, therefore, could not differentiate between these two possibilities, and its linearity is not sufficient to reject the divacancy-annealing mechanism.

It should also be pointed out that all that is required by the experimental data is two different annealing mechanisms, one involving vacancy migration to fixed sinks and the other involving vacancy combination with mobile defects. The present data cannot unambiguously define the mobile defect concerned. Energetic considerations, however, suggest that the divacancy is more likely to contribute to the vacancy annealing than any other point defect.

DIENES and DAMASK[6] have investigated the enhancement of diffusion in α-brass by neutron irradiation on the basis of a theoretical analysis similar to that presented in this paper. Their conclusion is that excess vacancies in α-brass anneal by a mechanism involving migration to vacancy sinks. Since their experiments were conducted at temperatures low compared to ordinary diffusion temperatures in α-brass, their results are in agreement with the results given in this paper.

5. SUMMARY AND CONCLUSIONS

It has been found that the self-diffusion coefficient in solid silver is proportional to the strain rate during compressive deformation with a proportionality constant that depends on temperature. At high temperatures the effect of the plastic flow on the diffusion rate is negligible, whereas at low temperatures the diffusion coefficient is markedly increased by the deformation.

An analysis of the mechanism of the production and annealing of vacancies during plastic deformation has been made on the basis of a simple theoretical model. The picture suggested by applying this analysis to the experimental data is that at low temperatures (below 1016°K) vacancies are produced by a temperature-independent mechanism and anneal by migrating to vacancy sinks. As the temperature increases, a shift in mechanism occurs and at high temperatures the predominant vacancy producing mechanism is thermally activated, and

the annealing takes place by the combination of vacancies with divacancies.

These conclusions are in accord with what is known about the enhancement of diffusion by radiation.

Acknowledgements—The authors wish to express their appreciation to Dr. ROBERT A. LAD for his assistance in formulating the problem and designing the experiments for measuring the diffusion coefficient during plastic deformation, and to Dr. D. R. BEHRENDT and Dr. H. H. GRIMES for detailed discussions concerning the interpretation of the data.

REFERENCES

1. MOLENAAR J. and AARTS W. H., *Nature, Lond.* **166,** 690 (1950).
2. BUFFINGTON F. S. and COHEN J., *J. Metals, N.Y.* **4,** 859 (1952).
3. SEITZ F., *Advances in Phys.* **1,** 43 (1952).
4. MOTT N. F., *Phil. Mag.* **44,** 741 (1953).
5. GIRIFALCO L. A. and GRIMES H. H., *Nat. Advis. Comm. Aeronautics Tech. Note* No. 4408 (1958).
6. DIENES, G. J. and DAMASK, A. C., *J. Appl. Phys.* **29,** 1713 (1958).
7. UJIIYE N., AVERBACH B. L., COHEN M. and GRIFFITHS V., *Acta Met.* **6,** 68 (1958).
8. HOFFMAN R. E. and TURNBULL D., *J. Appl. Phys.* **22,** 634 (1951).
9. DIENES G. J. and VINEYARD G. H., *Radiation Effects in Solids,* chap. 5. Interscience Publishers Inc., New York (1957).
10. MOTT N. F., *Proc. Phys. Soc.* **64,** 729 (1951).
11. DIENES G. J., DAMASK A. C. and WEIZER V. G., *Phys. Rev.* in the press.

VOL. 10 1959

J. Phys. Chem. Solids Pergamon Press 1959. Vol. 10. pp. 106–109.

STRUCTURE-SENSITIVITY OF THE HIGH-FREQUENCY NMR IN POWDERED ANTIFERROMAGNETIC MnF_2

J. L. DAVIS, G. E. DEVLIN, V. JACCARINO and A. L. SCHAWLOW

Bell Telephones Laboratories, Inc., Murray Hill, New Jersey

(*Received* 7 *October* 1958)

Abstract—Some structure-sensitive properties of the high-frequency nuclear magnetic resonance (NMR) of ^{19}F in powdered antiferromagnetic MnF_2 have been studied. The resonance is absent in powders obtained by precipitation whether sintered later or not. The resonance is readily observable however, in powders obtained by finely dividing single crystals. Successful attempts to modify the resonance properties by application of large pressures to powdered single crystals are described. Electron-microscope, X-ray-diffraction, and electron-spin-resonance studies were also made and lend support to our belief that strains induced in the nucleation of the precipitate powder broaden the bond-sensitive NMR to the point of rendering it unobservable.

A single crystal of MnF_2 was subjected to a uniaxial compression in the plane perpendicular to the direction of the antiferromagnetic spin alignment. The frequency shift is linear for small pressures with

$$\frac{dv}{dp} = +9{\cdot}2\times10^{-2}\text{kc/kg cm}^{-2}.$$

VOL.
10
195

In the course of making measurements[1] on the high-frequency "zero-field" nuclear magnetic resonance (NMR) of ^{19}F in antiferromagnetic MnF_2 at 4·2°K, we have observed that the resonances to be expected in powders using a frequency-swept NMR spectrometer are not to be found in the small, powdered particles of MnF_2 which are precipitated slowly when a solution of manganese carbonate is mixed with liquid HF. Indeed, in our earliest unsuccessful attempts to find the resonance we used freshly precipitated powder.[2] Nor was the resonance to be found if the same material was sintered in gaseous HF to a temperature several degrees below its melting point (whether it was later finely divided or not). However, since we had by then observed the resonance in large single crystals of MnF_2 with the same apparatus, we made the following studies to learn why the crystalline and powdered materials behaved so differently. Two explanations seemed possible: either the precipitated particle size was too small to support antiferromagnetism, or, more likely, the precipitated particles, whether sintered or not, were relatively strained and disordered and the resonance was broadened to the point where it was difficult to observe.

We attempted to ascertain whether particle size was involved in the observation of the resonance by finely dividing single crystals. We found that, no matter how finely we ground the crystals, the resonance was apparently as strong in the fine crystal powder as it was in the single crystals, and that the resonance was neither broadened nor shifted. Several tests were then made to determine the approximate nature of the particle sizes involved. An examination of the three different powders under a high-powered optical microscope revealed that all particles appeared to be smaller than could be resolved (i.e. $< 10^4$ Å). This was not surprising in view of the fact that both the powdered sintered material and the ground-up crystals appeared white even though they originally came from structures that had the pink color characteristic of manganous salts.

Electron-microscope studies were then made of the three samples. We noticed that the precipitate particles appeared to have an average size comparable with the particle sizes of the other two samples.

OL.
10
959

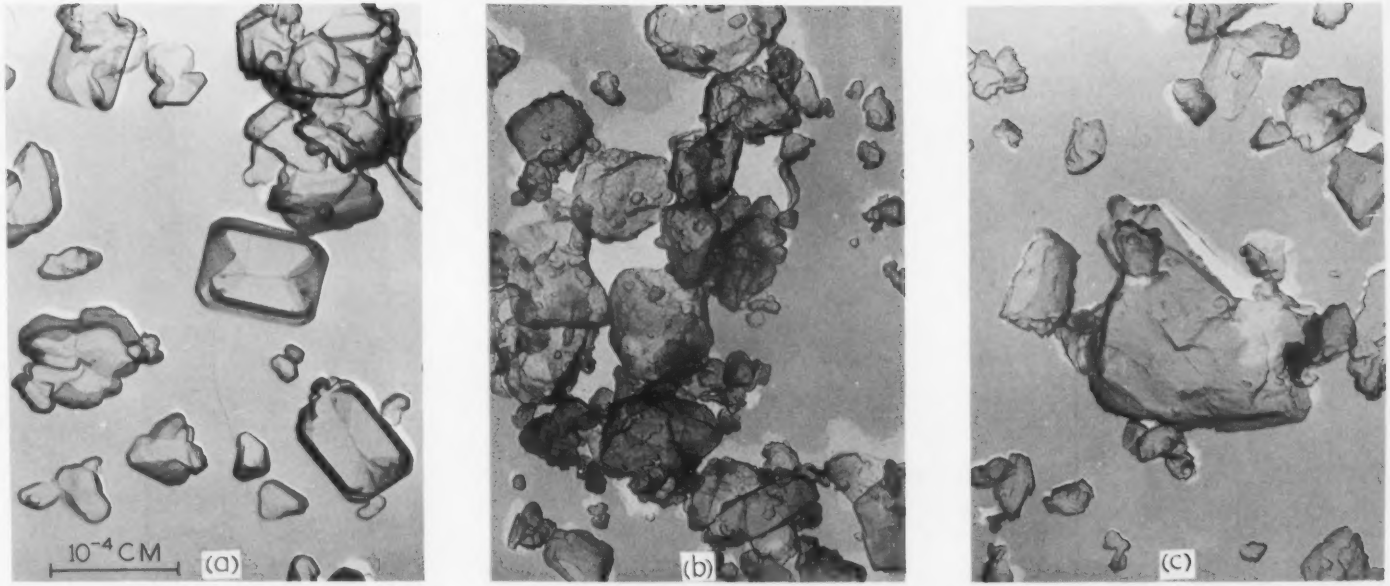

FIG. 1. Electron micrographs of three MnF_2 samples: (a) fresh precipitate powder, (b) precipitate material that had been sintered at 900°C and then finely divided, and (c) powder obtained from finely dividing a large single crystal. Notice that growth planes can be seen in some of the particles in (a). The process of sintering is seen in (b), where smaller particles have fused to larger ones. It should be pointed out that no conclusion of relative size of particles in the different samples can be drawn from these three pictures alone.

VOL.
10
1959

In all three cases there were definite indications of distinct crystal formations, but the edges of the precipitate crystals appeared to be rounded (Fig. 1a). The finely divided sintered material and the finely ground single-crystal powder electron micrographs indicated sharply broken crystalline specimens which are characteristic of a very brittle ionic crystal (Figs. 1b and c). However, even in electron-microscope stereoscopic pairs of the divided larger crystals, there were no more distinct crystal formations apparent than there were in the precipitate powders.

X-ray powder-pattern studies were then undertaken to determine whether the materials exhibited the characteristic MnF_2 X-ray diffraction pattern and also whether some additional information about particle size could be obtained. The main result of the X-ray studies was that in the sintered and ground single-crystal material there appeared to be a few particles large enough to give spots in the otherwise continuous ring patterns; whereas in the precipitate powders the rings were quite diffuse. In each case all lines present were those to be expected in the X-ray powder pattern of a pure MnF_2 sample. Previous chemical analyses have revealed that all impurities in these samples appear to be of the order of a few hundredths of a per cent or less, so that impurity considerations should not enter into the observability of the resonance. In addition, the X-ray powder-pattern studies ruled out any possibility of hydrate formation in any of the three materials.

In order to ascertain that the powders exhibited the strong, short-range exchange interaction which narrows the paramagnetic-resonance line widths, we examined the electron-spin resonance of the three powders at 9,000 Mc at room temperatures. All three samples gave a line width of 480 $\pm$15 Oe, which is characteristic of the line width observed in pure MnF_2 single crystals.[3] The intensity of the line was proportional to the masses of the material indicating again that as far as the electron-resonance properties were concerned, the materials in question were all identical.

The nuclear resonance is known to arise from the partial covalent character of the bond between the fluorine and manganese ions.[2] Since bond character is often a sensitive function of interatomic distance, it is reasonable to assume that the resonance might be affected by strains or imperfections. A similar dependence of frequency on covalent bond lengths has been reported for nuclear quadruple resonance.[4]

We supposed then that only in the powders of single-crystal origin was the local order perfect enough to keep the resonance line from being broadened as we presume it to be in the other two cases. Since we had positive evidence of an unbroadened line only in the case of the single-crystal powders and no resonances in the other two cases, we attempted to modify the former by embedding the finely divided single-crystal powders in a matrix of polystyrene cement and, upon its hardening, cooling it to liquid-helium temperatures. We observed (Fig. 2) that the resonance was both

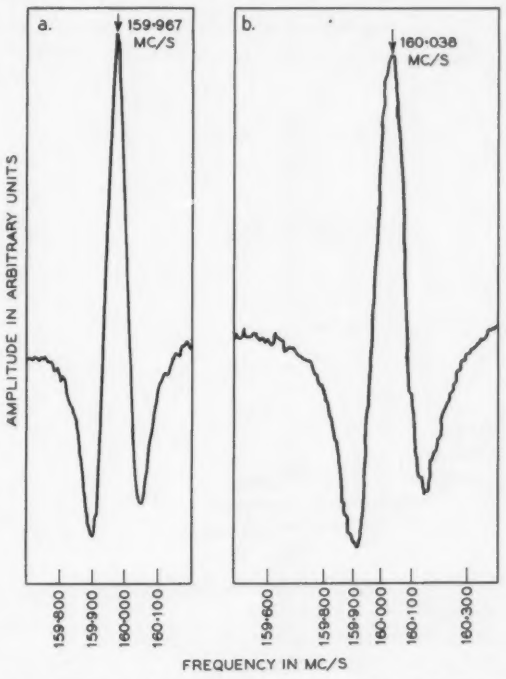

FIG. 2. The high-frequency NMR of ^{19}F in MnF_2 at 4·2°K in: (*a*) a sample from a finely divided single crystal; (*b*) the same material imbedded in a polystyrene matrix. In the recorded absorptions, the oscillator was swept in the direction of increasing frequency while a 100-cps modulation field of approximately 15 Oe was applied. A phase-sensitive detector with a 1-sec time constant followed the 200-c/s narrow-band audio amplifier. The asymmetry in the absorption results from partial saturation (see reference 2).

broadened by 50 per cent and shifted in frequency toward higher frequencies. The latter effect was to be expected in that the polystyrene upon contracting compressed the material and increased the overlap of the fluorine and manganese wave functions, thus causing an increased hyperfine interaction. The broadening presumably results from the nonuniformity of the applied local stress (the compression is not hydrostatic) and the anisotropy in the stress/strain relations for a tetragonal crystal.

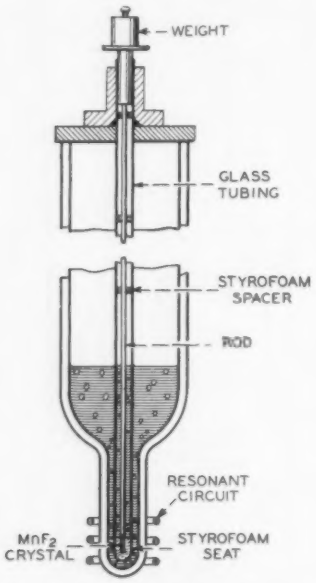

FIG. 3. A schematic representation of the apparatus used for observing the effects on the NMR of a uniaxial compression applied to a single crystal of MnF_2 at liquid-helium temperatures.

Since in the polystyrene matrix the magnitude of the stress applied to an individual particle is unknown, an attempt was made to determine an approximate pressure-frequency shift relation by applying a uniaxial compression to a single crystal of MnF_2, using the apparatus schematized in Fig. 3. All measurements were made at 4·2°K. The magnitude of the stresses applied and the observed frequency shifts are given in Fig. 4. The frequency shift was observed to be linear for the relatively small stresses applied in the experiment. From these data we obtain the pressure-dependence of the frequency shift as:

$$\frac{d\nu}{dp} = +9{\cdot}2\times10^{-2}\text{kc/kg cm}^{-2}.$$

The frequency shift may not be isotropic in this plane and, without knowledge of the elastic constants,* it was deemed not worthwhile at present to measure the anisotropy surface for $d\nu/dp$. It would be interesting to know the volume-dependence of the frequency shift.

These data are sufficient for us to infer that the

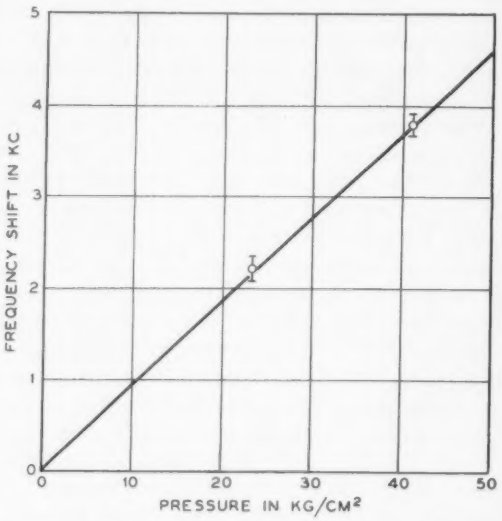

FIG. 4. A plot of the frequency shift versus applied pressure in the uniaxial compression experiment. The direction of applied pressure was perpendicular to the direction of antiferromagnetic alignment.

amounts of strain which could plausibly exist in the precipitated powder would broaden the nuclear resonance so much as to make it unobservable. For a value of Young's modulus of the order of 10^{12} dynes cm^{-2} (which is indicated by a preliminary measurement by H. J. McSKIMIN), a longitudinal stress of 10^8 dynes cm^{-2} produces a longitudinal strain of 10^{-4}. If Poisson's ratio is 1/4 (and here we have no data), the volume strain is approximately half as large, i.e. 5×10^{-5}. From our uniaxial compression measurement, a stress of 10^8 dynes cm^{-2} corresponds to a 9-kc shift, so that the shift per unit strain is of the order of 18×10^4 kc.

* D. F. GIBBONS, of Bell Telephone Laboratories, Inc., is now engaged in such measurements.

In its growth, each of the precipitate grains has been nucleated separately and must contain some nucleus. If the nucleus is a *single* dislocation, the strain at a distance of d atomic spacings from the dislocation is approximately $1/2\pi d$. For a particle of 1000 Å diameter (some 300 atom spacings), an average value of d would be about 75, corresponding to a strain of the order of 2×10^{-3}. The shift frequency corresponding to this strain is 380 kc. Since the strain could be positive in some places and negative in others, we would expect the resonance line width to be of the order of 500 kc. When we recall that this width corresponds to a single dislocation per particle, it is not unreasonable to assume that at least an order-of-magnitude *increase* in line width is to be expected in the precipitated powders as compared to that of the single crystal. Under these conditions, the resonance would be difficult to observe.

Just what the failure to observe the resonance means in the sintered material follows quite readily from our previous argument. The process of sintering presumably corresponds to the agglomeration of smaller particles (with large surface-to-volume ratio) with larger particles before the latter actually melt (this can be seen in Fig. 1*b*). Although larger particles are formed in this process, the absence of the resonance suggests that the original dislocations have yet to be annealed.

Conclusion

The sum total of these observations leads us to believe that the high-frequency nuclear magnetic resonance in the antiferromagnetic state is a measure of local order to which other means of examination that we have employed are largely insensitive. There are other indirect evidences for effects similar to these in the observations of the absence and the broadening of pure quadrupole resonances which have an origin not unlike that of the ^{19}F resonances in antiferromagnetic MnF_2. Since the resonance appears in the very finely divided single-crystal powders, it might be worthwhile to pursue the subdivision of particles still further to determine whether there is a minimum particle size to support the resonance in the antiferromagnetic state. Particle size in the vicinity of 10^{-5} cm or less would be necessary for such an experiment.

Irradiation Effects on the Structure-Sensitive NMR

We have, in addition, examined the high-frequency NMR in a single crystal of MnF_2 after exposure of 231 hr in a flux of $1{\cdot}3\times10^{13}$ neutrons cm^{-2} sec^{-1} in the Brookhaven National Laboratory reactor. At 4·2°K neither the line width nor the resonant frequency is changed, indicating that the local order for the large majority of ^{19}F sites is undisturbed. An order-of-magnitude reduction in the nuclear spin-lattice relaxation time was observed, however.[2] If we assume the fast neutron flux to be approximately one-fourth of the total flux, we may estimate the number of defects produced to be of the order of 10^{-3} of the number of undisturbed sites.[5]

Acknowledgements—We are indebted to S. E. Koonce for the electron micrographs, to S. Geller for the X-ray diffraction work and to J. F. Dillon both for the electron-spin-resonance measurements and for many interesting discussions. E. F. Dearborn and J. W. Nielsen have contributed immeasurably by supplying all samples for this work. Our thanks are due S. C. Abrahams for facilitating the neutron irradiation and to W. T. Reed for a helpful discussion.

REFERENCES

1. Jaccarino V. and Walker L. R., *International Conference on Magnetism, Grenoble, France* (July 1958).
   Jaccarino V. and Walker L. R., *Phys. Rev.* To be published.
2. Jaccarino V. and Shulman R. G., *Phys. Rev.* **107,** 1196 (1957).
   Shulman R. G. and Jaccarino V., *Phys. Rev.* **108,** 1219 (1957).
3. Dillon J. F. and Jaccarino V., *Phys. Rev.* To be published.
4. Kushida T., Benedek G. B., and Bloembergen N., *Phys. Rev.* **104,** 1364 (1956).
5. Seitz F. and Koehler J. S., *Solid State Physics* (Ed. F. Seitz and D. Turnbull) Vol. 2, Academic Press Inc., New York (1956).

J. Phys. Chem. Solids Pergamon Press 1959. Vol. 10. pp. 110–119.

A THEORY OF EDGE-EMISSION PHENOMENA IN CdS, ZnS AND ZnO

J. J. HOPFIELD

Bell Telephone Laboratories, Inc., Murray Hill, New Jersey

(*Received* 1 *December* 1958)

Abstract—Tentative symmetry assignments of p valence bands and s conduction bands can be made for ZnO and CdS on the basis of a tight-binding model. The six-fold degenerate p-bands are split in hexagonal crystals into a four-fold degenerate and a two-fold degenerate band. The four-fold degeneracy is split by spin-orbit coupling. The polarization of recombination radiation depends upon which band the hole belongs to, and is almost independent of the recombination mechanism. The polarization of the edge emission (the series of equally spaced emission lines) should be strongly temperature-dependent. Quantitative agreement is obtained between the predictions of this band model for CdS and the edge-emission polarization experiments of DUTTON (*J. Phys. Chem. Solids* **6**, 101 (1958)). It is shown that the spectra of edge-emission cannot be reasonably explained without the introduction of impurities or surfaces to absorb crystal momentum. In CdS, recombination from a shallow trap seems necessary to explain the large coupling to the lattice apparent in the observed emission spectrum. The edge-emission spectrum should approximate a Poisson distribution for recombination from a trap. The mean number of emitted phonons is a measure of the radius of the trapped carrier-wave function.

1. INTRODUCTION

THE polar crystals ZnS, CdS and ZnO are all observed to be luminescent when irradiated in the fundamental absorption band. The luminescence lies to the long-wavelength side of the fundamental absorption band. The principal feature of this emission spectrum is the occurrence of a series of equally spaced, narrow emission lines, decreasing in intensity at longer wavelengths (see, for example, Fig. 1). This emission has been the subject of extensive experimental investigation.[1,2] On the theoretical side, KRÖGER and MEYER[1] have suggested that the separation between the emission lines corresponds to the energy of a longitudinal optical phonon. (An up-to-date comparison of the observed line separation with the calculated energy of the $\boldsymbol{k} = 0$ longitudinal optical phonons is given in Table 1.) The emission process was hypothesized at the time to be recombination of excitons with phonon emission. More recently, LAMBE *et al.*[3] have performed experiments indicating that the emission in CdS is associated with recombination of a hole with a trapped electron. Experiments have recently been performed on the absorption edges of CdS,[4] ZnO[5] and ZnS[6] in polarized light. Polarization of the edge emission of the light from CdS has recently been observed.[7]

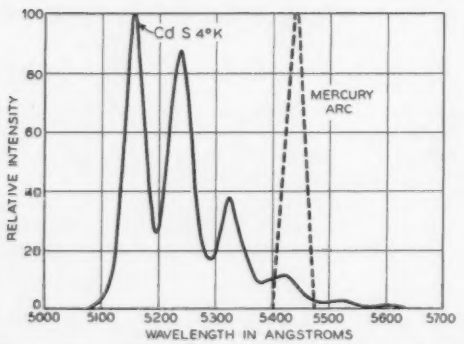

FIG. 1. The spectrum of the edge emission of CdS at 4°K. The dotted line shows the spectrometer window. (After KLICK[9].)

We wish to point out the relation between the absorption and the emission polarization experiments, and to demonstrate that the details of the polarization of the edge emission follow from the

polarization effects observed in the absorption spectrum. The polarization effects yield information about the band structure, but in general do *not* yield information about the mechanism of recombination. The theoretical aspects of the polarization phenomena are discussed in Sections 2 and 3. In Section 4, a theoretical argument is advanced for the necessity of the participation of an impurity to absorb crystal momentum. A shallow-trap model of the recombination center, similar to the *F*-center model of HUANG and RHYS[8], is proposed in Section 5. The model predicts the relative intensity of the multiphonon emission lines. A two-parameter fit of the intensity distribution gives quantitative agreement with the CdS emission spectrum measured by KLICK[9].

Table 1. *Restrahl parameters and edge-emission line spacings*

Material	ZnS (hex)	CdS (hex)	ZnO (hex)
Transverse optical frequency		241 cm^{-1}†	414 cm^{-1}†
n	2·356* 2·378*	2·411* 2·436*	1·93‖ 2·00†
ϵ_s	other data available	9·3†	8·5‡ 8·15†
Longitudinal optical frequency	for cubic phase	305 cm^{-1}§†	591 cm^{-1}§†
Emission spectrum spacing (main lines)	368 cm^{-1}*	320 cm^{-1}* 296 cm^{-1}*	571 cm^{-1}* 550 cm^{-1}*

* From the table of KRÖGER and MEYER.[1]

† COLLINS R. J. (to be published) best fit to restrahl measurements.

‡ HUTSON A. R., *Phys. Rev.* **108,** 222 (1957).

§ Calculated assuming the validity of $\lambda_t = \sqrt{(\epsilon/n^2)}\lambda_l$ for these crystals, which exhibit only minor optical and infrared anisotropies.

‖ An extrapolation by HUTSON A. R. of the data of MOLLWO E., *Z. angew. Phys.* **6,** 257 (1954) to zero frequency.

2. THE BAND STRUCTURE OF ZnS, ZnO AND CdS

The details of the band structures of these crystals are, by and large, unknown. The symmetry of the bands can, however, be estimated from a tight-binding model (even though the tight-binding model will give very poor estimates of the energies) and this is all that is required to discuss the polarization phenomena. The symmetry assignments given here reproduce the currently known polarization phenomena in absorption and edge emission.*

The effective charge on the ions (as calculated from lattice optical absorption spectra) is of the order of unity for all the crystals under consideration. We take for qualitative argument a crystal made up of $Zn^+(Cd^+)$ ions and $S^-(O^-)$ ions, the metal ions having one occupied and one unoccupied orbital *s*-state, the nonmetal ions having five occupied and one unoccupied *p*-orbitals. The lowest-energy electron and hole states probably correspond to a return to a configuration nearer free atoms, i.e. a second hole in a *p*-orbital of the anion or a second electron in an *s*-orbital of the cation. ZnS and CdS both exist in hexagonal and cubic forms. We first discuss the cubic forms and the hypothetical cubic modification of ZnO. At $\boldsymbol{k} = 0$, the conduction bands will be *s*-bands and the valence bands will be *p*-bands. Neglecting spin-orbit coupling, the band structure near $\boldsymbol{k} = 0$ in a [100] direction will be of the form shown in Fig. 2.

At $\boldsymbol{k} = 0$, the three degenerate *p*-states can be labeled P_x, P_y, P_z, according to the direction of the matrix element of the operator $\boldsymbol{r}$ between the *p*-state and an *s*-state. (It is, of course, not known whether these bands have maxima or minima at $\boldsymbol{k} = 0$.)

Imagine a distortion of the crystal into the hexagonal (wurtzite) phase. The tetrahederal nearest-neighbor configuration is present in both phases. The *P*-states which were triply degenerate at $\boldsymbol{k} = 0$ now are split by the crystalline field into two "P_x, P_y" states (x, y are perpendicular to the c-axis of the hexagonal crystal) degenerate at $\boldsymbol{k} = 0$, and a "P_c" state which is to lowest order split away

* *Note added in proof:* The same band symmetries and splittings have previously been suggested by BIRMAN, J. L., *Phys. Rev. Letters* **2,** 157 (1959). The author wishes to thank Dr. BIRMAN for a preprint of the above work and for correcting an error in our group theory.

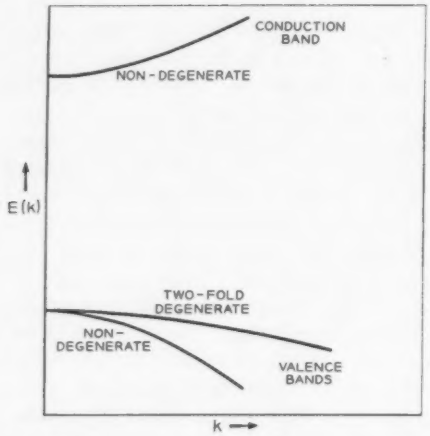

FIG. 2. The valence and conduction band structure for a cubic ZnO, ZnS or CdS crystal in a [100] direction near $\boldsymbol{k} = 0$.

from the "P_x, P_y" states in energy, but suffers no wave-function alteration. The nondegenerate S-state undergoes at worst a change in energy. Near $\boldsymbol{k} = 0$, the energy bands in a direction perpendicular to the c-axis now behave as shown in Fig. 3. The sign of δE is not determined by the argument.

Let it be assumed that the valence-band maximum is at $\boldsymbol{k} = 0$ and that the minimum vertical distance between the valence band and the conduction band is at $\boldsymbol{k} = 0$. The optical anisotropy

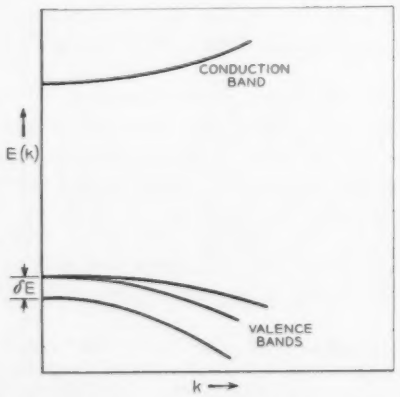

FIG. 3. The valence and conduction band structure for a hexagonal ZnO, ZnS or CdS crystal in a direction perpendicular to the c-axis near $\boldsymbol{k} = 0$.

can then be derived from the band symmetry. The optical properties near the direct absorption edge are determined by the wave-function symmetry at the point in $\boldsymbol{k}$-space corresponding to the smallest vertical distance between the bands. To the lowest order in the crystal field splitting, and neglecting the effect of the degeneracy of the "P_x, P_y" states at $\boldsymbol{k} = 0$ on exciton states, the optical properties of the crystal for the electric vector polarized parallel to the c-axis and photons of energy E should be approximately the same as the optical properties for the electric vector polarized perpendicular to the c-axis and photons of energy $E-\delta E$, if E is in the dispersion region near the band gap. An example of the phenomenon is given in Fig. 4, which shows the reflection coefficient of

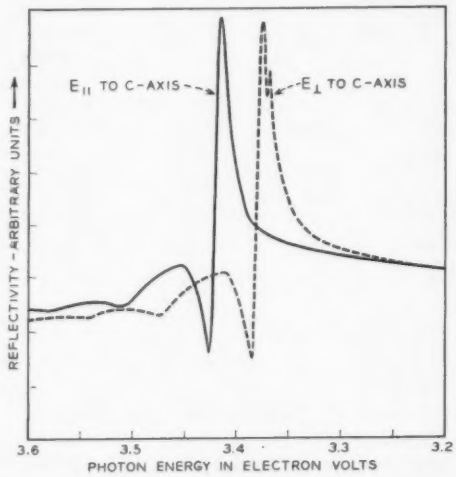

FIG. 4. The reflectivity of a single crystal of ZnO at 78°K for polarized light. (After THOMAS[5].)

ZnO (wurtzite structure) near the band edge for the two different polarizations. The magnitude of δE is 0·046 eV for ZnO* and 0·016 eV for CdS† In both cases the "P_c" band lies below the "P_x, P_y" bands at $\boldsymbol{k} = 0$.

The hexagonal phase has two molecules per unit cell. The additional bands at $\boldsymbol{k} = 0$ in the hexagonal phase are analogous to zone-boundary states of the cubic phase. It is assumed, for lack of other

* Calculated from the reflectivity data of THOMAS.[5]

† Calculated from the polarized-light excitation spectrum of DUTTON.[7]

information, that the top of the valence band and the bottom of the conduction band at $\boldsymbol{k} = 0$ will be the same as for the cubic crystals (i.e. will be $\Gamma_1+\Gamma_5$ and Γ_1, respectively.)

The band-symmetry assignments tentatively arrived at here are not directly verified by experimental data like that of Fig. 4. (Fig. 4 suggests only the symmetry of the combined bands at the point in $\boldsymbol{k}$-space of minimum vertical separation of the bands,* not the symmetry of the individual bands.) Lacking further evidence, however, we shall accept the suggested symmetry assignment for use in predicting the details of the polarization of edge emission. The group theory of the splitting and selection rules is given in the Appendix.

3. THE POLARIZATION OF EDGE EMISSION

Assume that by some process a hexagonal crystal is excited into a state from which it can emit edge radiation and that the edge emission is to be observed in a direction perpendicular to the c-axis. Most optical processes are slow compared to the scattering lifetime of an electron or hole, so it is reasonable (at least at sufficiently high temperatures) to suppose that the hole states are thermalized before the edge emission takes place. Since the recombination radiation involving holes in "P_x, P_y" states is polarized perpendicular to the hexagonal axis and radiation involving holes in "P_c" states is polarized parallel to the hexagonal axis, the polarization of the edge radiation is determined by the occupancy of the two kinds of hole states. If, for example, edge emission involves the recombination of a free hole, then the relative intensity of the two polarizations should be

$$\frac{I_\perp}{I_\parallel} = \left(\frac{m_\perp}{m_\parallel}\right)^{\frac{1}{2}} \left|\frac{H_\perp}{H_\parallel}\right|^2 \exp(\delta E/\kappa T),$$

where $m_\perp$ and $m_\parallel$ are the density of state masses of holes in the "P_x, P_y" bands and the "P_c" band and $H_\perp$ and $H_\parallel$ are the matrix elements for recombination with photon emission. ($|H_\parallel| = |H_\perp|$ in the tight-binding model.) No factor of 2 occurs as a result of the two "P_x, P_y" bands, because only one of these bands can be observed in a given direction.

If, on the other hand, recombination occurs through holes trapped in potential wells of high enough symmetry that "P_x, P_y" states are not mixed with "P_c" states, the polarization should be given by:

$$\frac{I_\perp}{I_\parallel} = \left|\frac{H_\perp}{H_\parallel}\right|^2 \exp[(E_\parallel - E_\perp)/\kappa T],$$

where $E_\parallel$ is the energy of the state having a hole in the "P_c" band and $E_\perp$ is the energy of the analogous state having a hole in the "P_x, P_y" bands. Except for corrections due to mass differences, $E_\parallel - E_\perp = \delta E$. This expression is also valid for recombination through exciton states, with the inclusion of a density-of-states factor to account for the translational degrees of freedom of the exciton.

The long-wavelength optical phonons should not cause an appreciable mixing of the different "P" states. With the hole-thermalization assumption, the following predictions can be made for hexagonal crystals in the lowest approximation of the theory (i.e. neglecting band mixing and the failure of the selection rules away from $\boldsymbol{k} = 0$.)

(1) The edge emission consists of two series of lines, identical except for an intensity factor and a shift δE between the two series. (If n different types of recombination centers give rise to edge emission, there would be $2n$ series.)

(2) Each of the series is 100 per cent polarized; one series is polarized parallel to the c-axis and the other series polarized perpendicular to it.

(3) The ratio of these two series is given approximately by

$$\frac{I_\perp}{I_\parallel} \approx \exp(\delta E/\kappa T)$$

independent of the method of excitation and of the recombination mechanism. This ratio is for observations in a direction normal to the c-axis.

In the Appendix the effects of spin-orbit coupling (which is unimportant in ZnO, but may be of importance in CdS) on the polarization of the emission is briefly discussed.

Recent experiments by DUTTON[7] on CdS at 90°K bear out many of the detailed predictions. Our estimate of δE has been taken from his excitation measurements with polarized light. DUTTON

* Reflection measurements are rather insensitive to indirect absorption processes, since for crystals having a band gap of a few eV it is necessary for the absorption constant to be of order of 10^5 cm^{-1} before absorption appreciably affects the reflectivity.

did not look for the two series, but did observe polarization of the edge emission. Two main points are verified:

(1) The polarization of the edge emission is independent of the polarization and energy of the exciting radiation.

(2) The measured ratio $I_\perp/I_\parallel$ is 6·3. The rough theory predicts $I_\perp/I_\parallel = \exp(0{\cdot}016/0{\cdot}00775) = 7{\cdot}8$. (Because of the exponential, this ratio is a sensitive function of δE. The agreement is within the accuracy of δE. A value of δE of 0·0143 eV would yield the experimental intensity ratio.)

The ZnO edge emission spectrum[10] at 85°K exhibits a series of lines spaced 0·071 eV apart, beginning at about 3755 Å, and one faint line lying 0·039 eV higher in energy than the first line of the main sequence. The near agreement between this energy separation and δE suggests that the weak line is the first line of the $E_\parallel$ series, that both series are completely polarized, and that the intensity ratio is given by the appropriate Boltzmann factor, in this case a factor of about 300 at liquid-nitrogen temperatures.

FURLONG[11] has observed a second series of edge-emission lines in CdS at 4°K, displaced 0·025 eV to higher energy than the main sequence of lines. If our polarization theory is correct, these two sequences of lines are probably due to different recombination processes, since the separation of the lines does not agree with the separation measured in absorption. If the hole-thermalization assumption is valid at this low temperature, both of these observed series should be 100 per cent polarized at this temperature.

4. THE SYSTEMATICS OF EDGE EMISSION

A brief investigation has been undertaken to try to determine under what conditions an edge-emission spectrum having the character of the observed spectra could occur. The basic question a theory must answer is this: under what circumstances is it possible that the mean number of phonons emitted during the radiative recombination of an electron and hole be about 1 (which seems necessary to fit the emission data)? An argument based chiefly on phase-space considerations indicates that the observed spectrum is reasonable only if recombination makes use of impurities or surfaces to absorb crystal momentum. The assumption that free-electron–free-hole recombination produces edge emission will be shown to lead to an absurdly large mass for one of the carriers. The assumption that edge emission is due to exciton recombination would lead to similar difficulties.

For simplicity, the case of parabolic bands with the minimum of the conduction band and the maximum of the valence band at $\boldsymbol{k} = 0$ is treated. It will be assumed that one carrier is so much heavier than the other that the coupling of the lattice to the lighter particle can be ignored. Denote the bare masses by m_l and m_h. For a coupling constant which would be necessary to explain edge emission (a coupling constant α of about 2), the intermediate coupling wave function of LEE *et al.*[12] should be adequate.

If optical transitions are allowed at $\boldsymbol{k} = 0$, and H is the optical matrix element for such a transition, then the squared matrix elements (neglecting the kinetic energy of the electron and the hole) for the recombination of a hole in state $\boldsymbol{k}$ and an electron in state $\boldsymbol{k}'$ with the emission of phonons $\boldsymbol{q}, \boldsymbol{q}' \ldots$ are given by

0 phonons $\quad |H|^2 \exp(-N)\delta_{\boldsymbol{k}',\boldsymbol{k}}$

1 phonon $\boldsymbol{q}$ $\quad |H|^2 \exp(-N)|f(\boldsymbol{q})|^2\delta_{\boldsymbol{k}',\boldsymbol{k}+\boldsymbol{q}}$

2 phonons $\boldsymbol{q}, \boldsymbol{q}'$

$$|H|^2 \exp(-N)|f(\boldsymbol{q})|^2||f(\boldsymbol{q}')|^2\delta_{\boldsymbol{k}',\boldsymbol{k}+\boldsymbol{q}'+\boldsymbol{q}}$$

where

$$f(\boldsymbol{q}) = i\frac{\hbar\omega_0}{|\boldsymbol{q}|}\left(\frac{\hbar}{2m_h\omega_0}\right)^{\frac{1}{4}}\left(\frac{4\pi\alpha}{V}\right)^{\frac{1}{2}}\left[\hbar\omega_0+\frac{\hbar^2\boldsymbol{q}^2}{2m_h}\right]^{-1},$$

$\hbar\omega_0$ is the energy of a longitudinal optical phonon, and N = mean number of virtual phonons present $= \alpha/2$.

For algebraic simplicity, the thermal spread of the light particle in $\boldsymbol{k}$-space is neglected, and the thermal spread for the heavy particle is approximated by a sphere of radius

$$\boldsymbol{k}_0 = \left(\frac{\kappa T m}{2\hbar^2}\right)^{\frac{1}{2}}.$$

(m is the polaron mass of the heavy carrier.) Then the total transition probability W_0 for emission of a photon and zero phonons is given by

$$W_0 = C\left(\frac{\hbar^2}{2\kappa T m}\right)^{\frac{1}{4}}|H|^2 \exp(-N)$$

where C is a constant of proportionality. The transition probability W_q for the emission of a phonon q and a photon is zero if $|q| > k_0$, for the emission of a phonon q implies the existence of an occupied initial state with wave-vector q. The total probability W_1 for emission of a photon and one phonon is

$$W_1 = C\left(\frac{\hbar^2}{2\kappa Tm}\right)^{\frac{1}{2}} |H|^2 \exp(-N) \sum_{|q|<k_0} |f(q)|^2$$

or

$$W_1 \approx W_0 N \left(\frac{\kappa T}{\hbar\omega_0}\right)^{\frac{1}{2}},$$

if $f(k)$ is approximated by

$$|f(k)|^2 = \frac{N}{4\pi k^2}\left(\frac{\hbar}{2m\omega}\right)^{\frac{1}{2}} \quad \text{for } |k| < \left(\frac{2m\omega}{\hbar}\right)^{\frac{1}{2}}$$

$$|f(k)|^2 = 0 \qquad \text{for } |k| > \left(\frac{2m\omega}{\hbar}\right)^{\frac{1}{2}}.$$

Similarly,

$$W_n \approx W_0 \frac{N^n}{n!}\left(\frac{\kappa T}{\hbar\omega_0}\right)^{\frac{1}{2}} \frac{1}{n}.$$

(These expressions are valid only in the absence of thermal optical phonons, i.e. for $\kappa T \ll \hbar\omega_0$.)

Measurements by KLICK[9] on CdS indicate no temperature-dependence of the relative line intensities, thus implying that if the process observed involves the recombination of free electrons and free holes, then direct recombination without phonons is forbidden. If this is the case, then the intensity ratio of the first and second lines as measured would require a bare mass of about 80 m_e for the heavy particle (i.e. would require $\bar{N} \approx 4$), which seems out of reason. If, on the other hand, the recombination takes place in the field of an imperfection (which can relax the wave-vector conservation rule and thus eliminate the density-of-states reduction of the transition probability), the probability of the emission of a photon with n phonons would be proportional to $N^n/n!$. For this case $\bar{N}$ need only be of the order of 1, and $m \approx 5m_e$ (in ZnO, the comparable figure is $m \approx 2m_e$) would produce a sufficiently large coupling constant.

The same qualitative density-of-states argument applies to exciton recombination (with the zero-phonon-emission case impossible). In this case, however, the coupling constant is appreciably smaller for any given values of the particle masses, because the exciton as a whole is electrically neutral.

The physical reason behind the algebraic result is clear. In order to emit an average of one phonon in the photon process, at least one virtual phonon must be present in the initial state. If one virtual phonon is present in the initial state, the occupation probability of a state having n virtual phonons present is approximately $e^{-1}(n!)^{-1}$. Most of the component of the wave function having n virtual phonons present is wasted from the point of view of optical transitions, for the component having n virtual phonons present ($n \neq 0$) contains chiefly electron components from which optical transitions cannot take place. To raise the mean number of *emitted* phonons to a value near 1 requires a coupling constant which is not physically reasonable. We conclude that the observed edge-emission spectrum cannot be due to properties of the pure bulk crystal.

There exists fairly direct evidence in CdS that edge emission takes place through recombination involving a trapped carrier.[3] If free–free or exciton recombination in the field of an impurity is responsible for edge emission, it requires a heavy carrier of mass about $5m_e$. DEXTER[13] has recently done cyclotron-resonance experiments on CdS and has found carriers having masses $0{\cdot}1m_e$ and $0{\cdot}36m_e$. (This, of course, does not necessarily imply that a carrier having a mass several times m_e cannot occur in CdS.) These experimental facts make it of interest to investigate a trapping model.

5. A SHALLOW-TRAP MODEL OF EDGE EMISSION

We assume, following the reasoning of Section 4, that edge emission is due to the recombination of a trapped electron (or hole) with a free hole (or electron). Experiment[9] indicates that these traps cannot be very deep, being of the order of 0·12 eV in CdS from the estimation of the energy difference between the location of the absorption edge and the location of the first edge-emission line (which is assumed to correspond to the emission of zero phonons). Since the binding energy of a trapped carrier is a factor of 3 greater than the energy of a longitudinal optical phonon, to a first approximation the wave function of the crystal

(lattice and trapped carrier) can be written as a product of the carrier-wave function and the lattice-wave function (in a manner analogous to the theory of the F-center of HUANG and RHYS[8]).

We shall assume that the trapping potential well is near enough to cubic symmetry that, if the hole is the carrier which is trapped, the $P_\perp$ bands are not mixed with the $P_\parallel$ band. This assumption will be valid only, if the wave function of the trapped particle is made up of wave functions from a small fraction of the Brillouin zone. (This assumption will turn out to be self-consistent by a fit of the experimental data to the predictions of the model.) The effect of the degeneracy of the $P_\perp$ bands at $\boldsymbol{k}=0$ will be neglected for simplicity.

The interaction of the longitudinal optical lattice vibrations with the trapped carrier is of electrostatic origin and is essentially independent of the details of the electronic band structure. For simplicity, a continuum model of the longitudinal optical lattice vibrations is used. In the effective mass approximation, the Hamiltonian of the trapped carrier, the longitudinal optical vibrations and the trapping center is

$$H = E\left(\frac{\hbar\nabla}{i}\right)+\hbar\omega_0\sum_{\boldsymbol{k}}(a_{\boldsymbol{k}}^*a_{\boldsymbol{k}}+\tfrac{1}{2})+U(\boldsymbol{r})+$$

$$+\left(\frac{2\pi}{V}\hbar\omega_0e^2\right)^{\frac{1}{2}}\left(\frac{1}{n^2}-\frac{1}{\epsilon_0}\right)^{\frac{1}{2}}\times$$

$$\times\sum_{\boldsymbol{k}}\frac{i}{|\boldsymbol{k}|}(a_{\boldsymbol{k}}^*\exp(-i\boldsymbol{k}\cdot\boldsymbol{r})-a_{\boldsymbol{k}}\exp(i\boldsymbol{k}\cdot\boldsymbol{r}),$$

where $a_{\boldsymbol{k}}^*$ and $a_{\boldsymbol{k}}$ are creation and annihilation operators for phonons $\boldsymbol{k}$. The potential $U(\boldsymbol{r})$ is the potential due to the trapping center, including the static lattice distortion which surrounds the unoccupied trap. The Hamiltonian is valid as long as the lattice distortion around an unoccupied trap is small enough to be elastic.

The adiabatic wave function is assumed to have the form $\psi_{\text{carrier}}\phi_{\text{lattice}}$. Since $U(\boldsymbol{r})$ is unknown, we shall assume ψ_{carrier} is known and vary ϕ_{lattice} to minimize the energy of the state. The expectation value of H, taken over the carrier coordinate, is simply

$$\langle H\rangle_{\text{electron}} = \text{const.}+\hbar\omega_0\sum_{\boldsymbol{k}}(a_{\boldsymbol{k}}^*a_{\boldsymbol{k}}+\tfrac{1}{2})+$$

$$+\left(\frac{2\pi}{V}\hbar\omega_0e^2\right)^{\frac{1}{2}}\left(\frac{1}{n^2}-\frac{1}{\epsilon_0}\right)^{\frac{1}{2}}\times$$

$$\times\sum_{\boldsymbol{k}}\frac{i}{|\boldsymbol{q}|}(a_{\boldsymbol{k}}^*\rho_{\boldsymbol{k}}^*-a_{\boldsymbol{k}}\rho_{\boldsymbol{k}}),$$

where $\rho_{\boldsymbol{k}}$ is the $\boldsymbol{k}$th Fourier coefficient of the electron charge density $|\psi_{\text{electron}}(\boldsymbol{r})|^2$. (Thus $\rho_{\boldsymbol{k}}=\rho_{\boldsymbol{k}}^*$.) This reduced Hamiltonian for the lattice vibrations can be solved by a shift of lattice vibration origin. If Φ_0 is the ground-state wave function of the lattice with no carrier present, the ground-state wave function of the lattice in the presence of a trapped carrier is

$$\psi_G = [\exp(-\tfrac{1}{2}\sum_{\boldsymbol{k}}|f_{\boldsymbol{k}}|^2+\sum_{\boldsymbol{k}}f_{\boldsymbol{k}}a_{\boldsymbol{k}}^*)]\Phi_0,$$

where

$$f_{\boldsymbol{k}} = -i\left(\frac{2\pi}{V}\frac{e^2}{\hbar\omega_0}\right)^{\frac{1}{2}}\left(\frac{1}{n^2}-\frac{1}{\epsilon_0}\right)^{\frac{1}{2}}\frac{\rho_{\boldsymbol{k}}^*}{|\boldsymbol{k}|}.$$

The probability W_0 for the emission of a photon and the simultaneous emission of no phonons by recombination of a carrier of opposite sign with the trapped carrier is proportional to the squared matrix element for photon emission.

$$W_0 = C|H|^2(\exp\{-\sum_{\boldsymbol{k}}|f_{\boldsymbol{k}}|^2\})\times$$

$$\times|\langle\psi_0|\exp\sum_{\boldsymbol{k}}f_{\boldsymbol{k}}a_{\boldsymbol{k}}^*|\psi_0\rangle|^2$$

$$= C|H|^2\exp(-\sum_{\boldsymbol{k}}|f_{\boldsymbol{k}}|^2)$$

where $H\equiv\langle\psi_{\text{free carrier}}|P|\psi_{\text{trapped carrier}}\rangle$. If the energy of an optical phonon is neglected in comparison with the photon energy, the probability of emission of a photon accompanied by one optical phonon is (for $\kappa T\ll\theta$ optical)

$$W_1 = C|H|^2\exp(-\sum_{\boldsymbol{k}}|f_{\boldsymbol{k}}|^2)\times$$

$$\times\sum_{\boldsymbol{k}}|\langle\psi_0|a_{\boldsymbol{k}}\exp(\sum_{\boldsymbol{k}'}f_{\boldsymbol{k}'}a_{\boldsymbol{k}'}{}^*)|\psi_0\rangle|^2$$

$$= C|H|^2\exp(-\sum_{\boldsymbol{k}}|f_{\boldsymbol{k}}|^2)\sum_{\boldsymbol{k}}|f_{\boldsymbol{k}}|^2.$$

Similarly, the probability of emission of n phonons with the photon is simply

$$W_n = C|H|^2\exp(-\sum_{\boldsymbol{k}}|f_{\boldsymbol{k}}|^2)\frac{(\sum_{\boldsymbol{k}}|f_{\boldsymbol{k}}|^2)^n}{n!}.$$

The mean number of emitted phonons is

$$\bar{N} = \sum_{\boldsymbol{k}}|f_{\boldsymbol{k}}|^2,$$

and the number of emitted phonons is given by a Poisson distribution of mean $\bar{N}$.

A fit of the Poisson distribution to the photoelectric measurement of the peak heights of the edge emission of CdS as measured by KLICK[9] is

shown in Table 2 for $\bar{N} = 0{\cdot}87$. The deviation of the 5-phonon line from the theoretical value could easily be due to the fact that the measured peak height (which has been assumed to be proportional to the integrated intensity) contains a contribution from the wings of adjacent lines due to the relatively large spectrometer slit width used by KLICK. These tails would become increasingly more important as the ratio of adjacent line intensities becomes large (large n). Alternatively, the disagreement could be due to the fact that the adiabatic approximation becomes increasingly poor for components of the wave function involving large numbers of phonons. The correlation between the trapped carrier-wave function and the lattice-wave function will then alter the relative probability of emitting large numbers of phonons.

Table 2. Measured[9] and trapping-model line intensities for CdS. $\bar{N} = 0{\cdot}87$

Number of phonons	Measured peak height	Theory
0	1·00	1·00
1	0·87	0·87
2	0·38	0·38
3	0·12	0·11
4	0·030	0·024
5	0·015	0·004

To check the model for internal consistency, the radius of the bound state corresponding to $\bar{N} = 0{\cdot}87$ in CdS will be calculated. We assume the charge distribution of the trapped carrier can be approximated by the Gaussian

$$\rho(r) = (\pi^{\frac{1}{2}}a)^{-3} \exp(-r^2/a^2).$$

For this charge distribution, $\bar{N}$ is given by

$$\bar{N} = \left(\frac{e^2}{a}\right)\left(\frac{1}{\hbar\omega_0}\right)\frac{1}{\sqrt{(2\pi)}}\left(\frac{1}{n^2} - \frac{1}{\epsilon_0}\right).$$

Thus for CdS, a is approximately 11 Å. Since a is ≈ 2 lattice constants, the radius of $|f_{\boldsymbol{k}}|^2$ (i.e. the mean value of $|\boldsymbol{k}|$ for the virtual phonons) in $\boldsymbol{k}$-space is about one-sixth of the distance from the center to the edge of the Brillouin zone, and the assumption that the trapped wave function contained components only in a small fraction of the Brillouin zone seems justified.* All that can be said about the binding energy is that it is not inconsistent with a mean radius of 22 Å (the mean radius is approximately $2a$) for the trapped carrier.

A crude estimate of the line width due to the dispersion of the optical phonons can be made by approximating the optical phonon-dispersion relation near the center of the zone by

$$E(\boldsymbol{k}) \approx \hbar\omega_0\left[1 - A\left(\frac{|\boldsymbol{k}|}{\boldsymbol{k}_{\max}}\right)^2\right],$$

where A should be of the order of unity. This would produce a line width of about 2 Å, an order of magnitude too small to account for the width of 10 Å measured by KLICK. A second source of line width within the theory is the width due to the kinetic energy of the free carrier. On the basis of a very simple band model, this broadening would predict a spectral shape $E^{\frac{1}{2}}e^{-E/\kappa T}$ and a full width at half maximum of about $1{\cdot}8\ \kappa T$. This width is about a factor of 2 too small to fit the experimental data at 77°K and an order of magnitude too small to fit the data at 4°K. If the proposed model is qualitatively correct, it must be concluded that the observed width is due, at least at low temperatures, to some minor perturbation not treated in the model (e.g. acoustic lattice vibrations, the influence of imperfections on the binding energy of the trapped carrier or lifetime broadening).

The chief qualitative feature of trapping is the fact that a trapped carrier can have a relatively large amount (compared to a free electron) of lattice polarization (virtual phonons) associated with it. At the same time, the selection rules are relaxed. It is then possible, in a trapping model, to obtain multiphonon emission with a large probability without the necessity of having a heavy carrier.

* The depolarization due to the mixing in of states lying a large distance from $\boldsymbol{k} = 0$ is not necessarily observable in the edge emission. If the conduction-band minimum is at $\boldsymbol{k}_0$, then only the component of trapped hole wave function at $\boldsymbol{k} = \boldsymbol{k}_0$ contributes to optical transitions. If, for example, $\boldsymbol{k}_0 = 0$, then the effects of the large $\boldsymbol{k}$ components of the trapped hole are not observable. The same is true, if $\boldsymbol{k}_0$ lies along symmetry directions in which the longitudinal and transverse "P" functions are not mixed.

6. CONCLUSION

Further polarization experiments need to be done to test the predictions of our tentative theory of the polarization of edge emission. The temperature-dependence of the polarization of the edge emission would seem to be the most definitive experiment. The observation of (or the failure to observe) a second series of lines in CdS would also be a critical experiment. Unfortunately, it does not appear that the polarization of edge emission can give an appreciable amount of evidence about the recombination mechanism if the theory is correct, although it would yield useful information about the valence band.

If, as both experiment and theory seem to indicate, edge emission is associated with impurities, then the edge emission lines may be expected to approximate a Poisson distribution. (The fact that the trapping model yielded exactly a Poisson distribution was a consequence of the rather drastic assumption made about the form of the wave function.) The mean number of phonons determined by the fit to the measured spectrum is a measure of the mass of the heavy carrier, if recombination of free carriers occurs, and is a measure of a trapping radius for trapped recombination.

The recombination theory of Sections 4 and 5 shows the theoretical possibility of edge emission in the presence of impurities. The theory does not indicate which of the possible recombination mechanisms involving impurities actually occurs.

Acknowledgements—The author wishes to thank Dr. A. R. HUTSON for many interesting discussions on edge luminescence and the properties of ZnO. He further wishes to thank Dr. D. G. THOMAS and Dr. R. J. COLLINS for making available unpublished experimental data.

APPENDIX

If spin-orbit coupling is neglected, the point group of the wurzite structure is isomorphic to the hexagonal group without inversions. The group character table is given in Table 3. The valence-band states at $\boldsymbol{k} = 0$ must belong to one of the six irreducible representations of the hexagonal group. The three degenerate atomic P states are split by the crystalline field into "P_x, P_y" (or $P_x + iP_y$, $P_x - iP_y$) (basis functions for Γ_5) and "P_c" (basis function for Γ_1). The kernel of the argument of Section 2 is that the splitting between the Γ_1 and Γ_5 states at $\boldsymbol{k} = 0$ should be small because the crystal structure is closely related to a cubic structure.

Table 3. Group character table for energy bands at $\boldsymbol{k} = 0$ in the wurtzite lattice (without spin-orbit coupling)

Representation	Class					
	E	$3C_2$	$3C_2$	$2C_1$	$2C_6^2$	C_6^3
$\Gamma_1(S,z)$	1	1	1	1	1	1
Γ_2	1	−1	−1	1	1	1
Γ_3	1	1	−1	−1	1	−1
Γ_4	1	−1	1	−1	1	−1
$\Gamma_5(x, y)$	2	0	0	1	−1	−2
Γ_6	2	0	0	−1	−1	2

For a conduction band belonging to Γ_1 and valence bands belonging to Γ_1 and Γ_5, the selection rules for $\boldsymbol{k} = 0 \rightarrow \boldsymbol{k} = 0$ optical transitions are

$$E_{\parallel} \text{ to } c\text{-axis} \qquad \Gamma_1 \rightarrow \Gamma_1$$

$$E_{\perp} \text{ to } c\text{-axis} \qquad \Gamma_5 \rightarrow \Gamma_1.$$

The selection rules do not determine the relative matrix elements for the two transitions. For estimating the relative sizes of the two matrix elements, an argument such as that in Section 2 is necessary.

Spin-orbit coupling has been neglected throughout the paper. This is probably a more serious error in CdS than in ZnO. Both CdS and ZnO seem to exhibit a shift in their optical properties in polarized light. Such a shift (in contrast with a change in shape[14]) must involve crystal-field splitting, not spin-orbit splitting alone. Spin-orbit coupling alters the polarization phenomena to some extent, but does not eliminate them. In the presence of spin-orbit coupling, the "P_x, P_y" band is split into two bands. One of these bands is completely polarized; the other band contains a mixture of "P_c" state. The "P_c" state similarly acquires a "P_x, P_y" component. A knowledge of the percentage depolarization and the location of the different bands allows a computation of the polarization of the edge emission. A large qualitative change from the predictions of Section 3 occurs only if the highest-lying valence band is a mixed band. In this case, for κT much less than the band splittings, the polarization of the edge emission should approach a constant value. Because the polarization of the edge emission arises from detailed balance considerations, the polarization can still be predicted from a knowledge of the absorption-edge polarization phenomena.

REFERENCES

1. For a bibliography of experimental work before 1954, see KRÖGER F. A. and MEYER H. J. G., *Physica, 's Grav.* **20,** 1149 (1954).
2. DIEMER G., VAN GURP G. J. and MEYER H. J. G., *Physica, 's Grav.* **23,** 987 (1957).
3. LAMBE J., KLICK C. C. and DEXTER D. L., *Phys. Rev.* **103,** 1715 (1956).
4. GROSS E. F. and JACOBSEN M. A., *Doklady Akad. Nauk SSSR,* **102,** 485 (1955).
5. THOMAS D. G. To be published.
6. PIPER W. W., MARPLE D. T. F. and JOHNSON P. D., *Phys. Rev.* **110,** 323 (1958).
7. DUTTON D., *J. Phys. Chem. Solids* **6,** 101 (1958).
8. HUANG K. and RHYS A., *Proc. Roy. Soc.* A**204,** 406 (1950).
9. KLICK C. C., *J. Opt. Soc. Amer.* **41,** 816 (1951).
10. EWLES J., *Proc. Roy. Soc.* A**107,** 34 (1938).
    RANDALL J. T., *Trans. Faraday Soc.* **35,** 1 (1939).
11. FURLONG L. R., *Phys. Rev.* **95,** 1086 (1954).
12. LEE T. D., LOW F. E., and PINES D., *Phys. Rev.* **90,** 297 (1953).
13. DEXTER R. N., *International Conference on Semiconductors Abstracts,* p. 47 (1958).
14. See DRESSELHAUS G., *Phys. Rev.* **105,** 135 (1957).

VOL.
10
959

J. Phys. Chem. Solids Pergamon Press 1959. Vol. 10. pp. 120–125.

LOW-TEMPERATURE HEAT CAPACITIES AND THERMODYNAMIC PROPERTIES OF ZINC FERRITES—III

EFFECT OF COPPER SUBSTITUTION

EDGAR F. WESTRUM, JR. and D. M. GRIMES

Department of Chemistry, University of Michigan, Ann Arbor, Michigan

(*Received 3 November* 1958)

Abstract—The heat capacities of annealed and quenched samples of $Cu_{0.05}Zn_{0.90}Fe_{2.05}O_4$ have been determined over the range 5–350°K. The Néel temperature is the same as that previously reported for a similar lithium-substituted zinc ferrite. The result is discussed in terms of the sublattice-population and molecular-field coefficients.

VOL. 10 1959

1. INTRODUCTION

THE low-temperature heat capacity and thermodynamic properties of zinc ferrite and of a solid solution of composition 90 mole per cent zinc ferrite ($ZnFe_2O_4$) and 10 mole per cent lithium ferrite ($Li_{0.5}Fe_{2.5}O_4$) have been studied and reported previously.[1] The data were taken on samples which, after forming spinels from the constituent oxides, had been annealed and on similar samples which had been quenched from 1100°C in distilled water. It was found[2] that the annealed samples had λ-type anomalies in the vicinity of 9°K. This effect has been associated with an antiferromagnetic-type ordering in zinc ferrite.[3] The heat-capacity curve for the quenched samples showed inflections at about 9°K, but a local maximum did not exist. These effects were explained on the basis of sublattice populations and freezing in the 1400°K population equilibrium by the water quench. Similar experimental data have now been obtained on other samples of quenched and annealed ferrite. The samples were solid solutions of composition 90 mole per cent zinc ferrite and 10 mole per cent copper ferrite ($Cu_{0.5}Fe_{2.5}O_4$). The copper ferrite was prepared in such a way that, according to STIERSTADT,[4] it should be in the univalent state.

2. EXPERIMENTAL

The samples were prepared as described previously[2], except that a Szegvari mixer was used in place of the ball mill. The results of chemical analyses on the samples for iron and copper are shown in Table 1.

Table 1. *Analyses of copper–zinc ferrites*

Sample treatment	Percentage by weight			
	Observed		Theoretical	
	Cu	Fe	Cu	Fe
Annealed	1·33	47·68	1·32	47·60
Quenched	1·29	47·37	1·32	47·60

The cryogenic technique was as described previously,[2,5] except that calorimeter of laboratory designation W-10 was employed for these measurements. This calorimeter is similar to calorimeter W-9 previously described,[2] but has a slightly greater volume and lacks heat-conduction vanes. The masses of the calorimetric samples were 187·486 g of annealed and 166·54 g of quenched $Cu_{0.05}Zn_{0.90}Fe_{2.05}O_4$. The gram-molecular weight was taken to be 240·51 g.

3. RESULTS

The values of heat capacity, corrected for "curvature" and in terms of the defined thermochemical calorie of 4·1840 absolute J, and an ice point of 273·15°K are presented in Table 2. The

discussion of precision and intrinsic errors of the previous work[1,2] applies equally to the present results. Values of the heat capacity at selected temperatures, together with the standard entropy increment and enthalpy function, are presented for the two samples in Tables 3 and 4.

4. DISCUSSION

The results at temperatures above 20°K are depicted graphically in Fig. 1, as the deviation of the heat capacities of the measured ferrites from those of annealed zinc ferrite. Only the smooth curve for the lithium–zinc ferrites and for the quenched zinc ferrite are shown; the curves for the copper–zinc ferrites are shown with the data points representing the actual determinations. The most striking characteristic of the curves is that, for the quenched samples, the copper–zinc ferrite resembles closely in properties the zinc ferrite itself, while the annealed copper–zinc ferrite more nearly resembles the lithium–zinc ferrite.

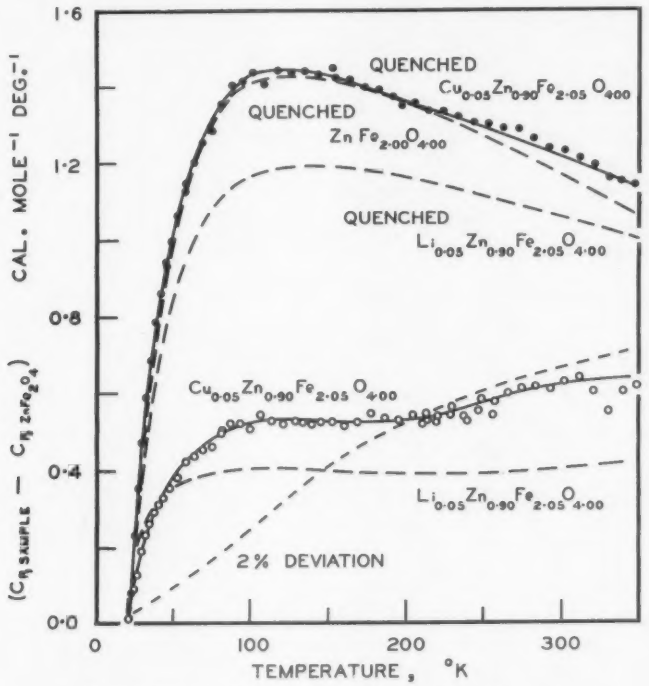

FIG. 1. The deviation of the heat capacities of copper-zinc and lithium–zinc ferrites from those of annealed zinc ferrite.

A major difference between the copper- and the lithium-containing ferrites is that the copper can migrate between sublattices at the temperature of firing, while the lithium cannot. Moreover, the mass of the copper is much greater than that of the lithium. Table 5 shows the idealized sublattice populations in terms of the ferric ions and the closed-shell ions.

The slight difference in absolute value of heat capacity between annealed lithium- and copper-containing ferrites is not explicable on the basis of the idealized sublattice populations. It might be due, however, to differences in the lattice heat capacity, to imperfect ordering of the copper-containing ferrite, to the presence of divalent copper or to different values of exchange coefficients.

Within experimental error, and certainly within 0·1°K, the temperature of the anomalous peak is the same in both annealed lithium-containing and in annealed copper-containing ferrites (cf. Fig. 2).

Table 2. Heat capacities of copper–zinc ferrites in cal(deg. mole)$^{-1}$

Annealed $Cu_{0.05}Zn_{0.90}Fe_{2.05}O_4$

Series I

T(°K)	C_p
211·01	27·29
219·18	28·03
228·15	28·83
237·29	29·56
246·28	30·31
255·09	30·93

Series II

T(°K)	C_p
131·98	17·56
137·33	18·36
143·72	19·30
150·86	20·30
158·54	21·33
167·02	22·44
175·75	23·53
184·33	24·52
193·49	25·52
202·80	26·49
211·90	27·36
208·95	27·07
217·89	27·90
226·90	28·71
235·95	29·47
245·10	30·20
254·46	30·85
263·88	31·55
273·13	32·15
282·23	32·70
291·36	33·22
300·67	33·71
310·12	34·23
319·62	34·65
329·21	35·04
338·90	35·50
347·53	35·87

Series III

T(°K)	C_p
6·46	0·67
6·49	0·69
6·67	0·84
6·96	1·30
7·16	2·01
7·34	2·70
7·72	3·33
8·03	2·96
8·23	2·86
8·39	2·83
8·53	2·74
8·66	2·72
8·81	2·71
8·96	2·66
9·14	2·64

Series IV

T(°K)	C_p
5·53	0·35
6·01	0·46
6·63	0·80
7·09	1·50
7·69	3·42
8·10	2·90
8·65	2·65
9·46	2·60
10·08	2·550
10·53	2·495
11·18	2·454
11·97	2·350
12·78	2·297

Series V

T(°K)	C_p
5·24	0·34
5·78	0·47
6·20	0·67
6·69	0·86
7·13	1·82
7·38	3·05
7·76	3·33
17·19	1·964
18·64	1·889
20·80	1·826
23·32	1·821
25·88	1·879
28·42	1·994
31·07	2·173
33·76	2·402
36·45	2·673
39·26	2·990
42·38	3·374
46·18	3·888
51·17	4·607
56·68	5·460
62·28	6·337
67·90	7·239
73·75	8·178
80·15	9·246

Series VI

T(°K)	C_p
5·33	0·34
5·84	0·43
6·20	0·53
6·50	0·62
6·62	0·71
6·88	1·13
7·46	2·63
7·82	3·02
8·09	2·96
8·64	2·69
9·23	2·631
9·87	2·571
10·52	2·502
11·12	2·460
11·58	2·419
12·25	2·332
13·22	2·262
14·22	2·168
15·40	2·086
16·67	1·994
17·95	1·921
19·17	1·870

Series VII

T(°K)	C_p
79·46	9·130
85·46	10·144
91·50	11·133
97·88	12·161
104·90	13·343
112·02	14·449
119·26	15·60
127·28	16·85

Quenched $Cu_{0.05}Zn_{0.90}Fe_{2.05}O_4$

Series I

T(°K)	C_p
93·82	12·402
99·48	13·356
106·98	14·539
115·57	15·91
124·36	17·31
133·17	18·66
142·05	19·96
151·03	21·22

Series II

T(°K)	C_p
4·82	0·28
13·18	1·56
14·24	1·59
15·68	1·62
4·57	0·19
4·68	0·22
5·04	0·38
5·71	0·72
6·67	1·01
7·83	1·21
9·07	1·36
44·10	4·193
47·32	4·682
51·49	5·333
56·42	6·147

Series III

T(°K)	C_p
7·23	1·12
10·34	1·43
11·75	1·518
13·31	1·569
14·99	1·608
16·71	1·640
18·45	1·685
20·29	1·739
22·31	1·836
24·37	1·957
26·39	2·098
28·73	2·291
31·35	2·547
34·15	2·860
37·25	3·247
40·49	3·681
43·95	4·177
56·27	6·108
61·73	7·015
67·27	7·942
73·38	8·943
79·84	10·047
86·43	11·183
93·32	12·320

Series IV

T(°K)	C_p
152·30	21·39
161·81	22·66
171·34	23·86
180·63	24·95
189·73	25·96
195·16	26·52
203·90	27·42
212·90	28·26
222·17	29·09
231·74	29·90
241·26	30·66
250·88	31·37
260·78	32·04
270·55	32·67
280·48	33·25
290·44	33·80
300·44	34·34
310·47	34·82
320·38	35·28
329·06	35·64
336·67	35·96
345·33	36·31

VOL. 10 1959

Table 3. Molal thermodynamic functions for annealed copper–zinc ferrite ($Cu_{0.05}Zn_{0.90}Fe_{2.05}O_4$) *at selected temperatures*

T(°K)	C_p (cal/deg. mole)	$S°-S_0°$ (cal/deg. mole)	$H°-H_0°$ (cal/mole)	$\frac{H°-H_0°}{T}$ (cal/deg. mole)	T(°K)	C_p (cal/deg. mole)	$S°-S°$ (cal/deg. mole)	$H°-H_0°$ (cal/mole)	$\frac{H°-H_0°}{T}$ (cal/deg. mole)
10	2·554	1·297	9·954	0·995	170	22·82	19·882	1788·1	10·518
15	2·121	2·245	21·56	1·437	180	24·03	21·221	2022·4	11·235
20	1·844	2·810	31·36	1·568	190	25·15	22·551	2268·3	11·938
25	1·852	3·218	40·49	1·620	200	26·20	23·868	2525·1	12·625
30	2·094	3·573	50·27	1·676	210	27·18	25·170	2792·0	13·295
35	2·522	3·927	61·75	1·764	220	28·09	26·455	3068·3	13·947
40	3·077	4·299	75·70	1·893	230	28·97	27·724	3353·7	14·581
45	3·720	4·697	92·66	2·059	240	29·79	28·974	3647·5	15·198
50	4·429	5·126	113·0	2·260	250	30·53	30·206	3949·2	15·797
60	5·978	6·069	165·0	2·749	260	31·25	31·417	4258·1	16·377
70	7·569	7·109	232·7	3·324	270	31·94	32·609	4574·0	16·941
80	9·218	8·227	316·6	3·957	280	32·57	33·783	4896·6	17·488
90	10·85	9·407	419·5	4·661	290	33·17	34·936	5225·3	18·018
100	12·49	10·635	536·2	5·362	300	33·73	36·070	5559·8	18·533
110	14·10	11·901	669·2	6·083	350	35·98	41·449	7305·8	20·874
120	15·71	13·198	818·2	6·819	273·15	32·14	32·981	4674·4	17·113
130	17·25	14·516	983·1	7·562					
140	18·76	15·850	1163·2	8·308	298·15	33·63	35·861	5497·6	18·439
150	20·17	17·193	1357·9	9·052					
160	21·52	18·538	1566·3	9·790					

However, the transition temperature is lower in the lithium-containing ferrite than in a nickel-containing zinc ferrite.[2] One of the differences noted was that annealed lithium ferrite without zinc forms an ordered array of lithium ions on the *B* sublattice. Such is not the case for copper ferrite, yet the transition temperature is the same in copper- as in lithium-containing zinc ferrite. Therefore, it is concluded that the decrease in transition temperature is not due to intrasublattice ionic ordering.

The presence of divalent copper would require a change in oxidation state in some other ferrite constituent for a fixed oxygen content. The most probable ion to change oxidation state is, of course, ferric iron. Both divalent copper and divalent iron ions possess permanent magnetic moments, as does divalent nickel. The fact that the annealed copper-containing sample has a transition similar to the lithium-containing sample in both anomaly shape and temperature and not to the nickel-containing

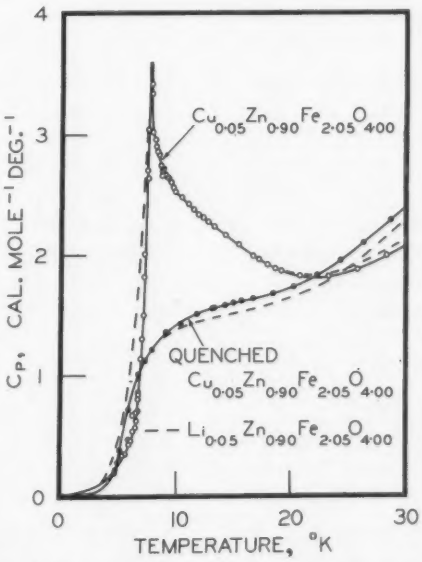

FIG. 2. The heat capacities of zinc ferrites at low temperatures.

Table 4. Molal thermodynamic functions for quenched copper–zinc ferrite ($Cu_{0.05}Zn_{0.90}Fe_{2.05}O_4$) *at selected temperatures*

T(°K)	C_p (cal/deg. mole)	$S°-S_0°$ (cal/deg. mole)	$H°-H_0°$ (cal/mole)	$\frac{H°-H_0°}{T}$ (cal/deg. mole)	T(°K)	C_p (cal/deg. mole)	$S°-S_0°$ (cal/deg. mole)	$H°-H_0°$ (cal/mole)	$\frac{H°-H_0°}{T}$ (cal/deg. mole)
10	1·428	0·834	5·873	0·587	170	23·69	20·363	1893·6	11·139
15	1·607	1·455	13·55	0·903	180	24·88	21·751	2136·5	11·869
20	1·730	1·932	21·86	1·093	190	25·98	23·126	2390·8	12·583
25	1·998	2·344	31·13	1·245	200	27·02	24·486	2655·9	13·279
30	2·410	2·743	42·08	1·403	210	27·99	25·828	2931·0	13·957
35	2·964	3·155	55·47	1·585	220	28·90	27·151	3215·5	14·616
40	3·612	3·592	71·88	1·797	230	29·76	28·455	3508·8	15·256
45	4·329	4·058	91·70	2·038	240	30·56	29·738	3810·4	15·877
50	5·098	4·554	115·3	2·305	250	31·30	31·001	4119·8	16·479
60	6·728	5·626	174·3	2·905	260	31·99	32·242	4436·3	17·063
70	8·386	6·788	249·9	3·570	270	32·62	33·461	4759·4	17·627
80	10·08	8·017	342·2	4·277	280	33·22	34·659	5088·6	18·174
90	11·78	9·302	451·5	5·017	290	33·78	35·835	5423·6	18·702
100	13·43	10·630	577·6	5·776	300	34·31	36·989	5764·0	19·213
110	15·04	11·984	719·9	6·544	350	36·48	42·448	7536·2	21·532
120	16·64	13·361	878·3	7·319	273·15	32·82	34·841	4862·4	17·801
130	18·18	14·754	1052·4	8·095					
140	19·67	16·156	1241·6	8·869	298·15	34·21	36·777	5700·6	19·120
150	21·08	17·562	1445·4	9·636					
160	22·43	18·965	1662·9	10·393					

sample indicates further that the copper is monovalent.

The ferritic compound is considered as $Me_xZn_{1-2x}Fe_{2+x}O_4$ where Me represents a univalent nonmagnetic ion such as those of Li or Cu. The ferrite is assumed to consist of two B sublattices, B^+ and B^-, and a single A sublattice. For annealed samples the Me ions are assumed to be randomly distributed on the B sublattice. The governing equations in the nonordered state are (by an extension of the treatment of TACHIKI and YOSIDA[6]):

$$\left.\begin{aligned} TM_{B^+} &= [1-(x/2)]C_{B^+}[H-(\alpha/2)M_{B^+}-\alpha M_{B^-}-\beta M_A] \\ TM_{B^-} &= [1-(x/2)]C_{B^-}[H-\alpha M_{B^+}-(\alpha/2)M_{B^-}-\beta M_A] \\ TM_A &= 2xC_A[H-\beta M_{B^+}-\beta M_{B^-}-\gamma M_A]. \end{aligned}\right\} \quad (1)$$

It will be assumed that the Lande g-factors are equal, i.e. $g_{B^+}=g_{B^-}=g_A$, so $C_{B^+}=C_{B^-}=C_A$. The condition that a nontrivial solution of equations (1) exists when $H=0$ is that the determinant of the coefficients of the M's be zero. The resulting cubic equation contains the root,

$$T=\frac{\alpha C}{2}\left(1-\frac{x}{2}\right), \quad (2)$$

which is independent of the magnitudes of β and λ.

If the moments on the A sublattice are considered to be resolved into two sublattices, the treatment of YAFET and KITTEL[7] is applicable. Their result for the antiferromagnetic ordering temperature on the B sublattice, T_{C2}, reduces to equation (2) above.

For the ferrites measured, $x=0{\cdot}05$, so the ratio

Table 5. Idealized sublattice populations

Sublattice	Ion	Zn ferrite	Li–Zn ferrite	Cu–Zn ferrite
		Annealed samples		
A	*R**	1·00	0·90	0·90
	Fe	0	0·10	0·10
B	*R*	0	0·05	0·05
	Fe	2·00	1·95	1·95
		Quenched samples		
A	*R*	0·333	0·305	0·317
	Fe	0·667	0·695	0·683
B	*R*	0·667	0·645	0·633
	Fe	1·333	1·355	1·367

* R = ions with zero intrinsic moment.

of Néel temperatures in the mixed ferrites to that in the zinc ferrite, for constant α, is 0·975. The measured ratio was 0·8. If the difference is attributed to variations of α with x, it should be noted that the shift in α is the same for Li^{+1} (radius of 0·78 Å) and Cu^{+1} (radius of 0·96 Å).

The magnetic moments of the quenched samples at 0°K are, ideally, the moments of 0·667, 0·660 and 0·684 ferric ions per formula for zinc, mixed lithium–zinc and mixed copper–zinc ferrites, respectively. Since the dependence of the magnetic moment upon temperature is not known as a function of x, it is not possible to correlate the moments with the heat-capacity curve at present.

Acknowledgements—The authors acknowledge with gratitude the contribution of NORMAN E. LEVITIN, who collaborated in the calorimetric measurements on the samples, and of LYSANDER ASHLOCK, who collaborated in the preparation and analysis of the samples.

REFERENCES

1. WESTRUM E. F., Jr. and GRIMES D. M., *J. Phys. Chem. Solids* **3,** 44 (1957).
2. WESTRUM E. F., Jr. and GRIMES D. M., *J. Phys. Chem. Solids* **6,** 280 (1958).
3. HASTINGS J. M. and CORLISS L. M., *Phys. Rev.* **102,** 1460 (1956).
4. STIERSTADT K., *Z. Phys.* **146,** 169 (1956).
5. BENJAMINS E. and WESTRUM E. F., Jr., *J. Amer. Chem. Soc.* **79,** 287 (1957).
6. TACHIKI M. and YOSIDA K., *Progr. Theor. Phys.* **17,** 223 (1957).
7. YAFET Y. and KITTEL C., *Phys. Rev.* **87,** 292 (1952)

J. Phys. Chem. Solids Pergamon Press 1959. Vol. 10. pp. 126–137.

SUR LE DEPLACEMENT DE KNIGHT DANS LES ALLIAGES

A. BLANDIN et E. DANIEL

Physique des Solides, Paris*

(*Received* 8 *November* 1958)

Resumé—La dissolution dans un métal d'atomes de taille ou de valence différentes de celles des atomes du solvant crée des oscillations de densité électronique autour de chaque atome dissous. Nous montrons que ce phénomène peut expliquer les variations du déplacement de Knight de la matrice, mesurées par différents auteurs sur plusieurs alliages. Cette explication rend également compte de l'élargissement considérable observé pour les raies de résonance. En accord avec les résultats expérimentaux, nous trouvons qu'aux concentrations faibles la variation relative du déplacement de Knight est proportionnelle à la concentration des atomes dissous, tandis que l'élargissement des raies croît comme la racine carrée de la concentration. La même théorie rend compte d'effets analogues observés sur des alliages liquides de métaux alcalins. Enfin, nous étudions l'influence des impuretés de transition.

Abstract—Dissolving in a metal atoms of different type or valence than those of the solvent produces oscillations of electronic density around each dissolved atom. We show that this phenomenon can explain the variations in the Knight shift of the matrix, as measured by different authors on several alloys. This explanation accounts equally well for the considerable observed broadening of the resonance lines. In agreement with experiment we find that at low concentrations the relative variation of the Knight shift is proportional to the concentration of dissolved atoms, whereas the broadening of the lines increases as the square of the concentration. The same theory accounts for analogous effects observed in liquid alloys of alkali metals. Finally, we study the influence of transition metal impurities.

1. INTRODUCTION

DES mesures récentes faites par DRAIN[1], principalement sur **Ag** Cd,† et par ROWLAND[2], en particulier sur **Ag** Cd, **Ag** In, **Ag** Sn et **Ag** Sb, ont révélé que le déplacement de Knight de l'argent dans ces alliages diminue proportionnellement à la concentration des atomes dissous, au moins tant que celle-ci n'est pas trop élevée. Des effets analogues ont été observés sur des alliages liquides de métaux alcalins[3] et sur des alliages de métaux de transition avec les métaux nobles.[1,2,4] Les raies de résonance nucléaire du solvant s'élargissent considérablement dans tous ces alliages, mais l'élargissement croît nettement moins vite que la concentration. Dans la série des alliages d'argent, par exemple, ces phénomènes vont en s'accentuant du cadmium à l'antimoine, c'est-à-dire à mesure que la valence du soluté augmente.

Les modifications observées sont beaucoup trop fortes pour être dues simplement à la distorsion du solvant par des atomes dissous de volume atomique différent. Elles varient de façon trop régulière avec la concentration pour pouvoir être attribuées à des changements de caractère *s-p* près d'une limite de zone de Brillouin.[5] Nous pouvons au contraire expliquer ces effets comme dûs à la polarisation des électrons de conductibilité de l'alliage par les atomes dissous.[6] La substitution d'un atome B de valence $Z+1$ à un atome A monovalent apporte Z électrons de conductibilité à l'alliage; mais le gaz d'électrons de conductibilité de l'alliage se

* Ecole des Mines, 60 boulevard Saint-Michel—Paris 6e France.

† Par **AB**, nous désignons un alliage formé d'un peu de métal B dissous dans la matrice A.

polarise sur l'atome B et à son alentour de façon à faire écran à son excès de charge ionique par rapport à A.[7,8] Cette polarisation a pour effet de localiser une charge électronique égale à Z au voisinage de B. Dans l'approximation de Thomas–Fermi, l'accroissement de la densité des états au niveau de Fermi de l'alliage, dû à l'augmentation du nombre des électrons, se trouve ainsi compensé par une diminution de la densité électronique de chaque état dans la matrice. FRIEDEL en avait conclu que le déplacement de Knight de la matrice ne devait pas être modifié par la dissolution de faibles quantités d'impuretés.[9]

Mais il existe un autre effet de la polarisation du gaz d'électrons que l'approximation de Thomas–Fermi ne révèle pas : c'est de produire des fluctuations oscillantes de densité électronique autour de chaque impureté.[10] Ces fluctuations se manifestent à assez grande distance dans la matrice. Nous allons montrer qu'elles sont la cause des variations observées du déplacement de Knight. On remarquera l'analogie qui existe entre ce phénomène et ce qui se passe dans le couplage d'échange indirect des spins nucléaires par l'intermédiaire des électrons de conductibilité :[11,12] dans ce cas, par interaction de contact, un noyau attire les électrons d'une direction de spin et repousse ceux de spin opposé, sans déplacement net de charge; il en résulte, autour du noyau, des oscillations de la densité des électrons ayant une direction de spin, ce qui a pour effet de stabiliser une direction de spin des noyaux voisins par rapport à l'autre. C'est par un phénomène analogue, mais en considérant les spins des atomes magnétiques que BLANDIN et FRIEDEL[13] ont proposé d'expliquer les propriétés magnétiques d'alliages désordonnés à faible teneur des métaux de transition.

Dans cet article, nous montrons d'abord comment la formation de l'écran d'un atome dissous dans un métal s'accompagne de fluctuations de densité électronique dans la matrice, entrainant un étalement de la fréquence de résonance nucléaire de celle-ci. Nous calculons ensuite la loi du déplacement de la fréquence de résonance moyenne avec la concentration de l'alliage. Le troisième paragraphe est consacré à l'élargissement des raies de résonance. Dans le quatrième, nous étendons notre théorie au cas des alliages liquides, et finalement, dans le cinquième, nous considérons le cas des solutés de transition.

2. FLUCTUATIONS DE DENSITE ELECTRONIQUE AUTOUR D'UNE IMPURETE

L'effet d'écran autour d'une impureté B dans le métal A est tel que le potentiel perturbateur ne s'étend guère au-delà de la sphère atomique de B.[8] Nous admettons que le potentiel perturbateur dû à l'atome B dans l'alliage **AB** a la symétrie sphérique et qu'il s'annule à l'extérieur de la sphère atomique de B. Pour l'étude du déplacement de Knight seuls les électrons au niveau de Fermi dans l'alliage nous intéressent. Nous allons montrer que la diffusion de ces électrons par le potentiel perturbateur de l'atome B crée autour de celui-ci des fluctuations de densité électronique de caractère oscillant. Nous utilisons un modèle d'électrons libres; plus exactement, nous admettons que la fonction de Bloch d'un électron au niveau de Fermi dans le métal A pur peut s'écrire

$$\Psi_A = u(\mathbf{r})\exp(i\mathbf{k}\,.\,\mathbf{r})$$

où $u(\mathbf{r})$ est la fonction d'onde au bas de la bande de conductibilité. A cette fonction Ψ_A correspond alors dans la matrice de l'alliage **AB**, c'est-à-dire de la sphère atomique de B, la fonction d'onde

$$\Psi = u(r)[\exp(i\mathbf{k}\,.\,\mathbf{r})+\Psi_k(r)]$$

où $\exp(i\mathbf{k}\,.\,\mathbf{r})+\Psi_k(\mathbf{r})$ est la fonction d'onde d'un électron libre d'énergie $h^2k^2/2m$ diffusé par le potentiel perturbateur de l'atome B. Soit $\rho(r)$ la densité, par unités d'énergie et de volume, des électrons au niveau de Fermi au point $\mathbf{r}$ du métal A pur :

$$\rho(\mathbf{r}) = \sum_k u^*(\mathbf{r})u(\mathbf{r}) = gu^*(\mathbf{r})u(\mathbf{r}), \qquad (1)$$

g étant le nombre d'électrons par unité d'énergie et de volume au niveau de Fermi.

Dans l'alliage, au point correspondant de la matrice, cette densité est devenue :

$$\rho(\mathbf{r})+\Delta\rho(\mathbf{r}) = \sum_k u^*(\mathbf{r})u(\mathbf{r})[\exp(-i\mathbf{k}\cdot\mathbf{r})+\Psi_k^*(\mathbf{r})][\exp(i\mathbf{k}\,.\,\mathbf{r})+\Psi_k(\mathbf{r})] \qquad (2)$$

Soit θ l'angle du vecteur $\mathbf{k}$ avec la direction de diffusion déterminée par $\mathbf{r}$. Analysons les fonctions d'ondes en composantes sphériques autour du noyau B. On a :

$$\left.\begin{aligned}\exp(i\mathbf{k}\,.\,\mathbf{r}) &= \sum_{l=0}^{\infty} i^l\sqrt{[2(2l+1)]}j_l(kr)P_l(\cos\theta);\\ \exp(i\mathbf{k}\,.\,\mathbf{r})+\Psi_{\mathbf{k}}(\mathbf{r}) &= \sum_{=0}^{\infty} i^l\exp(i\eta_l)\sqrt{[2(2l+1)]}f_l(kr)P_l(\cos\theta),\end{aligned}\right\}\quad(3)$$

avec

$$f_l = j_l\cos\eta_l - n_l\sin\eta_l.$$

Dans ces formules, j_l et n_l sont respectivement les fonctions sphériques de Bessel et de Neumann, P_l le polygone de Legendre normé d'ordre l, η_l le déphasage introduit par le potentiel diffuseur dans la $l^{\text{ème}}$ composante sphérique de l'onde plane incidente. En portant les développements (3) dans les égalités (1) et (2) et en remplaçant dans celles-ci la somme sur les vecteurs $\mathbf{k}$ par une intégrale sur la sphère de Fermi, on obtient pour la variation relative de densité au point $\mathbf{r}$:

$$\frac{\Delta\rho(\mathbf{r})}{\rho(\mathbf{r})} = \sum_{1}(2l+1)\{[n_l^2(kr)-j_l^2(kr)]\sin^2\eta_l - j_l(kr)n_l(kr)\sin 2\eta_l\}.\quad(4)$$

Cette quantité est alternativement positive et négative quand r croit; pour les grandes valeurs de r, l'amplitude de ses oscillations décroit comme $1/r^2$.*

Soit $\mathbf{R}_j$ le rayon vecteur du $j^{\text{ème}}$ noyau A autour du noyau B. Dans le métal A pur, la densité $\rho(\mathbf{R}_j)$ a la même valeur ρ pour tous les noyaux. Dans l'alliage, cette densité $\rho+\Delta\rho(\mathbf{R}_j)$ varie d'un noyau à l'autre. Comme le déplacement de Knight $K = \Delta H/H$ de la résonance magnétique est proportionnel à la densité électronique au noyau,[14] chaque noyau A dans l'alliage a sa fréquence de résonance particulière, donc son propre déplacement de Knight dont la variation relative $\Delta K_j/K$ au $j^{\text{ème}}$ noyau A est égale à celle de la densité électronique au même noyau :

$$\frac{\Delta K_j}{K} = \frac{\Delta\rho(\mathbf{R}_j)}{\rho}.\quad(5)$$

On obtient donc dans l'alliage un véritable spectre de fréquences de résonance.

Pour évaluer la répartition des déplacements de Knight dans l'alliage, nous choisissons le potentiel le plus simple qui puisse représenter l'effet de l'impureté : un puits sphérique de rayon égal à celui de l'atome B dissous et de profondeur telle qu'il attire exactement les Z charges électroniques nécessaires à la formation de l'écran. Dans ces conditions, les déphasages doivent vérifier la règle de FRIEDEL :[8]

$$Z = \frac{2}{\pi}\sum_{l}(2l+1)\eta_l.$$

Si les métaux A et B ont des volumes atomiques différents, il est possible de tenir compte de l'effet de taille dans l'alliage par le procédé de BLATT[15] qui remplace dans la condition ci-dessus la charge Z par une charge effective Z' plus grande ou plus petite que Z suivant que l'atome B est plus petit

* On s'en rend compte clairement sur sa forme asymptotique :

$$\frac{\Delta\rho(r)}{\rho(r)} \to \sum_{l}(-1)^l(2l+1)\sin\eta_l\frac{\sin(2kr+\eta_l)}{(kr)^2}\quad\text{pour } r\to\infty.$$

VOL. 10 1959

ou plus gros que l'atome A. On calcule aisément les déphasages pour ce potentiel diffuseur.[16] Ils sont d'ailleurs à peu près négligeables au-delà de $l = 2$ ou 3, ce qui limite les sommations sur l. En fait, pour **Ag** Cd, **Ag** In, **Ag** Sn et **Ag** Sb, nous avons utilisé directement les déphasages que tions d'autant plus importantes que la charge Z est plus grande. De part et d'autre d'une raie centrale intense et quelque peu élargie correspondant aux noyaux A éloignés, on devrait, en principe observer des raies satellites dues aux fréquences de résonance différentes des couches d'atomes A

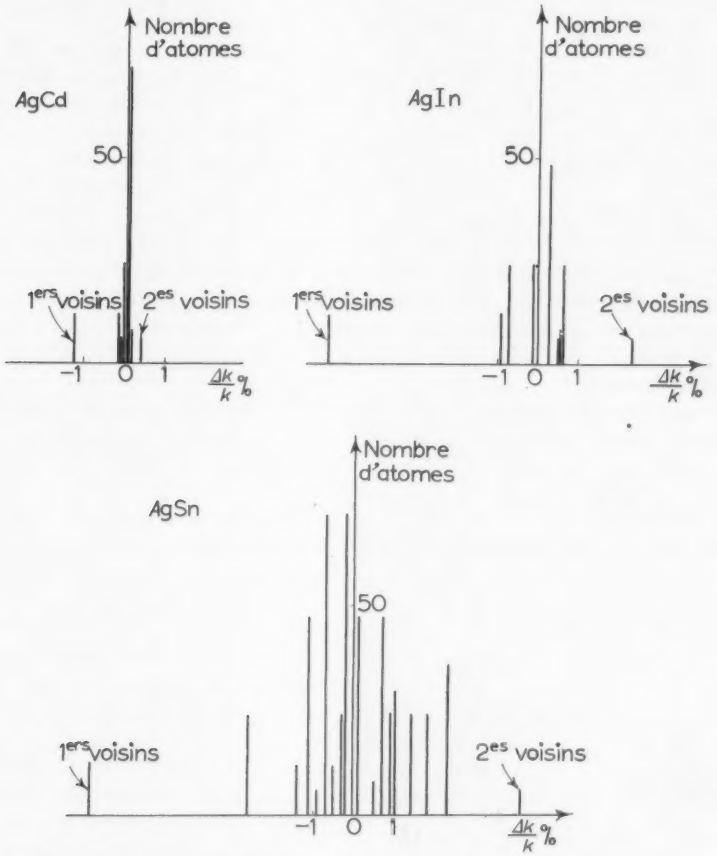

FIG. 1. Raies satellites de la résonance nucléaire de l'argent contenant une impureté dissoute.

Blatt avait calculés pour l'étude de la résistivité résiduelle de ces alliages aux basses températures.[15]

Les résultats, illustrés par la Fig. 1, montrent que la polarisation des électrons par l'atome B affecte fortement la fréquence de résonance des noyaux A premiers et seconds voisins, et qu'elle crée dans les couches plus éloignées des fluctuations d'autant plus importantes que la charge Z est plus grande. De part et d'autre d'une raie centrale intense et quelque peu élargie correspondant aux noyaux A éloignés, on devrait, en principe observer des raies satellites dues aux fréquences de résonance différentes des couches d'atomes A voisines de l'impureté. Bien entendu, même aux concentrations les plus faibles, ces raies sont élargies du fait qu'on a toujours un grand nombre d'atomes dissous, répartis de façon aléatoire dans l'alliage, et on ne peut guère espérer distinguer que les raies satellites des premiers et seconds voisins. Les observations de Rowland semblent confirmer ce point.[2]

3. CALCUL DU DEPLACEMENT DE KNIGHT MOYEN

Nous considérons maintenant un alliage de substitution **AB**, parfaitement désordonné, dans lequel la concentration c des atomes B est faible, mais non infiniment petite. Moyennant certaines hypothèses nous allons montrer que, dans ces conditions, le déplacement de Knight moyen des noyaux A est proportionnel à la concentration c et évaluer le coefficient de proportionnalité.

Nous faisons les trois hypothèses suivantes :

(1) l'alliage est parfaitement désordonné;

(2) les diffusions multiples des électrons au niveau de Fermi par les atomes dissous, sont négligeables;

(3) la première hypothèse étant satisfaite, on ne commet pas d'erreur appréciable en additionnant en chaque point les excès de densité électronique créés par chaque impureté isolée. On se rend compte assez aisément que cette dernière approximation est valable au premier ordre en c à la limite des concentration faibles.

Soient N et n les nombres respectifs d'atombres A et B dans l'alliage; le $i^{\text{ème}}$ atome B crée au $j^{\text{ème}}$ atome A la variation relative de densité $\Delta\rho(R_j-R_i)/\rho$. D'après la relation (5), avec les hypothèses que nous venons de faire, le déplacement de Knight moyen dans la matrice est, en valeur relative :

$$\frac{\Delta K}{K}=\frac{1}{N}\sum_{j=1}^{N}\sum_{i=1}^{n}\frac{\Delta\rho(\mathbf{R}_j-\mathbf{R}_i)}{\rho}=\frac{n}{N}\sum_{j=1}^{N}\frac{\Delta\rho(\mathbf{R}_j)}{\rho}$$

compte tenu de l'équivalence statistique de tous les atomes B. Puisque $c=n/N+n$ et que la probabilité d'occupation d'un noeud du réseau par un atome A est $N/N+n$, on voit que :

$$\frac{\Delta K}{K}=c\sum_{\mathbf{R}}\frac{\Delta\rho(\mathbf{R})}{\rho} \qquad (6)$$

la somme étant faite sur tous les noeuds du réseau autres que l'origine. Le déplacement de Knight moyen de la matrice varie proportionnellement à la concentration c de l'alliage.

En remplaçant, dans la relation (6), $\Delta\rho(\mathbf{R})/\rho$ par sa valeur donnée par la formule (4), on obtient :

$$\frac{1}{c}\frac{\overline{\Delta K}}{K}=\sum_{l}(\alpha_l\sin^2\eta_l+\beta_l\sin^2\eta_l). \qquad (7)$$

Dans cette formule, les coefficients :

$$\alpha_l=(2l+1)\sum_{\mathbf{R}}[n_l^2(kR)-j_l^2(kR)]$$

et

$$\beta_l=-(2l+1)\sum_{\mathbf{R}}j_l(kR)n_l(kR)$$

ne dépendent pratiquement que de la matrice A. En effet, pour des concentrations faibles d'atomes dissous, les distorsions du réseau modifient peu les distances entre noyaux, de sorte que nous pouvons conserver aux atomes A de l'alliage leurs positions dans la matrice non déformée. L'essentiel de l'effet de taille est contenu dans les déphasages. Dans la mesure où les électrons de conductibilité se comportent comme des électrons libres, le produit kr_s du rayon de la sphère de Fermi par celui de la sphère atomique est constant et égal à $(9\pi/4)^{1/3}$ pour tous les métaux monovalents. Par conséquent, les quantités kR ne dépendent que du réseau cristallin du métal A. Quant aux déphasages η_l, ils dépendent essentiellement du solute par sa valence $Z+1$ et un peu du solvant pour l'effet de taille.

Pour l'étude des alliages d'argent ou de cuivre, nous considérons un réseau cubique à faces centrées (c.f.c.). Les fonctions $(n_l^2-j_l^2)$ et $j_l n_l$ prennent des valeurs oscillantes dont l'amplitude ne décroit que comme $1/R^2$ aux grandes distances R du noyau B; par conséquent leurs sommes sur les points éloignés de B dans la matrice ne donnent de valeurs nulles qu'en moyenne. Pour évaluer numériquement les coefficients α_l et β_l, nous calculons les sommes sur les N' premiers voisins de l'atome B, c'est-à-dire pratiquement sur tous les noeuds du réseau de la matrice situés à l'intérieur d'une sphère de rayon $R_1=\sqrt[3]{(N'+1)}r_s$; à l'extérieur de cette sphère, nous remplaçons les sommes sur les points du réseau par des intégrales de volume. En prenant $N'=140$, ce qui correspond à $kR_1\simeq 10\simeq 5{,}2kr_s$ nous avons obtenu les résultats du tableau 1 (sauf pour α_0).

Nous avons calculé le coefficient α_0 avec précision par une autre méthode, développée en annexe, mais qui, ne s'applique pas au calcul pratique des autres coefficients. L'écart de 7% entre la valeur 1,052 obtenue ainsi et le nombre approché $1{,}1_3$ calculé par le procédé indiqué

VOL. 10 1959

ci-dessus permet d'avoir une idée de la validité des chiffres du Tableau 1.

Tableau 1. *Coefficients de la formule* (7) *pour un solvant* A *monovalent c.f.c.*

$\alpha_0 = 1{,}052$	$\beta_0 = 0{,}1_7$
$\alpha_1 = -2{,}3_7$	$\beta_1 = -1{,}2_0$
$\alpha_2 = -1{,}9_1$	$\beta_2 = 2{,}4_0$
$\alpha_3 = 4{,}8_7$	$\beta_3 = 3{,}5_2$

Dans le Tableau 2, nous comparons aux valeurs expérimentales les déplacements de Knight relatifs, par unité de concentration, calculés suivant la formule (7), en utilisant les déphasages de BLATT[15]

Tableau 2. *Comparaison des résultats théoriques et expérimentaux*

Alliage	$-(1/c)(\Delta K/K)$		
	Mesuré		Calculé
Ag Cd	0,34	[1]	$0{,}1_5$
Ag Cd	0,4	[2]	
Ag In	0,7	[2]	0,7
Ag Sn	1,1	[2]	1,1
Ag Sb	1,2	[2]	1,0
Cu Zn	0,15	[4]	0,1
Cu Sn	1,2	[4]	0,9

L'accord est satisfaisant dans l'ensemble, surtout quand l'effet de valence est assez fort. Notre résultat trop faible pour **Ag** Cd est à rapprocher du fait que ROWLAND[2] observe aussi une diminution du déplacement de Knight de l'argent dans les alliages **Ag** Au, proportionnelle à la concentration en or. Puisque, dans ces derniers alliages, il n'y a ni effet de valence, ni effet de taille important, la façon simple suivant laquelle nous avons développé notre théorie devient insuffisante, car elle ne conduit à aucune variation du déplacement de Knight. En fait, notre modèle suppose que les électrons au niveau de Fermi dans la matrice se comportent comme des électrons libres dont la fonction d'onde est simplement modulée par la fonction d'onde au bas de la bande de conductibilité. Autrement dit, nous admettons que la surface de Fermi est sphérique et que les électrons ont un caractère purement s et une masse effective égale à la masse normale.

En réalité, les différences de densités d'états au niveau de Fermi observés pour l'argent et l'or par chaleur spécifique indiquent que leurs structures électroniques sont un peu différentes. La dissolution d'or dans l'argent doit donc créer des perturbations qui se traduisent par des déphasages petits mais non nuls pour les fonctions d'onde dans l'argent. De petites corrections analogues seraient sans doute à faire dans la série **Ag** Cd, In, Sn, Sb, mais elles ne sont sensibles que pour **Ag** Cd.

4. ELARGISSEMENT DES RAIES

Rappelons que nous nous limitons à des concentrations faibles d'atomes dissous, répartis de façon parfaitement désordonnée dans la matrice.

Dans la mesure où les autres causes d'élargissement sont négligeables on peut assimiler la demi-largeur de raie δH à la racine carrée du second moment de la raie de résonance. En effet, si M_2 et M_4 sont les second et quatrième moments de la raie on a :

$$\frac{M_4}{M_2^2} = \frac{1}{cz} \quad \text{où} \quad z = \frac{[\sum_i \Delta\rho^2(r_i)]^2}{\sum_i \Delta\rho^4(r_i)}$$

z est un paramètre qui donne une indication sur la portée des interactions: $z = N_1$, nombre de premiers voisins, s'il n'y a interaction qu'entre premiers voisons; $3 \gg N_1$ si les interactions sont à longue distance.

Si $M_4/M_2^2 \gg 3$, le courbe ressemble à une courbe de Lorentz, si $M_4/M_2^2 \lesssim 3$, à une courbe de Gauss. Donc, si $c \ll 1/3$, la raie de résonance est de genre Lorentzien, si $c \gtrsim 1/3z$, elle est du genre gaussien. Ici, $z \simeq 14$, 18, 35, 80 pour Cd, In, Sn, Sb respectivement. Donc, dès que c est supérieur à 2% pour Cd et In, 1% pour Sn, 0,5% pour Sb, la raise et "gaussienne" et le second moment donne alors une mesure acceptable du carré de la demi-largeur.

On a donc, avec les notations du paragraphe précédent et en appelant ΔH le déplacement de Knight absolu, en gauss, du metal A :

$$\frac{\delta H}{\Delta H} = \sqrt{\left[\overline{\left(\frac{\Delta K}{K}\right)^2} - \left(\overline{\frac{\Delta K}{K}}\right)^2\right]}$$

$$= \sqrt{\left[\overline{\left(\frac{\Delta\rho}{\rho}\right)^2} - \left(\overline{\frac{\Delta\rho}{\rho}}\right)^2\right]}$$

les moyennes étant faites sur tous les atomes A de l'alliage. La deuxième égalité vient de la proportionnalité du déplacement de Knight d'un atome A à la densité électronique à son noyau.

Avec les hypothèses faites au paragraphe précédent, on trouve facilement

$$\overline{\left(\frac{\Delta\rho}{\rho}\right)^2} = c\sum_{\mathbf{R}}\frac{\Delta\rho^2(\mathbf{R})}{\rho^2} = cD^2,$$

le nombre D ne dépendant que de la nature de l'alliage tant que la concentration c demeure faible. Quant au terme $\overline{(\Delta\rho/\rho)^2}$, il se déduit immédiatement des résultats du paragraphe précédent; les relations (5) et (6) montrent qu'il est proportionnel à c^2.

Si $\delta_0 H$ est la demi-largeur de raie dans le métal A pur, la demi-largeur dans l'alliage sera :

$$\delta_1 H = \sqrt{[(\delta_0 H)^2 + cD^2(\Delta H)^2]} \quad \text{pour } c \text{ petit} \quad (8)$$

Pour l'argent, $(\delta_0 H)^2 \simeq 0{,}1$ gauss^2; le terme $cD^2(\Delta H)^2$ a sensiblement la même valeur pour $c = 1\,\%$ pour-cent dans le cas de l'alliage **Ag** Cd; il devient beaucoup plus grand quand on passe à des atomes dissous de valence supérieure (In, Sn, Sb). Par conséquent, pour des concentrations c de quelques pour-cents où la formule (8) est encore valable, quand l'élargissement dû aux impuretés est bien supérieur à la largeur propre de la matrice, la largeur de raie doit croître sensiblement comme $\sqrt{c}$.

D'après la formule (4), la quantité $\Delta\rho^2(Rj)/\rho^2$ décroit rapidement quand R_j augmente. Par conséquent, ce sont surtout les atomes A voisins des atomes B qui contribuent à D^2. Notre calcul ne doit plus être valable quand chaque atome B cesse d'être entouré en moyenne d'au moins une couche complète d'atomes A, c'est-à-dire quand la concentration c dépasse 7 à 8 pour-cent. La Fig. 2 permet de comparer les résultats expériementaux de DRAIN et de ROWLAND aux courbes déduites du calcul précédent pour **Ag** Cd, **Ag** In, **Ag** Sn, **Ag** Sb. L'accord est satisfaisant dans l'ensemble surtout si l'on tient compte des approximations faites dans les calculs et de l'incertitude assez grande de plusieurs valeurs expérimentales.

Nous avons négligé dans ce calcul la variation de la largeur par interaction de superéchange. Si $\delta'_0 H$ est la demi-largeur due au superéchange dans l'argent pur, on peut montrer que, pour une concentration c, elle devient : $\sqrt{[(\delta'_0 H)^2 + cD'^2]}$. Mais D'^2 est petit par rapport à $D^2(\Delta H)^2$: pour **Ag** Cd, par exemple, $D'^2/D^2(H)^2 \simeq 1/30$ dans un champ de 10,000 gauss. Il en est de même de la variation de

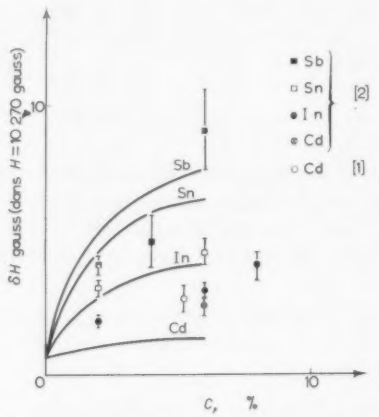

FIG. 2. Elargissement de la raie de résonance de l'argent en fonction de la concentration c pour quelques alliages. Courbes théoriques, selon le paragraphe 4, et points expérimentaux d'après (1) et (2).

l'élargissement dipolaire quand on remplace des atomes d'argent par des atomes étrangers. Il convient de remarquer que ces dernières causes d'élargissement (l'interaction dipolaire des noyaux et leur couplage d'échange indirect) ne dépendent pas du champ magnétique appliqué dans l'expérience de résonance. Le terme en ΔH de la formule (8), dû aux variations de densité électronique, est au contraire proportionnel au champ appliqué.

Enfin, on peut vérifier s'il est permis de négliger ce qui se passe au-delà des premiers voisins d'un atome dissous. En effet, après les formules (6) et (8), on doit avoir dans ces conditions :

$$\frac{\sqrt{[(\delta_1 H)^2 - (\delta_0 H)^2]}}{H\overline{\Delta H}} = \frac{1}{\sqrt{(N_1 c)}},$$

N_1 étant le nombre des premiers voisins.

Cette formule n'est pas suivie par ces alliages, en particulier par **Ag** Sn et **Ag** Sb. Ceci montre bien que les perturbations s'étendent plus loin que les premiers voisins.

VOL. 10 1959

5. APPLICATION AUX ALLIAGES LIQUIDES

Il est possible de modifier le calcul du paragraphe 3 de facon à l'adapter au cas d'alliages liquides près du point de fusion. Dans ces conditions, il subsiste en général un ordre local, ce qui suggère le procédé suivant pour calculer les coefficients α_l et β_l de la formule (7) : sommer sur les positions des N_1 noyaux premiers voisins prises comme dans le réseau cristallin de la matrice A et intégrer à l'extérieur d'une sphère de volume $v_B+N_1v_A$, où v_A désignant le volume atomique de A et v_B celui de B. Ne connaissant pas son volume molaire partiel, nous avons admis que l'atome B conserve son volume normal dans l'alliage liquide, ce qui modifie légèrement la distance de son noyau aux noyaux de ses plus proches voisins.

Nous avons appliqué ce procédé au cas des alliages fondus **Na** K, **Na** Rb et **Rb** Na. D'après la remarque de la fin du paragraphe 3, nous ne devons pas nous attendre à un très bon accord pour ces alliages où seul l'effet de taille nous permet de calculer des déphasages par la méthode de Blatt.

Les volumes atomiques du potassium et du rubidium étant de l'ordre du double de celui du sodium, nous envisageons deux possibilités pour l'environnement de l'atome dissous dans le sodium : soit huit premiers voisins, comme dans la structure cubique centrée (c.c.) du sodium, soit un environment plus compact de douze premiers voisins, comme dans une matrice cubique à faces centrées (c.f.c.) Nous comparons dans le Tableau 3 les résultats de notre calcul aux mesures de BLOEMBERGEN[3]. On voit que notre calcul rend compte non seulement du signe mais de l'ordre de grandeur des effets observés. Ceux-ci seraient en meilleur accord avec un empilement cubique à faces centrées des premiers voisins pour **Na** K et **Na** Rb ou le soluté est plus gros que le solvant; l'empilement cubique centré semble se produire pour **Rb** Na où le soluté est plus petit que le solvant.

Tableau 3. *Comparaison des valeurs calculées et mesurées pour les alliages liquides* **Na** K, **Na** Rb, **Rb** Na

Alliage	$(1/c)(\Delta K/K)$		
	Mesuré	Calculé c.c.	Calculé c.f.c.
Na K	0,35	0,1	0,25
Na Rb	0,5	0,15	0,4
Rb Na	−0,25	−0,23	

6. EFFET DES IMPURETES DE TRANSITION

L'étude de la structure électronique des impuretés de transition dans les métaux[17,13] conduit aux résultats suivants : l'impureté peut être déduite par un état lié virtuel *d* se remplissant progressivement, les déphasages η_2 des ondes *d* au niveau de Fermi vérifiant la régle de somme de Friedel. Mais si la matrice a une bande de conductibilité étroite et si le nombre d'électrons ou de trous dans la couche *d* est suffisamment grand, l'énergie d'échange entre électrons *d* peut créer un potentiel dépendant du spin et introduire des déphasages différents pour les deux directions de spin. L'impureté porte alors un moment magnétique donnant lieu à un paramagnétisme de Langevin à haute température. On peut alors dresser le Tableau 4 où sont indiqués par + ou par −, s'il y a, ou non, découplage des deux directions de spin, en accord avec les résultats théoriques et expérimentaux (susceptibilité magnétique et résistivité électrique). Les résultats doivent être analogues, que l'on ait *Z* électrons ou *Z* trous *d*. On doit donc s'attendre à un tableau à peu près symétrique de celui-ci par rapport au chrome

Tableau 4. *Découplage des spins des impuretés de transition*

	Solvant	Ag ou Au	Cu	Zn	Al
	Niveau de Fermi	5,5 eV	7 eV	9,5 eV	13 eV
Solutés	Cr	+	+	+	−
	Mn	+	+	+	−
	Fe	+	+	−	−
	Co	+	−	−	−
	Ni	−	−	−	−

pour la première moitié de la série : ceci est en accord avec les propriétés électriques.

On peut donc prévoir deux comportements très différents pour la variation du déplacement de Knight des spins nucléaires de la matrice, suivant que les impuretés ont leurs spins couplés ou non.

6.1 *Impuretés à spins appariés*

Les oscillations de densité électronique créés par l'impureté doivent donner les mêmes effets que pour les impuretés normales. Ce déplacement de Knight doit être indépendant de la température, proportionnel à la concentration et observable pour des concentrations notables d'impuretés. La largeur réduite de la raie de résonance $\delta H/\Delta H$ doit varier à peu près proportionnellement à $\sqrt{c}$.

trop forts. L'effet d'écran réel doit être intermédiaire entre ces deux extrèmes, avec une couche d plus remplie et plus stable pour le Pd que pour le Pt. Ceci est en accord avec la stabilité des couches d pour ces deux éléments à l'état atomique.

6.2. *Impuretés à spins découplés*

L'impureté porte un moment magnétique permanent. Si celui-ci avait une direction fixe, les spins nucléaires de la matrice seraient soumis à deux effets : l'effet dipolaire produit par le moment magnétique et les fluctuations de la densité électronique $\Delta\rho(r)$ des deux directions de spin qui crèent, par leur interaction de contact avec le spin nucléaire, un déplacement de la fréquence de résonance :

$$\frac{\Delta K}{K} = c\frac{\Delta\rho(r)}{\rho}$$

$$\Delta\rho(r) = \frac{5}{2\pi^2}\int_0^{k_0} k^2 dk[(\eta_2^2(kr) - j_2^2(kr)(\sin^2\eta_2^{\uparrow} - \sin^2\eta_2^{\downarrow}) - j_2(kr)\eta_2(kr)(\sin 2\eta_2^{\uparrow} - \sin 2\eta_2^{\downarrow})]$$

Expérimentalement, ceci est observé dans les alliages **Ag** Pd,[1] **Ag** Pt,[2] **Cu** Ni, **Cu** Ti, **Al** Mn.[4]

Nous avons calculé numériquement le déplacement $\Delta K/K$ par unité de concentration pour les alliages **Ag** Pd et **Ag** Pt, dans les deux cas extrèmes suivants :

— puits de potentiel sphérique repoussant une charge d'électronique dans la bande de conductibilité (a).

— charge d'écran totalement fournie par les électrons d (b). Ces résultats sont reportés dans le Tableau 5.

Tableau 5

Alliage	$\Delta K/K$		
	a	b	exp.
Ag Pd	+0,4	−1,6	−0,4
Ag Pt	+0,4	−1,6	−0,8

Le modèle d'état lié virtuel (b) donne des résultats numériques du bon signe, mais nettement

où $\eta_2^{\uparrow}$ et $\eta_2^{\downarrow}$ sont les déphasages des deux directions de spin pour un électron d'énergie $E = (\hbar^2/2m)k^2$ et k_0 le niveau de Fermi.

Quand l'impureté est soumise à un champ magnétique H à la température T, le spin nucléaire est soumis à l'effet dipolaire *moyen* et à l'interaction de contact *moyenne* sur toutes les directions de spins; en effet le temps de relaxation des spins nucléaires est grand et ceux-ci ne voient que la moyenne statistique des effets provoqués par les impuretés. Si le spin et le moment magnétique attachés à l'impureté sont S et μ, les effets sont alors à multiplier par le facteur $B_s(\mu H/kT)$ où B_s est la fonction de Brillouin d'ordre S.

L'interaction dipolaire est nulle en moyenne pour une poudre cristalline et la variation relative du déplacement de Knight est alors uniquement due au second effet soit quand $\mu H/kT \ll 1$:

$$\frac{\Delta K}{K} = \frac{2(S+1)}{9} v_A \frac{E_0}{kT}\gamma c$$

E_0 est l'énergie de Fermi et $\gamma = \sum_i \Delta\rho(r_i)$, somme étendue à tous les sites du réseau.

Dans les mêmes conditions, la forme et la largeur dépendent à la fois de l'effet dipolaire et de l'interaction de contact : le second moment doit être proportionnel à $\sqrt{(c/T)}$. L'élargissement est considérable, si bien qu'on ne peut observer la raie de résonance qu'à très faible concentration d'impuretés ; il peut masquer le déplacement de Knight: c'est sans doute pourquoi deux mesures sur **Cu** Mn[18,19] ne donnent aucun déplacement alors qu'une série de mesure sur **Cu** Cr, **Cu** Mn, **Cu** Fe[4] a permis d'en déceler. Dans ces dernières mesures, les déplacements de Knight diminuent quand la température augmente : nous avons essayé de comparer les valeurs mesurées à celles que donnent le modèle : les valeurs calculées sont du bon ordre de grandeur mais dépendent fortement de la forme et de la largeur de l'état lié virtuel d; celles-ci ne sont pas connues de façon assez précises pour que l'on puisse faire une comparaison quantitative.

La largeur des raies de résonance est trop grande pour être due uniquement à l'effet dipolaire[20] nettement insuffisant, et le modèle d'états liés virtuels découplés pourrait ici expliquer aussi les très forts élargissements observés.

Remerciments—Les auteurs remercient le Professeur FRIEDEL qui a dirigé ce travail ainsi que le Professeur BLOEMBERGEN et les Drs. DRAIN, ROWLAND, RIMAI et SUGAWARA qui ont aimablement communiqué leurs résultats expérimentaux avant publication et fait part de leurs commentaires.

ANNEXE

Remarque sur le calcul du coefficient α_0

Soit une fonction $f(\mathbf{r})$ possédant une transformée de Fourier

$$\phi(\mathbf{k}) = \int f(\mathbf{r}) \exp(i\mathbf{k} \cdot \mathbf{r})\, d^3\mathbf{r}$$

et ayant une valeur finie pour $\mathbf{r} = 0$. Nous voulons calculer :

$$L = \sum_i f(\mathbf{r}i)$$

la somme étant étendue à tous les points d'un réseau cristallin donné sauf $\mathbf{r} = 0$.

On peut écrire :

$$L = \int f(\mathbf{r}) d^3\mathbf{r} \left[\sum_j \delta(r - r_j) - \delta(r) \right]$$

(somme j sur *tous* les points du réseau) et, développant, la fonction δ en série de Fourier :

$$L = \frac{1}{(2\pi)^3} \int f(\mathbf{r}) d^3r \times$$

$$\times \int \exp(i\mathbf{k} \cdot \mathbf{r}) \left(\sum_i \exp(-i\mathbf{k}\mathbf{r}_i) - 1 \right) d^3\mathbf{k}$$

or,

$$\sum_i \exp(-i\mathbf{k} \cdot \mathbf{r}_i) = \frac{(2\pi)^3}{v_0} \sum_\tau \delta(\mathbf{k} - \boldsymbol{\tau})$$

où v_0 est le volume de la maille élémentaire du réseau direct et la somme sur $\boldsymbol{\tau}$ est étendue à tous les noeuds du réseau réciproque.

On a alors :

$$L = \frac{1}{v_0} \sum_\tau \phi(\boldsymbol{\tau}) - \frac{1}{(2\pi)^3} \int \phi(\mathbf{k}) d^3\mathbf{k}.$$

Nous appliquons cette méthode au calcul de α_0 : la fonction $f(\mathbf{r})$ est $\eta_0^2\ (k_0 r) - j_0^2(k_0 r) = \cos^2 k_0 r/(k_0 r)^2$ où k_0 est le vecteur d'onde à la surface de Fermi. La fonction $f(\mathbf{r})$ est infinie à l'origine et il faut définir un processus de convergence : soient $f(\mathbf{r})$ la moyenne de la fonction r sur un petit cube de dimensions δ et d'arêtes parallèles aux axes de coordonnées, $\overline{\phi(\mathbf{k})}$ sa transformée de Fourier; on a alors en sommant à l'intérieur d'une volume v

$$\alpha_0 = \lim_{\delta \to 0} \lim_{V \to \infty} \left[\frac{1}{v_0} \sum_{\tau \alpha v} \phi(\mathbf{r}) - \frac{1}{(2\pi)^3} \int_v \phi(\mathbf{k})\, d^3\mathbf{k} \right].$$

On peut intervertir les deux limites et passer à la limite $\delta = 0$

$$\alpha_0 = \lim_{V \to \infty} \left[\frac{1}{v_0} \sum_{\tau \alpha v} \phi(\boldsymbol{\tau}) - \frac{1}{(2\pi)^3} \int_v \phi(\mathbf{k})\, d^3\mathbf{k} \right].$$

Avec la fonction

$$f(\mathbf{r}) = \frac{\cos 2k_0 r}{(k_0 r)^2},$$

on a :

$$\phi(\mathbf{k}) = 2\pi \int_0^\infty \frac{\cos^2 k_0 r}{{k_0}^2}\, dr \int_0^\pi \exp(ikr\cos\theta)\sin\theta\, d\theta$$

$$= \frac{4\pi}{{k_0}^2 k} \int_0^\infty \frac{\sin(k+2k_0)^2 + \sin(k-2k_0)r}{2r}\, dr$$

$$= \begin{cases} \dfrac{2\pi^2}{{k_0}^2 k} \text{ si } k > 2k_0 \\ \dfrac{\pi^2}{2{k_0}^3} \text{ si } k = 2k_0 \\ 0 \quad \text{si } k < 2k_0. \end{cases}$$

La fonction $\phi(\mathbf{k})$ est représentée par Fig. 3.

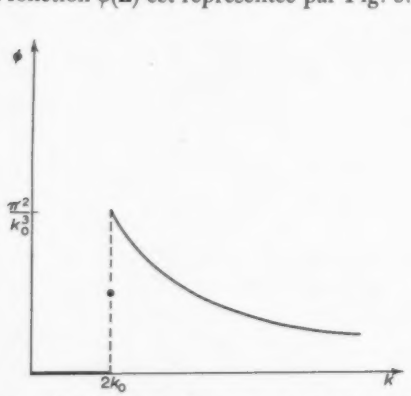

FIG. 3. Tranformée de Fourier de la fonction $n_0^2(k_0 r) - j_0^2(k_0 r)$.

On peut écrire

$$\phi(\mathbf{k}) = \frac{2\pi^2}{{k_0}^2}\left[\frac{1}{k} - \psi(\mathbf{k})\right] \text{ avec } \psi(\mathbf{k}) = \begin{cases} \dfrac{1}{k} \text{ si } k < 2k_0 \\ \dfrac{1}{k_0} \text{ si } k = 2k_0 \\ 0 \text{ si } k > 2k_0 \end{cases}$$

$$\alpha_0 = \frac{2\pi^2}{v_0 {k_0}^2} \lim_{V\to\infty}\left[\sum_{|\vec{\tau}|<v} \frac{1}{\tau} - \frac{v_0}{(2\pi)^3}\int_v \frac{1}{k}\, d^3\mathbf{k}\right] +$$

$$+ \frac{1}{4{k_0}^2}\int_{k<2k_0} \frac{1}{k}\, d^3\mathbf{k} - \frac{2\pi^2}{v_0 {k_0}^2}\sum_{|\tau|<2k_0} \psi(\tau).$$

Dans le premier terme, le crochet représente le potentiel électrostatique créé en un point du réseau réciproque par une distribution de charge $+1$ aux autres points du réseau et une distribution continue de charges négatives de densité $v_0/(2\pi)^3$ assurant la neutralité électrostatique à l'intérieur de tout volume, sauf la cellule élémentaire centrée à l'origine.

Pour un réseau *direct* cubique à faces centrées, le potentiel doit être calculé sur le réseau réciproque cubique centré. Le calcul a été fait par WIGNER et SEITZ[21] et donne

$$-\frac{3{,}6391}{d}$$

où d est l'arête de la maille élémentaire du réseau cubique centré :

$$d = \left(\frac{16\pi}{3}\right)^{\frac{1}{3}} k_0$$

pour une matrice monovalente.

Dans une matrice monovalente, les premiers voisins du réseau réciproque sont à l'extérieur de la sphère de rayon $2\,k_0$ et la somme

$$\sum_{|\vec{\tau}|<2k_0} \psi(\vec{\tau}) = 0.$$

On a alors la valeur

$$\boxed{\alpha_0 = 1{,}052}$$

Pour une matrice divalente, les premiers voisins du réseau passent à l'intérieur de la sphère $2\,k_0$: c'est-à-dire la sphère de Fermi déborde la première zone de Brillouin. Pour une sphère de Fermi touchant la zone, on obtiendrait une discontinuité de α_0 (β_0 devenant infini). Cela signifie que l'on somme les excès de densité électronique en des points qui sont en phase. Mais, on sait que si la surface de Fermi est proche de la zone de Brillouin, elle n'est plus sphérique et l'approximation initiale n'est plus valable. Au contraire, si la surface de Fermi est, soit nettement à l'intérieur de la zone de Brillouin, soit la déborde largement (cas des matrices mono et divalentes), l'approximation d'une surface sphérique ne doit pas être trop mauvaise.

BIBLIOGRAPHIE

1. DRAIN L. E., à paraître.
2. ROWLAND T. J., communication privée.
3. BLOEMBERGEN N., communication privée, cf. RIMAI L., Thèse à paraître, Harvard University.
4. SUGAWARA T., *J. Phys. Soc. Japan* **12,** 309 (1957); et articles à paraître au *J. Phys. Soc. Japan.*
5. COHEN M. H. et HEINE V., *Advanc. Phys.*, **7,** 395 (1958).
6. BLANDIN A., DANIEL E. et FRIEDEL J., *Phil. Mag.* **4,** 180 (1959).
7. MOTT N. F. et JONES H., *Metals and Alloys.* Oxford University Press (1936).
8. FRIEDEL J., *Advanc. Phys.* **3,** 466 (1954).
9. FRIEDEL J., *J. Phys. Rad.* **16,** 44 (1955).
10. FRIEDEL J., *Nuovo Cimento.* **2,** 287 (1958).
11. RUDERMANN M. A. et KITTEL C., *Phys. Rev.* **96,** 99 (1954).
12. BLOEMBERGEN N. et ROWLAND T. J., *Phys. Rev.* **97,** 1679 (1955).
13. BLANDIN A. et FRIEDEL J., *Colloque International de Magnétisme de Grenoble.* A paraître dans *J. Phys. Rad.* (1958).
14. KNIGHT W. D., *Solid State Physics* **2,** 93 (1956).
15. BLATT F. J., *Phys. Rev.* **108,** 285 (1957).
16. MOTT N. F. et MASSEY H. S. W., *Atomic Collisons.* Oxford University Press (1949).
17. DE FAGET DE CASTELJAU P. et FRIEDEL J., *J. Phys. Rad.* **17,** 27 (1956).
18. OWEN J., BROWN M. E., KNIGHT W. D. et KITTEL C., *Phys. Rev.* **102,** 1501 (1956).
19. POULIS N., *Physica, 's Grav.* **23,** 797 (1957).
20. BEHRINGER R. E., *J. Phys. Chem. Solids* **2,** 209 (1957).
21. WIGNER E. P. et SEITZ F., *Phys. Rev.* **46,** 509 (1934).

OL.
10
959

J. Phys. Chem. Solids Pergamon Press 1959. Vol. 10. pp. 138–146.

THE USE OF POLARIZED NEUTRONS IN DETERMINING THE MAGNETIC SCATTERING BY IRON AND NICKEL*

R. NATHANS
Pennsylvania State University, University Park, Pennsylvania, and Brookhaven National Laboratory, Upton, New York

C. G. SHULL
Massachusetts Institute of Technology, Cambridge, Mass.

G. SHIRANE
Brookhaven National Laboratory, Upton, New York

and

A. ANDRESEN
Brookhaven National Laboratory, Upton, New York and Joint Establishment for Nuclear Research, Kjeller, Norway

(*Received* 29 *December* 1958)

Abstract—The polarized neutron-beam technique is discussed and utilized in determining the magnetic scattering by iron and nickel. Procedures for obtaining and using polarized beams of monochromatic neutrons are outlined, and experimental data are presented on the performance of two polarizing crystals, Fe_3O_4 and 92 Co–8 Fe alloy. The reflectivity of neutrons of different polarization states by single crystals of iron and nickel has been studied and used for determining the magnetic scattering amplitudes at various scattering angles. Comparison is then made between the observed magnetic form values and theoretical values derived from calculated 3*d* wave functions.

1. INTRODUCTION

THE advantages in using polarized beams of neutrons in diffraction studies of magnetic materials have been known for some time, and the present report (*a*) summarizes some of the experiences gained in modifying a typical neutron-diffraction spectrometer to polarized-beam use and (*b*) presents experimental data obtained with this technique on the absolute magnetic scattering of the ferromagnetic elements, iron and nickel. The ferromagnetic scattering for these elements as measured with unpolarized radiation is unfortunately rather small in comparison with the nuclear scattering, about 8 and 0·6 per cent, respectively, so that it is difficult to measure this quantitatively for comparison with the expected absolute level or to draw comparisons with the theoretical form-factor variation. Much of this difficulty is surmounted by the use of polarized radiation, whereby it becomes possible to measure accurately very small magnetic scattering cross-sections.

In addition to the enhanced sensitivity of the polarized-beam method, two other advantages are worthy of mention. It is possible by these techniques to determine the absolute sign of the magnetic scattering amplitude associated with a particular magnetic lattice reflection, thereby resolving certain ambiguities that arise in the determination of a magnetic crystal structure. This has been utilized in a study of the magnetic structure existing in ordered Fe_3Al and is described in a companion publication.[1] Additionally there exist interesting changes in polarization upon magnetic scattering as predicted by the early theory, and these have been confirmed by experiment and utilized to establish[2] details of the magnetic axis orientation in the antiferromagnetic materials Cr_2O_3 and α-Fe_2O_3.

* This research was supported by the U.S. Atomic Energy Commission, the National Security Agency and the Air Force Office of Scientific Research.

2. GENERAL CONCEPTS AND TECHNIQUES

HALPERN and JOHNSON have shown,[3] in a comprehensive treatment of the magnetic scattering theory, that the scattering cross-section for a magnetic ion is given by:

$$\sigma = 4\pi(b^2+p^2q^2+2bp\mathbf{q}\cdot\boldsymbol{\lambda}), \tag{1}$$

where b and p are the nuclear and magnetic scattering amplitudes, $\boldsymbol{\lambda}$ is the unit vector describing the neutron polarization directed along its spin axis, and

$$\mathbf{q} = \mathbf{e}(\mathbf{e}\cdot\boldsymbol{\varkappa})-\boldsymbol{\varkappa} \tag{2}$$

with $\mathbf{e}$ the unit scattering vector and $\boldsymbol{\varkappa}$ the unit vector along the spin direction of the magnetic ion. If $\boldsymbol{\varkappa}$ is arranged perpendicular to the scattering vector $\mathbf{e}$, then $|\mathbf{q}| = q$ becomes unity, and the cross-sections for the two neutron spin states (analyzed such that $\mathbf{q}\cdot\boldsymbol{\lambda} = \pm 1$) that make up an unpolarized neutron beam can be written as

$$\sigma_+ = 4\pi(b+p)^2 \text{ with } \mathbf{q}\cdot\boldsymbol{\lambda} = +1 \tag{3}$$

and

$$\sigma_- = 4\pi(b-p)^2 \text{ with } \mathbf{q}\cdot\boldsymbol{\lambda} = -1.$$

With unpolarized incident radiation, the scattering cross-section becomes half of the sum of the two spin-state cross-sections or

$$\sigma_0 = 4\pi(b^2+p^2), \tag{4}$$

which can be considered to be the sum of the nuclear and magnetic scattering cross-sections.

It is obvious that a magnetic ion for which b is closely equal to p will scatter neutrons of only one spin state under the above conditions and hence a high polarization P will result in the scattered beam, where

$$P = \frac{I_1-I_2}{I_1+I_2} \tag{5}$$

and I_1 and I_2 are the intensities of the two neutron spin states. Unequal scattering amplitudes will of course yield only partial polarization.

The detection and utilization of such a polarized neutron beam has been discussed in the literature,[4,5] and the present investigation was undertaken as an extension of these studies. It was desired to study the polarizing efficiency of various crystals for quantitative comparison with that predicted from the known scattering amplitudes and to use such polarized radiation in a quantitative study of the magnetic scattering from iron and nickel. It is apparent from the form of equations (3) and (4) that the contribution of a weak magnetic scattering amplitude to the scattering cross-section will be more pronounced for the polarized-beam case.

For the production of a monochromatic polarized beam, we have used Bragg scattering by a suitable ferromagnetic crystal which exhibits the favorable balance of nuclear and magnetic scattering indicated above. The (220) reflection of Fe_3O_4 has been known to produce high polarization,[4] and a study has been made of the polarizing efficiency of this crystal as a function of crystal thickness, lack of magnetic saturation in the crystal and the presence of extinction effects. Additionally when single crystals of a cobalt–iron alloy became available, for which a favorable balance of the scattering amplitudes also occurs, these were studied and their superiority over Fe_3O_4 crystals was demonstrated.

3. POLARIZED BEAM SPECTROMETER

A schematic diagram of our experimental arrangement is shown in Fig. 1. It consists of a modified double-crystal neutron spectrometer in

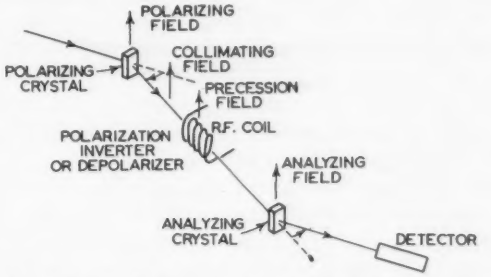

FIG. 1. Schematic diagram of polarized neutron spectrometer.

which the first crystal is replaced with a magnetized polarizing crystal and the second crystal serves as a polarization analyzer or a specimen crystal. It is necessary to magnetize the polarizing crystal to insure that $\boldsymbol{\varkappa}$ and hence $\mathbf{q}$ above be unidirectional, and for this a permanent magnet giving a field of 2200 Oe over a $\frac{3}{4}$-in. gap was used. The reflected

monochromatic neutrons pass along a magnetic collimator which maintains a uniform field of 150 Oe, in the same sense as the polarizing field, throughout the trajectory between the polarizing crystal and the second crystal. An electromagnet served for magnetizing the analyzing or test crystal with fields up to 7500 Oe over a $\frac{3}{4}$-in gap. Considerable care had to be taken to control the magnetic field over the entire path from polarizer to analyzer to prevent induced transitions from one neutron spin state to another, thereby affecting the degree of polarization in the beam. For certain types of measurement it was desirable to depolarize the beam completely, and this was accomplished by passing the beam through a thin foil of unmagnetized iron (0·020 in thick). In such an unmagnetized foil, the random direction of the magnetic domains cause many spin transitions and the emerging beam is completely depolarized.

Provision was also incorporated into the measurement technique for reversing the neutron polarization relative to the sense of magnetization for the analyzing or test crystal. Merely reversing the analyzing magnetic field direction does not accomplish this, since the neutron polarization would tend to follow the field reversal along its trajectory. If the field reversal region can be made small enough so that the neutron transit time through this region is small compared to its Larmor precession time, the neutron polarization will be maintained and the polarization will be reversed with respect to the analyzing field as desired. This method has been used by BURGY *et al.*[6] In the present experiments it was found difficult to meet the stringent requirements of this procedure, and accordingly an alternative method of invoking the neutron spin transition through resonant spin flipping was utilized.* In this procedure a radio-frequency field, applied at right angles to the neutron polarization, is matched in frequency to the Larmor precessional frequency of the neutron spin in a uniform magnetic field. If the strength of the r.f. field is adjusted properly relative to the neutron transit time, complete transition is possible, and this has been confirmed to a high degree by experiment. Thus, by merely turning on or off the r.f. flipper, the neutron polarization can be kept parallel or antiparallel to the common field direction in the polarizing, intermediate, and analyzing regions.

It is of convenience in treating the experimental measurements to make use of a quantity S, commonly called the *shim ratio* and defined as the ratio of the scattering intensity obtained with a polarized beam of polarization P_i to that obtained with a depolarized beam. Thus:

$$S_+ = \frac{I_+}{I_0} \text{ and } S_- = \frac{I_-}{I_0} \tag{6}$$

with I_+ and I_- being the scattered intensity with incident neutron polarization being parallel and antiparallel to the magnetization of the scattering crystal and I_0 the scattered intensity with a depolarized incident beam. This term has been called the shim ratio because in practice it is obtained by inserting a thin shim of unmagnetized ferromagnetic material in the beam thereby depolarizing it. Of usefulness is a related quantity R called the *polarization ratio* defined as the ratio of I_+ to I_- so that

$$R = \frac{I_+}{I_-} = \frac{S_+}{S_-}. \tag{7}$$

For a test crystal whose polarizing efficiency is P_x, defined in the sense of equation (5), it can be easily shown that

$$S = 1 + P_i P_x \tag{8}$$

where it is to be recognized that the intrinsic polarizing efficiency P_x will depend upon the degree of extinction present in the crystal, since this will affect the spin-state scattered intensities. P_i represents the degree of polarization in the neutron beam incident on the test crystal. For the extinction-free case, P_x will be simply related to the cross-sections:

$$P_x = \frac{\sigma_+ - \sigma_-}{\sigma_+ + \sigma_-} = \frac{2bp}{b^2 + p^2}. \tag{9}$$

Equation (8) can be used for assessing the relative polarizing efficiencies of different crystals, but a knowledge of P_i is necessary to determine the absolute efficiency.

It has been found experimentally that sizeable depolarization of the neutron beam accompanies its passage through crystals, and hence that it is necessary to include a depolarization factor in

* STANFORD *et al.*[5] have utilized this technique.

equation (8). It is convenient to define the *polarization transmission*, D, such that

$$P = P_0 \cdot D = P_0 \exp(-\mu_p t)$$

with P being the transmitted polarization, P_0 the incident polarization, μ_p the linear depolarization coefficient, and t the traversed thickness of the crystal. With this definition, equation (8) becomes

$$S = 1 + P_i \frac{1}{\mu_p t}[1 - \exp(-\mu_p t)]P_x \qquad (10)$$

and for small depolarization

$$S = 1 + P_i\left(1 - \frac{\mu_p t}{2}\right)P_x = 1 + P_i\sqrt{D} \cdot P_x. \qquad (11)$$

The polarization transmission will be strongly dependent upon the magnetization of the scattering crystal, approaching unity as the magnetization approaches saturation. With less than saturation, the neutron passage from one domain to another will be effective in changing the neutron polarization state as HALPERN and HOLSTEIN[7] have considered.

4. MEASUREMENTS ON POLARIZING EFFICIENCIES OF CRYSTALS

Experiments were first performed on a number of Fe_3O_4 polarizing and analyzing crystals cut from natural magnetite ingots. These crystals were cut with different shape factors, ranging from blocks to plates to pillars, and with different thicknesses so as to permit study of the internal depolarization effects. With a common polarizing crystal whose polarizing efficiency was later determined, the shim ratio S of a series of analyzing crystals was measured as a function of analyzing field strength and crystal thickness. Fig. 2 shows the variation of S obtained with a series of crystal pillars of common area (19·1 × 3·2 mm), but with different thicknesses with each maintained in a magnetic field of 6900 Oe. The variation of S with thickness shows that the effective polarizing efficiencies of these pillars decreases as the thickness is increased, and this is considered to result from the increased internal depolarization within the crystal. The alternative explanation that such a variation could result from increased extinction effects was eliminated by a calculation making use of the known mosaic distribution in these crystals.

Measurements were next made of the polarization transmission D for different crystals, so that the true polarizing efficiencies could be assessed. This was performed by placing the test crystal

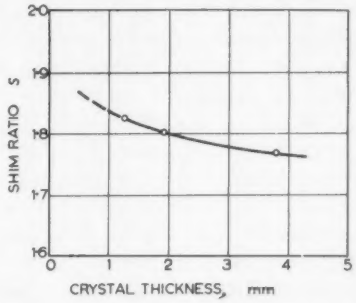

FIG. 2. Variation of shim ratio S with Fe_3O_4 crystal thickness.

directly in front of, and in the same magnetic field as, an analyzing crystal. The polarized beam from the polarizer then passed through the test crystal, but was not scattered by it, before being Bragg scattered by the analyzer. Measurements of the shim ratio with and without the test crystal could then be used to determine directly the polarization

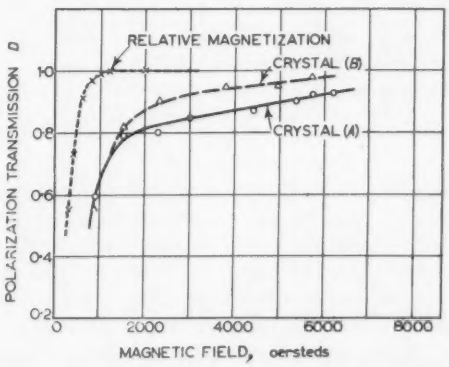

FIG. 3. Dependence of polarization transmission D upon magnetic field applied to crystal for two different Fe_3O_4 crystals. The relative magnetization for crystal (B) is also shown.

transmission of the test crystal. This was studied as a function of magnetic field strength, and typical results are shown in Fig. 3 for two crystals. Crystal (A), of dimensions 19·2 × 3·2 mm area and 1·24

mm thick was cut so that a [100] axis was parallel to the long dimension and the magnetic field was applied in this direction. Crystal (B), of dimensions 16·5 × 3·5 mm area and 2·1 mm thick, was cut with a [111] direction parallel to the long dimension and again the magnetic field was applied in this direction. Also shown in Fig. 3 are measured values for the relative magnetization of crystal (B). It is seen that the polarization transmission is exceedingly sensitive to departure from magnetic saturation, as had been predicted by HALPERN and HOLSTEIN[7] and studied experimentally by HUGHES and colleagues,[6,8] Since the easy direction of magnetization in magnetite is along the [111] direction, the depolarization effects are expected to be somewhat less for crystals magnetized in this fashion and the data of Fig. 3 demonstrate this.

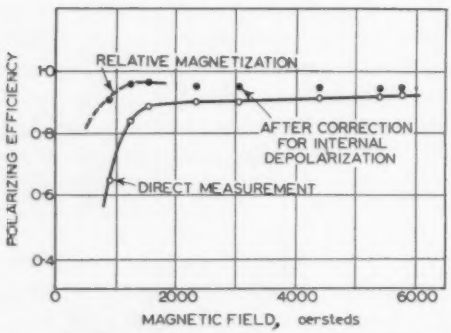

FIG. 4. Polarizing efficiency of Fe_3O_4 crystal (B) as a function of applied magnetic field.

Once the depolarization factors have been evaluated, a pair of crystals having the same intrinsic polarizing efficiency can be used as a polarizing-analyzing combination to determine the individual polarizing efficiency. Data obtained in this fashion for crystal (B) above are illustrated in Fig. 4. Here the polarizing efficiency of this crystal has been evaluated from shim ratio measurements as a function of applied magnetic field. Also shown in the figure is the variation of the intrinsic polarizing efficiency after correction for internal depolarization through the use of the polarization transmission data for this crystal from Fig. 3. Even after correction for depolarization effects, the intrinsic polarizing efficiency should fall off in the low-field region because of the reduction in crystal magnetization. It can be easily shown that

$$\frac{P_x}{P_x(\max)} = \frac{M}{M_s}$$

and a comparison is illustrated in Fig. 4 of the intrinsic polarizing efficiency and the relative magnetization in a limited low field region.

As seen in Fig. 4, the maximum value for the intrinsic polarizing efficiency of crystal (B) is seen to be about 95 per cent. A number of different Fe_3O_4 crystals have been studied, and some variation in this maximum value has been noted. Values as high as 98 per cent have been obtained, this having been measured with the particular crystal used in the early study of reference (4). Since all of the crystals studied have been cut from natural mineralogic ingots of unmeasured purity, these relatively small variations are not unexpected.

Similar studies have been carried out on polarizing and analyzing crystals of cobalt–iron alloy. For the composition 92 atomic per cent cobalt, this crystallizes from the melt* in the face-centered cubic phase, and by calculation, the intrinsic polarizing efficiency in the (111) reflection should be 99·1 per cent. In this phase, magnetic saturation

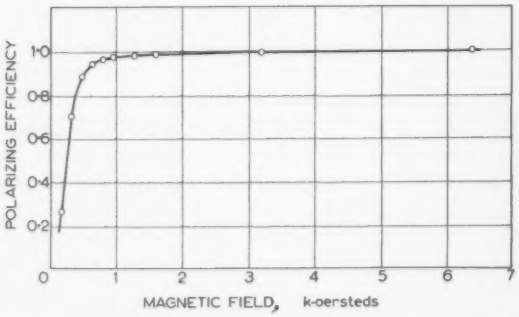

FIG. 5. Polarizing efficiency of cobalt–iron crystal as a function of applied magnetic field.

is approached with rather low fields. Fig. 5 illustrates the variation of the intrinsic polarization efficiency as a function of field for a crystal of dimensions 19·2 × 3·4 mm in area and 1·1 mm in thickness, with the magnetic field applied along the

* We are much indebted to Messrs. R. M. BOZORTH and A. J. WILLIAMS, of the Bell Telephone Laboratories, for supplying such a crystal to us.

[110] direction parallel to the long axis. This is seen to approach a value of 99–100 per cent. It has been found in general that the depolarizing effects are smaller for the case of the metallic crystals than has been observed for magnetite and hence smaller magnetic fields can be tolerated.

It should be mentioned that the neutron-polarization direction obtained with the metallic crystals is reversed from that obtained with the (220) Fe_3O_4 reflection. This follows from the fact that the magnetic ions responsible for the scattered intensity in (220) Fe_3O_4 are directed opposite to the applied field on the crystal, since it is a ferrimagnetic substance and these ions are in the minority. In contrast the magnetic ions in the metallic crystal are all parallel to the applied field direction. Thus the polarized neutrons in the (220) Fe_3O_4 reflection have their magnetic moments aligned parallel to the field on the crystal, whereas in the (111) cobalt–iron reflection, the neutron moments are antiparallel to the field direction. This absolute sense of direction follows from a theoretical assay of the absolute signs of the magnetic and nuclear scattering amplitudes and has been examined experimentally in a neutron STERN–GERLACH type of experiment by SHERWOOD *et al.*[9]

A decided advantage to the use of cobalt–iron polarizing crystals lies in their greater neutron reflectivity than is the case for the (220) Fe_3O_4 reflection. This arises because of the more favorable crystal-structure factor and the greater density of the magnetic scattering ions. Moreover the higher-order contaminant neutrons are largely absent in the metallic-crystal case. The magnetic structure of Fe_3O_4 is such that the (440) reflectivity is approximately 15 times larger than the (220) reflectivity, and hence in scattering neutrons of wavelength λ from the (220) reflection there is a strong component of $\lambda/2$ scattered simultaneously. The $\lambda/2$ component is partially polarized in the opposite direction, and it is necessary to absorb this with a suitable neutron filter. This was done in all of the above Fe_3O_4 measurements with a plutonium filter (useful when $\lambda = 1{\cdot}05$ Å) and this necessarily absorbs some of the desired intensity as well. This problem does not arise in the case of the (111) cobalt–iron polarizing reflection, since the (222) crystal-structure factor is of the same order of size as the (111) and no enhancement of the $\lambda/2$ component is thus obtained.

5. MAGNETIC SCATTERING RESULTS ON IRON AND NICKEL

The study of the angular dependence of the absolute magnetic scattering in these metals was made by measuring the polarization ratios (R) for the various Bragg reflections present. As a typical example of such a measurement, Fig. 6 shows the

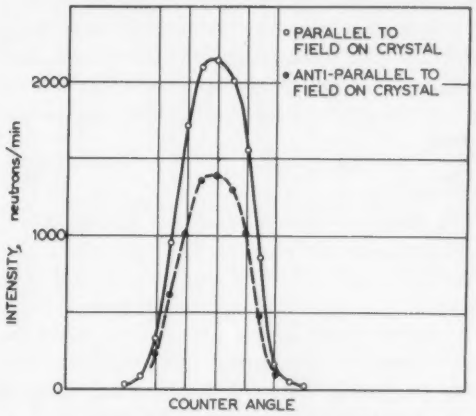

FIG. 6. Intensity in the (111) nickel reflection for incident neutron beams of different polarizations.

intensities observed for the nickel (111) reflection with incoming neutrons polarized first parallel and then antiparallel to the magnetic field on the crystal. The sizeable intensity change for the two orientations of scattered neutrons (1·5 : 1) is to be compared with the 0·6 per cent obtained in the usual technique with unpolarized neutrons. From the observed values of R_{hkl} the intrinsic polarizing efficiencies for various Bragg reflections can be evaluated after the necessary corrections have been made for extinction and depolarization. The final result is a value for the ratio of the magnetic scattering amplitude to the nuclear scattering amplitude, that is p_{hkl}/b_{hkl}. Since the coherent nuclear scattering amplitudes for these two metals are well established ($1{\cdot}03 \times 10^{-12}$ cm for nickel and $0{\cdot}96 \times 10^{-12}$ cm for iron) and are independent of angle, the magnitude of p_{hkl} follows.

In the study of both of these metals, the measurements were made, for the most part, with single-crystal pillars placed in the high magnetic field of the analyzing magnet. Intensities were recorded over short-time intervals alternately with r.f. field on and off. Each run was repeated several

times, and the uncertainty in the final results was established from the standard deviations between the different runs. Since the data accumulation extended over a considerable period of time, it was necessary to establish the stability of the incident neutron polarization and the efficiency of the r.f. coil in reversing the neutron polarization. For this purpose the (111) reflection of a cobalt–iron crystal was used as a standard. Measurements of the polarization ratio for this standard were made before and after each run on the test crystal, and the required adjustments, although small, were made to the observed polarization ratio on the test crystal.

(a) *Nickel*

The single crystal of nickel was cut so that it could be magnetized along the [110] direction. The pillar measured 19·1×3·2 mm in area and 0·55 mm in thickness. A chemical analysis revealed only small traces of impurities. Calculations using the known mosaic distribution and measurements taken at several different neutron wavelengths showed the extinction effects to be negligible. As an additional check, the polarization ratio for the most intense nickel reflection was repeated on a pillar of polycrystalline nickel and yielded the same result as the single-crystal sample. Finally, by the method outlined above, it was demonstrated that there was no significant depolarization of the neutron beam within the nickel sample.

Table 1 lists the resultant values of p, the magnetic scattering amplitude, and f, the magnetic form factor for the various Bragg reflections on which data were taken. These figures are plotted in Fig. 7 as a function of $4\pi \sin\theta/\lambda$. In the forward direction the magnetic scattering amplitude is proportional to the room-temperature saturation moment of nickel, and this value is shown on the curve. For comparison with the neutron data, we have drawn in the Hartree–Fock calculated atomic form factor for the 3d electrons in Cu^+, which possesses the same number of outer electrons as nickel. A significant variation between the two curves is evident. Recalling that the neutron magnetic scattering comes from the difference between the electrons in the two spin states in the 3d shell in nickel, while the Cu^+ data represents the sum of all the 3d electrons, the curves in Fig. 7 suggest that there is a difference in the electronic configurations of the two groups of 3d electrons in nickel. Such a separation can result from the intra-atomic exchange forces which will be more effective for greater number of positive spin electrons than for the lesser number of electrons in the negative spin state.

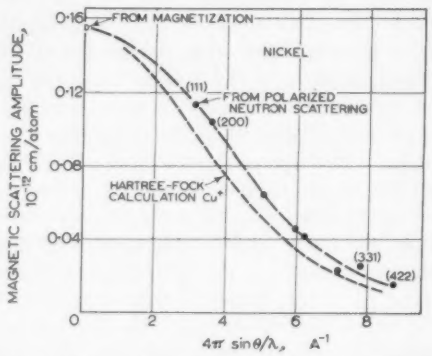

FIG. 7. Observed magnetic scattering amplitudes for different nickel reflections and comparison with theoretical form-factor curve.

Table 1. *Nickel magnetic scattering amplitudes and form-factor values for observed reflections*

hkl	p (10^{-12} cm)	f
(111)	0·1140±0·0015	0·739±0·010
(200)	0·1046±0·0010	0·678±0·006
(220)	0·0646±0·0016	0·419±0·010
(311)	0·0459±0·0012	0·297±0·008
(222)	0·0418±0·0015	0·271±0·010
(400)	0·0234±0·0021	0·152±0·014
(331)	0·0258±0·0030	0·167±0·019
(333)	0·0160±0·0035	0·104±0·023

(b) *Iron*

In obtaining the iron data, we used a single crystal of an iron–silicon alloy (3·9 weight per cent silicon). This crystal again was cut in the form of a thin pillar (19·2×3·9 mm in area and 0·41 mm thick) with its long axis as a [100] direction. A part of the data was collected on two crystals of widely differing thickness for the purpose of detecting and estimating the effects of extinction. These effects were studied, in this case, by a procedure somewhat different from the standard techniques. Of

particular use with polarized beams, this method utilizes the fact that the magnitude of the structure factor of the test crystal, and hence the degree of extinction, is changed by reversing the direction of the incident neutron polarization without altering the sample. If now one records the polarization ratio, R, of a particular reflection for a fixed counter angle as the crystal is rotated off the Bragg peak, the presence of extinction becomes quite evident.

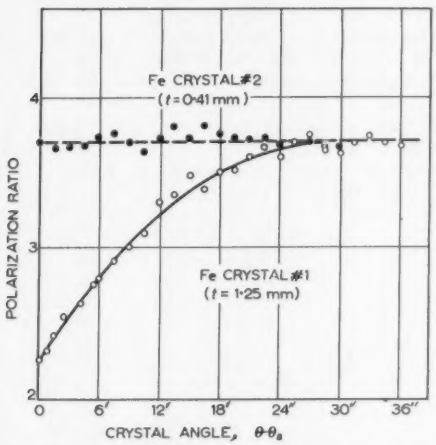

FIG. 8. Polarization ratio as a function of crystal rocking angle for thick and thin iron crystals.

Fig. 8 shows the results of such a series of measurements taken on two iron crystals for the (110) reflection. For the thicker crystal (Fe No. 1) the polarization ratio at the Bragg peak is suppressed. As the crystal is rotated off the peak, where fewer mosaic domains in the crystal are in a position to reflect, the suppression of R caused by the secondary extinction is reduced—in the limit approaching the extinction free value for crystal angles sufficiently removed from the Bragg peak position. For Fe No. 2, a crystal only one-third as thick, we observed a polarization ratio which remains unchanged as the crystal is rotated, and has a value equal to the limiting ratio observed for the much thicker crystal. This test for extinction strongly suggests that crystal Fe No. 2, which was used for the main body of the iron data, is free of extinction. It should be noted that this technique for estimating extinction is useful only in cases where the width of the observed Bragg reflection is due to the mosaic distribution and not a result of the spread in the wavelength of the scattering neutrons.

Table 2. Iron magnetic scattering amplitudes and form-factor values for observed reflections

hkl	$\bar{p}$ (10^{-12} cm)	f
(110)	0·3340±0·0027	0·619±0·006
(200)	0·2180±0·0014	0·405±0·004
(220)	0·0951±0·0024	0·176±0·005
(310)	0·0609±0·0020	0·113±0·004
(400)	0·0348±0·0100	0·065±0·020

Our results for iron are summarized in Table 2 and illustrated in Fig. 9. Also drawn in are the form-factor curves calculated by WOOD and PRATT[10] for the free iron atom ($3d_+^5$, $3d_-$, $4s^2$).

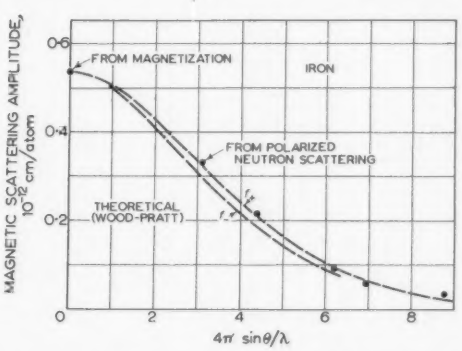

FIG. 9. Observed magnetic scattering amplitudes for different iron reflections and comparison with theoretical form-factor curves.

These theoretical curves have been normalized to agree with the experimental plot in the forward direction. The f_+ curve represents the electronic configuration of the five $3d_+$ electrons, while the curve f_- corresponds to the single $3d_-$ electron. If, as in nickel, the neutron data were to represent the difference between the spin density in two antiparallel electron groups, one would expect the experimental points in Fig. 9 to fall somewhat above both the f_+ and f_- curves. Instead, we find the experimental points to be in good agreement with the f_+ curve representing the electrons in the positive

spin group. Such agreement is consistent with a model for iron in which the magnetic spin density comes from electrons in a single spin state only. This result has been strongly indicated in the recent report of WEISS and DEMARCO[11] based on their measurements of X-ray scattering factors in the first transition group. A further interpretation of the combined neutron and X-ray results for nickel and iron will be found in the companion paper[12] following this report.

Acknowledgement—We wish to thank Dr. A. W. MCREYNOLDS for conceptual and executional assistance during early stages of this research.

REFERENCES

1. NATHANS R., PIGOTT M. T. and SHULL C. G., *J. Phys. Chem. Solids* **6,** 38 (1958).
2. NATHANS R., RISTE T., SHIRANE G. and SHULL C. G. In the press.
3. HALPERN O. and JOHNSON M. H., *Phys. Rev.* **55,** 898 (1939).
4. SHULL C. G., *Phys. Rev.* **81,** 626 (1951).
5. STANFORD C. P., STEPHENSON T. E., COCHRAN L. W. and BERNSTEIN S., *Phys. Rev.* **94,** 374 (1954).
6. BURGY M. T., HUGHES D. J., WALLACE J. R., HELLER R. B. and WOOLF W. E., *Phys. Rev.* **80,** 953 (1950).
7. HALPERN O. and HOLSTEIN T., *Phys. Rev.* **59,** 960 (1941).
8. HUGHES D. J., WALLACE J. R. and HOLTZMAN R. H., *Phys. Rev.* **73,** 1277 (1948).
9. SHERWOOD J. E., STEPHENSON T. E. and BERNSTEIN S., *Phys. Rev.* **96,** 1546 (1954).
10. WOOD J. H. and PRATT G. W., *Phys. Rev.* **107,** 995 (1957).
11. WEISS R. J. and DE MARCO J. J., *Rev. Mod. Phys.* **30,** 59 (1958).
12. WEISS R. J. and FREEMAN A. J., *J. Phys. Chem. Solids* **10,** 147 (1959).

VOL.
10
1959

J. Phys. Chem. Solids Pergamon Press 1959. Vol. 10. pp. 147–161.

X-RAY AND NEUTRON SCATTERING FROM ELECTRONS IN A CRYSTALLINE FIELD AND THE DETERMINATION OF OUTER ELECTRON CONFIGURATIONS IN IRON AND NICKEL

R. J. WEISS and A. J. FREEMAN†

Materials Research Laboratory, Ordnance Materials Research Office, Watertown, Massachusetts

(*Received* 30 *December* 1958)

Abstract—The effect of nonspherical charge distributions on X-ray and neutron scattering factors has been calculated for *d*- and *f*-electrons in cubic, tetrahedral, and hexagonal crystalline fields. The theory indicates that large deviations from the usual spherically symmetric approximation are to be expected, especially from electrons in a hexagonal environment, and that these deviations lead to a new technique for determining the spatial symmetry of the outer electrons in crystalline fields.

Using this technique the measured X-ray and neutron scattering factors have been analyzed to determine the outer electron distribution in iron and nickel and compared with the calculated effects of asphericity. The polarized neutron data of NATHANS, SHULL, *et al.* indicates that in b.c.c. iron the doubly and triply degenerate orbitals are equally populated, while in nickel the holes are 75 per cent in the triply degenerate orbitals and 25 per cent in doubly degenerate orbitals. Combining these results with the X-ray data, further analysis shows that in b.c.c. iron the spin density arises from 2·2 3*d* atom-like electrons in one spin direction, whereas in nickel the spin density arises from 5·0 3*d* atom-like electrons with spin up and 4·4 3*d* atom-like electrons with spin down. In nickel it is shown that the spin-up electrons have a radial charge density slightly more compressed than that of the spin-down electrons.

1. INTRODUCTION

As is well known, the basic integrals that appear in a calculation of the scattering factor are the matrix elements

$$f_{ij} = \int \psi_i^* \psi_j \exp(i\kappa \boldsymbol{S} \cdot \boldsymbol{r})\, dv, \qquad (1)$$

where $\kappa = 2\pi/\lambda$, λ is the wavelength of the incident radiation, $\boldsymbol{S} = \boldsymbol{s} - \boldsymbol{s}_0$, $\boldsymbol{s}$ and $\boldsymbol{s}_0$ are unit vectors along the reflected and incident directions, and the ψ are the individual one-electron wave functions. Only if the charge density, $\psi_i^* \psi_j$, is spherically symmetric, is the observed scattering independent of the orientation of the scattering vector $\boldsymbol{S}$, and one may then choose $\boldsymbol{S}$ in any convenient direction. Before considering the general case, let us calculate the scattering for the special case when $\boldsymbol{S}$ is chosen parallel to the z-axis, along which the orbitals are quantized. To evaluate the f_{ij}'s of equation (1), the expansion of $\exp(ikr\cos\theta)$ as a sum over products of Legendre functions and spherical Bessel functions is introduced. If further the ψ_i are written in the separable form $[R_i(r)/r]\Theta_{l_i}^{m_i}(\cos\theta)\Phi_{m_i}(\phi)$ with $\Theta_{l_i}^{m_i}(\cos\theta)$ the normalized associated Legendre functions,[1] the matrix elements in equation (1) may be written as

$$f_{ij} = \sum_n i^n (2n+1) C^n(l_i m_i;\, l_j m_j) \int_0^\infty R_i R_j j_n(kr)\, dr. \qquad (2)$$

Here the coefficients $C^n(l_i m_i;\, l_j m_j)$ are the integrals of the product of three associated Legendre functions (conveniently tabulated by CONDON and SHORTLEY[1]), $k = \kappa|\boldsymbol{s}| = 4\pi \sin\theta/\lambda$, and $j_n(kr)$

† Part of this work was performed as a Guest of the M.I.T. Solid State and Molecular Theory Group, Cambridge, Mass.

are the spherical Bessel functions. From this we see that the scattering matrix elements are linear combinations of integrals of products of radial charge densities and spherical Bessel functions with coefficients which depend only on the angular distribution of the one-electron wave functions. (In what follows, these radial integrals will be denoted by the symbol $\langle j_n \rangle_{ij}$.) These coefficients are listed in Table 1 for the matrix elements, f_{ij}, of d-like and f-like one-electron wave functions; the 0, +1, +2, +3 subscripts denote the component of angular momentum along the axis of quantization. Only if the one-electron charge density is spherically symmetric does equation (2) reduce to the familiar form

$$\int_0^\infty R_i R_j \sin kr/kr \, dr = \langle j_0 \rangle_{ij}.$$

When the charge density is not spherically symmetrical, the scattering for $\boldsymbol{S}$ in an arbitrary direction will no longer be equal to that calculated for $\boldsymbol{S}$ parallel to the z-axis. The scattering must be calculated as a function of this orientation, with of course an accompanying loss of the above-mentioned mathematical simplifications. In a previous paper,[2] one of the authors has shown that by use of the results of group theory the well-known selection rules are retained and the dependence of the scattering on atomic orientation may be described in terms of the scattering matrix elements given in equation (2). In this formalism the charge density in equation (1) is transformed from the xyz frame in which they are defined into a coördinate system $x'y'z'$ in which $\boldsymbol{S}$ is parallel to z'. Using the representations of the rotation group in three dimensions, it can be shown that under a rotation, the spherical harmonics transform linearly among themselves. Hence in the rotated system, the matrix elements f'_{ij} are linear combinations of the matrix elements in the unrotated system.[2]

As an example of this scheme we will write down the dependence of the scattering factor for atomic electrons of d-like symmetry ($l = 2$).

Writing

$$f_m(d) = \int R_d^2(r)[\Theta_2^m(\cos\theta)]^2 \times \times \exp(ikr\cos\theta)\sin^2\theta \, d\theta d\phi dr, \qquad (3)$$

as the scattering factor of a d-orbital with $m = |m_l|$, calculated when $\boldsymbol{S}$ is parallel to z, then the relation between the scattering factors in the primed to the unprimed system is

$$\begin{aligned} f_2'(d) &= \tfrac{1}{8}(1+6\cos^2\beta+\cos^4\beta)f_2(d)+\tfrac{1}{2}(1-\cos^4\beta)f_1(d)+\tfrac{3}{8}(1-2\cos^2\beta+\cos^4\beta)f_0(d) \\ f_1'(d) &= \tfrac{1}{2}(1-\cos^4\beta)f_2(d)+(\tfrac{1}{2}-\tfrac{3}{2}\cos^2\beta+2\cos^4\beta)f_1(d)+\tfrac{3}{2}(\cos^2\beta-\cos^4\beta)f_0(d) \\ f_0'(d) &= \tfrac{3}{4}(1-2\cos^2\beta+\cos^4\beta)f_2(d)+3(\cos^2\beta-\cos^4\beta)f_1(d)+(\tfrac{1}{4}-\tfrac{3}{2}\cos^2\beta+\tfrac{9}{4}\cos^4\beta)f_0(d). \end{aligned} \qquad (4)$$

Here β is the angle between $\boldsymbol{S}$ and the z-axis and the simplified notation $f_i = f_{ij}$ when $i = j$ has been introduced. When $\beta = 0$, then $f'_m(d) = f_m(d)$. Equation (4) gives the variation of the scattering from a particular d-orbital as a function of the angle of orientation of the scattering vector. Only for $\beta = 0$ may we speak of a unique scattering factor, i.e. $f_m(d)$. For $\beta \neq 0$, the symmetry of the orbitals, as represented by their momentum quantization, no longer exists and now the scattering factors $f_m'(d)$ are mixtures of the $f_m(d)$,

Table 1. Coefficients of $\langle j_n \rangle$ for the matrix elements f_{ij}

f_{ij}	$\langle j_0 \rangle_{ij}$	$\langle j_2 \rangle_{ij}$	$\langle j_4 \rangle_{ij}$	$\langle j_6 \rangle_{ij}$
$f(d)$ 0, 0	1	−10/7	18/7	
$f(d)$ ±1, ±1	1	−5/7	−12/7	
$f(d)$ ±2, ±2	1	10/7	3/7	
$f(f)$ 0, 0	1	5/3	3/11	a
$f(f)$ ±1, ±1	1	0	−7/11	$-6a$
$f(f)$ ±2, ±2	1	−1	1/11	$15a$
$f(f)$ ±3, ±3	1	−4/3	6/11	$-20a$

Where $a = [13/8\sqrt{(7361)}] = 0{\cdot}0189$.

Table 2. Principal scattering factors for d electrons in Co, Ni, Cu^+, and Fe

	Co*				Ni*			
Sin θ/λ	$f_2(d)$	$f_1(d)$	$f_0(d)$	$\overline{f(d)}$	$f_2(d)$	$f_1(d)$	$f_0(d)$	$\overline{f(d)}$
0	1·000	1·000	1·000	1·000	1·000	1·000	1·000	1·000
0·1	0·965	0·884	0·857	0·911	0·962	0·887	0·862	0·912
0·2	0·857	0·617	0·583	0·706	0·859	0·622	0·585	0·710
0·3	0·730	0·324	0·332	0·488	0·733	0·336	0·337	0·496
0·4	0·599	0·093	0·170	0·311	0·604	0·110	0·177	0·322
0·5	0·480	−0·062	0·091	0·186	0·485	−0·045	0·096	0·197
0·6	0·381	−0·157	0·064	0·102	0·390	−0·142	0·059	0·113
0·7	0·301	−0·206	0·063	0·050	0·310	−0·194	0·052	0·059
0·9	0·188	−0·230	0·094	0·002	0·196	−0·221	0·070	0·006
1·1	0·114	−0·187	0·089	−0·012	0·122	−0·189	0·075	−0·010
	Cu^+				Fe			
Sin θ/λ	$f_2(d)$	$f_1(d)$	$f_0(d)$	$\overline{f(d)}$	$f_2(d)$	$f_1(d)$	$f_0(d)$	$\overline{f(d)}$
0	1·000	1·000	1·000	1·000	1·000	1·000	1·000	1·000
0·1	0·960	0·887	0·867	0·912	0·969	0·881	0·852	0·910
0·2	0·861	0·626	0·590	0·713	0·856	0·611	0·580	0·703
0·3	0·736	0·348	0·346	0·504	0·728	0·312	0·324	0·481
0·4	0·610	0·125	0·190	0·333	0·590	0·092	0·140	0·309
0·5	0·496	−0·031	0·105	0·209	0·473	−0·077	0·079	0·174
0·6	0·399	−0·128	0·066	0·124	0·371	−0·172	0·057	0·091
0·7	0·320	−0·182	0·053	0·068	0·291	−0·219	0·061	0·041
0·9	0·204	−0·212	0·059	0·011	0·177	−0·230	0·090	−0·003
1·1	0·130	−0·191	0·071	−0·008	0·104	−0·177	0·080	−0·013

* Interpolated values.

the principal scattering factors for *d*-electrons in an atom. It follows from the relations given that, for *d*-electrons, the atomic scattering factor is known once the three principal scattering factors and the angle β are given.

In a previous paper[3] one of us has used Hartree–Fock wave functions to calculate these principal scattering factors for the transition elements Ti^+, V^{+2}, Mn^+ and Fe. We have also calculated these $f_m(d)$'s for Cu^+ and used these data to interpolate for the scattering factors for nickel and cobalt. These principal scattering factors are tabulated in Table 2 as a function of $\sin\theta/\lambda$ in A^{-1} units.

Similarly for atomic *f*-electrons ($l = 3$), principal scattering factors may be calculated according to the scheme already outlined. In this case, however, it proves to be simpler to calculate the matrix elements f_{tj} of equation (1) as a function of the orientation of the scattering vector by an expansion formula which gives the results directly in terms of the $\langle j_n \rangle_{tj}$. Here we do not rotate the charge density, as was done earlier, but instead use the expansion

$$\exp(i\boldsymbol{k}\cdot\boldsymbol{r}) = 4\pi \sum_{n=0}^{\infty} \sum_{m=-n}^{+n} i^n j_n(kr)\Theta_n{}^m(\cos\theta)\Phi_m(\phi)\cdot\Phi_n{}^m(\cos\beta)\Phi_m(\gamma),$$

where β, γ describe the direction of the scattering vector, $\boldsymbol{k}$. Proceeding in the way described earlier and integrating over the angular coördinates results in

$$f_{ij} = \sum_n \sqrt{(4\pi)} i^n \sqrt{(2n+1)} C^n(l_i m_i;\, l_j m_j) \langle j_n \rangle_{ij} \Theta_n^{m_i - m_j}(\cos\beta) \Phi_{m_i - m_j}(\gamma), \tag{5}$$

which reduces to

$$f_{ij} = \sum_n i^n (2n+1) C^n(l_i m_i;\, l_j m_i) \langle j_n \rangle_{ij} P_n(\cos\beta), \tag{6}$$

when $m_i = m_j$. The $P_n(\cos\beta)$ are the ordinary Legendre functions. Equation (5) has the same form as (2), with the angular dependence of the scattering vector appearing as a modulating factor to the $\langle j_n \rangle$. Here too, principal scattering factors may be defined (see Table 1) and the variation of these scattering factors with orientation given as in equation (4).

It was also shown in reference (2) that the average scattering from an electron of any orbital symmetry corresponds exactly to the scattering per electron from a half-closed shell of electrons. The scattering from a half-closed shell is angle-independent, since the charge density is spherically symmetric. For example, the total scattering from a half-closed shell of f-electrons is given by

$$\sum_{m_i=-l}^{+l} f_{m_i}'(f) = 2f_3'(f) + 2f_2'(f) + 2f_1'(f) + f_0'(f)$$
$$= 2f_3(f) + 2f_2(f) + 2f_1(f) + f_0(f),$$

and the "mean" scattering factor for any f-electron (defined by averaging over all values of β weighted with the element of solid angle $2\pi \sin\beta\, d\beta$) is

$$\overline{f(f)} = \tfrac{1}{7}(2f_3 + 2f_2 + 2f_1 + f_0). \tag{7}$$

Furthermore, the apparent success of the usual calculations of such scattering factors, in which the charge density is assumed spherical and only the $\langle j_0 \rangle$ term retained, follows from the fact that the $\langle j_0 \rangle$ term is exactly equal to the "mean" scattering factor of equation (7).

2. SCATTERING FROM ELECTRONS IN A CRYSTALLINE FIELD

In the preceding section we have discussed the scattering from electrons in free atoms. For any real case of scattering from a solid, the electrons find themselves in a field of lower symmetry than that of the free atom, and so we must expect the scattering factor to be dependent upon the particular crystalline environment considered. It is this dependence that we shall treat in the present section, not by considering the actual crystal electronic wave functions (since these are not known), but by restricting ourselves to the case of an atom in a crystalline field. In this way we may retain the formalism already discussed and also have accurate wave functions for some of our numerical applications.

(a) *d electrons in a cubic field*

The effect of a cubic field is to split the five-fold degeneracy of d-electrons into a triply degenerate set (of xy, xz, and yz symmetry, called T_{2g} orbitals) and a doubly degenerate set ($3z^2 - r^2$ and $x^2 - y^2$, called E_g orbitals).[4] Expressing these orbitals as linear combinations of our previous atomic orbitals which are eigenfunctions in a spherical field, we find the following expressions for the scattering factors:

$$f'(T_{2g}) = \tfrac{1}{5}\{2f_1' + f_2' - \tfrac{1}{2}(f'_{2,-2} + f'_{-2,2})\}$$
$$f'(E_g) = \tfrac{1}{2}\{f_0' + f_2' + \tfrac{1}{2}(f'_{2,-2} + f'_{-2,2})\}. \tag{8}$$

The cross term

$$f'_{2,-2} = \tfrac{1}{8}\sin^4\beta \exp(i4\gamma)(3f_0 + f_2 - 4f_1)$$
$$= \tfrac{15}{8}\sin^4\beta \exp(i4\gamma)\langle j_4(kr)\rangle,$$

and

$$f'_{2,-2} = f'^{*}_{-2,2}.$$

In terms of the $\langle j_n \rangle$ integrals these expressions simplify to

$$f'(T_{2g}) = \langle j_0 \rangle - A(\beta, \gamma)\langle j_4 \rangle,$$
$$f'(E_g) = \langle j_0 \rangle + \tfrac{3}{2}A(\beta, \gamma)\langle j_4 \rangle, \tag{9}$$

where

$$A(\beta, \gamma) = \tfrac{1}{8}(35\cos^4\beta - 30\cos^2\beta + 1) + \tfrac{5}{8}\sin^4\beta\cos 4\gamma,$$

VOL. 10 1959

and γ is the azimuthal angle of the scattering vector. In terms of the Miller indices, hkl,

$$A(\beta, \gamma) = \frac{h^4+k^4+l^4-3(h^2k^2+h^2l^2+k^2l^2)}{(h^2+k^2+l^2)^2}.$$

As an example of these results* we plot in Fig. 1 the scattering factors for the E_g and T_{2g} orbitals of Fe[3] for some important symmetry directions along with the free atom values. For comparison, the spherically symmetric result is also given. The differences between these scattering curves are quite striking and point up the importance of orientation effects on the scattering factor.

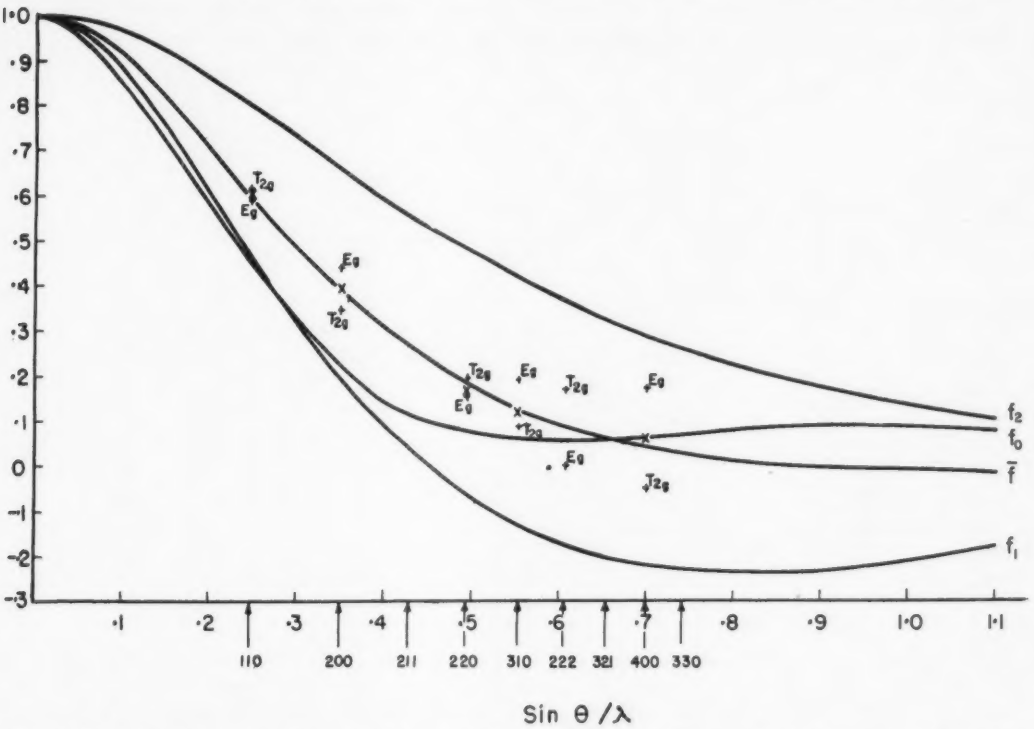

FIG. 1. The observed neutron form factor for Fe (×); the calculated free-atom principal scattering factors, f_2, f_1, f_0 and the spherically symmetric form factor, $\bar{f}$; and the calculated form factors for the Bragg reflections from the doubly degenerate orbitals, E_g, and the triply degenerate orbitals, T_{2g}, in a cubic field.

(b) *d electrons in a tetrahedral field*

In a tetrahedral environment d-electrons behave in exactly the same way as if the symmetry were cubic. Hence we need no results other than those given in the previous section.

(c) *d electrons in an hexagonal close-packed field*

In an hexagonal field the atomic degeneracy of d-electrons is split into two double degenerate sets and a single non-degenerate state. These sets have wave functions with an angular dependence like (x^2-y^2 and xy), called E_{2g}, (xz and yz), called E_{1g}, and ($3z^2-r^2$), called A_{1g}, respectively. Proceeding as before, we find that the scattering factors for these sets correspond exactly to those already given in equation (4), i.e.

$$f'(E_{2g}) = f_2'(d), f'(E_{1g}) = f_1'(d) \text{ and } f'(A_{1g}) = f_0'(d).$$

This follows from the fact that the c-axis in an hexagonal close-packed system defines an axis of quantization for the orbitals, corresponding to the

* A brief guide to the use of these formulae is given in Appendix II.

quantization of the angular momentum in the free atom. The symmetry operations corresponding to rotations about this axis then serve to split the free atom (spherical) degeneracy in the way already indicated, since functions of different m_l are readily distinguished by their different transformation properties under such rotations.

$f_m(d)$'s are given in Table 3 for the Bragg reflections plotted in Fig. 2.

Fig. 2 is quite striking in that it predicts much larger deviations from the usual spherically symmetric result than for d electrons in a cubic field. Furthermore, no smooth curve can be drawn through these points, since the variation is

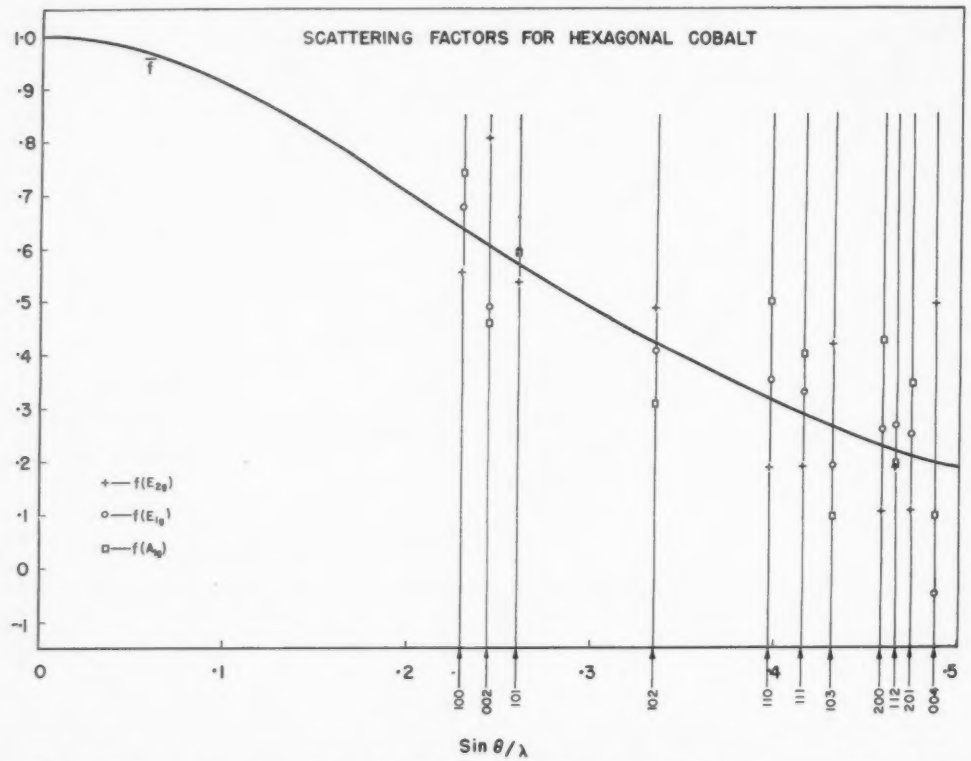

FIG. 2. Calculated scattering factors for the Bragg reflections for hexagonal Co compared with the spherically symmetric result, $\bar{f}$. (E_{2g} and E_{1g} are the doubly degenerate d-orbitals and A_{1g} the non-degenerate d-orbital in an hexagonal field).

As an illustration of the magnitude of the variation of these scattering factors expected for an hexagonal system, we plot in Fig. 2 the scattering factors $f'(E_{2g})$, $f'(E_{1g})$ and $f'(A_{1g})$ for cobalt for a number of Bragg reflections labelled by the indices hkl, calculated at the observed $c/a = 1{\cdot}63$ and with $c = 4{\cdot}105$. The atomic scattering factors, $f_m(d)$, were obtained by interpolating the known results for Cu^+ and Fe. The coefficients of the large from reflection to reflection corresponding to different scattering angles.

(d) f-*electrons in a cubic field*

In a cubic environment f-states split into three sets having different symmetry properties. These consist of a triply degenerate set, which we call δ, having an angular dependence $5z^3-3zr^2$, $5y^3-3yr^2$ and $5x^3-3xr^2$; another triply degenerate

Table 3. Coefficients of the principal scattering factors, f_m, for the scattering from d-electrons in hexagonal cobalt

	$f(E_{1g})$			$f(E_{2g})$			$f(A_{1g})$		
hkl	f_2	f_1	f_0	f_2	f_1	f_0	f_2	f_1	f_0
111	0·4963	0·3858	0·1179	0·1904	0·4963	0·3133	0·6265	0·2359	0·1376
100	0·500	0·500	0·000	0·125	0·500	0·375	0·750	0·000	0·250
102	0·3594	0·2670	0·3736	0·5579	0·3594	0·0827	0·1654	0·7473	0·0873
002	0·000	1·000	0·000	1·000	0·000	0·000	0·000	0·000	1·000
110	0·500	0·500	0·000	0·125	0·500	0·375	0·750	0·000	0·250
201	0·4978	0·4098	0·0924	0·1750	0·4978	0·3272	0·6543	0·1848	0·1609
112	0·4626	0·2394	0·2980	0·3394	0·4626	0·198	0·3959	0·5960	0·0081
103	0·2425	0·4535	0·3040	0·7275	0·2426	0·0299	0·0599	0·6081	0·3320
101	0·4758	0·2667	0·2575	0·2961	0·4758	0·2281	0·4562	0·5150	0·0288

set, ϵ, of symmetry $z(x^2-y^2)$, $y(z^2-x^2)$ and $x(y^2-z^2)$; and finally a non-degenerate term, β, of xyz symmetry. In terms of our previous definitions for the scattering factors we find:

$$
\begin{aligned}
f'(\beta) &= f_2'-\tfrac{1}{2}(f'_{2,-2}+f'_{-2,2}) \\
f'(\delta) &= \tfrac{1}{4}\tfrac{1}{8}\{16f_0'+20f_3'+12f_1'+2\sqrt{(15)}(f'_{3,-1}+f'_{-1,3}+f'_{1,-3}+f'_{-3,1})\} \\
f'(\epsilon) &= \tfrac{1}{4}\tfrac{1}{8}\{16f_2'+12f_3'+20f_1'+8(f'_{2,-2}+f'_{-2,2})-2\sqrt{(15)}(f'_{3,-1},+f'_{-1,3}+f'_{1,-3}+f'_{-3,1})\}.
\end{aligned}
\tag{10}
$$

Putting in the dependence on the scattering direction and expressing the final result in terms of the $\langle j_n \rangle$, results in the follcwing expressions:

(e) f *electrons in an hexagonal field*

It follows from the discussion already given for the case of *d*-electrons in an hexagonal field that

$$
\begin{aligned}
f'(\beta) = {} & \langle j_0\rangle+\tfrac{7}{8}\tfrac{7}{8}\langle j_4\rangle\{[-35\cos^4\beta+30\cos^2\beta-3]+\sqrt{(2)}\cos 4\gamma[-15\cos^4\beta+30\cos^2\beta-15]\}+ \\
& +\tfrac{3}{6}\tfrac{9}{4}(7361)^{-\frac{1}{2}}\langle j_6\rangle\{[-231\cos^6\beta+315\cos^4\beta-105\cos^2\beta+5]+ \\
& \quad +\cos 4\gamma[462\cos^6\beta-966\cos^4\beta+546\cos^2\beta-42]\} \\
f'(\delta) = {} & \langle j_0\rangle-\tfrac{7}{1}\tfrac{7}{6}\langle j_4\rangle\{[-35\cos^4\beta+30\cos^2\beta-3]+\sqrt{(2)}\cos 4\gamma[-15\cos^4\beta+30\cos^2\beta-15]\}+ \\
& +\tfrac{6}{2}\tfrac{5}{5}\tfrac{5}{6}(7361)^{-\frac{1}{2}}\langle j_6\rangle\{[-231\cos^6\beta+315\cos^4\beta-105\cos^2\beta+5]+ \\
& \quad +\cos 4\gamma[462\cos^6\beta-966\cos^4\beta+546\cos^2\beta-42]\} \\
f'(\epsilon) = {} & \langle j_0\rangle+\tfrac{7}{5}\tfrac{7}{2}\tfrac{7}{8}\langle j_4\rangle\{[-35\cos^4\beta+30\cos^2\beta-3]+\sqrt{(2)}\cos 4\gamma[-15\cos^4\beta+30\cos^2\beta-15]\}- \\
& -\tfrac{3}{7}\tfrac{5}{6}\tfrac{1}{8}(7361)^{-\frac{1}{2}}\langle j_6\rangle\{[-231\cos^6\beta+315\cos^4\beta-105\cos^2\beta+5]+ \\
& \quad +\cos 4\gamma[462\cos^6\beta-966\cos^4\beta+546\cos^2\beta-42]\}.
\end{aligned}
\tag{11}
$$

For the actual Bragg reflections observed in cubic crystals, we list in Table 4 the numerical coefficients required to calculate these scattering factors. All one needs then are the values of the $\langle j_n \rangle$, which may be calculated when Hartree–Fock free-atom wave functions become available for the rare earths.

the degeneracy of atomic *f*-electrons is split in an hexagonal environment into four groups distinguished by their m_l quantum numbers. These

Table 4. Coefficients of $\langle j_4 \rangle$ and $\langle j_6 \rangle$ for the scattering from f-electrons in a cubic field

	$f'(\beta)$		$f'(\delta)$		$f'(\epsilon)$	
*hkl**	$\langle j_4 \rangle$	$\langle j_6 \rangle$	$\langle j_4 \rangle$	$\langle j_6 \rangle$	$\langle j_4 \rangle$	$\langle j_6 \rangle$
111	0·9975	−0·3788	−0·4987	−0·1578	0·1663	0·2841
110	1·4488	0·3338	−0·7243	0·1391	0·2415	−0·2504
211	0·4105	−0·08260	−0·2050	−0·03442	0·06836	0·06195
200	−1·9261	−0·2628	0·9630	−0·1095	−0·3211	0·1971
310	−0·7108	−0·04797	0·3554	−0·01999	−0·1185	0·03598
311	−0·4349	−0·01505	0·2174	−0·006271	−0·07250	0·01129
332	1·2329	−0·2356	−0·6164	−0·09818	0·2055	0·1767
321	0·9425	0·03188	−0·4712	0·01328	0·1571	−0·02391
411	−0·9531	−0·05693	0·4765	−0·02372	−0·1589	0·04270
531	0·7143	0·1235	−0·3571	0·05146	0·1191	−0·09263
511	−1·2559	−0·1045	0·6279	−0·04356	−0·2093	0·07841
331	1·3938	0·1149	−0·6968	0·04788	0·2323	−0·08620
420	0·2342	0·1191	−0·1171	0·04962	0·03904	−0·08933

* These values refer to all orders of a given $h\,k\,l$.

scattering factors then are precisely those values calculated earlier for a free atom. Again, as in the case for *d*-electrons in an hexagonal field, these splittings are expected to be largest for *f*-electrons in this crystalline environment.

3. ANALYSIS OF THE X-RAY AND NEUTRON EXPERIMENTS ON IRON AND NICKEL

We now shall analyze the X-ray [5] and neutron [6] experimental results for the scattering factors of iron and nickel. (Details and discussion of the neutron results are given in the preceding paper.)

The neutron scattering factor in electron units is obtained from the unpaired spin density and is given by

$$f_N(k) = \int_\tau [A|\psi_\uparrow|^2 - B|\psi_\downarrow|^2]\exp(i\mathbf{k}\cdot\mathbf{r})\,d\tau. \tag{12}$$

$|\psi_\uparrow|^2$ and $|\psi_\downarrow|^2$ are the charge density per unit volume per electron for electrons of spin up and spin down, respectively, and A and B are the number of electrons of spin up and spin down respectively. The integration $d\tau$ is taken over the Wigner–Seitz cell.

The X-ray scattering factor in electron units is obtained from the total charge density and is given by

$$f_x(k) = \int_\tau [A|\psi_\uparrow|^2 + B|\psi_\downarrow|^2]\exp(i\mathbf{k}\cdot\mathbf{r})\,d\tau, \tag{13}$$

$f_N(0) = A-B$ is the Bohr magneton number (0·6 for Ni, 2·2 for Fe)* and $f_x(0) = A+B = Z$ is the atomic number of the atom (28 for Ni, 26 for Fe). The eighteen electrons comprising the "argon core" ($1s^2$, $2s^2$, $2p^6$, $3s^2$, $3p^6$) are assumed to be unchanged from the free atom to the solid. For neutrons these eighteen electrons contribute a negligible amount to the scattering factor, since $A|\psi_\uparrow|^2 \cong B|\psi_\downarrow|^2$ everywhere,† while for X-rays their contribution to the scattering factor can be subtracted by evaluating it from a free-atom self-consistent field calculation.

We are now left with the contribution from the $3d$, $4s$–$4p$ electrons, and all subsequent discussions will concern this outer electron charge density.

(a) *Iron*

In Fig. 3 are plotted the neutron and X-ray outer-electron scattering factors in electron units for b.c.c. iron. In order to determine this outer-electron charge density from these curves, we proceed as follows.

We extend the neutron scattering factors to $\sin\theta/\lambda = 0$ by using the data of SHULL and WILKINSON [7] on $Fe_{0.7}$ $Cr_{0.3}$ (disorder magnetic

* There is actually a small orbital contribution which can be approximately treated as additive.

† A small exchange contribution is discussed in Appendix I.

scattering) given in our Fig. 3. In this alloy the iron atoms retain the same Bohr magneton number as in pure iron and since their interatomic distance is unaltered from that of pure iron it is

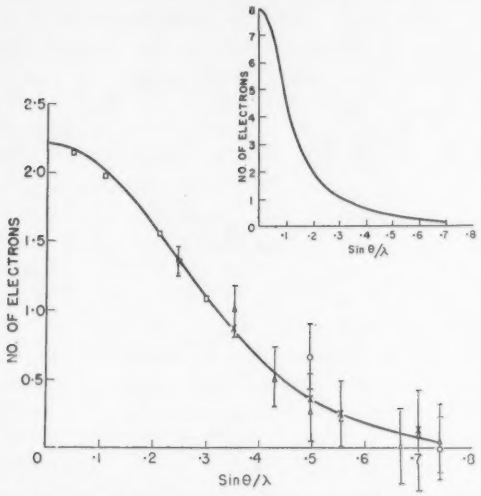

FIG. 3. Absolute neutron (×) and X-ray single crystal (○) and polycrystal (△) form factors for Fe. Included are the $Fe_{0.7}Cr_{0.3}$ disorder magnetic-scattering data of SHULL and WILKINSON[7] (□). The errors in the neutron measurements are small compared to the X-ray measurements. Two small corrections have been made to the X-ray data, −0·1 electron for the Honl correction and −0·2 electron to account for the contraction of the argon core based on our final charge densities.

assumed that the spin density is little altered in this alloy. The solid curve is the calculated curve from the WOOD and PRATT 3*d* wave functions for the free atom of iron[8] which agrees remarkably well with the neutron data.

Within experimental error the X-ray scattering factor agrees with the neutron data; its extension to $\sin\theta/\lambda = 0$ has been performed by joining the data at $\sin\theta/\lambda = 0{\cdot}24$ (first Bragg peak) such that the scattering factor and slope are continuous, and extrapolating to $f(0) = Z-18 = 8$ as a quadratic function of $\sin\theta/\lambda$. This is shown in Fig. 3 (inset curve).

We can separate the contributions from the 3*d*-, 4*s*-, and 4*p*-electrons by the following considerations. Firstly, since the cubic crystalline field does not split the 4*p*-orbitals, their average charge density must be spherically symmetric, and therefore they can be combined with the spherically symmetric 4*s*-orbitals to give a non-3*d* atom-like charge density hereafter referred to as the "residual" charge density.* On the other hand the 3*d*-electrons are split into E_g and T_{2g} orbitals (doubly and triply degenerate, respectively) in a cubic crystalline field and can be treated as described earlier.

We now replace the Wigner–Seitz cell in equation (13) by a sphere of equal volume and shall examine its consequences later. The radius of this sphere will be $a/2(3/\pi)^{\frac{1}{3}}$ for the b.c.c. crystal and $a/2(3/2\pi)^{\frac{1}{3}}$ for the f.c.c. structure.

As was shown earlier (see equation (9)) the neutron scattering factor, $f_N(k)$, for the charge density within this sphere is for the b.c.c. structure

$$f_N(k) = \int_0^{a/2(3/\pi)^{\frac{1}{3}}} [CU_\uparrow(3d) - DU_\downarrow(3d)] \times$$

$$\times \left[j_0 + \begin{pmatrix} +3/2 \\ -1 \end{pmatrix} A(\beta, \gamma) j_4 \right] dr + \qquad (14)$$

$$+ \int_0^{a/2(3/\pi)^{\frac{1}{3}}} [EU_\uparrow(4s, 4p) - FU_\downarrow(4s, 4p)] j_0 \, dr,$$

where C and D are the number of 3*d*-electrons with spin up and spin down and $U_\uparrow(3d)$ and $U_\downarrow(3d)$ their respective radial charge densities, E and F the number of residual (4*s*, 4*p*) electrons with spin up and spin down, and $U_\uparrow(4s, 4p)$ and $U_\downarrow(4s, 4p)$ their respective radial charge densities. $C+E = A-9$ and $D+F = B-9$. The coefficients modifying the fourth-order spherical Bessel function refer to the E_g and T_{2g} orbitals, respectively ($3/2A(\beta, \gamma) \rightarrow E_g$; $-A(\beta, \gamma) \rightarrow T_{2g}$). An inspection of the neutron measurements reveals only small variations in a smooth form-factor curve, suggesting only small deviations from spherical spin density. We therefore rewrite equation (14) as:

$$f_N(k) = f_{N-0}(k) + f_{N-4}(k)$$

$$= \int_0^{a/2(3/\pi)^{\frac{1}{3}}} \{[CU_\uparrow(3d) + EU_\uparrow(4s, 4p)] -$$

* Actually the symmetry of the residual charge density cannot be experimentally determined.

$$-[DU_{\downarrow}(3d)+FU_{\downarrow}(4s,4p)]\}j_0(kr)\,dr+$$
$$+\int_0^{a/2(3/\pi)^{\frac{1}{3}}}[CU_{\uparrow}(3d)-DU_{\downarrow}(3d)]\times$$
$$\times\begin{pmatrix}+3/2\\-1\end{pmatrix}A(\beta,\gamma)j_4(kr)\,dr \qquad (15)$$

where $f_{N-0}(k)$ refers to the spherically symmetric part and $f_{N-4}(k)$ refers to the nonspherical part. We can now transform* the smooth form-factor curve (given in Fig. 3), which gives

$$[CU_{\uparrow}(3d)+EU_{\uparrow}(4s,4p)]-$$
$$-[DU_{\downarrow}(3d)+FU_{\downarrow}(4s,4p)] \qquad (16)$$
$$=\frac{2r}{\pi}\int_0^{\infty}kf_{N-0}(k)\sin rk\,dk,$$

and obtain the curve in Fig. 4. Since this curve agrees quite well with the $3d$ free-atom charge density of WOOD and PRATT[8], it appears as though

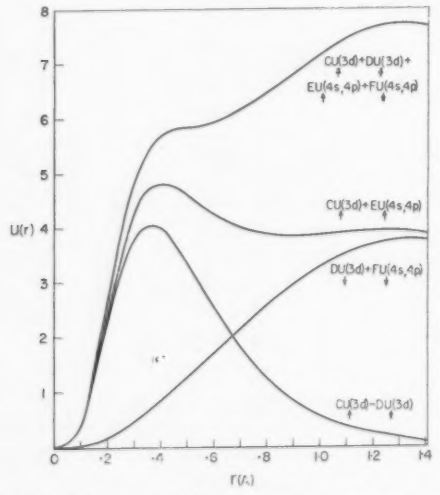

FIG. 4. The total radial distribution function of Fe, $CU_{\uparrow}(3d)+DU_{\downarrow}(3d)+EU_{\uparrow}(4s,4p)+FU_{\downarrow}(4s,4p)$; the spin radial distribution, $CU_{\uparrow}(3d)-DU_{\downarrow}(3d)$; the total spin-up radial distribution, $CU_{\uparrow}(3d)+EU_{\uparrow}(4s,4p)$; and the total spin-down radial distribution, $DU_{\downarrow}(3d)+FU_{\downarrow}(4s,4p)$.

* Actually, the Fourier transform is a sum over points in the reciprocal lattice, but owing to the sparsity of measured points we have drawn a smooth f-curve and replaced the sum by an integral.

there are negligible $(4s,4p)$ unpaired spins, since the corresponding charge density would be extended quite far radially. Hence we may set $EU_{\uparrow}(4s,4p)=FU_{\downarrow}(4s,4p)$. We now substitute $CU_{\uparrow}(3d)-DU_{\downarrow}(3d)$ from equation (16) into $f_{N-4}(k)$ (equation (15)) and determine the effect of the asphericity on the form factor. We have also plotted in Fig. 1 the resulting values of f if the spin density were either totally in the E_g or totally in T_{2g} orbitals. It is apparent that the effect of asphericity is indeed small and slightly favors the E_g orbitals. From the 400 peak we estimate that the spin density in iron is approximately equally populated in the E_g and T_{2g} orbitals. (As the spin density is quite small in the outer electron region, the replacement of the Wigner–Seitz cell by a sphere was justified.)

Since the neutron data indicate that the $3d$ charge density is approximately spherically symmetric, we can now simplify equation (13) in order to analyze the X-ray data. Here again we replace the Wigner–Seitz cell by a sphere of equal volume and discuss the consequences of this approximation below:

$$f_x(k)=\int_0^{a/2(3/\pi)^{\frac{1}{3}}}[CU_{\uparrow}(3d)+DU_{\downarrow}(3d)+$$
$$+EU_{\uparrow}(4s,4p)+FU_{\downarrow}(4s,4p)]j_0(kr)\,dr. \qquad (17)$$

Transforming the X-ray scattering-factor curve, we get the total outer-electron radial charge density shown in Fig. 4. Combining the neutron and X-ray results, which provide the difference and sum of the charge densities, we can determine the spin-up and spin-down charge densities separately and this is shown in Fig. 4. Since exchange effects will cause little change between $U_{\uparrow}(3d)$ and $U_{\downarrow}(3d)$ in the regions where the spin density $CU_{\uparrow}(3d)-DU_{\downarrow}(3d)$ is small and since $DU_{\downarrow}(3d)+FU_{\downarrow}(4s,4p)$ is small where the spin density is large, we can subtract from $CU_{\uparrow}(3d)+EU_{\downarrow}(4s,4p)$ a radial charge equal to $DU_{\uparrow}(3d)+FU_{\uparrow}(4s,4p)$ in order to pair it up and add this to $DU_{\downarrow}(3d)+FU_{\downarrow}(4s,4p)$ to give a final unpaired and paired radial distribution, i.e.

$$CU_{\uparrow}(3d)+EU_{\uparrow}(4s,4p)-DU_{\downarrow}(3d)-$$
$$-FU_{\downarrow}(4s,4p)\cong(C-D)U_{\uparrow}(3d)\text{ (unpaired)}$$
$$\text{since } E=F,$$

$$DU_{\downarrow}(3d)+FU_{\downarrow}(4s,\,4p)+DU_{\uparrow}(3d)+FU_{\uparrow}(4s,\,4p)$$
$$=D[U_{\uparrow}(3d)+U_{\downarrow}(3d)]+$$
$$+F[U_{\downarrow}(4s,\,4p)+U_{\uparrow}(4s,\,4p)]\,(\text{residual}).$$

These resulting separated charge densities are shown in Fig. 5 and are labelled $3d$ and residual

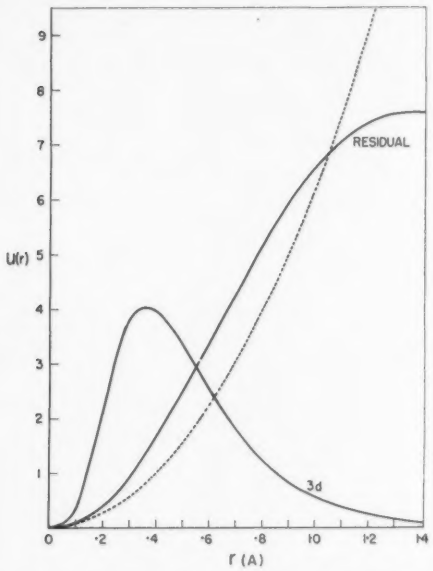

FIG. 5. The unpaired spin distribution ($3d$) and the paired radial distribution (residual) for Fe. The dotted curve is the radial distribution corresponding to a constant charge density.

respectively. It is apparent that there is no $3d$ atom-like radial component in the residual charge density and hence D equals zero and C must then be 2·3. We have finally

$$2{\cdot}2U_{\uparrow}(3d)\text{ unpaired},$$
$$2{\cdot}9(U_{\uparrow}(4s,\,4p)+U_{\downarrow}(4s,\,4p))$$
$$\cong 5{\cdot}8U(4s,\,4p)\text{ residual paired.}$$

The effect on the residual charge densities of replacing the Wigner–Seitz cell by a sphere of equal volume can be shown to be negligible from the following considerations. If the residual charge density were constant throughout the crystal, i.e.

$$|\psi|^2(\text{residual}) = \text{constant} = U(\text{residual})/4\pi r^2$$
$$U(\text{residual}) = \text{constant}\cdot 4\pi r^2,$$

shown in Fig. 5 (dotted curve), then f is identically zero at all Bragg reflections when the integral is taken over the Wigner–Seitz cell, i.e.

$$f=\int_{\tau}\text{const.}\,4\pi r^2\exp(i\mathbf{k}\cdot\mathbf{r})\,d\tau\cong 0,$$

for all Bragg reflections.

If we replace the integral by a sphere of equal volume, then the scattering per electron becomes

$$f=\frac{\int_0^{a/2(3/\pi)^{\frac{1}{3}}}\text{const.}\,4\pi r^2\sin kr/kr\,dr}{\int_0^{a/2(3/\pi)^{\frac{1}{3}}}\text{const.}\,4\pi r^2\,dr}$$
$$=\frac{3}{(kR)^3}[\sin kR-kR\cos kR],$$

where $R=a/2(3/\pi)^{\frac{1}{3}}$ and $k=4\pi\sin\theta/\lambda$. For a body-centered cubic lattice, the values of f are given in Table 5, and the error made by this approximation is seen to be small.

Table 5. Calculated values of f for a constant charge density for the Bragg reflections from a b.c.c. lattice based on the approximation of replacing the Wigner–Seitz cell by a sphere of equal volume

hkl	*f*
110	0·005
200	−0·08
211	−0·01
220	+0·03
310	+0·03
222	+0·009
321	−0·012
400	−0·02
(411)	−0·02
(330)	

It thus appears that the residual radial charge density in iron lies somewhere between the curve labeled residual and the constant charge density (dotted curve) in Fig. 5 and probably closer to the constant charge density.

(b) *Nickel*

The X-ray and neutron results for nickel are shown in Fig. 6, together with the calculated and observed X-ray results for copper. The good agreement with the copper results leads us to accept the total charge density for nickel as expected from band-theory considerations ($3d_{\uparrow}^{5}$, $3d_{\downarrow}^{4\cdot4}$). The spin density is also seen to extrapolate to 0·6, as expected from saturation magnetization measurements. We therefore accept the total $3d$ charge density as given by the calculated (Hartree–Fock) Cu^{+} charge density and normalize it to 9·4 $3d$-electrons. Since these electrons have very little charge density at the edges of the Wigner–Seitz cell, we are again justified in replacing the integration over the cell in equations (12) and (13) by spheres of equal volume. The 0·6 $4s$-electrons are assumed to be of uniform charge density and are neglected. From equation (16), letting $E = F = 0$, we determine the radial spin density $CU_{\uparrow}(3d) - DU_{\downarrow}(3d)$ and this is given in Fig. 7 (dashed curve, renormalized to 9·4). The total radial charge density is also given in Fig. 7 (solid curve), and we see a small but significant difference. Solving for $U_{\uparrow}(3d)$ and $U_{\downarrow}(3d)$, we plot this difference as $U_{\uparrow}(3d) - U_{\downarrow}(3d)$ per electron in Fig. 8 (dashed curve). Such a behavior is expected from the exchange effects which cause the five electrons with spin up to be more concentrated radially than the 4·4 electrons with spin down.

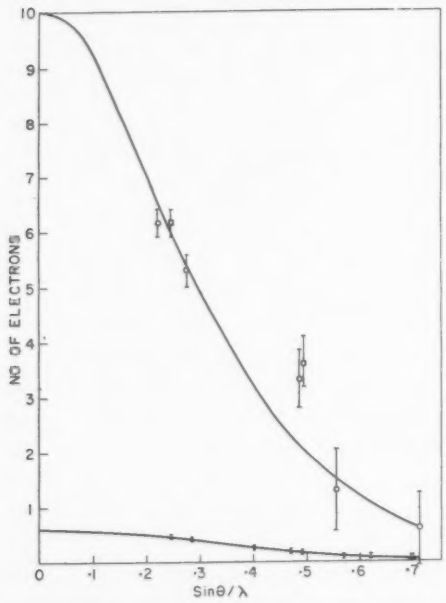

FIG. 6. Absolute neutron (I) and X-ray (□) form factors for nickel. Included are the X-ray measurements (○) and the calculated results for copper.

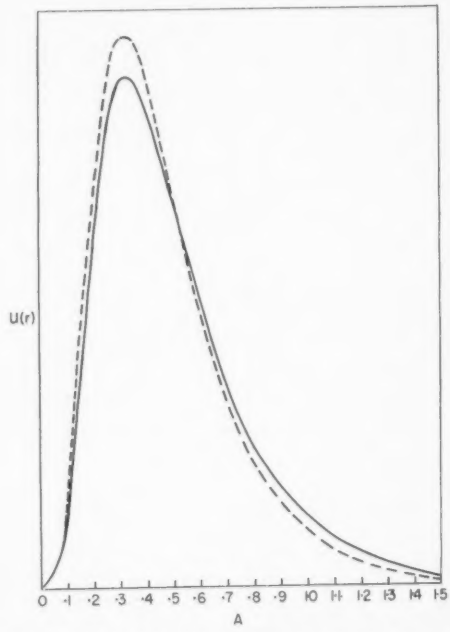

FIG. 7. The total radial charge distribution of nickel (solid curve) and the spin density radial distribution of nickel (broken curve) normalized to the total.

The magnitude of this effect is compared (Fig. 8) to the effect calculated by WOOD and PRATT[8] (solid curve) for the free atom of iron where the effect is larger, since iron has five electrons with spin up and only one electron with spin down. If we now substitute the radial spin density calculated from equation (16) into the aspherical part of (15), we can calculate the form factor, assuming the spin density to be entirely E_g or T_{2g}, and this is shown in Fig. 9. We observe that there is only a small deviation from spherical symmetry. From the 400 and 331 peaks we estimate that the hole population is 75 per cent T_{2g} and 25 per cent E_g, whereas it would be 60 : 40 for spherical symmetry.

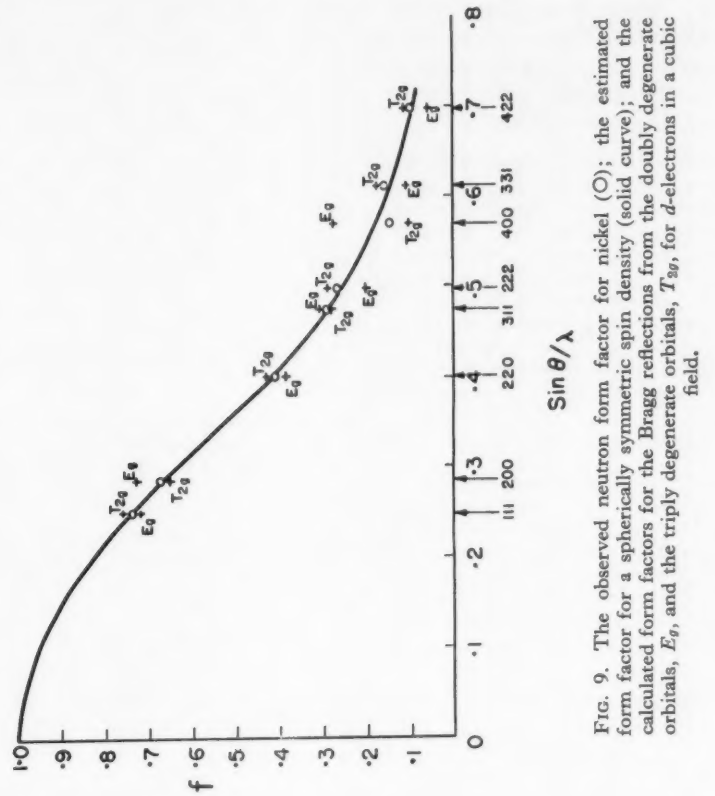

FIG. 9. The observed neutron form factor for nickel (○); the estimated form factor for a spherically symmetric spin density (solid curve); and the calculated form factors for the Bragg reflections from the doubly degenerate orbitals, E_g, and the triply degenerate orbitals, T_{2g}, for d-electrons in a cubic field.

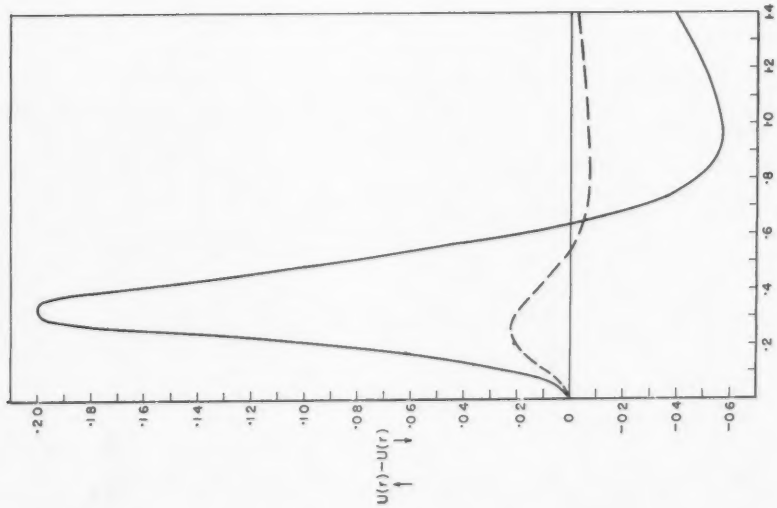

FIG. 8. The difference in charge density per electron for the two spin states of the free iron atom (solid curve) and of crystalline nickel (broken curve).

In conclusion it is important to point out that analysis of magnetic neutron-diffraction data must include the above considerations regarding lack of spherical symmetry, since the effects can be quite large, especially for non-cubic crystals.

Note added in proof : NATHANS and PAOLETTI[9] have reported preliminary results on the magnetic form factor of the face-centered cubic phase of metallic cobalt, which also indicates a deviation from spherical symmetry for its 3*d* spin density. From their published data we estimate that the hole population is 60 per cent E_g and 40 per cent T_{2g}. It is interesting to note that this result for f.c.c. cobalt is inverted from the results for f.c.c. nickel as stated in this paper. Calculations for f.c.c. cobalt also show that the five 3*d* electrons with spin up are more concentrated than the 3·3 3*d* electrons with spin down.

Acknowledgements—We are particularly indebted to Dr. R. NATHANS for his close co-operation. We are pleased to thank Dr. WALTER MARSHALL and Professor GEORGE KOSTER for helpful discussions and Dr. RALPH HARRISON for reading the manuscript. We are indebted to R. NATHANS, C. G. SHULL, G. SHIRANE, and A. ANDRESON for allowing us to use their data before publication.

APPENDIX I

The intra-atomic exchange effect giving rise to different radial distributions of the 3*d*-electrons in the two spin states also affects the radial distribution of other electrons close to the unpaired 3*d*-electrons, even though these other electrons are paired. These effects are most noticeable for the 3*p*-, 3*s*-, and 4*s*-electrons and give rise to coherent magnetic neutron scattering whose form factor has been evaluated for Fe $3d^6\ 4s^2$ (4 unpaired electrons) in Fig. 10. While the effect is small, it is not negligible and is estimated to reach a maximum of ~ 0·1 electron for atoms with five unpaired 3*d*-electrons.

APPENDIX II

The following formulae for the crystalline field scattering factors in terms of the principal scattering factors tabulated earlier (see Table 2) have been found to be useful.

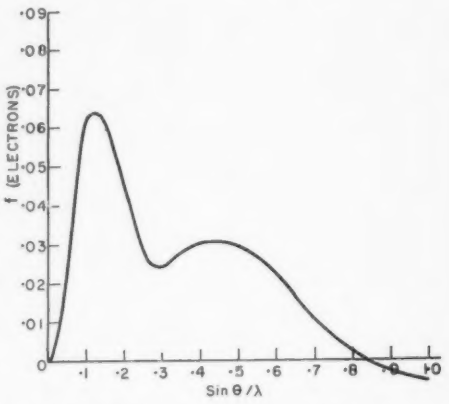

FIG. 10. The exchange form factor for non-3*d*-electrons in the iron free atom; 0·1 electron is equivalent to a scattering amplitude of $0{\cdot}027 \times 10^{-12}$ cm.

(a) d *electrons in a cubic or tetrahedral field*

Rewriting equation (9) we get

$$f(E_g) = \left(\frac{2}{5}+\frac{A}{10}\right) f_2(d)+ \\ +\left(\frac{2}{5}-\frac{2A}{5}\right) f_1(d)+\left(\frac{1}{5}+\frac{3A}{10}\right) f_0(d)$$

$$f(T_{2g}) = \left(\frac{2}{5}-\frac{A}{15}\right) f_2(d)+ \\ +\left(\frac{2}{5}+\frac{4A}{15}\right) f_1(d)+\left(\frac{1}{5}-\frac{3A}{15}\right) f_0(d)$$

where

$$A = \frac{h^4+k^4+l^4-3(h^2k^2+h^2l^2+k^2l^2)}{(h^2+k^2+l^2)^2}$$

(b) d *electrons in an hexagonal field*

Substituting $\cos\beta = 1/(B+1)^{\frac{1}{2}}$, where $B = 4/3(c/a)^2 (h+k/l)^2$, into equation (4) results in

$$f(A_{1g}) = \frac{1}{4\cdot(B+1)^2}[3B^2f_2(d)+12Bf_1(d)+(B-2)^2f_0(d)]$$

$$f(E_{1g}) = \frac{1}{2\cdot(B+1)^2}[(B^2+2B)f_2(d)+(B^2-B+2)f_1(d)+3Bf_0(d)]$$

$$f(E_{2g}) = \frac{1}{8\cdot(B+1)^2}[(B^2+8B+8)f_2(d)+4(B^2+2B)f_1(d)+3B^2f_0(d)]$$

(note that for $l = 0$ ($B = \infty$), all terms remain finite, for example

$$\frac{3B^2 f_2(d)}{4(B+1)^2} \rightarrow \tfrac{3}{4} f_2(d)).$$

From these formulae the crystalline field scattering factors may be calculated by the following procedure:

(a) Plot the values of the principal scattering factors $f_2(d)$, $f_1(d)$ and $f_0(d)$ (as listed for example in Table 2).

(b) Calculate A or B from the above formulae for the particular reflection desired from its Miller indices and (for a hexagonal crystal) the appropriate c/a ratio.

(c) For the sin θ/λ value at which the reflection occurs determine the values of the principal scattering factors from (a)

(d) Substitute these quantities into the above equations.

OL.
10
959

REFERENCES

1. We use the phase convention of CONDON E. U. and SHORTLEY G. H., *Theory of Atomic Spectra* p. 52. Cambridge University Press (1953).
2. FREEMAN A. J., *Phys. Rev.* **113,** 169 (1959).
3. FREEMAN A. J., *Acta Cryst.* **12,** 261 (1959).
4. VON DER LAGE F. C. and BETHE H. A., *Phys. Rev.* **71,** 612 (1947).
5. WEISS R. J. and DEMARCO J. J., *Rev. Mod. Phys.* **30,** 59 (1958).
6. NATHANS R., SHULL C. G., SHIRANE G., and ANDRESON A., *J. Phys. Chem. Solids.* **10,** 138 (1959).
7. SHULL C. G. and WILKINSON M. K., *Phys. Rev.* **97,** 304 (1955).
8. WOOD J. H. and PRATT G. W. Jr., *Phys. Rev.* **107,** 995 (1957).
9. NATHANS R. and PAOLETTI A., *Phys. Rev. Letters* **2,** 252 (1959).

J. Phys. Chem. Solids Pergamon Press 1959. Vol. 10. pp. 162–168.

MIGRATION BARRIERS FOR CATIONS AND ANIONS IN ALKALI HALIDE CRYSTALS

R. GUCCIONE* and M. P. TOSI†

Istituto di Fisica dell'Università, Palermo, Italy

and

M. ASDENTE

Laboratori CISE, Milano, Italy

(*Received* 24 *November* 1958)

VOL.
10
195

Abstract—The BORN–MAYER model is applied to the evaluation of the barriers for vacancy migration of cations and anions along the cube face diagonal in NaCl and KCl crystals. The effect of the hardness of the overlap interaction between ions at short distances is quantitatively investigated by using two different forms for the overlap repulsive potential. The values estimated for the energies of motion are compared with the available experimental data and with previous theoretical estimates for NaCl crystals; the hardness of the repulsive potential appears to be an important factor in determining the height of the migration barriers in crystals.

1. INTRODUCTION

THE role of mobile point imperfections in determining the physical properties of solids has been repeatedly stressed.[1] Various experimental methods, involving the study of ionic conductivity and of radioactive-tracer diffusion as functions of temperature in both "pure" and intentionally doped crystals, have been devised for the quantitative study of the concentrations and mobilities of point imperfections in the simplest ionic conductors, namely the alkali and silver halides.[2] On the theoretical side, while the model adopted by BORN and his collaborators[3] to describe the defect-independent properties of ionic solids allows fairly reliable estimates to be made of the energy of formation of Schottky defects in the alkali halides,[4–6] it has failed so far[4] to account for the height of the vacancy-migration barriers of ions and for the difference between the energies of vacancy migration for cations and anions indicated by the existing experimental evidence for most of these salts.[7] It has been suggested that in calculating migration barriers, both in alkali halides and in metals, the use of the equilibrium repulsive interaction potential in treating repulsive interactions between ions at distances considerably smaller (by something like 15 per cent in the alkali halides) than the equilibrium interionic distance in the crystal, may appreciably affect the results.[8] It also seems likely that in the case of the alkali halides a refined treatment of the lattice distortion around the moving ions and the explicit consideration of the repulsive interactions between ions other than nearest neighbours may increase the difference between the theoretical values of the vacancy-migration barriers of the two types of ions in the same crystal.[6]

We have applied the BORN model of ionic solids to the evaluation of the energy for vacancy migration of cations and anions in NaCl and KCl crystals, using two forms of different hardness for the repulsive interaction potential and taking into account also next-nearest-neighbour repulsive interactions. We shall restrict ourselves to a migration path along the cube face diagonal

* Now at the University of British Columbia, Vancouver, Canada.

† Now at the H.H. Wills Physics Laboratory, University of Bristol, England.

for both types of ions. Our results can thus be compared directly with the theoretical values reported by MOTT and LITTLETON [4] for the barriers for vacancy migration of cations and anions in NaCl crystals, immediately after the pioneer work by JOST and NEHLEP[9]. Although indirect migration paths outside the cube face diagonal appear conceivable in principle, we have not thought it advisable to calculate the saddle points for all the possible migration paths lying in the (110) plane passing through the vacancies. In this respect we would like to stress that the qualitative arguments put forward by LAURENT and BÉNARD[7] and by DRYDEN and MEAKINS[10] in favour of an indirect vacancy-migration path through the interstitial position for ions in alkali halide crystals cannot be considered as probative. In particular these arguments are based on simple geometrical considerations of the type first critically applied by BROOKS[11] for metals, and they thus neglect the fundamental role of the Coulombic interactions and of the ionic deformability. It should also be noted that the geometrical argument used by LAURENT and BÉNARD[7], when properly applied, leads generally to a saddle point for an indirect migration path of the anion near the interstitial position, and not at the centre of the triangle formed by three of the equilibrium neighbours of the moving anion as LAURENT and BÉNARD states[7]. However, the overlap and the Coulombic forces will tend to push the anion from the interstitial position towards the saddle position considered here.

2. THE ENERGY FOR VACANCY MIGRATION OF IONS IN ALKALI HALIDE CRYSTALS

The energy for vacancy migration U of an ion in an alkali halide crystal can be evaluated as the difference between the energy of the crystal in the saddle-point configuration (Fig. 1) and the energy of the crystal containing a single vacant lattice site; that is, as the difference between the energy E_2 to extract from a perfect crystal two next-nearest neighbour ions and to introduce one of them into the saddle-point position between the two neighbouring vacancies, and the energy E_1 to extract a single ion from a perfect crystal. A lattice calculation of both these energies involves the evaluation of potential energies at various ionic positions in the imperfect crystal containing the moving ion.

The relevant contributions to the potential energy of an ion in an alkali halide crystal are due to its electrostatic and overlap repulsive interactions with the other ions of the crystal, and these are the only interactions we shall consider here. For the overlap interaction energy, we use two different forms. The first (I) is the usual exponential form proposed by BORN and MAYER[3], while in the second (II) we substitute for the BORN–MAYER form a harder form of the type $A+Br^{-12}$ [12] whenever interactions between ions of opposite sign at a relative distance r smaller than the anion–cation equilibrium separation r_0 are involved. With both repulsive forms, overlap interactions between next-nearest-neighbour ions are taken into account. For the constants entering the calculation we adopt the numerical values referred to by FUMI and TOSI[6]. The numerical values of the parameters A and B appearing in the r^{-12} repulsive form are determined by assuming that the repulsive energy of two ions of opposite sign interacting at a relative distance r_0 have the same value and the same derivative as in the exponential BORN–MAYER form.

3. THE ENERGY OF THE CRYSTAL CONTAINING A SINGLE VACANCY

The MOTT type of procedure for evaluating the energy required to extract a single ion from a perfect crystal, as one-half of the negative of the potential energies at the position of the ion to be removed before and after its removal, has been described elsewhere.[6] Some numerical results, obtained by using the BORN–MAYER repulsive form and the SHOCKLEY ionic polarizabilities, but neglecting the elastic distortion around the vacancy, have been reported already.[13] These results are collected in Table 1, together with the corresponding results obtained by using the BORN–MAYER–VERWEY repulsive form. Clearly, the increased hardness of the repulsive interaction between ions of opposite sign at short distances reduces the lattice distortion around the defect, and thus its final effect is an increase in the energy required to create the defect. This effect is particularly large in the case of the anion vacancy, as the soft BORN–MAYER repulsion allows quite large distortions around it.[13]

Table 1. *Energy* (*in* eV) *to extract a single ion from* NaCl *and* KCl *crystals*

	E_1^+(I)	E_1^-(I)	E_1^+(II)	E_1^-(II)
NaCl	4·78*	4·49	4·89	4·76
KCl	4·44*	4·45	4·54	4·63

* These numerical values are given by Tosi and Fumi[13].

4. THE ENERGY OF THE CRYSTAL IN THE SADDLE-POINT CONFIGURATION

To evaluate the energy of the saddle-point configuration relative to a perfect crystal, we need to know the lattice distortion around the defects at the saddle point. Whereas in the previous theoretical estimates[9,4] only the nearest neighbours of the moving ion at the saddle point were given an

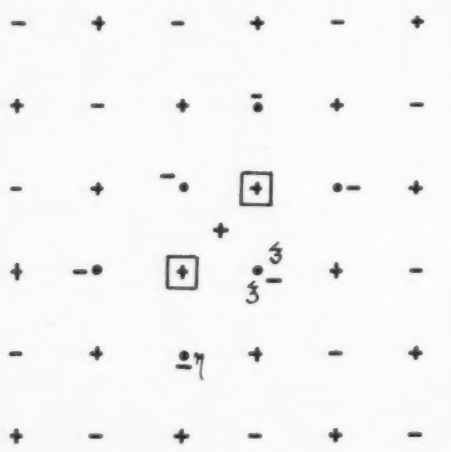

Fig. 1. The saddle-point configuration for the vacancy migration of a cation along the cube face diagonal in the NaCl lattice. The ions above and below the two vacancies are assumed to be displaced by the amount ηr_0 along the cube edge normal to the plane of the figure.

actual displacement, we allow all the neighbours of the defects to be displaced. The displacement and polarization of the other ions of the crystal is accounted for by attaching a displacement and polarization dipole[4] to the lattice position of each of them. Our approximation for the ions adjacent to the defects is illustrated in Fig. 1. For the two immediate neighbours of the ion in the saddle-point position, the displacement $\sqrt{2}\zeta r_0$ takes place along the cube face diagonal; for all the immediate neighbours of a vacancy an equal displacement ηr_0 along the cube edge is assumed. The quantities ζ and η are determined by minimizing the energy of the distorted configuration, that is, by maximizing the decrease in energy of the crystal upon distortion.[9] We have taken into account[13] the change in the Coulombic interaction energy of the ten nearest neighbours of the defects with the rest of the lattice and among themselves, the change in the repulsive interaction energy of the ten nearest neighbours of the defects among themselves and with their nearest and next-nearest neighbours,

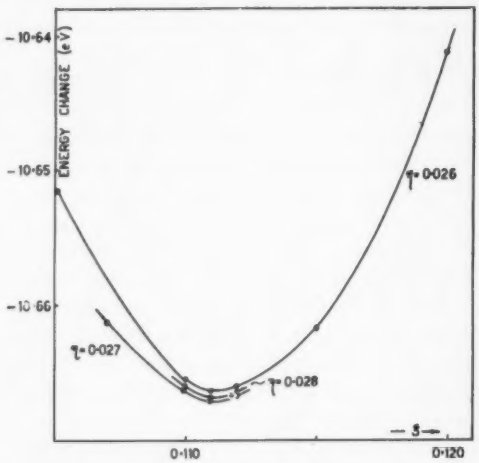

Fig. 2. Determination of the displacements of the nearest neighbours of the defects at the saddle point for the case of the vacancy migration of the cation in KCl (r^{-12} repulsive form).

and finally the change in polarization energy of the nearest neighbours of the defects due to the change of their electronic dipoles upon displacement. In calculating this last energy change, we have considered the electric field acting on a displaced ion as determined by the effective charges of the defects and by the ionic displacements of the other displaced ions. The determination of the displacements is illustrated in Fig. 2 for one case (cation migration in KCl, r^{-12} repulsive form), and all the values obtained for the quantities ζ and η are collected in Table 2. The increase in the hardness of the overlap interaction between ions of opposite

Table 2. Lattice distortion around the saddle point for vacancy migration in NaCl *and* KCl *crystals*

	Cation				Anion			
	η(I)	ζ(I)	η(II)	ζ(II)	η(I)	ζ(I)	η(II)	ζ(II)
NaCl	0·045	0·050	0·028	0·101	0·095	0·078	0·062	0·114
KCl	0·042	0·090	0·027	0·111	0·061	0·099	0·043	0·115

sign at short distances brings about an increase in the value of ζ and a decrease in the value of η, as one would expect.

To evaluate the energy of the crystal in the saddle-point configuration relative to the perfect crystal, it is necessary to add the decrease in energy of the crystal upon distortion that we have just discussed to the energy relative to the perfect crystal of the unrelaxed saddle-point configuration, in which the neighbours of the defects are held in their normal lattice positions. The Coulombic (and repulsive) part of this energy is evaluated as the sum of the Coulombic (and repulsive) interaction energy of the ion in the saddle-point position and the rest of the lattice, and the work to be done against the Coulombic (and repulsive) forces to create the two neighbouring vacancies in an undistorted lattice. The relevant formulae are:

$$E^{\mathrm{Coul}} = \frac{e^2}{r_0}\left(2\alpha_M + \frac{1}{\sqrt{2}} - \frac{2}{\sqrt{(2)/2}}\right) \qquad (1)$$

$$\begin{aligned} E^{\mathrm{rep}} = {} & 2w[r_0\sqrt{(2)/2}] + 4w[r_0\sqrt{(6)/2}] + \\ & + 4w[r_0\sqrt{(10)/2}] + 8w[r_0\sqrt{(14)/2}] - 12w(r_0) + \\ & + 4w\{r_0\sqrt{(6)/2}\} + 4w\{r_0\sqrt{(10)/2}\} + \\ & + 8w\{r_0\sqrt{(14)/2}\} - 23w\{r_0\sqrt{(2)}\} \end{aligned} \qquad (2)$$

where α_M is the Madelung constant referred to the nearest-neighbour distance and $w[r]$ and $w\{r\}$ are the overlap interaction energies of two ions, of opposite and equal sign respectively, at a distance r apart in the undistorted lattice. The first and second terms in equation (1) give the increase in the Coulombic energy of the crystal due to the extraction of two ions of the same sign at the distance of next-nearest neighbours from a perfect lattice; the third term gives the Coulombic interaction energy between the two vacancies and the ion in the saddle-point position, the Coulombic interaction energy between this ion and the perfect crystal being zero. Finally, the polarization energy term can be evaluated as one-half of the sum of the potential energies in the positions of the three defects, due to the polarization created in the medium by the effective charges of the defects. The final formula is, for the case of the cation vacancy migration (for the case of the anion vacancy migration, one has to substitute the cation polarizability α_+ for the anion polarizability α_- and to interchange M_+' and M_-'):

$$\begin{aligned} E^{\mathrm{pol}} = {} & -2{\cdot}490\alpha_- \frac{e^2}{r_0^4} - \\ & - \frac{e^2}{r_0}[M_+'(S_{11}^+ + \tfrac{1}{2}S_{33}^+ + S_{12}^+ - 2S_{13}^+) + \\ & + M_-'(S_{11}^- + \tfrac{1}{2}S_{33}^- + S_{12}^- - 2S_{13}^-)] \\ = {} & -2{\cdot}490\alpha_- \frac{e^2}{r_0^4} - \frac{e^2}{r_0}(2{\cdot}441M_+' + 1{\cdot}755M_-') \end{aligned} \qquad (3)$$

where[6]

$$M_\pm' = \frac{1}{4\pi}\left(1 - \frac{1}{K}\right)\frac{\alpha + \alpha_\pm}{\frac{1}{2}(\alpha_+ + \alpha_-) + \alpha} \qquad (4)$$

(α is the displacement polarizability;[6] K is the static dielectric constant). The first term in equation (3) gives the contribution of the electronic polarization of the neighbours to the defects, which actually cancels out in the final expression for E_2; the other terms give the contributions of the electronic and displacement polarizations of

the other ions. The $S_{ij}^{\pm}$ are lattice sums, respectively over positive and negative ions, of the type

$$S_{ij} = r_0^4 \sum{}' \frac{\cos(r_i, r_j)}{r_i^2 r_j^2} \qquad (5)$$

(the prime denoting that the contributions of the vacant lattice sites and of the nearest neighbours of the defects are to be excluded) and r_1, r_2 and r_3 are the distances of a given ion from the two vacancies and from the ion in the saddle-point position. The lattice sums $S_{ii}^{\pm}$ can be obtained directly from the lattice sums evaluated by LENNARD-JONES and INGHAM;[14]* the others have been computed by direct summation up to distances where the contribution by every ion shell can be approximated with sufficient accuracy by the corresponding contribution to the LENNARD-JONES and INGHAM series.

Table 3. Energy (in eV) of the saddle point for vacancy migration of cations and anions in NaCl *and* KCl *crystals, relative to the perfect crystal.*

	E_2^+(I)	E_2^-(I)	E_2^+(II)	E_2^-(II)
NaCl	4·86	4·97	5·76	5·87
KCl	4·97	5·09	5·67	5·81

* Apart from the contributions of the vacant lattice sites and of the nearest neighbours of the defects, which are to be subtracted from the LENNARD-JONES and INGHAM sums, the lattice sums $S_{33}^{\pm}$ are related to the sums A_4 and C_4 over points of a simple cubic and of a face-centred cubic lattice, evaluated by LENNARD-JONES and INGHAM,[14] by the simple relation $S_{33}^{+} = S_{33}^{-} = \frac{1}{3}C_4 - \frac{1}{6}A_4$.

The final results for the energy E_2 of the saddle point for vacancy migration relative to the perfect crystal are reported in Table 3.

5. DISCUSSION OF THE RESULTS

The values reported in Table 1 for the work to extract an isolated ion from a perfect crystal and in Table 3 for the energy of the saddle point for vacancy migration of an ion relative to the perfect crystal, give at once the values of the migration barriers of ions in NaCl and KCl crystals. These are reported in Table 4, together with the contributions arising from the Coulombic, repulsive and polarization energies. The effect of a harder overlap interaction between ions of opposite sign on migration barriers in alkali halides is not simply an increase in the repulsive-energy contribution to the energy of motion, but also a sizable increase in the Coulombic-energy contribution (see Table 4), which is essentially due to the larger ionic displacements of the two ions nearest to the moving ion in the saddle position.

The values that we have computed for the vacancy-migration barriers of ions in NaCl crystals can be compared directly with the theoretical values reported by MOTT and LITTLETON[4] (0·51 eV for the cation and 0·56 eV for the anion). These authors adopted for the repulsive interaction energy a form whose hardness lies between the hardness of the BORN–MAYER form and that of the VERWEY form, and they neglected repulsive interactions between non-nearest ions; moreover, in calculating the energy E_2 they apparently attributed an actual displacement only to the two ions nearest to the moving ion in the saddle position. Thus, the inclusion of the repulsive interactions

Table 4. Barriers for vacancy migration of cations and anions in NaCl *and* KCl *crystals (in* eV).

	BORN–MAYER repulsion				BORN–MAYER–VERWEY repulsion			
	U^{Coul}	U^{rep}	U^{pol}	U	U^{Coul}	U^{rep}	U^{pol}	U
NaCl:								
cation	−1·69	1·57	0·20	0·08	−1·32	1·83	0·36	0·87
anion	−2·02	2·10	0·40	0·48	−1·60	2·29	0·42	1·11
KCl:								
cation	−1·32	1·52	0·33	0·53	−1·17	1·92	0·38	1·13
anion	−1·49	1·75	0·38	0·64	−1·38	2·16	0·40	1·18

between next-nearest neighbours and a more refined treatment of the lattice distortion around the saddle point do in fact increase the separation between the theoretical migration barriers of the two types of ions, as suggested previously.[6] The slight decrease in the difference between the theoretical migration barriers for the two types of ions, in passing from the BORN–MAYER to the BORN–MAYER–VERWEY repulsive form, is largely due to the fact that the soft BORN–MAYER potential yields too low a value for the energy required to extract a negative ion from the perfect lattice, as discussed in section 3.

The theoretical values for the vacancy-migration barriers of ions in NaCl and KCl crystals reported in Table 4 can also be compared with the experimental values, which in these crystals are known with some certainty for the cation and can be estimated from indirect evidence for the anion. For the cation the best experimental values of the vacancy-migration barriers, which are obtained from the study of the temperature-dependence of the ionic conductivity and of the cation self-diffusion in the impurity range, are about 0·8 eV in both NaCl[15] and KCl[16] crystals. This figure is in agreement with the experimental value for the activation energy for dielectric loss of complexes in doped specimens, which is about 0·7 eV in both NaCl and KCl.[10] This activation energy is most probably the vacancy-migration barrier for a cation around a substitutional divalent impurity cation, and one may expect this barrier to be somewhat lower than the vacancy-migration barrier of a cation far removed from the impurity, owing to the inward displacements of the nearest neighbours of the impurity. The observed increase in the activation energy for the dielectric loss of complexes with increasing radius of the added impurity in doped KCl crystals[10] confirms this view. For the anion vacancy-migration barriers, of which no direct experimental determinations have been made, rough "experimental" values can be obtained from the measured activation energies for the anion diffusion in the intrinsic range (2·2 eV[7] and 2·3 eV[17] in NaCl; 2·0 eV[7] and 2·3 eV[18] in KCl), if one uses the known values for the energy of formation of Schottky defects (2·0 eV in NaCl[15]; about 2·2 eV in KCl[6]). In this way we obtain for the anion vacancy-migration barriers the approximate values 1·2–1·3 eV in NaCl and 0·9–1·2 eV in KCl. While the theoretical values of the vacancy-migration barriers obtained with the BORN–MAYER repulsive form are considerably lower than the experimental values above, the values computed with the harder repulsive form lie in the range of the experimental values. This fact supports the view that the use of the expression of the repulsive interaction energy obtained from equilibrium crystal data is a poor approximation for use in treating interactions at short distances,[8,6] and indicates that the hardness of the repulsive interaction is an important factor in determining the height of migration barriers in crystals. The BORN–MAYER repulsive form appears to provide a better approximation in KCl than in NaCl to the true repulsive interaction energy over the range of interionic distances of interest. However, it should be emphasized that the theoretical migration barriers that we have computed with the BORN-MAYER–VERWEY form for the overlap interaction energy should not be expected to represent necessarily the true migration barriers. On the one hand, the real migration path may differ somewhat from the migration path that we have considered; on the other, the VERWEY repulsive potential has an essentially heuristic character, as precise information on the actual hardness of the repulsive potential for ions interacting at short distances in alkali halide crystals is still lacking. The available quantitative experimental data on the behaviour of alkali halides under high hydrostatic pressures[19] refer to compressive strains much smaller than those involved in the present problem.

Acknowledgements—The authors are deeply indebted to Professor F. G. FUMI, who proposed this investigation, for valuable suggestions and for his critical reading of the manuscript. One of us (M.P.T.) acknowledges the tenure of a British Council Scholarship during the final stages of this work and the preparation of the manuscript.

REFERENCES

1. See, e.g., MOTT N. F. and GURNEY R. W., *Electronic Processes in Ionic Crystals*. Oxford University Press (1948); SEITZ F., *Imperfections in Nearly Perfect Crystals* (Ed. W. SHOCKLEY *et al.*) p. 3. John Wiley and Sons, New York (1952).
2. For a recent review, see LIDIARD A. B., *Handbuch der Physik* Vol. 20, p. 246. Springer, Berlin (1957).

3. BORN M. and GOEPPERT-MAYER M., *Handbuch der Physik* Vol. 24 (2), p. 633. Springer, Berlin (1933).
BORN M. and MAYER J., *Z. Phys.* **75,** 1 (1932).
HUGGINS M. L. and MAYER J., *J. Chem. Phys.* **1,** 643 (1933).
4. MOTT N. F. and LITTLETON M. J., *Trans. Faraday Soc.* **34,** 485 (1938).
5. BRAUER P., *Z. Naturforsch.* A**7,** 372 (1952).
6. FUMI F. G. and TOSI M. P., *Disc. Faraday Soc.* **23,** 92 (1957).
7. LAURENT J. F. and BÉNARD J., *J. Phys. Chem. Solids* **3,** 7 (1957).
8. FUMI F. G., *Phil. Mag.* **46,** 1007 (1955).
9. JOST W. and NEHLEP G., *Z. phys. Chem.* B**32,** 1 (1936).
10. DRYDEN J. S. and MEAKINS R. J., *Disc. Faraday Soc.* **23,** 39 (1957).
11. BROOKS H., *Impurities and Imperfections* p. 1. American Society for Metals, Cleveland, O. (1955).
12. VERWEY E. J. W., *Rec. Trav. Chim. Pays-Bas* **65,** 521 (1946).
13. TOSI M. P. and FUMI F. G., *Nuovo Cimento* **7,** 95 (1958).
14. LENNARD-JONES J. E. and INGHAM A. E., *Proc. Roy. Soc.* A**107,** 636 (1925).
15. ETZEL H. W. and MAURER R. J., *J. Chem. Phys.* **18,** 1003 (1950).
MAPOTHER D., CROOKS H. N., and MAURER R. J., *J. Chem. Phys.* **18,** 1231 (1950).
ASCHNER J. F., *Self-Diffusion in Sodium and Potassium Chloride,* Ph.D. Thesis, University of Illinois (1954).
16. KELTING H. and WITT H., *Z. Phys.* **126,** 697 (1949).
WAGNER C. and HANTELMANN P., *J. Chem. Phys.* **18,** 72 (1950).
17. HARRISON L. G., MORRISON J. A., and RUDHAM R., *Trans. Faraday Soc.* **54,** 106 (1958).
18. MORRISON J. A., unpublished work. The authors are indebted to Dr. MORRISON for communication of his results prior to publication.
19. BRIDGMAN P. W., *Proc. Amer. Acad. Arts Sci.* **76,** 1 (1945).

VOL.
10
195

J. Phys. Chem. Solids Pergamon Press 1959. Vol. 10. pp. 169–173.

RADIATION-INDUCED CHANGES IN THE FERROELECTRIC PROPERTIES OF SOME BARIUM TITANATE-TYPE MATERIALS*

ISSAI LEFKOWITZ†

Brookhaven National Laboratory, Upton, Long Island, New York

(*Received* 5 *December* 1958)

Abstract—Measurements of ceramic $BaTiO_3$ dielectric constant versus temperature as a function of pile irradiation showed modification of the Curie-point transition. In the case of commercially pure ceramic $BaTiO_3$ there was a depression of the dielectric-constant peak with little modification of the room-temperature dielectric constant. Ceramics made with additives showed a shift of the Curie point as well as a depression of the dielectric-constant peak. Material that had been exposed to an integrated pile dosage of 1×10^{18} *nvt* would not support reversible dielectric polarization.

EARLY work on radiation effects of ferroelectric materials has been sparse, and changes in the properties of ferroelectrics as a result of radiation have not been available in the literature. The results reported in the present paper were obtained during an investigation made to evaluate possible mechanisms for a charge-release phenomenon observed as a result of exposure of ferroelectric materials to low fluxes in a nuclear reactor. This experimental work is still in progress, but the results obtained are thought to be of sufficient interest to be reported at this time.

One of the earliest investigations reported was that of ROGERS[1], who measured the change in the dielectric constant versus temperature curve that resulted from a very large integrated exposure in the reactor. The reported dielectric constant versus temperature curve of the original ceramic material left considerable doubt as to its composition and density, since the room-temperature dielectric constant was quoted as being about 600, and the dielectric-constant peak about 1800. All of the published values for the ceramic material indicate very much higher values.[2] In addition, deterioration of the electrode coating resulting from the long integrated dosage further complicated the interpretation of the measurements. The measuring techniques did not make it possible to establish clearly the change in Curie point as a result of irradiation. In barium titanate one observes thermal hysteresis of the Curie point. This thermal hysteresis is clearly demonstrated in the study of cell-dimension variation versus temperature by KAY and VOUSDEN[3]. A curve plotted from measurements made in both directions obscures the Curie temperature by broadening the dielectric-constant peak. It is, therefore, important to make dielectric measurements continuous in one direction, i.e. either up or down in temperature to establish the dielectric peak temperature. Further, ROGERS did not report any measurements of tan δ and of the change in conductivity.

More recently, WITTELS and SHERRILL[4] have shown that a phase transformation occurs in a single crystal of barium titanate, from the tetragonal to the cubic structure, as a result of exposure to an integrated flux of 1×10^{20} *nvt*. The changes in the lattice parameters were measured by X-ray diffraction, and the cubic symmetry was confirmed by optical polarization microscopy. However, this work does not fully determine the fundamental changes in ferroelectric properties as a function of irradiation. One might wonder, for example, if the cubic–tetragonal transition point had been

* Work supported jointly by the U.S. Atomic Energy Commission and Frankford Arsenal.

† Gulton Industries: Guest Scientist, Brookhaven National Laboratory.

drastically shifted to much lower temperatures, or if the metastable cubic phase of NOVOTSILTSEV and KHODAKOV[8] had been formed (discussed later).

Modification of the dielectric constant versus temperature curve is important from an applied standpoint. Shifts of the dielectric temperature coefficient caused by a change in the Curie point would materially affect some capacitor and transducer applications.

In the course of the present study, measurements were made before and after reactor irradiation of dielectric constant versus temperature, tan δ versus temperature and spontaneous polarization versus temperature. Non-irradiated control samples showed no appreciable change in those properties over the time period of the experiment. Data on our commercially pure barium titanate follow published values quite closely.[2] Measurements were made on 12 typical ferroelectric ceramics, all based on the barium titanate system with additives. The samples designated by K and KEX had strontium additives, thereby shifting the Curie point toward room temperature,[5] while those designated by F100 and 103 were made with lead titanate, to enhance their piezoelectric properties, as well as to shift the Curie point. The irradiations were made in the Brookhaven reactor at an ambient temperature of about 50°C.

The results are plotted for two radiation levels one at an *nvt* of 1×10^{15} fast flux (fast flux being defined as neutrons with energies from 0·4 eV through the fission spectrum) and the second at 1×10^{18} *nvt*. Measurements were also made at 1×10^{13} *nvt*, but insufficient statistics left some doubt about the position of the corresponding curve. The data indicated that it would fall approximately between the normal material and the curve plotted for 1×10^{15} *nvt*.

Figs. 1 and 2 are a composite plot of dielectric constant versus temperature and tan δ versus temperature for barium titanate with the previously mentioned lead titanate additive (4 per cent). As can be seen from the shift in dielectric constant with radiation dose, there is a clear depression of

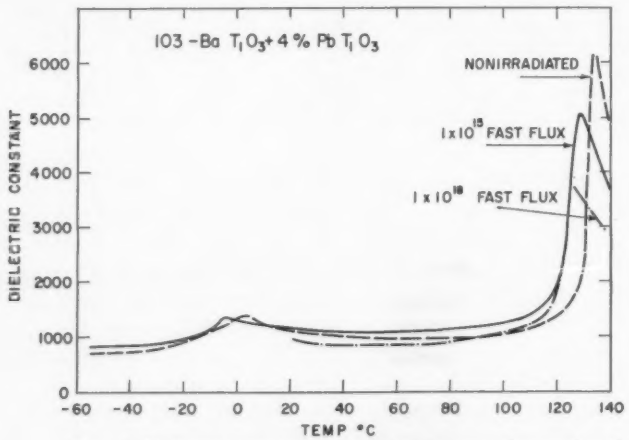

FIG. 1. Dielectric constant versus temperature of normal and reactor-irradiated $BaTiO_3$ + 4 per cent $PbTIO_3$.

the dielectric-constant peak at the Curie point and also a significant change of the Curie temperature to a lower value. It is also interesting to note that these same effects appear at the lower transition of 5°C. The tan δ shows a continuous increase as a function of the radiation. SUITA[6], of Osaka University, has reported that tan δ in an alkali halide also showed an increase as a result of radiation. This increase in tan δ was time-dependent, although there was a continually increased stable tan δ after several radiation exposures.

Table 1 is a composite listing of the results obtained from the other ferroelectric materials. It is interesting to note that the pure barium titanate showed no shift of the Curie temperature. The majority of the materials containing additives

VOL. 10 1959

showed changes of the Curie temperature, suggesting added sensitivity of the room-temperature dielectric constant of these materials in a radiation field environment. Analysis of the changes in the Curie point reported by previous investigators, both by ion replacement[5] and by hydrostatic pressure,[7] indicates that a decrease in cell dimension should depress the Curie temperature. Conversely an increase of cell dimension should be accompanied by an increase in the Curie temperature. The data reported here indicate that the changes observed would be too small to be detected by normal X-ray methods. Using the empirical formula suggested by MERZ[7]

$$\frac{\Delta x}{\Delta \theta} = 0{\cdot}303 \times 10^{-3}\ \text{Å}/^{\circ}\text{C},$$

one can obtain a value for the change of cell dimension (Δx) versus Curie temperature ($\Delta\theta$).

The largest change in the Curie temperature induced by radiation was 8°C, indicating that if this change is related to the lattice dimension it would result in a Δx of $2{\cdot}4 \times 10^{-3}$ Å, a value probably too small to be detected easily by normal X-ray methods.

One of the requirements for a ferroelectric material is that the reversible polarization should show a dielectric hysteresis loop. Measurements were made with a Sawyer–Tower circuit and the results are shown in Fig. 3, where the spontaneous polarization as a function of temperature was obtained from the hysteresis loop. After 1×10^{18} *nvt*, practically no hysteresis loop could be formed, yet some of the other properties associated with ferroelectrics still were present at this dosage, i.e. high dielectric constant rising to a peak near the Curie point. At this dosage no measurable shifts in lattice parameters were reported by WITTELS and SHERRILL[4].

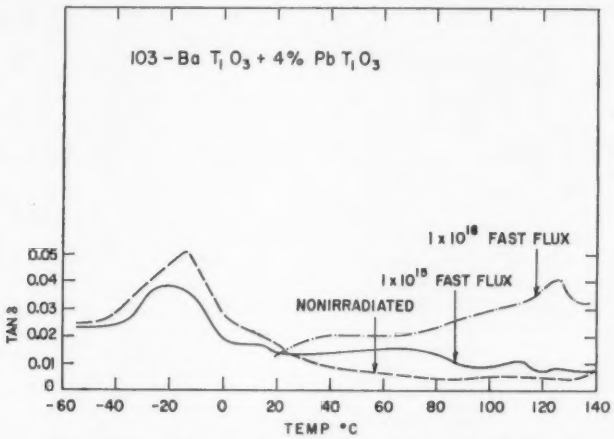

FIG. 2. Tan δ versus temperature of normal and reactor-irradiated $BaTiO_3$.

The material formed after 1×10^{20} *nvt* shows several similarities to the metastable cubic form of barium titanate that was reported by NOVOTSILTSEV

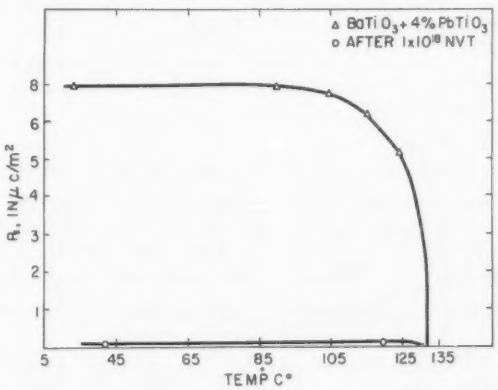

FIG. 3. Spontaneous polarization versus temperature of normal and reactor-irradiated $BaTiO_3$+4 per cent $PbTiO_3$.

Table 1. *Changes in dielectric properties as a function of reactor irradiation*

Material	Integrated dosage *nvt* (fast)	Dielectric constant at 28°C	Dielectric loss tangent at 28°C	Curie point (°C)	Curie point ϵ	Curie point, loss tangent
$BaTiO_3$	0	2600	0·01	119	9800	0·004
	1×10^{18}	1020	0·04	119	2520	0·04
$BaTiO_3$	0	1050	0·012	134	6400	0·005
with 4 per cent	1×10^{15}	1100	0·013	129	5200	0·008
$PbTiO_3$	1×10^{18}	900	0·017	126	3800	0·041
K-9000	0	8500	0·006	25	8600	0·008
	1×10^{18}	6500	0·076	< 25	7200	0·078
K-4000B	0	4800	0·011	20	4950	0·014
	1×10^{18}	2580	0·044	< 23	2760	0·042
K-1200	0	1510	0·014	119	1740	0·016
	1×10^{18}	970	0·031	≈ 122	1050	0·039
KEX 118 I	0	4550	0·014	8	5450	0·038
	1×10^{18}	3150	0·072			
$BaTiO_3$ with	0	1400	0·054	132	7150	0·016
4 per cent $PbTiO_3$	1×10^{18}	1050	0·011	132	4100	0·015
thin sheet						
F 100	0	1800	0·050	95	8050	0·01
	1×10^{18}	1350	0·032	89	3230	0·065

and KHODAKOV[8]. This cubic barium titanate is grown from a melt at 850°C. It reverts to normal tetragonal $BaTiO_3$ if it is heated to above 1000°C. This material is not ferroelectric, but does show an anomaly at about −50°C, suggesting that it transforms directly to the rhombohedral phase below this temperature.

The cubic form of barium titanate, grown by NOVOTSILTSEV and KHODAKOV, reportedly has a cell volume slightly greater than the tetragonal form. It was reported in an earlier paper[9] that the closer the c/a ratio is to unity the larger the volume of the unit cell, another similarity to the material produced by radiation damage.

To summarize briefly, low dosages of pile radiation produce measurable changes in some of the fundamental electrical properties of these materials. Tan δ goes up, the Curie-point peak is depressed, and when the ceramic is fabricated with additives there are indications of changes in the Curie temperature. The ferroelectric character of the material is sufficiently altered, so that it will no longer demonstrate reversible spontaneous polarization after a reactor irradiation of only 1×10^{18} *nvt*.

Acknowledgements—The pre-irradiated ϵ measurements were made under the direction of Mr. N. RUDNICK and Mr. G. HOWATT of Gulton Industries, both of whom also gave valuable advice.

I would like to express my indebtedness to Dr. ROSENBLATT and Dr. KROEGER of the Frankford Arsenal and Dr. B. C. FRAZER and Dr. G. J. DIENES of Brookhaven National Laboratory.

REFERENCES

1. ROGERS F. T. Jr., *J. Appl. Phys.* **27**, 1066 (1956).
2. VON HIPPEL, *Dielectrics and Waves* Figs. 28.6 and 28.9. John Wiley and Sons, New York (1954).

3. KAY H. F. and VOUSDEN P., *Phil. Mag.* **40,** 1019 (1949).
4. WITTELS N. C. and SHERRILL F. A., *J. Appl. Phys.* **28,** 606 (1957).
5. RUSHMAN D. F. and STRIVENS M. A., *Trans. Faraday Soc.* **42A,** 231 (1946).
6. Private communication.
7. MERZ W. J., *Phys. Rev.* **78,** 52 (1950).
8. NOVOTSILTSEV N. S. and KHODAKOV A. L., *Dokl. Akad. Nauk S.S.S.R.* **85,** 1263 (1952).
9. BELYAER I. N., NOVOTSILTSEV N. S., KHODAKOV A. L. and FESENKO E. G., *Dokl. Akad. Nauk S.S.S.R.* **78,** 875 (1951).

OL.
10
959

J. Phys. Chem. Solids Pergamon Press 1959. Vol. 10. pp. 174–181.

SUR LE DEPLACEMENT DE KNIGHT DES IMPURETES DANS LES METAUX

E. DANIEL

Physique des Solides, Paris.*

(*Received* 28 *October* 1958; *in revised form* 8 *December* 1958)

Résumé—Une étude théorique permet de justifier certaines hypothèses simplificatrices faites par Knight pour rendre compte du déplacement de Knight des impuretés dissoutes dans les métaux. Nous montrons ainsi que l'on peut négliger la polarisation des électrons de conductibilité par le noyau de l'atome d'impureté et qu'un même facteur permet de passer, pour l'impureté et la matrice, de la fonction d'onde de bas de bande à la fonction d'onde atomique correspondante. Les écarts observés entre les résultats expérimentaux et la formule empirique de Knight sont en général assez faibles, et de même ordre de grandeur que les erreurs introduites par les approximations faites.

Summary—Some simplifying assumptions made by Knight to explain the Knight shift of impurities in metals have been justified by a theoretical study. We show that one can neglect the polarization of the conductive electrons by the nucleus of an impurity atom; there is also a nearly constant ratio between the wave function at the bottom of the conduction band and the corresponding function for a free atom. The departure of measurements from Knight's empirical formula is often small and of the same order of magnitude as the errors due to the approximation used.

1. INTRODUCTION

Dans un métal pur, la résonance magnétique nucléaire est déplacée vers les fréquences élevées par rapport à celle qu'on observe pour le même métal dans un sel.[1] Le déplacement relatif $\Delta\nu/\nu$ est de l'ordre de 0,1 à 1 pour-cent. On l'explique par le paramagnétisme de Pauli des électrons de conductibilité.[2] Au niveau de Fermi, ces électrons s'orientent dans le champ magnétique statique H appliqué à l'échantillon; l'interaction de contact de leurs moments magnétiques avec ceux des noyaux équivaut à un accroissement local ΔH du champ magnétique tel que

$$\frac{\Delta\nu}{\nu} = \frac{\Delta H}{H} = \frac{8\pi}{3}\chi\langle|\psi_F(0)|^2\rangle.$$

χ désigne la susceptibilité paramagnétique de Pauli par atome, proportionnelle à la densité $n(E_F)$ par unité d'énergie des états au niveau de Fermi; $\langle|\psi_F(0)|^2\rangle$ est la valeur moyenne de la densité électronique au noyau prise, par unité d'énergie, sur la surface de Fermi, les ψ_F étant normalisées dans le volume atomique.

Dans un alliage **A**B, la densité des états au niveau de Fermi varie avec la concentration du soluté B dans la matrice A. De même, les fonctions d'ondes ψ_F se modifient tant aux noyaux A qu'aux noyaux B, ce qui altère leurs déplacements de Knight respectifs. Si, en particulier, un atome du métal B possède Z électrons de valence de plus qu'un atome du métal A, dans l'alliage cette charge électronique Z reste concentrée au voisinage de ce noyau B pour faire écran à la charge positive Z supplémentaire introduite en substituant B à A.[3,4] Nous avons étudié dans un autre article[5] comment varient avec la concentration de l'alliage les déplacements de Knight du solute et du solvant.

Nous discutons ici le déplacement de Knight des atomes *dissous* B aux faibles concentrations, et l'applicabilité d'une formule empirique proposée par Knight.[1] Nous trouvons que la polarisation des électrons au niveau de Fermi et au noyau de l'impureté est faible, et qu'elle ne suffit pas à expliquer les écarts entre la formule de Knight et les résultats expérimentaux.

* Ecole des Mines, 60 boulevard Saint-Michel, Paris 6e, France.

2. LA FORMULE EMPIRIQUE DE KNIGHT

Knight obtient un assez bon accord avec plusieurs résultats expérimentaux en supposant que, dans l'alliage :

(1) La susceptibilité paramagnétique électronique à employer dans la formule ci-dessus est celle de la matrice pure;

(2) La modification du caractère s de la fonction d'onde d'un électron au niveau de Fermi par rapport à celle d'un électron de valence de l'atome libre est la même pour l'atome dissous que dans la matrice.

C'est dire que, dans l'alliage **AB**, le déplacement de Knight relatif $\Delta\nu/\nu$ de l'atome dissous B est égal à celui des atomes A de la matrice, multiplié par le rapport des probabilités de présence des électrons de valence aux noyaux des atomes libres :

$$\frac{\Delta\nu}{\nu} \simeq \frac{\Delta\nu_A}{\nu_A} \times \frac{|\Phi_B(0)|^2}{|\Phi_A(0)|^2}$$

où les Φ désignent les fonctions d'ondes *atomiques*.

La première hypothèse semble assez justifiée : χ est proportionnelle à la densité des états au niveau de Fermi, qui se confond, aux dilutions infinies, avec celle de la matrice pure. Les corrélations ont certes sur χ une influence non négligeable; celle-ci est différente dans la matrice et dans le volume de l'atome dissous;[6] mais, faute d'une estimation précise, nous négligerons ce facteur, qui est sans doute petit.

La discussion qui suit analyse la *deuxième* hypothèse, qui peut s'écrire

$$\frac{\langle|\psi_F(\boldsymbol{r}_B)|^2\rangle}{|\Phi_B(0)|^2} \simeq \frac{\langle|\psi_F(\boldsymbol{r}_A)|^2\rangle}{|\Phi_A(0)|^2} \qquad (2)$$

où $\boldsymbol{r}_A$ et $\boldsymbol{r}_B$ indiquent respectivement les positions des atomes A et B.

Soit ψ_A la fonction d'onde d'un électron du bas de la bande de conductibilité dans le métal A pur, l'origine des coordonnées étant prise à un noyau. Soit de même ψ_B la fonction de bas de bande d'un métal qui serait formé d'atomes B seulement et tel que le potentiel subi par un électron dans chaque cellule y soit le même que lorsque l'atome B est dissous dans la matrice A.

Nous montrerons au paragraphe suivant que, si les électrons de conduction peuvent être traités comme assez libres, on a l'égalité approximative :

$$\frac{\langle|\psi_F(\boldsymbol{r}_B)|^2\rangle}{|\psi_B(0)|^2} \simeq \frac{\langle|\psi_F(\boldsymbol{r}_A)|^2\rangle}{|\psi_A(0)|^2}, \qquad (3)$$

c'est-à-dire que les électrons au niveau de Fermi de l'alliage contribuent très peu à l'écran produit par l'atome dissous sur son noyau. Nous vérifierons ensuite sur un modèle simple l'égalité approximative :

$$\frac{|\psi_B(0)|^2}{|\Phi_B(0)|^2} \simeq \frac{|\psi_A(0)|^2}{|\Phi_A(0)|^2}. \qquad (3a)$$

L'hypothèse de Knight qui correspond à l'égalité (2) sera ainsi justifiée.

3. CALCUL DE L'EFFET D'ECRAN

Il n'est pas question de calculer directement les fonctions d'ondes électroniques dans l'alliage. Ce que nous allons faire, c'est chercher la meilleure façon de ramener le calcul de la polarisation au problème simple de la diffusion d'électrons libres par un puits de potentiel.

3.1. *Difficultés du problème*

La substitution d'un atome B à un atome A équivaut à l'introduction d'une charge nucléaire supplémentaire Z. Elle modifie localement le potentiel du réseau d'une façon très forte, dans une région où, précisément, il n'est pas possible de considérer les électrons comme libres. Pour calculer la variation de densité électronique correspondante, on ne peut pas appliquer la méthode de Thomas–Fermi ou une méthode de perturbation usuelle. En effet, la méthode de Thomas–Fermi ne s'applique qu'avec un potentiel lentement variable; elle est inutilisable au voisinage du noyau et y donnerait d'ailleurs une densité infinie. Soit, d'autre part, ψ_A une fonction d'onde électronique solution de l'équation de Schrödinger avec le potentiel V_A du réseau de la matrice et pour l'énergie E_A du bas de la bande de conductibilité* :

$$\Delta\psi_A + 2(E_A - V_A)\psi_A = 0. \qquad (4)$$

Dans l'alliage infiniment dilué, on aura pour l'énergie E une nouvelle fonction $\phi\psi_A$ solution de

* Nous utiliserons dans la suite les unités atomiques $e = \hbar = m = 1$.

l'équation de Schrödinger avec le potentiel perturbateur V_p :

$$\Delta(\phi\psi_A)+2(E-V_A-V_p)\phi\psi_A = 0.$$

Compte tenu de l'équation (4), celle-ci devient :

$$\psi_A[\Delta\phi+2(E-E_A-V_p)\phi]+2\nabla\phi\nabla\psi_A = 0.$$

Si l'on pouvait négliger le terme $\nabla\phi\nabla\psi_A$, on retrouverait pour la fonction ϕ l'approximation classique d'un électron libre d'énergie $E-E_A$ diffusé par le potentiel perturbateur V_p.[3]

La fonction ψ_A varie très rapidement au voisinage d'un noyau; on ne peut donc pas négliger le facteur $\nabla\psi_A$ si ϕ varie rapidement elle-même, ce qui est le cas pour un potentiel coulombien avec écran, par exemple, de la forme $V_p = (Z/r)\exp(-qr)$. Le terme $\nabla\phi\nabla\psi_A$ devient même prépondérant au voisinage des nœuds de ψ_A, ce qui rend le calcul très malaisé et imprécis. On ne peut donc pas traiter les électrons de l'alliage comme des électrons libres, diffusés par le potentiel perturbateur V_p.

3.2 *Modèle utilisé*

Nous allons pouvoir éliminer la difficulté dûe au terme $\nabla\phi\nabla\psi_A$ en procédant de la façon suivante. On sait que dans un alliage AB à faible concentration, l'écran est très concentré autour des atomes B dissous et ne s'étend guère au-delà des polyèdres atomiques correspondants.[3,4] Nous admettons donc qu'au-delà de la sphère atomique d'un atome B dissous dans A, le potentiel subi par un électron est celui de la matrice. D'autre part, dans les métaux purs les fonctions d'onde de bas de bande ne présentent d'oscillations que dans un volume très limité autour des noyaux et elles sont très constantes au-delà,[3] comme le montre la Fig. 1 pour l'argent. Ce caractère doit subsister dans les alliages, où ces fonctions doivent se raccorder sans grandes modifications. Dans la matrice, la fonction d'onde d'un électron au bas de la bande de conductibilité satisfait à l'équation (4). Avec les notations correspondantes, dans la sphère atomique du métal B dissous, on a, *pour le bas de bande d'un métal pur qui serait fait d'atomes B* :

$$\Delta\psi_B+2(E_B-V_B)\psi_B = 0 \qquad (5)$$

Dénotons par $\phi\psi$ *la fonction d'onde d'un électron d'énergie* E *dans l'alliage*. A l'extérieur de la sphère atomique de B, c'est-à-dire pour $r > R$, rayon atomique, cet électron est soumis au potentiel V_A, à l'approximation que nous avons indiquée ci-dessus; il est soumis au potentiel V_B pour $r < R$. Prenons alors $\psi = \psi_B$ pour $r < R$ et $\psi = \psi_A$ pour $r > R$. En tenant compte des équations (4) et (5),

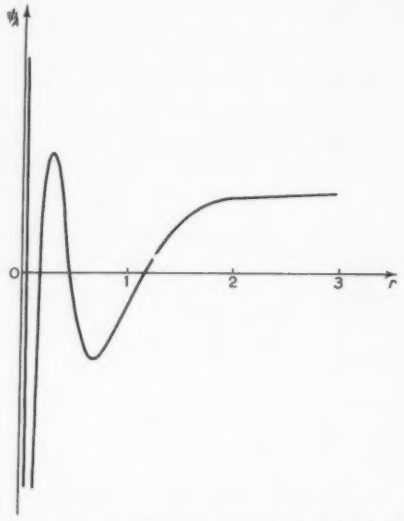

FIG. 1. Fonction d'onde de bas de bande de l'argent (d'après (3)).

nous voyons que ϕ doit satisfaire aux conditions suivantes :

$$\psi_A[\Delta\phi+2(E-E_A)\phi]+2\nabla\phi\nabla\psi_A = 0 \qquad \text{si } r > R \qquad (6a)$$

$$\psi_B[\Delta\phi+2(E-E_B)\phi]+2\nabla\phi\nabla\psi_B = 0 \qquad \text{si } r < R. \qquad (6b)$$

Nous allons maintenant ramener le problème à celui de la diffusion d'électrons libres par un puits de potentiel, en négligeant les termes de la forme $\nabla\phi\nabla\psi$. Avec le choix que nous avons fait des fonctions ψ_A et ψ_B, ceci est justifié par les considérations suivantes :

(1) $\nabla\psi_A$ est pratiquement nul dans la plupart du volume de la matrice et $\nabla\phi$ n'y devient jamais grand. Nous pouvons donc négliger $\nabla\phi\nabla\psi_A$ dans l'équation (6a). Ceci revient à supposer que la masse effective des électrons est voisine de la masse normale, ce qui est vrai dans les métaux ordinaires. Nous obtenons ainsi pour dans la matrice A l'équation d'onde d'un électron libre d'énergie $\frac{1}{2}k^2 = E-E_A$.

(2) A l'intérieur de la sphère B, $\nabla\psi_B$ est aussi à peu près nul à des distances du noyau supérieures à environ une unité atomique. Par contre, au voisinage immédiat du noyau, ψ_B oscille rapidement. C'est alors le facteur $\nabla\phi$ qui s'annule, permettant à son tour de négliger le terme $\nabla\phi\nabla\psi_B$ dans l'équation (6b). En effet, pour les petites valeurs de r, l'équation (6b) admet, si $\nabla\phi\nabla\psi_B$ est négligé, une solution $\phi \sim \sin\sqrt{2(E-E_B)}r/r$ pour laquelle $\nabla\phi(0) = 0$ dans tout le centre de l'atome d'impureté. Nous pouvons donc prendre pour fonctions ϕ les solutions à symétrie s de l'équation :

$$\Delta\phi+2(E-E_i)\phi = 0 \qquad \text{avec} \quad \begin{matrix} E_i = E_B & \text{si } r < R; \\ E_i = E_A & \text{si } r > R, \end{matrix} \tag{7}$$

les autres étant nulles à l'origine.

(3) L'équation (7) est celle de la diffusion d'électrons libres d'énergie $\frac{1}{2}k^2$ par un puits de potentiel de rayon R et de profondeur $\frac{1}{2}k_0^2 = E_A-E_B$.

Les fonctions d'onde ψ_A et ψ_B normalisées dans une sphère atomique n'ont pas, en général, strictement la même valeur pour $r = R$. La continuité de la fonction d'onde totale sur la sphère atomique :

$$\psi_A(R)\phi_A(R) = \psi_B(R)\phi_B(R)$$

entraine une discontinuité de la fonction ϕ, qui prend la valeur $\phi_A(R)$ pour $r = R+0$ et la valeur $\phi_B(R)$ pour $r = R-0$. La continuité en R de la dérivée de la fonction d'onde totale impose la même discontinuité pour les dérivées de ϕ de part et d'autre de la surface de la sphère :

$$\psi_A(R)\left(\frac{d\phi_A}{dr}\right)_{r=R+0} = \psi_B(R)\left(\frac{d\phi_B}{dr}\right)_{r=R-0}$$

car :

$$\left(\frac{d\psi_A}{dr}\right)_{r=R} = \left(\frac{d\psi_B}{dr}\right)_{r=R} = 0.$$

Par conséquent, la dérivée logarithmique de ϕ est continue en R. Dans ces conditions les déphasages créés par le puits de potentiel dans les composantes sphériques de la fonction d'onde ϕ sont les mêmes que pour une fonction d'onde d'électrons libres de même énergie satisfaisant aux conditions habituelles de continuité pour $r = R$. L'amplitude de la fonction ϕ se trouve simplement multipliée par le facteur $\psi_A(R)/\psi_B(R)$ pour $r < R$. Celui-ci est très voisin de l'unité, car les calculs de fonctions d'onde de bas de bande montrent que l'amplitude de ces fonctions dans la partie du volume atomique où elles sont presque constantes, est sensiblement celle qui correspondrait à un électron uniformément réparti dans le volume atomique.[3] Nous ne tiendrons donc pas compte de cette petite correction dans la suite.

Lorsque les volumes atomiques des métaux A et B sont les mêmes, nous prenons R égal à leur rayon atomique commun; dans le cas contraire, il nous semble raisonnable, en l'absence d'autre critère, d'adopter le rayon d'équilibre calculé selon l'élasticité classique. En l'absence d'effet de taille, nous déterminons la profondeur du puits de façon que la charge totale des électrons de conductibilité qu'il attire autour de B fasse exactement écran à l'excès Z des charges positives de l'ion B sur l'ion A qu'il remplace

On a, suivant la règale de FRIEDEL :[4]

$$Z = \frac{2}{\pi}\sum_{l=0}^{\infty}(2l+1)\eta_l,$$

où η_l est le déphasage introduit par le puits dans la composante sphérique d'ordre l de la fonction d'onde d'un électron libre diffusé et ayant l'énergie de Fermi de la matrice. Quand les volumes atomiques des métaux A et B diffèrent, nous en tenons compte dans le calcul de la charge d'écran selon le procédé utilisé par BLATT[7] dans son calcul de la résistivité résiduelle des alliages de cuivre et d'argent.*

* D'une façon générale, les déphasages η_l créés par un puits de potentiel de rayon a et de profondeur $\frac{1}{2}k_0^2$ pour un électron libre d'énergie $\frac{1}{2}k^2$ se calculent aisément au moyen des formules suivantes :

$$\operatorname{tg}\eta_l = \frac{kaj_{l-1}(ka)-\beta_l j_l(ka)}{kan_{l-1}(ka)-\beta_l n_l(ka)},$$

$$\beta_1 = k'a\frac{j_{l-1}(k'a)}{j_l(k'a)} \qquad \text{pour } l > 0$$

$$\operatorname{tg}\eta_0 = \frac{kaj_1(ka)+\beta_0 j_0(ka)}{kan_1(ka)+\beta_0 n_0(ka)}, \qquad \beta_0 = k'a\frac{j_1(k'a)}{j_0(k'a)}$$

dans lesquelles $k' = \sqrt{(k_0^2+k^2)}$ tandis que j_l et n_l sont respectivement les fonctions de Bessel et de Neumann sphériques. On déduit facilement ces formules de celles données d'habitude avec les fonctions de Bessel ordinaires.[8] Elles présentent l'intérêt de permettre l'emploi direct des tables des fonctions j_l et n_l.[9]

3.3 Calcul du facteur de polarisation p

Soit $E_F = E_A + \frac{1}{2}k_F^2$ l'énergie d'un électron au niveau de Fermi de l'alliage. Aux dilutions extrêmes, ce niveau de Fermi est le même que dans le métal A pur. Nous explicitons l'équation (7), pour les solutions qui nous intéressent, de la façon suivante :

$$\frac{d^2}{dr^2}(r\phi)+k^2{}_F(r\phi) = 0 \qquad \text{pour } r > R \text{ (8a)};$$

$$\frac{d^2}{dr^2}(r\phi)+k'^2(r\phi) = 0 \qquad \text{pour } r < R \text{ (8b)};$$

avec la condition de régularité : $r\phi \to 0$ quand $r \to 0$. Le problème se ramène donc au calcul simple de la fonction d'onde d'un électron libre diffusé par un puits de potentiel de rayon R et de profondeur (Fig. 2) :

$$\tfrac{1}{2}k_0^2 = \tfrac{1}{2}(k'^2 - k_F^2).$$

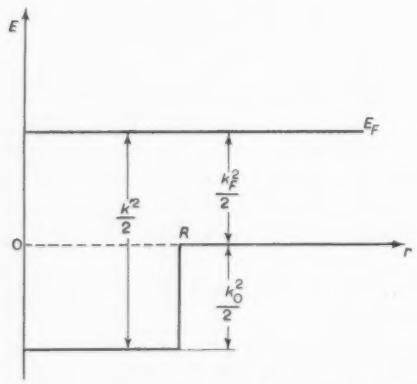

FIG. 2. Schéma du puits de potentiel.

A une solution de l'équation (8b) :

$$\phi = \frac{C}{r}\sin k'r$$

correspond la solution de l'équation (8a) :

$$\phi = \frac{1}{r}\sin(k_F r+\eta_0)$$

pourvu que la continuité de ϕ et de $d\phi/dr$ soit assurée pour $r = R$ par :

$$k' \operatorname{tg}(k_F R+\eta_0) = k_F \operatorname{tg} k'R$$

$$\text{et } C \sin k'R = \sin(k_F R+\eta_0). \qquad (9)$$

L'amplitude à l'origine de la fonction d'onde $\phi\psi$ correspondante est alors : $Ck'|\psi_B(0)|$. Dans le métal A pur, avec la même normalisation, on aurait $k_F|\psi_A(0)|$. Le rapport des densités au niveau de Fermi sur les noyaux de B et de A est donc, en reprenant les notations du paragraphe 2 :

$$\frac{\langle|\psi_F(r_B)|^2\rangle}{\langle|\psi_F(r_A)|^2\rangle} = P \cdot \frac{|\psi_B(0)|^2}{|\psi_A(0)|^2} \qquad (10)$$

avec, d'après (9) :

$$P = \left(\frac{Ck'}{k_F}\right)^2 = \frac{1}{1-\dfrac{k_0^2}{k'^2}\sin^2 k'R}. \qquad (11)$$

P est le facteur de polarisation produite par le puits carré sur la fonction d'électron libre ϕ. La courbe de la Fig. 3 montre comment il varie en

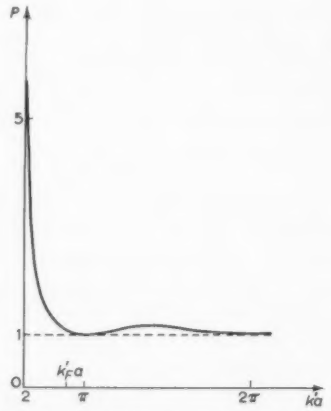

FIG. 3. Contribution à l'écran des électrons de la bande de conductibilité.

fonction de k dans la bande de conductibilité. En particulier pour un métal A monovalent avec $Z = 1$ ou $Z = 2$, le facteur P ne diffère de l'unité que de quelques centièmes au niveau de Fermi. Ceci montre que *la formation de l'écran autour de B intéresse peu les électrons* au niveau de Fermi et sur les noyaux B. On voit maintenant comment l'égalité (10) entraîne l'égalité approximative (3). Ce résultat n'est évidemment pas parfaitement rigoureux; il faudrait tenir compte des corrections dûes au terme $\nabla\phi\nabla\psi$ pour savoir dans quelle mesure il affecte le caractère s–p des fonctions

d'onde quand on passe du bas de la bande au niveau de Fermi. Ceci demanderait une étude particulière difficile.[10]

Le Tableau 1 donne les valeurs des paramètres pour le calcul de l'effet d'écran dans divers alliages pour lesquels existent des résultats expérimentaux, et les valeurs de P qui en résultent :

Tableau 1.

Alliage	R	k_F	Z	Z'	$k'R$	k_{0R}	P
* **Cu** Ga	2,8	0,72	2	1,84	2,76	1,89	1,07
Cu Al	2,8$_5$	0,72	2	+1,79	2,77	1,86	1,06
+ **Al** Cu	2,7$_5$	0,92	−2	−1,25	1,91	1,65	0,73
* **Ag** Cu	2,8	0,64	0	0,18$_5$	1,92	0,68$_5$	1,13
* **Ag** Cd	3,11	0,64	1	0,89	2,42	1,39	1,16
Ag Al	3	0,64	2	2	2,87	2,13	1,04
* **Au** Cu	2,8	0,64	0	0,21	1,92	0,73$_5$	1,15
Au Al	3	0,64	2	2	2,87	2,13	1,04

Le signe * indique les valeurs tirées des calculs de BLATT[9]. + Pour **Al** Cu ($Z' < 0$), il faut remplacer k_0^2 par $-k_0^2$ dans la formule (11).

Ces valeurs sont effectivement voisines de l'unité, à 10 pour-cent près environ. Avec la relation (10), ceci justifie approximativement la condition (3). Il est plus difficile de prouver que la condition (3a) est remplie. Nous nous bornerons à montrer qu'elle est vraie pour un modèle simple. Elle devient beaucoup moins sûre dans les cas réels, ce qui explique sans doute en partie les écarts entre les résultats expérimentaux et ceux qu'on obtient au moyen de la formule de Knight.

4. INFLUENCE DE LA FONCTION DE BAS DE BANDE

4.1 *Schéma de fonction de bas de bande dans le métal*

Nous avons vu que les fonctions d'onde de bas de bande calculées pour différents métaux présentent un caractère commun : elles oscillent fortement dans un rayon a sensiblement moitié du rayon atomique R; tous les nœuds sont concentrés dans l'intervalle $(0, a)$; elles sont au contraire très constantes au-delà avec une amplitude qui diffère peu de celle qu'aurait une fonction d'onde d'électron libre dans les mêmes conditions de normalisation. Nous obtenons qualitativement ce comportement en schématisant le potentiel V subi dans une sphère atomique par un électron au bas de la bande de conductibilité de la façon suivante (Fig. 4) :

$$\text{pour } r < a : V = -\frac{\lambda^2}{2} = -\tfrac{1}{2}(\mu^2+\rho^2)$$

$$\text{avec } \mu a = (2n-1)\frac{\pi}{2},$$

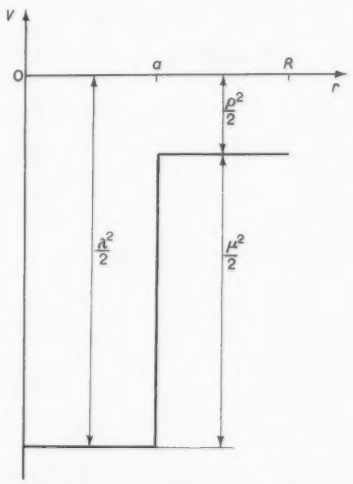

FIG. 4. Schéma du potentiel dans une sphère atomique.

si la bande de conductibilité correspond à la couche atomique de nombre quantique principal n;

$$\text{pour } a < r < R : V = -\frac{\rho^2}{2} = E_0,$$

où E_0 est précisément l'énergie au bas de la bande.

Dans ce conditions, la fonction d'onde de bas de bande est :

$$\psi_0 = A\frac{\sin \mu r}{r} \qquad \text{pour } r < a,$$

et

$$\psi_0 = (-1)^{n-1}\frac{A}{a} \qquad \text{pour } a < r < R,$$

avec

$$A^2 a = \left[\frac{4\pi}{3}\left(\frac{R^3}{a^3} - \frac{1}{2}\right)\right]^{-1}$$

lorqu'on la normalise dans la sphère atomique. Elle présente $(n-1)$ nœuds dans l'intervalle $(0, a)$, qui correspondent aux $(n-1)$ couches internes. Elle ne dépend pas de ρ et par conséquent ne change pas si on modifie ρ^2 d'une quantité constante.

En particulier, à l'effet de taille près, nous obtenons dans ce schéma la même fonction ψ_B dans le métal B pur et pour l'atome B dissous dans la matrice A; dans ce dernier cas, elle se raccorde exactement à la limite de la sphère atomique avec la fonction d'onde ψ_0 de la matrice calculée sur le même modèle.

Nous pouvons montrer avec ce modèle qu'il est correct à mieux que 10 pour-cent près de calculer les variations de densité à l'origine avec la dilatation du réseau, pour un métal pur, comme si l'on avait affaire à des électrons libres, même dans les cas réels. En effet, nous avons :

$$\frac{1}{|\psi(0)|^2}\frac{d}{dR}|\psi_{(0)}| = -\frac{3}{R}\frac{1}{1-\frac{1}{2}\frac{a^3}{R^3}}$$

$$= -\frac{1}{v}\frac{dv}{dR}\cdot\frac{1}{1-\frac{1}{2}\frac{a^3}{R^3}}$$

où $v = (4\pi/3)R^3$ est le volume atomique du métal. Puisque a vaut, à très peu près, la moitié de R, le terme correctif est inférieur à 10 pour-cent. Avec les potentiels réels qui sont plus attractifs au voisinage des noyaux, la variation relative doit être encore plus faible.

4.2 *Schéma correspondant de fonction d'onde atomique* Φ

Une certaine incertitude règne sur le potentiel qu'il est raisonnable d'adopter pour un électron de valence s dans l'atome libre. Nous montrerons sur un exemple que les résultats sont les mêmes à 10 pour-cent près dans les deux cas limites suivants :

(1) Nous conserverons le même potentiel que ci-dessus et seules les conditions aux limites changent. La fonction d'onde Φ peut s'étendre au-delà de R; elle n'est plus astreinte à avoir une dérivée nulle pour $r = R$, mais elle doit s'annuler à grande distance de façon à rester normalisable. L'énergie de l'électron s dans cet état est supérieur à E_0; c'est, en principe, l'énergie d'ionisation changée de signe.

Nous obtenons donc dans ce cas :

$$\text{pour } r < a : \Phi = A_0\frac{\sin \alpha r}{r};$$

$$a < r < R : \Phi = B\frac{\sin(\beta r + \eta)}{r}$$

$$r > R : \Phi = C\frac{e^{-\gamma r}}{r}.$$

Les relations

$$\begin{cases} \alpha^2 - \beta^2 = \mu^2 \\ \beta^2 + \gamma^2 = \rho^2, \end{cases}$$

les conditions de continuité de Φ et $d\Phi/dr$ en a et R :

$$A_0 \sin \alpha a = B \sin(\beta a + \eta),$$

$$\alpha a \operatorname{tg}(\beta a + \eta) = \beta a \operatorname{tg} \alpha a,$$

$$Ce^{-\gamma R} = B \sin(\beta R + \eta),$$

$$\beta R = -\gamma R \operatorname{tg}(\beta R + \eta),$$

et la normalisation de Φ permettent de calculer le déphasage η et les coefficients α, β, γ, A_0, B, C quand on connait les valeurs de a, R, E_0 et du coefficient n introduit dans la définition de μ.

(2) Le schéma précédent ne tient pas compte du fait que dans un atome bivalent les électrons de valence subissent en moyenne un potentiel plus attractif que dans l'atome monovalent qui le précède immédiatement. Une façon grossière d'en tenir compte consiste à remplacer, dans le calcul précédent ρ^2 par $\rho'^2 = \rho^2 + k_0^2$.

A titre d'exemple, pour un métal de la période de l'argent ($n = 5$) en prenant $a = 1{,}57$, $R = 3$, $\rho = 1$, nous trouvons dans la première hypothèse, quelque soit d'ailleurs la valence de ce métal, la valeur :

$$\frac{\psi_0^2(0)}{\Phi(0)^2} = 0{,}56$$

et en prenant pour l'atome dans la seconde hypothèse $\rho' = 1{,}2$, c'est-à-dire $k_0 R = 2$ (ce qui correspond $Z = 2$), nous trouvons

$$\frac{\psi^2(0)}{\Phi^2(0)} = 0{,}52.$$

L'écart entre les deux résultats est inférieur à 10 pour-cent. La relation (3a) est donc sans doute valable dans les mêmes limites tant que la valence de l'atome dissous ne dépasse pas 3.

5. CONCLUSION

Nous reproduisons dans le Tableau 2 les valeurs expérimentales et calculées par la formule de Knight du déplacement de Knight $\Delta\nu/\nu$ de l'atome B dans l'alliage dilué **AB** au déplacement $\Delta\nu_B/\nu_B$ dans le métal B pur, concernant quelques alliages pour lesquels nous connaissons des résultats.

Tableau 2

Alliage	$\frac{\Delta\nu}{\nu} / \frac{\Delta\nu_B}{\nu_A}$		P × Knight
	Expérience	Knight	
Cu Ga[1]	0,71	0,75	0,80
Cu Al[1]	0,64	0,70	0,74
Al Cu[1]	1,45	1,4	1,05
Ag Cu[1]	1,03	1,2	1,35
Ag Cd[11]	1,6	0,37	0,43
Ag Al[1]	0,95	0,82	0,85

Les chiffres des deux premières colonnes montrent que la formule de Knight est valable à 20 pour-cent près, sauf dans le cas de l'alliage **Ag** Cd. Ceux de la dernière colonne montrent que la polarisation électronique P joue un rôle restreint et ne suffit pas à expliquer les différences entre les deux premières colonnes. Il faut par conséquent chercher dans les approximations faites l'origine des écarts observés. Il faudrait savoir en particulier comment varient dans l'alliage la susceptibilité paramagnétique des électrons, leur masse effective et le caractère s des fonctions d'ondes quand on passe du bas de la bande de conductibilité au niveau de Fermi dans l'alliage. Des mesures systématiques précises seraient d'un grand intérêt pour la connaissance de la structure électronique des alliages et fourniraient à une étude théorique approfondie une base qui manque actuellement.

BIBLIOGRAPHIE

1. KNIGHT W. D., *Solid State Physics* **2,** 93 (1956).
2. TOWNES C. H., HERRING C. and KNIGHT W. D., *Phys. Rev.* **77,** 852 (1950).
3. MOTT N. F. and JONES H., *Metals and Alloys.* Oxford University Press (1936).
4. FRIEDEL J., *Advanc. Phys.* **3,** 446 (1954).
5. BLANDIN A., DANIEL E. et FRIEDEL J., *Phil. Mag.* **4,** 180 (1959).
6. PINES D., *Solid State Physics* **1,** 367 (1955).
7. BLATT F. J., *Phys. Rev.* **108,** 285 (1957).
8. MOTT N. F. and MASSEY H. S. W., *The Theory of Atomic Collisions.* Oxford University Press (1949).
9. *Tables of Spherical Bessel Functions.* Columbia University Press, New York (1947).
10. COHEN M. H. et HEINE V., *Advanc. Phys.* **7,** 395 (1958).
11. DRAIN L. E., Metallurgy Division, A.E.R.E. Communication privée.

J. Phys. Chem. Solids Pergamon Press 1959. Vol. 10. pp. 182–186.

THE FERRIMAGNETISM AND CRYSTAL CHEMISTRY OF SUBSTITUTED MANGANESE–TIN SPINELS

M. A. GILLEO* and D. W. MITCHELL

Bell Telephone Laboratories, Inc., Murray Hill, New Jersey

(*Received* 17 *December* 1958)

Abstract—In a $Me_2^{2+}Sn^{4+}O_4$ spinel, Sn^{4+} is known to occupy octahedral sites. Therefore manganese-tin spinel, (Mn)[MnSn]O_4, should be antiferromagnetic because of the strong interaction between octahedral and tetrahedral ions characteristic of magnetic spinels. The magnetic exchange interaction in a (Mn^{2+})–O^{2-}–$[Mn^{2+}]$ linkage is of particular interest because it is known to be much weaker than is the case for Fe^{3+}, with which Mn^{2+} is isoelectronic; magnetic measurements on Mn_2SnO_4 yield a Néel temperature of 58°K.

When the initial equality of the sublattice magnetizations of Mn^{2+} ions in octahedral and tetrahedral sites is upset by partial substitution of the nonmagnetic, divalent ions Mg^{2+} and Zn^{2+} for Mn^{2+}, spontaneous magnetization appears. The Néel temperature is decreased by these substitutions largely as a consequence of the smaller number of interactions between the reduced number of Mn^{2+} ions in the two different sites. For equal substitutions for Mn^{2+} in Mn_2SnO_4, the moment changes more rapidly in the case of Mg^{2+} than Zn^{2+}. The moment depends upon the size of the substituent ion because, in this case, the ions involved are spherical and of the same valence. The small size of the substituent ions leads to a predominance of occupation of the octahedral sites because substitution there will increase the Madelung potential both by reduction of the lattice constant and increase of the oxygen parameter. The sequence, Mg^{2+}, Zn^{2+}, Mn^{2+}, of increasing ionic sizes corresponds to that of increasing lattice constants, 8·60, 8·67, 8·88 Å, of the respective tin spinels. Substitution of Ge^{4+} for Sn^{4+} ultimately takes place principally in tetrahedral sites because of the very small size of Ge^{4+}.

Similarly, spontaneous magnetization arises with oxidation of Mn_2SnO_4. The resultant oxidized manganese ions (presumably Mn^{3+}) are of the same average valence, though of smaller size, than the octahedral ions and, therefore, also appear in octahedral sites. Because Sn^{4+} is rejected to maintain valence balance, the octahedral sublattice magnetization is increased by oxidation.

1. INTRODUCTION

THE Fe^{3+}–O^{2-}–Fe^{3+} linkage is of fundamental importance to the antiferro- and ferrimagnetism of a large number of magnetic oxides,[1] many of which are of practical value. Despite the fact that Mn^{2+} is isoelectronic with Fe^{3+}, the corresponding linkage seems to have very much less interaction strength. In order to gain a better understanding of the Mn^{2+}–O^{2-}–Mn^{2+} linkage, a spinel system was sought which would contain this linkage and which would be isostructural with one containing Fe^{3+}.

It was thought that the composition Mn_2SnO_4 would meet these requirements. Presumably it would form a spinel because the spinels Zn_2SnO_4[2] and Mn_2TiO_4[3] have already been reported; this was found to be the case. Zinc–tin spinel is inverse,[4] (Zn)[ZnSn]O_4, where ( ) indicates a tetrahedral site, 8(*a*), and [ ] indicates an octahedral site, 16(*d*). Accordingly, Mn–Sn spinel was also found to be inverse, so that we have linkages of the type (Mn^{2+})–O^{2-}–$[Mn^{2+}]$ present which are entirely analogous with linkages in the ferrites containing Fe^{3+} (ferrimagnetic spinels containing iron).

2. EXPERIMENTAL

The Mn–Sn spinels were prepared by solid–solid reaction of the constituent oxides, which were mixed by hand in a mortar. All MnO employed was pre-fired in hydrogen at 1100°C in order that no manganese should be present with a valence

* Present address: Lockheed Aircraft Corporation, Missiles and Space Division, Palo Alto, California.

greater than two. The oxides SnO_2, MgO and ZnO were pre-fired in oxygen at 1100°C and GeO_2 at 1000°C. All raw materials were spectrochemically analyzed qualitatively for impurities prior to use.

After an initial firing at 1000°C for 16 hr in nitrogen, the material was reground in a mortar and refired in nitrogen at 1150–1300°C for 2–4 hr. The house nitrogen contained a small amount of oxygen so that it was passed through copper turnings at 850°C when a less-oxidized Mn–Sn spinel was desired.

The firing time at higher temperatures was kept as short as was compatible with satisfactory reaction, as determined from X-ray powder photographs taken with Cr$K\alpha$ radiation. In this way the loss of tin oxide was kept small.

The final material was analyzed for total manganese by the bismuthate method with sulfuric acid as the solvent. The average valence of manganese was determined by the oxidation of a ferrous chloride–hydrochloric acid solution which resulted from the dissolution of a sample of material in a sealed-off tube; the excess ferrous chloride was determined by titration with a ceric sulfate solution.

Magnetic measurements in the temperature range 1·3–300°K were made in magnetic fields of 1000–12,500 Oe with the pendulum magnetometer of BOZORTH. The samples were cylinders with a length-to-diameter ratio of about 3:1 and weights of 0·6–1·0 g.

The Curie temperature, T_C, was determined from the inflection point[5] of the n_B versus T curve for a constant applied field,* H_a, of 7700 Oe (Fig. 1); n_B is the magnetic moment in Bohr magnetons, μ_B, per nominal formula unit.

The saturation moment, $n_B(\infty, 0)$, at infinite field (i.e. a field adequate for saturation) and zero temperature was determined by extrapolation of curves of n_B versus H at a constant temperature of 1·3–4·2°K, which is substantially zero; H is H_a less the demagnetizing field for the particular cylindrical specimen.

* In the case of a perfect antiferromagnetic material, such as stoichiometric Mn_2SnO_4, a spontaneous moment is not present. Therefore, this definition is not applicable. The temperature at which order in the orientation of the moments of the magnetic ions disappears will be referred to as the Néel temperature.

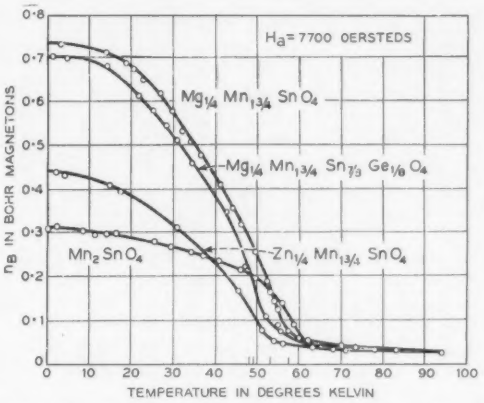

FIG. 1. Curves of n_B versus T at constant H_a for Mn–Sn spinels.

3. INTERPRETATION OF MAGNETIC DATA

Magnetic and crystal-chemical data for the Mn–Sn spinels which were prepared (Table 1) provide us with the information necessary for a good picture of this spinel system. Because the compounds examined contained manganese with an average valence greater than two, it is first necessary to understand the effect of Mn^{3+} on the magnetic moment. The ion Mn^{3+} is smaller than Mn^{2+} and of higher valence. Therefore, it would probably occupy an octahedral site to maximize the Madelung constant, M.[4,6]

The effect of oxidation on Mn_2SnO_4 may be expressed by the reaction

$$Mn_2SnO_4+\frac{b}{4+b}O_2 \rightarrow \frac{4}{4+b}(Mn^{2+})\times$$
$$\times\left[Mn^{2+}_{1-(b/2)}Mn^{3+}_{b}Sn^{4+}_{1-(b/2)}\right]O_4+\frac{3b}{4+b}SnO_2. \quad (1)$$

In terms of the average valence $\bar{v}$ of manganese, we have

$$b = 4(\bar{v}-2)/(4-\bar{v}) \quad (2)$$

and

$$n_B = (3/2)b = 6(\bar{v}-2)/(4-\bar{v})\,\mu_B, \quad (3)$$

where moments of 5 and 4 μ_B have been assumed for Mn^{2+} and Mn^{3+} respectively. For Mn_2SnO_4 oxidized to $\bar{v} = 2{\cdot}12$ ((a), Table 1), we find $b = 0{\cdot}255$ and $n_B = 0{\cdot}38\,\mu_B$. When the observed value of $0{\cdot}35\,\mu_B$ is adjusted for the amount of

Table 1. Crystal-chemical and magnetic data for manganese-tin spinels

Nominal composition	$\bar{v}$	T_C(°K)	$n_B(\infty, 0)$* (μ_B)	a_0(Å)
(a) Mn_2SnO_4	$2{\cdot}12 \pm 0{\cdot}01$	58 ± 3	0·35	8·84†
(b) $Mn_2Sn_{\frac{7}{8}}Ge_{\frac{1}{8}}O_4$	2·10	—	0·40	8·82
(c) $Mg_{\frac{1}{4}}Mn_{1\frac{3}{4}}SnO_4$	2·14	53	0·81	8·83
(d) $Mg_{\frac{1}{4}}Mn_{1\frac{3}{4}}SnO_4$	2·23	—	0·78	8·81
(e) $Mg_{\frac{1}{4}}Mn_{1\frac{3}{4}}Sn_{\frac{7}{8}}Ge_{\frac{1}{8}}O_4$	2·13	49	0·77	8·81
(f) $Zn_{\frac{1}{4}}Mn_{1\frac{3}{4}}SnO_4$	2·10	48	0·50	8·82

* Saturation moment per nominal formula unit at 0°K.

† A lattice constant of 8·88 Å has been obtained for $\bar{v} = 2$ by extrapolation from points for several values of $\bar{v}$.

magnetic phase present according to equation (1) and for the change in molecular weight with oxidation, the value of $n_B(\infty, 0)$ observed for the oxidized phase becomes 0·37 μ_B. The agreement is quite good, so that the oxidation reaction and the origin of the moment assumed may be correct.

However, it remains to be shown experimentally that Mn^{3+} is present in octahedral sites, as in equation (1), and that the moment of the octahedral magnetic ions exceeds that of the tetrahedral ions. It is known that the Ge^{4+} ion is sufficiently small so that it will exclusively occupy the tetrahedral site in spinels formed with divalent transition metal ions.[7] Therefore, the partial substitution of Ge^{4+} for Sn^{4+} should cause an increase of the moment above that observed for oxidized Mn–Sn spinel.* This expectation is borne out by $Mn_2Sn_{\frac{7}{8}}Ge_{\frac{1}{8}}O_4$ ((b), Table 1) with $\bar{v} = 2{\cdot}10$. For this compound $n_B(\infty, 0) = 0{\cdot}4\ \mu_B$ (Fig. 2), which is greater than that for Mn_2SnO_4 ((a), Table 1) even though it has a larger value, 2·12, of $\bar{v}$. Quantitative conclusions are difficult because some Ge^{4+} may be rejected by oxidation according to equation (1).

When the smaller ion, Mg^{2+}, is substituted partially for Mn^{2+}, it would be expected to occupy predominantly the octahedral sites. This preference is caused by the increase of the Madelung constant M brought about by the decrease of lattice constant (a_0, Table 1) and the increase of the oxygen parameter u in adjustment for a smaller average size of a divalent ion in octahedral sites; a decrease of u for a smaller ion in a tetrahedral site would decrease M.[4,6]

For replacement of $[Mn_{\frac{1}{4}}^{2+}]$ by $[Mg_{\frac{1}{4}}^{2+}]$, the magnetic moment of the octahedral ions would decrease by 1·25 μ_B per formula unit. For the compound $Mg_{\frac{1}{4}}Mn_{1\frac{3}{4}}SnO_4$ ((c), Table 1), a moment $n_B(\infty, 0) = 0{\cdot}81\ \mu_B$ was observed (Fig. 2), which must now arise from a preponderance of the tetrahedral moment. The change in the octahedral moment with $[Mg_{\frac{1}{4}}^{2+}]$ substitution observed in partially oxidized Mn–Sn spinel is about 0·35+

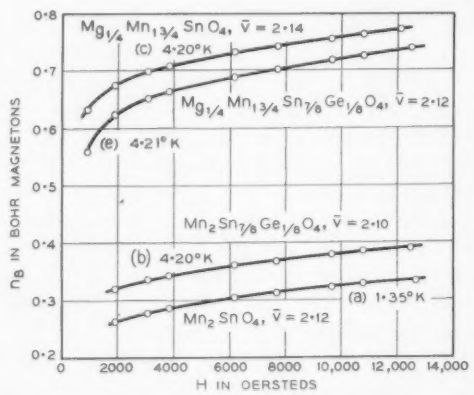

FIG. 2. The effect of partial replacement of Sn^{4+} by Ge^{4+} on the saturation moment of Mn–Sn spinels.

* For small substitutions the increase of the average valence of the tetrahedral ions which would result from the entry of Ge^{4+} into these sites is probably insufficient to cause M to alter favorably.[6] Therefore, Ge^{4+} will probably be present predominantly in octahedral sites with initial substitution. It has been presumed that u for Mn–Sn spinel may be in the neighborhood of 0·385, because the size of the Sn^{4+} ion approaches that of the larger Mn^{2+} ion in octahedral coördination.

$+0{\cdot}81 = 1{\cdot}16\ \mu_B$. With increased oxidation of a $[Mg_{\frac{1}{4}}^{2+}]$-substituted Mn–Sn spinel, the moment should decrease; such a decrease was observed, though the change was rather small (Fig. 3).

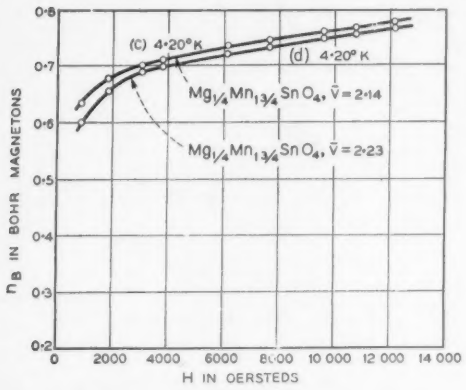

FIG. 3. The effect of oxidation on the saturation moment of Mg-substituted Mn–Sn spinel.

With a partial substitution of Ge^{4+} for Sn^{4+} in a $[Mg_{\frac{1}{4}}^{2+}]$-substituted compound, $n_B(\infty, 0)$ should also decrease, which it did for $Mg_{\frac{1}{4}}Mn_{1\frac{1}{2}}Sn_{\frac{3}{4}}Ge_{\frac{1}{4}}O_4$ ((e), Table 1) (Fig. 2). The decrease of $0{\cdot}04\ \mu_B$ was larger than the increase for the same Ge^{4+} substitution in oxidized Mn_2SnO_4 (Fig. 2); it happens that the changes of $\bar{v}$ involved have opposite effects in the two cases.

Finally, Zn^{2+} was substituted partially for Mn^{2+}. The Zn^{2+} ion is somewhat larger than Mg^{2+}, but smaller than Mn^{2+}, as can be seen from the lattice constants of the Mg–, Zn– and Mn–Sn spinels, which are 8·60,[8] 8·67[2] and 8·88 Å (Table 1), respectively. For $Zn_{\frac{1}{4}}Mn_{1\frac{1}{2}}SnO_4$ ((f), Table 1), the moment ($0{\cdot}5\ \mu_B$) was smaller than for the same Mg^{2+} substitution ($0{\cdot}81\ \mu_B$ for (c) Table 1) (Fig. 4). Presumably the increased size of the substituent ion has reduced the energy difference for occupancy of the different sites.

In all cases a fractional substitution of a nonmagnetic ion for Mn^{2+} decreased T_C (Table 1). However, the value of T_C is most sharply reduced by the entry of the nonmagnetic ions Ge^{4+} and Zn^{2+} into the tetrahedral sites. The sharp reduction probably occurs because of the rapid decrease in the coherence of the magnetic exchange interactions; the newly appeared randomness in the distribution of magnetic ions in tetrahedral sites, in addition to the randomness inherent in the distribution of magnetic ions over the octahedral sites, is probably responsible.

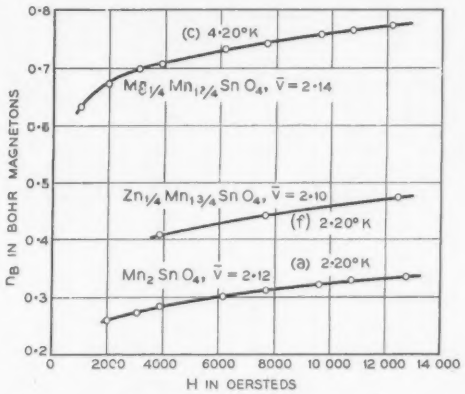

FIG. 4. The effect of fractional substitution of Mg and Zn for Mn on the saturation moment of partially oxidized Mn–Sn spinel.

The Curie temperature of about 58°K for somewhat oxidized (Mn)[MnSn]O_4 is less than one-tenth that of the corresponding ferrite (Fe)[FeMg]O_4, for which the Curie temperature extrapolates to 690°K.[9] Thus the importance of the electronic configuration to the strength of the exchange interaction is emphasized by the great difference in its strength for the isoelectronic ions, Mn^{2+} and Fe^{3+}, in isostructural compounds. Of course, the distances are longer in Mn–Sn spinel ($a_0 = 8{\cdot}88$ Å, Table 1) than in Mg–Fe spinel (for (Fe)[FeMg]O_4, $a_0 = 8{\cdot}37$ Å by extrapolation),[10] which would also reduce the interaction strength.

Acknowledgements—We are greatly indebted to Dr. R. M. BOZORTH for the use of his apparatus for low-temperature measurements and to Mr. A. J. WILLIAMS for his help. Discussions with Dr. S. GELLER of the crystallographic parts of the problem were a valuable aid.

REFERENCES

1. GILLEO M. A., *Phys. Rev.* **109,** 777 (1958).
2. TAYLOR N. W., *Z. phys. Chem.* B**9,** 241 (1930).
3. HOLGERSSON S. and HERRLIN A., *Z. anorg. allg. Chem.* **198,** 69 (1931).

4. VERWEY E. J. W. and HEILMAN E. L., *J. Chem. Phys.* **15,** 174 (1947).
5. CURIE P., *Ann. Phys.* (*Paris*) **5,** 289 (1895).
6. VERWEY E. J. W., DE BOER F. and VAN SANTEN J. H., *J. Chem. Phys.* **16,** 1091 (1948).
See also GORTER E. W., *Philips Res. Rep.* **9,** 295 (1954) for an extensive discussion.
7. ROMEIJN F. C., *Philips Res. Rep.* **8,** 304 (1953).
8. NOTTA G. and PASSERINI L., *Atti Accad. naz. Lincei* **9,** 557 (1929).
9. EPSTEIN D. J. and FRACKIEWICZ B., *J. Appl. Phys.* **29,** 376 (1958).
10. KRIESSMAN C. J. and HARRISON S. E., *Phys. Rev.* **103,** 857 (1956).

VOL.
10
1959

J. Phys. Chem. Solids Pergamon Press 1959. Vol. 10. pp. 187–190.

THE INTERACTION OF MAGNETIC IONS IN $Gd_3Mn_2Ge_2GaO_{12}$ AND RELATED GARNETS

M. A. GILLEO* and S. GELLER

Bell Telephone Laboratories, Inc., Murray Hill, New Jersey

(*Received* 17 *December* 1958)

Abstract—The existence of appreciable (c)–(a) ferrimagnetic exchange interaction in the garnet structure has been established by the observation of ferrimagnetism in $\{Gd_3\}[Mn_2](Ge_2Ga)O_{12}$. The Néel temperature is about 8°K; the $1/\chi$ versus T curve is linear for $T > 35$°K with an intercept of -8°K at $1/\chi = 0$ and a Curie constant of $5{\cdot}6 \times 10^{-3}$ μ_B deg. per Oe per formula unit. The magnetic moment at 0°K probably corresponds to $3n_B\{Gd^{3+}\} - 2n_B[Mn^{2+}] = 11$ μ_B, because the moments observed at temperatures between 4·2 and 1·5°K extrapolate to not less than 9·6 μ_B at 0°K. The moment decreases for the compositions $\{MnGd_2\}[Mn_2](Ge_3)O_{12}$ and $\{CaGd_2\}[Mn_2](Ge_3)O_{12}$ in that order. In these three cases the $1/\chi$ versus T curves are concave downward below 20°K, as would be expected in the case of ferrimagnetism.

No spontaneous magnetization is observed in $\{MnY_2\}[Mn_2](Ge_3)O_{12}$ and $\{CaY_2\}[Mn_2](Ge_3)O_{12}$ down to 1·3°K. For these compounds the $1/\chi$ versus T curve is concave upward below 20°K, as would be expected for a weak (a)–(a) antiferromagnetic interaction. Only a very weak (c)–(a) interaction is present in the first case as a consequence of one-third occupancy of dodecahedral sites by Mn^{2+} ions.

1. INTRODUCTION

OXIDE compounds in the garnet structure system (space-group $O_h(10)-Ia3d$) are of a general formula which may for our purposes be conveniently written

$$\{A_3\}[B_2](C_3)O_{12}$$

where { } represents a site, (c), dodecahedrally surrounded by oxygen ions, [ ] an octahedral site, (a), and ( ) a tetrahedral site, (d). The presence of three crystallographically different sites accessible to magnetic ions makes the garnet structure system valuable in the study of superexchange interactions.

In yttrium–iron garnet, $\{Y_3\}[Fe_2](Fe_3)O_{12}$, a negative superexchange interaction between the $[Fe^{3+}]$ and (Fe^{3+}) ions through the intervening oxygen ions results in ferrimagnetism with a Curie temperature, T_C, of 545°K.[1,2] The ferrimagnetism can be well described by the molecular field theory of NÉEL[3] with interaction coefficients† $n_{aa} = -352$, $n_{ad} = 742$, $n_{dd} = -211$. From these coefficients it is easily seen that the $[Fe^{3+}]$–O^{2-}–(Fe^{3+}) linkages, which correspond to n_{ad}, must be the source of the strongest interactions. The geometry of the linkages as determined by X-ray diffraction studies[4] is clearly consistent with that required for substantial interaction in the theoretical treatment of ANDERSON[5].

In the case of gadolinium–iron garnet, $\{Gd_3\}[Fe_2](Fe_3)O_{12}$, additional interaction coefficients, n_{cc}, n_{ca}, n_{cd}, must be taken into account. Because each of these coefficients is known to be small and under the assumption that the iron–iron interactions are little altered by the substitution of gadolinium for yttrium, PAUTHENET[6] and ALÉONARD and BARBIER[7] evaluated these interactions as follows: $n_{ca} = -20$, $n_{cd} = 35$, $n_{cc} \simeq 0$. For these reasons the accuracy of the n values is smaller for the gadolinium–iron than for the iron–iron system.

The existence of a (c)–(a) interaction is only implied in the case of gadolinium–iron garnet. Furthermore, the interaction geometry is quite unfavorable to superexchange interaction; the

* Present address: Lockheed Aircraft Corporation, Missiles and Space Division, Palo Alto, California.

† The double subscript indicates the sites between which interaction takes place.

included angles in the $\{Gd^{3+}\}$–O^{2-}–$[Fe^{3+}]$ linkages are probably similar to the 102·8° and 104·7° angles found for yttrium–iron garnet.[4] It is known from theory[5] and observation[8] that in oxide systems superexchange interaction may be considered negligible for included angles near 90°. Consequently, we considered that explicit experimental evidence for the existence of (*c*)–(*a*) interaction would reinforce the interpretation of the magnetic properties of gadolinium–iron garnet in terms of the NÉEL theory.

In the course of attempts to learn more about these interactions and of the crystal chemistry of the garnets, GELLER and MILLER[9] synthesized a number of garnets $\{M^{2+}R_2^{3+}\}[Mn_2](Ge_3)O_{12}$ Among these were the following:

$$\{CaY_2\}[Mn_2](Ge_3)O_{12}$$

$$\{CaGd_2\}[Mn_2](Ge_3)O_{12}$$

$$\{MnY_2\}[Mn_2](Ge_3)O_{12}$$

$$\{MnGd_2\}[Mn_2](Ge_3)O_{12}$$

For these compounds, the distribution of the ions is deduced on crystal-chemical grounds.* However, the $\{Gd^{3+}\}$–O^{2-}–$[Mn^{2+}]$ interaction is so weak that the dilution of $\{Gd^{3+}\}$ by $\{Ca^{2+}\}$ seriously reduces the feasibility of observing it. Therefore the compound

$$\{Gd_3\}[Mn_2](Ge_2Ga)O_{12}$$

was synthesized also. This compound gave the most conclusive results yet obtained on (*c*)–(*a*) interactions. Magnetic measurements on the four other compounds provided additional data valuable to the understanding of magnetic interactions in garnet-structure compounds.

2. EXPERIMENTAL

The samples were prepared by solid–solid reaction.[9] Crystal-chemical data for all compounds except $\{Gd_3\}[Mn_2](Ge_2Ga)O_{12}$ are given by GELLER and MILLER[9]; the lattice constant for the latter compound is 12·550±0·003 Å. Analysis for the average valence of manganese in this compound by D. W. MITCHELL yielded a value of 2·08.

Magnetization measurements were carried out in the temperature range 1·3–300°K in fields of 1000–12,000 Oe by means of the pendulum magnetometer of BOZORTH[10]. The specimens were long cylinders or spheres. Demagnetizing field corrections based on geometry and relative density were applied. Magnetic moments, n_B, are given in Bohr magnetons, μ_B, per formula unit to permit interpretation in terms of composition and crystal structure. Susceptibility, χ_n, is given in units of Bohr magnetons per oersted per formula unit.

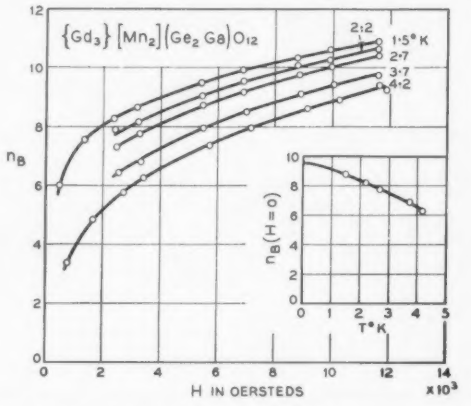

FIG. 1. Magnetic moment versus field at constant temperature for $\{Gd_3\}[Mn_2](Ge_2Ga)O_{12}$ and (insert) $n_B(H = 0)$ versus temperature.

The most extensive magnetic data were taken for $\{Gd_3\}[Mn_2](Ge_2Ga)O_{12}$ because it exhibited ferrimagnetism most clearly among the compounds examined at temperatures of 4·2–1·5°K. The magnetic moment was measured as a function of H at constant T (Fig. 1). The curves of n_B versus H show no saturation at high field because the Curie temperature is sufficiently low so that the field applied is of the order of magnitude of the Weiss molecular (or exchange) field.

The spontaneous magnetization for $H = 0$ has, therefore, been obtained by extrapolation under the assumption that

$$n_B(H, T) = n_B(0, T) + \chi_n(H, T)H$$

is a reasonable approximation to the nearly linear portion of the curves. On this basis $n_B(0, T)$ is

* The ionic size of Mn^{2+} is substantially greater than that of Fe^{3+}, so that the presence of Ge^{4+} in octahedral sites as reported by TAUBER *et al.* [*J. Appl. Phys.* **29**, 385 (1958)] for $\{MnY_2\}Fe_4GeO_{12}$ seems unlikely in this case. The distribution given for the magnetic ions is also supported by the magnetic data.

about 9·6 μ_B (insert Fig. 1) by extrapolation to $T = 0$.

A plot of $1/\chi_n$ versus T for $\{Gd_3\}[Mn_2](Ge_2Ga)O_{12}$ is concave downward, as it should be for a ferrimagnetic material (Fig. 2); the linear extrapolation intersects $1/\chi_n = 0$ at about $-8°$K. From the

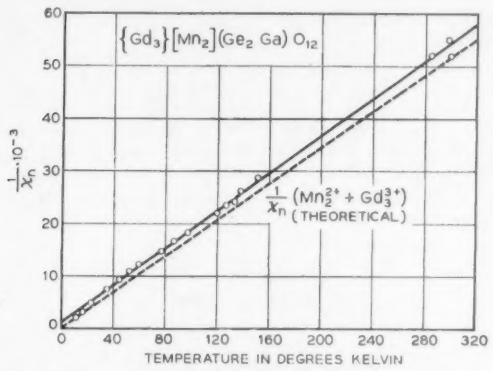

FIG. 2. Reciprocal susceptibility ($1/\chi$) versus temperature for $\{Gd_3\}[Mn_2](Ge_2Ga)O_{12}$.

$1/\chi_n$ versus T and $n_B(H = 0)$ versus T curves, it is roughly estimated that $T_C = 8 \pm 2°$K. From the slope of the $1/\chi_n$ versus T curve, a Curie constant of $5{\cdot}62 \times 10^{-3}$ μ_B deg./Oe is obtained, which is about 2 per cent less than the value calculated for free ions with a small correction for the Mn^{3+} present by analysis.

Similar measurements were carried out for $\{CaGd_2\}[Mn_2](Ge_3)O_{12}$. For this compound the Curie temperature may be about $6 \pm 2°$K as judged from the n_B versus H and $1/\chi_n$ versus T curves. However, the spontaneous magnetization is difficult to estimate even at 1·3°K, because of the curvature of the n_B versus H curves (Fig. 3). Again the $1/\chi_n$ versus T curve is concave downward at low temperature.

In the case of $\{MnGd_2\}[Mn_2](Ge_3)O_{12}$ it is also difficult to estimate the spontaneous magnetization. Though there is no doubt that this compound is ferrimagnetic, the susceptibility below T_C is greater than in the previous cases. Probably $\{Mn^{2+}\}$ remains paramagnetic at the temperatures employed, whereas $\{Ca^{2+}\}$, which it replaces, is nonmagnetic; $\{Gd^{3+}\}$, which it may also be regarded to replace, contributes less to the susceptibility because of saturation by the exchange field below T_C.

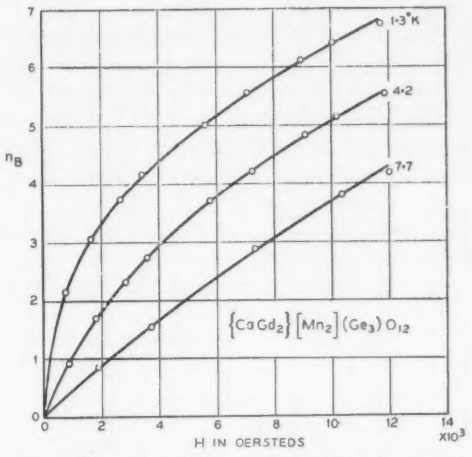

FIG. 3. Magnetic moment versus field at constant temperature for $\{CaGd_2\}[Mn_2](Ge_3)O_{12}$.

Measurements on $\{MnY_2\}[Mn_2](Ge_3)O_{12}$ show no evidence of spontaneous magnetization at temperatures down to 3·2°K. However, the $1/\chi_n$ versus T curve (Fig. 4) is slightly concave upward

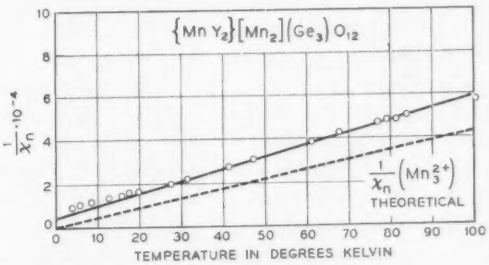

FIG. 4. Reciprocal susceptibility ($1/\chi$) versus temperature for $\{MnY_2\}[Mn_2](Ge_3)O_{12}$.

below 20°K, indicating that antiferromagnetic exchange interaction may be present. Similar observations were made for $\{CaY_2\}[Mn_2](Ge_3)O_{12}$, except that the upward concavity of the $1/\chi_n$ versus T curve is less pronounced at low temperatures.

3. DISCUSSION

The observation in $\{Gd_3\}[Mn_2](Ge_2Ga)O_{12}$ of spontaneous magnetization which extrapolates to 9·6 μ_B at 0°K clearly indicates that a $\{Gd^{3+}\}$–O^{2-}–$[Mn^{2+}]$ exchange interaction (a (c)–(a) interaction) is present; a moment of $3n_B\{Gd^{3+}\} - 2n_B[Mn^{2+}] = 3\times7 - 2\times5 = 11$ μ_B would be

expected. The presence of Mn^{2+} ions in octahedral sites alone is thus supported; a random distribution of Mn^{2+} ions over the octahedral and tetrahedral sites would undoubtedly so destroy the coherence of interaction with $\{Gd^{3+}\}$ that spontaneous magnetization would not be observed; loss of a few $[Mn^{2+}]$ ions to tetrahedral sites should lead to a moment greater than 11 μ_B.

This is the first case in which exchange interaction has been explicitly observed to take place between one rare-earth and one transition-metal ion magnetic sublattice through the intervening O^{2-} ions. The weakness of the interaction ($T_C/n \simeq \simeq 8/(48/5) = 5/6°$)* may be partly attributed to unfavorable geometry. Weakness of exchange interaction is also characteristic of Mn^{2+} in oxides and fluorides. The interaction between Gd^{3+} and Fe^{3+} in gadolinium–iron garnet is also known to be weak.

From magnetic measurements on $\{Gd_3\}[Ga_2](Ga_3)O_{12}$ crystals[11] and ceramics,[12] it is known that the interaction between $\{Gd^{3+}\}$ ions is very weak because the departure of the $1/\chi_n$ versus T curve from a purely paramagnetic character is unnoticeable. Therefore we would expect n_{cc} to be very small, as was found for gadolinium–iron garnet. The (a)–(a) interaction of the $[Mn^{2+}]$ ions is also weak, because of the small departure of the $1/\chi_n$ versus T curve for $\{CaY_2\}[Mn_2](Ge_3)O_{12}$ from a purely paramagnetic one.

There must be, however, some distinct differences in the relationship of the NÉEL interaction coefficients involving (c) and (a) in $\{Gd_3\}[Mn_2](Ge_2Ga)O_{12}$ from that in $\{Gd_3\}[Fe_2](Fe_3)O_{12}$. In the latter case we had $-n_{aa} \gg -n_{ca} \gg -n_{cc} \simeq 0$. For $\{Gd_3\}[Mn_2](Ge_2Ga)O_{12}$ we have found by implication that $n_{ca} \gg -n_{cc} \simeq 0$† as before; however, we must now have $-n_{aa} < n_{ca}$ in order that the ferrimagnetic (c)–(a) interaction will dominate. The very great change of the relationship of n_{ca} to n_{aa} could possibly be explained by the replacement of Fe^{3+} by Mn^{2+} even though these ions are isoelectronic.

Acknowledgements—The authors are indebted to Dr. R. M. BOZORTH for the use of his apparatus for the low-temperature magnetic measurements and to Mrs. V. KRAMER and Messrs. A. J. WILLIAMS and C. E. MILLER for their assistance.

REFERENCES

1. ALÉONARD R., BARBIER J.-C. and PAUTHENET R., *C.R. Acad. Sci. (Paris)* **242,** 2531 (1956).
2. GILLEO M. A. and GELLER S., *Phys. Rev.* **110,** 73 (1958).
3. NÉEL L., *Ann. Phys. (Paris)* **3,** 137 (1948).
4. GELLER S. and GILLEO M. A., *J. Phys. Chem. Solids* **3,** 30 (1957).
5. ANDERSON P. W., *Phys. Rev.* **79,** 350 (1950).
6. PAUTHENET R., Thesis, Grenoble (1957) as given in reference (7).
7. ALÉONARD R. and BARBIER J.-C., *C.R. Acad. Sci. (Paris)* **245,** 831 (1957).
8. GILLEO M. A., *Phys. Rev.* **109,** 777 (1958).
9. GELLER S. and MILLER C. E. To be published.
10. BOZORTH R. M., WILLIAMS A. J. and WALSH D. E., *Phys. Rev.* **103,** 572 (1956).
11. BOZORTH R. M. Private communication.
12. PAUTHENET R., *Colloque Internat. Magnétisme Grenoble,* Paper No. 66 (July 2–6, 1958).

* There are 48 interactions for the 5 magnetic ions per formula unit, so that $n = 48/5$ in the terminology of reference (8). See reference (2) for interaction geometry.

† Signs have been changed in order to make the interaction coefficient responsible for spontaneous magnetization positive.

J. Phys. Chem. Solids Pergamon Press 1959. Vol. 10. pp. 191–200.

MATERIALS FOR THERMOELECTRIC REFRIGERATION

F. D. ROSI, B. ABELES and R. V. JENSEN

R.C.A. Research Laboratories, David Sarnoff Research Center, Princeton, New Jersey

(*Received* 5 *December* 1958; *revised* 27 *January* 1959)

Abstract—The electrical conductivity, thermoelectric power and thermal conductivity were measured on Bi_2Te_3 and the alloy systems $(Bi,Sb)_2Te_3$, $Bi_2(Te,Se)_3$ and $(Bi_2Sb)_2(Te,Se)_3$. Criteria determining the optimum properties of the materials for thermoelectric refrigeration are discussed. Thermocouples made up of the above materials have yielded a maximum cooling corresponding to a temperature difference of 65°C between the hot and cold junctions, with the hot junction at 300°K.

VOL. 10 959

1. INTRODUCTION

More than a century has passed since the discovery of the Peltier effect. However, not until recently has serious attention been devoted to the practical utilization of this effect for cooling. Early attempts to devise efficient refrigerators were unsuccessful because materials were not available with the requisite properties for use as thermoelements. These early attempts were made with metals and metal alloys which had too low a thermoelectric power.

In recent years, the great interest which has been centered on the properties of semiconductors has led to the development of materials with a large enough thermoelectric power to permit the construction of thermoelements with much higher efficiencies than was possible with metals. This realization has brought about considerable research activity on the properties of semiconductor materials that could be utilized in thermoelectric devices. The early information[1–4] showed that the most promising thermoelectric materials consist of compounds resulting from combination of elements from Groups V and VI, Groups IV and VI, and Groups II and V of the Periodic Table. In addition, the early theoretical considerations of A. F. Ioffe *et al.*[5] on the thermal conductivity and thermoelectric power in various alloy systems, and the more recent experimental work of Steele and Rosi[6] on the Ge–Si system showed that solid-solution alloying can result in an improvement in the figure of merit of thermoelements by decreasing the thermal conductivity without affecting the thermoelectric power and resistivity. This is due to distortions of the lattice on alloying which enhance the scattering of phonons, but are ineffective in scattering electrons that have longer wavelengths than the phonons. The awareness of this phenomenon made it advisable to investigate solid-solution alloys of compound semiconductors.

In the present work, data will be presented on the thermoelectric properties of bismuth telluride (Bi_2Te_3) and solid-solution alloys of Bi_2Te_3 with Sb_2Te_3 and Bi_2Se_3. These materials have provided the best properties for thermoelectric refrigeration to date.

2. THERMOELECTRIC REFRIGERATION

The performance of a refrigeration thermocouple is described in the literature by three different quantities: "coefficient of performance", "figure of merit" and "maximum cooling".[7] If the properties of the thermocouple are temperature-independent, these three quantities are simply related as follows:

The heat-balance equation at the cold junction of a refrigeration thermocouple is:

$$H = QIT_c - \tfrac{1}{2}I^2R - (T_h - T_c)K, \qquad (1)$$

and the electrical power P driving the thermocouple is:

$$P = I[RI + Q(T_h - T_c)]. \qquad (2)$$

Here H is the external heat input to the cold junction; T_h and T_c are the temperatures of the hot and cold junctions, respectively; I is the electrical

current through the thermocouple; K is the thermal conductance of the two thermocouple arms in parallel; R is the electrical resistance of the thermocouple arms in series; and Q is the algebraic sum of the thermoelectric powers of the thermocouple arms:

$$\left.\begin{aligned} Q &= Q_a+Q_b \\ R &= (l_a/A_a)\rho_a+(l_b/A_b)\rho_b \\ K &= (A_a/l_a)\kappa_a+(A_b/l_b)\kappa_b \end{aligned}\right\} \quad (3)$$

where l is the length and A the cross-sectional area of the thermocouple arm; ρ, the specific electrical resistivity; and κ, the specific thermal conductivity; subscripts a and b denote the two arms, respectively.

The coefficient of performance η of a refrigeration thermocouple (heat absorbed/electrical energy input) is given by the ratio of equations (1) and (2). η can be maximized by the proper choice of I, A and l. The maximum value of η is given by:

$$\eta_{\max} = \left[\frac{T_c}{T_h-T_c}\right]\left[\frac{(1+z\bar{T})^{\frac{1}{2}}-(T_h/T_c)}{(1+z\bar{T})^{\frac{1}{2}}+1}\right] \quad (4)$$

where

$$\bar{T} = (T_h+T_c)/2$$

and

$$z = \frac{(Q_a+Q_b)^2}{[(\kappa_a\rho_a)^{\frac{1}{2}}+(\kappa_b\rho_b)^{\frac{1}{2}}]^2}. \quad (5)$$

The quantity z, defined by equation (5), is referred to as the figure of merit.

The current I_0 for which η is maximum is given by:

$$I_0 = \frac{Q}{R}(T_h-T_c)\left[\frac{1+(1+z\bar{T})^{\frac{1}{2}}}{z\bar{T}}\right], \quad (6)$$

and the ratio of the dimensions of the arms satisfy the condition

$$(A_a l_b)/(A_b l_a) = [(\rho_a\kappa_b)/(\rho_b\kappa_a)]^{\frac{1}{2}}. \quad (7)$$

The maximum cooling $\Delta T_{\max}$ is defined as the maximum temperature difference attainable between the hot and cold junctions when the cold junction is thermally insulated. $\Delta T_{\max}$ is obtained by setting the right side of equation (1) to zero, solving for T_h-T_c, and maximizing with respect to I:

$$\Delta T_{\max} = (\tfrac{1}{2})zT_c^2. \quad (8)$$

Since the coefficients z, $\eta_{\max}$ and $\Delta T_{\max}$ are usually measured under different temperature conditions, the simple relations between them given by equations (4), (5) and (8) exist only if the properties of the materials are temperature independent.

3. PREPARATION OF MATERIALS

In the preparation of Bi_2Te_3 and its alloys with Sb_2Te_3 and Bi_2Se_3, a special high-purity grade (99·999 per cent) of the component elements was used. The tellurium and selenium were obtained from the American Smelting and Refining Company, and the antimony from the National Lead Company. Before reacting to form the compounds, the elements were melted in a high vacuum and then zone-refined.

The compounds were prepared by reacting the constituent elements in stoichiometric proportions at their melting points in horizontal, evacuated quartz tubes, which had been previously flushed with purified hydrogen. Since these compounds dissociate on melting, a measured excess of the volatile constituent was placed in the evacuated sealed tube to maintain stoichiometry. After melting, the compounds were allowed to solidify by the Bridgman technique at a rate of 6 mm hr^{-1}. A slow rate of crystallization was desirable to avoid internal stresses and micro-cracks as a result of the expansion of Bi_2Te_3 on solidification. In general, the resulting ingots were not single crystals, but consisted of very coarse grains with the (0001) plane within 10° of the growth direction, or specimen axis. This preferred crystallographic orientation results from the significantly greater thermal conductivity,[8] and hence heat dissipation, parallel to the (0001) plane in Bi_2Te_3. In the case of the solid-solution alloys, the melt was superheated, mechanically agitated and then held 50°C above the melting point for approximately 10 hr prior to crystallization. This was done in order to achieve chemical homogeneity. X-ray, wet-chemical analyses, and electrical-resistivity measurements were used to check the homogeneity of the crystals.

Semiconductor materials for thermoelectric cooling should be close to degeneracy for optimum efficiency.[4,7] In the case of Bi_2Te_3 this requires impurity additions which will provide a carrier concentration of approximately 10^{19} cc^{-1} or a resistivity of approximately 1×10^{-3} Ω-cm. Studies

were carried out on the effect of impurity additions over a wide range of concentrations. Elements in Groups IV and V, such as Sn, Pb, Sb, As and excess Bi, provide free holes. Unless otherwise noted, excess bismuth was used in the present work to provide the *p*-type Bi_2Te_3 and its alloys.

For *n*-type materials it was necessary to use compound doping. It was found that many elements in Groups I, II, III and VI of the Periodic Table either form tellurides which are not soluble in Bi_2Te_3, or have a limited solid solubility which prevents attainment of the desired carrier concentration. Our initial *n*-type Bi_2Te_3 was prepared by additions of cuprous sulfide (Cu_2S) in accordance with the earlier work of BUSANOVICH.[9] However, Cu_2S was not effective as an *n*-type impurity in the $(Bi, Sb)_2Te_3$ alloys. This was due to preferential formation of Sb_2S_3, which has very little solid solubility in these alloys. On the other hand, additions of Cu_2S did provide the necessary electron concentration in the $Bi_2(Te, Se)_3$ alloys, because Cu_2S has a higher free energy of formation than the Bi_2S_3, so that the latter compound did not form. These results clearly pointed to the need for doping with compounds which have a higher free energy of formation, and hence chemical stability, than the similar compound with either bismuth or antimony. This led to a detailed investigation of impurity additions with the halides of copper, silver, antimony and bismuth, most of which were found to have sufficiently high solid solubilities in Bi_2Te_3 and the $Bi_2(Te, Se)_3$ and $(Bi, Sb)_2Te_3$ alloys to provide the desired low electrical resistivity. Best results were obtained with the iodides and bromides of copper and silver, in general agreement with the most recent work of SINANI and GORDIAKOVA[10] on the Bi_2Te_3–20 per cent Bi_2Se_3 alloy.

In connection with the extent of solid solubility of the various halides in Bi_2Te_3, present results strongly suggest a size-factor relationship, since maximum solid solubility is generally obtained when the tetrahedral covalent radii of the Group I and Group VII elements of the halide are similar to the radii of the Bi and Te, respectively. For example, the covalent radii of Ag (1·53 Å) and I (1·28 Å) are most similar to those of Bi (1·46 Å) and Te (1·32 Å), respectively; and it was found that of the halides AgI appeared to have the largest solid solubility in Bi_2Te_3. Similarly, it was also found that the solid solubility of the silver halides in Bi_2Te_3 decreased slightly on going from AgI → AgBr → AgCl. It is apparent that this concept of size-factor can also be extended to the compound alloys.

4. MEASURING TECHNIQUES

Measurements of the room-temperature values of the thermal conductivity, thermoelectric power and electrical conductivity were made on the materials described in the previous section. The thermal conductivity was measured by an absolute method. A sketch of the apparatus is shown in Fig. 1. The crystals were cut into short rods, 1 cm long and 1 cm diameter. The sample *C* was placed between a copper sink *S* and a flat electrical heater *H* made out of copper. The temperatures were measured by copper/Constantan thermocouples soldered to the heater and sink. The thermoelectric power was measured against the copper members of the thermocouples. The measurements were made in a vacuum of about 10^{-4}mm Hg.

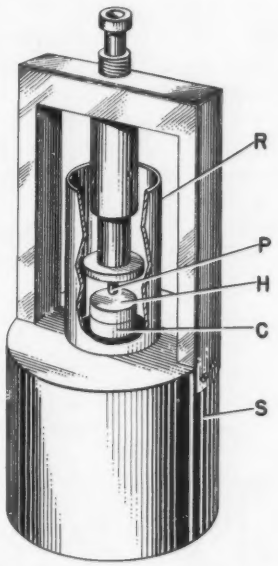

FIG. 1. Apparatus for measuring thermal conductivity: *H* heater, *S* copper sink, *C* crystal, *P* spring-loaded nylon plunger, *R* radiation shield.

Two sources of errors are inherent in the above method of measuring thermal conductivity. In addition to the heat conducted through the sample,

heat is also transferred by radiation from the heater and sample to the colder surrounding. This was minimized by making the physical size of the heater as small as possible, and silver plating and polishing its surface to reduce its emissivity. Further, the sample and heater were surrounded by a radiation shield in thermal contact with the sink. Under these conditions the radiation losses from the heater and sample were reduced to less than 5 per cent of the output of the heater. The second source of error is the thermal contact resistance between the sample and the heater and sink. To ensure a low contact resistance the heater, sink and samples were lapped, and then a thin layer of silicone oil was introduced between the lapped surfaces. With these precautions the contact resistance was less than 1 per cent of the thermal resistance of the samples. Both errors, radiation losses and contact resistance, were determined by measuring on samples of varying length. All the results were corrected for radiation losses and contact resistance.

Measurements of Peltier cooling were made on selected materials with the arrangement shown in Fig. 2. A thermocouple was assembled by soldering two rods, N and P, of n-type and p-type materials respectively, to copper electrodes 1, 2 and 3. The soldered joints were made by nickel plating the surfaces to be joined and using Wood's metal as solder. The thermocouple was held in position by a method in which strains on the thermocouple branches were avoided.[11] Two copper rods A with hemispherical heads fitted closely into hemispherical holes in electrodes 1 and 2. Good thermal contact between the electrodes and rods A was obtained by applying a thin layer of silicone oil. Rods A were threaded into two copper blocks B through which cooling water was circulated by means of copper tubes C. Heavy current leads were soldered directly to the electrodes 1 and 2. The whole assembly was enclosed under a bell jar E and evacuated. The thermocouple and electrical leads were brought outside through the Kovar seal G. Direct current was passed through the thermocouple in such a direction that Peltier heat was absorbed at electrode 3 (cold junction) and generated at electrodes 1 and 2 (hot junctions). The hot junctions were maintained at 300°K by the circulating water. An electric heater was wound around the cold junction so that measurements of the coefficient of performance could be made. Temperatures of the hot and cold junctions were measured by copper/Constantan thermocouple soldered to the copper electrodes.

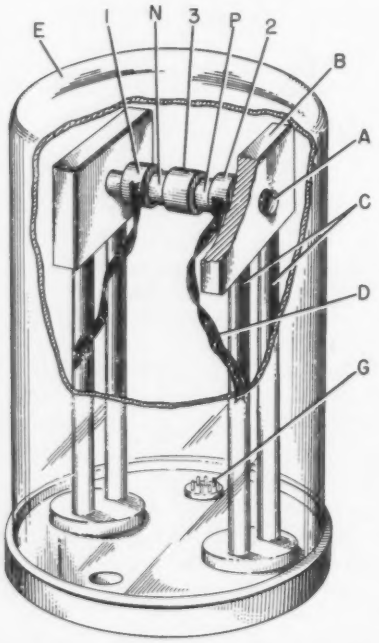

FIG. 2. Apparatus for measuring Peltier cooling.

5. RESULTS AND DISCUSSION

(a) *Bismuth telluride* (Bi_2Te_3)

Measurements of thermoelectric power, electrical conductivity and thermal conductivity were made on a number of p-type and n-type Bi_2Te_3 polycrystals at 300°K. The p-type material had excess Bi and the n-type was doped with CuI. The measurements were made on short cylinders with the electrical current or temperature gradient applied in the direction of the axis of the cylinder. As a result of the growth conditions, this direction was very nearly parallel to the (0001) plane of the crystallites.

The dependence of the thermoelectric power Q on the electrical conductivity σ is shown in Fig. 3. In the high-conductivity range, the thermoelectric power drops off due to the onset of degeneracy. In the low-conductivity range, Q drops off again due to intrinsic conduction. In p-type material Q

decreases more rapidly than in n-type as one approaches degeneracy. This indicated that the electrons either have a larger mobility or a larger density of states effective mass than the holes.* Mobility measurements in Bi_2Te_3 have been made

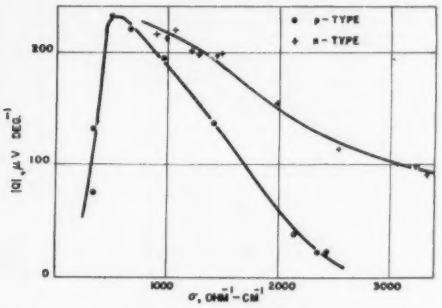

FIG. 3. Dependence of thermoelectric power on electrical conductivity in Bi_2Te_3.

by a number of workers.[12–16] The largest reported values for the mobilities parallel to the cleavage plane at room temperature are 1250 $cm^2V^{-1}sec^{-1}$ for electrons[16] and 680 $cm^2V^{-1}sec^{-1}$ for holes.[15] Both results are for specimens having resistivities of about 10^{-3} Ω-cm.

The thermal conductivity is given by:

$$\kappa = \kappa_{ph} + \kappa_{el} + \kappa_{amb} \quad (9)$$

$$\kappa_{el} = S(k/e)^2 T\sigma \quad (10)$$

$$\kappa_{amb} = (k/e)^2 T(\sigma_n\sigma_p/\sigma)[(Eg/kT)+4]^2. \quad (11)$$

Here κ_{ph} is the lattice thermal conductivity and κ_{el} is the electronic contribution to κ given by the Wiedemann–Franz law.[17] S is a factor which depends on the degree of degeneracy and the type of scattering of the carriers; for a Boltzmann distribution and thermal scattering $S = 2$, and for degeneracy $S = \pi^2/3$. κ_{amb} is the ambipolar contribution due to diffusion of electron–hole pairs,[18] where Eg is the band gap of the semiconductor, and σ_n and σ_p are the electrical conductivities of the electrons and holes, respectively. For equation (11) thermal scattering and non-degeneracy is assumed, and the temperature-dependence of Eg has been neglected. In the intrinsic range κ_{amb} is appreciable and κ_{el} is small. As σ increases, κ_{amb} decreases rapidly to zero, and κ_{el} increases. This gives rise to a minimum in the thermal conductivity, as shown in Fig. 4. The dashed lines in Fig. 4 were calculated from equations (9) and (10),

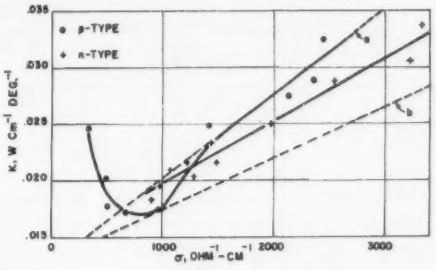

FIG. 4. Dependence of thermal conductivity on electrical conductivity in Bi_2Te_3.

assuming $\kappa_{ph} = 0{\cdot}013$ $Wdeg^{-1}cm^{-1}$ independent of σ, and $\kappa_{amb} = 0$. Line a is for $S = \pi^2/3$; and line b for $S = 2$. κ for p-type Bi_2Te_3 follows a in the high-electrical-conductivity range and tends to b as σ decreases until the onset of ambipolar conduction. κ for n-type Bi_2Te_3 falls intermediate between lines a and b. Similar results were recently obtained by GOLDSMID,[19] who suggests that the lower values of κ for the n-type materials is due to a decrease in the lattice thermal conductivity due to additional scattering of the phonons by the halide impurities.

In order to calculate the dependence of κ_{amb} on σ, a detailed knowledge of the position of the Fermi level and density of states would be necessary. The calculation is, however, simplified for intrinsic material. Equation (11) then reduces to:

$$\kappa_{amb} = (k/e)^2 T\sigma[2+b+(1/b)]^{-1}[(Eg/kT)+4]^2, \quad (12)$$

where b is the ratio of electron to hole mobilities. Substituting in equation (11), $b = 2$, $\sigma = 300$ $\Omega^{-1}cm^{-1}$ and for the band gap[20] $Eg = 0{\cdot}15$ eV, we obtain $\kappa_{amb} = 0{\cdot}014$ $Wdeg^{-1}cm^{-1}$. From equation (10) we calculate $\kappa_{el} = 0{\cdot}0014$ $Wdeg^{-1}cm^{-1}$, and, substituting in equation (9) for κ_{amb} and κ_{el} the calculated values and for $\kappa_{ph} = 0{\cdot}013$ $Wdeg^{-1}cm^{-1}$, we obtain $\kappa = 0{\cdot}028$ $Wdeg^{-1}cm^{-1}$. This is in good agreement with the experimental value $\kappa = 0{\cdot}025$ $Wdeg^{-1}cm^{-1}$ for intrinsic Bi_2Te_3.

* More precisely it can be shown that $m_n^{3/2}\mu_n > m_p^{3/2}\mu_p$, where m is the effective density of states mass, μ the mobility, and n and p refer to electrons and holes, respectively.

The figure of merit, $z = Q^2\sigma/\kappa$, is plotted in Fig. 5 against σ. It may be seen that in p-type Bi_2Te_3, z has a sharp maximum of $2{\cdot}2\times10^{-3}$ deg^{-1} at 900 $\Omega^{-1}cm^{-1}$. In the n-type material the

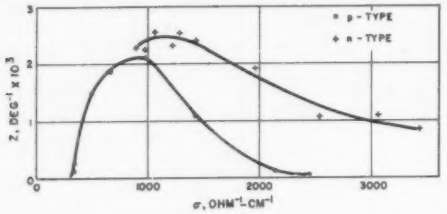

FIG. 5. Variation of figure of merit with electrical conductivity in Bi_2Te_3.

maximum value of z is $2{\cdot}6\times10^{-3}$ deg^{-1}, and the curve is more shallow. It is clear from Fig. 5 that for p-type Bi_2Te_3 very close tolerances of electrical conductivity must be maintained for optimum z.

(b) *(Bi, Sb)$_2$Te$_3$ alloys*

Studies of the $(Bi, Sb)_2Te_3$ alloys were confined to p-type (excess-Bi) material, since until recently it was not possible to produce n-type alloys. In addition, the early work of LINDENBLAD[21] showed that a (Bi, 20 per cent Sb)$_2$Te$_3$ alloy produced good p-type thermoelements for refrigeration.

The variation in the thermal conductivity κ with alloying in the $(Bi, Sb)_2Te_3$ system was examined over the entire range of composition at 300°K, and the results are summarized in Table 1 and Fig. 6. The electronic component, κ_{el}, of the thermal conductivity was determined from equation (10), assuming degeneracy $S = \pi^2/3$, as indicated by the low values of thermoelectric power. The phonon

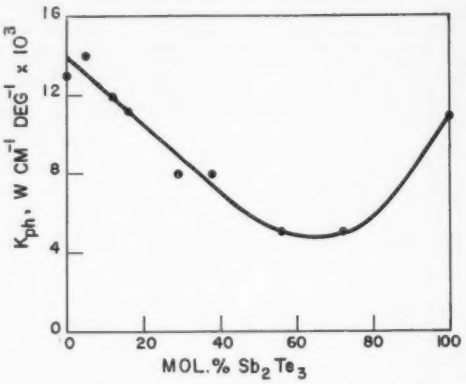

FIG. 6. Dependence of lattice thermal conductivity on solid-solution alloying in the Bi_2Te_3–Sb_2Te_3 system.

contribution, κ_{ph}, was then determined by simply subtracting κ_{el} from κ. It should be pointed out, however, that the large electronic contribution to κ introduces considerable uncertainty in the calculated values of κ_{ph}. The selection of degenerate samples was considered necessary in order to avoid the ambipolar contribution to the thermal conductivity. This was particularly important in the Sb_2Te_3-rich alloys, since the intrinsic resistivity for Sb_2Te_3 is about 5×10^{-4} Ω-cm as compared to about 3×10^{-3} Ω-cm for Bi_2Te_3; and the variation in the intrinsic resistivity with alloying is approximately linear.

It may be seen from Fig. 6 that κ_{ph} decreases on alloying Bi_2Te_3 with Sb_2Te_3 to a minimum value of 0·005 $Wcm^{-1}deg^{-1}$ corresponding to an alloy of Bi_2Te_3–65 per cent Sb_2Te_3. However, in spite of this large decrease in κ_{ph}, it is not possible to increase significantly the figure of merit of p-type

Table 1. Thermal-conductivity data for the (Bi, Sb)$_2$Te$_3$ alloys

Crystal No.	Sb_2Te_3 (Mol.-%)	$\rho(\Omega$ cm $\times 10^{-4})$	κ (W $cm^{-1}deg^{-1}$)	κ_{el} (W $cm^{-1}deg^{-1}$)	κ_{ph} (W $cm^{-1}deg^{-1}$)
BST 13	6	6·6	0·025	0·011	0·014
BST 9	12	5·3	0·026	0·014	0·012
BST 8	16	5·2	0·025	0 014	0 011
BST 7	29	6 2	0 020	0 012	0·008
BST 10	38	4·9	0·023	0·015	0·008
BST 11	56	4·0	0·023	0·018	0·005
BST 12	72	2·9	0·030	0·025	0·005
SbTe	100	2·1	0·045	0·034	0·011

Bi_2Te_3 with additions of Sb_2Te_3. In order to avoid the ambipolar effect, the materials had to be doped down well below the intrinsic resistivity; but with the small band gaps of the above compound alloys,* this degree of doping results in degeneracy and consequently a lowering of the figure of merit. Generally, the value of the figure of merit will not be as high in a material with a small band gap, where the ambipolar contribution and onset of degeneracy overlap, as in a similar material with a larger band gap.

The best *p*-type figure of merit obtained in the Bi_2Te_3–Sb_2Te_3 system was $2{\cdot}2\times10^{-3}$ deg^{-1} for a Bi_2Te_3–25 per cent Sb_2Te_3 alloy at a conductivity of $1{\cdot}1$–$1{\cdot}4\times10_3$ Ω^{-1}cm^{-1}, which is not better than that for the best *p*-type Bi_2Te_3.

It is noteworthy that in the case of the Bi_2Te_3–25 per cent Sb_2Te_3 alloy the distribution coefficient, k, of Sb_2Te_3 was found to be ~ 1. Thus, ingots of this alloy showed uniform alloy composition along their length. Since the value of k was found to be < 1 for alloys containing < 25 per cent Sb_2Te_3 and > 1 for alloys with composition above 30 per cent Sb_2Te_3, one can conclude that a minimum occurs in the solid-solubility curve in the Bi_2Te_3–Sb_2Te_3 phase diagram at approximately 30 per cent Sb_2Te_3.

(c) *Bi_2(Te, Se)$_3$ alloys*

Early studies on the Bi_2(Te, Se)$_3$ alloys showed that, for *p*-type material in the desired alloy range (20–30 per cent Bi_2Se_3), degeneracy set in at too high a resistivity ($\sim 2\times10^{-3}$ Ω-cm) to effect an improvement in the figure of merit over Bi_2Te_3. Consequently, detailed studies of this alloy system were confined to *n*-type, CuBr-doped material.

Fig. 7 shows the variation in the lattice thermal conductivity, κ_{ph}, at 300°K in the Bi_2(Te, Se)$_3$ system over the entire range of compositions. The value of κ_{ph} was obtained by subtracting the electronic component, κ_{el}, from the measured thermal conductivity, κ, using equation (10). In the resistivity range used, it was possible to avoid any ambipolar contribution to the thermal conductivity.

It may be seen from Fig. 7 that the dependence of κ_{ph} on alloying Bi_2Se_3 to Bi_2Te_3 exhibits two minima corresponding to values of 0·009 and 0·013

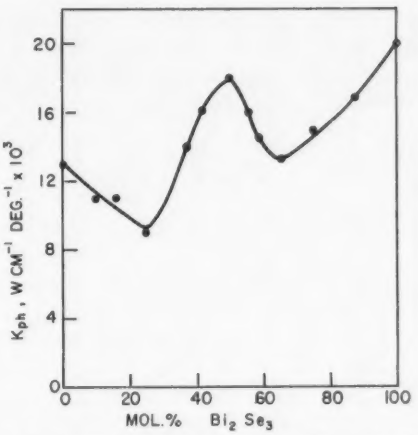

FIG. 7. Dependence of lattice thermal conductivity on solid-solution alloying in the Bi_2Te_3–Bi_2Se_3 system.

Wcm^{-1}deg^{-1} at alloy compositions of Bi_2Te_3–25 per cent Bi_2Se_3 and Bi_2Te_3–65 per cent Bi_2Se_3, respectively. The decrease in κ_{ph} to 0·009 Wcm^{-1} deg^{-1} is comparable to that obtained in the (Bi, Sb)$_2$Te$_3$ system (see Table 1 and Fig. 6) for the same alloy composition. The anomalous sharp rise in κ_{pn} in the 25–50 per cent Bi_2Se_3 alloy range suggests superlattice formation. In this connection it is interesting to note that AUSTIN and SHEARD[20] recently reported an anomalous maximum in the band gap in this alloy system corresponding to the Bi_2Te_3–33 per cent Bi_2Se_3 alloy composition. However, X-ray analysis in the present work, as well as that of AUSTIN and SHEARD, indicated a single-phase structure with no evidence of superlattice or compound formation. Thus, there does not seem to be a simple explanation to this anomaly.

Studies of the variation in the figure of merit, $Q^2/\rho\kappa$, with resistivity for the *n*-type Bi_2Te_3–25 per cent Bi_2Se_3 alloy showed that an optimum value of $2{\cdot}7\times10^{-3}$ deg^{-1} is obtained over the resistivity range 1–$1{\cdot}5\times10^{-3}$ Ω-cm. This represents a slight improvement over the $2{\cdot}6\times10^{-3}$ deg^{-1} value for *n*-type Bi_2Te_3.

(d) *(Bi, Sb)$_2$(Te, Se)$_3$ alloys*

It was mentioned that the figure of merit for *p*-type Bi_2Te_3 could not be significantly improved by alloying with Sb_2Te_3 in spite of a large decrease in the lattice thermal conductivity. This was attributed to a decrease in the energy band gap and,

* The fact that the band gap decreases was inferred from a corresponding decrease in the intrinsic resistivity.

hence, a decrease in the intrinsic resistivity with alloying, which caused an overlap between the ambipolar contribution to the thermal conductivity and degeneracy. This is indicated in Fig. 8

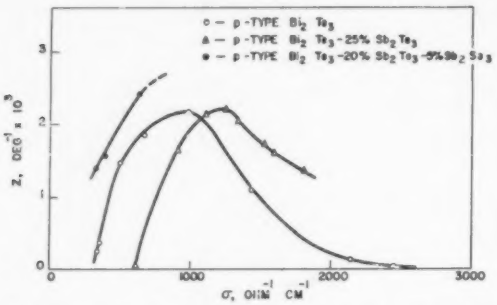

FIG. 8. Variation of figure of merit with electrical conductivity in p-type materials.

by the variation of the figure of merit, z, with electrical conductivity σ for p-type Bi_2Te_3 and Bi_2Te_3–25 per cent Sb_2Te_3 alloy. The sharp drop in z at the lower values of σ for each material is due to a sudden decrease in the thermoelectric power as a result of intrinsic conduction. The shift in the σ associated with this sharp decrease in z is ascribed to a change in the energy band gap of the material.

To avoid overlap between the ambipolar effect and degeneracy in the Bi_2Te_3–25 per cent Sb_2Te_3 alloy, it would be desirable to increase its band gap through small additions of a higher-band-gap material which is soluble in the alloy. This was accomplished by adding 5 per cent of Sb_2Se_3 to the Bi_2Te_3–20 per cent Sb_2Te_3 alloy, as may be seen in Fig. 8 by the marked shift of the onset of intrinsic conduction (and consequent low figure of merit, z) to lower values of σ. This ternary solid-solution alloy has provided a figure of merit of $2{\cdot}4\times10^{-3}$ deg^{-1} which is the best value, to date, for p-type material. More important, there is good reason to believe that this value can be further improved by: (1) increasing the alloy proportions of the Sb_2Te_3 and Sb_2Se_3 in order to make use of the low 0·005 Wcm^{-1}deg^{-1} lattice conductivity in the Bi_2Te_3–Sb_2Te_3 alloy system (see Fig. 6), and (2) investigating other alloy systems which provide a variation in band gap by suitable additions of a third compound in solid solution.

6. PELTIER COOLING

Thermoelectric data pertinent for evaluating four Peltier thermocouples are given in Table 2. Listed are the materials used in constructing the branches of the thermocouple, the type of impurity added to obtain the desired electrical conductivity, the conductivity type, the figure of merit ($Q^2/\rho\kappa$)

Table 2. Thermoelectric data on thermocouples of different materials

Material	Impurity added	Conductivity type	$Q^2/\rho\kappa$, (deg$^{-1}\times10^{-3}$)	ΔT_{max} (°C)	ΔT_{meas} (°C)
Bi_2Te_3	CuI	n	2·5	65	59
Bi_2Te_3	Bi	p	2·2		
Bi_2Te_3	AgI	n	2·6	66	60
Bi_2Te_3–25%Sb_2Te_3	Bi	p	2·2		
Bi_2Te_3–25%Bi_2Se_3	CuBr	n	2·7	67	62
Bi_2Te_3–25%Sb_2Te_3	Bi	p	2·2		
Bi_2Te_3	AgI	n	2·6	68	65
Bi_2Te_3–20%Sb_2Te_3–5%Sb_2Se_3	Bi	p	2·4		

determined from measured properties, the maximum cooling (ΔT_{max}) calculated from measured properties using equation (8) and a hot junction temperature (T_h) of 300°K, and the maximum cooling measured (ΔT_{meas}) with the hot junction at 300°K.

It is apparent from the data in Table 2 that with *p*- and *n*-type Bi_2Te_3 a Peltier cooling of 59°C from 300°K is possible; and by the use of solid-solution alloys this cooling can be increased to 65°C. The actual Peltier cooling curves for three of the thermocouples are shown in Fig. 9. The resistances

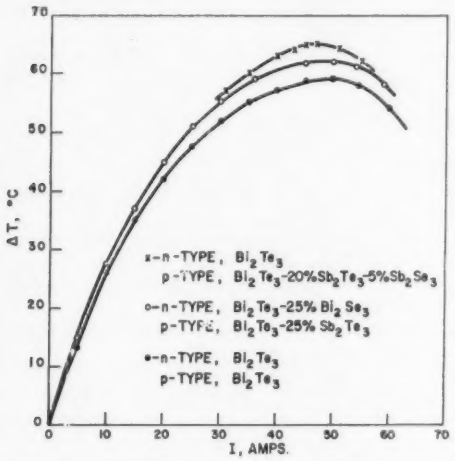

FIG. 9. Temperature difference between hot and cold junction measured as a function of electrical current for a number of thermocouples.

of the thermocouples were about $2 \times 10^{-3}\ \Omega$ and the maximum ΔT was obtained at an optimum current of about 45 A.

The data in Table 2 further show that there is a mean difference of ~ 5°C between ΔT_{max} and ΔT_{meas}. This cannot be attributed to the resistance at the junctions of the thermocouple, since this resistance was found to be two orders of magnitude less than the sum of the branch resistances. Rather, this difference of 5°C in Peltier cooling results from a change in the thermoelectric properties of the material with decreasing temperature and a consequent lowering of the figure of merit. This is demonstrated by the curves in Fig. 10, which describe the temperature-dependence of the thermoelectric power, Q, and resistivity, ρ, for the *p*-type Bi_2Te_3–25 per cent Sb_2Te_3 alloy. Both Q

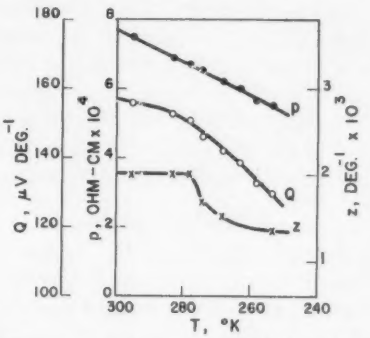

FIG. 10. Temperature-dependence of resistivity, thermoelectric power and figure of merit in *p*-type Bi_2Te_3–25 per cent Sb_2Te_3 alloy.

and ρ decrease with decreasing temperature, but at different rates. κ was assumed to be independent of temperature. This assumption is reasonable, since κ is the sum of an electronic and a lattice component of the same order but opposite temperature dependencies. The more rapid drop in Q^2 than in ρ results in a decrease of z with temperature. It can be shown that the amount by which z decreases with temperature would account for the 5°C difference between ΔT_{max} and ΔT_{meas}. This suggests that, by proper impurity grading along the branches of the thermocouple, it should be possible to obtain the ΔT_{max} of 68°C in Table 2 with the *p*-type ternary alloy and *n*-type Bi_2Te_3. For the *n*-type solid-solution alloys, Q did not decrease as rapidly with temperature and hence z did not vary significantly down to ~ 250°K.

It is also noteworthy from Fig. 10 that z remains relatively constant over the temperature range 276°–300°K. Therefore the efficiency, or coefficient of performance, for a thermoelectric refrigerator operating over this temperature range would not be significantly effected by the temperature-dependence of the thermoelectric properties in Fig. 10.

A final observation of interest is that the coefficient of performance for a thermoelectric refrigerator, calculated from equation (4) using the highest values of z given in Table 2, is 0·65. This coefficient of performance was calculated by assuming $T_h = 300$°K and $T_c = 266$°K. The values of T_h and T_c were measured by LINDENBLAD[22] on his 4-ft³ thermoelectric refrigerator-freezer. This coefficient of performance is to be compared with

that of approximately 1·45 for a compressor-type refrigerator without freezer.[23] This relative performance would be even better if one considered refrigerators of smaller volume, since the coefficient of performance would not be expected to decrease with size for the thermoelectric refrigerator, as in the case of the conventional compressor-type.

7. CONCLUSIONS

Solid-solution alloying of Bi_2Te_3 with Sb_2Te_3 and Bi_2Se_3 results in only a small increase in the Peltier cooling in spite of a marked decrease in the lattice thermal conductivity on alloying. In the case of the Bi_2Te_3–Sb_2Te_3 alloys, this is attributed to a decrease in the energy band gap on alloying which results in an overlap between degeneracy and the ambipolar contribution to the thermal conductivity. It was found that additions of a third compound to the binary alloys enable one to increase the band gap in such a manner as to avoid the above-mentioned overlap and thereby improve the figure of merit. Such ternary alloys, the Bi_2Te_3–Sb_2Te_3–Sb_2Se_3 system, have yielded a Peltier cooling of 65°C from 300°K.

Acknowledgements—The authors are indebted to H. H. WHITAKER and J. WHITE for X-ray and chemical analyses on the solid-solution alloys, and to D. O. NORTH for constructive criticism of the manuscript.

REFERENCES

1. TELKES M., *J. Appl. Phys.* **18,** 1116 (1947).
2. JUSTI E. and LAUTZ G., *Z. Naturforsch.* **7a,** 602 (1952).
3. GOLDSMID H. J. and DOUGLAS R. W., *Brit. J. Appl. Phys.* **3,** 383 (1954).
4. STIL'BANS L. S., IORDANISHVILI E. K., and STAVITSKAYA T. S., *Izv. Akad. Nauk S.S.S.R. Ser. Fiz.* **20,** 81 (1956); English Translation: Russian Literature Survey, SEM–1–56, London.
5. IOFFE A. F., AIRAPETYANTS S. V., IOFFE A. V., KOLOMOETS N. V., and STIL'BANS L. S., *Dokl. Akad. Nauk. S.S.S.R.*, **106,** 981 (1956).
6. STEELE M. and ROSI F. D., *J. Appl. Phys.* **29,** 1517 (1958).
7. IOFFE A. F., *Poluprovodnikovye Termoelementy*. Akad. Nauk S.S.S.R., Moscow (1956).
8. GOLDSMID H. J., *Proc. Phys. Soc.* B **69,** 203 (1956).
9. BUSANOVICH C. J. Private communication (1956).
10. SINANI S. S. and GORDYAKOVA G. N., *Zh. Tekh. Fiz.* **26,** 2398 (1956).
11. LINDENBLAD N. E. Private communication (1957).
12. SHIGETOMI S. and MORI S., *J. Phys. Soc. Japan* **11,** 915 (1956).
13. HARMAN T. C., PARIS B., MILLER S. E., and GOERING H. L., *J. Phys. Chem. Solids* **2,** 181 (1957).
14. SATTERTHWAITE C. B. and URE R. W., *Phys. Rev.* **108,** 1164 (1957).
15. BLACK J., CONWELL E. M., SEIGLE L., and SPENCER C. W., *J. Phys. Chem. Solids* **2,** 240 (1957).
16. WOLFE R., GROVES R. D., and DRABBLE J. R., *Bull. Amer. Phys. Soc.* **3,** 121 (1958).
17. WILSON A. H., *The Theory of Metals* p. 200. Cambridge University Press (1953).
18. PRICE P. J., *Phil. Mag.* **46,** 1252 (1955).
19. GOLDSMID H. J., *Proc. Phys. Soc.* **72,** 17 (1958).
20. AUSTIN I. G. and SHEARD A., *J. Electronics and Control* **3,** 236 (1957).
21. LINDENBLAD N. E., U.S. Patent No. 2,734,344.
22. LINDENBLAD N. E., *Elect. Engng.* **77,** 802 (1958).
23. STOLL G. H., Private communication (August 1958).

J. Phys. Chem. Solids Pergamon Press 1959. Vol. 10. pp. 201–203.

THERMAL OSCILLATIONS IN *n*-GERMANIUM AT LOW TEMPERATURE

S. H. KOENIG and R. D. BROWN III

International Business Machines Watson Laboratory, Columbia University, New York, New York

(*Received* 6 *January* 1959)

Abstract—The low-temperature breakdown in germanium is shown to be unstable under certain circumstances. The instability occurs when a small increase in current in part of the sample produces a local temperature rise which cannot be dissipated before it in turn causes a further current increase. The instability generally results in thermal relaxation oscillations of the sample with associated electrical relaxation oscillations of the measuring circuitry. The oscillations cause an effective negative resistance to appear when d.c. measurements are made in the usual manner.

VOL. 10 959

It has been known for some time that an apparent negative resistance region occurs in the current density versus electric field characteristics of *n*-germanium at the onset of the breakdown that occurs at low temperatures.[1] This effect, varying greatly from sample to sample, from one set of contacts to another, and from day to day, has been variously attributed by different workers to contacts, anisotropy, geometric distortion of the current paths, and other causes.

The purpose of this communication is to point out that the apparent negative resistance is associated with a high-frequency (typically ~ 1 Mcs) relaxation oscillation of the sample and the associated circuitry, and that under these conditions one simply measures an average electric field across the sample which, by the nature of the oscillations, is always lower than the equilibrium breakdown field. These oscillations are *thermal* in nature,* and their dependence on temperature, T, and sample doping can be understood quantitatively in terms of what is presently known about the variation of breakdown field with T and sample purity,[1–3] which in turn can be understood in terms of the electron velocity and temperature-dependence of the cross-sections for impact ionization A_I and for single electron capture B_T.[4]

* The negative resistance observed on *p*-germanium at M.I.T. Lincoln Laboratories (cf. their *Quarterly Report, Solid State Research*, 1 Aug. 1958, p. 94) is presumably of a similar nature.

Fig. 1 shows the circuit that was used to study the oscillations and the voltage waveforms observed between various points of the circuit. The

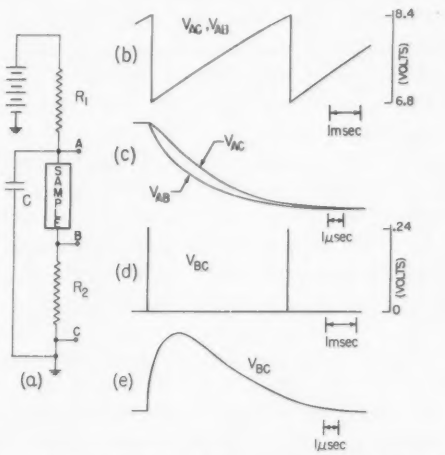

FIG. 1. (a) The circuit used to observe oscillations. For the data shown in (b)–(d), the sample is 3Ω cm Sb-doped Ge, $0{\cdot}98 \times 0{\cdot}27 \times 0{\cdot}19$ cm in dimensions, $R_1 = 10^5\Omega$, $R_2 = 10\Omega$, $C = 0{\cdot}1\mu$F. The circuit parameters were chosen to clarify the various effects.

circuit parameters shown were chosen to separate the various effects that occur. The slow rise of V_{AC} and V_{AB} is exponential with a time constant given by R_1C. The fast decay of V_{AC} and V_{BC} has a time constant $(R_2+R_S)C$, with the intervening

sample contributing an effective resistance, R_S, of the order of 40Ω. The main rise of V_{BC}, proportional to the current through the sample, occurs in less than 1 μsec, and is limited in ultimate speed (as will be seen) by the rate at which the carrier density in the sample can increase, by impact ionization, from its initial negligibly small value. The increase in the total number of carriers in the sample during this time is from $\sim 10^6$ to $\sim 10^{12}$.

The oscillations are presumed to occur in the following manner: After the d.c. voltage is applied, V_{AB} increases until the breakdown field is reached. The current density through the sample increases to a critical value ($\sim 1\ \mu A/cm^2$), at which point a region in the interior of the sample becomes thermally unstable. When this region is heated slightly by the current, B_T decreases, and the balance between impact ionization and single electron capture, which characterizes the breakdown,[3] is destroyed, resulting in a rapid increase in carrier density. The subsequent discharge of capacitor C through the sample causes additional heating. This continues regeneratively until the saturation current is reached (cf. Fig. 1, reference 3). C then discharges through the sample and R_2, the discharge current maintaining all or part of the sample (depending on R_2 and C) at a temperature sufficient to allow conduction with negligible impedance. The criterion for the current to be critical is that a small increase in current produce a temperature rise which cannot be dissipated before the carrier density increases sufficiently to increase the current further. Too large a bias current on the other hand will maintain the sample at a steady state temperature above the maximum temperature for oscillation.

The above mechanism is strongly substantiated by Fig. 2, which shows the temperature-dependence of both the breakdown field and the amplitude of oscillation. It is seen from this figure that the magnitudes of the oscillations correspond to a thermal swing given by the difference between 6°K (above which no oscillations occur) and the initial temperature, assuming (as is the case) that the critical current is in the breakdown region.

The remaining question is whether the known power dissipation (Fig. 1) in the sample can change the temperature by the appropriate amount in the available time. Assuming the sample has once reached 6°K on the discharge cycle (of the condenser), the current is sufficient to maintain the sample at this temperature against the calculated losses to the exchange gas ambient. However, the power input to the sample during the first μsec is only sufficient (using the known heat capacity[5]) to heat a region along the center of the bar of the

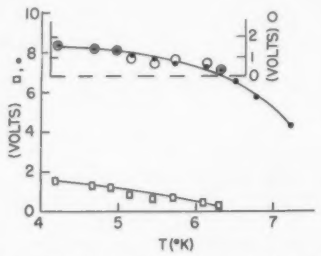

FIG. 2. The solid circles show the variation of breakdown voltage versus temperature for the sample of Fig. 1. The open squares show the amplitude of oscillation (of V_{AB}, Fig. 1a) versus temperature. The open circles are the oscillation-amplitude data superimposed on the breakdown curve to show the relation between the oscillations and the temperature variation of breakdown voltage.

order of 10^{-2} cm diameter to the required temperature. Using a mean specific heat of 4×10^{-4} J/cm³.°K, a thermal conductivity of ~ 1 W unit and a transverse sample dimension ~ 2 mm, the time constant for this heat to equilibrate in the bulk is $(4\times10^{-4}\ J/cm^3.°K)\times(10^{-1}\ cm)^2/(1\ J/°K.\ cm) \sim 4$ μsec. Therefore this small region can heat essentially adiabatically in the rise time of V_{BC} and the necessary instability can arise. In addition, the ionization rate required to produce the observed carrier increase in the time available is consistent with existing data.[6]

As a further check, the oscillations were studied in a sample 0·3 mm on a side ($\sim 1/50$ the cross-sectional area of the sample of Fig. 1 and cut from the same crystal). The oscillations in the two samples were identical. The maximum current the samples would deliver during the fast rise of V_{BC} (as determined by reducing the series resistor R_2) were the same, which is consistent with the picture that only a small part of each carried the current. In addition, as would be expected, the critical current *densities*, which are uniform across the sample before the oscillations start, were the same, though of course the critical currents were different.

Why high-purity samples generally do not oscillate, whereas material with room-temperature resistivity $\sim 4\Omega$ cm or less do, can be understood in terms of the impurity-dependence of the variation of breakdown field with temperature. This will be discussed in more detail in a subsequent publication.[3]

REFERENCES

1. KOENIG S. H. and GUNTHER-MOHR G. R., *J. Phys. Chem. Solids* **2,** 268 (1957).
2. SCLAR N. and BURSTEIN E., *J. Phys. Chem. Solids* **2,** 1 (1957).
3. FINKE G. and LAUTZ G., *Z. Naturforsch.* **12a,** 223 (1957).
4. KOENIG S. H., *Phys. Rev.* **110,** 986 (1958).
   KOENIG S. H. To be published.
5. LAX M., *J, Phys. Chem. Solids* **8,** 66 (1959).
6. KEESOM P. H. and PEARLMAN N., *Phys. Rev.* **91,** 1347 (1953).
7. KOENIG S. H., *International Conference on Solid State Physics in Electronics and Telecommunications, Brussels* (June 1958). Proceedings to be published.

OL.
10
959

J. Phys. Chem. Solids Pergamon Press 1959. Vol. 10. pp. 204–210.

THERMAL, ELECTRICAL AND OPTICAL PROPERTIES OF (In,Ga)As ALLOYS

M. S. ABRAHAMS, R. BRAUNSTEIN and F. D. ROSI

R.C.A. Research Laboratory, David Sarnoff Research Center, Princeton, New Jersey

(*Received* 15 *January* 1959)

Abstract—The (In,Ga)As system exhibits complete solid miscibility. Homogeneous alloys were produced across the entire system by using the method of zone-levelling. Physical measurements show that the lattice thermal conductivity decreases markedly with alloying and exhibits a minimum value of about 0·05 $Wdeg^{-1}cm^{-1}$ at an alloying composition of about 50 per cent. The thermoelectric power varies linearly with the logarithm of the carrier concentration for non-degenerate crystals, and from these data it appears that the "density of states mass" is independent of alloying. The mobility of electrons decreases monotonically with increasing percentages, up to about 70 per cent of GaAs. The band gap varies continuously with composition, and a concave upward dependence is observed on going from InAs to GaAs.

VOL.
10
195

1. INTRODUCTION

THE recent work of FOLBERTH[1] on alloy systems of III–V compounds has indicated that the GaAs–GaP and InAs–InP systems exhibit complete solid solubility, and that by suitable alloying one can obtain a wide range of semiconducting properties. In view of these results, it was thought that the system InAs–GaAs might also exhibit solid miscibility. This was considered possible, since a favorable size-factor exists for these two compounds, with due realization that size-factor alone is not a sufficient criterion. Complete solid

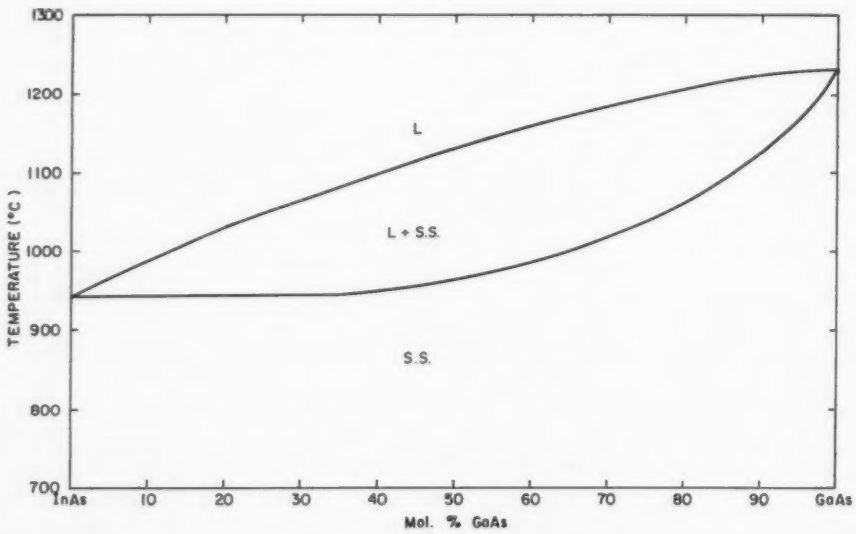

FIG. 1. The system InAs–GaAs.

miscibility in this system would be most desirable in view of the marked difference in the physical properties of the component compounds.

Phase-equilibrium studies by VAN HOOK and LENKER[2] have shown complete solid miscibility in the system InAs–GaAs. The phase diagram for this system, shown in Fig. 1, is characterized by a simple ascendent liquidus and solidus. The present work was undertaken to investigate the variation with composition of typical thermal, electrical and optical properties. The properties investigated were the lattice thermal conductivity, the Hall electron mobility and the band gap. In addition, the dependence of the thermoelectric power on carrier concentration was studied.

2. EXPERIMENTAL PROCEDURE

(a) *Preparation of alloys*

The alloys were prepared by reacting indium arsenide with a predetermined amount of gallium arsenide, either by gradient freezing or by zone-levelling.[3] The indium arsenide and gallium arsenide, which were used in preparing the final ingots, were obtained by reacting the elements in a graphite crucible which was contained in an evacuated silica tube. The crucible was heated to the melting point of the compound in a horizontal, resistance-type furnace and held at this temperature for about 1 hr. After this, the crucible was slowly cooled to room temperature with solidification proceeding from one end of the ingot to the other.

The (In,Ga)As alloys were prepared by placing the desired amount of InAs and GaAs in a graphite crucible, and then sealing the crucible and its contents in a silica tube under a vacuum of about 10^{-7} mm Hg. A 1 per cent excess of arsenic was used in preparing these alloy ingots, as well as in the preparation of the components InAs and GaAs. The silica tube was long enough so that at all times there was a portion within the after-heater section of the furnace, which was controlled at 600°C. The after-heater served to maintain the arsenic vapor pressure at about 1 atm.

In gradient freezing, the tube containing the crucible with the charge was maintained stationary while the furnace was moved from the front end of the ingot at constant speed. With this method, homogeneous sections of the ingots were produced with compositions up to 30 molecular per cent of either compound. Growth rates of 1-3 in./day were employed. Alloys with compositions greater than 30 per cent had a composition spread as large as 12 per cent. These composition variations were determined from lattice-constant measurements, using X-ray diffraction methods.

In zone-levelling, a molten zone was passed from the front to the tail end of the ingot and then in the reverse direction. The overall ingot length was 8 in. and the length of the molten zone was about 1 in. In all cases the ingots were given two passes. Zoning rates of 5 and 10 in./day were used. The homogeneity of the alloys was strongly dependent on growth rate. The slower zoning rate produced alloys near the middle of the system with composition spreads of 4 per cent compared to the 12 per cent spread observed on gradient freezing. Homogeneity not only improves with decreased zoning rates, but also with decreased alloying at a constant zoning rate. This is to be expected in view of the occurrence of constitutional supercooling[4] on solidification. Alloys produced near the ends of the phase diagram exhibited composition spreads < 2 per cent when zone-levelled at 5 in./day.

The ingots were polycrystalline with very coarse grains elongated parallel to the growth direction There was no evidence of microcracks or porosity when grown in a graphite crucible. Chemically, the ingots contained 10–100 p.p.m. of spectrographically detectable impurities. The elements found in order of decreasing abundance were: Cu, Al, Si, Mg, Pb, Ag.

(b) *Physical measurements*

The electrical resistance was determined by voltage scanning. An a.c. current method was used in order to eliminate spurious thermoelectric c.m.f. due to Joule heating. The a.c. voltage drop across the crystal was scanned by a motor-driven potential probe, and was fed into a synchronous detector whose output was recorded on a d.c. recorder. Before each measurement, the apparatus was calibrated by switching the detector across a standard resistor.

The thermal conductivity was determined by employing the technique of placing the specimen between a heater and a sink. The heater was

energized by passing an electric current through a resistance wire embedded in the heater. Copper–constantan thermocouples, the junctions of which were soldered into small holes located in the heater and sink, were used to measure the temperatures of the heater and sink. The diameters of the thermocouple wires were so chosen as to make the heat transfer along the thermocouples negligible. The reference junctions of the thermocouples were maintained at 0°C. Measurements were carried out in a vacuum of about 10^{-4}mm Hg. Details of this apparatus and that used to measure the electrical resistance are given in a previous paper.[5] The thermal conductivity κ was determined from the relation,

$$\kappa = (W/\Delta T)(l/A), \tag{1}$$

where W(watts) is the heat input to the heater, ΔT (°C) is the temperature difference between the heater and the sink, l (cm) is the length and A (cm^2) is the cross-sectional area of the sample with dimensions, 1 cm × 0·5 cm^2. All the results were corrected for radiation losses which amounted to 2–4 per cent of the measured value of κ. The error due to the thermal contact resistance between the sample and the heater and sink was minimized by the use of a thin layer of silicone oil at the contact surfaces. This correction amounted to about 0·2–0·4 per cent of the measured value of κ.

The thermoelectric power was measured in the thermal conductivity apparatus. The voltage (V) between the copper wires of the heater and sink thermocouples was measured, using the same specimens as that used in measuring κ. The thermoelectric power is given by

$$Q = V/\Delta T, \tag{2}$$

where ΔT has been defined above.

The electron mobility was determined by measuring the Hall effect. The magnetic field intensity across the thickness of the specimen was equal to 2400 G, and a direct current of 10 mA was used along the length of the specimen. The specimen size was about 1 × 2 × 7 mm. Ohmic contacts were obtained in all cases by using indium dots between the specimen and the contact points of the apparatus.

3. RESULTS AND DISCUSSION

(a) *Thermal conductivity*

The lattice thermal conductivity, κ_{ph}, in extrinsic material is related to the measured total thermal conductivity, κ, by the equation,

$$\kappa = \kappa_{ph} + \kappa_{el}, \tag{3}$$

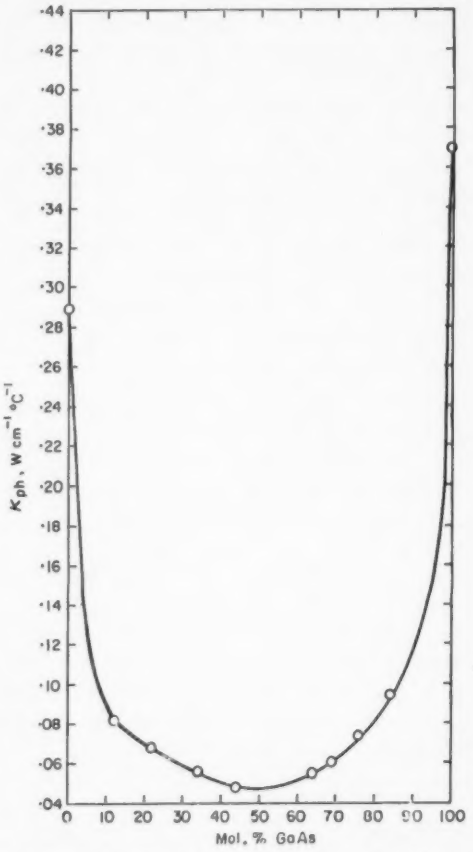

FIG. 2. Variation of lattice thermal conductivity, κ_{ph}, with composition in the InAs–GaAs system.

where κ_{el} is the electronic component and is directly related to the electrical conductivity, σ, and the temperature, T, by the expression

$$\kappa_{el} = S(k/e)^2 T\sigma. \tag{4}$$

The constant S has the numerical value of 2 for non-degenerate electrons and lattice scattering, 4 for non-degenerate electrons and impurity scattering, and $\pi^2/3$ for degenerate electrons.[6] Thus, if the test temperature and electrical conductivity are known, κ_{el} may be evaluated from equation (4) and κ_{ph} from equation (3).

In Fig. 2, the lattice thermal conductivity at 300°K is plotted as a function of composition. The measured values of electrical conductivity indicate that κ_{el} is negligible for all the crystals except the one containing 36 per cent InAs. For the degenerate alloy containing 36 per cent InAs, κ_{el} is equal to 13 per cent of the total thermal conductivity. It is apparent from Fig. 2 that κ_{ph} decreases rapidly with alloying and achieves a minimum of 0·047 $Wdeg^{-1}cm^{-1}$ corresponding to an alloy composition of $\sim$ 50 per cent. This decrease in κ_{ph} is most likely due to scattering of phonons[7] due to lattice strains resulting from the solid-solution alloying and, perhaps, from a mass effect due to the difference in weight of the gallium and indium atoms. The effectiveness of a small alloying addition on lowering the thermal conductivity of either InAs or GaAs is remarkable. A 10 per cent addition of either constituent into the respective pure compound lowers the thermal conductivity of the lattice by about 70 per cent.

(b) *Thermoelectric power*

The thermoelectric power[8–10] for a non-degenerate semiconductor with a single sign of carrier predominating may be expressed as:

$$Q = \pm 86{\cdot}2\left[\ln\frac{4{\cdot}70\times10^{15}}{n}+\right.$$

$$\left.+\tfrac{3}{2}\ln\frac{m^{(N)}}{m}+\frac{|\Delta\epsilon_T|}{T}+\tfrac{3}{2}\ln T\right]. \quad (5)$$

Here, Q is the thermoelectric power in $\mu V\ deg^{-1}$, and n is the carrier concentration per cm^3 HERRING[8] refers to the quantity, $m^{(N)}$, as the "density of states mass." $|\Delta\epsilon_T|$ represents the average kinetic energy of the electrons relative to the band edge. From equation (5), at constant temperature Q may be expected to vary as $-\ln n$ with a slope equal to 86·2 $\mu V\ deg^{-1}$, if the "density of states mass" and kinetic energy term are constant. In Fig. 3, Q is plotted against the logarithm of n at 300°K for a series of alloys ranging in composition from 0 to 100 molecular per cent InAs. Since all the points corresponding to the non-degenerate samples fall along a straight line having the required slope, it appears that the sum of the contribution due to the "density of states mass" and the kinetic-energy terms does not vary with alloying. Since the kinetic-energy term depends upon the type of scattering and, hence, n, $|\Delta\epsilon_T|$ can be expected to be constant in view of the high carrier concentration of the measured samples. Therefore, the dominant scattering mechanism in these samples may be regarded as one of impurity

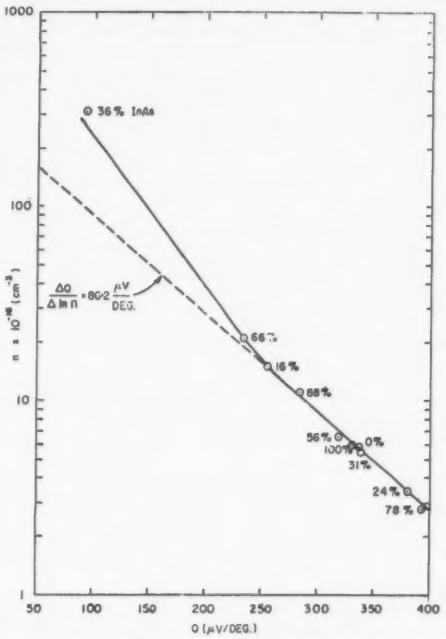

FIG. 3. Log n versus Q for (In,Ga)As alloys.

scattering. This is substantiated by the fact that a calculation of the kinetic-energy term, $|\Delta\epsilon_T|/kT$, from equation (5) yields the value of 3·1, which is in good agreement with the value reported by SPITZER and HÄRM[11] for pure ionized-impurity scattering. This calculation was carried out from the data on pure InAs, using the optical value reported by SPITZER and FAN[12] of 0·03 for $m^{(N)}/m$. Thus, from the apparent constancy of $|\Delta\epsilon_T|$ with alloying, it would appear that $m^{(N)}/m$ is invariant with alloying.

(c) *Electron mobilities*

Ideally, the electron mobility, μ, should be plotted as a function of composition at constant carrier concentration. Unfortunately, the available

data do not permit this to be done. In Fig. 4, however, several points have been chosen which are not widely different with respect to their carrier concentration. It can be seen that with decreasing percentages of InAs, the Hall electron mobility drops almost linearly down to about 30 per cent

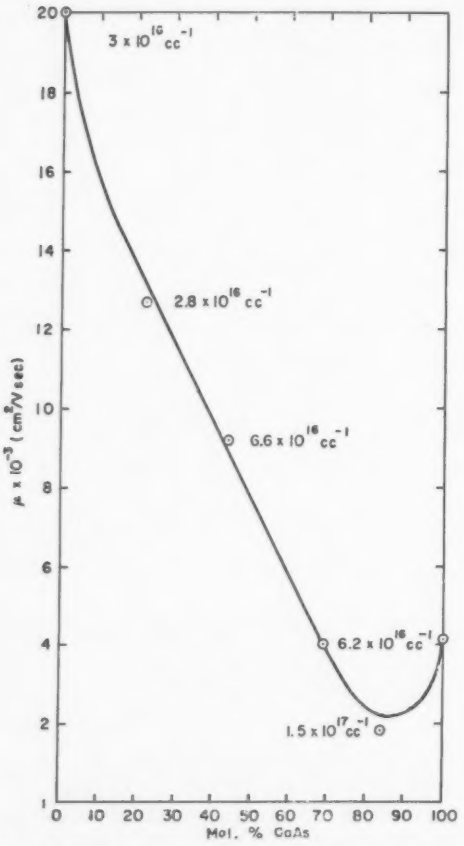

FIG. 4. Variation of mobility with composition in the InAs–GaAs system.

InAs. This is to be compared to the work of FOLBERTH,[1] who found a monotonic decrease in the mobility of InAs on alloying with InP.

(d) *Energy band gap*

The variation in band gap with composition in the InAs–GaAs system is shown in Fig. 5. These data were obtained from infrared transmission measurements made on optically polished, 20-mil-thick samples, employing CaF_2 optics; the usual sample-in–sample-out technique was used. A typical transmission curve is reproduced in Fig. 6. It was found that for samples relatively homogeneous in composition the transmission curves were parallel in the steep portions, and the band gap was arbitrarily taken as the energy at half the maximum transmission. In samples with large inhomogeneities in composition, the absorption edges were more diffuse. In no case did X-ray analysis and annealing studies indicate the presence of a second phase. It is interesting to note that it is now possible to produce material having any desired band gap in the range from 0·35 to 2·24 eV by solid-solution alloying. The range 0·35–1·35 eV is covered by the InAs–GaAs system, while the range 1·35–2·24 eV is covered by the GaAs–GaP system.[1]

The concave upward dependence of the band gap on composition for InAs–GaAs, shown in Fig. 5, is to be contrasted with similar studies on other alloy systems. In the InAs–InP system,[1] a linear dependence of band gap on composition is observed, while in the GaAs–GaP system[1] a concave downward dependence is observed. In the Ge–Si system,[13] a distinct discontinuity of the rate of change of band gap versus composition is observed, and this indicates that the band edges shift to different positions in momentum space.[14] From the results in the InAs–GaAs system, no definite break in the slope is indicated, and consequently the band edges in this system probably remain essentially at the same position in k-space. This conclusion is consistent with the results of the thermoelectric-power measurements, where it appears that the density of states effective mass does not vary with alloying. The effective masses of electrons in GaAs and InAs are $\sim 0{\cdot}043m$[15] and $0{\cdot}03m$,[11] respectively, as determined from optical measurements. Since it appears that such small effective masses are characteristic of conduction-band minima that lie at the center of the Brillouin zone,[12] the lowest conduction-band minima are probably those with $k = 0$ for all compositions of InAs and GaAs.

4. SUMMARY

(*a*) Some properties of the InAs–GaAs system, which exhibits complete solid solubility, have been examined.

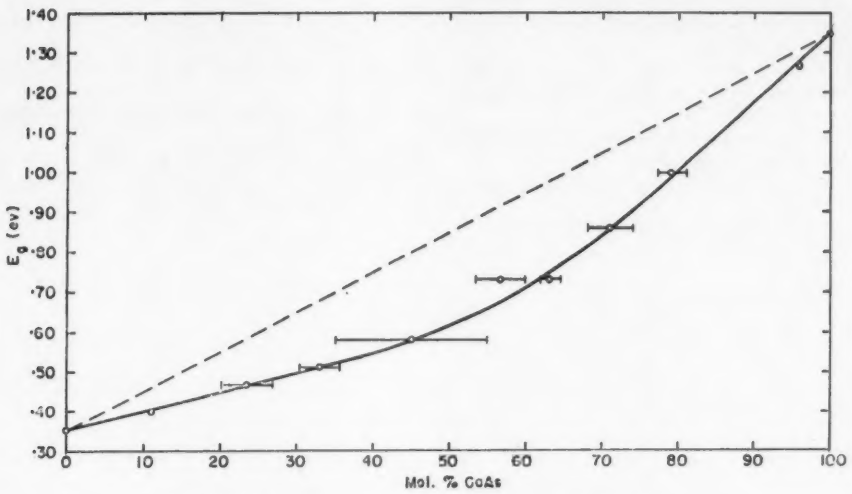

FIG. 5. Band gap versus composition in the InAs–GaAs system.

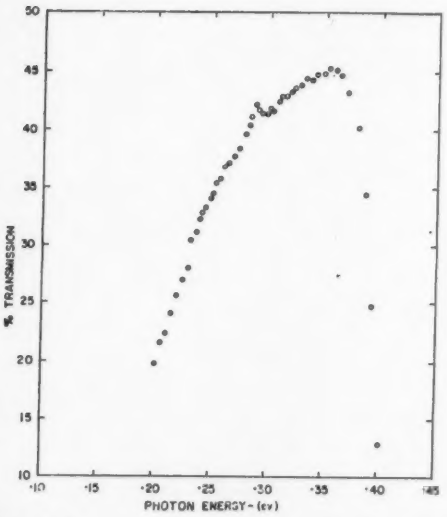

FIG. 6. Transmission versus photon energy for an alloy containing 11 per cent GaAs. Band gap = 0·40 eV.

(*b*) The process of zone-levelling has produced homogeneous alloys across the entire system. Homegeneity is favored by slow zoning rates.

(*c*) The lattice thermal conductivity, κ_{ph}, decreases markedly with alloying and exhibits a minimum at an alloying composition of ~ 50 per cent.

(*d*) The thermoelectric power varies linearly with the logarithm of the carrier concentration for non-degenerate crystals. It appears that the "density of states mass" is independent of alloying.

(*e*) The Hall electron mobility decreases monotonically with increasing percentages, up to about 70 per cent, of GaAs.

(*f*) The band gap varies continuously with composition for the entire system. A concave upward dependence is observed on going from InAs to GaAs.

Acknowledgements—The authors would like to express their appreciation to Mr. P. D. DOWNEY for assisting in the preparation of the alloys; to Mr. D. A. KRAMER for assisting in the physical measurements; to Mr. H. H. WHITAKER for performing the spectrographic analyses; to Dr. J. WHITE and Mr. W. C. ROTH for performing the X-ray diffraction studies; and to Messrs. H. J. VAN HOOK and E. S. LENKER for permission to reproduce the InAs–GaAs phase diagram.

REFERENCES

1. FOLBERTH O. G., *Z. Naturforsch.* **10a,** 502 (1955).
2. VAN HOOK H. J., and LENKER E. S., *The System InAs–GaAs.* In course of publication.
3. PFANN W. G., *Trans. Amer. Inst. Min (Metall.) Engrs.* **194,** 747 (1952).
4. RUTTER J. W. and CHALMERS B., *Canad. J. Phys.* **31,** 15 (1953).

5. ROSI F. D., ABELES B., and JENSEN R. V., *Materials for Thermoelectric Refrigeration, J. Phys. Chem. Solids* **10,** 191 (1959).
6. BLATT F. J., *Solid State Physics* (Ed. F. SEITZ and D. TURNBULL) Vol. 4, p. 221. Academic Press, Inc., New York (1957).
7. KLEMENS P. G., *Handbuch der Physik* Vol. 14, p. 198. Springer-Verlag, Berlin (1956).
8. JOHNSON V. A. and LARK-HOROVITZ K., *Phys. Rev.* **92,** 226 (1953).
9. YAMASHITA J., *J. Phys. Soc. Japan* **4,** 310 (1949).
10. HERRING C., *Phys. Rev.* **96,** 1163 (1954).
11. SPITZER L. Jr. and HÄRM R., *Phys. Rev.* **89,** 977 (1953).
12. SPITZER W. G. and FAN H. Y., *Phys. Rev.* **106,** 882 (1957).
13. JOHNSON E. R. and CHRISTIAN S. M., *Phys. Rev.* **95,** 560 (1954).
14. HERMAN F., *Phys. Rev.* **95,** 847 (1954).
15. BARCUS L. C., PERLMUTTER A., and CALLAWAY J., *Phys. Rev.* **111,** 167 (1958).

VOL
10
195

J. Phys. Chem. Solids Pergamon Press 1959. Vol. 10. pp. 211–216.

TRAPPED CHARGE AND THE LOW-TEMPERATURE LUMINESCENCE OF UNDOPED KI*

K. TEEGARDEN and R. WEEKS†

The Institute of Optics, University of Rochester, Rochester, N.Y.

(*Received* 5 *December* 1958; *revised* 7 *January* 1959

Abstract—New data are presented on the previously reported low-temperature blue luminescence of undoped KI. It is shown that the emission previously observed during irradiation in the fundamental bands can also be stimulated by irradiation in the *F*- and *F'*-bands formed by exposure to ultraviolet light at 93°K. The crystals display a burst of red luminescence when warmed after irradiation with light absorbed in the fundamental bands at 93°K. No emission upon irradiation in the *F*-band at 93°K occurs if the *F*-centers have been formed at room temperature. It is suggested that the red luminescence occurs when holes are released from traps during warming and that the blue luminescence is due to the recombination of electrons with trapped holes at 93°K.

1. INTRODUCTION

SOME time ago, one of the authors reported on the luminescence of undoped KI stimulated by irradiation in the fundamental band region at low temperature.[1] It was shown then that single crystals of KI emitted light in a band centered at about 3·3 eV with a quantum efficiency between 0·5 and 1·0 when so illuminated. Recently a similar emission from single RbI crystals has been observed. Since then work has been going on to determine the mechanism for this luminescence. It is of great interest to know whether or not the luminescence is directly associated with the decay of excitons, for example. The work is not yet completed, but results have been obtained which shed some light on the processes involved.

2. EXPERIMENTAL PROCEDURE

The single crystals used in this work were cleaved from boules grown by Dr. KARL KORTH of Kiel, Germany. No trace of common activators such as the heavy metals was observed in either the optical absorption spectrum of the crystals or their excitation and emission spectra.

The apparatus and procedure used to obtain the excitation and emission spectra shown in Figs. 1 and 2 have been described in a previous

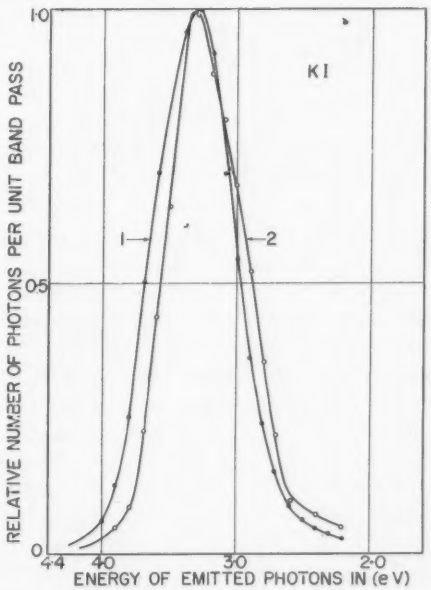

FIG. 1. The emission spectrum of KI at 93°K. Curve 1 shows the emission excited by 6·1-eV photons. Curve 2 shows the emission excited by 1·8-eV photons during exposure to 6·1-eV radiation.

* Research supported in part by the U.S. Air Force through the Air Force Office of Scientific Research of the Air Research and Development Command.

† Now at the Richard D. Brew Company, Inc., Concord, N. H.

paper.[1] It should be noted, however, that the excitation spectrum shown in Fig. 2 extends to shorter wavelengths than those previously presented. The instrument used to obtain the new data was a Bausch and Lomb single monochromator equipped with fused-silica prisms and lenses. This material is more transparent in the far ultraviolet than the original crystal quartz used in the monochromator. The instrument was operated in a nitrogen atmosphere, since oxygen absorbs below about 6·7 eV. The new prisms did not significantly change the dispersion of the monochromator. Band-pass figures previously given for excitation-spectra measurements can therefore be used in connection with Fig. 2.[1]

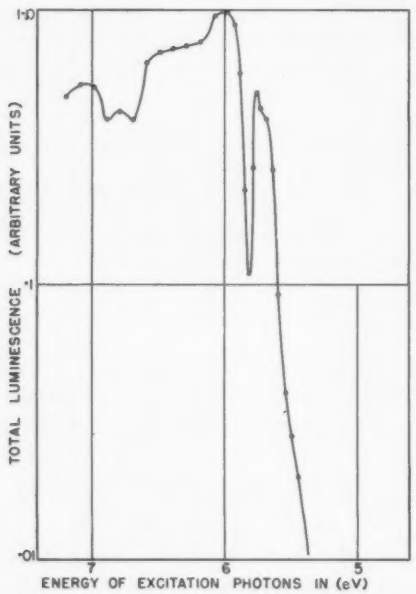

FIG. 2. The excitation spectrum for 3·3-eV emission in the region of the fundamental bands of KI.

An important part of this work is concerned with the stimulation of luminescence by irradiation with light absorbed in the *F*-band of KI. In this experiment the *F*-centers were formed by irradiation in the fundamental bands of the crystals and presumably were accompanied by trapped holes. Under these circumstances the *F*-band bleached readily, and the quantum yield for luminescence per incident photon decreased with time of irradiation. It was found that excitation intensities great enough to show an observable luminescence bleached the *F*-band in a few seconds. Because of this, measurements of excitation and emission spectra for excitation in the *F*-band were made as described below.

The crystal was illuminated simultaneously with a constant intensity of ultraviolet light absorbed in the fundamental band region and red light chopped at 15 c/s. A monochromator with fused-silica optics was used to provide the ultraviolet radiation. The slits of this instrument were set to give a band pass of about 0·2 eV at 6·1 eV. Red light was obtained from a single monochromator with glass prisms and a band pass of about 0·2 eV at 2·0 eV. No measurement was made of the absolute intensity of the red light used. From past experience one would estimate 10^{13}–10^{14} quanta incident per sec as a reasonable value. The emission of the crystal was analyzed with a third monochromator equipped with crystal-quartz optics, as described in a previous paper.[1] The signal from a 6199 photomultiplier placed at the exit slit of this monochromator was fed into an amplifier tuned to 15 c/s. The output of the amplifier was measured with an electronic voltmeter. Care was taken to be sure that the signal attributed to luminescence stimulated by light absorbed in the *F*-band only occured when the crystal was also irradiated with ultraviolet light. As would be expected, scattered light from the glass prism monochromator caused a 15 c/s signal to appear in the output of the photomultiplier even when the crystal was not luminescing. To correct for this, scattered-light measurements were made with the ultraviolet light off, so that no *F*-centers were present in the crystal. The continuous background of scattered light determined in this way was subtracted from the readings taken with the ultraviolet on. This correction amounted to about 10 per cent in the peak of the 3·3 eV emission band.

It should be noted that excitation spectra made in the region of the *F*-band were not measured with a constant incident intensity. Corrections for the changing dispersion of the glass prism monochromator and changing intensity of the tungsten light source were not made. Both these factors would probably lead to an increase in the quantity "total luminescence" with increasing wavelength.

There is no reason to suspect that this increase was anything but monotonic, however. The essential features of Fig. 3 are therefore most likely correct.

Measurements of the temperature-dependence of the luminescence stimulated by light absorbed

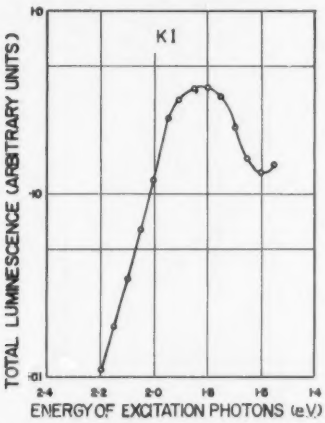

FIG. 3. The excitation spectrum for 3·3-eV emission in the region of the *F*-band of KI. This spectrum was measured with the crystal exposed to a constant flux of 6·1-eV photons.

in the fundamental bands were taken in the usual way by warming the crystal slowly with a thermocouple attached to record the temperature. The rate of warming was kept small enough to prevent thermally stimulated luminescence from interfering with the measurements. A typical value for the rate of warming was 3° min.

3. RESULTS

The previously reported emission spectrum of single undoped crystals of KI for excitation with light absorbed in the fundamental band region at 93°K is shown by the curve marked (1) in Fig. 1. The excitation spectrum of the luminescence is shown in Fig. 2. It has long been known that *F*-centers are produced in alkali halide single crystals when they are exposed to light absorbed in the fundamental bands.[2] The number of *F*-centers so formed is quite small, but the concentration may be quite high when the light is absorbed very near the surface. An attempt was made to determine the number of *F*-centers present after irradiation by measuring a change in the optical density of the crystals at the wavelength of the peak of the *F*-band. No such change was observed. Since a density change of 0·05 was the smallest measurable, the number of *F*-centers in the 1-mm-thick crystals must have been less than $10^{14}/cm^2$. One must remember, however, that all of the coloration occurred in a layer about 10^3 Å thick, because of the high absorption constant of KI at 6·1 eV. Thus color-center densities as high as $10^{19}/cm^3$ may have been present.

We have found that crystals previously exposed to ultraviolet at 93°K luminesce when irradiated with light absorbed in the *F*-band at 93°K. This luminescence is hard to observe because during the irradiation the *F*-centers are bleached. One sees a luminescence which decays away with a time constant of the order of seconds with reasonable excitation intensities. To measure the emission and excitation spectra of this luminescence, it is necessary to maintain a constant concentration of *F*-centers by simultaneous irradiation with ultraviolet light. By using a steady ultraviolet illumination and chopping the red light, it was possible to observe only the luminescence produced by the red light, as described in the section above. Emission spectra of the luminescence measured in this way are shown by the curve marked (2) in Fig. 1. It is to be noted that the emission bands for ultraviolet and *F*-center light excitation are almost identical.

The position of the peak of the emission for *F*-center excitation was also located roughly by the laborious process of irradiating first with ultraviolet and then with light absorbed in the *F*-band and taking the initial height of the pulse of luminescence as a measure of the relative number of emitted photons. This method gave the same result as the more sophisticated process described above.

The red and near-infrared excitation spectrum for 3·3-eV emission in the case of KI crystal previously exposed to 6·1-eV radiation at 93°K is shown in Fig. 3. There is a peak in this spectrum at 1·8 eV. This corresponds to the peak of the *F*-band in KI. The rise towards longer wavelengths below 1·65 eV may be due to the presence of *F'*-centers, although this is not certain.

After exposure to light absorbed in the

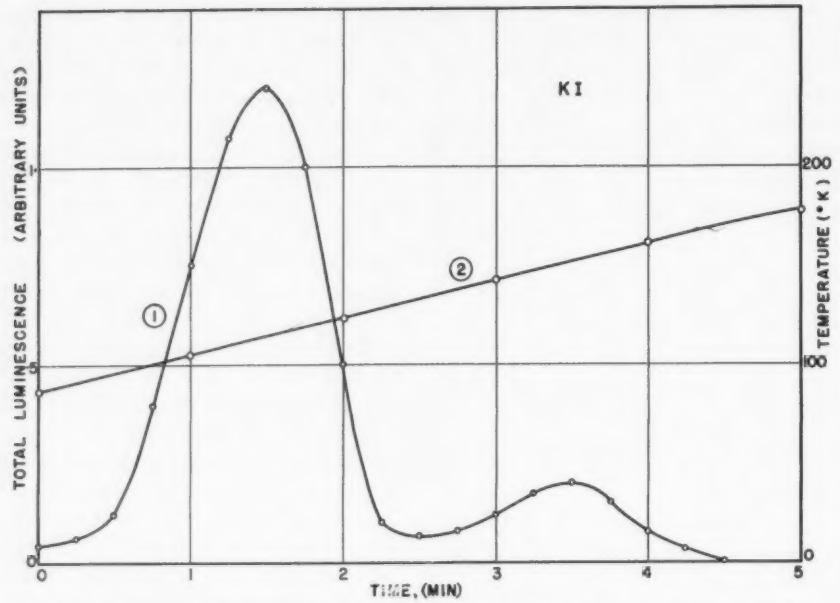

FIG. 4. A thermal-glow curve for KI taken after exposure to 6·1-eV photons at 93°K. Curve 1 gives the total luminescence of the crystal during warming. Curve 2 shows the temperature of the crystal.

fundamental bands at 93°K, the crystals exhibited a burst of luminescence when warmed. The maximum of this thermal glow peak occurred at 118°K. A typical thermal glow curve is shown in Fig. 4. It was determined by means of filters (Wratten numbers 26 and 34) that the emission from the crystals during warming lay in the red at about 2·0 eV. The response of the photomultiplier used was very low in this region, so that no accurate determination of the emission spectrum was possible.

When the crystals were exposed to light absorbed in the fundamental bands at 93°K and subsequently exposed to light absorbed in the *F*-band, the ultraviolet being shut off, a burst of 3·3 eV emission was observed, as has been described above. This is illustrated in Fig. 5. If, however, the exposure to ultraviolet light occurred at a temperature somewhat above the temperature of the thermal burst of luminescence, subsequent exposure to light absorbed in the *F*-band at 93°K produced less emission, as is shown in Fig. 5. If the crystal was irradiated with 6·1 eV photons at room temperature, no luminescence

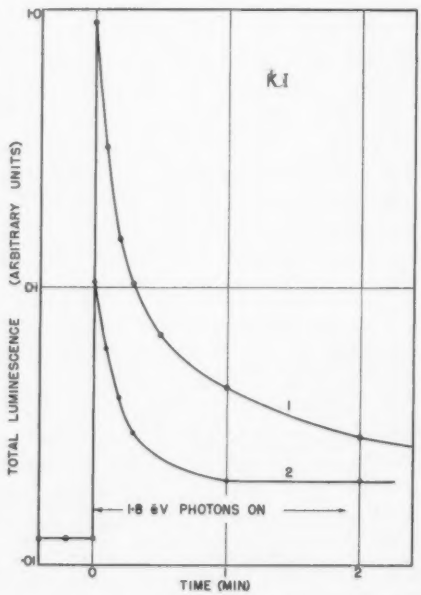

FIG. 5. Pulses of luminescence stimulated at 93°K by 1·8-eV photons after exposure to 6·1-eV photons at: (1) 93°K, (2) 144°K.

could be observed upon illumination with F-band light at 93°K.

The temperature-dependence of the relative quantum efficiency of the 3·3 eV emission for stimulation with 6·1 eV photons is shown in Fig. 6. It is interesting to note that the quantum efficiency for the luminescence is down by a factor of about 5 at 118°K, the temperature of the thermal burst of red luminescence.

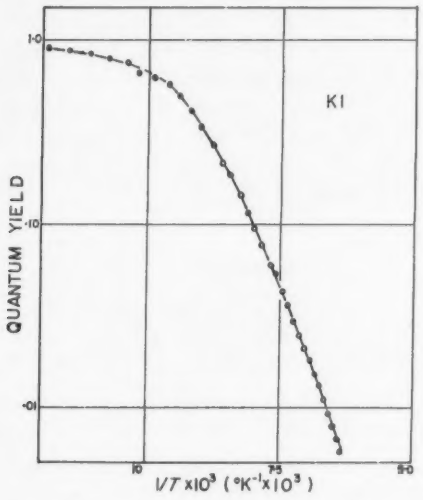

FIG. 6. The temperature-dependence of the quantum efficiency of the 3·3-eV emission for stimulation with 6·1-eV photons.

Photoconductivity measurements were made on crystals of KI after irradiation with light absorbed in the fundamental bands to form F-centers. For example, a crystal was first exposed to 6·1 eV radiation at room temperature and then with light of wavelength greater than 6000 Å selected with a Wratten no. 26 filter. The red light gave rise to a pulse of photoconductivity which decayed away in a time of the order of seconds. The source of this current was undoubtedly F-centers formed by the ultraviolet light. At room temperature no F'-centers are formed by the ultraviolet.[3] If the crystals were irradiated with red light at 118 or 93°K after exposure to ultraviolet at room temperature, the photocurrents were more than a factor of 10 smaller than those observed at room temperature. This type of measurement is being extended to crystals irradiated with ultraviolet at 93°K to determine the effect of F'-centers on the photoconductivity.

4. CONCLUSIONS

In interpreting the data presented above we must utilize the large store of information about photochemical processes in the alkali halides which has been accumulated during past years. We can draw on this store to make analogies between the behavior of KI and the other alkali halides and to point out differences between the different substances.

Irradiation in the fundamental band region of KI produces trapped charge in the form of F-centers and probably trapped holes as it does in the other alkali halides.[2,4,5] In the case of KI at low temperature, such radiation also produces a high-efficiency luminescence with emission principally at 3·3 eV.[1] Subsequent irradiation in the F-band bleaches the F-center and produces luminescence as has been shown in this paper. We know that irradiation in the F-band leads to the excitation of electrons bound to negative ion vacancies. The observed emission must be due to the interaction of these electrons with some trap. In view of past experience with the alkali halides, a possible hypothesis is that the electrons recombine with trapped holes.[6] Since the emission during irradiation with light absorbed in the F-band is the same as the high-efficiency emission observed during irradiation in the fundamental band region, the conclusion is that this latter emission must also be due to electrons interacting with the same trap, i.e., by hypothesis, trapped holes. In this case the electrons and holes are formed by band-to-band transitions or by the dissociation of excitons.

There has been much work done in the past on the properties of trapped holes in the alkali halide. It has been shown that there are many hole traps which form at low temperature, but which ionize when the crystals are warmed to room temperature.[5–11] In KCl and KBr bursts of free charge and luminescence occur during warming after exposure to ultraviolet radiation or X-rays at low temperature.[7] By analogy with these results we may tentatively attribute the burst of red luminescence observed in the present warming experiments to the release of trapped holes. As was demonstrated in the present work, F-centers

formed in KI above the temperature of this burst of red luminescence are less efficient in producing luminescence at 93°K. This would be the case, if the trapped holes destroyed by warming were the recombination centers necessary for the electrons to cause luminescence at 93°K or if fewer F-centers were produced at the higher temperatures. However, from the photoconductivity data it is evident that some F-centers are formed when KI is irradiated with 6·1-eV photons at temperatures above 118°K. Further, SMAKULA has shown that more F-centers are produced for a given number of quanta absorbed in the tail of the fundamental band at room temperature than at 93°K for KBr.[2] The experiments of APKER and TAFT and PHILIPP and TAFT indicate that F-center concentrations of the order of $10^{19}/cm^3$ are obtained at room temperature when KI single crystals are irradiated with light absorbed in the first fundamental band.[4] There seems to be no reason to suspect that the number of F-centers produced with ultraviolet radiation is much different at 93°K and room temperature. It is therefore suggested that the thermal burst of red luminescence is connected with the ionization of holes from traps and that these trapped holes constitute the recombination centers giving rise to 3·3-eV emission at 93°K.

Considering the high efficiency of the low-temperature luminescence, it is probable that these recombination centers represent a major trap for electrons at low temperatures and considerably reduce photocurrents below 118°K. In the case of photoelectrons from F-centers, this reduction would be obscured by the rapid decrease in the quantum yield for free electrons with temperature. F'-centers are ionized at any temperature, however, and these may be used to study the dependence of the schubweg of free electrons on temperature. One would expect to find that the ranges of electrons from F'-centers at 93°K are greatly enhanced, if the F-centers are formed with ultraviolet radiation above the temperature at which the recombination centers ionize, i.e. 118°K.

It should be noted that if a strict relation between free electrons and the 3·3-eV luminescence can be established, a study of the excitation spectrum of this luminescence will provide information about the production of free electrons in the fundamental band region of KI.

REFERENCES

1. TEEGARDEN K., *Phys. Rev.* **105,** 1222 (1957).
2. SMAKULA A., *Z. Phys.* **63,** 762 (1930).
3. GLASER G., *Nachr. Akad. Wiss. Göttingen* **3,** 31 (1937).
4. APKER L. and TAFT E., *Phys. Rev.* **79,** 964 (1950).
5. CHIAROTTI G. and INCHAUSPE N., Private communication.
6. See SEITZ F., *Rev. Mod. Phys.* **18,** 384 (1946); **26,** 7 (1954).
7. DUTTON D. and MAURER R. J., *Phys. Rev.* **90,** 126 (1953).
8. DUTTON D., HELLER W. R. and MAURER R. J., *Phys. Rev.* **84,** 363 (1951).
9. DORENDORF H., *Z. Phys.* **129,** 317 (1951).
10. CASTNER T. G. and KÄNZIG W., *J. Phys. Chem. Solids* **3,** 178 (1957).
11. CASLER R., PRINGHEIM P. and YUSTER P. H., *J. Chem. Phys.* **18,** 877, 1564 (1950).

J. Phys. Chem. Solids Pergamon Press 1959. Vol. 10. pp. 217–221.

THE CATHODIC SPUTTERING OF SILVER

G. J. OGILVIE and M. J. RIDGE*

Division of Tribophysics, Commonwealth Scientific and Industrial Research Organization, University of Melbourne, Australia

(*Received* 31 *December* 1958; *revised* 29 *January* 1959)

Abstract—Single and polycrystalline specimens of silver have been sputtered at pressures in the ranges $10–50 \times 10^{-3}$ and $0{\cdot}1–1{\cdot}0 \times 10^{-3}$ mm Hg. It has been shown that sputtering with helium, argon and xenon ions does not roughen the surface, but tends to make it smooth. Mercury and oxygen produce facets. A polycrystalline specimen sputtered with inert-gas ions develops steps at the boundaries between adjacent crystals. This is shown to be due to the sputtering rate being dependent on the orientation of the exposed crystal face.

1. INTRODUCTION

THE erosion of the cathode in a glow discharge by positive-ion bombardment or cathodic sputtering has been extensively studied not only for its intrinsic interest but also because of its usefulness as an experimental tool. The principal uses to which sputtering has been put are:

(*a*) etching of metal specimens for microscopic examination,

(*b*) production of clean surfaces,

(*c*) coating of surfaces with materials removed from the cathode. The subject has been reviewed from different points of view by HOLLAND[1], FRANCIS[2], MASSEY and BURHOP[3], and WEHNER[4].

Although studies of sputtering have been made for more than a century, the processes responsible for the removal of atoms from the cathode are only poorly understood, and there are not sufficient data on which to base a satisfactory theory. Experimental studies of sputtering are liable to be in error because of the large number of variables which should be controlled. An attempt at a systematic study of etch figures produced on the cathode surface has been made by WEHNER[4–6], who sputtered a number of metals, including silver, with mercury ions with a nominal energy of 100–300 eV. Mercury, however, is not chemically inert with respect to these metals, and WEHNER's observations need amplification by parallel experiments with inert-gas ions before the full significance of his results can be assessed.

It is hoped that the experiments described in this and subsequent papers will fill, at least in part, the gap in the experimental data about the changes produced in a surface by sputtering. In the present paper some of the larger-scale effects due to sputtering are studied. Both single-crystal and polycrystalline specimens of silver have been sputtered with inert-gas ions and also with oxygen and mercury ions. Crystals with flat surfaces were used to examine the change in topography by means of multiple-beam interferometry, and cylindrical crystals with very smooth surfaces were used to determine the relative rates of sputtering of faces of different crystallographic orientations.

2. EXPERIMENTAL

(a) *Preparation of specimens*

The two shapes of single crystals were grown by slow solidification in graphite moulds placed in an evacuated chamber. The dimensions of the moulds used to make the crystals are given in Figs. 1 and 2. The critical surfaces of the crystals were made by casting against silica incorporated in the moulds. To prevent the silver from sticking to the silica, it was covered by a thin evaporated film of carbon. The flat silica inserts were given their graphite coating by the method due to BRADLEY[7]. The inner surface of the cylindrical insert was coated by passing a current pulse along a graphite filament which was placed along the tube axis.

The moulds have separate melting and casting chambers connected by a small feeder channel. The

* Now at Division of Building Research, Commonwealth Scientific and Industrial Research Organization, Highett, Victoria, Australia.

melting chamber is charged with silver ingots which have been previously melted in hydrogen and as they melt the casting chamber is progressively filled. Without this procedure gas bubbles formed at the silica/silver interface, despite the fact that the chamber was evacuated to a

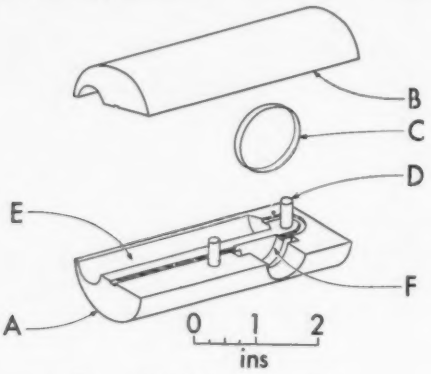

FIG. 1. Mould for flat crystals.

KEY

A, B Two halves of graphite mould.
C Silica disc.
D Graphite dowels.
E Melting chamber.
F Casting chamber.

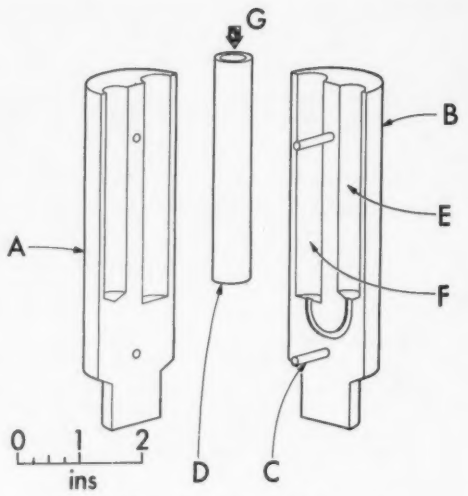

FIG. 2. Mould for cylindrical crystals,

KEY

A, B Two halves of graphite mould.
C Graphite dowel.
D Silica tube.
E Melting chamber.
F Casting chamber which houses the silica tube.
G Load for silica tube to prevent it floating upwards.

pressure $< 2 \times 10^{-4}$ mm Hg. Preliminary experiments showed that it was necessary to have the silica surfaces approximately parallel to the direction of heat flow from the mould, otherwise a fairly regular pattern of voids appeared at the silver/silica interface. These voids were probably due to the contraction during solidification of liquid trapped between dendrites of the advancing crystal.

The melting and solidification of the silver was effected by one pass of a travelling furnace (15 cm/hr) in an upwards direction and single crystals were nearly always produced.

Polycrystalline specimens were prepared by melting silver in a simple mould and electropolishing prior to sputtering.

(b) *Observation of surface and measurement of diameter*

The contour of the flat surfaces before and after sputtering was studied by multiple-beam interferometry. The comparison surface was a partly silvered face of an optically flat glass disc. Where necessary, a portion of the original surface was protected from the discharge by a shield in order that the thickness of material removed could be measured.

The diameters of the cylindrical specimens were measured at 10° intervals, using the apparatus whose construction is shown in Fig. 3. The crystal is located laterally by four cylinders. End-wise location is effected by the rounded end of the crystal bearing against a flat lapped plate. A long, thin rod is tightly fitted into a hole drilled in one end of the specimen, and this rod rests against a series of horizontal cylindrical stops sticking out of a plate at one end of the specimen holder. The position of these stops is adjusted so that the specimen rotates through 10° when the specimen rod engages successive stops. The specimen is pushed against the vertical cylinders and the lapped plate with a camel-hair brush before each diameter measurement is made. This arrangement enables the specimens to be replaced in a given angular position with a high degree of precision before and after sputtering so that the diameters can be measured in the same plane.

Three balls were inserted in the base of the measuring device and, in conjunction with the locating device on the stage of a Vickers projection microscope, it is possible to remove the measuring device and replace it in the identical position it had occupied before.

The diameters were measured optically. The specimen was illuminated from above by a beam of parallel light. Beneath a hole in the base of the measuring device, two parallel-sided glass blocks with optically worked faces were supported with one face in contact and with equal, opposite tilts about the direction of the incident beam. The shadow edges cast by the specimen were translated laterally by refraction at the surfaces of the inclined glass blocks so that by using a long-focus objective beneath the glass blocks, images of the two sides of the crystal were brought nearly coincident in the field of view of the microscope. The images of the opposite

sides of the specimen are projected on to a ground-glass screen at sufficient magnification to see the diffraction pattern at the edges of the specimen. By measuring the distance between identical parts of the diffraction patterns before and after sputtering, very small changes in diameter can be determined, provided that the microscope focussing motions are locked and not disturbed during a series of measurements on any one crystal.

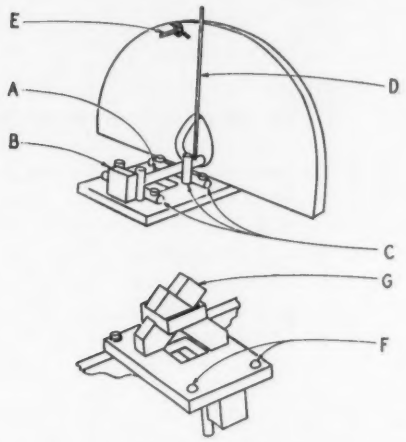

FIG. 3. Device for measuring the changes in diameter of cylindrical crystals after sputtering.

KEY

A Crystal.
B End stop.
C Locating rods.
D Indexing pointer.
E Indexing stop. There are 18 of these spaced at 10° intervals.
F Locating balls.
G Prism assembly.

(c) *Sputtering apparatus*

Experiments were made in gas pressures of 0·1–1·0 × 10^{-3} and 10–50 × 10^{-3} mm Hg. The higher of these two ranges was maintained in the sputtering chamber by an oil-diffusion pump backed by a rotary pump, while the gas was admitted through a leak valve. For the lower pressures it was found necessary, however, to use a mercury diffusion pump, because carbonaceous films sometimes appeared if the discharge voltage was low. Sputtering was effected at the high gas pressures by a simple glow discharge, the specimen being made the cathode. The cylindrical specimens were surrounded by a co-axial cylindrical anode, while the flat specimens had a parallel plate as anode. In both cases the electrode separation was 5 cm, and rectified and smoothed d.c. supplies were used. Sputtering in the low-pressure range was carried out in an apparatus based on the Penning gauge; this apparatus is described by OGILVIE.[8]

3. RESULTS

(1) Smooth single crystals of silver sputtered at about 30 × 10^{-3} mm Hg in argon show no observable roughening. Fig. 4 shows a sequence of three multiple-beam interference patterns taken from the same area of a crystal, in its original state and after two successive sputterings.

(2) An originally rough surface of a silver crystal is smoothed by sputtering. A flat crystal with etch pits (Fig. 5a) obtains a very gently undulating surface by the bombardment (Fig. 5b). On further sputtering, the surface becomes so smooth that the photograph would show no features if the illumination were not changed by closing the aperture iris. Fig. 5 also shows the effects due to the disappearance of one graphite inclusion and the uncovering of another.

(3) The same results have been obtained for sputtering at low argon pressures between 1 and 0·1 × 10^{-3} mm Hg for voltages between 20 V and 4 kV and many experiments have shown that sputtering with helium and xenon has the same effect.

(4) A polycrystalline specimen of silver was ground on 400 and 600 metallographic papers and finally polished on a diamond-impregnated cloth (4–8μ), and then sputtered in a series of stages. A sequence of photographs taken from this specimen is shown in Fig. 6. The sputtering first reveals effects due to the scratches from the abrasive papers, and after sufficient silver has been removed the crystals of the underlying material can be distinguished as lines appear at their boundaries. Interferometric observation shows that the boundaries are outlined because of differences in level of the crystal surfaces and not because grooves are formed (see Fig. 7).

(5) This result indicates that different crystallographic faces of the silver sputter at different rates. To make this statement quantitative, three single-crystal cylinders of different orientations were sputtered in argon (25 × 10^{-3} mm Hg, 3kV, 7 mA) and the resulting changes in diameters measured. The orientation of each crystal was determined from Laue back-reflection patterns. On the assumption that the crystal was truly cylindrical, the orientation of the surface at any point was then

determined and plotted in the standard triangle. The surface orientations corresponding to each of the measured diameters were plotted, and at each point a number proportional to the change in diameter after sputtering was inserted. The largest change in diameter was given the arbitrary value of 10·0 and the other data from the crystal giving this largest diameter change were adjusted accordingly. Data from the other two crystals were multiplied by a factor found by comparison between nearly overlapping values from the different crystals. The results (Fig. 8) show that surfaces parallel to

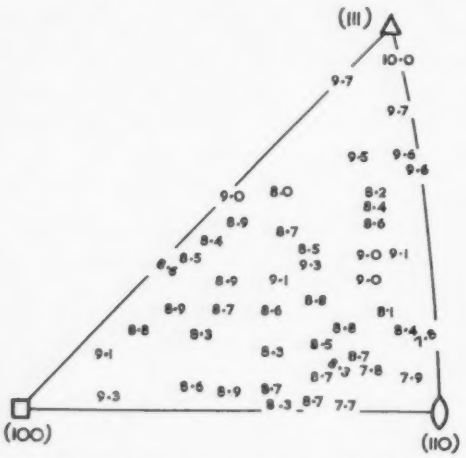

FIG. 8. Stereographic triangle showing relative sputtering rates for different orientations.

{111} sputter most rapidly and surfaces parallel to {110} least rapidly, whilst other orientations are intermediate in sputtering rate.

When the crystals were sputtered they were entirely surrounded by discharge. Therefore, variations in anode geometry would have no effect on the sputtering rate. One of the important errors in the measurements lies in the determination of the orientation of the element of surface corresponding to the measured diameter. This error is due to the crystal not having a truly cylindrical cross-section, as assumed in deriving the orientation. However, data from different crystals frequently overlapped and at these places in the triangle the trend was the same for each crystal. This fact was taken to justify the presentation of the results in a composite diagram.

(6) It is only for inert gases that the above observations apply. Sputtering in mercury vapour or oxygen produces characteristic patterns of facets on the surface (Fig. 9). These facets are very similar to the facets produced by thermally etching the same crystal.

4. DISCUSSION

The smooth erosion of a single crystal of silver by ions of an inert gas is in sharp contrast to the facets developed by bombarding with ions of mercury. Since mercury is known to amalgamate with silver and to form intermetallic compounds, it seems likely that the chemical forces between silver and mercury are significant. The formation of facets on a silver crystal may be due to these forces. This idea is supported by the observation that facets form in the surface of a single crystal of silver when it is heated to red heat in mercury vapour (thermal etching), and these facets are very similar to those produced by sputtering the same crystal with mercury ions.[9]

Sputtering in an inert gas tends to smooth a deliberately roughened surface of a single crystal of silver. FETZ[10] and WEHNER[4,5] have demonstrated that the sputtering yield increases as the angle of incidence of the ions increases. In the experiments described above, the ions are always directed normal to the mean plane of the surface. The rough surface has parts inclined to the direction of the incident ions, and consequently these parts of the surface will tend to be eroded faster than the parts of the surface perpendicular to the direction of the incident ions. This will result in a tendency to flatten the rough regions. In addition, surface atoms will receive blows from the ions with components parallel to the surface, and many of these will not have sufficient energy to escape from it. It seems likely then that an accelerated surface diffusion will occur during sputtering, and this process also will tend to flatten surface projections.

The experiments show that a crystal immersed in a glow discharge is eroded most rapidly from a surface parallel to {111}, and least rapidly from a surface parallel to {110}. WEHNER,[5] using 150-eV Hg ions bombarding silver, quotes a similar conclusion and gives rate {111}/rate {110} $\simeq$ 1·6. He comments that this ratio "seems to be higher at lower ion energies". The present results cannot be directly compared with WEHNER's, as his crystals would have developed facets, and he has shown

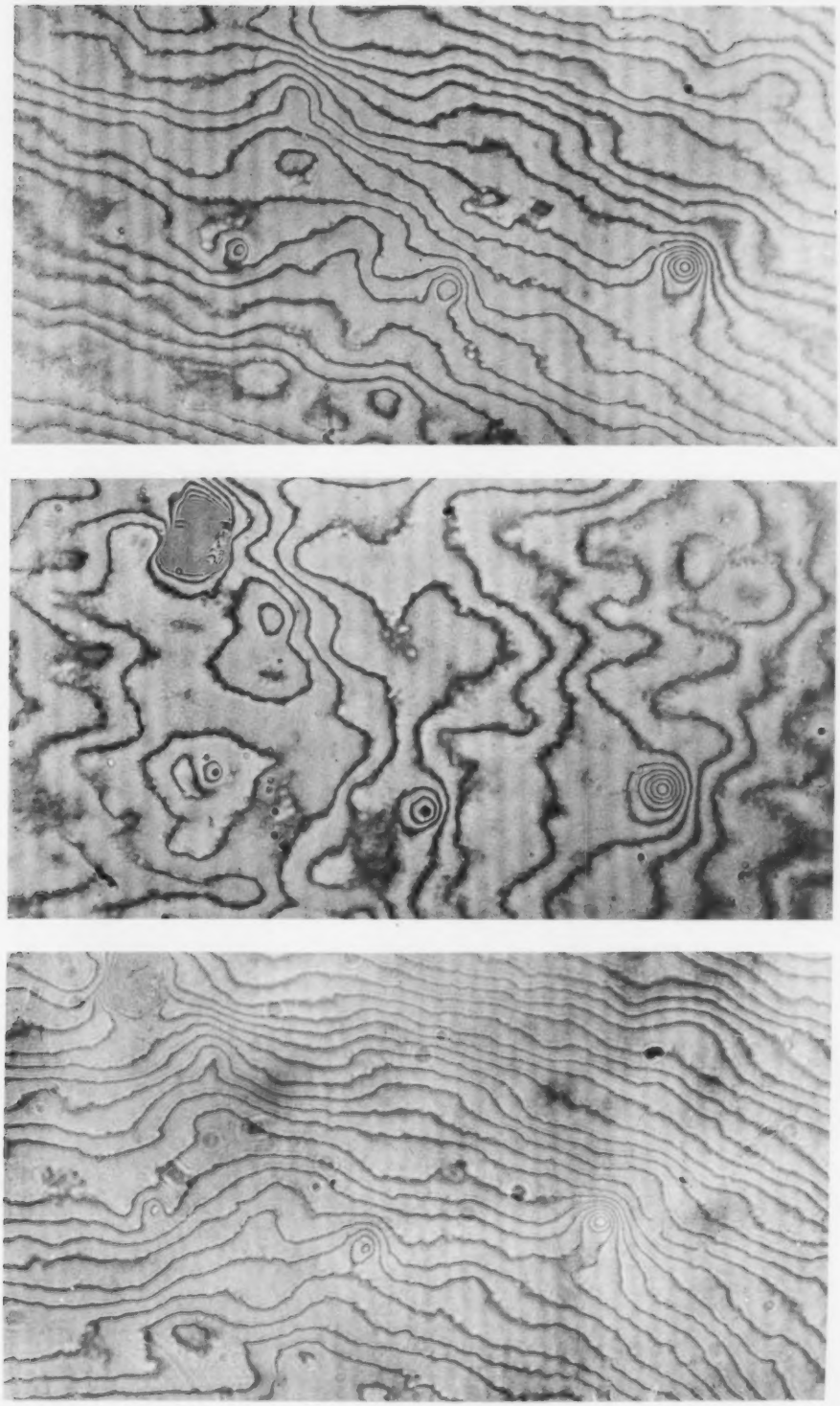

FIG. 4. Multiple-beam interference patterns obtained from the same area of a single crystal of silver. (a) Electropolished. (b) 1μ removed by sputtering. (c) 5μ removed by sputtering. Magnification: × 50. Discharge conditions: 2 kV, $\frac{1}{2}$ mA/cm^2, 30×10^{-3} mm Hg.

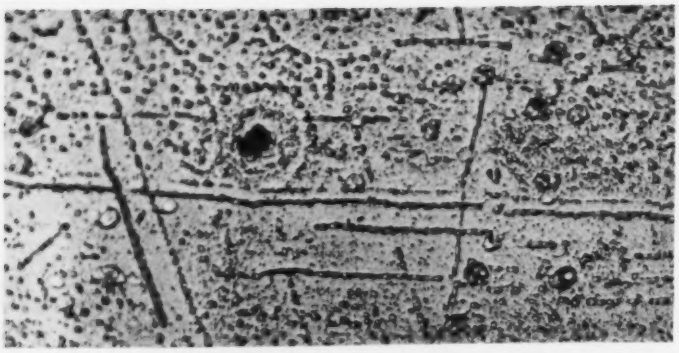

(a)

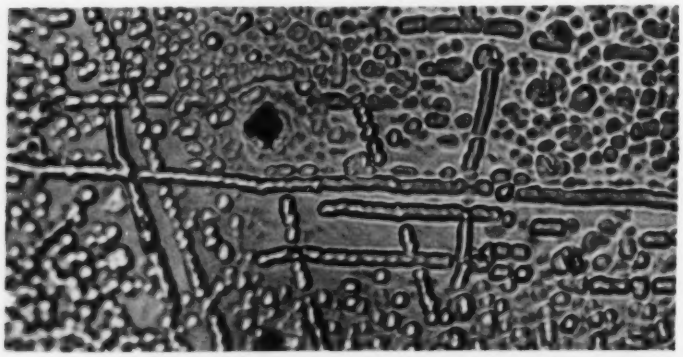

(b)

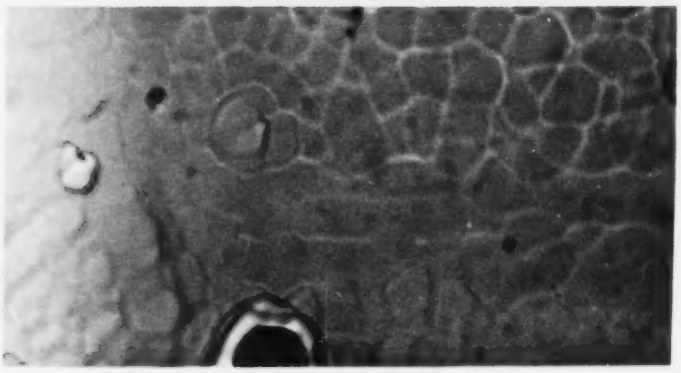

(c)

FIG. 5. Smoothing produced by sputtering. (a) Single crystal of silver etched in 1 part concentrated nitric acid and 2 parts water for 5 min. (b) Sputtered in argon at a pressure of 25×10^{-3} mm Hg, 0·5 mA/cm², 2 kV, to remove 0·3μ from the surface. (c) Sputtered under the same conditions to remove 2·2μ. Magnification: × 75.

VOL
10
195

VOL. 10 959

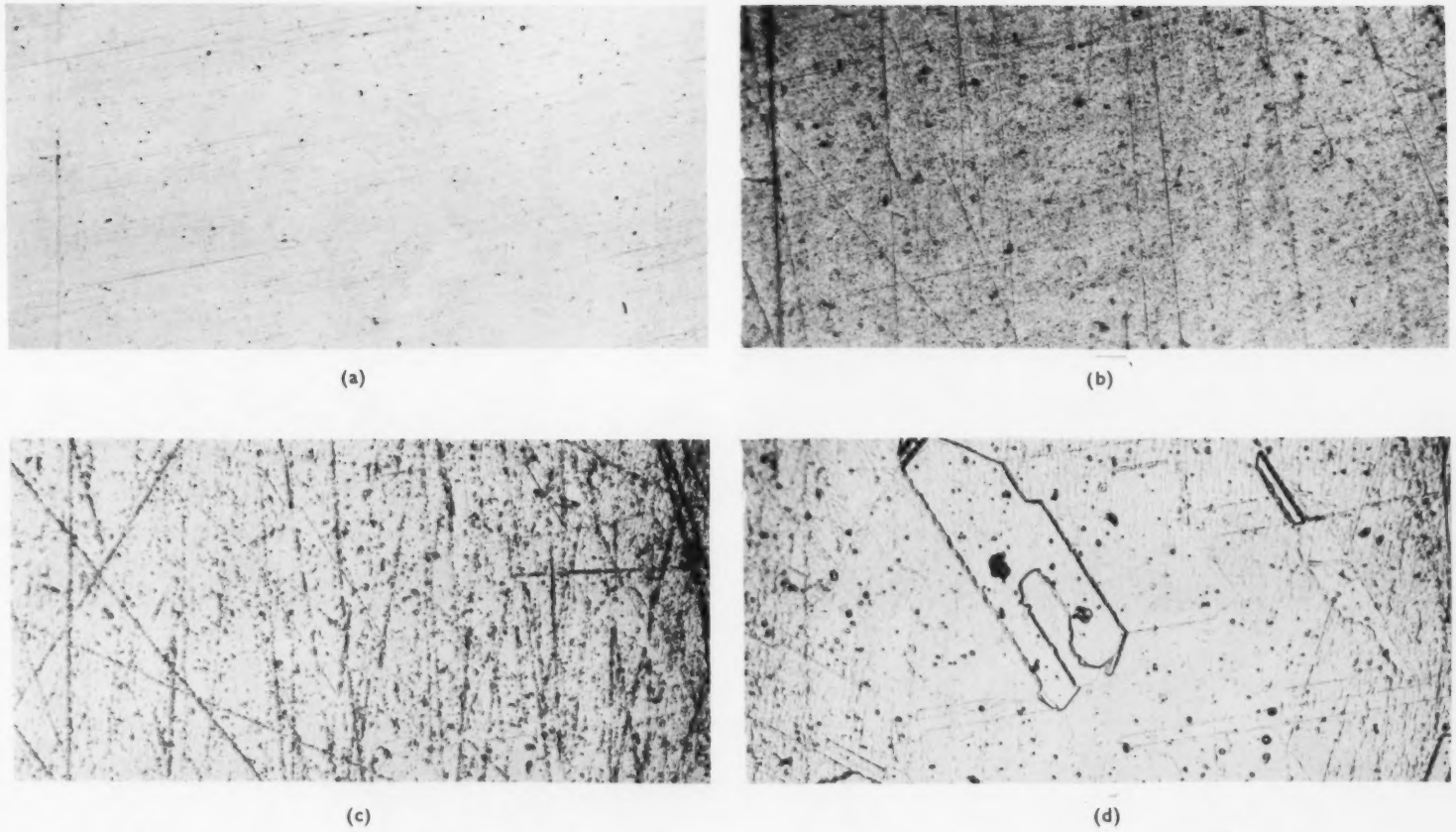

FIG. 6. Series of photographs of the same place of a single crystal of silver which had been: (a) Ground on 400 and 600 papers and finished on a cloth impregnated with diamond particles of $4-8\mu$; (b) sputtered in argon to remove $0{\cdot}7\mu$; discharge conditions; 3 kV, $\frac{1}{2}$ mA/cm^2, 20×10^{-3} mm Hg; (c) sputtered under the same conditions to remove $0{\cdot}52\mu$; (d) sputtered under the same conditions to remove $1{\cdot}85\mu$. Magnification: $\times$ 65.

FIG. 7. Difference in level at crystal boundaries produced by sputtering. Multiple-beam interference pattern of a polycrystalline specimen of silver sputtered at 1 kV in argon at 30×10^{-3} mm Hg to produce a mean removal of 30μ. Magnification: $\times$ 40.

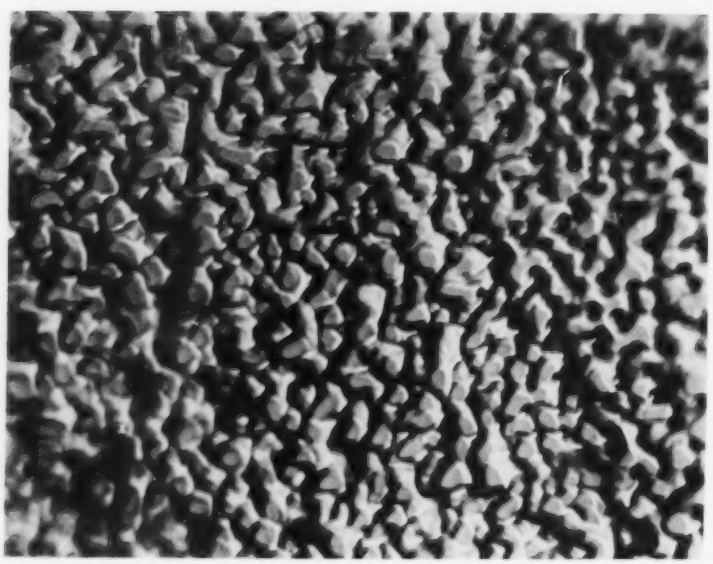

FIG. 9. Etched surface of a single crystal of silver with its surface parallel to {111} sputtered in mercury vapour at a pressure of 1×10^{-3} mm Hg. Discharge conditions: 300 V, 3 mA. Magnification: $\times$ 1400.

VOL
10
195

that as a surface becomes increasingly irregular, the sputtering yield falls. This accords with his observation that the ratio rate {111}/rate {110} "tends to decrease with increasing amount of material removed", that is, as the facets develop and the surface becomes rougher.

When a polycrystalline silver target is sputtered with ions of an inert gas, the boundaries between adjacent crystals are delineated by sudden changes in level. These changes in level are due to the different rates of erosion of crystals with different orientations. It has been believed that the delineation of a crystal boundary by sputtering is due to a groove.[1,11–13] WEHNER[6] has demonstrated that grooves appear at low-angle boundaries in germanium polycrystals sputtered with mercury ions. In the present study grooves were not found at the boundaries of crystals of a silver specimen sputtered with inert-gas ions. Consequently, it is likely that groove formation is connected with a chemical interaction between the atoms of the gas supporting the discharge and the atoms in the surface of the specimen.

Acknowledgement—The authors wish to thank Mr. A. A. THOMSON for his able assistance with the experiments.

REFERENCES

1. HOLLAND L., *Vacuum Deposition of Thin Films* Chapman and Hall Ltd., London (1956).
2. FRANCIS Q., *Handbuch der Physik* Vol. 22, p. 53. Springer-Verlag, Berlin (1956).
3. MASSEY H. S. W. and BURHOP E. H. S., *Electronic and Ionic Impact Phenomena*. Oxford University Press (1952).
4. WEHNER G. K., *Advances in Electronics and Electron Physics* Vol. 7, p. 239. Academic Press, Inc., New York (1955).
5. WEHNER G. K., *Phys. Rev.* **102,** 690 (1956).
6. WEHNER G. K., *J. Appl. Phys.* **29,** 217 (1958).
7. BRADLEY D. E., *J. Appl. Phys.* **27,** 1399 (1956).
8. OGILVIE G. J., *J. Phys. Chem. Solids* **10,** 222 (1959).
9. HONDROS E. D. and MOORE A. J. W. Private communication.
10. FETZ H., *Z. Phys.* **119,** 590 (1942).
11. DEO P. G. and SHERMA B. D., *Nature* (*Lond.*) **178,** 175 (1956).
12. HENSCHKE E. B., *Phys. Rev.* **106,** 738, section 6.1 (1957).
13. BAUM T., *Z. Phys.* **40,** 686 (1927).

J. Phys. Chem. Solids Pergamon Press 1959. Vol. 10. pp. 222–228.

THE SURFACE STRUCTURE OF SILVER CRYSTALS AFTER ARGON-ION BOMBARDMENT

G. J. OGILVIE

Division of Tribophysics, Commonwealth Scientific and Industrial Research Organization, University of Melbourne, Australia

(*Received* 31 *December* 1958)

Abstract—Three single crystals of silver in the form of thin sheets with surfaces parallel to (111), (110) and (100), respectively, have been bombarded with argon ions at several energies in the range 12–4000 eV. Electron-diffraction patterns, taken by transmission and reflection, show short arcs and some streaks not present in the diagrams taken before bombardment. It has been found that after bombardment the surface contains disoriented crystallites. In general, the crystallite orientations are related to the original orientation by tilts about ⟨112⟩ axes lying in or near the surface of the crystal. It is suggested that the bombarding ions can easily penetrate the lattice if directed parallel to close-packed directions and are arrested near dislocation lines giving rise to a high concentration of point defects. These in turn give rise to a net current of interstitial atoms diffusing away from the primary dislocation. This net transfer of material is thought to be the cause of the tilting of lattice blocks.

1. INTRODUCTION

In a previous paper[1] the surfaces of both single-crystal and polycrystalline specimens of silver were studied by optical methods after they had been bombarded by positive ions of argon. No roughening of the surface was found, although layers of considerable thickness were removed by sputtering (the term "sputtering" is here used as a synonym for the process of ion bombardment of a surface). The rate of removal from the surface depended upon its orientation, being a maximum when it was parallel to (111) and a minimum when it was parallel to (110).

However, positive-ion bombardment of a surface may produce effects other than the removal of material from it. In particular, the surface layers of atoms may be disturbed by the impact of the ions. This effect has been reported by a number of investigators; for example, Trillat[2] showed, by using a transmission electron-diffraction technique, that a single-crystal film of gold is progressively disoriented by 12-keV ions until the film is converted to a random polycrystalline aggregate.

The only detailed study of this phenomenon has been made by Gianola[3], who bombarded silicon with 30-keV helium ions and subsequently prepared taper sections of the specimens. He obtained information about the surface structure directly from reflection electron-diffraction patterns, and indirectly by studying rectification at a junction formed between the crystal and a fine probe which was placed at various points on the surface of the taper section. He found that the silicon crystal was changed in its properties to a depth of about 1 μ and a thinner layer was changed to a "quasi-stable amorphous form which may be partially restored to the crystalline state after annealing". This estimate of the depth of penetration of the effect of the positive ions agrees with an earlier result of Heinz *et al.*,[4] who found a value of 0·6μ for silicon bombarded with helium ions.

Farnsworth *et al.*[5] for germanium and titanium, Farnsworth and Woodcock[6,7] for nickel and platinum, and Schlier and Farnsworth[8] for germanium have shown that bombardment by argon ions introduces a disturbance into the crystal lattice near the surface of these metals. They have not reported a detailed study of this disturbance.

In the present paper the disturbance of the surface layers of metal crystals by bombardment with positive ions has been studied. The results

obtained are of wider interest, since ion bombardment is often used as a method for cleaning a surface before its properties are investigated. In particular, the catalytic activity has been studied by using as catalysts crystals of the same orientations, bombarded under the same conditions, as the crystals in the present investigation.[9]

2. SPUTTERING APPARATUS

The sputtering chamber and schematic circuit are shown in Figs. 1 and 2. The chamber is evacuated by a

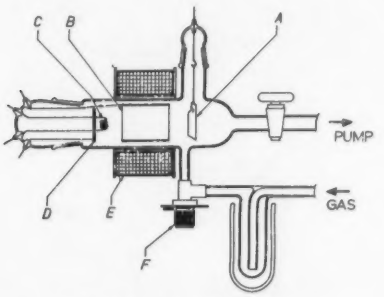

FIG. 1. Sputtering apparatus.

KEY

A	Specimen.	D	Cathode 1.
B	Anode.	E	Coil.
C	Filament.	F	Leak valve.

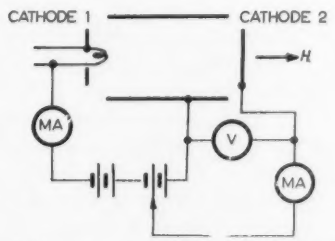

FIG. 2. Schematic circuit of sputtering apparatus.

standard pumping system comprising a mercury diffusion pump and two liquid-air traps in series between the pump and the chamber. Prior to each bombardment the chamber was evacuated to a pressure $< 5\times10^{-6}$ mm Hg. The gas in which the bombardment was to take place (helium, argon or xenon) was then admitted through a leak valve to a pressure of about 10^{-3} mm Hg.

The electrode arrangement is based on the Philips ionization gauge[10] (Penning gauge) and is capable of producing large currents of positive ions bombarding the specimen (cathode 2) even for an accelerating voltage of the ions of as low as 12 V. In order that the discharge shall operate, an axial magnetic field of about 250 Oe is necessary. The discharge takes place in the space between cathode 1 and cathode 2, and the anode; for voltages above 350–400 V the hot filament is not used, and cathodes 1 and 2 are kept at the same potential. In order to operate the discharge at high voltages without necessitating a corresponding large decrease in the pressure, cathode 1 was varied in area. The filament only was used at the highest voltages. In this way the voltage range was covered with a pressure change of only 2×10^{-4} to 2×10^{-3} mm Hg.

Electrons originating from the impact of positive ions on the cathode surfaces are accelerated in the cathode dark space and are constrained to move in helices under the action of the magnetic field until they ionize atoms by impact. The discharge is then self-sustaining if sufficient secondary electrons are emitted by the cathodes, but below applied voltages of 350–400 V the secondary-electron-emission coefficient becomes so low that the discharge stops. By using the hot filament the discharge can be re-started and can be made to run reliably to well below 50 V with argon. Below about 80 V the discharge current becomes small, but it can be increased by biassing cathode 2 with respect to cathode 1.

The potential between cathode 1 and the anode was held constant at 90 V for all bombarding voltages below 80 V, and satisfactory positive-ion currents could be collected by cathode 2 down to an applied voltage of 14 V. For 30-V ions it is easy to get a current of 0·1 mA/cm² by adjusting the filament temperature so that the current passing to cathode 1 was about 15 mA. Considerably larger currents could be obtained if desired.

3. PREPARATION AND EXAMINATION OF SILVER SPECIMENS

Three silver crystals in the form of thin sheets (approximately $2\times1\times0{\cdot}005$ in.) were used, having (111), (110) and (100) planes, respectively, parallel to the surface of the sheet. They were made by slow solidification in a graphite mould and then electropolished in the same way as the crystals prepared for the catalysis study.[9] A small region of each crystal was then electrolytically polished until a hole appeared. Around the edge of this hole regions sufficiently thin to give good transmission electron-diffraction patterns could be usually found.

Each side of the crystal was then bombarded at each voltage in turn until the diffraction patterns at that voltage were unaltered with further bombardment.

The power input to the crystal was kept at about 0·1 W so that the temperature of the crystal never exceeded 100°C during bombardment. This temperature was measured by allowing two thermocouple wires sharpened at their ends to touch the specimen surface. The minimum sputtering time necessary to give a surface whose structure did not change with further bombardment was found to be 4 hr on each side of the crystal when the accelerating voltage was 22½ V, whilst with 4 kV, 15 min. on each side was more than sufficient.

After the bombardment the silver crystals were examined by both transmission and reflection

techniques in an electron-diffraction camera, using an accelerating voltage of 50 kV. Sequences of bombardments have been made with both increasing and decreasing voltages in the range from 12 to 4000 V, and the diffraction patterns were found to be typical of the bombarding voltage whatever the previous treatment.

4. RESULTS

The results presented below all refer to surfaces which had been sputtered in argon. Helium and xenon give results which are essentially the same, but a detailed comparison of the effects of different ions will be given later. The plates reproduced in the figures have been selected from many patterns from several parts of the three crystals. These sets are, in fact, obtained from nearly the same region of a hole in each crystal. The patterns showed that different areas behaved in a similar manner to the areas for which patterns are shown. Only those regions which gave diffraction patterns with the correct symmetry with the electron beam perpendicular to the surface of the crystal (that is, where the diffracting volume has the same orientation as the rest of the crystal) have been considered.

Figures 3–5 are portions of transmission and reflection patterns obtained after bombarding, at several voltages, the crystal having its surface nearly parallel to (111). The transmission patterns, apart from the 22½-V pattern, show many spots and short arcs which do not appear in the diagram of the unbombarded surface. The pattern is indexed in Fig. 6. The indices of the primary spots (present in the original diagram) are underlined to distinguish these from the new interferences. The extra streaks clearly have a simple crystallographic relationship to the primary spots.

These transmission patterns give clear evidence that the surface contains many small crystallites whose orientations are related in some simple fashion to the primary orientation.

In the reflection patterns the interferences corresponding to the original orientation are streaked by refraction and broadened laterally; in addition, except for the 22½-V pattern, they have rings with the spacings of silver.

Figures 7–9 show a similar series of transmission and reflection patterns obtained from the crystal having its surface nearly parallel to (110). As above, the transmission patterns have extra interferences which would not be present if the crystal surface did not contain disoriented elements. In addition, the 12-V, 46-V and 500-V patterns show complete spotty rings with spacings corresponding to

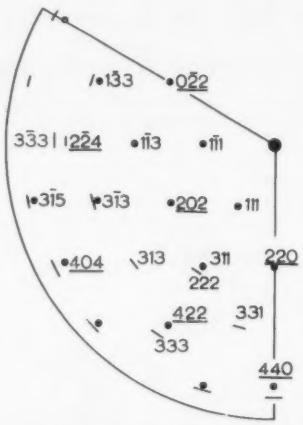

FIG. 6. Diagram showing the indices of the interferences in the pattern from the crystal with (111) parallel to the surface bombarded at 4 kV.

silver. All the reflection patterns have the primary spots broadened laterally, but, with the exception of the 12-V pattern, the silver rings are weak or absent.

Figures 10 and 11 give a series of transmission and reflection patterns for the crystal with (100) parallel to the surface. No extra interferences appear in the transmission patterns, with the exception of the 22½-V pattern, where the relationship between the primary and the extra interferences is different from the relationship for the first two crystals. The 16-V pattern shows complete spotty rings. Some of the reflection patterns show faint rings with parameters corresponding to silver, and the primary interferences are broadened laterally.

Some other minor differences and details can be found in the diffraction patterns (for example, spots and faint streaks probably due to stacking faults), but these details will not be considered further in this paper.

5. INTERPRETATION OF THE TRANSMISSION DIFFRACTION PATTERNS

The appearance of the extra spots and arcs in

OL.
10
959

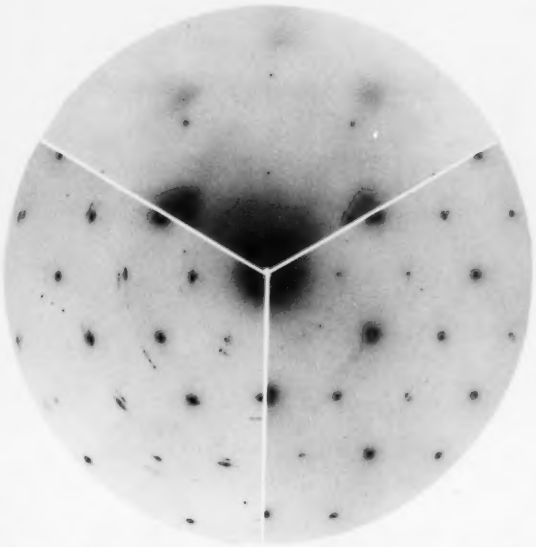

FIG. 3. Transmission electron-diffraction patterns from the silver crystal with surfaces parallel to (111) bombarded at 22½, 30 and 86 V.

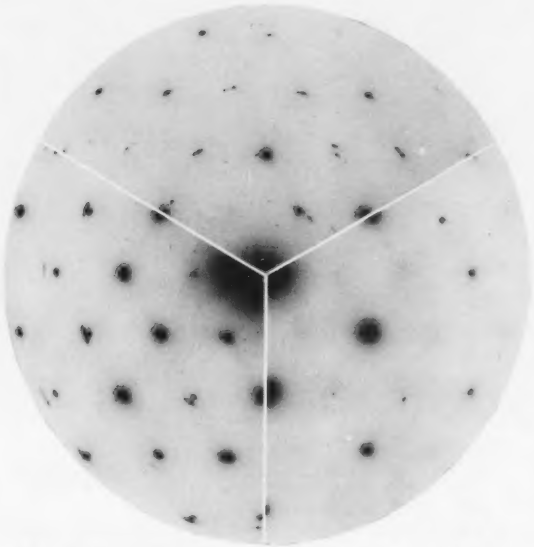

FIG. 4. Transmission electron diffraction patterns from the silver crystal with surfaces parallel to (111) bombarded at 130, 300 V, and 4 kV.

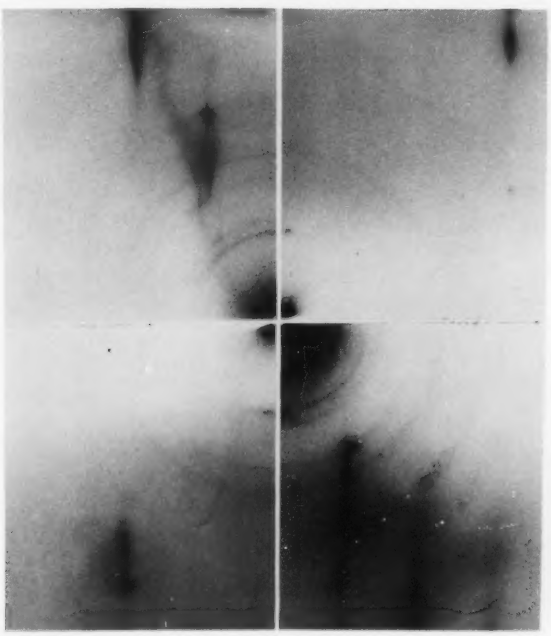

FIG. 5. Reflection electron-diffraction patterns from the silver crystal with surfaces parallel to (111) bombarded at 30, 86, 300 V, and 4 kV.

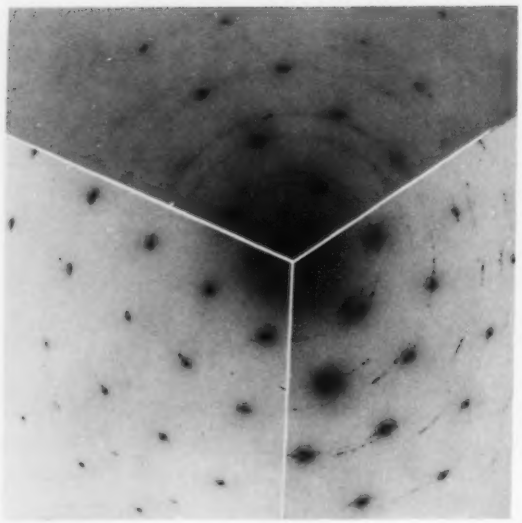

FIG. 7. Transmission electron-diffraction patterns from the silver crystal with surfaces parallel to (110) bombarded at 12, 22½ and 46 V.

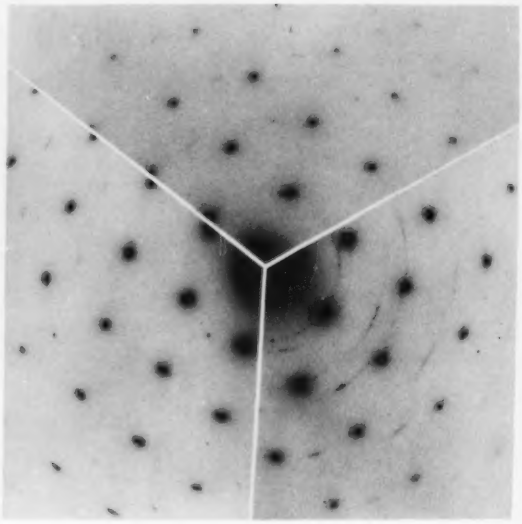

FIG. 8. Transmission electron-diffraction patterns from the silver crystal with surfaces parallel to (110) bombarded at 130, 500 V, and 4 kV.

VOL
10
195

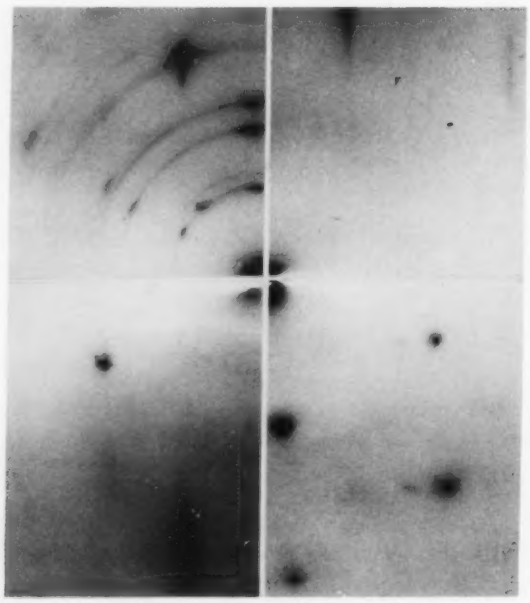

FIG. 9. Reflection electron-diffraction patterns from the silver crystal with surfaces parallel to (110) bombarded at 12, 46, 500 V, and 4 kV.

VOL.
10
959

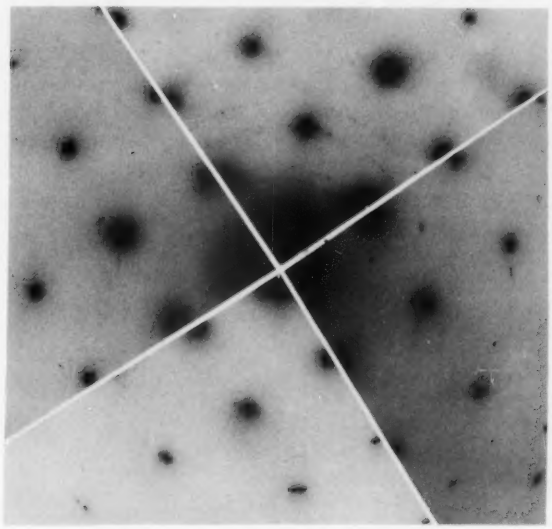

FIG. 10. Transmission electron-diffraction patterns from the silver crystal with surfaces parallel to (100) bombarded at 16, 22½, 300 V, and 4 kV.

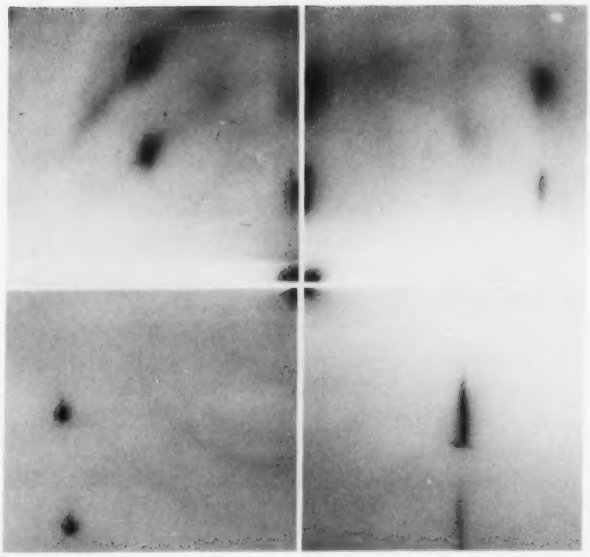

FIG. 11. Reflection electron-diffraction patterns from the silver crystal with surfaces parallel to (100) bombarded at 16, 22½, 300 V, and 4 kV.

VOL
10
195

the transmission patterns for the crystal with (111) parallel to the surface can be accounted for by the texture shown in the pole figure of Fig. 12. The

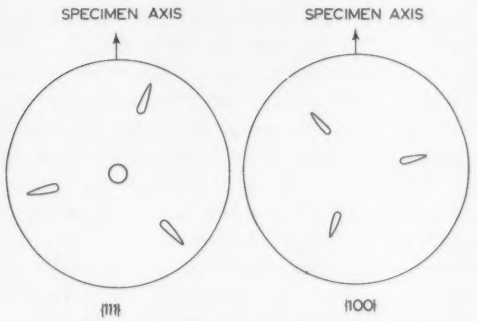

FIG. 12. {111} and {100} pole figures for the surface texture of the silver crystal with surfaces parallel to (111). These figures are qualitative only.

effect of this texture on the reciprocal lattice of the crystal is shown schematically in Fig. 13. The individual crystallites are rotated with respect to the

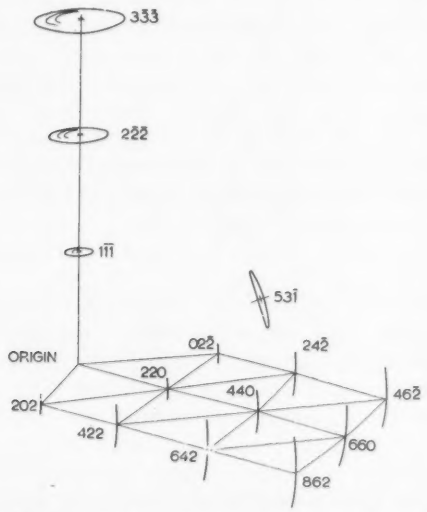

FIG. 13. Schematic representation of the effect of the texture described in Fig. 12 on the reciprocal lattice of the crystal with surfaces parallel to (111).

original lattice about axes lying in the plane of the surface. From the diffraction patterns one cannot decide whether the tilt axes are likely to be ⟨110⟩, ⟨112⟩ or ⟨123⟩. As the tilt of a particular crystallite becomes larger, rotation of the crystal about a second axis starts to take place. For example, crystallites tilted through 10° about an axis in the surface plane ($1\bar{1}3$ reflection) have rotations of less than $\pm 1°$ about an axis normal to the surface; for a tilt of 19° (111 reflection) the maximum rotation about the normal to the surface is about $\pm 4°$.

The transmission diffraction patterns from the crystal with (110) parallel to the surface can be interpreted in a similar fashion. The array of possible tilt axes which could produce the patterns does not include ⟨123⟩, but ⟨110⟩ and ⟨112⟩ are possible.

On the other hand, the crystal having (100) parallel to the surface does not give diffraction patterns with extra spots in positions expected if rotation took place about axes in the surface plane. Furthermore, the reflections associated with the primary orientation are drawn out into short arcs. The extra spots that do appear are consistent with rotation of the crystallites about ⟨112⟩, but are not consistent with rotations about ⟨110⟩.

Even for the lowest energies used, the crystals with (110) and (100) parallel to the surface showed marked disorientation. Intense silver rings appear on both the reflection and transmission pictures. The size of the individual spots on the rings is such that the lateral dimensions of the individual crystallites cannot be less than 200 Å. On the other hand, the thickness of the region giving transmission patterns is not much greater than 400 Å, and so the crystallites are probably about 100 Å thick. Sputtering of alloys provides data to confirm this estimate.[11]

6. INTERPRETATION OF THE REFLECTION DIFFRACTION PATTERNS

The reflection patterns, in general, show little evidence of the texture found by the transmission patterns but are not inconsistent with it. Diffraction effects due to such a texture would tend to disappear into the background of a reflection picture because:

(i) The background is considerably higher than for a comparable transmission photograph from the same specimen.

(ii) The interferences, in general, will be drawn out perpendicular to the shadow edge by refraction.

(iii) All the extra reflections (in the absence of refraction) would be drawn out into arcs.

The principal effect on the pattern would be a lateral broadening of the main interferences and the appearance of fainter extra reflections, and these features are to be found most obviously in the patterns obtained from the crystals with (100) and (110) parallel to the surface sputtered at 16 and 500 V, respectively.

A number of the patterns show interferences typical of a surface which contains facets. The reason for the appearance of these facets might be small differences in level between a crystallite and the original crystal due to a dependence of sputtering rate on orientation.[1]

7. DISCUSSION

The experiments described above have shown that an originally nearly perfect surface of a silver single crystal is disoriented by the action of positive ions directed on it. After a bombardment the surface region contains an array of very small crystallites, some of which have been tilted through a range of angles with respect to the parent orientation. The disorientation is most marked for very low-energy ions (12 V) bombarding surfaces parallel to (110) to (100). The interaction of the ions with the atoms in the surface of the crystal must, therefore, result in the generation of dislocation lines, though it is clear that a low-energy ion has insufficient energy to produce a dislocation directly and that some cumulative process must operate. The most obvious mechanism which could produce the observed tilts is by a co-operative movement of point defects generated by the impact of the ions.

It seems likely that point defects generated by the collision of the ions with atoms at the surface of the crystal will appear uniformly over the surface area. Some of these defects would be expected to associate to form dislocation lines, but these lines would appear at random places near the crystal surface, and to account for the formation of tilted crystallites a process must operate which causes dislocations to appear at certain preferred places. It has been imagined that the stresses associated with thermal spikes can generate dislocation loops.[12] This process will not operate for the lowest-energy ions used in this study, but could be increasingly important for ion energies above 100 eV. In any case, the dislocation loops will be produced at random and will not be directly responsible for tilting small blocks of crystal.

To account for the experimental results, it is first noted that the ions can enter the crystal,[13] and if, after entering the crystal, they are travelling parallel to a close-packed direction in the crystal, it is assumed that their range is greater than theory predicts. It is also assumed that very low-energy (say 5–50 eV) particles travelling in a close-packed direction will displace atoms only when the particle meets a region where the atomic arrangement of the crystal is distorted. In this region, for example, it might be imagined the particle is guided so that it makes a near head-on collision with an atom and causes its displacement into an interstitial position. This is most likely to happen when the particle is directed at the stacking fault between two partial dislocations. Another possibility is that atoms are less firmly bound to their sites in such a region than where the crystal is perfect. Thus it is imagined that near a dislocation line, vacant sites, interstitial silver atoms, interstitial argon atoms, and substitutional argon atoms are to be found. It has already been pointed out by SHOCKLEY[14] that if vacant sites and interstitial atoms are generated continuously in equal numbers at a particular place in a crystal, there will probably be a net current of interstitial atoms moving away from that region because of the higher rate of migration of interstitials.

Now, unless a hole is formed in the crystal, the surface layers will tend to be pulled downwards above the dislocation line, and some distance away the surface will tend to be pushed upwards by the relatively high concentration of interstitial atoms. Thus the crystal on either side and above the dislocation line tends to tilt. The stresses produced by this process must eventually become so large that appropriate dislocations appear in the regions of highest stress and so form the crystallite boundary. It is more likely that these dislocations are generated from surface sources than by spontaneous creation. The dislocations attracted to the boundaries parallel to, but not directly above, the original dislocation will be edge dislocations so oriented that ions passing through them have the smallest chance of making head-on collisions with lattice atoms. As a consequence, the tilt increases with time. The

gradually increasing tilt is balanced by the erosion of the surface by sputtering, and so an equilibrium disorientation is found if sputtering continues long enough.

Where dislocation lines cross or intersect, the tilt produced by this process is probably more complex, since the boundary between two tilted blocks must be of a complex nature. Also, if the bombardment conditions are such that the tilts can become very large, then less favourably oriented dislocation lines can produce observable tilts. Therefore, it is to be expected that, as the tilts about an axis lying in the surface increase, tilts about axes not lying in the surface should become observable. This is found to be so, since the interferences produced by crystals tilted through small angles are sharp, whereas those interferences associated with large tilts are drawn out round the Debye–Scherrer circles.

The number of tilted elements in the surface of the crystal has not been determined accurately because of uncertainties in the area of the specimen transmitting electrons, but it seems likely that more crystallites are present than would be predicted on the basis of the above mechanism from the number of dislocations to be expected in an annealed crystal.

The discrepancy can be accounted for in terms of climb of edge dislocations.[15] An edge dislocation further in than the range of the bombarding ion is likely to be the sink of interstial atoms in its vicinity. A proportion of these dislocations will therefore climb towards the surface. When those dislocations which climb towards the surface are in the region acted on by the incoming argon ions, they will have atoms knocked away from them and so there is a tendency for their motion to be reversed. Thus, they will lie at some equilibrium distance from the surface and also the dislocation line will be turned parallel to the surface. Therefore, the dislocation density near the surface will be higher than the original density. Another factor tending to increase the density is that the free surface of the crystal is continuously advancing into it while the bombardment is proceeding. Hence, with time, more dislocations are caught in the subsurface zone as its sweeps through the crystal.

From observations of the nature of the tilts for the three orientations used, evidence has been found that the tilt axes tend to be ⟨112⟩. This observation is consistent with the idea that the disorientation is due primarily to edge dislocations which find a stable position parallel to, and a short distance away from the surface.

The very marked disorientation found for the low-energy bombardment of the crystals with (110) and (100) parallel to the surface is not found for the crystal with (111) parallel to the surface. It has been supposed above that the incident ions must penetrate into the crystal with sufficient energy remaining after the penetration to displace silver atoms. With very low-energy ions only those which enter the crystal without losing much of their energy by surface collision will be able to cause displacements. For a crystal with (111) parallel to the surface, the chance of an ion penetrating with enough energy to cause displacement is clearly less than for a crystal with (110) or (100) parallel to the surface.

8. CONCLUSION

It has been shown that, when a single crystal of silver is bombarded by ions having energies in the range 12–4000 V, the surface is partly covered by a layer of crystallites of about 100 Å linear dimension. The orientation of a given crystallite is related to the parent orientation by a rotation about ⟨112⟩ lying in or near the surface plane. This phenomenon has been accounted for by assuming that low-energy ions or atoms can move easily along close-packed directions in the lattice and are arrested in the neighbourhood of dislocation lines. Here interstitial atoms and vacant sites are produced which give rise to a net current of interstitial atoms away from the dislocation line with the consequent production of tilted crystal blocks.

Acknowledgements—The author is very grateful to Mr. A. A. THOMSON for his great help with the experimental work. He wishes to thank Dr. J. V. SANDERS for helpful criticism and Mr. E. GILLAM for many discussions.

REFERENCES

1. OGILVIE G. J. and RIDGE M. J., *J. Phys. Chem. Solids* **10,** 217 (1959).
2. TRILLAT J. J., *J. Chim. Phys.* **53,** 570 (1956).
3. GIANOLA U. F., *J. Appl. Phys.* **28,** 868 (1957).
4. HEINZ O., GYORGY E. M., and OHL R. S., *Rev Sci. Instrum.* **27,** 43 (1956).
5. FARNSWORTH H. E., SCHLIER R. E., GEORGE T. H., and BURGER R. M., *J. Appl. Phys.* **26,** 252 (1955).

6. FARNSWORTH H. E. and WOODCOCK R. F., *Industr. Engng. Chem.* **49,** 258 (1957).
7. FARNSWORTH H. E. and WOODCOCK R. F., *Advances in Catalysis* Vol. 9, p. 123. Academic Press Inc., New York (1957).
8. SCHLIER R. E. and FARNSWORTH H. E., *Semiconductor Surface Physics* p. 3. University of Pennsylvania Press, Philadelphia (1957).
9. SOSNOVSKY H. M. C., *J. Phys. Chem. Solids.* To be published (1959).
10. BACKUS J., *Gaseous Electrical Discharges in Magnetic Fields* p. 345. McGraw-Hill, New York (1949).
11. GILLAM E., *J. Phys. Chem. Solids.* To be published (1959).
12. SEITZ F. and KOEHLER J. S., *Solid State Physics* Vol. 2, p. 305. Academic Press, Inc., New York (1956).
13. LE CLAIRE A. D. and ROWE A. H., *Rev. Métall.* **52,** 94 (1955).
14. SHOCKLEY W., *Dislocations and Mechanical Properties of Crystals* p. 581. John Wiley, New York (1957).
15. BARNES R. S., *Acta Met.* **2,** 380 (1954).

VOL
10
195

J. Phys. Chem. Solids Pergamon Press 1959. Vol. 10. pp. 229–241.

SYMMETRY PROPERTIES OF THE WURTZITE STRUCTURE

M. L GLASSER*

RCA Laboratories, David Sarnoff Research Center, Princeton, N.J.

(*Received* 1 *October* 1958; *revised* 17 *November* 1958)

Abstract—The space group of the wurtzite structure is considered, and character tables are given for the important symmetry elements in the Brillouin zone. Symmetrized combinations of plane waves are worked out for the most important points. A discussion is given of the probable forms of energy bands in wurtzite crystals.

VOL. 10 959

1. INTRODUCTION

In recent years, interplay between theory and experiment has greatly expanded our knowledge of the electronic structure of many types of solids. This seems most evident in the case of crystals which have the diamond or zinc-blende structures, e.g. silicon, germanium, InSb and GaAs. As a survey of the literature shows, much of this progress was initiated by the band studies of HERMAN and others.[1,2] Now, as more and more attention is directed to the technological applications of photoconductors, phosphors, semiconductors and thermoelectric materials, there is increasing interest in the electronic energy bands of these substances, many of which have the wurtzite structure. Band calculations for many of these, such as CdS, ZnS, BeO, etc., would be valuable guides for further theoretical and experimental work.

Thorough band studies depend very much on a knowledge of the symmetry properties of the system considered. Not only does the usual group theory furnish a description of the possible degeneracies and transformation properties of the wave functions, but many general features of the band structure may be delineated in advance, thus eliminating a good deal of otherwise necessary computation.

In this paper, a discussion is given of the space group and Brillouin zone of the wurtzite lattice. This includes spin-orbit splittings at the symmetry points and selection rules for perturbative matrix elements. Symmetrized plane-wave combinations are discussed and given for several points in the zone.

2. THE WURTZITE SPACE GROUP

A simplified picture of a solid is that of a large number of noninteracting electrons moving in a fixed potential field having the symmetry of the crystalline lattice. Each electron will obey a Schroedinger equation

$$H\psi = (\boldsymbol{p}^2 + V(\boldsymbol{r}))\psi = E\psi, \tag{1}$$

and the group of the Hamiltonian is just the crystal space group plus, possibly, time inversion. Several good accounts have recently been given of the general theory of space groups and their representations,[3,4] and the reader is referred to them for details.

The space group of a crystalline solid consists of all coördinate transformations $\{\alpha|\boldsymbol{t}\}$ which leave the lattice invariant, where α is a rotation or reflection and $\boldsymbol{t}$ a translation: $\{\alpha|\boldsymbol{t}\}\boldsymbol{r} = \alpha\boldsymbol{r} + \boldsymbol{t}$. SEITZ proved that each irreducible representation of a space group may be labeled by a wave vector $\boldsymbol{k}$ in the reciprocal space of the lattice. Furthermore, only those $\boldsymbol{k}$ vectors which are not related by symmetry and lie in a symmetrical region, called the Brillouin zone, give distinct irreducible representations. Each irreducible representation can be

* Present address: Physics Department, Carnegie Institute of Technology, Pittsburgh 13, Pennsylvania.

constructed from one of the irreducible representations of a subgroup of the space group, which is associated with the labeling $\boldsymbol{k}$ vector. This group of $\boldsymbol{k}$ is related to the symmetry which $\boldsymbol{k}$ has in the Brillouin zone.

The quantum-mechanical significance of these considerations was first discussed in classic papers by SEITZ[5a] and BOUCKAERT *et al.*[5] In particular, the preceding remarks may be shown to imply that the eigenstates of (1) may be labeled by a $\boldsymbol{k}$ (reduced wave vector) from the Brillouin zone and that states with the same reduced wave vector form bases for the irreducible representations of the group of $\boldsymbol{k}$. In this way the reduced wave vector furnishes a good quantum number for the eigenstates in a crystal. For these reasons, attention is directed primarily toward obtaining the irreducible representations of the symmetry-point groups in the Brillouin zone.

The wurtzite lattice consists of two interpenetrating close-packed hexagonal lattices (Fig. 1) and

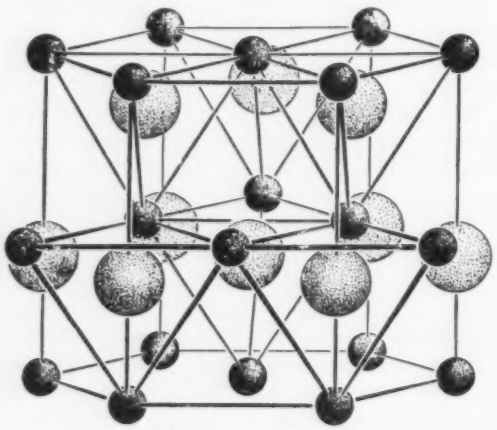

FIG. 1. The wurtzite lattice.

has space group $C_{6v}{}^4$. This differs from the space group of the close-packed hexagonal lattice principally by the absence of a horizontal mirror plane. With respect to a set of cartesian coördinates, the vectors which span the unit cell may be taken as:

$$\left.\begin{aligned} \boldsymbol{a}_1 &= a(1/2, -\sqrt{(3)}/2, 0) \\ \boldsymbol{a}_2 &= a(1/2, \sqrt{(3)}/2, 0) \\ \boldsymbol{a}_3 &= c(0, 0, 1). \end{aligned}\right\} \quad (2)$$

The reciprocal lattice is hexagonal and the basis vectors are:

$$\left.\begin{aligned} \boldsymbol{b}_1 &= a^{-1}(1, -1/\sqrt{(3)}, 0) \\ \boldsymbol{b}_2 &= a^{-1}(1, 1/\sqrt{(3)}, 0) \\ \boldsymbol{b}_3 &= c^{-1}(0, 0, 1). \end{aligned}\right\} \quad (3)$$

The point group of the lattice is C_{6v} and consists of the following operations:

ϵ The identity.
δ_6, $\delta_6{}^{-1}$ Six-fold rotations about the z-axis.
δ_3, $\delta_3{}^{-1}$ Three-fold rotations about the z-axis.
δ_2 Two-fold rotation about the z-axis.
ρ_i'' Reflection in a plane containing $\boldsymbol{a}_3$ and $\boldsymbol{a}_i$, $i = 1, 2, 4$.
ρ_i' Reflection in a plane containing $\boldsymbol{a}_3$ and perpendicular to $\boldsymbol{a}_i$ for $i = 1, 2, 4$.

The Brillouin zone shown in Fig. 2 has volume $2(a^2c/3)^{-1}$ and holds two states per unit cell. Some

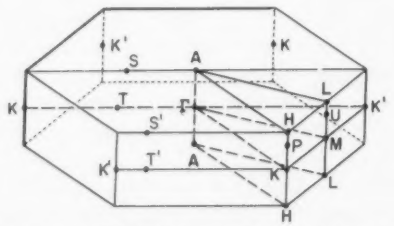

FIG. 2. The first Brillouin zone. Points and lines of symmetry are indicated.

Table 1. *Symmetry elements in the Brillouin zone. The coördinates are with respect to the reciprocal basis* (3)

Pt.	Coördinates	Group
Γ	$2\pi(0, 0, 0)$	C_{6v}
A	$2\pi(0, 0, 1/2)$	C_{6v}
Δ	$\Gamma-A$ axis	C_{6v}
H	$2\pi(-1/3, 2/3, 1/2)$	C_{3v}
K	$2\pi(-1/3, 2/3, 0)$	C_{3v}
P	$K-H$ axis	C_{3v}
L	$2\pi(0, 1/2, 1/2)$	C_{2v}
M	$2\pi(0, 1/2, 0)$	C_{2v}
U	$L-M$ axis	C_{2v}
S	$\Gamma-K$ axis	C_{1v}
T	$A-H$ axis	C_{1v}
π	$AL-LA$ plane	C_{1v}
ψ	Square face	C_{1v}

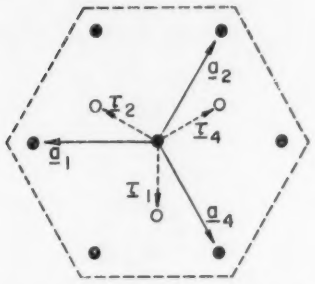

FIG. 3. An outline of the unit cell.
$\mathbf{a}_4 = -\mathbf{a}_1 - \mathbf{a}_2$, $\tau_1 = a/2\,(-1, -1/3, c/a)$
$\tau_2 = a/2(1, -1/3, c/a)$,
$\tau_3 = a/2(0, 2/3, c/a$. (Atoms of one kind lying above the basal plane are shown.)

3. DOUBLE GROUPS

If spin is also considered in the one-electron problem above, the wave functions become spinors and are no longer left invariant by 360° rotations. An elegant way of including this is by the introduction of double groups, as discussed by BETHE[7] and OPECHOWSKI[8] for point groups and by ELLIOTT[9] for space groups.

The essential feature is that the groups involved are doubled by Kronecker multiplication with the spin group. In the process, new classes, and hence new irreducible representations, may be added. The original (single) representations are simply

Table 4. Character table for the representations of the single groups of R, Σ, and π

2	$R,\ \Sigma,\ \pi$	$4_1,\ \Sigma_1,\ \pi$	$R_2,\ \Sigma_2,\ \pi_2$
1	$\{\epsilon\|0\}$	1	1
1	$\{\rho_1'\|0\}$	1	−1
		$\{z\}$	$\{x\}\{y\}$

Table 2. Character table for the representations of the single group of Δ

$\omega = \exp(-ik \cdot \tau_2)$.

12	Δ	Δ_1	Δ_2	Δ_3	Δ_4	Δ_5	Δ_6
1	$\{\epsilon\|0\}$	1	1	1	1	2	2
2	$\{\delta_6^{-1}, \delta_6\|\tau_2\}$	ω	ω	$-\omega$	$-\omega$	$-\omega$	ω
2	$\{\delta_3^{-1}, \delta_3\|0\}$	1	1	1	1	−1	−1
1	$\{\delta_2\|\tau_2\}$	ω	ω	$-\omega$	$-\omega$	2ω	-2ω
3	$\{\rho_i'\|0\}$	1	−1	1	−1	0	0
3	$\{\rho_i''\|\tau_2\}$	ω	$-\omega$	$-\omega$	ω	0	0
		$\{z\}$				$\{x, y\}$	$\{xy, x^2-y^2\}$

important symmetry elements and their groups are given in Table 1. The characters given in Tables 2–6 were worked out using the methods given by HERRING for the close-packed structure.[6]

Table 3. Character table for the representations of the single group of P

$\alpha = \exp(-ik_z \cdot \tau_1)$ where k_z is the component of k along a_3. $\omega = \exp(-ik_z \cdot \tau_2)$. For H, $\omega = -i$; for K, $\omega = 1$. Products of the above classes by $\{\epsilon|a_1\}$ and $\{\epsilon|2a_1\}$ have characters multiplied by α and α^2, resp.

18	P	P_1	P_2	P_3
1	$\{\epsilon\|0\}$	1	1	2
2	$\{\delta_3\|0\}$	$-\alpha$	$-\alpha$	α
	$\{\delta_3^{-1}\|0\}$	α^2	α	$-\alpha^2$
3	$\{\rho_1''\|\tau_1\}$	$\omega\alpha^2$	$-\omega\alpha^2$	0
	$\{\rho_2''\|\tau_1\}$	ω	$-\omega$	0
	$\{\rho_4''\|\tau_4\}$	$-\omega\alpha$	$\omega\alpha$	0
		$\{z\}$		$\{x, y\}$

Table 5. Character table for the representations of the single groups of U

$\omega = \exp(-ik \cdot \tau_1)$. For M, $\omega = 1$; for L, $\omega = -i$.

4	U	U_1	U_2	U_3	U_4
1	$\{\epsilon\|0\}$	1	1	1	1
1	$\{\delta_2\|\tau_1\}$	ω	$-\omega$	$-\omega$	ω
1	$\{\rho_1'\|0\}$	1	1	−1	−1
1	$\{\rho_1\|\tau_1\}$	ω	$-\omega$	ω	$-\omega$
		$\{z\}$	$\{x\}$	$\{y\}$	

Table 6. Character table for the representations of the single groups of T, S, and ψ

$\omega_z = \exp(-ik_z \cdot \tau_1)$, where k_z is the component of k along a_3. $\omega = \exp(-ik \cdot \tau_1)$.

2	S, T, ψ	S_1, T_1	S_2, T_2	ψ_1	ψ_2
1	$\{\epsilon\|0\}$	1	1	1	1
1	$\{\rho_1''\|\tau_1\}$	ω	$-\omega$	ω_z	$-\omega_z$

repeated for the new elements, i.e. $X(\bar{E}A) = X(A)$. The extra irreducible representations induced at the various points are given in Tables 7–11. The

Table 7. Character table for the extra representations of the double groups of Δ

24	Δ	Δ_7	Δ_8	Δ_9
1	$\{\epsilon\|0\}$	2	2	2
1	$\{\bar{\epsilon}\|0\}$	-2	-2	-2
2	$\{\delta_6, \delta_6^{-1}\|\tau_2\}$	$\omega\sqrt{(3)}$	$\omega\sqrt{(3)}$	0
2	$\{\bar{\delta}_6, \bar{\delta}_6^{-1}\|\tau_2\}$	$-\omega\sqrt{(3)}$	$\omega\sqrt{(3)}$	0
2	$\{\delta_3, \delta_3^{-1}\|0\}$	1	1	-2
2	$\{\bar{\delta}_3, \delta_3^{-1}\|0\}$	-1	-1	2
2	$\{\delta_2, \bar{\delta}_2\|\tau_2\}$	0	0	0
6	$\{\rho_i', \bar{\rho}_i\|0\}$	0	0	0
6	$\{\rho_i'', \bar{\rho}_i''\|\tau_2\}$	0	0	0

effect of the spin-orbit interaction is to split the degenerate states and these split-off states will transform according to the extra irreducible representations in the double group. A splitting is indicated, if the product of the representation which

Table 9. Character table for the extra representations of the double group of U

8	U	U_5
1	$\{\epsilon\|0\}$	2
1	$\{\bar{\epsilon}\|0\}$	-2
2	$\{\delta_2, \bar{\delta}_2\|\tau_1\}$	0
2	$\delta\rho_1', \bar{\rho}_1'\|0\}$	0
2	$\{\rho_1'', \bar{\rho}_1''\|\tau_1\}$	0

Table 10. Character table for the extra representations of the double groups of R, Σ, and π

4	R, Σ π	R_3, Σ_3	R_4, Σ_4	π_3	π_4
1	$\{\epsilon\|0\}$	1	1	1	1
1	$\{\bar{\epsilon}\|0\}$	-1	-1	-1	-1
1	$\{\rho_1'\|0\}$	1	-1	1	-1
1	$\{\bar{\rho}_1'\|0\}$	-1	1	-1	1

Table 11. Character table for the extra representations of the double groups of S, T, and ψ

4	S, T ψ	S_3 T_3	S_4 T_4	ψ_3	ψ_4
1	$\{\epsilon\|0\}$	1	1	1	1
1	$\{\bar{\epsilon}\|0\}$	-1	-1	-1	-1
1	$\{\rho_1''\|\tau_1\}$	ω	$-\omega$	ω_z	$-\omega_z$
1	$\{\bar{\rho}_1''\|\tau_1\}$	$-\omega$	ω	$-\omega_z$	ω_z

Table 8. Character table for the extra representations of the double group of P

See caption for Table 3.

36	P	P_4	P_5	P_6
1	$\{\epsilon\|0\}$	1	1	2
1	$\{\bar{\epsilon}\|0\}$	-1	-1	-2
2	$\{\delta_3\|0\}\{\delta_3^{-1}\|0\}$	$\alpha, -\alpha^2$	$\alpha, -\alpha^2$	$-\alpha, \alpha^2$
2	$\{\bar{\delta}_3\|0\}\{\bar{\delta}_3^{-1}\|0\}$	$-\alpha, \alpha^2$	$-\alpha, \alpha^2$	$\alpha, -\alpha^2$
3	$\{\rho_i'\|\tau_i\}$	$-i\omega\alpha^2, -i\omega, \omega\alpha$	$i\omega\alpha^2, i\omega, -i\omega\alpha$	0
3	$\{\bar{\rho}_i''\|\tau_i\}$	$i\omega\alpha^2, i\omega, -i\omega\alpha$	$-i\omega\alpha^2, -i\omega, \omega\alpha$	0

Table 12. Matrices for the irreducible representations of C_{6v}

	$\{\epsilon\}$	δ_6	δ_6^{-1}	δ_3	δ_3^{-1}	δ_2
Γ_1	1	1	1	1	1	1
Γ_2	1	1	1	1	1	1
Γ_3	1	−1	−1	1	1	−1
Γ_4	1	−1	−1	1	1	−1
Γ_5	$\begin{bmatrix}1 & 0\\ 0 & 1\end{bmatrix}$	$\frac{1}{2}\begin{bmatrix}-1 & -\sqrt{(3)}\\ \sqrt{(3)} & -1\end{bmatrix}$	$\frac{1}{2}\begin{bmatrix}-1 & \sqrt{(3)}\\ -\sqrt{(3)} & -1\end{bmatrix}$	$\frac{1}{2}\begin{bmatrix}-1 & \sqrt{(3)}\\ -\sqrt{(3)} & -1\end{bmatrix}$	$\frac{1}{2}\begin{bmatrix}-1 & -\sqrt{(3)}\\ \sqrt{(3)} & -1\end{bmatrix}$	$\begin{bmatrix}1 & 0\\ 0 & 1\end{bmatrix}$
Γ_6	$\begin{bmatrix}1 & 0\\ 0 & 1\end{bmatrix}$	$\frac{1}{2}\begin{bmatrix}1 & -\sqrt{(3)}\\ \sqrt{(3)} & 1\end{bmatrix}$	$\frac{1}{2}\begin{bmatrix}1 & \sqrt{(3)}\\ -\sqrt{(3)} & 1\end{bmatrix}$	$\frac{1}{2}\begin{bmatrix}-1 & -\sqrt{(3)}\\ \sqrt{(3)} & -1\end{bmatrix}$	$\frac{1}{2}\begin{bmatrix}-1 & \sqrt{(3)}\\ -\sqrt{(3)} & -1\end{bmatrix}$	$\begin{bmatrix}-1 & 0\\ 0 & 1\end{bmatrix}$

	ρ_1'	ρ_2'	ρ_4'	ρ_1''	ρ_2''	ρ_4''
Γ_1	1	1	1	1	1	1
Γ_2	−1	−1	−1	−1	−1	−1
Γ_3	1	1	1	−1	−1	−1
Γ_4	−1	−1	−1	1	1	1
Γ_5	$\begin{bmatrix}1 & 0\\ 0 & -1\end{bmatrix}$	$\frac{1}{2}\begin{bmatrix}-1 & -\sqrt{(3)}\\ -\sqrt{(3)} & 1\end{bmatrix}$	$\frac{1}{2}\begin{bmatrix}-1 & \sqrt{(3)}\\ \sqrt{(3)} & 1\end{bmatrix}$	$\begin{bmatrix}1 & 0\\ 0 & -1\end{bmatrix}$	$\frac{1}{2}\begin{bmatrix}-1 & -\sqrt{(3)}\\ \sqrt{(3)} & 1\end{bmatrix}$	$\frac{1}{2}\begin{bmatrix}-1 & \sqrt{(3)}\\ \sqrt{(3)} & 1\end{bmatrix}$
Γ_6	$\begin{bmatrix}-1 & 0\\ 0 & 1\end{bmatrix}$	$\frac{1}{2}\begin{bmatrix}1 & -\sqrt{(3)}\\ -\sqrt{(3)} & -1\end{bmatrix}$	$\frac{1}{2}\begin{bmatrix}1 & \sqrt{(3)}\\ \sqrt{(3)} & -1\end{bmatrix}$	$\begin{bmatrix}1 & 0\\ 0 & -1\end{bmatrix}$	$\frac{1}{2}\begin{bmatrix}-1 & \sqrt{(3)}\\ \sqrt{(3)} & 1\end{bmatrix}$	$\frac{1}{2}\begin{bmatrix}-1 & -\sqrt{(3)}\\ -\sqrt{(3)} & 1\end{bmatrix}$

corresponds to a given state and the spin representation $D_{1/2}$* can be decomposed into two or more extra representations. The splittings for Δ and P are given in Table 13.

There is no extra degeneracy due to time reversal in k_xk_y plane.[9,10] Furthermore, the lack of an inversion center implies that a two-fold degeneracy throughout the zone is not required. Since there are sixteen electrons per unit cell, eight of each spin, the gap will occur between the eighth and ninth bands (see Fig. 4), each band holding one electron of each spin, per unit cell.

* The characters of $D_{1/2}$ are defined by $X(E) = X(\bar{E}) = 2$, $X(A) = 2\cos\pi/n$, where A is an n-fold rotation.

Table 13. Spin orbit splittings at Δ and P

Δ_i	Δ_1	Δ_2	Δ_3	Δ_4	Δ_5	Δ_6
$\Delta_i \times D_{1/2}$	Δ_7	Δ_7	Δ_8	Δ_8	$\Delta_7+\Delta_9$	$\Delta_7+\Delta_9$

P_i	P_1	P_2	P_3
$P_i \times D_{1/2}$	P_6	P_6	$P_4+P_5+P_6$

4. COMPATIBILITY RELATIONS

BOUCKAERT *et al.*[5] have pointed out the connection that exists between the topology of

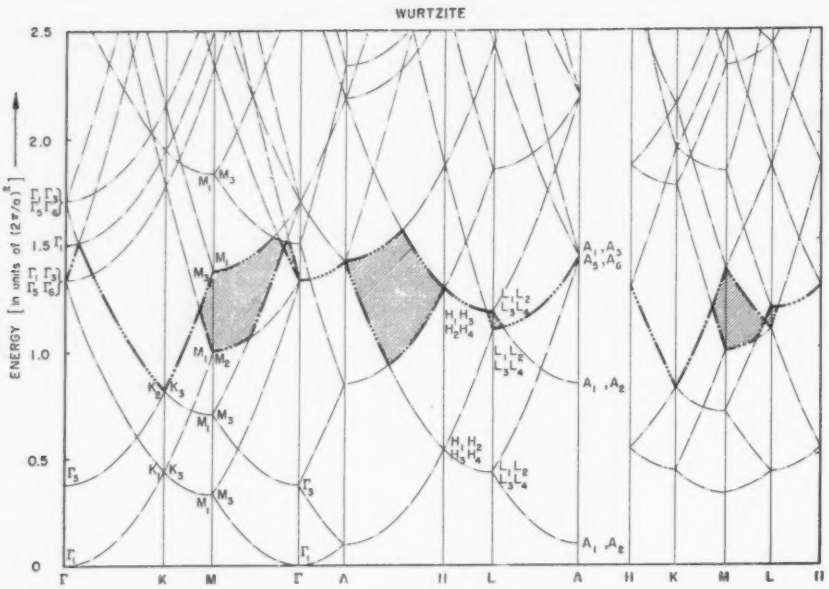

FIG. 4. The empty lattice structure for wurtzite-type crystals. (Drawn for ideal c/a ratio.)

irreducible representations in the zone and the "sticking" of energy surfaces. By deriving relations which can be deduced from the character tables, the splitting of degeneracies and the sequence of states, as one moves from points of higher to lower symmetry in the zone, can be determined. For example, along the Δ and U axes, we have the possible sequence of states:

$$\Gamma_1-\Delta_1-A_1-\Delta_2-\Gamma_2-A_2-\Delta_1-\Gamma_1$$

$$\Gamma_3-\Delta_3-A_3-\Delta_4-\Gamma_4-A_4-\Delta_3-\Gamma_3$$

$$\Gamma_5-\Delta_5-A_5-\Delta_6-\Gamma_6-A_6-\Delta_5-\Gamma_5$$

$$M_1-U_1-M_1-U_2-M_2-U_2-U_2-U_1-M_1$$

$$M_3-U_3-M_3-U_4-M_4-U_4-M_3-U_3-M_3.$$

Compatibility relations for most symmetry elements are given for the double groups, in Table 14.

5. SYMMETRIZED COMBINATIONS OF PLANE WAVES

Suppose it is desired to solve equation (1) by expanding ψ in a Fourier series, $\psi = \Sigma a_j \exp(i\boldsymbol{k}_j \cdot \boldsymbol{r})$. Putting this into equation (1) leads in the usual way to the secular equation

$$\det|\langle \boldsymbol{k}_i|H|\boldsymbol{k}_j\rangle - E\langle \boldsymbol{k}_i|\boldsymbol{k}_j\rangle| = 0,$$

where

$$\langle \boldsymbol{k}| = \langle \exp(i\boldsymbol{k}\cdot\boldsymbol{r})|.$$

To find a particular state, and to obtain a convergent result, in general a very large number of terms is needed in the expansion and a large secular equation may result. This procedure may be greatly simplified as follows. We know that a solution must have the Bloch form

$$\psi_{\boldsymbol{k}} = \exp(i\boldsymbol{k}\cdot\boldsymbol{r})U_{\boldsymbol{k}}(\boldsymbol{r}),$$

where $U_{\boldsymbol{k}}$ is lattice-periodic and hence has a Fourier expansion in plane waves whose wave vectors are reciprocal lattice vectors. Thus $\psi_{\boldsymbol{k}}$ may be expanded in a series of the form: $\psi_{\boldsymbol{k}} = -a_j \exp(i(\boldsymbol{k}+\boldsymbol{k}_j)\cdot\boldsymbol{r})$. Furthermore, $\psi_{\boldsymbol{k}}$ must transform according to an irreducible representation of the group of $\boldsymbol{k}$. Thus we need merely expand $\psi_{\boldsymbol{k}}$ in linear combinations of the plane waves which have the appropriate symmetry. This, in effect, factors the original secular determinant into smaller ones and the labor is greatly reduced.

The plane-wave combinations for an expansion at a point in the zone are thus obtained by adding

Table 14. Compatibility relations

$\Gamma_1 \to \Delta_1$,	T_1,	Σ_1
$\Gamma_2 \to \Delta_2$,	T_2,	Σ_2
$\Gamma_3 \to \Delta_3$,	T_2,	Σ_1
$\Gamma_4 \to \Delta_4$,	T_1,	Σ_2
$\Gamma_5 \to \Delta_5$,	T_1+T_2,	$\Sigma_1+\Sigma_2$
$\Gamma_6 \to \Delta_6$,	T_1+T_2,	$\Sigma_1+\Sigma_2$
$\Gamma_7 \to \Delta_7$,	T_3+T_4,	$\Sigma_3+\Sigma_4$
$\Gamma_8 \to \Delta_8$,	T_3+T_4,	$\Sigma_3+\Sigma_4$
$\Gamma_9 \to \Delta_9$,	T_3+T_4,	$\Sigma_3+\Sigma_4$
$A_1 \to \Delta_1$,	R_1,	S_1
$A_2 \to \Delta_2$,	R_2,	S_2
$A_3 \to \Delta_3$,	R_1,	S_2
$A_4 \to \Delta_4$,	R_2,	S_1
$A_5 \to \Delta_5$,	R_1+R_2,	S_1+S_1
$A_6 \to \Delta_6$,	R_1+R_2,	S_1+S_2
$A_7 \to \Delta_7$,	R_3+R_4,	S_3+S_4
$A_8 \to \Delta_8$,	R_3+R_4,	S_3+S_4
$A_9 \to \Delta_9$,	R_3+R_4,	S_3+S_4

$H_1 \to P_1$,	S_1
$H_2 \to P_2$,	S_2
$H_3 \to P_3$,	S_1+S_6
$H_4 \to P_4$,	S_3
$H_5 \to P_5$,	S_4
$H_6 \to P_6$,	S_3+S_4
$M_1 \to U_1$,	Σ_1
$M_2 \to U_2$,	Σ_2
$M_3 \to U_1$,	Σ_1
$M_4 \to U_4$,	Σ_2
$M_5 \to U_5$,	$\Sigma_3+\Sigma_4$
$K_1 \to P_1$,	T_1
$K_1 \to P_2$,	T_2
$K_3 \to P_3$,	T_1+T_2
$K_4 \to P_4$,	T_3
$K_5 \to P_5$,	T_4
$K_6 \to P_6$,	T_3+T_4

$L_1 \to U_1$,	R_1
$L_2 \to U_2$,	R_2
$L_3 \to U_3$,	R_1
$L_4 \to U_4$,	R_2
$L_5 \to U_5$,	R_3+R_4

to the point vector all reciprocal lattice vectors, and forming linear combinations of the resulting degenerate plane waves. These combinations may be formed by the projection technique discussed by EYRING *et al.*[11] and ASENDORF[4].

To each symmetry operation $\{\boldsymbol{\alpha}|\boldsymbol{t}\}$ there corresponds an operator $P\{\boldsymbol{\alpha}|\boldsymbol{t}\}$ defined as follows:

$$P\{\boldsymbol{\alpha}|\boldsymbol{t}\}F(\boldsymbol{r}) = F(\{\alpha|\boldsymbol{t}\}^{-1}\boldsymbol{r}) = F(\alpha^{-1}\boldsymbol{r}-\alpha^{-1}\boldsymbol{t}).$$

Thus, $P\{\boldsymbol{\alpha}|\boldsymbol{t}\}F(\boldsymbol{r})$ expresses $F(\boldsymbol{r})$ in terms of a coördinate system transformed from the original by $\{\boldsymbol{\alpha}|\boldsymbol{t}\}$. When $F(\boldsymbol{r})$ is a plane wave, $\exp(i\boldsymbol{k}\cdot\boldsymbol{r})$, we have,

$$\begin{aligned} P\{\boldsymbol{\alpha}|\boldsymbol{t}\}\exp(i\boldsymbol{k}\boldsymbol{r}) &= \exp[i\boldsymbol{k}\cdot(\alpha^{-1}\boldsymbol{r}-\alpha^{-1}\boldsymbol{t})] \\ &= \exp\{-i\boldsymbol{k}\cdot\alpha^{-1}\boldsymbol{t}\}\exp\{i\boldsymbol{k}\cdot\alpha^{-1}\boldsymbol{r}\} \\ &= \exp\{-i\alpha\boldsymbol{k}\cdot\boldsymbol{t}\}\exp\{i\alpha\boldsymbol{k}\cdot\boldsymbol{r}\}, \end{aligned}$$

where the last equality follows from the fact that $\boldsymbol{\alpha}$ is an orthogonal transformation. The symmetrized combinations of plane waves (SCPW) are obtained for a degenerate set of waves by operating on any member with the projection operator

$$E_i\gamma = \Sigma X_i^*(A)P(A). \qquad (4)$$

Here the sum is over all elements A of the group of the point considered; γ labels the irreducible representation in question, and X_i is the appropriate character, if γ is one-dimensional, and one of the diagonal elements of the representation matrix if γ is degenerate. This operator projects out the linear combination belonging to the i^{th} row of the representation γ of the group of the $\boldsymbol{k}$ vector.

As an example, the SCPW for the point H which transforms according to H_1 for the waves of least kinetic energy is worked out. With respect to the set of cartesian coördinates, the elements of the group of H are:

$$\{\epsilon|0\}: \begin{bmatrix} 1 & 0 & 0 \\ 0 & 1 & 0 \\ 0 & 0 & 1 \end{bmatrix} \qquad \{\delta_3|0\}:\tfrac{1}{2}\} \begin{bmatrix} -1 & -\sqrt{(3)} & 0 \\ \sqrt{(3)} & -1 & 0 \\ 0 & 0 & 1 \end{bmatrix}$$

$$\{\delta_3^{-1}|0\}: \tfrac{1}{2}\begin{bmatrix} -1 & \sqrt{(3)} & 0 \\ -\sqrt{(3)} & -1 & 0 \\ 0 & 0 & 1 \end{bmatrix}, \quad \{\rho_1''|\tau_1\}\left\{\tfrac{1}{2}\begin{bmatrix} 1 & 0 & 0 \\ 0 & -1 & 0 \\ 0 & 0 & 1 \end{bmatrix}\middle|\frac{a}{2}\begin{pmatrix} -1 \\ -1/\sqrt{(3)} \\ c/a \end{pmatrix}\right\}$$

$$\{\rho_2''|\tau_2\}: \quad \left\{\tfrac{1}{2}\begin{bmatrix} -1 & \sqrt{(3)} & 0 \\ \sqrt{(3)} & 1 & 0 \\ 0 & 0 & 1 \end{bmatrix}\middle|\frac{a}{2}\begin{pmatrix} 1 \\ -1/\sqrt{(3)} \\ c/a \end{pmatrix}\right\}$$

$$\{\rho_4''|\tau_4\}: \tfrac{1}{2}\left\{\begin{bmatrix} -1 & -\sqrt{(3)} & 0 \\ \sqrt{(3)} & 1 & 0 \\ 0 & 0 & 1 \end{bmatrix}\middle|\frac{a}{2}\begin{pmatrix} 0 \\ 2/\sqrt{(3)} \\ 2/a \end{pmatrix}\right\}$$

Tables 15–20. *Symmetrized combinations of plane waves (unnormalized) for* Γ, A, H, K, L, *and* M

$\alpha = \exp(-\pi i/3)$. $[k_1, k_2, k_3]$ denotes $\exp(2\omega i\mathbf{k}\cdot\mathbf{r})$ where the components are given with respect to the reciprocal basis (3)*

$(\Gamma+k)$	Γ_1	Γ_2	Γ_3	Γ_4	$\Gamma_5(1)$	$\Gamma_5(2)$	$\Gamma_6(1)$	$\Gamma_6(2)$
[000]	1	0	0	0	0	0	0	0
[001]	0	0	1	0	0	0	0	0
[00$\bar{1}$]	0	0	1	0	0	0	0	0
[100]	2	0	2	0	1	3	3	1
[$\bar{1}$10]	2	0	2	0	2	0	0	−2
[0$\bar{1}$0]	2	0	2	0	1	−3	−3	1
[$\bar{1}$00]	$2\alpha^2$	0	$-2\alpha^2$	0	α^2	$3\alpha^2$	$-3\alpha^2$	$-\alpha^2$
[1$\bar{1}$0]	$2\alpha^2$	0	$-2\alpha^2$	0	$-2\alpha^2$	0	0	$2\alpha^2$
[010]	$2\alpha^2$	0	$-2\alpha^2$	0	α^2	$-3\alpha^2$	$3\alpha^2$	$-\alpha^2$
[101]	2		2		1	3	3	1
[$\bar{1}$11]	2		2		−2	0	0	−2
[0$\bar{1}$1]	2		2		1	−3	−3	1
[011]	$-2\alpha^2$		$2\alpha^2$		$-\alpha^2$	$3\alpha^2$	$-3\alpha^2$	α^2
[$\bar{1}$01]	$-2\alpha^2$		$2\alpha^2$		$-\alpha^2$	$-3\alpha^2$	$3\alpha^2$	α^2
[1$\bar{1}$1]	$-2\alpha^2$		$2\alpha^2$		$2\alpha^2$	0	0	$-\alpha^2$
[10$\bar{1}$]	2		2		1	3	3	1
[$\bar{1}$1$\bar{1}$]	2		2		−2	0	0	−2
[0$\bar{1}\bar{1}$]	2		2		1	−3	−3	1
[01$\bar{1}$]	$-2\alpha^2$		$2\alpha^2$		$-\alpha^2$	$3\alpha^2$	$-3\alpha^2$	α^2
[$\bar{1}$0$\bar{1}$]	$-2\alpha^2$		$2\alpha^2$		$-\alpha^2$	$-3\alpha^2$	$3\alpha^2$	α^2
[1$\bar{1}\bar{1}$]	$-2\alpha^2$		$2\alpha^2$		$2\alpha^2$	0	0	$-\alpha^2$
[002]	1		0					
[00$\bar{2}$]	1		0					

* More extensive tables have been published in an RCA Technical Report, which may be obtained by writing the author.

The cartesian coördinates of H are $(2\pi/a)[\frac{1}{3}, \frac{1}{3}, \frac{1}{2}(a/c)]$ and the first degenerate set may be formed by adding the lowest reciprocal lattice vector, (0, 0, 0), to H. Coördinates in square brackets denote that they are to be taken with respect to the reciprocal basis (3). The same symbol is also used for the corresponding plane wave; which meaning is intended should be clear from the context.

It is easily seen that:

$$\{\epsilon|0\}\boldsymbol{H} = [-\tfrac{1}{3}, \tfrac{2}{3}, \tfrac{1}{2}]$$
$$\{\delta_3|0\}\boldsymbol{H} = [-\tfrac{1}{3}, -\tfrac{1}{3}, \tfrac{1}{2}]$$
$$\{\delta_3^{-1}|0\}\boldsymbol{H} = [\tfrac{2}{3}, -\tfrac{1}{2}, \tfrac{1}{2}].$$

The factor $-i$ is $\exp(\alpha\boldsymbol{H}\cdot\boldsymbol{\tau}_j)$ in each case. Thus we have:

The characters for H_1 are given in Table 3 and are:

$$X\{\epsilon|0\} = 1 \qquad X\{\rho_1''|\tau_1\} = -i\alpha^2$$
$$X\{\delta_3|0\} = -\alpha \qquad X\{\rho_2''|\tau_2\} = -i$$
$$X\{\delta_3^{-1}|0\} = \alpha^2 \qquad X\{\rho_4''|\tau_4\} = i\alpha$$

Thus from an application of (4) the desired SCPW is (unnormalized)

$$2[-\tfrac{1}{3}, \tfrac{2}{3}, \tfrac{1}{2}]+2\alpha^2[-\tfrac{1}{3}, \tfrac{1}{3}, \tfrac{1}{2}]-2\alpha[\tfrac{2}{3}, -\tfrac{1}{3}, \tfrac{1}{2}].$$

$$\{\rho_1''|\tau_1\}\boldsymbol{H} = -i[\tfrac{2}{3}, -\tfrac{1}{3}, \tfrac{1}{2}]$$
$$\{\rho_2''|\tau_2\}\boldsymbol{H} = -i[-\tfrac{1}{3}, -\tfrac{1}{3}, \tfrac{1}{2}]$$
$$\{\rho_4''|\tau_4\}\boldsymbol{H} = -i[-\tfrac{1}{3}, \tfrac{2}{3}, \tfrac{1}{2}].$$

The SCPW for Γ, A, H, K, L, M, are listed in Tables 15–20.

$$P\{\epsilon|0\}\exp i\boldsymbol{H}\cdot\boldsymbol{r} = [-\tfrac{1}{3}, \tfrac{2}{3}, \tfrac{1}{2}] \quad P\{\rho_1''|\tau_1\}\exp i\boldsymbol{H}\cdot\boldsymbol{r} = -i[\tfrac{2}{3}, -\tfrac{1}{3}, \tfrac{1}{2}]$$
$$P\{\delta_3|0\}\exp i\boldsymbol{H}\cdot\boldsymbol{r} = [-\tfrac{1}{2}, -\tfrac{1}{3}, \tfrac{1}{2}] P\{\rho_2''|\tau_2\}\exp i\boldsymbol{H}\cdot\boldsymbol{r} = -i[-\tfrac{1}{3}, -\tfrac{1}{3}, \tfrac{1}{2}]$$
$$P\{\delta_3^{-1}|0\}\exp i\boldsymbol{H}\cdot\boldsymbol{r} = [\tfrac{2}{3}, -\tfrac{1}{3}, \tfrac{1}{2}] \quad P\{\rho_4''|\tau_4\}\exp i\boldsymbol{H}\cdot\boldsymbol{r} = -i[-\tfrac{1}{3}, \tfrac{2}{3}, \tfrac{1}{2}].$$

Table 16

$2(A+h)$	A_1	A_2	A_3	A_4	$A_5(1)$	$A_5(2)$	$A_6(1)$	$A_6(2)$
[001]	1							
[00$\bar{1}$]	1							
[201]	2		2		1	3	3	1
[021]	$2\alpha^2$		$-2\alpha^2$		α^2	$3\alpha^2$	$-3\alpha^2$	$-\alpha^2$
[2$\bar{2}$1]	$2\alpha^2$		$-2\alpha^2$		$2\alpha^2$	0	0	$-2\alpha^2$
[$\bar{2}$21]	2		2		-2	0	0	-2
[0$\bar{2}$1]	2		2		1	-3	-3	1
[$\bar{2}$01]	$2\alpha^2$		$-2\alpha^2$		$-\alpha^2$	$-3\alpha^2$	$3\alpha^2$	α^2
[20$\bar{1}$]	2		2		1	3	3	1
[02$\bar{1}$]	$-2\alpha^2$		$2\alpha^2$		$-\alpha^2$	$-3\alpha^2$	$3\alpha^2$	$-\alpha^2$
[2$\bar{2}$$\bar{1}$]	$-2\alpha^2$		$2\alpha^2$		$-2\alpha^2$	0	0	$2\alpha^2$
[$\bar{2}$2$\bar{1}$]	2		2		-2	0	0	-2
[0$\bar{2}$$\bar{1}$]	2		2		1	-3	-3	1
[$\bar{2}$0$\bar{1}$]	$-2\alpha^2$		$2\alpha^2$		α^2	$3\alpha^2$	$-3\alpha^2$	$-\alpha^2$
[003]			1					
[00$\bar{3}$]	1							
[203]	2		2		1	3	3	1
[023]	$-2\alpha^2$		$2\alpha^2$		$-\alpha^2$	$-3\alpha^2$	$3\alpha^2$	$-\alpha^2$
[2$\bar{2}$3]	$-2\alpha^2$		$2\alpha^2$		$-2\alpha^2$	0	0	$2\alpha^2$
[$\bar{2}$23]	2		2		-2	0	0	-2
[0$\bar{2}$3]	2		2		1	-3	-3	1
[$\bar{2}$03]	$-2\alpha^2$		$2\alpha^2$		α^2	$3\alpha^2$	$-3\alpha^2$	$-\alpha^2$

6. SELECTION RULES

It is possible to obtain the behaviour of bands in the neighborhood of a point at which energy levels and wave functions are known, by the following procedure. If we write the wave functions in Bloch form the cell periodic function U_k satisfies the equation

$$[p^2+V+\boldsymbol{k}\cdot\boldsymbol{p}]U_k(r)=(E-k^2)U_k.$$

The corresponding equation for U_{k+K} is

$$[p^2+V+\boldsymbol{k}\cdot\boldsymbol{p}+\boldsymbol{K}\cdot p]U_{k+K}=[E-(\boldsymbol{k}+\boldsymbol{K})^2]U_{k+K}.$$

By taking $\boldsymbol{K}$ to be a small vector, the term $\boldsymbol{K}\cdot\boldsymbol{p}$ may be treated as a perturbation, and the appropriate degenerate or non-degenerate perturbation theory may be used. When working out the matrix elements for this approach, it is helpful to use group-theoretical selection rules. Since the momentum operator transforms as a vector, matrix elements $\langle\psi_{\boldsymbol{k}}{}^i|\boldsymbol{p}|\psi_{\boldsymbol{k}}{}^j\rangle$ will vanish unless the direct product $R^{i*}\times R^v\times R^j$, where R^v is the representation of the group of $\boldsymbol{k}$ according to which a vector transforms, contains the totally symmetric representation. Thus, $\boldsymbol{K}\cdot\boldsymbol{p}$ will mix with $\psi_{\boldsymbol{k}}{}^i$ only those states $\psi_{\boldsymbol{k}}{}^j$ where R^j is in the decomposition of $R^{i*}\times R^v$. The selection rules for the Zone center are given in Table 21. In the case of points whose elements contain nonprimitive translations this procedure is no longer strictly applicable. The momentum operator is generally translation-invariant and may not transform according to any representation at a point if there are translational phase factors. In this case, however, representations $\bar{R}_t$ of the underlying (isomorphic) point group

Table 17

$6(H+h)$	H_1	H_2	$H_3(1)$	$H_3(2)$
[$\bar{2}$43]	2	0	1	3
[$\bar{2}\bar{2}$3]	$2\alpha^2$	0	$-2\alpha^2$	0
[4$\bar{2}$3]	-2α	0	$-\alpha$	3α
[$\bar{2}$43]	0	2	3	1
[$\bar{2}\bar{2}$3]	0	$2\alpha^2$	0	$-2\alpha^2$
[4$\bar{2}$3]	0	-2α	3α	$-\alpha$
[443]	2	0	4	0
[$\bar{8}$43]	$2\alpha^2$	0	$-2\alpha^2$	0
[4$\bar{8}$3]	-2α	0	2α	0
[44$\bar{3}$]	0	2	0	2
[$\bar{8}$4$\bar{3}$]	0	$2\alpha^2$	0	$-2\alpha^2$
[4$\bar{8}$3]	0	-2α	0	2α
[$\bar{2}$49]	0	2	3	1
[$\bar{2}\bar{2}$9]	0	$2\alpha^2$	0	$-2\alpha^2$
[4$\bar{2}$9]	0	-2α	3α	$-\alpha$
[$\bar{2}$49]	2	0	1	3
[$\bar{2}\bar{2}$9]	$2\alpha^2$	0	$-2\alpha^2$	0
[4$\bar{2}$9]	-2α	0	$-\alpha$	3α
[$\bar{2}$109]	1	1	2	2
[$\bar{8}$29]	α^2	α^2	$-\alpha^2$	$-\alpha^2$
[10$\bar{8}$9]	$-\alpha$	$-\alpha$	α	α
[10$\bar{2}$9]	$-\alpha^2$	α^2	$-2\alpha^2$	$2\alpha^2$
[$\bar{8}$109]	α	$-\alpha$	$-\alpha$	α
[$\bar{2}$89]	-1	1	1	-1

Table 18

$3(K+h)$	K_1	K_2	$K_3(1)$	$K_3(2)$
[$\bar{1}$20]	2	0	1	3
[$\bar{1}\bar{1}$0]	$2\alpha^2$	0	$-2\alpha^2$	0
[2$\bar{1}$0]	-2α	0	$-\alpha$	3α
[$\bar{1}$23]	0	2	3	1
[$\bar{1}\bar{1}$3]	0	$2\alpha^2$	0	$-2\alpha^2$
[2$\bar{1}$3]	0	-2α	3α	$-\alpha$
[$\bar{1}$2$\bar{3}$]	0	2	3	1
[$\bar{1}\bar{1}$3]	0	$2\alpha^2$	0	$-2\alpha^2$
[2$\bar{1}$3]	0	-2α	3α	$-\alpha$
[220]	2	0	2	0
[$\bar{4}$20]	$2\alpha^2$	0	$-\alpha^2$	0
[240]	-2α	0	α	0
[223]	0	2	0	2
[$\bar{4}$23]	0	$2\alpha^2$	0	$-\alpha^2$
[2$\bar{4}$3]	0	-2α	0	α
[22$\bar{3}$]	0	2	0	2
[$\bar{4}$2$\bar{3}$]	0	$2\alpha^2$	0	$-\alpha^2$
[2$\bar{4}$3]	0	-2α	0	α
[$\bar{1}$50]	1	1	2	2
[$\bar{4}\bar{1}$0]	α^2	α^2	$-\alpha^2$	$-\alpha^2$
[5$\bar{4}$0]	$-\alpha$	$-\alpha$	α	α
[5$\bar{1}$0]	α^2	$-\alpha^2$	$2\alpha^2$	$-2\alpha^2$
[$\bar{4}$50]	$-\alpha$	α	α	$-\alpha$
[$\bar{1}\bar{4}$0]	1	-1	-1	1
[$\bar{1}$26]	2	0	1	3
[$\bar{1}\bar{1}$6]	$2\alpha^2$	0	$-2\alpha^2$	0
[2$\bar{1}$6]	-2α	0	$-\alpha$	$3\alpha^2$

Table 19

$2(L+h)$	L_1	L_2	L_3	L_4
[011]	1	1	1	1
[0$\bar{1}$1]	α^2	$-\alpha^2$	$-\alpha^2$	α^2
[$\bar{1}$01]	1	1	−1	−1
[101]	$-\alpha^2$	α^2	$-\alpha^2$	α^2
[01$\bar{1}$]	1	1	1	1
[0$\bar{1}\bar{1}$]	$-\alpha^2$	α^2	α^2	$-\alpha^2$
[$\bar{1}$0$\bar{1}$]	1	1	−1	−1
[10$\bar{1}$]	α^2	$-\alpha^2$	α^2	$-\alpha^2$
[$\bar{2}$11]	1	1	1	1
[2$\bar{1}$1]	1	−1	−1	1
[$\bar{1}$21]	1	1	−1	−1
[1$\bar{2}$1]	−1	1	−1	1
[$\bar{2}$1$\bar{1}$]	1	1	1	1
[2$\bar{1}\bar{1}$]	−1	1	1	−1
[$\bar{1}\bar{2}\bar{1}$]	1	1	−1	−1
[1$\bar{2}\bar{1}$]	1	−1	1	−1
[013]	1	1	1	1
[0$\bar{1}$3]	$-\alpha^2$	α^2	α^2	$-\alpha^2$
[$\bar{1}$03]	1	1	−1	−1
[103]	α^2	$-\alpha^2$	α^2	$-\alpha^2$
[01$\bar{3}$]	1	1	1	1
[0$\bar{1}$3]	α^2	$-\alpha^2$	$-\alpha^2$	α^2
[$\bar{1}$03]	1	1	−1	−1
[10$\bar{3}$]	$-\alpha^2$	α^2	$-\alpha^2$	α^2

may be used. Thus $\langle \psi^i_k | \psi_k{}^j \rangle$, vanishes unless $\bar{R}^{i*} \times \bar{R}^v \times \bar{R}^j$ contains the totally symmetric representation. For example, at the point A, $\bar{R}^{vy}$ (the representation to which the y component of a vector belongs in C_{6v}) is, in standard notation,[11] E_1. Thus $\langle \psi_A{}^{A_3} | p_y | \psi_A{}^{A_4} \rangle = 0$, since $B_1 \times E_1 \times B_2 = E_1$. In this way the selection rules at any point may be worked out as desired. These remarks can be extended to the double group in the same way as done by DRESSELHAUS[12] for the zinc-blende structure.

7. DISCUSSION

In a recent review article,[1] HERMAN pointed out the resemblance that sometimes exists between empty lattice bands and the results of elaborate calculations. He suggested that an informed deformation of the empty lattice structure may give a good indication of the actual band shapes. Starting with the crystal-field splittings of the empty bands and using what theoretical or experimental evidence is available, it is interesting to speculate on the band structures of some wurtzite crystals.

A tight binding calculation has been done for the valence-band structure of BeO by O'SULLIVAN.[13] No details were assumed about the crystal potential, except that the Be^{++} and O^{--} ions are in their lowest spherically symmetric configurations. Up to and including third nearest-neighbor interactions were taken into account. Admittedly this is probably a poor approximation to the state of affairs, and several more sets of neighbors may have to be included before convergence is assured,[14] but some general features may be indicated. O'SULLIVAN concludes that the valence-band edge is nondegenerate and lies near the point M. He does not determine the symmetry of the states, but a possible ordering is shown in Fig. 5, we consider the lines A–Γ–M. In general, the valence bands

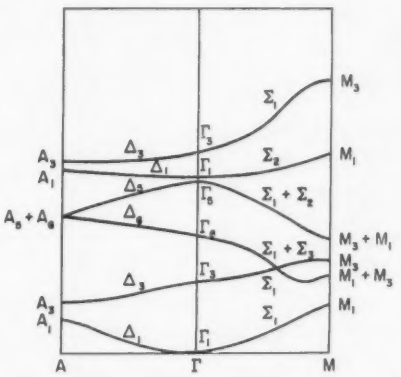

FIG. 5. Valence-band structure in BeO, according to O'SULLIVAN.[13]

will be sensitive to the ionic character of the crystal, since the more tightly bound states will pile up charge in accordance with the ionicity. Γ_1 represents a p-state along the hexagonal axis and will probably be more tightly bound than Γ_3 or Γ_5, which have predominant d-character. Also, Γ_6 represents the degenerate x and y p-orbitals. Thus it seems strange that Γ_5 and Γ_6 should both be depressed below the top of the valence band. Probably if the ionic and covalent nature of the crystal were considered more carefully, and the calculation extended to further neighbors, the following would

Table 20

$2(M+k)$	M_1	M_2	M_3	M_4
[010]	1	1	1	1
[0$\bar{1}$0]	α^2	$-\alpha^2$	$-\alpha^2$	α^2
[$\bar{1}$00]	1	1	−1	−1
[100]	$-\alpha^2$	α^2	$-\alpha^2$	α^2
[$\bar{2}$10]	1	1	1	1
[2$\bar{1}$0]	1	−1	−1	1
[$\bar{1}$20]	1	1	−1	−1
[1$\bar{2}$0]	−1	1	−1	1
[012]	1	1	1	1
[0$\bar{1}$2]	$-\alpha^2$	α^2	α^2	$-\alpha^2$
[$\bar{1}$02]	1	1	−1	−1
[102]	α^2	$-\alpha^2$	α^2	$-\alpha^2$
[01$\bar{2}$]	1	1	1	1
[0$\bar{1}\bar{2}$]	$-\alpha^2$	α^2	α^2	$-\alpha^2$
[$\bar{1}$0$\bar{2}$]	1	1	−1	−1
[10$\bar{2}$]	α^2	$-\alpha^2$	α^2	$-\alpha^2$
[212]	1	1	1	1
[2$\bar{1}$2]	−1	1	1	−1
[$\bar{1}$22]	1	1	−1	−1
[1$\bar{2}\bar{2}$]	1	−1	1	−1
[$\bar{2}$1$\bar{2}$]	1	1	1	1
[2$\bar{1}\bar{2}$]	−1	1	1	−1
[$\bar{1}\bar{2}\bar{2}$]	1	1	−1	−1
[1$\bar{2}\bar{2}$]	1	−1	1	−1

similar to the above, a reasonable picture would be: a degenerate valence band with the maximum at $\boldsymbol{k} = 0$ and a (probably) non-degenerate many-valley conduction band. From the empty lattice, the point $\boldsymbol{K}$ seems reasonable for the conduction-band edge. There is some evidence that the same situation may prevail in ZnS.[15]

DRESSELHAUS[16] has given a scheme for obtaining information from the apparent shift in the optical absorption-band edge with polarization. He gave a discussion for wurtzite crystals, but his results are vitiated by the use of an incorrect character table. As has been noted by others,[17] the correct group is C_{6v} rather than D_6. The effect is that p_z transforms as Γ_1 rather than Γ_2 and different selection rules must be used. A rough calculation shows that his expression for the optical matrix element $\langle\psi_{\gamma 1}(\boldsymbol{k})|\epsilon\cdot\boldsymbol{p}|\psi_{\gamma 2}(\boldsymbol{k})\rangle$ has a more complicated $\boldsymbol{k}$-dependence and the forms of the corresponding coefficients $\boldsymbol{K}_{\gamma 1,\ \gamma 2}$ will be altered. The correct selection rules are those given in Table 20.

Acknowledgements—I wish to express my appreciation to Dr. FRANK HERMAN, who suggested this problem, for his helpful advice and criticism. I was aided at the beginning by some preliminary work of Dr. R. H. PARMENTER, and I have included the tables he worked out for the symmetry planes. I have also benefited from conversations with F. QUELLE, who has also worked on this problem.

Table 21. *Selection rules for matrix elements of the momentum at the zone center*

Γ_i	Γ_1	Γ_2	Γ_3	Γ_4	Γ_5	Γ_6	
$\Gamma_1\times\Gamma_1$	Γ_1	Γ_2	Γ_3	Γ_4	Γ_5	Γ_6	$\{z\}$
$\Gamma_1\times\Gamma_5$	Γ_5	Γ_5	Γ_6	Γ_6	$\Gamma_1+\Gamma_2+\Gamma_6$	$\Gamma_3+\Gamma_7+\Gamma_5$	$\{x, y\}$

occur. Γ_3 and Γ_5 would probably lie in the conduction band; because the z p-orbital should be more tightly bound than the x or y p-orbitals, the top valence band would probably be Γ_6. At the same time, in accordance with the empty lattice structure, the band edge would probably shift closer to A or Γ.

Recent experimental data on CdS seem to indicate that the valence-band maximum probably lies at the center of the zone, with the conduction-band edge at some other point. By considerations

REFERENCES

1. HERMAN F., *Rev. Mod. Phys.* **30,** 102 (1958).
2. LAX B., *Rev. Mod. Phys.* **30,** 122 (1958).
3. KOSTER G., *Solid State Physics* (Ed. F. SEITZ and D. TURNBULL) Vol. 5, Academic Press, New York (1957).
4. ASENDORF R., *Application of Group Theory to Quantum Mechanics of the Solid State.* Westinghouse Research Labs. Scientific Paper 60–94439–1–P3.
5. BOUCKAERT L. P., SMOLUCHOWSKI R. and WIGNER E., *Phys. Rev.* **50,** 58 (1936).

5a. SEITZ F., *Ann. Math.* **37,** 17 (1936).
6. HERRING C., *J. Franklin Inst.* **233,** 525 (1942).
7. BETHE H., *Ann. Phys. (Leipzig)* **3,** 133 (1929).
8. OPECHOWSKI W., *Physica* **7,** 552 (1940).
9. ELLIOTT R. J., *Phys. Rev.* **96,** 280 (1954).
10. HERRING C., *Phys. Rev.* **52,** 361 (1937).
11. EYRING H., KIMBALL G. E. and WALTER J., *Quantum Chemistry* Chap. 5. John Wiley and Sons, New York (1944).
12. DRESSELHAUS G. F., *Phys. Rev.* **100,** 580 (1955).
13. O'SULLIVAN W. J., *Univ. Pennsylvania Tech. Rep.* TN–58–474.
14. CORBATO F. J., Ph.D. Thesis, MIT (1956) (unpublished); see also *Quarterly Progress Report, Solid State and Molecular Theory Group MIT,* No. 21, p. 23 (1956) (unpublished).
15. BIRMAN J., private communication.
16. DRESSELHAUS G. F., *Phys. Rev.* **105,** 135 (1957).
17. BIRMAN J., QUELLE F. and HERMAN F., private communications.

VOL.
10
1959

Crystal structure and electroluminescence in ZnS

(*Received* 19 *January* 1959)

A.C. electroluminescence has been extensively studied since it was first described by G. DESTRIAU[1]. Efficient E.L. phosphors, are in general, of the sulphide type, in most cases the host matrix being zinc sulphide. As is well known zinc sulphide exists both in cubic and hexagonal forms with a transition temperature of 1024°C. Electroluminescent phosphors of each type have been described.[2–4] In this Laboratory electroluminescent phosphors co-activated with aluminium, gallium and indium have been investigated. In all cases the powders were prepared by firing the mix in a gentle oxidizing atmosphere such as wet hydrogen sulphide[5] at temperatures above the transition point (1024°C). Copper activated phosphors containing less than 10^{-4} g Cu/g ZnS have been shown by X-ray diffraction to be hexagonal in crystal structure. Increasing the copper concentration causes the appearance of a cubic phase and the crystals are predominately cubic for copper concentrations above 10^{-3} g Cu/g ZnS. This phase change coincides with the appearance of electroluminescence in the crystals, and also with the precipitation of copper sulphide on the surface. Manganese co-activated and sensitized phosphors exhibit the same effect.

It is generally maintained that the separation of this electron rich phase is the necessary condition for electroluminescence. That it is not sufficient is indicated by a study of silver activated phosphors. The hexagonal to cubic transition occurs for this activator at 10^{-2} g Ag/g ZnS and again is associated with the appearance of electroluminescence. The precipitation of silver is observed at lower concentrations and does not cause the phosphor to exhibit this phenomenon. Thermoluminescence experiments on the same phosphors have shown that when the phase transformation occurs there is a redistribution of trapping states, the deeper traps vanishing.

Preliminary work indicated that, whereas hexagonal zinc sulphide single crystals grown from the vapour phase are not electroluminescent or only feebly so, doping with copper produces an increase in efficiency and the conversion of the crystal to fourfold symmetry.

A.C. electroluminescence is associated, therefore, with a phase change corresponding to the appearance of one dimensional disorder in the lattice, and to the disappearance of deeper traps. It is not clear at present whether these phenomena are interdependent or whether each is a necessary condition for electroluminescence.

D. W. G. BALLENTYNE

Research Laboratory
Siemens Edison Swan Limited
West Road
Templefields
Harlow
Essex
England

REFERENCES

1. DESTRIAU G., *Phil. Mag.* **38,** 770 (1947).
2. HOMER H. H., RULON R. M., and BUTLER K. H., *J. Electrochem. Soc.* **100,** 566 (1953).
3. ZALM P., DIEMER G., and KLASENS H., *Philips Res. Rep.* **9,** 81 (1954).
4. FRÖEHLICH H. C., *J. Electrochem. Soc.* **100,** 280 (1953).
5. BALLENTYNE D. W. G., *Marconi Rev.* **123,** 160 (1956).

Magnetic properties of solid solutions of Fe_3O_4 and $FeAl_2O_4$

(*Received* 5 *February* 1959)

IN previous cases where the saturation moments[1] and the Curie temperatures[2] of aluminum-substituted magnetite were measured, the phase limit of the substitution could not be made to exceed 20 mol per cent. In this range the moment (given in Bohr magnetons per molecule) followed the relation $\mu = 4-3x$, where x is the number of Al^{3+} ions replacing Fe^{3+} ions per molecule of Fe_3O_4. If the Al^{3+} replaced Fe^{3+} on the B sites of the spinel lattice, as it should according to Verwey's rules,[3] one would expect the relation to be $\mu = 4-5x$. To obtain the former expression

($\mu = 4-3x$), for each Al^{3+} ion substituted it is necessary to transfer an Fe^{2+} ion from the B to the A site, which could be effected simply by the transfer of an electron. In this manner the structure would change continuously from the inverse to the normal spinel arrangement as the composition went from magnetite ($x = 0$) to hercynite ($x = 2$).

The entire range of compositions $0 \leqslant x \leqslant 2$ has now been synthesized by a method employing a buffer[4] to control the partial pressure of oxygen. The magnetic measurements are summarized in the accompanying graphs. The magnetization curves measured in a field of 6300 Oeds are reproduced in Fig. 1 in normalized form. In Fig. 2 the moments (extrapolated to infinite field and zero temperature) are plotted as a function of composition, while Fig. 3 shows the Curie temperatures observed for the series. Compositions with $x = 1{\cdot}8$ and $2{\cdot}0$ were found to possess no spontaneous moment at 77°K.

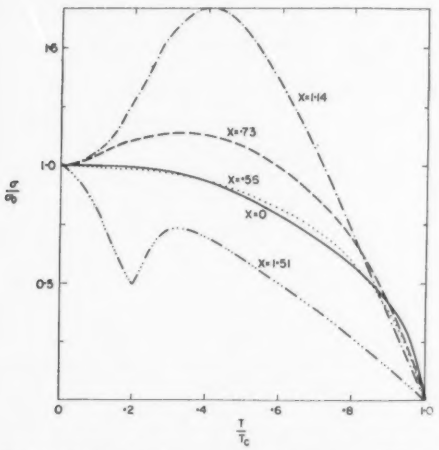

FIG. 1. Normalized magnetization curves of $Fe_{3-x}Al_xO_4$ as a function of reduced temperature.

It will be noted in Fig. 1 that magnetization curves for $x = 0{\cdot}73$ and $x = 1{\cdot}14$ are the Néel *P* type[5], where the moment increases with increasing temperature. This type of magnetization was previously observed[6] for the substitution of Al^{3+} in $NiFe_2O_4$ at compositions near the compensation point (zero net moment). The curve for $x = 1{\cdot}51$, however, is suggestive of type *N*, where the moment passes through zero at some temperature below the Curie point. As Gorter has shown[7] from the simple theory with one type of magnetic ion, type *N* should occur on the opposite side of the compensation point from type *P*. On the basis of this criterion, the moment for $x = 1{\cdot}51$ should be considered as negative and a compensation point occurs somewhere between $x = 1{\cdot}14$ and $x = 1{\cdot}51$.

From Fig. 2 it can be seen that the present results, taken in conjunction with those of

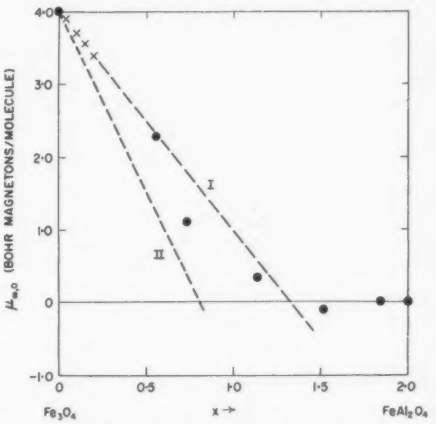

FIG. 2. Magnetic moment in Bohr magnetons per molecule of $Fe_{3-x}Al_xO_4$ as a function of composition. Values found in the present work are marked by ●, those of Gillaud and Michel by ×. Curve I: $\mu = 4-3x$. Curve II: $\mu = 4-5x$.

GILLAUD and MICHEL[1], show that the moment follows the relation $\mu = 4-3x$, at least as far as $x = 0{\cdot}6$. It should be pointed out that the samples had to be prepared by quenching in order to prevent exsolution of two phases, and that a different dependence of moment on composition might hold for annealed samples.[6] If the transition from the inverse to the normal structure is occurring, the compositional formula (using brackets to enclose B site ions) is written $Fe_{1-x}^{3+}Fe_x^{2+}[Fe_{1-x}^{2+}Fe^{3+}Al_x^{3+}]O_4$ for $x \leqslant 1$, and $Fe^{2+}[Fe_{2-x}^{3+}Al_x^{3+}]O_4$ for $1 < x \leqslant 2$. From these formulae a compensation point is expected at $x = 1{\cdot}2$, in fair agreement with the observations.

The exact Curie point of the composition $x = 1{\cdot}51$ is difficult to fix because of the extremely low moment. Bearing in mind, however,

that at $x = 1{\cdot}8$ the transition temperature is below 77°K, one can extrapolate the curve of Curie temperature vs. composition in Fig. 3

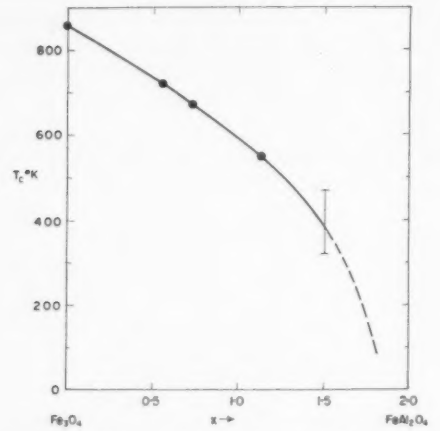

FIG. 3. Curie temperatures of $Fe_{3-x}Al_xO_4$ as a function of composition. The dotted line is the extrapolation mentioned in the text.

towards $x = 2{\cdot}0$, and it is clear that the hercynite ($FeAl_2O_4$) would order at very low temperatures if at all. This is consistent with a normal structure and the usual assumption of a very weak magnetic interaction between A site ions in the spinels.

We are indebted to Mr. E. P. Wenzel for assistance in making the magnetic measurements.

S. J. PICKART*
A. C. TURNOCK†

**U.S. Naval Ordnance Laboratory*
White Oak
Maryland

†*Geophysical Laboratory*
Carnegie Institution of Washington, D.C.
and The Johns Hopkins University

REFERENCES

1. GILLAUD C. and MICHEL A., *J. Phys. Radium* **12,** 65 (1951).
2. MICHEL A. and POUILLARD E., *C.R. Acad. Sci., Paris* **227,** 194 (1948).
3. VERWEY E. J. W. and HEILMANN E. L., *J. Chem. Phys.* **51,** 174 (1947).
4. EUGSTER H. P., *J. Chem. Phys.* **26,** 1760 (1957).
5. NÉEL L., *Ann Phys. Paris* **3,** 137 (1948).
6. MAXWELL L. R. and PICKART S. J., *Phys. Rev.* **92,** 1120 (1953).
7. GORTER E. W., *Philips Res. Rep.* **9,** 295 (1954).

VOL.
10
195

J. Phys. Chem. Solids Pergamon Press 1959. Vol. 10. pp. 245–253. Printed in Great Britain.

NUCLEAR QUADRUPOLAR RELAXATION IN IONIC CRYSTALS

JUN KONDO and JIRO YAMASHITA

Institute for Solid-State Physics, University of Tokyo, Tokyo, Japan

(*Received* 5 *December* 1958)

Abstract—The nuclear quadrupolar relaxation time of alkali halide crystals is investigated by the Heitler–London approximation. We use the Slater determinant which is constructed by the Hartree–Fock wave functions of the free ions. The charge distribution around an ion is not spherically symmetrical because of mutual overlap of the atomic wave functions of nearest-neighbor ions. Moreover, the charge distribution around an ion changes its shape during thermal vibrations of the ions, because the degree of the overlap depends upon the distance apart of the ions. Therefore, the quadrupolar interaction in alkali halide lattices is the resultant of a combination of the thermal vibration with the charge overlap. As illustrations of the theory, we have computed the quadrupolar relaxation time of the ^{39}K and the ^{35}Cl nuclei in the KCl crystal, and the ^{23}Na nucleus in the NaCl crystal. The theoretical results are in good agreement with those of experiments. We have also computed the ratio of the quadrupolar relaxation time of the metal nucleus to that of the halogen nucleus for some alkali halide crystals. After computing the same ratio by the covalent model and the deformation model, we have compared these results with the available experimental data. Finally, by using the same overlap model as that mentioned previously, we have developed a formula which gives the chemical shift of ionic crystals.

1. INTRODUCTION

IT is very important in solid-state physics to investigate the nature of binding in some representative crystals. Usually we classify crystals into four types: metals, valency crystals, ionic crystals and molecular crystals. Here we define an ideal ionic crystal as follows: an ionic crystal is produced by combining highly electropositive metals and highly electronegative elements. Each constituent ion becomes a positive or negative ion with a definite number of valency. Each ion has a closed shell structure and it is well separated from other ions. There are no crystals in nature which fulfil these conditions completely, although some of the alkali halide crystals seem to approach the ideal. In general it is rather difficult to compute a wave function in a crystal with considerable accuracy. However, in the case of simple ionic crystals the situation is much easier. As long as we are concerned with their ground state, the Slater determinant which is constructured from solutions of Fock's equation for the free ions seems to be a good wave function. However, this does not mean that the idealized model of ionic crystals is a good approximation. The idealized model of ionic crystals is inadequate in three respects: (1) *Overlap.* In real crystals the ions overlap in some extent. If two ions approach so closely that their electron shells overlap, then there is a strong repulsive force between them. This force is short range in nature and arises mainly from the Pauli principle. The electrostatic force, which tends to contract the dimensions of the crystal, is balanced by the repulsive force at the observed lattice distance. (2) *Deformation.* In a crystal there exists a crystalline field. The origin of the crystalline field is rather complicated. It may come from electrostatic interactions, exchange interactions, and overlap interactions. At any rate, the wave functions of the ions are modified by the crystalline field. The simplest way of taking this into account is to mix some excited-state wave functions of the ions into the ground-state configuration. (3) *Covalency.* There is a small transfer of charge from the negative to

the positive ion.* Therefore, if we start from the idealized model of the ionic crystal, then we must modify it in the next approximation by considering the three respects mentioned previously.† Thus, we find it an interesting problem to determine to what extent these effects contribute to the binding in a certain ionic crystal.

The cohesive energy of the simple ionic crystals has been investigated by LÖWDIN[1]. The wave function of the total system is the Slater determinant constructed from the Hartree–Fock wave functions of the free ions. Effects of the overlap is automatically involved in this Slater determinant, because the wave functions which belong to different ions are not mutually orthogonal. LÖWDIN has developed a method by which overlap of wave functions is taken into account. Really he has shown that the theoretical results agree well with observed values, and an ionic lattice is not stable unless the overlap effect is taken into account. Although he did not consider the effect of the deformation and the covalency on the cohesive energy, the quantitative success of his computation suggests that these effects are relatively unimportant.

On the other hand, the recent development of techniques in micro- and radiowave regions enables us to obtain direct informations of the wave function in solids. Observations of the chemical shift and the nuclear quadrupolar relaxation time make it clear that the wave function of the ions in ionic crystals is somewhat different from that in the free ion. KRANENDONK[2] estimated the order of magnitude of the quadrupolar relaxation time by using the idealized ionic model. The result shows that the idealized ionic model is completely inadequate. Then, YOSIDA and MORIYA[3] have analysed the observed data on the assumption that the shift and the relaxation time come only from the covalency. They determined the mixing ratio of the covalency by using the observed data of the chemical shift. On the other hand, WIKNER and DAS[4] have explained the observed relaxation time by considering the deformation of the wave function by the crystalline field. Both works are very important for the purpose of obtaining detailed knowledge about the nature of binding in ionic crystals, but we think that we should investigate first whether the overlap effect gives the reasonable order of magnitude of the chemical shift or the relaxation time, because this idea is so successfully applied to simple ionic crystals by LÖWDIN in his computation of the cohesive energy. In the following we shall carry out a theoretical study of the consequences of the charge overlap for the nuclear quadrupolar relaxation time and the chemical shift in ionic crystals and compare the result with available experiments.

2. NUCLEAR QUADRUPOLAR RELAXATION TIME

In this section we calculate the relaxation time of a nuclear spin in an ionic crystal caused by electric quadrupolar interactions. The Hamiltonian of the quadrupolar interaction between a nuclear spin and electrons in the crystal is given by:[5]

$$V_Q = \sum_i \sum_\mu Q_\mu W_\mu(\boldsymbol{r}_i), \tag{1}$$

where

$$\begin{aligned} Q_0 &= 3I_z^2 - I(I+1), \\ Q_{\pm 1} &= \tfrac{1}{2}\{I_z(I_x \pm iI_y) + (I_x \pm iI_y)I_z\}, \\ Q_{\pm 2} &= (I_x \pm iI_y)^2, \end{aligned} \tag{2}$$

and

$$\begin{aligned} W_0(\boldsymbol{r}) &= -\frac{A}{2}\frac{e}{r^5}(3z^2 - r^2), \\ W_{\pm 1}(\boldsymbol{r}) &= -3A\frac{e}{r^5}(x \mp iy)z, \\ W_{\pm 2}(\boldsymbol{r}) &= -\frac{3}{4}A\frac{e}{r^5}(x \pm iy)^2. \end{aligned} \tag{3}$$

Here I_x, I_y, and I_z are components of the nuclear

* Usually we assume that the positive ion becomes an atom by receiving one electron and the orbital of the extra electron is equal to the valence orbital of the atom in the free state. However, it is rather difficult to imagine an outermost orbital of the metal atom preserving its original character in the crystal, because the orbit is so large compared with the lattice distance. Some variational procedures may be useful to determine such a covalent orbital, but the problem is rather complicated owing to the mutual overlap of these orbitals.

† The idea of the charge overlap is connected intimately with the Heitler–London approximation that is based on solutions of Fock's equations for the free ions. If we adopt the cellular method or the OPW method for computing the crystal wave function, there is no need to introduce the idea of overlap. It is a matter of convenience that we chose one of these as a starting approximation.

spin vector, whose magnitude is $\sqrt{I(I+1)}$, A is defined by:

$$A = eQ/2I(2I-1)$$

and $r_i(x_i, y_i, z_i)$ is a position vector of the i-th electron from the nucleus. The summation over i is extended over all electrons in the crystal. Let $\Psi(\boldsymbol{x}_1, \boldsymbol{x}_2 \ldots, \boldsymbol{x}_N)$ be the wave function of the total system, where $\boldsymbol{x}_i = (\boldsymbol{r}_i, \chi_i)$ denotes the spatial and spin co-ordinates of the i-th electron. Then the expectation value of V_Q over Ψ is given by:

$$\langle V_Q \rangle \equiv \int V_Q(\boldsymbol{r})\rho(\boldsymbol{r})\, d\boldsymbol{r}, \tag{4}$$

where

$$\rho(\boldsymbol{r}) = N \sum_{\chi=\pm\frac{1}{2}} \int |\Psi(\boldsymbol{r}, \chi; \boldsymbol{x}_2 \ldots, \boldsymbol{x}_N)|^2\, d\boldsymbol{x}_2 \ldots, d\boldsymbol{x}_N. \tag{5}$$

As an approximate wave function for Ψ, we use the Slater determinant which is constructed from the atomic orbitals of the free ions in the ground state. We denote the atomic orbitals of the ions by ϕ_μ. Following LÖWDIN, we construct an orthogonal set of wave functions which are denoted by φ_μ from the original set of the non-orthogonal wave functions ϕ_μ. The former set is related to the latter by the LÖWDIN transformation†:

$$\varphi_\mu = \sum_\nu (1+S)^{-\frac{1}{2}}_{\mu\nu}\phi_\nu, \tag{6}$$

where $S_{\mu\nu}$ is an overlap integral:

$$S_{\mu\nu} = \int \phi_\mu^*(\boldsymbol{r})\phi_\nu(\boldsymbol{r})\, d\tau - \delta_{\mu\nu}. \tag{7}$$

Then the charge distribution $\rho(\boldsymbol{r})$ is given by:

$$\rho(\boldsymbol{r}) = 2 \sum_\mu \sum_\nu (1+S)^{-1}_{\mu\nu}\phi_\nu^*(\boldsymbol{r})\phi_\mu(\boldsymbol{r}). \tag{8}$$

First we consider the NaCl-type lattice, in which the ions are in their equilibrium positions. Let us consider the following charge distribution

$$\rho_0(\boldsymbol{r}) = 2 \sum_\mu |\varphi_\mu(\boldsymbol{r})|^2,$$

where the summation μ is taken over the orbitals in an ion. We note that $\rho_0(\boldsymbol{r})$ is not a spherically symmetric function, but contains a cubic symmetric part which comes from the overlap integral S.

When the ions are displaced from the equilibrium positions by thermal vibrations, the charge distribution of each ion is deformed slightly by an induced field. However, even when we neglect the deformation of ions (the rigid ion approximation) the orthogonalized wave functions φ_μ are modified by thermal vibration through the factor S, because $S_{\mu\nu}$ are the function of mutual distances of the ions. Consequently, the thermal vibration brings forth a non-cubic field at the position of the nucleus through the variation of the wave functions, because six nearest-neighbour ions are no longer situated at the same distance from that nucleus.

Inserting equation (8) into equation (4), we obtain the expectation value of V_Q in the same order of the approximation as that which LÖWDIN has used in the computation of the cohesive energy of the simple ionic crystals. In practice we introduce some approximations. We consider the overlap integrals between the orbitals which belong to nearest-neighbour ions. We assume further that $S_{\mu\nu}$ is so small that we may expand $(1+S)^{-1}$ in a power series of S and retain terms up to the order of S^2. In the case of alkali halide crystals, these approximations are proved to be valid.[1] Moreover, when we compute the matrix element

$$\int \phi_\mu^*(\boldsymbol{r})(1/r^3)\phi_\nu(\boldsymbol{r})\, d\tau,$$

we consider only the case where both orbitals μ and ν belong to the same ion.

After simple computations we obtain:

$$\rho(\boldsymbol{r}) = 2[\sum_\mu |\phi_\mu(\boldsymbol{r})|^2 + \sum_\mu |\phi_\mu(\boldsymbol{r})|^2 \cdot \sum_\alpha |S_{\mu\alpha}|^2 + \\ + \sum_\mu \sum_\nu \phi_\nu^*(\boldsymbol{r})\phi_\mu(\boldsymbol{r}) \cdot \sum_\alpha S_{\mu\alpha}S_{\alpha\nu}], \tag{9}$$

where the orbitals μ and ν belong to the same ion and the orbitals α belong to their nearest-neighbour ions. Since the integral $S_{\mu\alpha}$ may become very small for the inner orbitals, we shall retain only the outermost orbitals in the second and third terms of equation (9). In the case of alkali halide crystals, these are p-orbitals, which we shall denote hereafter by ϕ_x^0, ϕ_y^0 and ϕ_z^0. Then we obtain an

† As long as we represent a state by the single Slater determinant, the observable quantities such as the total energy or the charge distribution are invariant under the LÖWDIN transformation. However, for the practice of a computation a set of orthogonalized functions is much easier to handle.

expression for $\rho(\boldsymbol{r})$:

$$\rho(\boldsymbol{r}) = 2\sum_{\mu}|\phi_{\mu}|^2 + |\phi_x^0|^2\sum_n \alpha_n^2\lambda_n + |\phi_y^0|^2\sum_n \beta_n^2\lambda_n + \\ + |\phi_z^0|^2\sum_n \gamma_n^2\lambda_n + 2\phi_x^0\phi_y^0\sum_n \alpha_n\beta_n\lambda_n + \\ + 2\phi_y^0\phi_z^0\sum_n \beta_n\gamma_n\lambda_n + 2\phi_z^0\phi_x^0\sum_n \gamma_n\alpha_n\lambda_n, \quad (10)$$

where n specifies one of the six nearest-neighbour ions whose co-ordinates are denoted by $\boldsymbol{R}_n(X_n, Y_n, Z_n)$, while we take the position of the central nucleus as the origin of the co-ordinate. The direction cosines of $\boldsymbol{R}_n$ are denoted by α_n, β_n and γ_n, respectively. The quantity λ_n is defined by:

$$\lambda_n = 2\sum_{\alpha}|S_{n,\alpha}|^2, \quad (11)$$

$$S_{n,\alpha} = \int \phi_n^0(\boldsymbol{r})\phi_{\alpha}(\boldsymbol{r})\,d\tau,$$

where the summation is taken over all orbitals of the n-th ion, and the orbital ϕ_n^0 is a p-orbital which is constructed by a linear combination of three orbitals ϕ_x^0, ϕ_y^0 and ϕ_z^0 so as to have a maximum overlap with the σ- and s-orbitals of the nth ion. (Here the σ orbital is axially symmetric around the line joining the two ions.) The contribution from overlap integrals between π-orbitals ($m = 1$), which we have neglected, may be one-tenth of that from the σ-orbitals ($m = 0$). The quantity λ_n is a function of the distance between the nth ion and the central ion. We see that the first term in equation (10) has no contribution to equation (4) and the contribution from other terms in equation (10) is proportional to λ_n. After simple calculations[3] we obtain:

$$\langle V_Q\rangle = \sum_{\mu} Q_{\mu}\int W_{\mu}(\boldsymbol{r})\rho(\boldsymbol{r})\,d\tau = \sum_{\mu} Q_{\mu}\langle W_{\mu}\rangle, \quad (12)$$

where

$$\langle W_0\rangle = A'\sum_n \lambda_n(\gamma_n^2 - \tfrac{1}{3}),$$

$$\langle W_{\pm 1}\rangle = 2A'\sum_n \lambda_n\gamma_n(\alpha_n \pm i\beta_n), \quad (13)$$

$$\langle W_{\pm 2}\rangle = \tfrac{1}{2}A'\sum_n \lambda_n(\alpha_n \pm i\beta_n)^2,$$

and

$$A' = -\tfrac{2}{5}Ae\langle 1/r^3\rangle_{Av}. \quad (14)$$

The interaction energy (12) is to be used in the computation of the relaxation time both of the metal nucleus and of the halogen nucleus.

In order to calculate the transition probability between the Zeeman levels, an accurate knowledge of the lattice vibration and of the numerical values of S as a function of distance is required. However, such knowledge of the lattice vibration is not available at present. Here we follow the approximate procedure by which KRANENDONK, and YOSIDA and MORIYA have investigated the same problem, although the treatment of the optical mode of vibration is not accurate enough. As for the overlap integral, on the contrary, LÖWDIN[1] has performed an accurate computation of S for several alkali halide crystals.

As an application of the theory developed here, we have computed the relaxation time of the ^{39}K and the ^{35}Cl nuclei in the KCl crystal at room temperature. By using the Hartree–Fock wave function of the Cl^- and K^+ ions, we have evaluated the S integral for several lattice distances. For convenience we represent λ by approximate analytical functions. The results are as follows:

$$\lambda_{Cl} = 2\{S^2(3p_z\,Cl^-;\ 3p_z\,K^+) + S^2(3p_z\,Cl^-;\ 3S\,K^+)\} \\ = 57{\cdot}32\exp(-1{\cdot}362r)$$

and

$$\lambda_K = 2S^2(3p_z\,Cl^-;\ 3p_z\,K^+) = 28{\cdot}89\exp(-1{\cdot}340r).$$

Other overlap integrals are so small that we can neglect them approximately. The average value of $\langle 1/r^3\rangle$ is also evaluated by using the Hartree–Fock functions.

(*a*) ^{35}Cl: Following YOSIDA and MORIYA's notation, we define W_1 and W_2 as follows: $W_1 = P(\frac{3}{2} \to \frac{1}{2}) = P(-\frac{1}{2} \to -\frac{3}{2})$ and $W_2 = P(\frac{3}{2} \to -\frac{1}{2}) = P(\frac{1}{2} \to -\frac{3}{2})$, respectively. Then, by using equation (4–31) of their paper, we obtain the value of W_1 and W_2 which are averaged over the field direction: $W_1 = 0{\cdot}0626\ sec^{-1}$ and $W_2 = 0{\cdot}0722\ sec^{-1}$. Therefore, the relaxation time $T_1 = (1/W_1)+(1/W_2)$ is evaluated as 30 sec.

(*b*) ^{39}K: The values of W_1 and W_2 are $0{\cdot}0788\ sec^{-1}$ and $0{\cdot}0909\ sec^{-1}$, respectively. The relaxation time is evaluated as 23·7 sec.† The ratio

† We have used the values: (^{39}K) $I = 3/2$, $Q = 0{\cdot}07\times10^{-24}\ cm^2$ and $\langle 1/r^3\rangle = 13{\cdot}05$ a.u.; (^{35}Cl) $I = 3/2$, $Q = -0{\cdot}0797\times10^{-24}\ cm^2$ and $\langle 1/r^3\rangle = 5{\cdot}71$ a.u.

$T_1(M)/T_1(X)$ is 0·79. On the other hand, ITOH and YAMAGATA[6] have observed the relaxation time of the ^{35}Cl and ^{39}K nuclei by the saturation method. The observed values are 26 and 19 sec, respectively. Then the observed ratio $T_1(M)/T_1(X)$ is 0·73. Thus, we find that the agreement between the theory and the experiment is quite good, although the accuracy of the theoretical value is somewhat ambiguous, because the treatment of the lattice vibration is not accurate enough as mentioned previously.

Next, we investigate the relaxation time of the ^{23}Na nucleus in the NaCl crystal at room temperature. By using LÖWDIN's result λ is approximately represented by an analytical function $\lambda = 11{\cdot}2 \exp(-1{\cdot}57r)$, where r is measured in atomic units. The calculated values of $1/W_1$ and $1/W_2$ are 158 and 40·6 sec, respectively, when H is parallel to (0, 0, 1), while we have: $1/W_1 = 37$ sec and $1/W_2 = 51$ sec, when H is parallel to (1, 1, 1). On the other hand, a determination of the relaxation time of ^{23}Na at room temperature has been carried out by BLOEMBERGEN and SOROKIN[7] using pulse techniques. The observed relaxation time is 14·5 sec and no dependence on the direction of the external field is observed. Since the theoretical values mentioned above should be compared with the observed values obtained by the saturation method, we must compute a relaxation time which can be compared with the pulse experiment. Although this is a rather complicated problem, we estimate it by computing a relaxation time which is taken to restore the thermal equilibrium from an initial state where four Zeeman levels are equally populated. On this assumption we need only to solve the usual differential equations concerning the time variation of populations under the initial condition: $n(3/2) = n(1/2) = n(-1/2) = n(-3/2) = N/4$, where $n(m)$ means the number of population in the level $I_z = m$. Then, we obtain the time variation of the magnetization M:

$$M = \sum_{m=-3/2}^{3/2} m \cdot n(m)$$

$$= \frac{N\hbar\omega_0}{2kT}\left(\tfrac{5}{2} - \tfrac{1}{2}\exp(-t/2W_1) - 2\exp(-t/2W_2)\right). \quad (15)$$

Inserting the values of W_1 and W_2 obtained previously into equation (15), we see that the time variation of equation (15) is well approximated by a single exponential function with a relaxation time of 25 sec for both directions of the magnetic field. Therefore, we find that the theoretical results are in fair agreement with the observation. WIKNER and DAS[4] have also computed the relaxation time of the ^{23}Na ion. They obtained a value of 27 min, which is too long as compared with 14·5 sec. The electronic core of the Na^+ ion may be too hard to be deformed appreciably by the crystalline field.

Observations of the relaxation time have been made for several other crystals.[9] We show some of these materials in Table 1. Unfortunately, we cannot obtain an accurate value of S for these materials, because the Fock wave functions are not available. We must content ourselves with estimating the ratio of the relaxation time of the metal nucleus to that of the halogen nucleus. Let

$$p = T_1(M)/T_1(X) \quad (16)$$

denote the ratio of the relaxation time of the metal nucleus to that of the halogen nucleus; then a simple computation shows that p is approximately given by:

$$p = \left(\frac{\langle 1/r^3\rangle_x}{\langle 1/r^3\rangle_{M,n,p}}\right)^2 \left(\frac{Q_x}{Q_M}\right)^2 \cdot \left(\frac{\lambda_x}{\lambda_M}\right)^2, \quad (17)$$

while in the covalent model it may be approximately given by:

$$p = \left(\frac{Q_x}{Q_M}\right)^2 \left(\frac{\langle 1/r^3\rangle_x}{\langle 1/r^3\rangle_{M,n+1,p}}\right)^2. \quad (18)$$

According to WIKNER and DAS's deformation model, p is also given by:

$$p = \left(\frac{Q_x}{Q_M}\right)^2 \left(\frac{(1-\gamma_\infty)_x}{(1-\gamma_\infty)_M}\right)^2. \quad (19)$$

We show in Table 1 experimental values of p for several alkali halide crystals, together with the theoretical values computed by equations (17), (18) and (19), where we put $(\lambda_x/\lambda_M) = 1$†. We see that the usual covalent model is inadequate for the

† We take the value of $\langle 1/r^3\rangle$ from BARNES and SMITH's paper.[8]

Table 1. *Ratio of the relaxation time of the metal nucleus to that of the halogen nucleus from*: (1) *the covalent model*, (2) *the deformation model and* (3) *the overlap model with the assumption* $(\lambda_x/\lambda_M) = 1$

Material	(1) Y–M	(2) W–D	(3) This model	Expt.
^{87}Rb ^{81}Br	900	15	1·4	1·7
^{133}Cs ^{35}Cl	2×10^4	140	40	154
^{133}Cs ^{81}Br	10^6	7000	2000	10^4
^{23}Na ^{81}Br	$2{\cdot}4\times10^4$	6000	5·0	76
^{23}Na ^{127}I	3×10^5	$1{\cdot}4\times10^5$	63	325

alkali halide crystals. The deformation model gives a reasonable value of p for heavy alkali halide crystals, although the absolute value of the relaxation time is sometimes too long as compared with the experimental values.[4]

However, this model is inadequate for sodium halide crystals, because the theoretical value of the relaxation time becomes too long for the Na nucleus according to the deformation model. As for the heavy alkali halide crystals, the overlap model would give also a fairly reasonable value of p, if we could take into account $(\lambda_x/\lambda_M)^2$ correctly. In the case of KCl this factor amounts to 4. On the other hand, the ratio in the sodium bromide crystal may be a little too small according to the overlap model, even if we consider the ambiguities in that factor and other points. The reason is not clear, but we suppose that this discrepancy arises from the negative ion, because this model seems to give the right order of the relaxation time for the Na nucleus. We might think that the effect of the deformation becomes important in the case of heavy negative ions, although the deformation model of WIKNER and DAS gives sometimes too long relaxation times. We must also note that they consider only a crystalline field caused by the point lattice, but this approximation may be insufficient. If we could develop a deformation model on a more reliable approximation, it would be possible to explain the quantitative discrepancies mentioned previously.

3. CHEMICAL SHIFT

In the present section we shall deal with the chemical shift of the nuclear magnetic resonance in ionic crystals. In this case the interaction Hamiltonian is given by:

$$V_L = V_1 + V_2, \tag{20}$$

where

$$V_1 = \sum_i 2\mu_B \mu l_{i\zeta}/r_i^3, \tag{21}$$

and

$$V_2 = \sum_i \mu_B H l_{i\zeta}. \tag{22}$$

Here μ_B is the Bohr magneton, μ is the magnetic moment of a nucleus, l is the angular momentum operator, r_i is the distance between the ith electron and the nucleus of the ion to which the electron belongs and, finally, ζ is the direction of the external field H. The summation is taken over all electrons in the crystal. We compute the energy correction which is linear both in μ and in H by the second-order perturbation theory:

$$E_2 = \sum_n{}' \frac{\langle 0|V_1|n\rangle\langle n|V_2|0\rangle}{E_0 - E_n} + \text{comp. conj.} \tag{23}$$

where 0 and n denote the ground state and the excited states of the total system, respectively. Here we define the coefficient of the chemical shift by a relation:

$$\sigma = E_2/\mu H. \tag{24}$$

We now replace the energy difference $(E_0 - E_n)$ in the denominator in equation (23) by an average value $-\langle \Delta E\rangle$ and take it out of the summation. Then we have:

$$E_2 = -(1/\langle \Delta E\rangle)\{[\langle 0|V_1V_2|0\rangle - \langle 0|V_1|0\rangle\langle 0|V_2|0\rangle] + \text{comp. conj.}\}. \tag{25}$$

It is easily seen that the energy correction vanishes in the idealized model of ionic crystals, because the free ion is in an s-state. YOSIDA and MORIYA computed this by mixing a covalent state to the ground state wave function. They determined the mixing ratio so as to give reasonable agreement with observed values. As mentioned previously, however, their wave functions failed to agree with the observed quadrupolar relaxation times. The deformation of ions from spherical symmetry due to the Sternheimer effect may also give rise to the chemical shift, although this aspect of the theory has not yet been developed. In the following we shall consider the effect of the charge

overlap to the chemical shift and compare the result with available observations. Here we adopt the Slater determinant constructed from a set of orbitals (6). Let Y denote $(0|V_1V_2+V_2V_1|0)$; then

$$E_2 = -\frac{Y}{\langle \Delta E \rangle} = -\frac{16}{3} Z \left\langle \frac{1}{r^3} \right\rangle \mu_B{}^2 \mu H \frac{\Lambda}{\langle \Delta E \rangle} \tag{33}$$

$$Y = 2\mu_B{}^2 \mu H \left(0 \left| \sum_i \frac{2 l_{i\zeta}{}^2}{r_i{}^3} + \sum_i \sum_{j \neq i} l_{i\zeta} l_{j\zeta} \left(\frac{1}{r_i{}^3} + \frac{1}{r_j{}^3} \right) \right| 0 \right). \tag{26}$$

By using the wave function mentioned previously, we have:

$$\begin{aligned} Y = 2\mu_B{}^2 \mu H \{ & \sum_\mu (\mu|H|\mu) + \sum_{\mu,\nu} [(\mu\nu|G|\mu\nu) - (\mu\nu|G|\nu\mu)] - \\ & - \sum_\mu \sum_\kappa P_{\mu\kappa} [(\kappa|H|\mu) - 2 \sum_\nu \{(\kappa\nu|G|\mu\nu) - (\kappa\nu|G|\nu\mu)\}] + \\ & + \sum_{\mu\nu} \sum_{\kappa\lambda} P_{\mu\kappa} P_{\nu\lambda} [(\kappa\lambda|G|\mu\nu) - (\kappa\lambda|G|\nu\mu)] \}, \end{aligned} \tag{27}$$

where

$$(\kappa|H|\mu) = \int \phi_\kappa{}^*(\boldsymbol{r}) (2 l_\zeta{}^2 / r^3) \phi_\mu(\boldsymbol{r})\, d\boldsymbol{r}, \tag{28}$$

$$(\kappa\lambda|G|\mu\nu) = \int \phi_\kappa{}^*(\boldsymbol{r}_1) \phi_\lambda{}^*(\boldsymbol{r}_2) l_{1\zeta} l_{2\zeta} \left(\frac{1}{r_1{}^3} + \frac{1}{r_2{}^3} \right) \phi_\mu(\boldsymbol{r}_1) \phi_\nu(\boldsymbol{r}_2)\, d\boldsymbol{r}_1 d\boldsymbol{r}_2, \tag{29}$$

and

$$P = 1 - (1+S)^{-1}. \tag{30}$$

When we carry out the computation in practice, we introduce the same approximation as in the preceding section. After some simple computations, we obtain the result:

$$Y = (16/3) Z \langle 1/r^3 \rangle \mu_B{}^2 \mu H \Lambda, \tag{31}$$

where Λ is defined by

$$\Lambda = \sum_\alpha |S_{z,\alpha}|^2 \tag{32}$$

Here $S_{z,\alpha}$ means an overlap integral between the outermost p-orbital having an axial symmetry about a z-axis and an orbital α in one of the nearest-neighbour ions. (We chose here the line joining the two ions as a z-axis.) The notation Z in equation (31) means the number of nearest neighbours, which is six in NaCl-type crystals and eight in CsCl-type crystals. The term $(0|V_1|0)(0|V_2|0)$ vanishes if we consider integrals

$$\int \phi_\mu{}^* (1/r^3) \phi_\nu \, d\boldsymbol{r}$$

only when both orbitals μ and ν belong to the same ion. Then the second-order perturbation energy (23) becomes:

Then we have from equation (24):

$$\sigma = -\frac{16}{3} Z \left\langle \frac{1}{r^3} \right\rangle \frac{\Lambda}{\langle \Delta E \rangle}. \tag{34}$$

It is to be noted that equation (34) is of the same form as YOSIDA and MORIYA's equation (2–13), if we replace $\lambda = (b/\Delta E)^2$ and ΔE by $2A$ and $\langle \Delta E \rangle$, respectively.

Experiments on the chemical shift of the nuclear resonance have been carried out on many ionic crystals, the shift in the aqueous solution being taken as a reference. It is not certain, however, that the ions at question are perfectly free in aqeous solutions, so that we cannot compare the theory directly with experiments as in the case of the quadrupolar relaxation time. However, let us assume provisionally that the observed data represent absolute values of the chemical shift. Then we can estimate values of S in equation (32) by comparing the theory with the experiments. The theoretical formula (34) contains the unknown factor $\langle \Delta E \rangle$, but we estimate $\langle \Delta E \rangle$ of a metal ion by equating it to the energy necessary to excite an outermost np-electron to the next higher $(n+1)$ p-orbital. These values are available from optical

data. We use also the values of $\langle 1/r^3 \rangle$ which were determined by BARNES and SMITH[8]. As for the overlap integrals, it may be sufficient to consider only those between the *np*-orbital of the metal ion and the outermost *s*- and *p*-orbitals of halogen ions, which are denoted by S_s and S_p, respectively. Then we have a relation: $\Lambda = S_s^2 + S_p^2$. Further, we estimate S_s by an approximate relation: $S_s = (1/3)S_p$, which may be reasonable in our rough estimation. If we assume tentatively that the chemical shift derives only from the overlap effect, we can determine the value of S_p for several ionic crystals by the aid of the formula (34) and the observed values of the chemical shift.

The results are shown in Table 2. As can be seen from the table, the estimated values of S appear fairly reasonable. However, we are not quite sure that this agreement has a real significance because of the ambiguity of the standard of the chemical shift. For bromides and iodides of rubidium and caesium, the chemical shift of the halogen nuclei were also observed. In our model the ratio of the shift of the metal nucleus to that of the halogen nucleus is given by:

$$q = \frac{\sigma(M)}{\sigma(X)} = r\frac{\langle 1/r^3 \rangle_M}{\langle 1/r^3 \rangle_X}, \tag{35}$$

where

$$r = \frac{\Lambda(M)}{\Lambda(X)} \cdot \frac{\langle \Delta E \rangle_X}{\langle \Delta E \rangle_M}. \tag{36}$$

Unfortunately, we have no means of estimating the value of $\langle \Delta E \rangle$ for halogen ions accurately, although it may be reasonable to assume that the ratio $\langle \Delta E \rangle_X / \langle \Delta E \rangle_M$ is of the order of one. If we assume tentatively that $r = 1$, we have a set of the theoretical values of the ratio which is shown in the third column of Table 3. The result does not seem to be unreasonable. However, since there are many ambiguities both in the theory and in the experiments, it is difficult to draw any definite conclusions from these comparisons.

Table 3. Ratio of the chemical shift of the metal nucleus to that of the halogen nucleus.

	q(expt.)	q(calc.)
RbBr	1·32	1·58
CsBr	0·76	2·14
RbI	0·88	1·19
CsI	0·5	1·61

Table 2. Chemical shift σ

Material	Nucleus	σ(expt.)$\times 10^4$	$\langle \Delta E \rangle$	$\langle 1/r^3 \rangle$	S_p
RbF	^{87}Rb	−0·6	20 eV	21·4	0·069
RbCl	^{87}Rb	−0·9	20 eV	21·4	0·084
RbBr	^{87}Rb	−1·6	20 eV	21·4	0·112
RbI	^{87}Rb	−1·5	20 eV	21·4	0·109
CsF	^{133}Cs	−0·9	17 eV	29	0·063
CsCl	^{133}Cs	−1·7	17 eV	29	0·076
CsBr	^{133}Cs	−1·9	17 eV	29	0·080
CsI	^{133}Cs	−2·5	17 eV	29	0·092
RbBr	^{81}Br	−1·2	– – –	13·55	– – –
CsBr	^{81}Br	−2·5	– – –	13·55	– – –
RbI	^{127}I	−1·7	– – –	18·0	– – –
CsI	^{127}I	−5·0	– – –	18·0	– – –

Acknowledgements—This work was undertaken by the suggestion of Professor J. ITOH, and we would like to express our thanks to him for suggesting this problem. He also made a preliminary discussion of this problem at the annual meeting of the Physical Society of Japan in 1957.

REFERENCES

1. LÖWDIN P. O., *A Theoretical Investigation into Some Properties of Ionic Crystals*. Thesis, Uppsala (1948).
2. VAN KRANENDONK J., *Physica* **20**, 781 (1954).

3. YOSIDA K. and MORIYA T., *J. Phys. Soc. Japan* **11,** 33 (1956).
4. WIKNER E. G. and DAS T. P., *Phys. Rev.* **109,** 360 (1958).
5. COHEN M. H. and REIF F., *Solid State Physics* (Ed. F. SEITZ and D. TURNBULL) Vol. 5, p. 322. Academic Press, New York (1957).
6. J. ITOH and YAMAGATA Y., Lecture given at the annual meeting of the Physical Society of Japan (1958).
7. BLOEMBERGEN N. and SOROKIN P. P., *Phys. Rev.* **110,** 865 (1958).
8. BARNES R. G. and SMITH W. V., *Phys. Rev.* **93,** 95 (1954).
9. WATKINS G. W. and POUND R. V., *Phys. Rev.* **89,** 658 (1953).
KANDA T., *J. Phys. Soc. Japan* **10,** 85 (1955).
BLOEMBERGEN N. and SOROKIN P. P., *loc cit.*
WIKNER E. G. and HAHN E. L., *Bull. Amer. Phys. Soc.* **3,** 325 (1958).

VOL.
10
959

J. Phys. Chem. Solids Pergamon Press 1959. Vol. 10. pp. 254–276. Printed in Great Britain.

QUANTUM THEORY OF TRANSVERSE GALVANOMAGNETIC PHENOMENA

E. N. ADAMS* and T. D. HOLSTEIN

Westinghouse Research Laboratories, Pittsburgh 35, Pennsylvania

(*Received* 25 *November* 1958)

Abstract—A quantum theory of electrical conduction in crossed electric and magnetic fields is given for the limit of very weak scattering. A density matrix formulation of the problem is used, and an arbitrary scattering mechanism is considered. The theory is found to be completely equivalent to theories given earlier by TITEICA and by DAVYDOV and POMERANCHUK.

Formulae are given for the resistivity in the quantum limit for both longitudinal and transverse orientations of electric field, for degenerate and non-degenerate statistics, and for several different scattering mechanisms. The oscillatory conductivity is calculated for acoustical and ionized-impurity scattering mechanisms. Formulae obtained for the quantum transport effects are in disagreement with the formulae of LIFSHITZ and of ARGYRES. The discrepancy is attributed to unwarranted approximations in those authors' treatments of scattering.

1. INTRODUCTION

GALVANOMAGNETIC effects are often measured in the "strong magnetic field" regime for which the cyclotron angular frequency ω is greater than the reciprocal time between collisions τ^{-1} or $\omega\tau \gg 1$. The study of the strong-field galvanomagnetic phenomena presents points of theoretical as well as of experimental interest. For example, it has been of particular interest to us that in the strong-field regime the individual quantum levels associated with the electrons circling motion become fairly well defined, so that it becomes possible for quantization to make its effects manifests in the transport properties.

When the quantization of the energy levels becomes important, the Boltzmann velocity space theory of galvanomagnetism is not applicable, and a quantum theory of galvanomagnetism must be used. This is possibly the theoretically simplest case of a transport problem which cannot be treated by the Boltzmann theory, and perhaps for that reason is of more than ordinary interest in connection with the general theory of transport phenomena. A number of theoretical discussions of galvanomagnetism in the quantum regime have been published, of which we will take note of the treatments of d.c. galvanomagnetic effects by TITEICA[1] and of DAVYDOV and POMERANCHUK[2], and more recently by ARGYRES and ADAMS[3], LIFSHITZ[4,5] and his coworkers, KUBO[6] and his coworkers, and ARGYRES[7,8]. These papers have concerned themselves with various matters of interest which may be grouped into two categories: first what might be called *practical* matters, i.e. matters of significance for the interpretation of details of experiment; and, second, what might be called *theoretical* matters, i.e. matters which involve the mathematical apparatus for treating transport phenomena when quantization plays a role and the interrelations of the galvanomagnetic properties in the quantum regime to the same properties in the regime of validity of the Boltzmann description. Topics of the first kind treated among the cited works include the dependence of the magnetoresistance on the mechanism of scattering and on the geometrical details of the energy surfaces. The topics of the second kind include the relationship of the oscillatory transport phenomena to the oscillatory phenomena in the magnetic

* Now at IBM Research Center, Yorktown Heights, New York.

VOL. 10 1959

susceptibility and certain matters concerning the correct deduction of a quantum transport theory from the postulates of quantum mechanics.

In this paper we present a quantum theory of the electrical conductivity in an electron gas in the regime $\omega\tau \gg 1$. Our aim is to provide a theory suitable for use in interpreting galvanomagnetic experiments made on semiconductors and semimetals in which the effective mass is so small that the separation between magnetic levels is comparable to or greater than both KT and the Fermi energy. One object of our work is to provide formulae applicable to all of the scattering mechanisms that may be thought to be of significance in these experiments. These formulae appear to be needed for the interpretation of existing data as well as for experiments currently in progress.

A second object of our work is to present a critique of certain aspects of existing theories, some of which we have found to be inadequate for treating the phenomena associated with the lowest quantum states and the quantum effects in general. For this purpose we present a deduction of the conductivity formulae that is somewhat different from previously given deductions, and which yields correct formulae for the transport quantities in the extreme quantum regime. Our theory is somewhat special in that it is derived only for static fields and for spherical energy surfaces. However, it permits us to elucidate matters of general qualitative significance as regards the quantum-galvanomagnetic effects and the representation of scattering in the quantum-mechanical theory of transport.

2. WAVE FUNCTIONS AND CURRENT DENSITY

In order to establish our notation, we give a few of the well-known equations for the energies and wave functions of an electron moving in crossed electric and magnetic fields.[9] We use the gauge in which the vector potential is

$$A(r) = (0, Bx, 0) \tag{2.1}$$

Here B is the magnetic field strength taken to be in the z-axis direction. The Hamiltonian will be denoted as H_0, since it does not include a scattering potential. It is given by:

$$H_0 = (1/2m)(p_x^2+p_z^2)+(1/2m)(p_y+m\omega x)^2-xF \tag{2.2}$$

Here F is the electric force field, taken to be in the positive x-direction, and ω is the cyclotron frequency (eB/mc).

It is useful to define the following quantities

$$L \equiv (\hbar c/eB)^{\frac{1}{2}}$$
$$X \equiv -(p_y/m\omega)+(F/m\omega^2) \tag{2.3}$$

and to measure lengths in units of L, momenta in units of $\hbar/L$, energies in units of $\hbar\omega$, and force in units of $(\hbar\omega/L)$. In the equations that follow we will ordinarily use wave numbers rather than momenta and will often write equations in dimensionless form, displaying dimensional factors only when it seems particularly helpful to do so.

In the above units the Hamiltonian becomes

$$H_0 = \tfrac{1}{2}(p_x^2+p_z^2)+\tfrac{1}{2}(x-X)^2-XF \tag{2.4}$$

Where no confusion would arise, the eigenfunctions and eigenvalues will be labeled with a single Greek index to denote the three quantum numbers k_y, k_z, N, as follows:

$$\Psi_\mu = \exp(ik_y y)\exp(ik_z z)\phi_N(x-X_\mu) \quad (\mu \equiv k_y k_z N)$$
$$E_\mu + \omega_\mu - X_\mu F = (N+\tfrac{1}{2})+\tfrac{1}{2}k_z^2-X_\mu F \tag{2.5}$$

Here we denote as X_μ the value of X for the state μ, ω_μ the part of the energy that is independent of the electric field, and $\phi_N(x)$ the N^{th} Hermite function of x. The orthonormal Hermite function $\phi_N(x)$ may be derived from the generating function:

$$G(x, s) \equiv \exp[-s^2+2sx-\tfrac{1}{2}x^2]$$
$$= \sum_{N=0}^{\infty} s^N[\sqrt{(\pi)}2^N/N!]^{\frac{1}{2}}\phi_N(x) \tag{2.6}$$

The physical quantity of particular interest to us is the electron current density. Omitting for the moment the factor $(-e)$ for the electronic charge, we may write the n^{th} component current of current density in a state described by a wave function ϕ as

$$J(r)^n = -\left[\frac{i}{2}\left(\phi^*\frac{\partial\phi}{\partial x_n} - \frac{\partial\phi^*}{\partial x_n}\phi\right)-x\delta_{ny}\phi^*\phi\right]^r \tag{2.7}$$

The generalization of equation (2.7) to an ensemble described by a density matrix ρ is

$$J(r)^n = -\sum_{\mu\nu}\left[\tfrac{1}{2}i\left(\phi_\mu^*\frac{\partial\phi_\nu}{\partial x_n} - \frac{\partial\phi_\mu^*}{\partial x_n}\phi_\nu\right)- -x\delta_{ny}\phi_\mu^*\phi_\nu\right]^r \rho_{\nu\mu} \tag{2.8}$$

The density matrix ρ for the transport ensemble will depend on the complete Hamiltonian for the transport problem, which will contain in addition to H_0 a scattering interaction V that is responsible for the dissipative

effects in the system. The dependence of the density matrix on the scattering interaction will be calculated in the next section. However, it is convenient to anticipate somewhat and use some of the results of that section to simplify the expression (2.8) for the current density. In the next section we will determine the density matrix in the form of a perturbation power series in the scattering interaction and will calculate the lowest approximation in which dissipative current is obtained. In this approximation the solution density matrix will have two properties (Cf. discussion following equation (3.12)) that we will wish to make use of here, viz.

(1) For the purpose of calculating the current, the matrix elements $\rho_{\mu\nu}$ are effectively different from zero only if the wave numbers of the states μ and ν are the same. We will denote these nonvanishing matrix elements as $D_{N\bar{N}}(k)$.

(2) The matrix elements $D_{N\bar{N}}$ do not depend on the wave number k_y. Thus we may denote the diagonal-in-wave number part of the density matrix in equation (2.8) as $\rho_{N\bar{N}}(k)$. Further, since the current density will be essentially independent of position, we will choose $r = 0$ in equation (2.8). We may then write the two components of the current as

$$J^x = -\tfrac{1}{2}i \sum_{k_y k_z N\bar{N}} \left[\phi_N(x-X) \frac{\partial \phi_{\bar{N}}}{\partial x}(x-X) - \right.$$

$$\left. - \frac{\partial \phi_N}{\partial x}(x-X) \phi_{\bar{N}}(x-X) \right]^{x=0} \rho_{\bar{N}N}(kz) \tag{2.9}$$

$$J^y = \sum_{k_y k_z N\bar{N}} [k_y \phi_N(x-X) \phi_{\bar{N}}(x-X)]^{x=0} \rho_{\bar{N}N}(k_z) \tag{2.10}$$

The summation over the variable $X = -k_y + F$ can be simplified by use of the familiar properties of the Hermite functions and the expressions (2.9) and (2.10) reduced to (by means of an average over k_y):

$$J^x = \frac{i}{2} \sum_{k_y k_z N} \sqrt{2(N+1)} (\rho_{N\,N+1} - \rho_{N+1\,N}) \tag{2.11}$$

$$J^y = F \sum_{k_y k_z N} \rho_{NN} +$$

$$+ \tfrac{1}{2} \sum_{k_y k_z N} \sqrt{2(N+1)} (\rho_{N\,N+1} + \rho_{N+1\,N}) \tag{2.12}$$

Combining equations (2.11) and (2.12) in a familiar way, we find:

$$J^y + iJ^x = F \sum_{N k_y k_z} \rho_{NN} + \sum_{N k_y k_z} \sqrt{2(N+1)} \rho_{N+1\,N} \tag{2.13}$$

3. CALCULATION OF THE DENSITY MATRIX

Equation (2.13) expresses the current in terms of the matrix elements ρ_{NN} and $\rho_{N+1\,N}$ of the density matrix, which connect states of the same wave number. Our next step will be to develop an expansion of ρ as a perturbation series in the scattering interaction V. We will use the Laplace transform method of solving the differential equation of motion of the density matrix. If the total Hamiltonian is denoted by H, then in our previous notation

$$H = H_0 + V \tag{3.1}$$

$$-i \frac{\partial \rho}{\partial t} = [\rho, H] \tag{3.2}$$

We will treat the scattering interaction V as static, although our equations will apply to interactions that vary at frequencies small compared to the electron energies of interest. Thus the entire Hamiltonian is independent of time. Let $P_{\mu\nu}(s)$ denote the Laplace transform† of $\rho_{\mu\nu}$, then

$$-isP(s) = [P(s), H] - is\rho(0) \tag{3.3}$$

By means of equation (3.3), $P(s)$ can be developed as a perturbation series in the interaction.

The physical problem of interest is one in which the current is independent of time, so the desired density matrix should be independent of time. We might consider either of two approaches for obtaining it. One approach is to choose an arbitrary initial density matrix $\rho(0)$ and find ρ after such a long time that all transients have disappeared. The other approach is to try to determine an initial density matrix so that its time variation is zero.

Both approaches to finding the density matrix would be straightforward were it not that, strictly speaking, ordinary irreversible phenomena cannot be deduced from the equation of motion (3.2). In order to obtain the kind of irreversible behavior present in the physical system, we need to augment the theoretical apparatus for treating the problem, either through a modification of the Hamiltonian or through some mathematical device for simulating the interaction of the system with external systems. In particular some local thermalizing interaction is required in order that the electrons do not heat up. We will avoid an explicit treatment of this problem, while recognizing what result any such treatment must yield. We will assume that the initial density

† We use the definition of Laplace transform for which the transform of unity is unity.

matrix $\rho(0)$ is very nearly that corresponding to a thermal ensemble, and has such a character that transient perturbations all decay with time. Very many such initial density matrices exist. If we compute the density matrix for a very great time such that all transients will have died out, it will then be immaterial exactly what the initial density matrix was and it may be taken to be exactly that of a thermal ensemble. We may then obtain the value of the density matrix at very large times the limit approached by the Laplace transform $P(s)$ because the Laplace parameter approaches zero through positive real values.

We will choose as the initial density matrix

$$\rho_{\mu\nu}(0) = \delta_{\mu\nu} f(\omega_\mu) \equiv \delta_{\mu\nu} f_\mu \tag{3.4}$$

where $f(E)$ is the Fermi function of E, ζ and T, and according to equation (2.5), ω_μ represents the part of the energy that does not depend on electric field. The choice (3.4) is made arbitrarily, and on the intuitive grounds that a flat distribution is what we want to find in the end. However, the method of solution must be such as to systematically remove any deficiency in the choice of initial distribution. Our choice is the best if we are to get a solution with no diffusion currents.

We will express the scattering interaction V in terms of its Fourier components V_q according to the formula:

$$V = (2\pi)^{-3} \int d^3q V_q \exp(iq \cdot r) \tag{3.5}$$

Finally we will express the Laplace transform $P(s)$ as the sum of three parts:

$$P_{\mu\nu}(s) = f_\mu \delta_{\mu\nu} + D_{\mu\nu}(s) + G_{\mu\nu}(s) \tag{3.6}$$

Here $f_\mu \delta_{\mu\nu}$ represents the Laplace transform of the initial density matrix, while $D_{\mu\nu}$ and $G_{\mu\nu}$ together represent the Laplace transforms of the change in the distribution function resulting from the combined action of the scattering and the electric fields. $D_{\mu\nu}$ is defined so that its matrix elements vanish except when μ and ν have the same wave number; $G_{\mu\nu}$ is defined so as to vanish unless μ and ν have different wave numbers. The "diagonal" matrix $D_{\mu\nu}$ is the only one that enters into the conductivity formulae. From equation (3.3) D and G satisfy

$$(\omega_{\mu\nu} - FX_{\mu\nu} - is) G_{\mu\nu} = f_{\mu\nu} V_{\mu\nu} + [D, V]_{\mu\nu} + [G, V]_{\mu\nu} \tag{3.7}$$

$$(\omega_{N\bar{N}} - is) D_{N\bar{N}} = [G, V]_{N\bar{N}} \tag{3.8}$$

Here $f_{\mu\nu}$, $\omega_{\mu\nu}$ and $X_{\mu\nu}$ denote, respectively, $f_\mu - f_\nu$, $\omega_\mu - \omega_\nu$, $X_\mu - X_\nu$, and the notation $D_{N\bar{N}}$ is used to call attention to the fact that D is diagonal in wave numbers.†

In order to find the density matrix to a given order, we solve equations (3.7) and (3.8) simultaneously to that order. This may be done very simply by iterating them.

The lowest non-vanishing approximations to the solutions of equations (3.7) and (3.8) are

$$G_{\mu\nu} = f_{\mu\nu} V_{\mu\nu} / [\omega_{\mu\nu} - X_{\mu\nu} F - is] \tag{3.9}$$

$$D_{N\bar{N}} = \frac{1}{\omega_{N\bar{N}} - is} \sum_\nu V_{N\nu} V_{\nu\bar{N}} \left[\frac{f_{N\nu}}{\omega_{N\nu} - X_{N\nu} F - is} - \frac{f_{\bar{N}\nu}}{\omega_{\bar{N}\nu} - X_{m\nu} F + is} \right] \tag{3.10}$$

The matrix element $V_{N\nu}$ in equation (3.13) depends upon various Fourier components V_q of the scattering interactions and the matrix elements of the function, $\exp(iq_x x + iq_y y)$, between the initial and final oscillator functions. We will denote the oscillator quantum number of the state ν by the letter M and define

$$\lambda \equiv q_y + iq_x. \tag{3.11}$$

By use of the generating function (2.6) we may express the matrix element $V_{qN\nu}$ for the Fourier component V_q of the interaction as

$$V_{qN\nu} = [2^{M+N} M! N!]^{-\frac{1}{2}} V_q \frac{d^N}{du^N} (2u - \lambda^*)^M \times \times \exp[u\lambda - \tfrac{1}{4}\lambda\lambda^* + \tfrac{1}{2} iq_x (X_N + X_\nu)] \tag{3.12}$$

in which $k_N = k_\nu + q$.

$V_{N\nu}(q)$ depends on the k_y values of the two states N and ν through the occurrence of the factor $\exp[\frac{1}{2} iq_x(X_N + X_\nu)]$. However, it is only the expression $V_{N\nu} V_{\nu\, N+1}$ that enters the expression for $D_{N\bar{N}}$. Writing this factor as $V_{N\nu}(q) V_{N+1\nu}{}^*(q)$, we readily see that the k_y-dependent phase factor drops out of the expression for D_{NN+1}. This establishes that the D_{NN+1} do not depend on k_y, one of the properties of the density matrix used in the previous section to simplify the expression for the conductivity.

We wish now to establish that the matrix element $G_{\mu\nu}$, for which the wave number changes between the initial and final state, is effectively zero for calculation of the current. For a random array of scatterers or a field of phonons, there will be no phase relationship between different Fourier components $V_{\mu\nu}$. More precisely $V_{\mu\nu}$

† In general where we use a capital Latin letter as a subscript to a state, its significance is the same as though a Greek letter had been used, i.e. it signifies a set of quantum numbers Nk_yk_z. The notation is supposed to imply that two states denoted by Latin capitals have the *same* wave number. Thus, $D_{N\bar{N}}$ means $D_{Nk_yk_z;\,\bar{N}k_yk_z}$, $D_{N\nu}\, D_{\nu\bar{N}}$ means $D_{Nk_yk_z;\,\nu} \cdot D_{\nu;\,\bar{N}k_yk_z}$.

will contain as a factor an infinite sum of the type $\sum_k \exp(iq_{\mu\nu}\cdot R)$ where, e.g. the various R are the positions of individual scattering centers and $q_{\mu\nu}$ denotes $k_\mu - k_\nu$. Considered as a function of $q_{\mu\nu}$, such a sum is of even more rapid variation the larger the system, and for systems of infinite size may be considered to be of infinite variation. The product of such a function with a smoothly varying function is effectively zero, since the average value of the sum is zero. This result holds not only for $V_{\mu\nu}$, but also for all of the matrix elements $G_{\mu\nu}$. It is to be noted that $|V_{\mu\nu}|^2$, while also a rapidly varying function, does not oscillate about zero, but about a value which is a smooth function of μ and ν. $|V_{\mu\nu}|^2$ may then be approximated by this mean smooth function.

An expansion of the current in powers of V corresponds to the classical strong field expansion of the galvanomagnetic coefficients in powers of $(\omega\tau)^{-1}$. Equation (3.10) permits us to calculate the current to the first power of this parameter. We need only the value approached by the expression (3.10) as s approaches zero through positive real values.

In evaluating this limit we may set s zero in (3.10) everywhere except where the denominators vanish. The contributions from the poles may be obtained by use of the relation

$$\lim_{s\to 0}\frac{1}{z-i|s|}=\pi i\delta(z) \tag{3.13}$$

The only part of the density matrix (3.10) that could give rise to a dissipative current is the contribution from the poles. Perhaps the simplest way to see this is to observe that since the direction of flow of the dissipative currents must be reversed if we reverse the sign of macroscopic time, and since s is the only thing in the formulae which changes sign with the sign of time, only terms that change sign with s can describe such dissipative processes. The contributions from the poles of (3.10) are the only such terms, since the principal value of the integral over a singularity does not depend on the sign of s. Thus the only part of $D_{N\bar{N}}(0)$ that we need evaluate comes from the poles.

Carrying out the integration over the poles, we obtain

$$D_{N\bar{N}}(0)=\frac{\pi i}{\omega_{N\bar{N}}}\sum_\nu V_{N\nu}V_{\nu\bar{N}}\{[f(\omega_N)-f(\omega_\nu)]\delta(\omega_{N\nu}-X_{N\nu}F)+[f(\omega_{\bar{N}})-f(\omega_\nu)]\delta(\omega_{\bar{N}\nu}-X_{\bar{N}\nu}F)\} \tag{3.14}$$

The weak-field electrical conductivity is obtained from (3.14) by developing it to the first power of F. We give only the expression applicable when $\bar{N}=N+1$.

$$D_{NN+1}(0)=\pi iF\sum_\nu V_{N\nu}V_{N+1\nu}{}^*X_{\nu N}\frac{df}{d\omega}(\omega_\nu)[\delta(\omega_{N\nu})+\delta(\omega_{N+1\nu})] \tag{3.15}$$

In order that our calculation be self-consistent, the summation right-hand side of equation (3.10) or (3.14) must vanish for $N=\bar{N}$. This is a stability condition for the distribution and in a sense replaces the transport equation that comes into the Boltzmann theory. It is readily verified that the summation does vanish to the order we work when our initial distribution function is used.

4. THE ELECTRICAL CONDUCTIVITY

If we insert the perturbation approximation (3.15) for the density matrix elements ρ_{NN+1} into the expression (2.13) for the current, we obtain a formula for the current density correct to order

$$J^y+iJ^x=F\sum_{Nk_yk_z}f_{NN}-$$

$$-\pi iF\sum_{Nk_yk_z\nu}\sqrt{2(N+1)}X_{\nu N}V_{N+1\nu}V_{\nu N}+$$

$$+\frac{df_\nu}{d\omega}[\delta(\omega_{N\nu})+\delta(\omega_{N+1\nu})] \tag{4.1}$$

The first term, which is real, describes a current in the y direction of magnitude

$$J^y=necE/B \tag{4.2}$$

in which n is the number density of electrons. The expression (4.2) is related to the well-known classical result that a charged particle in crossed electric and magnetic fields moves on the average in the direction $E\times B$. This current is independent of the scattering and is not affected by orbital quantization.

The second term in equation (4.1) can be written

$$-\pi iF\sum_{Nk_yk_z\nu}\delta(\omega_{N\nu})\frac{df_\nu}{d\omega}q_y+$$

$$+[\sqrt{2(N+1)}V_{N+1\nu}V_{\nu N}+\sqrt{(2N)}V_{N\nu}V_{\nu N-1}] \tag{4.3}$$

By use of the relations

$$\sqrt{2(N+1)}\phi_{N+1}(x) = \left(x - \frac{\partial}{\partial x}\right)\phi_N(x)$$
$$\sqrt{(2N)}\phi_{N-1}(x) = \left(x + \frac{\partial}{\partial x}\right)\phi_N(x) \tag{4.4}$$

the expression (4.3) may be written in terms of matrix elements involving only the indices N, ν. In Appendix A we show that by means of this device the expression (4.3) can be reduced to

$$-F\pi i \sum_{Nk_yk_z\nu q_x} \delta(\omega_{N\nu})\frac{df_\nu}{d\omega} q_y(q_y + iq_x)|V_{qN\nu}|^2 \tag{4.5}$$

The particular applications which we will be making all have the characteristic that the matrix element $|V_{qN\nu}|^2$ is an even function of q_x and also of q_y. For such cases the real part of the sum vanishes. For cases in which it does not vanish, it describes an anisotropy in the conductivity tensor which is an even function of the field magnitude. Such a term does not contribute to the Hall effect, but it does contribute to the magnetoresistance. Such anisotropic effects are clearly of no interest to us here.

The imaginary part of expression (4.5) is the dissipative current

$$J^x = -F \sum_{Nk_yk_z\nu q_x} 2\pi|V_{qN\nu}|^2\delta(\omega_{N\nu})\frac{df_\nu}{d\omega}\tfrac{1}{2}q_y{}^2 \tag{4.6}$$

Introducing the proper dimensional quantities into equations (4.2) and (4.6), we obtain for the transverse conductivity components the expressions

$$\sigma_{xy} = -(nec/B) \tag{4.7}$$

$$\sigma_{xx} = \sum_{Nk_yk_z} e^2\frac{df}{d\zeta}(E_N) \sum_{\nu}^{E_n = E_\nu} \tfrac{1}{2}X_{N\nu}{}^2\omega_{N\nu} \tag{4.8}$$

in which n denotes the electron density for a single spin, ζ the Fermi energy, and $\omega_{N\nu}$ is the Born approximation expression for the transition rate between states N and ν of the same energy. Throughout the manuscript we omit the spin degeneracy from our formulae. The expression (4.8) is closely related to the Einstein formula for the electrical conductivity in terms of the diffusivity. In order to make the relation evident, we define a relaxation time in terms of the total transition rate and rewrite (4.8) in the form of an Einstein relation

$$\sigma_{xx} = \frac{e^2}{\tau}\left\langle\frac{dn}{d\zeta}\langle\tfrac{1}{2}d^2\rangle\right\rangle \tag{4.9}$$

in which we have substituted

$$\frac{d}{d\zeta}\sum_{Nk_yk_z} f(E_N) = \frac{dn}{d\zeta} \tag{4.10}$$

and defined the mean square jump distance d^2 in the natural way as

$$\frac{1}{\tau}\langle\tfrac{1}{2}d^2\rangle \equiv \sum_{\nu}^{\bar{N}E = E_\nu} \omega_{N\nu}\tfrac{1}{2}X_{N\nu}{}^2 \tag{4.11}$$

The outer angular bracket in equation (4.9) denotes a thermal average, the inner an average over jumps.

These last observations show that our conductivity theory is essentially identical with that of TITEICA. Our treatment above may be regarded as establishing the analytical connection between the transition probability, diffusion theory of TITEICA, and a stationary density matrix calculation of the electrical conductivity. For the purpose of calculation the formulation in terms of transition probability is ordinarily more convenient and will be used in the applications made in later sections of the paper.

The experimental quantities most commonly measured in zero-frequency experiments are the Hall coefficient and the resistivity. To approximation $(\omega\tau)^{-1}$ these quantities are given by

$$R_H = -(1/nec) \tag{4.12}$$

$$\rho = \frac{m}{ne^2\tau}\left(\frac{\hbar\omega}{n}\right)\left\langle\frac{dn}{d\zeta}\middle/\left\langle\frac{d^2}{2L^2}\right\rangle\right\rangle \tag{4.13}$$

5. GALVANOMAGNETIC FORMULAE FOR THE QUANTUM LIMIT

Our equations for the conductivity are valid in the limit $\omega\tau \gg 1$. There are essentially three distinct experimental regimes in which these equations could be applied. One is the strong field "classical regime" with $\hbar\omega \ll KT$, $E \sim KT$, in which E denotes a typical electron energy. We will not treat this case, since the familiar Boltzmann velocity space theory is valid. The second regime of applicability is the regime $KT \ll \hbar\omega$, $E > \hbar\omega$, in which oscillatory effects are observed in the galvanomagnetic properties; the third is what we will call the "quantum limit" (QL), in which $\hbar\omega > E$ for all of the electron energies of interest. We will also speak of the "extreme quantum limit" (EQL) as the condition $\hbar\omega \gg E$.

The quantum limit is the only regime for which orbital quantization has a large effect on the average galvanomagnetic coefficients. In this section

we will treat several different scattering mechanisms in the quantum limit, comparing and contrasting the effects of quantization on the transverse and longitudinal resistivities. We will treat all of the interactions as elastic, although for application to low-temperature measurements such a treatment would not be valid for certain of the mechanisms considered. For these cases it should be considered that our treatment has as its purpose to illustrate the qualitative dependence of the quantum effects on scattering mechanism.

In the quantum limit only states of oscillator number $N = 0$ are available, so the matrix element for scattering is (in dimensionless units)

$$|V_{qN\nu}|^2 = |V_q|^2 \exp[-\tfrac{1}{2}(q_x^2+q_y^2)] \qquad (5.1)$$

The density of states $n(E)$ of a single spin is given by

$$n(E) = \frac{2\pi}{(2\pi\hbar)^3}(2mE_z)^{\frac{1}{2}}(2m\hbar\omega)^{\frac{1}{2}} \qquad (5.2)$$

The longitudinal momentum relaxation time is given by the relation

$$\tau_L(E)^{-1} = \hbar^{-1}\int dq_x\, dq_y \times \times \exp(-\tfrac{1}{2}q^2)|V_{q_x\, q_y,-2k_z}|^2 n(E) \qquad (5.3)$$

Here q^2 denotes $q_x^2+q_y^2$. The appearance of $-2k_z$ in the matrix element is because the only collisions that are effective in momentum transfer are those that reverse the momentum along the field. The transverse conductivity will be expressed in terms of a single-energy diffusivity $D(E)$

$$D(E_N) = \sum_{\nu}^{E_N=E_\nu} \tfrac{1}{2}X_{N\nu}^2\omega N\nu$$

$$D(E) = \tfrac{1}{4}\hbar^{-1}n(E)\int dq_x\, dq_y q_y^2 \times \times\{|V_{q_x q_y,-2k_z}|^2+|V_{q_x,q_y,0}|^2\}\exp(-\tfrac{1}{2}q^2) \qquad (5.4)$$

Several scattering mechanisms will be considered: (*a*) high-temperature acoustical scattering denotes that in which each oscillator has energy KT; (*b*) the low-temperature acoustical that in which each oscillator is in zero point motion; (*c*) the point scatterer mechanism[2] is identical with high-temperature acoustical in its energy dependence but not in its temperature-dependence; (*d*) the piezoelectric scattering[13] is of interest in ionic materials such as InSb; it can have either a low-temperature or high-temperature form also; (*e*) the optical mode scattering is in practice so inelastic that it can be treated as elastic only for very high energy electrons; however, it is of great experimental importance, so it is included;* (*f*) ionized impurity scattering is of great experimental interest, especially in low-temperature work. In all of the singular interactions we will assume that there exists a cutoff momentum of the order of the Debye screening length of the material. The analytical form we use for introducing this screening length is not exactly that given by theory in every case, but no serious error can result from this feature of our formulae.

The momentum-dependence of the scattering matrix element $|M|^2$ is given in Table 1 for each of the scattering mechanisms considered. The longitudinal momentum relaxation rates are given in Table 2 for each scattering mechanism, and the transverse diffusivity in Table 3. In Table 4 we give the dependence on field and temperature of the longitudinal conductivity and transverse

* The optical mode scattering might also be considered in a high-temperature as well as a low-temperature form. However, to the extent that the interaction is treated as elastic, the formulae obtained are identical except that in the low-temperature form $2kT/\hbar\omega_D$ is replaced by the Planck factor.

Table 1. 1. *Momentum-dependence of squared matrix element*

Scattering mechanism	$\|M\|^2$
Low-temperature acoustical	$A_1 q$
High-temperature acoustical	$A_1(2KT/\hbar S)$
Point defect	A_2
Low-temperature piezoelectric	$A_3 q^{-1}$
High-temperature piezoelectric	$A_3(q^2+q_S^2)^{-1}(2KT/\hbar S)$
High-temperature optical	$A_4(q^2+q_S^2)^{-1}(2KT/\hbar\omega_D)$
Ionized-impurity	$A_5(q^2+q_S^2)^{-2}$

Table 2. Longitudinal momentum relaxation rate τ_L^{-1}

Scattering Mechanism	$\left[\frac{2\pi}{\hbar} n(E)\tau_L\right]^{-1}$ Quantum limit	E.Q.L.
Low-temp. acoustical	$\frac{A_1}{L}\sqrt{\frac{\pi}{2}}\exp\left(\frac{4E}{\hbar\omega}\right)\left[1-\operatorname{erf}\left(\frac{8E}{\hbar\omega}\right)^{1/2}\right]$	$\frac{A_1}{L}\sqrt{\frac{\pi}{2}}$
High-temp. acoustical	$A_1\left(\frac{2KT}{\hbar S}\right)$	$A_1\left(\frac{2KT}{\hbar S}\right)$
Point defect	A_2	A_2
Low-temp. piezoelectric	$A_3L\sqrt{\frac{\pi}{2}}\exp\left(\frac{4E}{\hbar\omega}\right)\left[1-\operatorname{erf}\left(\frac{8E}{\hbar\omega}\right)^{1/2}\right]$	$A_3L\sqrt{\frac{\pi}{2}}$
High-temp. piezoelectric	$\frac{A_3L^2}{2}\left(\frac{2KT}{\hbar S}\right)\exp\left(\frac{4E+E_S}{\hbar\omega}\right)E_i\left(\frac{4E+E_S}{\hbar\omega}\right)$	$\frac{A_3L^2}{2}\left(-\ln\left[\frac{4E+E_S}{\hbar\omega}\right]\right)\left(\frac{2KT}{\hbar S}\right)$
High-temp. optical	$\frac{A_4L^2}{2}\left(\frac{2KT}{\hbar\omega_D}\right)\exp\left(\frac{4E+E_S}{\hbar\omega}\right)E_i\left(\frac{4E+E_S}{\hbar\omega}\right)$	$\frac{A_4L^2}{2}\left(-\ln\left[\frac{4E+E_S}{\hbar\omega}\right]\right)\left(\frac{2KT}{\hbar\omega_D}\right)$
Ionized-impurity	$\frac{A_5L^4}{4}\left[\frac{\hbar\omega}{4E+E_S}-\exp\left(\frac{4E+E_S}{\hbar\omega}\right)E_i\left(\frac{4E+E_S}{\hbar\omega}\right)\right]$	$\frac{A_5L^4}{4}\frac{\hbar\omega}{4E+E_5}$

resistivity for degenerate statistics and in the extreme quantum limit in order to show the great variety of dependences that are possible. More complicated statistical situations would have to be considered in practice, since the degree of degeneracy depends markedly on field. In these tables the quantity E_s denotes $\frac{1}{2}q_s^2$. We also give the ratio ρ_T/ρ_L of the transverse resistivity to the longitudinal resistivity calculated for the extreme quantum limit and completely degenerate statistics. It is to be noted that for all mechanisms except scattering by ionized impurities this ratio is proportional to H^2 and is within a factor two the same. In contrast, the ratio is almost independent of magnetic field for impurity scattering and is somewhat larger than unity. The relevant formulae for the degenerate case are:

$$\sigma_L = \frac{ne^2}{m}\tau(\zeta) \tag{5.5}$$

$$\rho_T = \left(\frac{m}{ne^2}\right)\left(\frac{D(\tau)}{L^2}\right)\left(\frac{\hbar\omega}{2\zeta}\right) \tag{5.6}$$

For non-degenerate statistics we cannot immediately calculate the resistivity, because the thermal average diverges logarithmically at energy zero. This divergence has its origin in the $E^{-\frac{1}{2}}$ singularity of the density of states, which enters twice, once directly in the thermal average and once indirectly through the effect on the scattering rate. In the physical situation this divergence is removed by one or another mechanism. In any particular case, the logarithm may be approximately evaluated by a simple estimate of the cutoff.

Three different physical cutoff mechanisms must be considered. One mechanism, collision broadening, always operates and will cut off the divergence at an energy

$$E_{\mathrm{CB}} \sim \hbar/\tau(E_{\mathrm{CB}}) \tag{5.7}$$

A second cutoff comes in as τ becomes small and the expansion in $(\omega\tau)^{-1}$ converges less rapidly, so that a better approximation to the distribution function must be used. In that case the divergent integral should have its integrand modified by a factor

$$[1+(1/\omega^2\tau^2)]^{-1} \tag{5.8}$$

This "classical" cutoff will cut off the divergence at the value

$$E_{\mathrm{Cl}} \sim E(\tau)|^{\omega\tau=1} \tag{5.9}$$

Finally, some of the scattering potentials have actual frequency-dependence. For such scattering interactions

Table 3. Transverse diffusivity D(E)

Scattering mechanism	$\frac{\hbar D(E)}{2\pi L^2 n(E)}$ Quantum limit	E.Q.L.
Low-temp. acoustical	$\frac{A_1}{4L}\left[\frac{3}{2}\sqrt{\frac{\pi}{2}}+\sqrt{\frac{\pi}{2}}\left(\frac{3}{2}-\frac{4E}{\hbar\omega}\right)\exp\left(\frac{4E}{\hbar\omega}\right)\left(1-\operatorname{erf}\left(\frac{8E}{\hbar\omega}\right)^{1/2}\right)+\frac{3}{2}\left(\frac{8E}{\hbar\omega}\right)^{1/2}\right]$	$\frac{A_1}{L}\frac{3}{4}\sqrt{\frac{\pi}{2}}$
High-temp. acoustical	$\frac{A_1}{2}\left[\frac{2KT}{\hbar S}\right]$	$\frac{A_1}{2}\left[\frac{2KT}{\hbar S}\right]$
Point defect	$\frac{A_2}{2}$	$\frac{A_2}{2}$
Low-temp. piezoelectric	$\frac{A_3L}{2}\left[\sqrt{\frac{\pi}{2}}+\sqrt{\frac{\pi}{2}}\left(1-\frac{8E}{\hbar\omega}\right)\exp\left(\frac{4E}{\hbar\omega}\right)\left(1-\operatorname{erf}\left(\frac{8E}{\hbar\omega}\right)^{1/2}\right)+\left(\frac{8E}{\hbar\omega}\right)^{1/2}\right]$	$A_3L\frac{1}{4}\sqrt{\frac{\pi}{2}}$
High-temp. piezoelectric	$\frac{A_3L^2}{8}\left[2-\left(\frac{4E+E_S}{\hbar\omega}\right)\exp\left(\frac{4E+E_S}{\hbar\omega}\right)E_i\left[\frac{4E+E_S}{\hbar\omega}\right]-\left(\frac{E_S}{\hbar\omega}\right)\exp\left(\frac{E_S}{\hbar\omega}\right)E_i\left(\frac{E_S}{\hbar\omega}\right)\right]\left(\frac{2KT}{\hbar S}\right)$	$A_3L^2\frac{1}{4}\left(\frac{2KT}{\hbar S}\right)$
High-temp. optical	$\frac{A_4L^2}{8}\left(\frac{2KT}{\hbar\omega_D}\right)\left[2-\left(\frac{4E+E_S}{\hbar\omega}\right)\exp\left(\frac{4E+E_S}{\hbar\omega}\right)E_i\left(\frac{4E+E_S}{\hbar\omega}\right)-\left(\frac{E_S}{\hbar\omega}\right)\exp\left(\frac{E_S}{\hbar\omega}\right)E_i\left(\frac{E_S}{\hbar\omega}\right)\right]$	$A_4L^2\frac{1}{4}\left(\frac{2KT}{\hbar\omega_D}\right)$
Ionized-impurity	$\frac{A_5L^4}{16}\left[\left(1+\frac{E_S}{\hbar\omega}\right)\exp\left(\frac{E_S}{\hbar\omega}\right)E_i\left(\frac{E_S}{\hbar\omega}\right)+\left(1+\frac{4E+E_S}{\hbar\omega}\right)E_i\left(\frac{4E+E_S}{\hbar\omega}\right)-2\right]$	$\frac{A_5L^4}{16}\left[-\ln\frac{E_S}{\hbar\omega}-\ln\left(\frac{4E+E_S}{\hbar\omega}\right)\right]$

VOL. 10, 1957

Table 4. Variation of resistivity with H, T, extreme quantum limit degenerate statistics

Scattering mechanism	ρ_T	ρ_L	ρ_T/ρ_L
Low-temp. acoustical	$\sim H^{11/2}T^0$	$\sim H^{5/2}T^0$	$\frac{3\hbar\omega}{8E_F}$
High-temp. acoustical	$\sim H^5T$	$\sim H^2T$	$\frac{1\hbar\omega}{4E_F}$
Point defect	$\sim H^5T^0$	$\sim H^2T^0$	$\frac{1\hbar\omega}{4E_F}$
Low-temp. piezoelectric	$\sim H^{9/2}T^0$	$\sim H^{3/2}T^0$	$\frac{1\hbar\omega}{8E_F}$
High-temp. piezoelectric	$\sim H^4T$	$\sim HT$	$\frac{1\hbar\omega}{4E_F\left[-\ln\left(\frac{4E_F+E_S}{\hbar\omega}\right)\right]}$
High-temp. optical	$\sim H^4T$	$\sim HT$	$\frac{1\hbar\omega}{4E_F\left[-\ln\left(\frac{4E_F+E_S}{\hbar\omega}\right)\right]}$
Ionized-impurity	$\sim H^3T^0$	$\sim H^3T^0$	$-\left(\frac{4E_F+E_S}{4E_F}\right)\left[\frac{\ln\left(\frac{E_S}{\hbar\omega}\right)+\ln\left(\frac{4E_F+E_S}{\hbar\omega}\right)}{2}\right]$

the divergence is cut off at an electron energy equal to that of the phonon with which the electron interacts. The situations are quite different for the cases optical and acoustical modes, since the acoustical mode frequency depends appreciably on wave number, while the optical mode frequency does not. The cutoffs are

$$E_{C\,OPT} \sim \hbar\omega_{OPT} \tag{5.10}$$

$$E_{C\,AC} \sim \sqrt{(6m^*S^2E)} \tag{5.11}$$

where S is the velocity of sound.

Of these cutoffs the classical cutoff is never important in the regime $\omega\tau \gg 1$, since collision broadening always gives a cutoff at a smaller scattering rate. To see this note that from equation (5.7) the collision broadening cutoff comes for values of

$$\omega\tau \sim \frac{\hbar\omega}{E_{CB}} > 1 \tag{5.12}$$

whereas the classical cutoff is at $\omega\tau \sim 1$. The cutoff because of the frequency of the vibrational quantum will usually be the physical one in the case of optical mode interactions, since the optical phonons are very energetic. However, in the case of acoustical interaction the collision broadening will usually be the physical cutoff in semimetals and semiconductors.

In Table 5 we give the dependence on field and temperature of the transverse resistivity and longitudinal conductivity in the extreme quantum limit and for nondegenerate statistics. We also give the ratio of the two resistivities. For the scattering mechanisms considered, the longitudinal conductivity is

$$\sigma_L = \frac{2ne^2}{\sqrt{(\pi)m}}\tau(KT) \tag{5.13}$$

except for ionized-impurity scattering, where the formula is

$$\sigma_L = \frac{4ne^2}{\sqrt{(\pi)m}}\tau(KT) \tag{5.14}$$

The transverse resistivity is given in each case by

$$\rho_T = (-\ln\epsilon)\left(\frac{mD(KT)}{ne^2L^2}\right)\left(\frac{\hbar\omega}{\sqrt{(\pi)}KT}\right) \tag{5.15}$$

The factor $(-\ln\epsilon)$ occurring in the formula for ρ_T is the cutoff logarithm

$$-\ln\epsilon = -\ln[E_c/KT] \tag{5.16}$$

where E_c is the proper physical cutoff energy.

Table 5. Variation of resistivity with H, T, *extreme quantum limit, non degenerate statistics*

Scattering mechanism	ρ_T	ρ_L	ρ_T/ρ_L
Low-temp. acoustical	$\sim H^{5/2}T^{-3/2}$	$\sim H^{3/2}T^{-1/2}$	$\frac{3\hbar\omega}{2\pi KT}(-\ln\epsilon)$
High-temp. acoustical	$\sim H^{2}T^{-1/2}$	$\sim HT^{1/2}$	$\frac{1\hbar\omega}{\pi KT}(-\ln\epsilon)$
Point defect	$\sim H^{2}T^{-3/2}$	$\sim HT^{-1/2}$	$\frac{1\hbar\omega}{\pi KT}(-\ln\epsilon)$
Low-temp. piezoelectric	$\sim H^{3/2}T^{-3/2}$	$\sim H^{1/2}T^{-1/2}$	$\frac{1\hbar\omega}{2\pi KT}(-\ln\epsilon)$
High-temp. piezoelectric	$\sim HT^{-1/2}$	$\sim H^{0}T^{1/2}$	$\frac{1\hbar\omega(+\ln\epsilon)}{\pi KT\ln\left(\frac{4KT+E_S}{\hbar\omega}\right)}$
High-temp. optical	$\sim HT^{-1/2}$	$\sim H^{0}T^{1/2}$	$\frac{1\hbar\omega(+\ln\epsilon)}{\pi KT\left[\ln\left(\frac{4KT+E_S}{\hbar\omega}\right)\right]}$
Ionized-impurity	$\sim H^{0}T^{-3/2}$	$\sim H^{0}T^{-3/2}$	$\frac{4}{\pi}\ln\epsilon\left[\ln\left(\frac{E_S}{\hbar\omega}\right)+\ln\left(\frac{E_S+4KT}{\hbar\omega}\right)\right]$

In examining the entries in Table 5 it is noteworthy that there is considerable variation of the field- and temperature-dependence from one mechanism to the other. The ratio of resistivities is proportional to $\hbar\omega/KT$ for all scattering mechanisms except again ionized-impurity scattering, for which it depends only weakly on field and temperature.

6. OSCILLATORY GALVANOMAGNETIC EFFECTS

In degenerate semiconductors and semimetals it is possible under certain circumstances to observe quantum effects in the electrical conductivity,[10,11] even though the Fermi level is so high that levels of several or even very many different principal quantum numbers are occupied. These effects are observed under the condition $\hbar\omega \gg KT$. In this case the position of the Fermi level is well defined within the level, and the values of the transport quantities depend on the scattering at the particular position of the Fermi level. As the field is varied the scattering will oscillate somewhat because of the non-smooth variation of the density of states with energy.

Several theories of these oscillations have been given.[2,5,7,8] However, we believe that some further discussion is justified in order to clarify the situation as regards the harmonic content of the oscillations, the dependence of amplitude on magnetic field, and the extent to which the phenomenon is sensitive to scattering mechanism. We will try to elucidate this last matter by considering two extreme examples. The first is high-temperature elastic acoustical lattice scattering, which is effectively of zero range. The second is ionized-impurity scattering, which is effectively of infinite range so that screening must ordinarily be introduced to obtain finite and reasonable values for the scattering rate.

Initially we will discuss the transverse conductivity on the basis of equation (4.6) and for the absolute zero of temperature. In dimensionless terms (4.6) yields

$$\sigma_{xx} = -\sum_{Nk_yk_zvq_x} \frac{df_\nu}{d\omega}\tfrac{1}{2}q_y{}^2 2\pi|V_{qN\nu}|^2\delta(\omega_{N\nu}) \tag{6.1}$$

where as before the wave number q denotes the wave number difference $k_N - k_\nu$. At the absolute zero, df/dE becomes a δ function and equation (6.1) can be rewritten

$$\sigma_{xx} = (2\pi)^{-3} \sum_{NM} (\zeta - N - \tfrac{1}{2})^{-\frac{1}{2}} \times$$

$$\times (\zeta - M - \tfrac{1}{2})^{-\frac{1}{2}} \left[\sum_{q_x q_y} q_y^2 2\pi |V_{qN\nu}|^2 \right]^{E_N = E_\nu} \tag{6.2}$$

In equation (6.2) M denotes as before the oscillator quantum number of ν, and q_z is to be expressed in terms of E_z and $E_{z\nu}$. There will in general be two values of q_z for which energy is conserved. The quantum numbers N and M each range from zero up to the largest value consistent with the conditions

$$\begin{aligned} \hbar\omega N &\leqslant \zeta \\ \hbar\omega M &\leqslant \zeta \end{aligned} \tag{6.3}$$

The bracketed quantity in equation (6.2) contains the information necessary for a description of the detailed way in which the conductivity depends on scattering mechanism. It is the factor which chiefly determines the magnitude and temperature-dependence of the conductivity. The two factors outside of the bracket are responsible for the oscillatory behavior. These factors are smooth functions of ζ (or H) except when ζ passes through a half integral value. For such values of ζ these factors provide a divergent contribution to the conductivity that is the primary cause of the oscillations.

We find it simpler to carry through the discussion of the oscillatory behavior by way of examples rather than in terms of general equations. We will begin by considering the acoustical scattering interaction which has the squared matrix element (in the notation of Section 5) $A_1 (2kT/\hbar s)$, a constant independent of q. This constant we will denote for brevity as C_1 in the following discussion. To evaluate the bracketed quantity in equation (6.2), we require the matrix elements

$$|V_{qN\nu}|^2 = C_1 |(\phi_N(x),\ \exp(iq \cdot x)\phi_M(x - q_y))|^2 \tag{6.4}$$

This quantity is a function of N and M and $q^2 = q_x^2 + q_y^2$. Its value is readily computed directly for any particular values of M and N. No simple formula for it may be given that is valid for all quantum numbers. However, an asymptotic formula valid for large values of the quantum numbers may be derived (cf. Ref. (1), equation (12)) which states that for large quantum numbers N and M, the acoustical lattice scattering may be described by the squared matrix element

$$|V_{qN\nu}|^2 = \frac{C_1}{\pi} [(N + M + 1)^2 q^2 - (N - M)^2 - \tfrac{1}{4} q^4]^{-\frac{1}{2}} \tag{6.5}$$

Even though we will not be interested exclusively in large quantum numbers, we will use the approximation (6.5) to evaluate the sum in equation (6.2). Equation (6.5) is used with the understanding that we sum only over values of q_x and q_y for which the expression (6.5) is real. The result of the integration over q_x and q_y is

$$\sum_{q_x q_y} \tfrac{1}{2} q_y^2 2\pi |V_{qN\nu}|^2 = C_1 (N + M + 1) \tag{6.6}$$

It may be shown that the result (6.6), derived using the large quantum number approximation (6.5) for $|V_{qN\nu}|^2$, is actually exact and is valid for arbitrarily small values of M, N.

If we substitute the result (6.6) in equation (6.2), we obtain for the (dimensionless) conductivity

$$\sigma_{xx} = (2\pi)^{-3} C_1 \sum_{MN} \frac{(M + N + 1)}{\sqrt{(\zeta - M - \tfrac{1}{2})}\sqrt{(\zeta - N - \tfrac{1}{2})}} \tag{6.7}$$

We will express the Fermi energy as the sum of an integer I and a non-integral part δ, between zero and unity

$$\zeta = I + \delta + \tfrac{1}{2} \tag{6.8}$$

Now by means of equation (6.8) we can express (6.7) as

$$\sigma_{xx} = 2(2\pi)^{-3} C_1 \times$$

$$\times \sum_{MN=0}^{I} \left[\frac{I + \delta + \tfrac{1}{2}}{\sqrt{(M + \delta)}\sqrt{(N + \delta)}} - \frac{\sqrt{(M + \delta)}}{\sqrt{(N + \delta)}} \right] \tag{6.9}$$

The sums in equation (6.9) can be expressed in terms of the electron concentration and the density of states

$$n = 2\sqrt{(2)}(2\pi)^{-2} \sum_{M=0}^{I} (M + \delta)^{\frac{1}{2}} \tag{6.10}$$

$$n(\zeta) = \frac{dn}{d\zeta} = \sqrt{(2)}(2\pi)^{-2} \sum_{M=0}^{I} (M + \delta)^{-\frac{1}{2}} \tag{6.11}$$

Then, finally, with the introduction of the dimensional factors we obtain an expression for the transverse conductivity

$$\sigma_{xx} = (e^2/m\omega^2) 2\pi C_1 n(\zeta) \hbar^{-1} [\zeta n(\zeta) - \tfrac{1}{2} n] \tag{6.12}$$

In the factor outside of the bracket in equation (6.12) appears the Born approximation to the relaxation rate τ^{-1} as ordinarily defined. The bracketed factor at large

quantum numbers oscillates around the value n. At sufficiently large quantum numbers the average behavior is such that $\zeta n(\zeta) \to \frac{3}{2}n$ and the expression (6.12) passes over to the simple expression

$$\sigma_{xx} = (ne^2/m\omega^2\tau) \tag{6.13}$$

Equation (6.13) describes the "classical" behavior for the conductivity in the limit $\omega\tau \gg 1$.

At small quantum numbers the conductivity equation (6.12) will exhibit an oscillatory behavior as function of field. The oscillatory behavior arises because the density of states $n(\zeta)$ is not a smooth function of field, and in fact exhibits a singularity for each field value such that the Fermi energy coincides with the threshold of another oscillator level. Strictly speaking ζ itself is not a smooth function of field, but, as will be shown immediately below, its variation is slight and may for most purposes be ignored until the field is so strong that the quantum limit is reached.

The singularities of $n(\zeta)$ occur when the field is such that $\delta = 0^+$. In dimensional units this requires that the field be such as to satisfy the integer condition (here given approximately (cf. Appendix B))

$$n = \frac{4\pi}{3}(2m\hbar\omega)^{\frac{3}{2}}(2\pi\hbar)^{-3}[(I+\tfrac{1}{2})^{\frac{3}{2}} - (\tfrac{1}{2})^{\frac{3}{2}}] \tag{6.14}$$

Since the electron concentration n is constant, equation (6.14) means that the integer conditions are fulfilled at nearly equal intervals of H^{-1}; the periodicity is exact to the extent that $(\frac{1}{2})^{\frac{3}{2}}$ can be neglected. Even for the very smallest integers, there is only a small deviation from periodicity, and except for this small deviation from periodicity the variation of Fermi level with H will play no significant role in the periodic phenomena for a single spherical surface.

The singular behavior of $n(\zeta)$ near the threshold of an oscillator level is described by the function $\delta^{-\frac{1}{2}}$. It is in this singularity that the oscillatory behavior originates. According to equation (6.12) the electrical conductivity has terms that are singular like $\delta^{-\frac{1}{2}}$ in the part proportional to $n(\zeta)$ and also terms that are singular like δ^{-1} which occur in the part proportional to $[n(\zeta)]^2$. In order to compare these two terms we will separate out the oscillatory behavior of $n(\zeta)$ explicitly.

The dependence of the density of states $n(\zeta)$ on the position of the Fermi level ζ may be represented with good accuracy by the approximate formula (cf. Appendix B):

$$n(\zeta) = 4\pi m(2\pi\hbar)^{-3}(2m\hbar\omega)^{\frac{1}{2}} \times \times [(I+\delta+\tfrac{1}{2})^{\frac{1}{2}} + \tfrac{1}{2}\delta^{-\frac{1}{2}} - (\delta+\tfrac{1}{2})^{\frac{1}{2}}] \tag{6.15}$$

The terms in $\delta^{-\frac{1}{2}}$, $(\delta+\frac{1}{2})^{\frac{1}{2}}$ are periodic functions of H^{-1}, and lead to oscillatory behavior. The term $(I+\delta+\frac{1}{2})^{\frac{1}{2}}$ is just $(\zeta/\hbar\omega)^{\frac{1}{2}}$, hence is a continuous function of the reciprocal field.

In order to discuss the oscillatory behavior, it is convenient to express equation (6.15) as

$$n(\zeta) = n_0(\zeta) + n_1(\zeta) \tag{6.16}$$

with

$$n_0(\zeta) = 4\pi m(2\pi\hbar)^{-3}(2m\zeta)^{\frac{1}{2}} \tag{6.17a}$$

$$n_1(\zeta) = n_0(\zeta)\zeta^{-\frac{1}{2}}[\tfrac{1}{2}\delta^{-\frac{1}{2}} - (\tfrac{1}{2}+\delta)^{\frac{1}{2}}] \tag{6.17b}$$

Inserting these expressions into equation (6.12) and noting that except for a small error in the lowest quantum state we may set $\zeta n_0(\zeta) = \frac{3}{2}n$, we obtain for the conductivity

$$\sigma_{xx} = \frac{2\pi C_1 e^2}{\hbar m\omega^2}\left[1 + \frac{5}{2}\frac{n_1(\zeta)}{n_0(\zeta)} + \frac{\zeta[n_1(\zeta)]^2}{nn_0(\zeta)}\right] \tag{6.18}$$

The first term represents the conductivity in the high-quantum-number limit, so it is convenient to re-express the conductivity (6.18) as

$$\sigma_{xx} = \sigma_0\left[1 + \frac{5}{2}\frac{n_1(\zeta)}{n_0(\zeta)} + \frac{\zeta[n_1(\zeta)]^2}{nn_0(\zeta)}\right] \tag{6.19}$$

The second and third terms of equation (6.19) represent quantum corrections to the conductivity of somewhat different types. We will denote these corrections as $\Delta\sigma_1$ and $\Delta\sigma_2$, respectively. $\Delta\sigma_1$ represents the contributions arising from scatterings between the states belonging to the oscillator level lying closest below the Fermi surface and those belonging to other oscillator levels, which contain rather large numbers of electrons. $\Delta\sigma_2$ represents the scatterings taking place between states entirely within the level lying closest to the Fermi surface. $\Delta\sigma_1$ contains singularities of the $\delta^{-\frac{1}{2}}$ type, while $\Delta\sigma_2$ contains the δ^{-1} singularity. This δ^{-1} singularity is analogous to the one we found in the quantum limit, and like that one, would lead to a logarithmic divergence in the conductivity, even after a thermal average.

The magnitudes of the two oscillatory conductivities $\Delta\sigma_1$ and $\Delta\sigma_2$ may be written down directly from equations (6.17) and (6.19).

$$\Delta\sigma_1 = \frac{5}{2}\sigma_0\left(\frac{\hbar\omega}{\zeta}\right)^{\frac{1}{2}}\left[\frac{1}{2}\left(\frac{\hbar\omega}{E_z}\right)^{\frac{1}{2}} - \left(\frac{1}{2}+\frac{E_z}{\hbar\omega}\right)^{\frac{1}{2}}\right] \tag{6.20}$$

$$\Delta\sigma_2 = \frac{3}{2}\sigma_0\left(\frac{\hbar\omega}{\zeta}\right)\left[\frac{1}{2}\left(\frac{\hbar\omega}{E_z}\right)^{\frac{1}{2}} - \left(\frac{1}{2}+\frac{E_z}{\hbar\omega}\right)^{\frac{1}{2}}\right]^2 \tag{6.21}$$

where $E_z = \zeta - (I+\frac{1}{2})\hbar\omega$.

Thus in the equations (6.20) and (6.21) E_z denotes the amount of energy by which the Fermi level exceeds the state of zero wave number along the field associated with the oscillator level just below the Fermi surface.

The infinite conductivities occurring for particular values of magnetic field strength would be observable were it not for the fact that the levels are broadened as a result of collisions.[2] Just as in the quantum limit case, the logarithmic divergence in equation (6.21) may also be affected by the finite frequency of the vibrational waves responsible for the scattering. For the purpose of the following discussion we will assume that only collision broadening plays a role. In that case we can estimate the maximum values attained in the conductivities $\Delta\sigma_1$ and $\Delta\sigma_2$ by making use of the fact that, roughly speaking, collision broadening levels off the density of states at the value for which $E_z \sim \hbar/\tau(E_z)$. On this basis we can estimate that the maximum values attained by the oscillatory conductivities are

$$\Delta\sigma_{1\,\max} \sim \frac{5}{2}\sigma_0\left(\frac{\hbar\omega}{\zeta}\right)^{\frac{1}{2}}\gamma^{-\frac{1}{2}} \tag{6.22}$$

$$\Delta\sigma_{2\,\max} \sim \frac{3}{2}\sigma_0\left(\frac{\hbar\omega}{\zeta}\right)\gamma^{-1} \tag{6.23}$$

where $\gamma = (\omega\tau_c)^{-1}$ is the collision-broadening cutoff parameter.

We are not in a position to make a quantitative theory of the cutoff time τ_c that enters equations (6.22) and (6.23). Clearly it should be smaller than the mean relaxation time for conduction as obtained from σ_0, since there is surely some increase in the scattering where the density of states is large near the edge. In most cases τ_c is probably not much smaller than the conductivity relaxation time, and the latter should in any case provide an order-of-magnitude estimate of τ_c.

In discussing the shape of the oscillations and the change of shape with temperature, it is a mathematical convenience to express the oscillator conductivity as a Fourier series in the harmonics of $2\pi\delta$. In the harmonic representation we can take account of the effect of collision or thermal broadening on, e.g. the M^{th} harmonic, by multiplying the amplitude of that harmonic by the Fourier transform of the corresponding distribution evaluated at $2\pi M$. This fact is a consequence of the *Faltung* theorem[12] for Fourier transforms.

In Appendix C we give the harmonic series representations for the oscillatory parts of the functions with which we have to deal. We will give the expressions here in terms of δ. They may be transformed into explicit functions of ζ and $\hbar\omega$ by substituting $\delta = (\zeta/\hbar\omega) - I - \frac{1}{2}$, which in each case has the effect of replacing δ by $(\zeta/\hbar\omega)$ and multiplying the summand by $(-)^M$.

Equation (C.3) gives the oscillatory part of the function $\delta^{-\frac{1}{2}}$ that enters $\Delta\sigma_1$. The new expression for $\Delta\sigma_1$, uncorrected for collision broadening, is

$$\Delta\sigma_1 = \sigma_0 5\sqrt{(\pi)}\left(\frac{\hbar\omega}{\zeta}\right)^{\frac{1}{2}} \times \times \sum_{M=1}^{\infty} (2\pi M)^{-\frac{1}{2}} \cos\left(2\pi M\delta - \frac{\pi}{4}\right) \tag{6.24}$$

We cannot compute $\Delta\sigma_2$ without considering the effect of collision broadening, since $\Delta\sigma_2$ has a logarithmic divergence at the edge[2] which we cannot Fourier transform. We have examined several crude ways of removing this difficulty, and found they lead to similar results. The formulae of Appendix C were obtained by using the function $\delta[\delta^2+\gamma^2]^{-1}$ to replace δ^{-1} near the point $\delta = 0$. With this we find as an approximation to $\Delta\sigma_2$, suitable for use in most cases, the formula:

$$\Delta\sigma_2 \approx \sigma_0\frac{3\pi}{2}\left(\frac{\hbar\omega}{\zeta}\right) \times \times \sum_{M=1}^{\infty} \exp(-2\pi M\gamma)\cos\left(2\pi M\delta - \frac{\pi}{2}\right) \tag{6.25}$$

A comparison of equations (6.24) and (6.25) indicates that there is a phase difference of $\pi/4$ between the arguments of the cosines. In order to compare the amplitudes we must take account of collision broadening in $\Delta\sigma_1$. This we can do in a crude way by means of the broadening distribution $\gamma/\pi[\delta^2+\gamma^2]$. Folding this distribution into $\delta^{-\frac{1}{2}}$ multiplies the summand in equation (6.24) by a factor $\exp(-2\pi M\gamma)$. In a similar way we take account of thermal broadening by averaging $\Delta\sigma_1$ and $\Delta\sigma_2$ over the thermal distribution

$$-\frac{df_0}{dE} = \{4KT\cosh^2[(E-\zeta)/KT]\}^{-1} \tag{6.26}$$

This thermal average introduces a factor

$$\left(\frac{2\pi^2 MKT}{\hbar\omega}\right)\Big/\sinh\left(\frac{2\pi^2 MKT}{\hbar\omega}\right) \tag{6.27}$$

into the summands of equations (6.24) and (6.25).

The relative importance of the two kinds of oscillatory term depends on the magnitude of the Fermi energy and of γ. If the oscillations are very large so that the amplitude of the oscillation is much greater than the smooth resistance, then the dominant term is $\Delta\sigma_2$. The resistivity in such a situation would exhibit high narrow maxima

separated by wide shallow minima, and the value at maximum would be given approximately by equation (6.23) suitably modified to take account of thermal broadening. If, on the other hand, the oscillations have an amplitude smaller than the magnitude of the steady conductivity, the conductivity $\Delta\sigma_1$ can be chiefly responsible for the oscillatory phenomena, which should then be analyzed using equations (6.20) and (6.22) with an appropriate value of the relevant parameters. We might expect that in general the importance of M, N, q_z, k_z will be different for each scattering mechanism. An especially important other mechanism is the scattering by ionized impurities. We have chosen to investigate it, both because of its importance for experiment and because it represents, with respect to the range of interaction, the opposite extreme case from lattice scattering.

Using the form $A=[q_s^2+q^2]^{-2}$ for the squared Fourier component of the interaction and the asymptotic formula (6.5), we obtained for the bracketed sum in equation (6.2) the expression

$$\left.\begin{aligned} I_{\pm} &= \frac{A}{4}\frac{[[M+N)(M+N+\epsilon^{\pm})-4MN]}{[(M+N+\epsilon^{\pm})^2-4MN]^{\frac{1}{2}}} \\ \epsilon_{\pm} &= \tfrac{1}{2}q_s^2+[\sqrt{(\zeta-M-\tfrac{1}{2})}\pm\sqrt{(\zeta-N-\tfrac{1}{2})}]^2 \end{aligned}\right\} \quad (6.28)$$

$\Delta\sigma_2$ will be limited to situations in which the Fermi energy is not very many times as great as the magnetic quantum, so that only a few oscillator levels are involved in the transport process. The chief practical difference between phenomena dominated by $\Delta\sigma_1$, and those dominated by $\Delta\sigma_2$ is in the phase of the oscillations.

Equation (6.27) shows that thermal broadening can substantially reduce the amplitude of the higher harmonics in a harmonic expansion. Thus raising the temperature acts to convert the oscillations to a progressively more perfect sinusoidal form. The effect of thermal broadening is somewhat larger than one would estimate from order-of-magnitude considerations, since the quantity $(kT/\hbar\omega)$ in the broadening formula appears multiplied by a coefficient $2\pi^2\sim 20$. Thus, for example, for experiments done with samples at the temperature of liquid helium the magnetic level spacing must be of the order of 0·01 eV in order that the oscillations be well defined.

The treatment of the oscillatory phenomena for scattering mechanisms other than acoustical scattering can be carried out along the same lines as the theory above. General formulae cannot be given, since the detailed dependence of the matrix elements $|V_{qN_\nu}|^2$ on the quantum numbers

The two signs in equation (6.28) refer to the two values of q_z which conserve energy in the transition from m to n for a given value of k_z. The expressions $I_\pm$ must now be inserted in equation (6.2) and summed over M and N.

The dependence of the expression (6.28) on the quantum numbers M and N is very complicated, and even if the sum (6.2) were carried out exactly it is doubtful that the formula would be especially useful in its exact form. It is not difficult to get good approximate formulae for the oscillatory phenomena if we take advantage of the fact that the steady part of the conductivity can be calculated by the same means as in the usual theory of transport phenomena at high quantum numbers. The term in the conductivity proportional to δ^{-1} is readily found to be

$$\Delta\sigma_2=(2\pi)^{-3}(A/16\delta\zeta^{\frac{1}{2}})[(E_s+4\delta)^{-\frac{1}{2}}+E_s^{-\frac{1}{2}}] \quad (6.29)$$

The term proportional to $\delta^{-\frac{1}{2}}$ can be calculated by noting that most of the contribution comes from states of quantum number near the maximum and making an appropriate expansion of the integrand of (6.2). The approximate value we obtained for this term is

$$\Delta\sigma_1=(2\pi)^{-3}(A/2\delta^{\frac{1}{2}}\zeta^{\frac{1}{2}})[\sinh(\zeta/E_s)^{\frac{1}{2}}-(\tfrac{1}{2}+\delta)^{\frac{1}{2}}] \quad (6.30)$$

In the same units the steady value of the conductivity is given by

$$\sigma_0=(2\pi)^{-3}(A/6)[\ln(4\zeta/E_s)-1] \quad (6.31)$$

Combining equations (6.29)–(6.31) and inserting dimensional units, we find in the same notation as used for equations (6.20), (6.21).

$$\Delta\sigma_1=\sigma_0\left[\ln\left(\frac{4\zeta}{E_s}\right)-1\right]^{-1}\left(\frac{\hbar\omega}{\zeta}\right)^{\frac{1}{2}}\left(\frac{\hbar\omega}{E_z}\right)^{\frac{1}{2}}\left\{\sinh^{-1}\left(\frac{\zeta}{E_s}\right)^{\frac{1}{2}}-\left(\frac{\tfrac{1}{2}\hbar\omega+E_z}{E_z}\right)^{\frac{1}{2}}\right\} \quad (6.32)$$

$$\Delta\sigma_2=\frac{3}{8}\sigma_0\left[\ln\left(\frac{4\zeta}{E_s}\right)-1\right]^{-1}\left(\frac{\hbar\omega}{\zeta}\right)^{\frac{1}{2}}\left(\frac{\hbar\omega}{E_z}\right)\left\{\left(\frac{\hbar\omega}{E_s+4E_z}\right)^{\frac{1}{2}}+\left(\frac{\hbar\omega}{E_s}\right)^{\frac{1}{2}}\right\}$$

VOL. 10 1959

We have separated the oscillatory terms into the two parts, although we have not gotten explicit expressions giving the shape in the part of the cycle when δ is not near zero. This should occasion no real difficulty in making a Fourier analysis, since the terms given in equations (6.29) and (6.30) are rapidly varying ones. In comparing the formula (6.32) with the formulae (6.20), (6.21) we will use the behavior near $\delta \simeq 0$ to estimate the relative magnitudes of the various quantities.

Comparing the term in equation (6.32) that varies like $\delta^{-\frac{1}{2}}$ with the oscillatory conductivity $\Delta\sigma_1$ given by equation (6.20) for $\zeta > E_s$ so that

$$\sinh^{-1}\left(\frac{\zeta}{E_s}\right)^{\frac{1}{2}} \sim \frac{1}{2}\ln\left(\frac{4\zeta}{E_s}\right)$$

we find that

$$(\Delta\sigma_1/\sigma_0)^{\text{Ion Imp}}/(\Delta\sigma_1/\sigma_0)^{\text{Ac Lat}} \approx \frac{6}{5}\ln\left(\frac{4\zeta}{E_s}\right)\Big/\left[\ln\frac{4\zeta}{E_s}-1\right] \sim 1^{+} \quad (6.33)$$

Similarly

$$(\Delta\sigma_2/\sigma_0)^{\text{Ion Imp}}/(\Delta\sigma_2/\sigma_0)^{\text{Ac Lat}} \approx \left(\frac{4\zeta}{E_s}\right)^{\frac{1}{2}}\Big/\left[\ln\left(\frac{4\zeta}{E_s}\right)-1\right] \gtrsim 2 \quad (6.34)$$

for representative values of the parameters ζ and E_s.

The correction $\Delta\sigma_1$ is the more important for large quantum numbers. We might conclude that the relative amplitudes of the oscillatory phenomena are very much the same for the mechanism of ionized-impurity scattering as for lattice scattering. In view of the fact that there is an undetermined dependence of the line broadening on scattering mechanism, a completely quantitative comparison can not be made on the above basis. It seems appropriate to comment on the similarity of the results, which are certainly closer than might have been predicted *a priori*.

7. DISCUSSION

(a) *Quantum limit*

Of the interactions listed in Table 1, each plays a role in galvanomagnetic phenomena in some range of temperature and/or concentration in some semiconductor or semimetal that has been extensively investigated (with the exception of the point defect scattering, which we include because it has been used in several theoretical papers as a basis for treating impurity scattering). In our treatment every scattering mechanism is treated as elastic; however, it requires no more than a minor modification of our formulae to take into account the finite energy of the quanta involved in the inelastic processes. We have discussed both the degenerate and the non-degenerate limits, since both cases can occur in practice.

Tables 2–5 show that a great variety of field- and temperature-dependences are possible to the extent that the various scattering mechanisms can be made dominant. It would probably not be feasible to investigate all of the scattering mechanisms using a single material. However, by varying temperature and magnetic field and by working with doped samples and hot carriers, one might arrange to observe several scattering mechanisms operative in a single material. In particular the very strong field-dependences of the scattering and the differences in the field-dependence for different scattering mechanisms offers the possibility of using a strong magnetic field to supplant one scattering mechanism by another in experiments done at a single temperature.

We have been particularly interested in experiments done on InAs and InSb. We do not desire to discuss such experiments in any detail here. However, we will point out that our theory may find experimental confirmation in the linear dependence of resistivity on magnetic field at large fields, recently observed by BATE *et al.*[14] in InSb at the temperature of liquid air. Under the conditions of these experiments the formulae of Table 5 should be expected to apply. An examination of this table shows that only for the optical mode or piezoelectric modes of scattering should such a linear dependence be observed. From other evidence it is expected that a combination of just these two modes should be dominant at the temperatures and fields used in the experiments.[15,16] This experiment is significant in that alternative theories[8] would lead to a different field-dependence for these same scattering mechanisms and under the conditions of the experiment.

The theory shows that the quantum limit offers certain unique features for experiment. Only in the quantum limit can really large changes in the scattering be induced by a magnetic field. The reason the effects are so much greater in this regime may be seen from the series of drawings

represented in Figs. 1–3. These drawings attempt to depict in a Fermi–Thomas sense how the distribution of the electrons in momentum space is affected by the magnetic field. These intuitive drawings

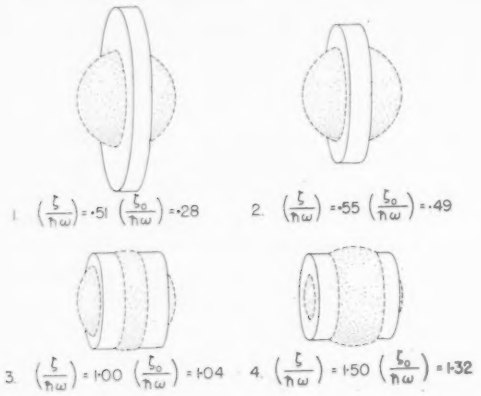

FIG. 1. Variation of Fermi surface with magnetic field in quantum limit. The sphere encloses the momentum states occupied when $H = 0$. The cylinder indicates the approximate volume of momentum space occupied in the presence of the field. The sequence progresses from stronger to weaker fields.

have their basis in the matrix elements and density of states that come into the theory. They show clearly that a large overall distortion of the Fermi surface occurs in the extreme quantum regime,

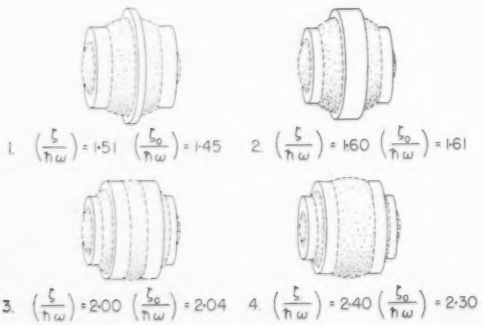

FIG. 2. Variation of Fermi surface with magnetic field when only states $N = 0$, $N = 1$ contain electrons. The progression is from strong to weak fields.

whereas only local distortions occur when the Fermi level is of the order $\hbar\omega$ or larger. This overall distortion has the result that the magnetoresistance effects in the quantum limit are much larger than other magnetoresistance effects, since the scattering matrix elements become a function of magnetic field as the Fermi surface becomes distorted.

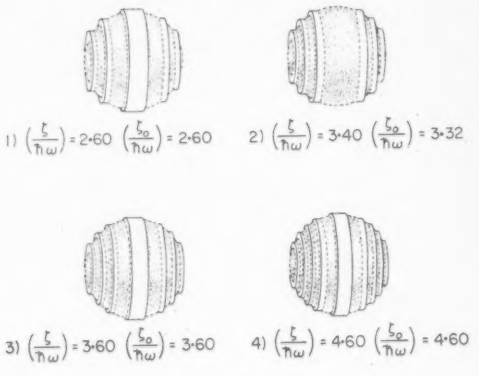

FIG. 3. Variation of Fermi surface with field, showing the increasingly spherical shape as the field becomes weaker.

A noteworthy feature of the quantum limit phenomena is that the ratio of transverse to longitudinal resistivity is approximately the same for all of the scattering mechanisms considered other than ionized-impurity scattering. The result that

$$(\rho_T/\rho_L)_{\text{Q.L.}} \sim \hbar\omega/\langle E_z\rangle \tag{7.1}$$

is in contrast to the normal classical situation in which ρ_T and ρ_L are very nearly the same. The inequality of these two resistivities is not related to the effect of quantization on the relaxation time: the classical formulae relating the resistivities to the relaxation time, viz.

$$\rho_L \sim m/ne^2\tau \tag{7.2}$$

$$\rho_T \sim \frac{m}{ne^2\tau}\cdot\frac{d\ln n}{d\zeta}\cdot\tfrac{1}{2}m\omega^2\langle d^2\rangle \tag{7.3}$$

remain valid. What is different about the quantum limit is that the mean square jump distance is now $L^2 \equiv \hbar/m\omega$ rather than $(E/m\omega^2)$ as in the high-quantum-number situation. Thus, in terms of the thermal energy of the carrier, the transverse resistivity in the quantum limit is anomalously large, in fact, just in the ratio $(\hbar\omega/E_z)$. This may be viewed as meaning that in the quantum limit the

jumping distance is determined by the zero point energy, rather than the thermal energy.

The above remarks apply for reasonably short-range interactions, for which large momentum transfer scattering predominates and a collision time exists which is much the same for all processes. In contrast, the Coulomb interaction is of such very long range that the collision time is no longer the same for all processes. For this interaction, and any interaction of longer range, the longitudinal momentum transfer time is shorter than the mean collision time for the transverse conduction in the ratio $E_s/\hbar\omega$. Thus for the Coulomb and other long-range interactions the ratio ρ_T/ρ_L will be approximately independent of field, just as in the classical case.

(b) *Oscillatory phenomena*

Our treatment of the transverse oscillatory conductivity comprises two parts. The first is the separation of the oscillatory conductivity into two parts, $\Delta\sigma_1$, which yields the main contribution at large quantum numbers, and $\Delta\sigma_2$, which is important when only a few quantum states are occupied, and to determine the field-dependence and harmonic composition of these. The relative magnitudes and relative importance of $\Delta\sigma_1$ and $\Delta\sigma_2$ was found to depend on the collision broadening of the energy levels near the edge of a new quantum level. Our crude treatment indicates that either $\Delta\sigma_1$ or $\Delta\sigma_2$ can be dominant and that the phase of the oscillatory phenomena is different by $\pi/2$ in the two cases.

The second part of this study was to investigate the dependence of the amplitude of the oscillatory conductivity on the nature of the scattering mechanism. We found (cf equation (6.33)) that the conductivity $(\Delta\sigma_1/\sigma_0)$ was virtually the same for acoustical scatterings as for ionized-impurity scattering. The quantity $\Delta\sigma_2/\sigma_0$ was about twice as large for the impurity-scattering mechanism (cf. equation (6.34)), as for the lattice-scattering mechanism. Our reaction to these results is that the dependence of the oscillations on scattering mechanism is not very important; one is unlikely to find much dependence of the oscillatory phenomena on scattering mechanism when the results are so much the same for two such different scattering mechanisms. However, one might be able to observe some dependence on scattering mechanism by studying the effects at very large fields so that there remain only a last few oscillations before the quantum limit is reached.

In view of the above discussion we would expect that the phase of the last few oscillations would in some cases be substantially different than is given by the high-quantum-number approximation. Of course, we cannot make quantitative statements about phases apart from assumptions about collision broadening. However, we observe that the phase of $\Delta\sigma_2$ could well differ from that of $\Delta\sigma_1$, by as much as $\pi/4$, and $\Delta\sigma_2$ becomes relatively more important as the field gets higher. For higher maxima, $(\Delta\rho > \rho_0)$, for which $\Delta\sigma_2$ dominates, $\Delta\sigma_2$ should fix the phase. As a consequence one might even find some dependence of phase on scattering mechanism at very high fields, to the extent that the scattering mechanism conditions the dominance of $\Delta\sigma_2$.

(c) *Comparison with other theories: quantum limit phenomena*

The theories which have explicitly been concerned with the quantum limit are the theories of TITEICA[1], of ARGYRES and ADAMS[3] for the longitudinal magnetoresistance, and of ARGYRES[7,8]. The more general theory of LIFSHITZ[4] is concerned only with the high-quantum-number situation. The theory of TITEICA, which treated acoustical scattering in the quantum limit, concerned itself with good metals in which the Fermi momentum is comparable to the Debye momentum. As a consequence his results are not directly comparable to ours, which are derived implicitly assuming that we have to do with semiconductors and semimetals. The only direct comparison of results which we can make is with the work of ARGYRES, who has given formulae for the Hall effect and resistivity in the quantum limit for the case of elastic acoustical scattering.

In order to compare ARGYRES's formulae with ours, it is necessary to reduce them so that only the lowest powers of $(\omega\tau)^{-1}$ occur. When this is done we find differences between our formulae for both the Hall effect and the magnetoresistance. The difference between our formulae for the Hall effect is that in addition to the zero-order term $1/Nec$, ARGYRES gives corrections which are apparently of the order $(\omega\tau)^{-1}$ when certain obvious corrections are made. We do not know what

feature of his calculation gives this result, since the relevant equations are not given. However, it seems that ARGYRES's corrections are erroneous. From our equation (4.5) it can be shown that when the conductivity is expanded as a power series in $(\omega\tau)^{-1}$ the first corrections to the Hall coefficient are of order $(\omega\tau)^{-2}$.

Comparing formulae for the resistivity, we find a sharp disagreement between the theories in the predicted dependence of the transverse resistivity on magnetic field. ARGYRES's formulae[8] have the resistivity substantially proportional to H^2 in the degenerate case and H^{+1} in the non-degenerate case, while our formulae have the resistivity proportional to H^5 in the degenerate case and H^2 in the non-degenerate case. We have traced the origin of this discrepancy to a difference in the treatment of scattering in the two theories. We will discuss this matter in more detail below, where we will show that as a consequence of the way ARGYRES treats scattering he should not find, as we did, an extra factor $(\hbar\omega/E)$ in the transverse resistivity in the quantum limit, and should find, as he does, that the ratio of longitudinal to transverse resistivity depends only weakly on field.

We attribute the discrepancy between the results of our theory and that of ARGYRES to approximations which he has made that are invalid for treating the phenomena at small quantum numbers. We do not wish to give a point-by-point discussion of his calculations, which would not in any case be profitable for our present purpose. However, we want to indicate what feature of his treatment of scattering makes it invalid at low quantum numbers. The theory of ARGYRES is based on an equation he deduces (cf. Ref. (8) equation (5.21)) for the time development of the density matrix, which is somewhat analogous to the Boltzmann equation. It can be written in the form

$$\frac{\partial\rho}{\partial t} = i[\rho, H_0]+i[\rho, -XF]+\frac{\partial\rho}{\partial t}\bigg|_{sc} \qquad (7.4)$$

where $\partial\rho/\partial t_{sc}$ is to be represented as arising from the effects of a collision operator on ρ, *this collision operator being dependent on the scattering interaction but not on the force field* F. Such description is valid for the ordinary d.c.-conductivity problems, where ρ may be replaced by the Boltzmann function f and the eigenvalues of energy have a continuous spectrum. ARGYRES has assumed that a direct matrix generalization is valid in the magnetic-field case where the spectrum is partly discrete, and has accordingly omitted terms of order higher than the second in the exact equation for $\partial\rho/\partial t|_{sc}$. The same approximation has been used by LIFSHITZ[4] in his theory, applied, however, only to the case of large quantum numbers.

We want to show now that the use of this "Boltzmann-like" approximation results in the absence of the "anomalous" factor $(\hbar\omega/E)$ which we observed in our transverse resistivity formulae. We note that in order to calculate the current one needs a solution of equation (7.4) of first order in F and the scattering, obtained as a perturbation series from the unperturbed density matrix ρ_0. In the quantum limit the only non-vanishing element of the unperturbed density matrix is ρ_{00}, i.e. only states in the lowest oscillator level are occupied and a complete description of the system is obtained by giving the populations of the states. From purely dimensional considerations it follows that the solution of equation (7.4) for the off-diagonal element ρ_{10} will be of the form

$$\rho_{01} = FL\rho_{00}/\hbar\left(\omega+\frac{i}{\tau}\right) \qquad (7.5)$$

The transverse current is obtained from the imaginary part of ρ_{01} and is the integral

$$J_x = -\frac{eF}{m\omega^2}\int\frac{\rho_{00}n(E)dE}{\tau} \qquad (7.6)$$

The corresponding equation from our theory will be

$$J_x = \frac{eF}{m\omega^2}\int\hbar\omega\frac{d\rho_{00}}{dE}\cdot\frac{n(E)dE}{\tau} \qquad (7.7)$$

Now, the τ occurring in the various theories are essentially the same, since they represent the reciprocal of the total transition rate out of a given state. We see, then, that the two theories differ in their predictions because of the presence in equation (7.7), but not in (7.6), of the dimensionless factor, $\hbar\omega/E$.

The presence of the factor $\hbar\omega(d\rho_{00}/dE)$ rather than ρ_{00} in our theory comes about because of the involvement of the electric field in the energy-conservation condition in scattering. The presence of the derivative represents the physical fact that the electric current flows *as a result of the effect of the electric field on the scattering*. This feature is absent from the theory of ARGYRES[8]; as a consequence his theory can not give the proper scattering behavior, at least until the temperature is so high that his factor $[\rho(E+\hbar\omega)-\rho(E)/\hbar\omega]$ can be replaced by $d\rho/dE$, which is to say, until $\hbar\omega \ll KT$. This entire question has analogues

VOL. 10 1959

in the theory of high-frequency electrical conduction,[17] where difficulty is encountered in the use of the ordinary Boltzmann transport equation.

(d) *Comparison with other theories: oscillatory phenomena*

Theories of the oscillatory phenomena have been given by DAVYDOV and POMERANCHUK[2], by LIFSHITZ[4], by LIFSHITZ and KOSEVITCH[5], and by ARGYRES[7,8]. The original work of DAVYDOV and POMERANCHUK is closely related to that of TITEICA[1], although they calculated the electrical conductivity directly rather than by use of the Einstein relation. Their work contains implicitly all of the results obtainable by our theory, although some of these were not written out explicitly. The model of point-defect scattering was used in this work, according to which the scattering matrix element is independent of wave number. As a consequence the results of DAVYDOV and POMERANCHUK should be compared with calculations of the acoustical lattice scattering. DAVYDOV and POMERANCHUK have not discussed the details of the general galvanomagnetic phenomena, being concerned principally with interpreting the phenomena for bismuth in terms of mass and number parameters. They did, however, point out the difference between the two kinds of processes that lead to $\Delta\sigma_1$ and $\Delta\sigma_2$, respectively, and they discussed the general qualitative features of the phenomena on the basis of theory. Their work is in essential agreement with ours.

LIFSHITZ and ARGYRES have given more elaborate theories of the transverse galvanomagnetic phenomena. LIFSHITZ[4] has treated the oscillatory phenomena for general energy surfaces and general scattering mechanisms. He has been concerned primarily with the relation of the galvanomagnetic phenomena to the de Haas–van Alphen effect and its use to give information about the shape of a Fermi surface. His treatment of the scattering mechanism in terms of the "classical mobility tensor" was designed to establish a connection between high-quantum-number "steady" galvanomagnetic phenomena, the de Haas–van Alphen effect, and the oscillatory galvanomagnetic phenomena at large quantum numbers. He realized that there would be other oscillatory phenomena at low quantum numbers. The feature of his results to which we will make reference is that he expressed the conductivity oscillations linearly in terms of the oscillatory moment with coefficients of proportionality derived from the "classical mobility tensor".

ARGYRES[8] has done a calculation using the same mechanical system (of free electrons) that we have studied and the acoustical lattice scattering interaction. ARGYRES and LIFSHITZ have both used density matrix formulations of the theory, and have used a similar treatment of the effect of collisions on the density matrix. We have described this treatment in discussing the quantum limit phenomena, where we have shown it is not really valid. We would not expect it to be valid in the region of the oscillatory phenomena either, since the replacement of $d\rho_0/dE$ by the function $[\rho(E+\hbar\omega)-\rho(E)/\hbar\omega]$ is in a sense equivalent to thermal broadening with a temperature of $(\hbar\omega/K)$. Thus we should expect these theories to give oscillations of less than the correct amplitude.

An examination of the formulae of ARGYRES and of LIFSHITZ for the oscillatory conductivity $\Delta\sigma_{xx}$ shows that in each case they do not in fact exhibit the oscillations characteristic of a singular function like $\delta^{-\frac{1}{2}}$, but rather those characteristic of $\delta^{\frac{1}{2}}$. Both authors find that the amplitude of the oscillations fall off like $(\hbar\omega/\zeta)^{\frac{1}{2}}$ and that the amplitude of the M^{th} harmonic is proportional to $M^{-\frac{1}{2}}$, whereas our formula (6.24) states that $\Delta\sigma_1$ falls off like $(\hbar\omega/\zeta)^{\frac{1}{2}}$ and the amplitudes of the M^{th} harmonic falls off like $M^{-\frac{1}{2}}$. Thus the extra averaging in these theories, by removing the singular behavior, has acted to substantially decrease the oscillatory behavior. The difference between $\delta^{-\frac{1}{2}}$ and $\delta^{\frac{1}{2}}$ is so great that an experimental differentiation between the two possibilities should be easily feasible.

It may be remarked that LIFSHITZ and KOSEVICH[5] predict a similar $\delta^{\frac{1}{2}}$-type oscillation in the longitudinal conductivity, whereas ARGYRES[7] finds there the $\delta^{-\frac{1}{2}}$ singularity which we would expect. This we take as an indication that LIFSHITZ's treatment also neglects the effect of quantization on the relaxation time, an effect which ARGYRES correctly takes into account.

Acknowledgements—We would like to acknowledge a number of helpful conversations with our colleagues EUGENE BLOUNT on various aspects of the quantum mechanical theory of transport and RONALD SLADEK on

the experimental quantum effects. We have also benefited from several conversations with Professor RYOGO KUBO who has kindly communicated some of his results prior to publication.

APPENDIX A

In this Appendix, the text equation (4.3), which reads

$$\Delta J^y+iJ^x=-\pi iF\sum_{Nk_yk_z\nu}q_y\delta(\omega_{N\nu})\frac{df_\nu}{d\omega}[\sqrt{[2(N+1)]}V_{N+1\nu}V_{\nu N}+\sqrt{(2N)}V_{N\nu}V_{\nu N-1}] \tag{A.1}$$

will be shown to be equivalent to the text equation (4.5).

We may begin by introducing the relations

$$\sqrt{[2(N+1)]}\phi_{N+1}(x)=\left(x-\frac{\partial}{\partial x}\right)\phi_N(x) \tag{A.2}$$

$$\sqrt{(2N)}\phi_{N-1}(x)=\left(x+\frac{\partial}{\partial x}\right)\phi_N(x) \tag{A.3}$$

(valid for harmonic-oscillator eigenfunctions) into (A1). The result is

$$\Delta J^y+iJ^x=-\pi iF\sum_{\mu\nu}\delta(\omega_{\mu\nu})\frac{df}{d\omega_\nu}q_y\left[\{(x-X_\mu)V\}_{\mu\nu}V_{\nu\mu}+V_{\mu\nu}\{V(x-X_\mu)\}_{\nu\mu}+\left(\frac{\partial}{\partial x}V\right)_{\mu\nu}V_{\nu\mu}+V_{\mu\nu}\left(V\frac{\partial}{\partial x}\right)_{\nu\mu}\right] \tag{A.4}$$

Here, the Greek letters μ and ν represent the quantum numbers N, k_y, k_z and N', k_y', k_z', respectively; also expressions of the type $[(\partial/\partial x)V]_{\mu\nu}$ and $(xV)_{\mu\nu}$ designate the matrix elements of operator products. The occurrence of the "orbit centers", X_ν and X_μ, arises from the circumstance that the wave functions, $\phi_{\mu,\nu}$, are centered about the $X_{\mu,\nu}$. Finally, in obtaining the third term in the square bracket of (A.4), an integration by parts was employed.

Let us now "symmetrize" (A.4) by adding to it the expression obtained by interchanging $_\mu$ and $_\nu$, and dividing by two. Then, remembering that $q_y\equiv X_\nu-X_\mu$ alters its sign in this interchange, we find

$$\Delta J^y+iJ^x=-\pi iF\sum_{\mu\nu}\delta(\omega_{\mu\nu})\frac{df_\nu}{d\omega}q_y[A_1+A_2+A_3] \tag{A.5}$$

where

$$A_1=(X_\nu-X_\mu)V_{\mu\nu}V_{\nu\mu} \tag{A.6}$$

$$A_2=\tfrac{1}{2}[(xV-Vx)_{\mu\nu}V_{\nu\mu}+V_{\mu\nu}(Vx-xV)_{\nu\mu}] \tag{A.7}$$

$$A_3=\tfrac{1}{2}\left[\left(\frac{\partial}{\partial x}V-V\frac{\partial}{\partial x}\right)_{\mu\nu}V_{\nu\mu}+V_{\mu\nu}\left(V\frac{\partial}{\partial x}-\frac{\partial}{\partial x}V\right)_{\nu\mu}\right] \tag{A.8}$$

With V being a function of r, the commutator $(xV-Vx)$ vanishes and hence A_2 is immediately seen to vanish whereas A_3 becomes

$$A_3=\tfrac{1}{2}\left[\left(\frac{\partial V}{\partial x}\right)_{\mu\nu}V_{\nu\mu}-V_{\mu\nu}\left(\frac{\partial V}{\partial x}\right)_{\nu\mu}\right] \tag{A.9}$$

At this point, it is desirable to express V in terms of its space-Fourier expansion:

$$V(r)=\sum_q\exp(iq\cdot r)V_q \tag{A.10}$$

in which, because of the reality (i.e. hermiticity) of $V(r)$,

$$V_{-q}=V_q^* \tag{A.11}$$

In substituting (A.10) into the A_i, one has to take account of the so-called "infinite-variation" property of the V_q's, discussed in the text. This property has the consequence that products of the type $V_{q'}V_q$ are to be taken equal to zero, except when $q'=-q$, i.e.

$$V_{q'}V_q=\delta_{q',-q}|V_q|^2 \tag{A.12}$$

Applying this recipe, one then has

$$A_1-\sum_q(X_\nu-X_\mu)|V_q|^2[\exp(iq\cdot r)]_{\mu\nu}|^2 \tag{A.13}$$

whereas

$$A_3 = \sum_q iq_x |V_q|^2 |[\exp(iq\cdot r)]_{\mu\nu}|^2 \quad \text{(A.14)}$$

Inserting (A.13) and (A.14) into (A.5), and remembering that $X_\nu - X_\mu = q_\nu$ we then have

$$\Delta J^y + iJ^x = -\pi i F \sum_{\mu\nu q} |V_q|^2 q_y(q_y + iq_x)|[\exp(iq\cdot x)]_{\mu\nu}|^2 \quad \text{(A.15)}$$

APPENDIX B

We wish to have analytic approximations for the sums

$$S(I, p) = \sum_{N=0}^{I} [N+\delta]^{\frac{1}{2}+p} \quad \text{(B.1)}$$

with $p = 1, 0-1$. We make use of the identity

$$\frac{(I+\frac{1}{2}+\delta)^{p+\frac{3}{2}}}{(p+\frac{3}{2})} = \frac{(\frac{1}{2}+\delta)^{p+\frac{3}{2}}}{(p+\frac{3}{2})} + \int_{-\frac{1}{2}}^{\frac{1}{2}} dx \sum_{N=1}^{I} [N+\delta+x]^{\frac{1}{2}+p} \quad \text{(B.2)}$$

Developing the integrand of the last term by the binomial theorem and integrating, we obtain

$$\frac{(I+\delta+\frac{1}{2})^{p+\frac{3}{2}} - (\frac{1}{2}+\delta)^{p+\frac{3}{2}}}{(p+\frac{3}{2})} = \sum_{N=1}^{I} \{[N+\delta]^{p+\frac{1}{2}} + \tfrac{1}{24}(p+\tfrac{1}{2})(p-\tfrac{1}{2})[N+\delta]^{p-\frac{3}{2}} + \ldots\} \quad \text{(B.3)}$$

The first omitted term in the series is at maximum of order 0·001. The last term retained is at maximum of the order of 5–10 per cent. Adding $\delta^{p+\frac{3}{2}}$ to each side and rearranging, we find

$$S(I, p) = \frac{(\zeta/\hbar\omega)^{p+\frac{3}{2}} - (\frac{1}{2}+\delta)^{p+\frac{3}{2}}}{(p+\frac{3}{2})} + \delta^{p+\frac{1}{2}} - \sum_{N=1}^{I} (p^2-\tfrac{1}{4})\tfrac{1}{24}[N+\delta]^{p-\frac{3}{2}} \quad \text{(B.4)}$$

The last term may be approximated by iteration, and we finally obtain

$$S(I, p) = \frac{(\zeta/\hbar\omega)^{p+\frac{3}{2}} - (\frac{1}{2}+\delta)^{p+\frac{3}{2}}}{p+\frac{3}{2}} + \delta^{p+\frac{1}{2}} - \tfrac{1}{24}(p+\tfrac{1}{2})[(\zeta/\hbar\omega)^{p-\frac{1}{2}} - (\tfrac{1}{2}+\delta)^{p-\frac{1}{2}}] \quad \text{(B.5)}$$

As an alternative to retaining the last term, one may treat *two* terms of the sum exactly and considerably increase the rate of convergence of the binomial series. Thus the remainder term is ordinarily only a few per cent in the following:

$$S(I, p) = \frac{(\zeta/\hbar\omega)^{p+\frac{3}{2}} - (\frac{3}{2}+\delta)^{p+\frac{3}{2}}}{p+\frac{3}{2}} + \delta^{p+\frac{1}{2}} + (1+\delta)^{p+\frac{1}{2}} \quad \text{(B.6)}$$

APPENDIX C

The Poisson sum formula for the oscillatory part of a function

$$f(x) = \sum_{n=-\infty}^{\infty} g(x+m) \quad \text{(C.1)}$$

is

$$f(x)_{\text{osc}} = \sum_{M\neq 0} \exp(2\pi i M x) G(2\pi M) \quad \text{(C.2)}$$

where $G(k)$ is the Fourier transform of $g(x)$. The applications in this paper are to the functions, the most strongly varying oscillatory parts of which are given below:

$$\delta^{-\frac{1}{2}} \approx 2\sqrt{(\pi)} \sum_{M>0} (2\pi M)^{-\frac{1}{2}} \cos\left(2\pi M\delta - \frac{\pi}{4}\right) \quad \text{(C.3)}$$

In terms of ζ and $\hbar\omega$ this is

$$\delta^{-\frac{1}{2}} \approx 2\sqrt{(\pi)} \sum_{M>0} (2\pi M)^{-\frac{1}{2}} (-)^M \cos\left(\frac{2\pi M\zeta}{\hbar\omega} - \frac{\pi}{4}\right) \quad \text{(C.3A)}$$

Other cases of interest include

$$\delta^{\frac{1}{2}} \approx \sqrt{(\pi)} \sum_{M>0} (2\pi M)^{-\frac{1}{2}} \cos\left(2\pi M\delta + \frac{\pi}{4}\right) \quad \text{(C.4)}$$

$$\delta^{\frac{3}{2}} \approx \tfrac{3}{2}\sqrt{(\pi)} \sum_{M>0} (2\pi M)^{-\frac{3}{2}} \cos\left(2\pi M\delta + \frac{3\pi}{4}\right) \quad \text{(C.5)}$$

In order to analyse δ^{-1} we must make some assumption about line broadening. To obtain the equations of Appendix C we rather arbitrarily replaced δ^{-1} by $\delta/[\delta^2+\gamma^2]$ for positive values of $R\delta$, 0 for negative values. The Fourier transform of this function is

$$F(k) = -\frac{\pi}{2} i \exp(-k\gamma) + \tfrac{1}{2}[1 + \exp(-2k\gamma)] \times$$

$$\times \int_0^\infty \frac{dx \exp(-x)}{x+k\gamma} + \tfrac{1}{2} \exp(-k\gamma) \int_{-k\gamma}^{k\gamma} \frac{\exp(-x)-1}{x} dx$$

$$F(-k) = F(k)^* \qquad \text{(C.6)}$$

This function may be approximated by

$$F(k) \doteq -\frac{\pi}{2} i \exp(-k\gamma) + \ln(k\gamma)^{-1} \qquad (k\gamma \ll 1)$$

$$F(k) \doteq \tfrac{1}{2}(k\gamma)^{-1} \qquad (k\gamma \gg 1) \qquad \text{(C.7)}$$

An approximation to (C.7) sufficient for our purpose allows us to represent δ^{-1} by

$$\delta^{-1} \doteq \sum_{M=1}^{\infty} \{\pi \exp(-2\pi M\gamma) \sin 2\pi M\gamma + [\ln(2\pi M\gamma)^{-1} - 1] \cos 2\pi M\gamma\} \qquad \text{(C.8)}$$

The second term is only significant relative to the first when γ is very small, so it can probably be neglected in most cases.

REFERENCES

1. Titeica S., *Ann. Phys.* (*Leipzig*) **22,** 128 (1935).
2. Davydov B. and Pomeranchuk I., *J. Phys., Moscow* **2,** 147 (1940).
3. Argyres P. N. and Adams E. N., *Phys. Rev.* **104,** 900 (1956).
4. Lifshitz E. M., *JETP* **3,** 774 (1956); *J. Phys. Chem. Solids* **4,** 11 (1958).
5. Lifshitz I. M. and Kosevich A. M., *J. Phys. Chem. Solids* **4,** 1 (1958).
6. Kubo R., Private communication; *Canad. J. Phys.* **34,** 1274 (1956); *Phys. Rev. Letters* **1,** 279 (1958).
7. Argyres P., *J. Phys. Chem. Solids* **4,** 19 (1958).
8. Argyres P., *Phys. Rev.* **109,** 1115 (1958).
9. Johnson M. and Lippman B., *Phys. Rev.* **76,** 1949. The paper contains a good summary of the required formulae.
10. de Haas W. J. *et al.*, *Commun. K. Onnes Lab. Leiden* No. 237 (1935).
11. Sladek R., *Phys. Rev.* **110,** 817 (1958). Fredrikse R. and Hosler W., *Phys. Rev.* **110,** 880 (1958). These works were carried out on semiconductors.
12. Feshbach H. and Morse P. M., *Methods of Theoretical Physics* Part I, p. 464. McGraw-Hill Book Co., New York (1953).
13. Meyer H. and Polder D., *Physica* **19,** 255 (1953).
14. Bate R., Willardson R., and Beer A., Private communication.
15. Harrison W., *Phys. Rev.* **100,** 903 (1956).
16. Ehrenreich H., *J. Phys. Chem. Solids* **2,** 131 (1957).
17. See, for example, Gurzhi R., *JETP* **6,** 352 (1958).

VOL. 10 195

J. Phys. Chem. Solids Pergamon Press 1959. Vol. 10. pp. 277–285. Printed in Great Britain.

CALCUL SEMI-EMPIRIQUE DE LA TEMPERATURE DE TRANSITION DES SUPERCONDUCTEURS ET DE L'EFFET DE LA PRESSION SUR LA TRANSITION

PIERRE MOREL*

École Normal Supérieure, Paris

(*Received* 1 *December* 1958)

Résumé—Le calcul de l'interaction électrons–phonons est compliqué, dans le cas des métaux polyvalents, par l'occurence des *Umklapprozesse* en plus des collisions normales (avec conservation de la quantité de mouvement). Une méthode numérique pour évaluer la contribution des *Umklapprozesse* est développée et appliquée au calcul—à partir des paramètres du cristal—de la résistivité des métaux normaux, de la température de transition T_c des superconducteurs normaux et de la variation de T_c en fonction de la pression. Il est fait usage des résultats de la théorie de l'état supraconducteur de BARDEEN, COOPER et SCHRIEFFER (*Phys. Rev.* **108,** 1175 (1957)).

Abstract—A method is developed to take into account the contribution of the *Umklapprozesse* to the electron–phonon interaction in polyvalent metals. This method is used to compute—from first principles—the high-temperature resistivity of non-transition metals as well as the transition temperature T_c of non-transition superconductors along the lines of BARDEEN, COOPER and SCHRIEFFER's theory of superconductivity (*Phys. Rev.* **108,** 1175 (1957)). The effect of pressure on T_c is also computed and its dependence upon the band structure is stressed.

1. INTRODUCTION

CET article expose une méthode pour calculer d'une façon approchée la contribution des *Umklapprozesse* (processus U) aux phénomènes où intervient l'interaction entre les électrons de conduction et les ions du réseau. Comme l'a, le premier, montré PEIERLS[1], les processus U jouent un rôle important dans la conductivité électrique en rendant possible les transitions d'électron d'un état k à un état k',† lorsque $(k'-k)$ est plus grand que le vecteur de propagation maximum des phonons (l'extrémité du vecteur $k'-k$ est alors extérieure à la première zone de Brillouin). En général, les transitions sont soumises à la règle de sélection :

$$k'-k = q+K_n \qquad (1)$$

où K_n est un vecteur du réseau réciproque (Fig. 1). Pour les métaux polyvalents les processus U produisent la contribution dominante à la résistivité à température ordinaire.[2] PINES[3] a montré que ces processus U jouent un rôle également important dans la théorie de la supraconductivité proposée

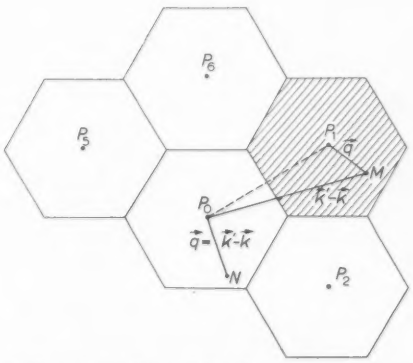

FIG. 1. Représentation schématique à deux dimensions d'une collision normale et d'un *Umklapprozess*.

* Actuellment aux Services Culturels de l'Ambassade de France, 972 5th Avenue, New York, N.Y.

† Les électrons de conduction sont traités comme des particules libres et représentés par des ondes planes $\exp(ikr)$.

par BARDEEN *et al.*[4] Il montre que la contribution nette des collisions normales, telles que :

$$k'-k=q \tag{2}$$

est très faible et que celle des processus U, essentielle, doit absolument être prise en compte pour calculer une valeur réaliste de l'interaction moyenne (paramètre V de la théorie de BARDEEN *et al.*[4]).

Notre méthode de calcul est décrite dans le paragraphe suivant. Dans la paragraphe 3, nous évaluons la résistivité des métaux normaux (à l'exclusion des métaux de transition). Dans le paragraphe 4, nous évaluons la paramètre d'interaction V tandis que la variation de V avec les dimensions cristallines, et par suite l'effet de la pression sur la température T_c de transition à l'état superconducteur sont étudiés au paragraphe 5.

2. CALCUL APPROCHÉ DE LA CONTRIBUTION DES PROCESSUS U

Si nous adoptons les notations de JONES (réf. 2, paragraphes 8 et 9), l'élément de matrice pour la transition $k \to k'$ est :

$$U_{kk'} = -\sqrt{(N)}a(q)\cdot I_{kk'} \tag{3}$$

où N est le nombre d'atomes par cm^3; le vecteur de propagation q du phonon qui participe à la transition est donné par les équations (1) ou (2); $a(q)$ est l'amplitude de ce phonon et $I_{kk'}$ est la transformée de Fourier du gradient du potentiel électron–ion. Le point essentiel du calcul de la conductivité à la température ordinaire aussi bien que du paramètre V, est l'évaluation de la moyenne du terme :*

$$\frac{|I_{kk'}|^2}{s^2|q|^2} \tag{4}$$

sur toutes les valeurs possibles de k et k'.

Les modules k et k' étant égaux au moment maximum k_0 de la distribution de Fermi, le domaine d'intégration est une sphère D de rayon $2k_0$ (Fig. 2). Le terme 4 devient infini aux noeuds P_i du réseau réciproque contenue dans D.† Nous choisissons définitivement $2k_0$ comme unité de longueur pour fixer l'échelle dans l'espace des moments. Nous posons donc :

$$|k'-k| = 2k_0 \sin(\theta/2) = 2k_0 x \tag{5}$$

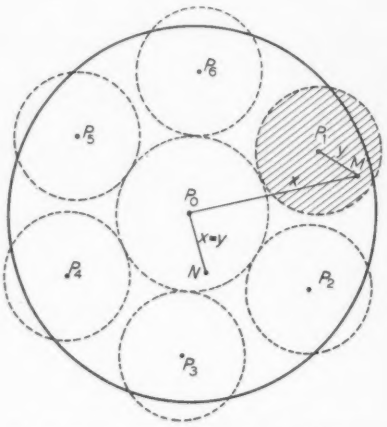

FIG. 2. Schéma du partage du domaine d'intégration en sphères entourant les pôles P_i.

où θ est l'angle entre k et k'; x est une nouvelle variable proportionnelle à la longueur P_0M (Fig. 1).

De même :

$$|q| = 2k_0 y \tag{6}$$

y étant proportionnel à MP_1 (Fig. 1). Il s'agit d'intégrer le produit d'une fonction $x^2f(x)$ assez lentement variable, par le terme $1/y^2$ qui augmente indéfiniment au voisinage des points P_i.

$$I = \int_D \frac{f(x)x^2\,dx}{y^2} \tag{7}$$

Au lieu de cela, nous partageons le domaine d'intégration D en un réseau de sphère S_i entourant chaque noeud P_i, et de rayon R_i choisis de façon à minimiser les recouvrements et les vides (Fig. 2). Un tel partage est aisé pour les réseaux cubiques (f.c.c. et b.c.c.). Il l'est moins pour les structures plus complexes (Hg, Ga, In, Sn). Lorsque l'extrémité du vecteur x est à l'intérieur d'une sphère S_i, son centre P_i est le noeud du réseau réciproque le plus proche et par conséquent y est le rayon vecteur issu de P_i. $4\pi x^2dx$ et $4\pi y^2dy$ étant des éléments de volume équivalents dans l'espace des

* Il est fait usage dans cette expression de l'approximation de Debye, très bonne lorsque q est petit, c'est-à-dire lorsque ce terme (4) est le plus grand.

† Le domaine D contient effectivement des noeuds du réseau réciproque pour tous les métaux polyvalents.

moments, on peut remplacer x^2dx par y^2dy à l'intérieur d'une sphère S_i :

$$I = \sum_i \int_{S_i} f(x)\,dy \tag{8}$$

On trouve que $f(x)$ varie assez lentement à l'intérieur de chaque sphère; on est donc justifié de remplacer ce facteur par une valeur moyenne, pratiquement sa valeur au centre P_i :

$$I = \sum_i f(x_i) \int_{S_i} dy = \sum_i R_i f(x_i) \tag{9}$$

La contribution des processus N, correspondant à la sphère de centre P_0 disparaît totalement dans ce calcul, $f(0)$ étant nul dans les cas que nous envisageons. Mais l'intégration exacte est alors élémentaire et l'intégrale totale, processus N et U (les premiers comptant pour quelques centièmes du total) est approximativement :

$$I = \int_0^{R_0} f(x)\,dx + \sum_i R_i f(x_i) \tag{10}$$

3. ÉVALUATION DE LA CONDUCTIVITÉ À LA TEMPERATURE ORDINAIRE

Dans l'approximation du temps de relaxation, la conductivité est donnée (cf. réf. 2, équation 7.12) par :

$$\frac{1}{\sigma} = \frac{m^2 k_0}{2\pi Z N e^2 \hbar^3} \int_0^{\pi} |U_{kk'}|^2 (1 - \cos\theta)\sin\theta\,d\theta \tag{11}$$

On se rappelle que :

$$|U_{kk'}|^2 = N|a \cdot I|^2 = \frac{N}{3}|a|^2 \cdot |I|^2 \tag{12}$$

D'après la loi d'équipartition de l'énergie

$$\tfrac{1}{3}M|a(q)|^2 \cdot \omega_q{}^2 = KT \tag{13}$$

où ω_q est la fréquence associée au phonon q :

$$\omega_q = s|q| \tag{14}$$

En utilisant le potentiel d'interaction entre les électrons et les ions calculé par BARDEEN et PINES[3,5], nous avons d'autre part :

$$I_{kk'} = -\frac{4\pi Z e^2 i(k'-k)}{|k'-k|^2 \epsilon(k'-k)} \tag{15}$$

qui peut être remplacé dans la limite des grandes longueurs d'ondes ($k'-k$ petit) par :

$$I_{kk'} = -\frac{4\pi Z e^2 i(k'-k)}{|k'-k|^2 + k_s{}^2} \tag{16}$$

Z est la valence du métal (nombre d'électrons de conduction par atome), ϵ la constante diélectrique du gaz d'électrons :

$$k^2\epsilon(k) = k^2 + k_s{}^2\left\{\tfrac{1}{2} + \frac{4k_0{}^2 - k^2}{8k_0 k}\,\mathrm{Log}\left(\frac{2k_0 + k}{2k_0 - k}\right)\right\} \tag{17}$$

k_s étant la constante d'écran du modèle de Fermi–Thomas :

$$k_s{}^2 = 4\pi N_F e^2 \tag{18}$$

où N_F est la densité d'état par unité d'énergie sur le niveau de Fermi. Cette dernière expression est d'ailleurs équivalente à :

$$\frac{k_s{}^2}{4k_0{}^2} = a^2 = 0{\cdot}167 r_s \tag{19}$$

où r_s est l'espacement moyen des électrons de conduction exprimé en unité atomique (a_0 = rayon de Bohr)

$$\frac{1}{ZN} = \frac{4\pi}{3}(a_0 r_s)^3 \tag{20}$$

On a supposé pour obtenir l'expression (15) que l'interaction entre les électrons et les ions est purement coulombienne. On a négligé ainsi les conséquences de la périodicité du cristal sur la réponse des électrons aux mouvements des ions. Pour des raisons de simplicité, nous avons utilisé l'expression (16) dans ce paragraphe. On a fait usage de (15) dans le paragraphe 4. Dans le cadre du modèle conduisant à l'expression (15), la vitesse du son s est :[5]

$$s = \frac{1}{k_s}\left(\frac{4\pi Z^2 e^2 N}{M}\right)^{\frac{1}{2}} \tag{21}$$

En groupant ces résultats (13), (14), (16), (21) avec (12), nous obtenons :

$$|U_{kk'}|^2 = \frac{KT\,4\pi e^2 k_s{}^2 |k'-k|^2}{|q|^2(|k'-k|^2 + k_s{}^2)^2} \tag{22}$$

et finalement avec l'aide de (5), (6), (19) et (20), l'expression de la résistivité (en $\mu\Omega$ cm) à la température $T = 273°K$:

$$\frac{1}{\sigma} = 0{,}16 r_s^4 \int_D \frac{a^2 x^5\, dx}{y^2(a^2+x^2)^2} \qquad (23)$$

Cette intégrale se prête bien au calcul indiqué dans la section 2. Nous avons évalué la résistivité des métaux normaux (à l'exclusion des métaux de transition). Les alcalins ont également été traités à titre de comparaison : dans leur cas la contribution des processus U a été négligée (comparer au calcul de JONES, réf. 2). Les résultats (Tableau 1) sont

Tableau 1. *Comparaison entre les valeurs de la résistivité mesurée et calculée avec l'expression* (23)

Métaux	r_s	a^2	I	$1/\sigma_{\text{calc.}}$	$1/\sigma_{\text{mes.}}$ [6]
Na	4,0	0,67	0,106	4,3	4,27
K	4,97	0,83	0,101	9,8	6,3
Rb	5,32	0,89	0,098	12,5	11,6
Cs	5,67	0,95	0,099	16,2	19,0
Mg	2,66	0,45	0,775	6,2	3,94
Ca	3,26	0,55	0,485	8,8	3,6
Sr	3,55	0,59	0,49	12,6	20
Ba	3,71	0,62	0,91	28	36
Zn	2,32	0,39	0,72	3,3	5,45
Cd	2,59	0,43	0,74	5,3	6,73
Hg	2,59	0,43	0,75	5,4	21,2
Al	2,07	0,346	0,75	2,2	2,5
Ga	2,18	0,364	1,72	6,2	13,7
In	2,40	0,40	1,40	7,4	8,2
Tl	2,48	0,415	0,85	5,1	15
Sn	2,21	0,37	1,18	4,5	10,1
Pb	2,30	0,384	0,79	3,5	19,3

Les résistivités sont évaluées en $\mu\Omega$ cm à la température normale (273°K).

comparés aux valeurs expérimentales compilées par GERRITSEN[6]. On notera l'accord satisfaisant pour les alcalins, alcalino-terreux et Zn, Cd, Al, In. Cependant le présent calcul sous-estime* notablement la résistivité des autres métaux Hg, Ga, Tl, Sn, Pb. On peut interpréter cet écart en remarquant que nous n'avons tenu compte que des transitions intra-bande en négligeant les transitions inter-bande qui seraient responsables d'une part de la résistivité.

Comme le montre PINES[3], ces transitions inter-bande ne jouent pas un rôle important dans le calcul du paramètre d'interaction V de BARDEEN *et al.*[4] L'accord des valeurs calculées de la résistivité avec les valeurs expérimentales pour les métaux où les transitions intra-bande sont dominantes, nous encourage donc à aborder par la même méthode le calcul de V.

* L'accord avec les résultats expérimentaux s'améliore d'ailleurs beaucoup dans le cas de Hg et Pb si on utilise la masse effective m^* au lieu de m.

4. ÉVALUATION DE L'INTERACTION MOYENNE V DANS L'ÉTAT SUPERCONDUCTEUR

Le paramètre d'interaction V de la théorie de BARDEEN *et al.*[4] est la moyenne, sur la surface de Fermi, de l'interaction nette électron–électron, soit :

$$V = \left\langle \frac{N|I_{kk'}|^2}{Ms^2|q|^2} - W_{kk'} \right\rangle_{\text{av}} \qquad (24)$$

en faisant usage de l'expression calculée par BARDEEN et PINES[5], de l'attraction entre électrons, induite par échange d'un phonon. Dans cette équation (24), $W_{kk'}$ est l'élément de matrice de l'interaction électrostatique répulsive entre électrons pour la transition $k \to k'$.

Le critère pour l'existence de l'état supraconducteur est que V soit positif (c'est-à-dire que l'interaction nette soit attractive. Dans ce cas, la température de transition T_c est donnée par (réf. 4, équation 3.29) :

$$KT_c = 1{,}14 \langle \hbar\omega_q \rangle_{\text{av}} \cdot \exp\left(-\frac{1}{N_0 V}\right) \qquad (25)$$

ou bien

$$T_c = 0{,}85 \Theta_D \exp\left(-\frac{1}{N_0 V}\right) \qquad (26)$$

Ici Θ_D est la température de Debye et N_0 la densité par unité d'énergie d'états *d'un seul spin* sur le niveau de Fermi.

Nous déduisons des équations (16) et (21) :

$$\frac{N|I_{kk'}|^2}{Ms^2|q|^2} = \frac{4\pi e^2 k_s^2 |k'-k|^2}{|q|^2\{|k'-k|^2 \epsilon(k'-k)\}^2} \qquad (27)$$

et par conséquent, avec l'aide de (5), (6) et (19) :

$$\left\langle \frac{N|I_{kk'}|^2}{Ms^2|q|^2} \right\rangle_{\text{av}} = \frac{\pi e^2}{k_0^2} \int_D \frac{2a^2 x^3\, dx}{y^2[x^2 \epsilon(x)]^2} = \frac{\pi e^2}{k_0^2} \chi(a^2) \qquad (28)$$

Le choix de la valeur de a^2 ou ce qui est équivalent de k_s (soit donné par l'équation (18), soit choisi pour accorder la valeur (21) de s avec la vitesse du son mesurée) n'est pas critique : il se produit en effet une compensation entre le numérateur et le dénominateur de (27), de sorte de $\chi(a^2)$ est sensiblement constant dans l'intervalle $0{,}3 < a^2 < 0{\cdot}6$. χ est donc bien définie même lorsque la valeur de k_s est incertaine.* Les courbes représentant χ en fonction de a^2 pour différents métaux présentent un plateau (Fig. 3). Nous prendrons comme valeur de χ l'ordonnée de ce plateau.

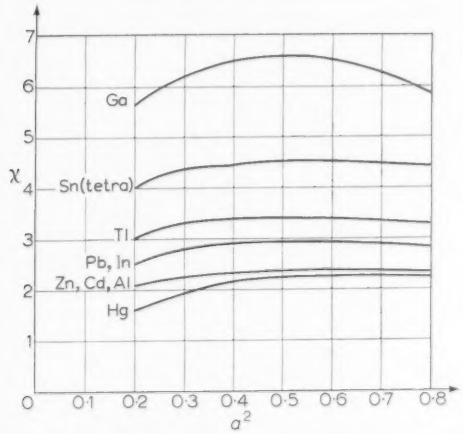

FIG. 3. Fonction $\chi(a^2)$ des métaux supraconducteurs (à l'exclusion des métaux de transition).

PINES a étudié le problème de déterminer l'élément de matrice $W_{kk'}$ de l'interaction électrostatique entre électrons; il offre deux solutions :

(*a*) Sur la base de travaux récents en collaboration avec P. NOZIERES, une interaction électrostatique dans un milieu de constante diélectrique ϵ définie par l'équation (17) :

$$W_{kk'} = \frac{4\pi e^2}{|k'-k|^2\epsilon(k'-k)} \tag{29}$$

dont l'expression approchée pour les grandes longueurs d'onde est :

$$W_{kk'} = \frac{4\pi e^2}{|k'-k|^2+k_s^2} \tag{30}$$

(*b*) Sur la base des travaux de BOHM et PINES, l'élément de matrice du potentiel de Coulomb coupé aux grandes longueurs d'onde; la limite est k_c :†

$$\frac{k_c}{k_0} = 0{,}47 r_s^{\frac{1}{2}} \tag{31}$$

telle que

$$W_{kk'} = 0 \qquad \text{si} |k'-k| < k_c$$
$$W_{kk'} = \frac{4\pi e^2}{|k'-k|^2} \qquad \text{si} |k'-k| > k_c \tag{32}$$

Le choix (*b*) conduit à une contribution électrostatique nettement supérieure à celle correspondant au choix (*a*) (Fig. 4). Nous avons utilisé dans

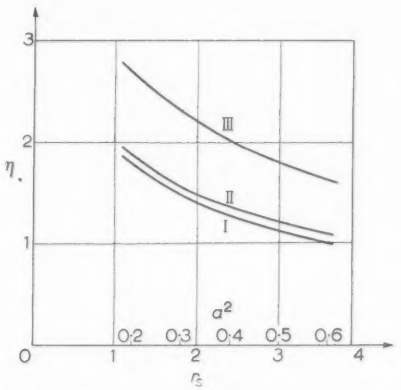

FIG. 4. Fonction $\eta(r_s)$ calculée avec différentes expressions de l'interaction électrostatique : Les courbes I, II, III correspondent respectivement aux éléments de matrice (29), (30) et (32) du texte. L'échelle a^2 convient aux courbes I et II seulement.

ce qui suit l'expression (29) consistante avec notre expression précédente (27). Nous avons posé :

$$\langle W_{kk'}\rangle_{\text{av}} = \frac{\pi e^2}{k_0^2}\int_D \frac{2x\,dx}{x^2\epsilon(x)} = \frac{\pi e^2}{k_0^2}\eta(a^2) \tag{33}$$

Finalement, en remplaçant $N_0 = \frac{1}{2}N_F$ par sa

* La constante d'écran du potentiel électron–ion peut être différente de celle du potentiel électron–électron auquel l'expression (18) s'applique.

† Ce choix correspond étroitement à la forme proposée par SAWADA, BRUECKNER, FUKUDA et BROUT dans leur article *Correlation energy of an electron gas at high density* (*Phys. Rev.* **108,** 507 (1957)). L'expression de k_c obtenue par ces auteurs (équation (9)) est très voisine de l'expression (31) ci-dessus.

Tableau 2. Comparaison entre les valeurs calculées (expression (34)) et expérimentales (expression (26)) du facteur N_0V de BARDEEN, COOPER *et* SCHRIEFFER[4]

Métaux	χ	η	$\chi-\eta$	m^*/m[7]	$N_0V_{calc.}$	$N_0V_{mes.}$	T_c[8] (°K)	Θ_D[9] (°K)
Zn	2,4	1,36	1,04	0,85	0,17	0,175	0,91	320
Cd	2,4	1,30	1,10	0,75	0,18	0,16	0,56	300
Hg	2,2	1,30	0,90	2,0	0,39	0,38	4,16	69
Al	2,4	1,45	0,95	1,6	0,26	0,175	1,2	419
Ga	6,5	1,41	5,09	0,4	0,37	0,19	1,1	240
In	2,9	1,35	1,55	1,35	0,48	0,30	3,37	109
Tl	3,4	1,32	2,08	1,15	0,49	0,28	2,38	100
Sn	4,4	1,40	3,0	1,2	0,67	0,29	3,73	140
Pb	3,0	1,37	1,63	2,1	0,66	0,41	7,22	96,3

valeur et en se rappelant de l'équation (18), nous obtenons :

$$N_0V = \frac{k_s^2}{8k_0^2}(\chi-\eta) = \frac{a^2}{2}(\chi-\eta) \qquad (34)$$

Cependant la densité N_0 mesurée (proportionnelle à la chaleur spécifique électronique) est souvent très différente de la densité d'un gaz d'électron libre. Etant donné l'importance de ce facteur, nous introduirons la valeur expérimentale de N_0 au lieu de son expression théorique.† Pour cela, il suffit de multiplier l'expression (34) par le rapport des chaleurs spécifiques électroniques mesurées et calculées (rapport connu sous la forme m^*/m) :

$$N_0V = \frac{a^2}{2}\cdot\frac{m^*}{m}(\chi-\eta) \qquad (35)$$

Les résultats de ce calcul ($N_0V_{calc.}$) sont comparés à la valeur expérimentale $N_0V_{mes.}$ déduite de (26) (Tableau 2). L'accord est quantitatif pour les métaux bivalents et qualitatif pour les autres.

5. EFFETS DE LA PRESSION SUR LA TEMPÉRATURE DE TRANSITION

Nous nous proposons d'étudier l'effet d'une pression hydrostatique‡ sur la température de transition T_c avec l'aide de notre expression (35). L'effet d'une telle pression étant de réduire proportionnellement toutes les dimensions cristallines, il est complètement traduit par une variation du paramètre r_s (ou du paramètre a^2 proportionnel à r_s). Nous déduisons de l'équation (26):

$$\frac{d\log T_c}{d\log r_s} = \frac{d\log\Theta_D}{d\log r_s} + \frac{r_s}{(N_0V)^2}\frac{d(N_0V)}{dr_s} \qquad (36)$$

Le premier terme du second membre est simplement -3γ, γ étant la constante de Gruneisen.§ Quant au second terme, on peut l'écrire :

$$\frac{1}{N_0V}\cdot\frac{d\log(N_0V)}{d\log r_s}$$

$$= \frac{1}{N_0V}\cdot\frac{d\left\{\log\left(a^2\frac{m^*}{m}\right)+\log(\chi-\eta)\right\}}{d\log r_s} \qquad (37)$$

En se rappelant que (équations (18), (34) et (35)):

$$a^2\frac{m^*}{m} = N_F\frac{\pi e^2}{k_0^2} \qquad (38)$$

† Nous introduisons ici un paramètre qui dépend d'une façon critique de la forme de la bande de conduction et par conséquent de la structure du solide.

‡ Les mesures de l'effet de contraintes sur la température de transition de spécimens monocristallins sont délicates et très peu nombreuses. Nous avons donc préféré nous limiter à l'effet d'une pression isotrope qui garde un sens pour les échantillons polycristallins.

§ La constante de Gruneisen est par définition ($V \equiv$ volume) :

$$\gamma = -\frac{d\log\Theta_D}{d\log V}$$

et que k_0 est proportionnel à r_s^{-1}, nous avons :

$$\frac{d\log\left(a^2\frac{m^*}{m}\right)}{d\log r_s}=\frac{d\log\left(\frac{N_F}{k_0^2}\right)}{d\log r_s}=\frac{d\log N_F}{d\log r_s}+2 \tag{39}$$

D'autre part, nous avons vu que la fonction $\chi(a^2)$ est peu sensible aux variations de a^2. En première approximation, nous négligerons $d\chi/dr_s$. Nous évaluerons $d\eta/dr_s$ en choisissant son expression simplifiée avec l'élément de matrice (30) :

$$\eta=\int_0^1\frac{2x\,dx}{x^2+a^2}=\log\frac{1+a^2}{a^2} \tag{40}$$

d'où

$$r_s\frac{d\eta}{dr_s}=a^2\frac{d\eta}{d(a^2)}=-\frac{1}{1+a^2} \tag{41}$$

En rassemblant ces expressions dans (36), nous obtenons finalement :

$$\frac{d\log T_c}{d\log r_s}=-3\gamma+\left[\log\left(\frac{0{,}85\Theta_D}{T_c}\right)\right]\left[\frac{d\log N_F}{d\log r_s}+2\right]+\left[\log\left(\frac{0{,}85\Theta_D}{T_c}\right)\right]^2\left[\frac{m^*}{m}\cdot\frac{a^2}{2(1+a^2)}\right] \tag{42}$$

Les trois termes du second membre (A, B et C de gauche à droite) sont comparés dans le Tableau 3.

Tableau 3. Comparaison entre les valeurs calculées (équation (42)) et mesurées de l'effet de la pression sur T_c

Métaux	$\frac{d\log N_F}{d\log r_s}$†	A	B	C	$\frac{d\log T_c}{d\log r_s}$ (calc.)	$\frac{d\log T_c}{d\log r_s}$ (mes.)	Références
Hg	6,6	−6,6	24,4	2,3	20,1	6,1 8,4 9,0	(10) (11) (14)
Al		−6,5		7,0		40,6 38	(11) (13)
In	5,1	−7,1	24,5	2,3	19,7	13,5 14,0 15,6	(10) (12) (13) (14)
Tl	9,9	−8,2	44	2,3	38,1	−2,2 −4,7 −8	(13) (10) (11)
Sn	1,5	−5,4	13	2,2	9,8	20 27,5 24,3	(10) (11) (13) (12) (14)
Pb	2,1	−8,2	10,5	1,9	4,2	9,5	(10) (12)
Ta	−120					17 15 4,5	(10) (11) (14)
V						−13,5	(10)

A, B, C sont respectivement les 1er, 2e et 3e termes du second membre de l'expression (42).

† Les valeurs portées dans cette colonne sont déduites des expériences de Olsen et Rohrer[10].

La valeur calculée $d \log T_c/d \log r_s$ est donnée en regard des valeurs expérimentales (on trouvera dans les références (10), (11) et (12) des mesures de la variation du champ critique en fonction de la pression; (13) donne directement la variation de la température de transition en fonction de la pression).

Tous les paramètres apparaissant dans (42) sont connus avec une précision raisonnable, sauf $d \log N_F/d \log r_s$. Pour le modèle de Fermi :

$$\frac{d \log N_F}{d \log r_s} = \frac{d \log k_0}{d \log r_s} = -1 \qquad (43)$$

OLSEN et ROHRER, analysant la variation de la température de transition en fonction de la pression et du champ critique déterminent expérimentalement ce paramètre (réf. 10, équation 16) :

$$\frac{d \log N_F}{d \log r_s} = \frac{d \log \gamma^*}{d \log r_s} = 3(g-1) \qquad (44)$$

Les valeurs mesurées sont toutes très différentes de -1 (Tableau 3).

6. CONCLUSION

PINES[3] déduit de la théorie de BARDEEN *et al.*[4] un critère très suggestif pour distinguer les éléments superconducteurs des non-supraconducteurs en les classant suivant les valeurs de r_s et de Z_s†; mais les valeurs de N_0V calculées avec sa formule (21) sont systématiquement inférieures aux valeurs expérimentales. Il apparaît donc que deux paramètres r_s et Z ne sont pas suffisants pour caractériser la transition à l'état supraconducteur.

En poursuivant la même voie que PINES dont nous avons adopté les expressions (15) et (29) des éléments de matrice $I_{kk'}$ et $W_{kk'}$ et en restant dans l'esprit du modèle choisi par BARDEEN *et al.* (électrons libres), nous avons introduit deux éléments dépendant de la structure :

(*a*) le calcul de la contribution des "processus U", lié à la forme du *réseau réciproque*;

(*b*) la valeur expérimentale de la densité d'états N_F sur le niveau de Fermi. La densité d'états dans la bande de conduction est généralement une fonction très compliquée de l'énergie : le paramètre N_F est donc très sensible à des modifications minimes du solide : distorsion mécanique, compression, présence d'impuretés,‡ etc.

L'introduction de ces deux éléments structuraux détruit la simplicité du critère de PINES, mais améliore sensiblement l'accord quantitatif entre les valeurs calculées et mesurées de N_0V. Ce résultat démontre qu'un calcul aussi précis que possible de la contribution des processus U doit être envisagé, pour évaluer quantitativement une grandeur liée à l'interaction électron–phonon (et en particulier T_c).

Cependant dans le cas particulier de la température de transition T_c, l'influence de la densité d'états N_F est essentielle. Alors que pour un solide donné, l'interaction induite est pratiquement constante, N_F au contraire est très sensible aux déformations minimes du cristal. Ceci peut expliquer les grandes variations de l'effet de la pression $d \log T_c/d \log r_s$ non seulement d'un métal à l'autre mais encore d'un spécimen à l'autre, de pureté différentes. Inversement, il serait possible de déduire de la mesure de $d \log T_c/d \log f_s$ la valeur de $d \log N_F/d \log r_s$ et par là, une estimation de la forme de la bande de conduction.

Remerciment—Je voudrais exprimer ma gratitude au Professeur PINES qui m'a suggéré le sujet de cette étude et m'a constamment aidé de ses conseils.

BIBLIOGRAPHIE

1. PEIERLS R., *Ann. Phys.* (*Leipzig*) **12,** 154 (1932).
2. JONES H., *Handbuch der Physik* Band 19. Springer, Berlin (1956).
3. PINES D., *Phys. Rev.* **109,** 280 (1958).
4. BARDEEN J., COOPER L. N., et SCHRIEFFER J. R., *Phys. Rev.* **108,** 1175 (1957).
5. BARDEEN J. et PINES D., *Phys. Rev.* **99,** 1140 (1955).
6. GERRITSEN A. N., *Handbuch der Physik* Band 19. Springer, Berlin (1956).
7. DAUNT J. G., *Progress in Low Temperature Physics* Vol. I. (Ed. C. J. GORTER). North Holland Publishing Co., Amsterdam (1955).
8. SHOENBERG D., *Superconductivity*. Cambridge University Press (1952).
9. EISENSTEIN J., *Rev. Mod. Phys.* **26,** 277 (1954) ou, à défaut, *American Institute of Physics Handbook*.
10. OLSEN J. L. et ROHRER H., *Helv. Phys. Acta* **30,** 49 (1957).

† Le calcul de PINES ne fait intervenir aucune donnée structurale.

‡ Comme le suggèrent E. ABRAHAM et B. SERIN (communication privée).

11. FISKE M. D., *J. Phys. Chem. Solids* **2,** 191 (1957).
12. CODY G., *Volume Changes Associated with the Superconducting Transition.* Communication, Conférence sur les Basses Températures, Madison (Wisconsin) (1957).
13. MUENCH N. L., *Phys. Rev.* **99,** 1814 (1955).
14. SWENSON C. A., *Effects of Elastic and Plastic Deformation on Properties of Superconductors.* Conf. on Electronic Properties of Metals at Low Temperature, Geneva, New York (1958).

VOL.
10
1959

J. Phys. Chem. Solids Pergamon Press 1959. Vol. 10. pp. 286–303. Printed in Great Britain.

ENERGY BANDS IN THE PRESENCE OF AN EXTERNAL FORCE FIELD—II.

ANOMALOUS VELOCITIES

E. N. ADAMS* and E. I. BLOUNT

Westinghouse Research Laboratories, Pittsburgh 35, Pennsylvania

(*Received* 9 *January* 1959)

Abstract—The theory of field-modified energy bands is extended to include the effect of weak scattering forces on the energy band structure. The modified current operator is found to contain terms giving anomalous currents of a type previously treated by KARPLUS and LUTTINGER (*Phys. Rev.* **95,** 1154 (1954)) in connection with electrical conduction in ferromagnets. The physical meaning of these currents is discussed, and they are shown to be analogous to spin-dependent currents in Dirac's theory of the electron. They may be regarded formally as resulting from a non-commutability of the components of the coördinates. It is shown that such currents, proportional to the acceleration, are caused by every accelerating mechanism, including scattering mechanisms. A classical transport theory including the anomalous currents is derived, valid for scattering mechanisms for which the momentum transfer per collision is small, and a very simple problem carried through by way of example. A formal theory including the anomalous transport currents is given for the general case of arbitrary scattering mechanism and overlapping bands. Finally, a critique is given of some recent theories of the spontaneous Hall effect in ferromagnetics.

VOL
10
195

1. INTRODUCTION

KARPLUS and LUTTINGER[1] and more recently KOHN and LUTTINGER[2] have given formal theories of electrical conduction which predict the existence of what we will refer to as *anomalous transport currents*. These currents are anomalous in that they are not simply proportional to the collision time for scattering of the electrons by the various aperiodic potentials present in the lattice. Both sets of authors suggest that such anomalous currents may be responsible for the spontaneous Hall effect in ferromagnets.

The existence of the anomalous transport currents has been inferred by each set of authors on the basis of an intricate calculation. In each case the calculation was made in the representation of the Bloch functions of a perfect crystal, and the anomalous effects were found to arise from off-diagonal matrix elements of the density matrix in this representation. Because of this circumstance, it is not straightforward to give an intuitive discussion of the meaning of the equations of the theory, or to make trustworthy estimates of the rather complicated quantities occurring in the formulae of the theory.

In the present work we present an alternative discussion of these anomalous currents based on a different approach. The scope of our work is the same as for the previous work, i.e. the application is to a gas of non-interacting electrons moving in a perturbed periodic potential. Our method is dissimilar to that of the previous authors, in that in our work we focus attention on the Hamiltonian of the system, rather than on the statistical ensemble. We are able, as a consequence, to give a more intuitive discussion of the anomalous currents and indeed to produce a classical Hamiltonian theory from which they arise naturally. Thus we establish contact with the usual pseudoclassical treatment of transport phenomena in solids.

Our treatment is based on the use of the "physical energy bands" of a crystal made imperfect by aperiodic perturbations, as recently discussed by several authors.[3–5] We will begin with a formal discussion of some matters concerning the "physical energy bands" and their general definition.

* Now at IBM Research Center, Yorktown Heights, New York.

2. MATRIX ELEMENTS OF THE COÖRDINATE

Initially we will express our quantum-mechanical operators in the representation generated by the Bloch functions associated to the energy bands of the unperturbed crystal. We will refer to this representation as the crystal momentum representation (CMR) and will use in the main a notation previously introduced by one of us.[6] In this work it was shown that the coördinate and momentum operators may each be conveniently divided into two parts, one which describes the "particle-like" behavior important for transport; the other which described the "atomic" behavior of the electron, which is analogous to that of an electron in an isolated atom and which is important, e.g., in optical absorption. The second quantity, which we will refer to as the "intracell" coördinate, represents in a certain sense the position of the electron within unit cell with reference to the arbitrary origin of coördinates in unit cell. In particular the μ^{th} component of the diagonal part of the coördinate matrix is of the form

$$x_{\text{diag}}{}^{\mu} = i\hbar\frac{\partial}{\partial p_{\mu}} + X_{nn}{}^{\mu}(p) \tag{2.1}$$

in the notation of reference (6). $X_{nn}{}^{\mu}(p)$ is the diagonal-in-bands part of the intracell coördinate operator. Roughly speaking it gives the position of the centroid of charge for the Bloch state ψ_{np} as measured from the origin in unit cell.[6] The effects of interest in this paper originate in the momentum-dependence of $X_{nn}(p)$.

We will denote as $x_c{}^{\mu}$ the operator for the μ^{th} component of the diagonal part of the coördinate operator, and refer to x_c as the *crystal coördinate*. For vanishing electromagnetic vector potential $x_c{}^{\mu}$ is given by the expression (2.1) for the crystal coördinate; the term $X_{nn}{}^{\mu}(p)$ is formally analogous to the vector potential in the familiar operator $p^{\mu}+(e/c)a^{\mu}(x)$. Thus in the CMR there are transformations[6] u of a unitary type analogous to the gauge transformations of the vector potential, in which the Bloch functions ψ_{np} are multiplied by complex factors of modulus unity and of the form $u_n = \exp(if_n(p)/\hbar)$. Under such a transformation

$$x_c{}^{\mu} \to x_c{}^{\mu} + \frac{\partial f_n}{\partial p^{\mu}}$$

These "phase" transformations are not special to crystal physics. When carried out in the usual momentum representation, they generate the transformations of the coördinate operator implied in the classical discussion of DIRAC[7]. However, even in the general form of the ordinary coördinate operator, the vector function of momentum must be the gradient of a scalar, in order that the components of the coördinate operator commute, whereas, the components of the crystal coördinate do not in general commute. From equation (2.1) the commutator is readily found to be

$$[x_c{}^{\mu}, x_c{}^{\nu}] = i\hbar\left[\frac{\partial X_{nn}{}^{\nu}}{\partial p^{\mu}} - \frac{\partial X_{nn}{}^{\mu}}{\partial p^{\nu}}\right] \tag{2.2}$$

or

$$[x_c{}^{\mu}, x_c{}^{\nu}] = i\hbar\delta_{\mu\nu\lambda}[\text{curl}_p X_{nn}]_{\lambda} \tag{2.3}$$

Equations (2.2) and (2.3) differ from the more familiar quantum-mechanical equations, in that the curl of $X_{nn}{}^{\mu}$ need not in general vanish.

It is a complication that the components of the crystal coördinate do not commute, but not to be excluded on simple *a priori* grounds. We will make use of this formal property of the crystal coördinate operator in what follows. The components of the true coördinate operator commute, of course. From this fact it follows that for each band n

$$\sum_{n'}{}' (X_{nn'}{}^{\mu}X_{n'n}{}^{\nu} - X_{nn'}{}^{\nu}X_{n'n}{}^{\mu}) = -[x_c{}^{\mu}, x_c{}^{\nu}]_{nn} \tag{2.4}$$

The $X_{nn'}{}^{\mu}$ are the interband matrix elements of the intracell coördinate operator. All of the matrix elements $X_{nn'}{}^{\mu}$ are functions of p.

In the case of a crystal with a center of symmetry, double degeneracy of bands persists throughout k-space. It is then convenient to modify slightly the above considerations. In this case, $X_{nn'}$ may be considered as containing matrix elements between bands of different energy, and X_{nn} as a Pauli 2×2 matrix connecting the two degenerate bands. The treatment is formally similar to the treatment of spin in regular non-relativistic quantum mechanics. In this theory $\nabla x X_{nn}$ is no longer phase-invariant, but the commutator $[x_c{}^{\mu}, x_c{}^{\nu}]$ is still phase-invariant and plays the same role as above.

3. EXTERNAL ELECTRIC AND MAGNETIC FIELDS

Several authors [3.5] have discussed the effect of external electric and magnetic fields on the energy band structure. They have shown that the "physical" energy bands in the presence of external fields do not correspond to the unperturbed Bloch states but to certain linear combinations of these. The case that has received the most detailed attention is that of the external electric field, although the basis for a treatment of the magnetic field has also been given. In this paper we will be interested in some results that are implicit in this previous work. Thus we will begin by recapitulating the findings already reported in the literature, pointing out certain significant features that were not commented on in the original papers.

In the CMR the Hamiltonian for an electron in a periodic potential perturbed only by an external force field F^ν is

$$H_{nn'} = \delta_{nn'}[E_n(p) - F^\nu x_c^\nu] - F^\nu X_{nn'}^\nu (1-\delta_{nn'}) \quad (3.1)$$

In order to get the corresponding equation for the "physical" energy bands in which the energy matrix is diagonal, one carries out a canonical transformation of which the generator is the completely non-diagonal matrix $S^{(F)}$ with matrix elements[4]

$$S_{nn'}^{(F)} = ihF^\nu \cdot X_{nn'}^\nu/(E_n - E_{n'}) \quad (3.2)$$

After the transformation the energy is diagonal to first order in the perturbation, and to this order its diagonal elements are the same as given in equation (3.1). In the new representation the diagonal part of the coördinate operator is

$$[U^{(F)} x_c^\mu \, U^{(F)-1}]_{nn} = x_c^\mu + \delta X_{nn}^\mu(p) \quad (3.3)$$

In a representation for which the energy is diagonal-in-bands, the average velocity is the commutator between the energy and the diagonal part of the coördinate. To first order in F the diagonal part of the velocity is

$$V_{nn}^\mu = \frac{\partial E}{\partial p^\mu} - [F \times \mathrm{curl}_p X_{nn}]_\mu \quad (3.4)$$

The quantity δX_{nn}^μ contributes to the velocity only a term of order F^2. The second term on the right-hand side of equation (3.4) is a correction to the velocity. We will refer to it as the operator for the "anomalous velocity engendered by the electric field".

In the example above the transformation which diagonalizes the energy is very simple in form, but for more complicated perturbations it will be more complicated to write down. It is fortunate, therefore, that there is a simple procedure of getting the desired matrix elements without a complicated calculation, which can be used even in the cases of the more complicated perturbations that we will want to consider. We notice that in the above example one may obtain the transformed coördinate and velocity matrices to the first order in the perturbation merely by *dropping the inter-band matrix elements from the expression on the right-hand side of equation* (3.1). Thus to get equation (3.4) we do not need actually to know the transformation (3.2) at all.

The analog of the above theory for the perturbing effect of a magnetic field presents some further complications. In the presence of a non-vanishing electromagnetic vector potential a^ν, of which the first, but no higher space derivates are appreciable, the Hamiltonian is given to first order in a^ν by:

$$H_{nn'} = \delta_{nn'}\left[E_n(p) + \frac{e}{2c}\left\{\frac{\partial E_n}{\partial p^\mu}, A^\mu(x_c)\right\} + \frac{e}{2c}\{V^\mu, X^\nu\}_{nn}\frac{\partial A^\mu}{\partial x^\nu}\right] + \\ + \frac{e}{2c}\frac{\partial A^\mu}{\partial x^\nu}(1-\delta_{nn'})\left[\{V^\mu, x_c^\nu\}_{nn'} + \{V^\mu, X^\nu\}_{nn'} + \left\{\frac{\partial E}{\partial p_\mu}, X^\nu\right\}_{nn'}\right] \quad (3.5)$$

An explicit formula for $\delta X_{nn}^\mu(p)$ can readily be obtained. As will be shown below, however, we do not need it, so we will not write it out here.

In equation (3.5) the symbols V^μ, X^ν denote the "atomic" part of the velocity and coördinate matrices, i.e. the parts that have no matrix elements

diagonal in the bands. Equation (3.5) is written in terms of the matrix elements of the velocity, so that it will be correct for problems involving spin-orbit interaction.

We shall not construct here the rather complicated transformation that diagonalizes the Hamiltonian, although it is straightforward to do so.[8] For the most part we do not need to use it. However, we call attention to that part of the generator of the transformation that affects the results to first order in the magnetic perturbation. This partial generator is the non-diagonal matrix $S_{nn'}{}^{(a1)}$ with matrix

$$S_{nn'}{}^{(a1)} = (e/2c)\{A^\mu(x_c),\, X^\mu\}_{nn'} \tag{3.6}$$

The transformation generated by equation (3.6) removes the mixing of energy bands arising from a *constant* vector potential. The generator $S^{(a)}$ for the transformation that completely diagonalizes H to first order in the magnetic field B contains besides $S^{(a1)}$ no other terms proportional to a, but only terms proportional to the space derivatives of a.

Carrying out the complete diagonalization of the energy to order a, we obtain, correct to first order in a,

$$H_{nn'} = \delta_{nn'}[E_n[p+(e/c)A(x_c)]+E_B(p)] \tag{3.7}$$

$$[u_a x_c{}^\mu u_a{}^{-1}]_{nn} = x_c{}^\mu[p+(e/c)A(x_c)]- \\ -(e/2c)\left\{A^\nu(x_c),\, \frac{\partial X_n{}^\nu}{\partial p^\mu}\right\}+\delta X_{nn}{}^\mu \tag{3.8}$$

The quantity $E_B(p)$ is a small first-order contribution to the energy of the general appearance of an orbital magnetic moment. Notationally we will omit it in the following discussion. In the expression (3.8) for the coördinate the quantity $\delta X_{nn}{}^\mu$ is of the same character as that encountered in the theory of the electric field perturbation and may be dropped in computing first-order effects. However, the second term on the right-hand side of equation (3.8) cannot be dropped, since it is required in order that the theory be gauge invariant and in order to preserve the commutation relations between p^μ, $x_c{}^\nu$. As a consequence the commutator $[x_c{}^\mu, x_c{}^\nu]$ is now of a more complicated form than previously, having in addition to the terms of equation (2.3) eight terms of relative order $(e/c)B$ (curl $_pX$). These terms are small, however, since the order of magnitude of curl $_pX$ is $L^2/\hbar$, where L is the lattice constant, and

$$\frac{eB}{c\hbar}\,\mathrm{curl}_p X_{nn} \sim \frac{eBLf^2}{\hbar c} \sim \frac{\omega_c}{\omega_E} \tag{3.9}$$

Here ω_E is an electronic energy of the order of electron volts, and ω_c is the cyclotron frequency for a free electron in field B. It would appear that in most experimental situations the magnetic-field-dependent terms in the commutator are very small relative to the field-independent terms, and may be dropped.

The appearance of the vector potential in the expression (3.8) for the coördinate operator originates in the dependence of the coördinate operator on p. That the form satisfies the requirements of gauge invariance is readily established by considering the transformations of the pair of operators:

$$\left.\begin{aligned} &p^\mu+(e/c)A^\mu(x_c) \\ &x_c{}^\mu-(e/2c)\left\{A^\nu(x_c),\, \frac{\partial X_{nn}{}^\nu}{\partial p^\mu}\right\} \end{aligned}\right\} \tag{3.10}$$

under the unitary transformations with generator $(e/\hbar c)\ G\ (x_c)$. It is easily shown that neglecting higher commutators the vector potential in both operators transforms to

$$A^\mu(x_c) \to A^\mu(x_c) - \frac{\partial G}{\partial x^\mu} \tag{3.11}$$

From equations (3.7) and (3.8) the diagonal part of the velocity operator may now be found to be:

$$V_{nn}{}^\mu = \frac{\partial E_n}{\partial p_\mu}[p+(e/c)A]+ \\ +(e/c)[[v_{nn}\times B]\times \mathrm{curl}_p X_{nn}]_\mu \tag{3.12}$$

The second term on the right-hand side of equation (3.12) is an anomalous velocity analogous to that found in the electric-field case. This term arises from the magnetic instead of the electric force. Both anomalous velocity operators can be comprised in the single formula:

$$\delta V_{nn}{}^\mu = -\left[\frac{d}{dt}\left(p+\frac{e}{c}A\right)\times \mathrm{curl}_p X_{nn}\right]_\mu \tag{3.13}$$

From the mathematical point of view these anomalous velocities are exact analogues of the

Lorentz force (with momentum and coördinate interchanged). They are present because the coördinate operator has a part $X_{nn}(p)$, which is the analogue of the vector potential in the familiar operator $p+(e/c)a$.

The transformation to the "physical energy bands" and the appearance of anomalous velocities has an exact formal analogy in the reduction of the Dirac theory to an energy representation and the consequent appearance of spin currents. This analogy is expounded more fully in Appendix A. The "physical energy bands" in the presence of the magnetic field are bands of Bloch-like states that are approximate eigenfunctions of $p+(e/c)a$ rather than of p. Since the components of $p+(e/c)a$ do not in general commute, it must be understood that the use of such transformations involves errors in quantum effects. Such a treatment is accurate only at high quantum numbers, where quasi-classical mechanics is valid. It is to be noted that the formulæ for the anomalous velocities do not involve $\hbar$ explicitly, and thus describe physical effects which can persist to high quantum numbers.

4. ANOMALOUS VELOCITIES DUE TO SCATTERING

In the last section we studied the effect of the external electric and magnetic fields on the bands, assuming that they are the only perturbations present. In so doing we omitted the interactions that effect the scattering of electrons. In a steady-state transport process these scattering interactions just equilibrate the force arising from the electric and magnetic perturbations. The effect of these interactions on the energy bands must then be of about the same magnitude as that of the other interactions. Further, since (dp/dt) caused by scattering just balances (dp/dt) caused by accelerations, we might expect anomalous currents arising directly from the scattering processes to be of the same order of magnitude as those found above.

Because the scattering interaction is not diagonal in momentum, the formal treatment of the modification of the bands is more complicated than was the case with the electric-field perturbation. So long as the interaction is weak, however, we may treat it by the method used in the last section, except that true scattering effects require special attention. Thus we may still obtain the matrix for the average velocity in the physical energy bands as the commutator of new Hamiltonian and coördinate operators obtained by the following procedure:

(1) Omit the interband matrix elements of the Hamiltonian between states of different energy, and replace the diagonal element $E_n[p]$ by $E_n[p+(e/c)a(x_c)]$.

(2) Replace the crystal coördinate x_c by its gauge invariant form as given by the right-hand side of equation (3.8).

In this section we will consider the especially simple problem for which the scattering potential is a function of position only and has only long-wavelength Fourier components. In these circumstances the matrix of the scattering potential can be approximated by

$$V_{nn'} = \delta_{nn'}V(x_c)+\frac{\partial V}{\partial x^\nu}(x_c)X_{nn'}{}^\nu(1-\delta_{nn'}) \quad (4.1)$$

We may neglect higher space derivatives, since equation (4.1) is an expansion in qX, where q is a typical Fourier component of the potential and X has eigenvalues of the order of the lattice dimension L. Similarly, under our assumptions the order of writing operators in the second terms of the right-hand side of equation (4.1) is immaterial, and the treatment of the scattering potential may be carried out by means of the same transformation used for the discussion of the uniform electric field. The application of the electric-field-type transformation to a scattering potential which varies slowly with position involves what might be called *local diagonalization*. For this case we are adjusting the bands at each point as though the scattering field at that point were homogeneous and extended to infinity. The transformed operators for the Hamiltonian, coördinate, and velocity are given, respectively, by:

$$H = E\left[p+\frac{e}{c}A(x_c)\right]-F^\nu x_c{}^\nu+V(x_c) \quad (4.2)$$

$$V_{nn}{}^\mu = \frac{\partial E}{\partial p^\mu}+\frac{i}{\hbar}\frac{\partial H}{\partial x^\nu}[x_c{}^\nu, x_c{}^\mu] \quad (4.3)$$

Equation (4.3) may also be expressed as

$$V_{nn}{}^\mu = \frac{\partial E}{\partial p^\mu}+\left[\frac{\partial H}{\partial x_c}\times \operatorname{curl}_p X_{nn}\right]_\mu \quad (4.4)$$

in which the force $-(\partial H/\partial x_c)$ includes not only the forces of the external fields but also those due to scattering. The equation (4.3) is what we expect from the interpretation of the last section that the anomalous current terms are the momentum space analogue of the Lorentz force. It may be remarked that all of the results of this section also apply to external fields which vary slowly in space or time.

5. SIMPLE THEORY OF ANOMALOUS TRANSPORT CURRENTS

In the previous section we obtained an expression for the anomalous velocity operators in a perturbed problem which includes both forces due to external electromagnetic fields and scattering forces. In this section we wish to investigate the overall effect of the anomalous velocities on the total current in a situation involving transport. In order to make the presentation as simple as possible, we will treat a very simple example, perhaps the simplest non-trivial application of the theory. We will calculate the electrical conductivity for a hypothetical material containing electrons in a single, non-degenerate energy band for which the effective mass is isotropic and constant and for which curl X_{nn} is a constant D independent of k for all occupied states. As in the last section the scattering potential V will be taken to be a slowly varying, function of position alone

$$V = \sum_e V_q \exp(iq \,.\, x_c + X) \tag{5.1}$$

We may conveniently choose the "gauge" so that for the occupied states

$$X_{nn}(k) = -\tfrac{1}{2} k \times D \tag{5.2}$$

The assumptions we make limit the applicability of our model to cases for which $q.X$ is very small, so that the local diagonalization approximation is valid. In this case we may justify neglecting $q.X$ in equation (5.1) and approximating the scattering interaction as

$$V = \sum_q V_q \exp(iq \cdot x_c) \tag{5.3}$$

To treat the role of the anomalous currents in transport, we may introduce a phase space density $\rho(p, x_c)$ and derive a classical transport theory. The Hamiltonian (4.2) leads to a Boltzmann equation, valid at high quantum numbers, in which the anomalous currents appear naturally. The Liouville equation is

$$\frac{d\rho}{dt} = \frac{\partial \rho}{\partial t} + [[H, \rho]] \tag{5.4}$$

in which the double bracket symbol denotes the Poisson bracket of the two quantities. For functions of p^ν, x^μ, the Poisson Bracket is just $(i/\hbar)$ times the commutator. For steady-state electric conduction, equation (5.4) becomes

$$\frac{\partial \rho}{\partial p^\nu} \cdot \frac{\partial H}{\partial x^\nu} - \frac{\partial \rho}{\partial x^\nu}\left[\frac{\partial E}{\partial p^\nu} + \frac{\partial H}{\partial x^\mu}[[x_c{}^\mu, x_c{}^\nu]]\right] = 0 \tag{5.5}$$

The last term on the right-hand side of equation (5.5) comes about from the non-vanishing P.B. of the components of $x_c{}^\mu$, and represents the transport arising from the anomalous velocities. The coefficient of $(\partial\rho/\partial x^\nu)$ is the complete velocity component, $[[H, x_c{}^\nu]]$. Thus the anomalous velocity operators enter the classical transport theory in the usual way, both in the expressions for the current and in the equation which the distribution function satisfies.

The electric current may be considered to consist of three parts, contributed respectively by the two anomalous velocities engendered by the electric field and the scattering forces, and by the "normal" velocity $(\partial E/\partial p)$. The average current contributions of the anomalous velocity operators may in our problem be calculated very simply. The velocity engendered by the electric force is the same for every state. Its contribution $\delta_F J$ to the total current is

$$\delta_F J = -neF \times D/\hbar \tag{5.6}$$

The current $\delta_s J$ resulting from the velocity engendered by scattering may be inferred immediately from the condition of overall momentum balance in the steady state. By equation (4.4) the anomalous velocity arising from scattering is just the gradient of the scattering potential multiplied times $\mathrm{curl}_p X_n$. Since in our example $\mathrm{curl}_p X_n$ is just a constant vector D, the sum of the anomalous velocities of all electrons is

$$\delta_s J = -e\left.\frac{dP}{dt}\right|_{sc} \times D/\hbar \tag{5.7}$$

where $dP/dt)_{sc}$ is the average rate of momentum transfer to the electrons from the scattering interaction. In the steady state the force exerted by the scattering interaction just equilibrates the force exerted by the electric field on the electrons, hence

$$\begin{aligned} \delta_s J &= neF \times D/\hbar \\ &= -\delta_E J \end{aligned} \tag{5.8}$$

Thus we find that the anomalous current engendered by the electric force exactly cancels the anomalous current engendered by scattering. This result is not a general one, but is a special consequence of the assumption that $\mathrm{curl}_k X_{nn} = D$ is constant, independent of k. If D varied significantly with k, the two anomalous currents would not cancel one another.

In addition to their direct contribution, the anomalous velocities make an indirect contribution to the current through their effect on the equation which the distribution function satisfies. Thus the "normal" current, i.e. the sum of $(\partial E/\partial p)$ for the carriers, is not the same as it would be if $\mathrm{curl}_k X = D$ were zero. If we discuss this matter in terms of an ordinary (three-space) momentum-space Boltzmann equation, there are corrections both to the "driving" terms, i.e. inhomogeneous terms, and to the "scattering" terms, i.e. terms homogeneous in the distribution function, for the effects of the anomalous velocities. These effects can be treated by means of our classical theory, but the calculation is fairly complicated. We will not give a derivation here. (We will present a general theory in the next section and Appendix B.) Instead we will close this section by describing the nature and origin of the additional terms in the complete transport equation.

The detailed calculation (cf. Appendix B and Section 5) shows that for our simple example the Boltzmann equation for the distribution function can be written

$$-\frac{f_k^{(1)}}{\tau} = \frac{df_k^{(0)}}{dE} F \cdot V_k^{(0)} + \frac{df_k^{(0)}}{dE} F \cdot \left.\frac{dp}{dt}\right|_{sc} \times D/\hbar + \\ + \sum_{k'} (f_k^{(1)} - f_{k'}^{(1)}) W_{kk'}^{(A)} \tag{5.9}$$

in which $f_k^{(0)}$ is the Boltzmann function for an equilibrium ensemble and $f_k^{(1)}$ is the deviation of the Boltzmann function from equilibrium. The second term on the right-hand side of equation (5.9) represents the additional driving term arising from the anomalous scattering velocity, while the third term represents the effect of the anomalous velocity on the scattering. $W_{kk'}^{(A)}$ denotes a transition rate that is antisymmetric for interchange of k and k', so vanishes for detailed balancing.

It is possible to understand the origin of the anomalous driving term in equation (5.9) if we recognize that scattering acts to oppose any steady current, whether we call it "anomalous" or "normal". First we note that $(dp/dt)_{sc}$ in the second term of the right-hand side can be written $-p/\tau$ in the relaxation time notation, so the anomalous driving term can be expressed as

$$\frac{df_k^{(0)}}{dE} V_k^{(0)} \cdot (mF \times D/\hbar) \tag{5.10}$$

Next we remark that there will be a steady average force F_s exerted by the scattering system in a direction to oppose any velocity v, no matter whether its origin is "normal" or "anomalous". This force is given by:

$$F_s = -m\langle v \rangle/\tau \tag{5.11}$$

In particular, the anomalous velocity engendered by the electric field evokes a force of scattering governed by equation (5.11). Its magnitude is

$$F_s = mF \times D/\hbar\tau \tag{5.12}$$

Comparing equation (5.12) with the anomalous driving term (5.10), one sees that the complete driving term in the Boltzmann equation (5.9) is just

$$\frac{\partial f}{\partial p} \cdot \frac{dp}{dt} = \frac{df_k^{(0)}}{dE} v_k \cdot [F + m(F \times D/\hbar\tau)] \tag{5.13}$$

The corrections to the scattering terms in the transport equation may be considered from the same point of view: the anomalous velocity engendered by the scattering force evokes a reaction force of scattering according to equation (5.11). However, in order actually to calculate this force is more difficult, since the anomalous velocity engendered by the scattering force varies from point to point along the trajectory. The

calculation is most easily carried out using quantum-mechanical methods and working with the Fourier components of the scattering interaction. In classical terms, the origin of these anomalous scattering terms is perhaps most easily visualized in terms of the effect of the anomalous velocity of scattering on the trajectory of a particle moving in a central field of force about a hypothetical "scattering center". In classical mechanics this motion follows a plane curve along which angular momentum is conserved, and the same trajectory may be traced in either direction. As a result of the action of the anomalous velocity, the trajectory will not in general be plane (there will be a *torsion* to the trajectory), the angular momentum will not be conserved, and the trajectory can be traced only in one sense. These features of the motion result in a scattering that is asymmetric, so that a current-carrying distribution, as it decays by scattering, rotates in such a way that the current arising in response to a steady driving field is not parallel to the field.

When expressed in terms suitable for use in the Boltzmann equation (5.9), the scattering corrections take the form of an asymmetric transition rate $W_{kk'}{}^{A}$. From considerations of time symmetry it may be shown that

$$W_{kk'}(D) = W_{k'k}(-D) \tag{5.14}$$

The simplest form of $W_{kk'}{}^{(A)}$ consistent with equation (5.14) is

$$W_{kk'}{}^{A} = -\tau_A{}^{-1} k \times k' \cdot D \tag{5.15}$$

Substituting the equation (5.15) for the scattering correction in equation (5.9), one may solve equation (5.9) by iteration in the usual way. The result is readily found to be

$$f_k{}^{(1)} = \left(-\frac{df_k{}^{(0)}}{dE}\right)[v_k \cdot F\tau + \\ + k \cdot F \times D - \tfrac{1}{3} v_k \cdot F \times D(k^2\tau^2/\tau_A)] \tag{5.16}$$

The current carried by the distribution (5.12) is

$$J = ne^2\left(-\frac{2}{3}E\frac{df^{(0)}}{dE}\right) \times \\ \times \left[\frac{F\tau}{m} - \frac{F \times D}{\hbar} + \left(\frac{1}{3}\frac{\tau^2 k^2}{m\tau_A}\right) F \times D\right] \tag{5.17}$$

The current given by equation (5.17) arises entirely from the "normal" currents, since the currents arising from the average of the anomalous velocities exactly cancelled. However, the anomalous terms in the "normal" current (5.17) are entirely similar in appearance to the "anomalous" currents $\delta_F J$ and $\delta_s J$. Since all of these anomalous currents have their origin in closely related phenomena, our classification of some as "normal" and some as "anomalous" is somewhat arbitrary. We think it useful to make distinctions among these various contributions, however, in order to better understand the relation between certain theories of KARPLUS and LUTTINGER and of SMIT concerning the spontaneous Hall effect in ferromagnets. As we will discuss more fully later, these authors suggest that the spontaneous Hall effect can be treated as an application of such a transport theory as we present here.

6. GENERAL THEORY OF ANOMALOUS TRANSPORT CURRENTS

In the previous section we discussed the anomalous electric current for an example chosen as simple as possible in order to minimize the purely computational intricacy. We there assumed $\mathrm{curl}_k X_{nn}$ constant, the energy band under consideration non-degenerate, and the scattering interaction slowly varying. Our purpose there was to convey an impression of what the existence of anomalous transport currents implies for a Boltzmann equation of the simplest type, i.e. what kind of corrections occur. In this section we present a theory of the same phenomena, i.e. electrical conductivity, which is more general in that none of these restrictions is made. As we would expect, the qualitative features of our previous results remain valid in the more general case. Some notational complication is unavoidable, however. We have tried to present the theory in such a way as to preserve the conceptual simplicity of our previous treatment.

The program for this section consists of three presentations. The first is a definition of the anomalous velocity operators for a general band structure. The second is a discussion of the formal characteristics of the transport equation and the conductivity. The third is the presentation of the results of a calculation which yields formulae for the various anomalous effects in terms of matrix elements of the scattering interaction.

We have seen how in the case of a simple band the concept of "anomalous velocity" arises in connection with the definition of field-dependent energy bands. We now want to demonstrate the generalization of this concept to a general band situation. A convenient means of going about this makes use of the expression for the electric current in a steady-state ensemble in terms of a time-independent density matrix which describes the ensemble. Let the motion of the system be governed by the Hamiltonian

$$H = H_0 + V - F \cdot x_c - F \cdot X \tag{6.1}$$

with the notation the same as in Section 4, so that X has no diagonal matrix elements. We now transform away the term $F \cdot X$ as in Section 3. This transformation will add a term linear in F to V and to X. (We assign the linear term added to x_c to X instead for convenience.) We need not indicate these corrections explicitly, since they do not affect the transport quantities to the order of perturbation theory of interest to us.

With this understanding of the notation, the current is then given by

$$J = Tr\{(i/\hbar)\rho[H_0 - F \cdot x_c + V, x_c + X]\} \tag{6.2}$$

We will begin by calculating the part of the expression (6.2) containing X explicitly; this we will show to vanish. Calling this contribution J_X, we rewrite it as the sum of three expressions

$$J_x = Tr\left\{\frac{i}{\hbar}[H_0 + V, \rho X]\right\} -$$

$$- Tr\left\{\frac{i}{\hbar}[F \cdot x_c, \rho X]\right\} - Tr\left\{\frac{i}{\hbar}[H, \rho]X\right\} \tag{6.3}$$

The first of the expression in equation (6.3) vanishes in virtue of the fact that it is the trace of a commutator of operators whose eigenvalues have a lower bound; the second trace vanishes because it is an integral over k of the derivative by k of a periodic function of k; the third trace vanishes in virtue of the Liouville equation for the density matrix

$$[H, \rho] = 0 \tag{6.4}$$

Thus the expression for the current reduces to

$$J^\mu = Tr\left\{\rho\frac{i}{\hbar}[H - F \cdot x_c - V, x_c{}^\mu]\right\} \tag{6.5}$$

The commutator appearing in equation (6.6) may be recognized as formally the same as our expression for the velocity in the field-dependent bands of simple type. We will regard it as the velocity operator for the general field-modified bands.

The definition of the velocity for the field-dependent bands may appear somewhat arbitrary in that we have retained X_{nn} in the expression x_c instead of transforming it away with X. The fact that we could have transformed X_{nn} away with X shows that the current $Tr\{(i/\hbar)\rho[H, X_{nn}]\}$ itself vanishes, a fact already suggested by SMIT. We choose to keep the combination x_c in the definitions to maintain the equations in a form that is manifestly phase-invariant. Clearly, however, the entire current is given by $Tr\{i\rho[H, (i\partial/\partial k)]\}$, which cannot be transformed away by the arguments above, because of the fact that $(i\partial/\partial k)$ is a singular operator whose eigenvalues are bounded neither above nor below.

We remark that it is not necessary to place emphasis on the diagonal matrix elements in computing the anomalous current; by a suitable use of the commutation relations for x_c and X we could express these current primarily in terms of the matrix elements of X. The principal reason for preferring the diagonal form is the closer relationship to the Boltzmann description and semiclassical ideas.

We now proceed to a discussion of the formal theory of the electrical conductivity. In the simplest theory of electrical transport the transport equation takes the form

$$F \cdot v_k \frac{df_k^{(0)}}{dE} = \sum_{k'} (f_{k'} - f_k) W_{k'k} \tag{6.6}$$

when considerations such as the failure of detailed balancing can be ignored. Here f_k denotes the term of the distribution function linear in the field F, $f^{(0)}$, the zero field distribution. For formal reasons we will re-express this as

$$-F \cdot v_m + \sum_{m'} R_{mm'} f_{m'} = 0 \tag{6.7}$$

where m denotes a wave number k, and

$$R_{mm} = \left(-1 \Big/ \frac{df_m^{(0)}}{dE}\right) W_{mm}$$

$$R_{mm'} = \left(1 \Big/ \frac{df_m^{(0)}}{dE}\right) W_{mm'}$$

In simple situations energy is conserved in scattering and $R_{mm'} = R_{m'm}$. In the above notation the μ^{th} component of current J is

$$J^\mu = \sum_m f_m v_m{}^\mu \tag{6.8}$$

and the $\mu\nu$ component of conductivity is

$$\sigma^{\mu\nu} = \sum_{mm'} v_m{}^\mu R^{-1}{}_{mm'} v_{m'}{}^\nu \tag{6.9}$$

From the symmetry of $R_{mm'}$ follows the symmetry of $\sigma^{\mu\nu}$.

We will now present the generalization of equations (6.7)–(6.9) that is required to describe the situation in a general band structure. The justification for the forms given here is contained in Appendix B, which comprises a transport theory after the manner of KOHN and LUTTINGER[2]. The general forms for the transport equation, the current and the conductivity, are, respectively,

$$-F^\mu[v_m{}^{0\mu} - v_m{}^{E\mu}] + \sum_{m'} R_{mm'} f_{m'} = 0 \tag{6.10}$$

$$J^\mu = \sum_m f_m[v_m{}^{0\mu} + v_m{}^{E\mu}] + \sum_m \frac{df_m^{(0)}}{dE}[F^\nu v_m{}^{0\nu} X_m{}^\mu - F^\nu X_m{}^\nu v_m{}^{0\mu}] \tag{6.11}$$

$$\sigma^{\mu\nu} = \sum_{mm'} [v_m{}^{0\mu} + v_m{}^{E\mu}] R^{-1}{}_{mm'} [v_{m'}{}^{0\nu} - v_{m'}{}^{E\nu}] - \sum_m \frac{df_m^{(0)}}{dE}[v_m{}^{0\mu} X_m{}^\nu - X_m{}^\mu v_m{}^{0\nu}] \tag{6.12}$$

In these equations v^0 and v^E represent "odd" and "even" parts of the velocity in a sense to be discussed more fully below. The index m now denotes a Bloch state (n, k, σ) with σ spin index. The transition probability in equation (6.10) need not be such as to give detailed balancing, so

$$R_{mm'} \neq R_{m'm} \tag{6.13}$$

The conductivity $\sigma^{\mu\nu}$ given by equation (6.12) may be symmetric or not. If the Hamiltonian of the system has time-inversion symmetry, σ is symmetric. For, if Km denotes the state corresponding to state m with the time reversed, it can be established that

$$\left.\begin{aligned} X_{mm'} &= X_{Km'Km} \\ v_m{}^0 &= -v_{Km}{}^0 \\ v_m{}^E &= v_{Km}{}^E \\ E_m &= E_{Km} \\ R_{mm'} &= R_{Km'Km} \end{aligned}\right\} \tag{6.14}$$

Substituting the equations (6.14) into the expression (6.12) and using the fact that the summation index Km is equivalent to the summation index m, one readily verifies that

$$\sigma^{\mu\nu} = \sigma^{\nu\mu}$$

If the Hamiltonian of the system does not have time-inversion symmetry, $\sigma^{\mu\nu}$ may have an antisymmetric part, and in general it will have. The antisymmetric part of σ may originate either in the antisymmetric way that v^E and X enter equation (6.12) or in the fact that $R^{-1}{}_{mm'}$ does not necessarily have the time-symmetry behavior (6.14). The contribution of v^E and X we have attributed to anomalous velocities. An asymmetric conductivity is thus the most favorable opportunity for observing the effects of anomalous velocities.

Explicit expressions for v^0, v^E and $R_{mm'}$ may be obtained by, e.g., the procedures of KOHN and LUTTINGER, in terms of the matrix elements of x_c, X, and the scattering interaction. An outline of such a transport theory is given in Appendix B, where expressions for v^0 and v^E are given. Explicit formulae for the quantities $R_{mm'}$ can be worked out from the formulae of KOHN and LUTTINGER. The general formulae are quite complicated, and could not be given here without extensive notational development which would be excessive for our purposes. Let it suffice to say that when $R_{mm'}$ is developed as a perturbation series of

powers of V, meaningful asymmetries occur in every order after the second. To second order in V the explicit expressions for the velocity are

$$v_m{}^{0\mu} = \frac{i}{\hbar}\frac{\partial}{\partial k^\mu}[E_m + E_m{}^{(2)}] \tag{6.15a}$$

$$v_m{}^{E\mu} = -\pi \sum_{m'} \delta(E_m - E_{m'})\{[V, x_c{}^\mu]_{mm'} V_{mm'} + \text{c.c.}\} \tag{6.15b}$$

Here $E_m{}^{(2)}$ denotes the second-order perturbation correction to the energy of state m.

The first feature of the equations (6.15) on which we wish to comment is the designations "even" and "odd" which we have employed in equation (6.10) and subsequent equations. These designations are descriptive of the two kinds of behavior of these velocities under the time-reversal operations as expressed in equations (6.14). The "odd" behavior of the normal velocity is usual. However, the "even" behavior of expression (6.15b), which involves the anomalous velocity engendered by scattering, deserves comment. It can be verified that $v_m{}^E = v_{Km}{}^E$ when time symmetry is present. (Note that in equation (6.15b) V in the commutator should include all of H except H_0, the unperturbed Hamiltonian, except that the electric-field terms are omitted in the Ohm's law approximation). This implies that the states m and Km have the *same* even current associated with them, so their even currents do not cancel one another. On the other hand, the sum of the even velocities of all states having the same energy clearly vanishes. Thus, if the distribution function is a function of energy alone, the even currents will add up to zero. If time symmetry is not present, such argument cannot be made. The states m and Km in general do not have the same energy, and no particular relation exists between $v_m{}^E$ and $v_{Km}{}^E$. Nevertheless, it follows immediately from equation (6.15b) that the sum of the even velocities associated with all of the states of a given energy vanishes. Thus a necessary condition that the even velocities (and, of course, the odd velocities) contribute to the total current is that the distribution function not be merely a function of energy.

The intimate involvement of $v_m{}^E$ with the scattering interaction implies that, strictly speaking, $v_m{}^E$ is not a property of the microscopic state m: ultimately $v_m{}^E$ depends also on the statistical ensemble describing the system in that the sign of $v_m{}^E$ *depends on the direction of physical time*.* Thus although $v_m{}^E$ is a microscopic variable in that it has a definite value for each microscopic state, that value is contingent on the overall macroscopic condition of the ensemble! As a final remark in this general connection, it is noteworthy that the even current can not contribute to entropy production.

Before concluding this section we wish to say a few more words about the part of the total current that is directly related to the anomalous velocity. This current contributes to the antisymmetric part of the conductivity σ, a part we will call σ_A.

$$\sigma_A{}^{\mu\nu} = \sum_{mm'} [v_m{}^{0\mu} R^{-1}{}_{mm'} v_{m'}{}^{E\nu} - v_m{}^{E\mu} R^{-1}{}_{mm'} v_{m'}{}^{0\nu}] - \sum_m \frac{df_m{}^{(0)}}{dE}[v_m{}^{0\mu} X_m{}^\nu - X_m{}^\mu v_m{}^{0\nu}] \tag{6.16}$$

We have seen that in the simple problem of Section 5 the two anomalous currents were exactly equal, and it might be expected that they would be of comparable magnitude. SMIT, in a paper which we will discuss in the next section, has suggested that the total current directly attributable to the anomalous velocities vanishes in general. In order to clarify what the real situation is, we wish to insert in equation (6.16) the exact expression (6.15b) for $v_n{}^E$ and show to what extent cancellation can be effected. Inserting the explicit expression for the matrix elements in equation (6.15b), one finds for the even velocity

$$v_m{}^{E\mu} = \pi i \sum_{m'} \delta(\omega_{mm'}) \left[\left\{ \left(\frac{\partial}{\partial k_\mu} + \frac{\partial}{\partial k_\mu{}'} \right) V_{mm'} \right\} V_{m'm} - \text{c.c.} \right] + 2\pi \sum_{m'} \delta(\omega_{mm'}) |V_{mm'}| \frac{df_m{}^{(0)}}{dE} (X_m{}^\mu - X_{m'}{}^\mu) \tag{6.17}$$

* We refer by this term to the time direction in which entropy increases in the ensemble under consideration. We use "physical" in distinction to "geometrical", since in dynamics time is simply a coördinate whose direction can be chosen arbitrarily.

VOL
10
195

To the perturbation approximation in which we work, the second summation may be expressed in terms of (the symmetric part of) $R_{mm'}$, and $v_m{}^E$ re-expressed as

$$v_m{}^{E\mu} = w_m{}^\mu + \sum_{m'} R_{mm'} X_{m'} \qquad (6.18)$$

where $w_m{}^\mu$ is just a notation for the first sum in (6.17). Inserting the expression (6.18) into (6.16), we find that the terms involving X_m explicitly cancel one another, and we are left with

$$\sigma_A{}^{\mu\nu} = \sum_{mm'} [v_m{}^{0\mu} R^{-1}{}_{mm'} w_{m'}{}^\nu - w_m{}^\mu \times R^{-1}{}_{mm'} v_{m'}{}^{0\nu}] \qquad (6.19)$$

The form (6.19) represents the maximum formal simplication which we have been able to make in the general case. However, the apparent simplification is somewhat illusory, since the summand of the expression (6.19) is not phase-invariant. Thus we have preferred to preserve the form (6.16) (which does not suffer from such a defect: the first summation in (6.16) is manifestly phase-invariant and the second summation becomes so after a trivial integration by parts). It should be noted that even for the simple example considered in Section 5 the conductivity (6.16) does not vanish.

7. SUMMARY AND DISCUSSION

Previous work had shown that when a crystal electron is accelerated by weak external fields the "physical energy bands" in which it can move are not the Bloch bands of the unperturbed crystal but "field-modified" Bloch states. In this paper we have shown that if we set up the quantum-mechanical equations in the "field-modified" band representation, the average velocity is changed, so that it comprises, in addition to the "normal" velocity $(\partial E/\partial p)$, anomalous velocities proportional to the gradient of the perturbing potential and to $\mathrm{curl}_k X_{nn}$. We have shown that formally the anomalous velocities may be viewed as arising from the non-commutability of the components of the crystal coördinate x_c.

In Sections 5 and 6 we have discussed the role of the anomalous velocities in electrical conduction, and have shown how the concept of anomalous velocities may be generalized to the case of a complex band structure with overlapping bands. We have seen that in problems for which time-reversal symmetry is absent the anomalous velocities can give rise to *anomalous transport currents*. We have given a theory of these currents, and in Appendix B we have established its connection to related theories of KOHN and LUTTINGER and of LUTTINGER, who have discussed such currents without the use of the concept "field-modified bands". We now want to give quantitative estimates of the importance of the anomalous currents in transport processes.

From the most general considerations we would expect that the average value of $\mathrm{curl}_k X_{nn}$ could hardly exceed L^2(L = the lattice spacing) for any considerable portion of the Brillouin zone. Using the formula (3.4) for the anomalous velocity engendered by the electric field, and expressing this velocity in terms of an equivalent mobility which would yield the same current, we find for this mobility

$$\mu_{eq} \lesssim (eL^2/\hbar) \sim 0{\cdot}1(\mathrm{cm}^2/\mathrm{vsec}) \qquad (7.1)$$

The mobility (7.1) is quite small compared to typical mobilities in metals or other solids to which the simple band theory might be properly applied. Moreover, the estimate (7.1) is an upper limit on what might be expected to be the average value of the equivalent mobility over a large fraction of a Brillouin zone. Thus there are probably few if any materials to which our theory is applicable and for which the anomalous currents are comparable in magnitude with the normal velocities of drifting in the electric field.

The direction of the anomalous velocity (viz. normal to the electric field) and its small magnitude suggest that it be compared with a Hall velocity, which is related to the electric field by

$$v_H \sim EB\mu_H{}^2 \qquad (7.2)$$

in which B is the magnetic induction and μ_H the Hall mobility. If we try to interpret the anomalous current as a Hall current, its magnitude will depend on the magnitude of B. With such an interpretation an analogous estimate to (7.1) above gives for the equivalent Hall mobility to yield the same current as the anomalous velocity

$$\mu_{Heq} \lesssim (eL^2/\hbar B)^{\frac{1}{2}} \sim 3\times 10^3 B^{-\frac{1}{2}}(\mathrm{cm}^2\mathrm{Oe}^{\frac{1}{2}}/\mathrm{vsec}) \qquad (7.3)$$

Taking as a typical saturation induction the value 10^4 Oe, we find from (7.3) a mobility of 30 cm^2/v sec. This mobility is comparable to that observed in many metals, so it seems entirely possible that the anomalous currents could lead to observable effects comparable to the Hall effect in such metals.

We were led to these last observations by the fact that KARPLUS and LUTTINGER[1] and later SMIT[9,10] have suggested that the origin of the spontaneous Hall effect in ferromagnets is in what we have called anomalous currents. Our estimate (7.3) is in accord with the conclusions of those authors that the anomalous currents are of the same order of magnitude as some of the observed effects in transition metals. KARPLUS and LUTTINGER have also shown that in a typical case the spin-orbit coupling in a ferromagnet would result in an average component of $\mathrm{curl}_k X_{nn}$ in the direction of the magnetization as required to produce the spontaneous Hall effect.

It should be emphasized that the spin-orbit interaction plays an essential role in producing a situation for which the anomalous currents do not vanish. Thus, for our transport theory to yield an asymmetric conductivity, in the absence of a magnetic field, it is required *both* that there be a finite magnetization, which destroys the time symmetry of the basic lattice, *and* that there be the spin-orbit coupling, which communicates the lack of time symmetry to the potential in which the electron moves. That is to say, in the absence of spin-orbit coupling the potential in which the electron moves still have time symmetry, even in the presence of a finite magnetization.

It is very difficult to conclude that the origin of the spontaneous Hall effect lies in the anomalous currents: the energy-band situation in a typical ferromagnet is very complicated, and it would be a major problem to carry through the transport theory with a realistic model of such a band structure. We will not attempt any such thing in this paper. However, we will discuss the theories of KARPLUS and LUTTINGER, of SMIT, and of LUTTINGER, since our theory permits us to clarify certain matters that were in controversy among these authors.

We have already noted the result of KARPLUS and LUTTINGER that if the crystal under consideration had a finite magnetization M (but no external magnetic field) there would be, in virtue of the spin-orbit interaction, a component of $\mathrm{curl}_k X_{nn}$ in the direction of the magnetization, and the anomalous transport currents would flow in the direction $E \times M$. KARPLUS and LUTTINGER have proposed a theory of the spontaneous Hall effect based on this fact. Their theory was not based on the idea of field-modified bands, but was carried out by means of a calculation using the Bloch functions of the unperturbed problem and a density matrix description of the transport ensemble.

In carrying out their transport theory they did not treat the mechanism of scattering explicitly. They did, however, attempt to take account of the effect of the electric perturbation on the scattering by assuming in effect that the density matrix relaxed toward $\rho_0(H_0 - F \cdot X_{nn})$ rather than towards $\rho_0(H_0)$. In the categories of this paper they took into account the anomalous velocity engendered by the electric field and part of the anomalous driving term in the transport equation, the part that comes from neglecting $w_m{}^\mu$ in (6.18). We may relate their expression for the conductivity to the expression (6.16) by remarking that they took account of the third and fourth summations in (6.16) together with that part of the second summation which is obtained by setting $w_m{}^\mu = 0$.

KARPLUS and LUTTINGER finally obtained for the current

$$J^\mu = \sum_m \left(-\frac{df_m^{(0)}}{dE} \right) \frac{\partial X_m{}^\mu}{\partial k^\nu} \frac{dk_\nu}{dt} \bigg|_{\text{el field}} \tag{7.4}$$

The expression (7.4) has a very simple interpretation: since the position operator is momentum-dependent, the electric force causes a change of position proportional to the *rate of change of momentum*. SMIT[9] critized the theory of KARPLUS and LUTTINGER, pointing out that it is inconsistent to include the effects (7.4) that result from the electric force but not the analogous effects that result from the force of scattering. He gave an argument that purports to prove that the average current associated with the anomalous currents is exactly zero when all of the effects are taken into account. SMIT's reasoning amounts to taking account of both the electric and the scattering

forces, but doing so in the same incomplete manner as KARPLUS and LUTTINGER had taken account of the electric force alone. As we showed at the end of the last section, such a treatment obtains a vanishing result by neglecting all of the contributions to σ_A from $w_m{}^\mu$. To neglect $w_m{}^\mu$ is in general wrong. Further, in the special example of Section 5 for which all of these effects can be evaluated, it is found that the part $w_k{}^\mu$ is twice as large as the other part of $v_k{}^{E\mu}$ and leads to a non-zero value of σ_A of the same magnitude (but opposite sign) as originally found by KARPLUS and LUTTINGER. Thus while SMIT is right that the forces of scattering result in anomalous effects comparable to the anomalous effects induced by the electric field, his conclusion that these effects exactly cancel out is incorrect. His error may be traced to an inconsistency involving an implicit change of representation of his density matrix in the course of his calculation of the current.

More recently SMIT[10] has proposed that the spontaneous Hall effect be attributed to the anisotropy in the scattering that can exist when the Hamiltonian of the system lacks overall time symmetry. This anisotropy is described in our theory by the anisotropy of $R_{mm'}$ of equation (6.10). In our opinion such effects are unquestionably comparable to those described by equation (6.16) and contribute significantly to the total current.

KOHN and LUTTINGER realized that in order to obtained satisfactory answers to questions that arose in connection with the theories discussed above, it would be necessary to extend the usual quantum-mechanical version of transport theory and to refine the systematics of its presentation. For the special case of impurity scattering, they developed a transport theory capable of treating the anomalous effects unequivocally. LUTTINGER[11] has recently applied this theory to calculate the electrical conductivity of a simple system very similar to that of our Section 5. He has evaluated the effects of all of the anomalous currents, including those originating in the asymmetry of $R_{mm'}$. His results are in quantitative agreement with ours for the example presented in Section 5. His results show that the effects arising from the asymmetry of $R_{mm'}$ depend strongly on the form of the scattering potential V. On the whole his work certainly gives support to the suggestion that the spontaneous Hall effect is a manifestation of the anomalous transport effects with which we have been concerned. While this more recent theory does not give a result agreeing quantitatively, or in sign, with the original theory of KARPLUS and LUTTINGER, we may say that it confirms their basic idea.

The theories of LUTTINGER and of SMIT treated the collisions according to the model of scattering by impurities. This theory has the feature that the largest effect comes from the corrections to $R_{mm'}$ of third order in the scattering interaction. This kind of theory leads to a spontaneous Hall coefficient proportional to the resistivity, whereas the observed spontaneous Hall coefficients vary as a higher power of the resistivity, often as the resistivity squared. If the important scattering interaction were phonon scattering it is to be expected that the largest effects would be comparable to those arising from the corrections to $R_{mm'}$ of fourth order in the scattering interaction. That is because, unless the anharmonic interactions between phonons are taken into account, phonon-scattering processes are always of even order in the scattering interaction. A fourth-order effect contribution to the current results in a spontaneous Hall coefficient that varies as resistivity squared.[1] We might expect in general that mixed scattering would have to be considered in analyzing experiments done on ferromagnetic alloys. A semi-empirical theory taking account of all such effects might well be feasible along the lines of our Section 6. To develop it any further, however, would too much enlarge the scope of this paper.

APPENDIX A

The Dirac Equation

Mathematically, the Dirac equation is equivalent to an extremely simple band structure. It therefore provides a simple example for the ideas outlined in this paper. The usual presentation of the Dirac theory is not given in terms of basis functions which are eigenfunction of the energy, as are Bloch functions in band theory. The transformation to such a basis has, however, been given by FOLDY and WOUTHUYSEN.[12]

The required transformation is

$$U = (E+H)/\sqrt{[2E_p(E_p+mc^2)]}$$

which is unitary and Hermitian. E_p is

$$\sqrt{(m^2c^4+p^2c^2)}$$

The velocity and coördinate are easily calculated

$$v^\mu = \beta v_p{}^\mu - c\alpha^\mu + [c^2\alpha\cdot pp^\mu/E_p(E_p+mc^2)] \quad \text{(A1a)}$$

$$x^\mu = \hbar i\frac{\partial}{\partial p^\mu} - \frac{\hbar(v_p\times\sigma)_\mu}{2(E_p+mc^2)} + \frac{ihc}{2E_p}\beta\alpha_\mu - \frac{i\hbar c\beta(\alpha\cdot p)p_\mu c^2}{2E_p{}^2(E_p+mc^2)} \quad \text{(A1b)}$$

where $v_p = (\partial E_p/\partial p)$. The first two terms constitute x_c, and the commutator $[x_c{}^\mu, x_c{}^\nu]$ is

$$[x_c{}^\mu, x_c{}^\nu] = i\delta_{\mu\nu\lambda}\sigma^\lambda\tfrac{1}{2}(\hbar/mc)^2 \quad \text{(A1c)}$$

If we now add a slowly varying external field to the problem, we find, as in Section 6, that the Hamiltonian is

$$H = E_p\beta + V(x_c+X) \quad \text{(A2a)}$$

$$\doteq E_p\beta + V(x_c) + X\cdot\frac{\partial V}{\partial x} \quad \text{(A2b)}$$

$$= E_p\beta + V\left(i\frac{\partial}{\partial k}\right) - \frac{\partial V}{\partial x}\cdot\frac{1}{2}\frac{\hbar(v\times\sigma)}{E_p+mc^2} + \text{terms in } \alpha \quad \text{(A2c)}$$

As in the body of this paper, the terms in $\bar{\alpha}$ can be removed by a transformation, leaving only the terms written explicitly in (A2c). The third term is, of course, the spin-orbit energy, which will be more readily recognized if we keep only lowest-order terms in the velocity.

$$H_{s.o.} \cong -\frac{\hbar}{4m^2c^2}\frac{\partial V}{\partial x}\cdot p\times\sigma \quad \text{(A3)}$$

The velocity is readily evaluated as

$$v = \frac{i}{\hbar}[H, x] \cong \beta\frac{p}{m} - \frac{1}{2}\left(\frac{\hbar}{mc}\right)^2\frac{\partial V}{\partial x}\times\sigma \quad \text{(A4)}$$

This is not $(\partial H/\partial p)$, whose second term would be only one-half that of (A4). The difference is the term $i[V, x_c]$, which can be interpreted as a change in the electric dipole-moment as the electron is accelerated. It is entirely analogous to the variation in $X_n(k)$ with k. Like the current due to the latter, it cannot be observed in any steady-state situation.

The last term in equation (A4) represents the "spin-current". It is the exact formal analogue of the anomalous velocities discussed in our paper.

APPENDIX B

In this Appendix we shall obtain the form of the Boltzmann equation used in Section 6 by methods closely related to those of KOHN and LUTTINGER.

We again consider a system whose Hamiltonian is

$$H = H_0 - F\cdot x_c + V$$

The properties of the system will be described by a density matrix, ρ, which we shall divide into two terms, P independent of the field and F proportional to it. F may in turn be split into a part f with only diagonal elements and a part g without diagonal elements. The equation of motion of the density matrix is

$$i[P, H_0+V] - i[P, F\cdot x_c] + i[F\cdot H_0+V] = 0 \quad \text{(B1)}$$

The first term is of zero order in the field, while the remainder are of first order. We write the latter in the term

$$-i[P, F\cdot x_c]_{mm} + i[g, V]_{mm} = 0 \quad \text{(B2a)}$$

$$-[P, F\cdot x_c]_{mm'} + [f, V]_{mm'} = -[g, H_0+V]_{mm'} \quad \text{(B2b)}$$

Since equation (B2b) is a linear equation for g, we can replace it with

$$g = g^{(1)} + g^{(2)} \quad \text{(B3a)}$$

$$-[P, F\cdot x_c]_{mm'} = -[g^{(1)}, H_0+V]_{mm'} \quad \text{(B3b)}$$

$$[f, V]_{mm'} = -[g^{(2)}, H_0+V]_{mm'} \quad \text{(B3c)}$$

Thus $g^{(1)}$ is driven by the electric field alone, while $g^{(2)}$ is driven by the diagonal elements f regardless of the field. (If we do not require the system to be stationary the term dg/dt can be similarly split, so that this feature holds for periodic, as well as steady-state processes.) This clearly permits a considerable simplification. We can now rewrite equation (B2a):

$$-i[P, F\cdot x_c] + i[g^{(1)}, V] + i[g^{(2)}, V] = 0 \quad \text{(B4)}$$

The first and third term are simply the usual driving and scattering terms of the Boltzmann equation, whereas the middle term is of a hybrid nature and can be discussed from either point of view. We shall treat it as part of the driving term, since it does not involve the perturbed distribution. We do not wish to embark at this point on a detailed discussion of transport theory. Consequently we shall regard the equations (B3) and (B4) as determining an iterative solution for f and g in powers of V, and shall content ourselves with the lowest orders so far as actual calculation are concerned. More general, but less physically clear, arguments verify the general nature of our conclusions.

We will need $P = P(H+V)$ to the following accuracy

$$P_m \equiv P_{mm} = \rho_m + \rho'_m\sum_{m'}\frac{|V_{mm'}|^2}{\omega_{mm'}} - \sum_{m'}(\rho_m-\rho_{m'})\left|\frac{V_{mm'}}{\omega_{mm'}}\right|^2 \quad \text{(B5a)}$$

$$P_{mm'} = \frac{\rho_m-\rho_{m'}}{\omega_{mm'}}V_{mm'} \quad \text{(B5b)}$$

where ρ_m is the zero-order density matrix.

For g we shall use

$$\left.\begin{aligned} g_{mm'}{}^{(1)} &= -\frac{[P, F\cdot x_c]}{\omega_{mm'}-is}{}_{mm'} \\ g_{mm'}{}^{(2)} &= \frac{(f_m-f_{m'})V_{mm'}}{\omega_{mm'}-is} \end{aligned}\right\} \quad \text{(B6)}$$

The term (is) in the denominator is a small imaginary term taken to approach zero, whose only function is to define the method of integration at the zeroes of $\omega_{mm'}$. The use of this term requires some justification, but such a discussion is beyond the scope of this paper. A similar term is used by KOHN and LUTTINGER[13] after a more elaborate preparation. The appearance of the imaginary part is standard in scattering theory, and is essential for obtaining irreversible behavior. Its presence results in certain irregular integrals containing a term $i\pi\delta(\omega_{mm'})$ in addition to $P(1/\omega_{mm'})$.

A. We now evaluate the driving terms. To obtain the second term of equation (B4), we substitute (B5b) into (B6):

$$g^{(1)}{}_{mm'} = \frac{iV_{mm'}}{\omega_{mm'}-is}F\cdot\left(\frac{\partial}{\partial k}+\frac{\partial}{\partial k'}\right)\left(\frac{\rho_m-\rho_{m'}}{\omega_{mm'}}\right)-\frac{(\rho_m-\rho_{m'})}{\omega_{mm'}}\frac{[V, F\cdot x_c]_{mm'}}{\omega_{mm'}-is}$$

$$i[g^{(1)}, V]_{mm} = -F\cdot\sum_{m'}\left(\frac{\partial}{\partial k}+\frac{\partial}{\partial k'}\right)\left(\frac{[\rho_m-\rho_{m'}]|V_{mm'}|^2}{\omega_{mm'}}\right)-\sum_{m'}\left|\frac{V_{mm'}}{\omega_{mm'}}\right|^2 F\cdot(\rho_m'v_m-\rho_{m'}'v_{m'})+$$

$$+\pi\sum_{m'}\delta(\omega_{mm'})\rho_{m'}'([V, F\cdot x_c]_{mm'}V_{m'm}+\text{c.c.}) \quad \text{(B7)}$$

Upon combining (B7) with $-i[P, F\cdot x_c]$, we obtain the total driving term (to the order considered):

$$D_m = -\bar{\rho}'_m F\cdot\frac{\partial}{\partial k}(H_0+H^{(2)})-$$

$$-\sum_{m'}\left|\frac{V_{mm'}}{\omega_{mm'}}\right|^2(\rho'_m v_m-\rho'_{m'}v_{m'})+$$

$$+\rho'_m\pi\sum_{m'}\delta(\omega_{mm'})([V, F\cdot x_c]_{mm'}V_{m'm}+\text{c.c.}) \quad \text{(B8)}$$

$$H^{(2)} = \sum_{m'}\frac{|V_{mm'}|^2}{\omega_{mm'}}$$

$$\bar{\rho} = \rho(H_0+H^{(2)})$$

B. We shall not obtain detailed expression for $i[g^{(2)}, V]$, but observe that since it is linear in the f_m, it can be written in the form:

$$i[g^{(2)}, V]_{mm} = \sum_{m'}(W_{mm'}f_{m'}-W_{m'm}f_m)$$

$$= \rho_m'\sum_{m'}R_{mm'}f_{m'} \quad \text{(B9)}$$

To second order in V, $W_{mm'}=W_{m'm}=2\pi\delta(\omega_{mm'})|V_{mm'}|^2$ so that R is symmetric and scattering conserves energy. To higher order, neither of these characteristics holds.

C. The current is

$$J = \sum_m f_m v_m+\sum_{mm'}g^{(2)}{}_{mm'}v_{m'm}+$$

$$+\sum_{mm'}g^{(1)}{}_{mm'}v_{m'm}-\sum_m\rho_m F\times(\nabla\times X_m)$$

The last term has been sufficiently discussed in Section 4. The third is of higher order than the others and will be discussed later. The first two can be rewritten, after solving (B3c) for to lowest order. We will call this part of J, J_d.

$$J_d = \sum_m f_m(v_m+\sum_{m'}\frac{V_{mm'}i}{\omega_{mm'}-is}[V, x_c]_{m'm}+\text{c.c.})$$

$$= \sum_m f_m\Big\{\frac{\partial}{\partial k}(H_m+H_m{}^{(2)})-$$

$$-\sum_{m'}\left|\frac{V_{mm'}}{\omega_{mm'}}\right|^2(v_m-v_{m'})-$$

$$-\pi\sum_{m'}\delta(\omega_{mm'})([V, x_c]_{mm'}V_{m'm}+\text{c.c.})\Big\} \quad \text{(B10)}$$

We see that there is a close formal relationship between (B8) and (B10). The only differences are due to (a) the fact that the last term has a different sign in the two expressions, and (b) the fact that, unlike f_m in (B10), ρ'_m cannot be factored out of (B8).

These dissimilarities and the asymmetry of R' result in much more cumbersome expressions than (6.10). Not all of these lead to actual asymmetrics in σ, however. We can obtain more compact expressions by making the unitary transformation generated by S,

$$S_{mm'} = P \cdot \frac{V_{mm'}}{\omega_{mm'}}$$

This results in the following expressions

$$v_{m'} = v_m{}^0 + v_m{}^E \tag{B11a}$$

$$D_{m'} = \bar{\rho}'_m F \cdot (v_m{}^0 - v_m{}^E) \tag{B11b}$$

$$v_m{}^0 = \frac{\partial}{\partial k}(H_m + H_m{}^{(2)}) \tag{B11c}$$

$$v_m{}^E = -\pi \sum_{m'} \delta(\omega_{mm'})([V, x_c]_{mm'} V_{m'm} + \text{c.c.}) \tag{B11d}$$

The form of (B9) is unchanged, but R is changed. These expressions are the ones used in (5.10).

An important feature of $v_m{}^E$ is that it is even under the symmetry operator time reversal, when this is a symmetry of the system. This is readily deduced from the fact that $V_{KmKm'} = V_{mm'}$ where K stands for the time-reversal operator. By contrast v^0 is odd under K, as a velocity should be. On the other hand, v^0 is unaffected by the sign of s, whereas v^E changes signs with s. This is the operator we have called physical time-reversal. If we perform both operations, both $v_m{}^E$ and $v_m{}^0$ change sign. The sensitivity of v^E to the sign of s suggests that it is clearly related to the scattering terms equation in (6.4). The intimacy of this connection is discussed below.

One may ask in what sense it is meaningful to describe the higher-order terms in equation (B11) as velocities. These terms represent the non-zero average of the fluctuations in velocity experienced by an electron as it goes through the scattering system. $g^{(2)}{}_{mm'}$ represents the fluctuation in the classical function of $f(p, x)$. The transformation S removes $g^{(2)}{}_{mm'}$ and averages the fluctuations in v. The delta-function contribution v^E must ultimately be attributed to the fact that the environment contains a statistical feature responsible for the increase in entropy, which establishes the direction of physical time.

A really satisfactory discussion of this point would require a more detailed discussion of irreversibility than has yet been given.

So far we have treated the term $i[g^{(1)}, v]_{mm}$ as a driving term in the Boltzmann equation. Alternatively we could have treated it as a scattering term, or more properly we could have considered the terms leading to v^0 as driving terms and the terms leading to v^E as scattering terms, a division which corresponds to separating the principal part contribution from the delta-function contribution of integral involving $(\omega_{mm'} - is)$. Had we done so, the scattering term would have had the form

$$\rho_{m'} w_m \cdot F + \sum_{m'} R_{mm'}(f_{m'} + F \cdot X_{m'} \rho_{m'}) \tag{B12}$$

where w is defined in equation (6.17).

The significance of the last term may be taken as being that f relaxes not to $\rho(H)$ but to $\rho(H - F \cdot X)$. This was assumed by KARPLUS and LUTTINGER in their treatment of the spontaneous Hall effect. It was never an entirely satisfactory assumption, however, since it is not phase-invariant. Clearly the presence of the term in w in (B12) rectifies this problem. This indicates that this term must be of a very similar nature. Indeed it is easy to show that (B12) can be rewritten in the form

$$\pi \sum_{m'} \delta(\omega_{mm'})(V_{mm'}[V, f + \rho' F \cdot x_c]_{m'm} + \text{c.c.}) \tag{B13}$$

Thus in some sense we can speak of f as relaxing to $\rho(H - F \cdot x_c)$. This is much preferable, since $x_c = [i(\partial/\partial k) + X_m]$ is a phase-invariant operator in the same sense that $v = [p + (e/c)a]$ is gauge invariant classically. The singular nature of $F \cdot x_c$ prevents us from rewriting this expression as

$$R_{mm'}(f_m + \rho_m' F \cdot x_c) \tag{B14}$$

In problems where the perturbing potential is not singular, however, this form or its equivalent can and indeed must be used. Thus it makes a profound difference in absorption of waves whether we relax to $\rho(H)$ or to $\rho(H - \phi)$. This was demonstrated by VAN VLECK and WEISSKOPF in the problem of collision broadening in gases, and was also pointed out by BLOUNT in a discussion of ultrasonic attenuation by electrons in metals. It is similarly crucial in the treatment of transport phenomena in large transverse magnetic fields as emphasized by ADAMS and HOLSTEIN[14].

Our results have been obtained rigorously only for terms of order $(V)^2$ smaller than those usually considered. Nevertheless, we anticipate that the important feature of a split into $v^{(0)}$ and $v^{(E)}$ will persist to all orders. New effects will also appear. These will be: (1) currents of the form $g^{(1)}{}_{mm'} v_{mm'}$ due to the part of g which is driven directly by the electric field, and (2) terms resulting from the field-dependence of V, pointed out in Section 6. This will lead to scattering terms like this:

$$F \cdot \sum_{m} (\bar{W}_{mm'} \rho_{m'} - \bar{W}_{m'm} \rho_m)$$

VOL. 10 195

This will give a non-zero effect only in higher-order terms, where scattering does not conserve energy.

REFERENCES

1. KARPLUS R. and LUTTINGER J., *Phys. Rev.* **95,** 1154 (1954).
2. KOHN W. and LUTTINGER J. M., *Phys. Rev.* **108,** 590 (1957).
3. WANNIER G. H., *Phys. Rev.* **100,** 1227 (1955); **101,** 1835 (1956).
4. ADAMS E. N. and ARGYRES P. N., *Phys. Rev.* **102,** 605 (1956).
5. ADAMS E. N., *Phys. Rev.* **107,** 698 (1957).
6. ADAMS E. N., *Phys. Rev.* **85,** 41 (1952).
7. DIRAC P. A. M., *The Principles of Quantum Mechanics* p. 92. Oxford University Press (1947).
8. ADAMS E. N., *Phys. Rev.* **89,** 633 (1953).
9. SMIT J., *Physica* **21,** 877 (1955).
10. SMIT J., *Physica* **24,** 39 (1958).
11. LUTTINGER J. M., *Phys. Rev.* **112,** 739, (1958).
12. FOLDY L. L. and WOUTHUYSEN S. A., *Phys. Rev.* **78,** 29 (1950).
13. LUTTINGER J. M. and KOHN W., *Phys. Rev.* **97,** 869 (1955).
14. ADAMS, E. N. and HOLSTEIN, T. D., *J. Phys. Chem. Solids* **10**, 254 (1959).

OL.
10
959

J. Phys. Chem. Solids Pergamon Press 1959. Vol. 10. pp. 304–310. Printed in Great Britain.

THE CATALYTIC ACTIVITY OF SILVER CRYSTALS OF VARIOUS ORIENTATIONS AFTER BOMBARDMENT WITH POSITIVE IONS

H. M. C. SOSNOVSKY

Division of Tribophysics, Commonwealth Scientific and Industrial Research Organization, University of Melbourne, Australia*

(*Received* 31 *December* 1958)

Abstract—Single crystals of silver with surfaces oriented parallel to (111), (110) and (100) have been bombarded with positive argon ions at voltages between 14 and 4000 V. The catalytic decomposition of formic acid has been used as a test reaction in the temperature range 150–250°C. The parameters log A and E found from Arrhenius plots change appreciably with bombarding ion energy and for each ion energy are different for the three orientations. It is concluded that the reaction occurs at sites where dislocation lines intersect the surface and that a compensating effect occurs which is associated with interaction between dislocations when their density is high.

VOL
10
195

1. INTRODUCTION

IT is well known that the activity of a catalyst can be greatly influenced by treatment of its surface. Ion bombardment has frequently been used to clean surfaces, but, in addition to being cleaned, a surface is damaged by bombardment even with low-energy ions.

FARNSWORTH and WOODCOCK[1] prepared clean surfaces by bombarding nickel and platinum with positive argon ions in a gaseous discharge at 250 V and found that the rate of hydrogenation of ethylene had been thereby increased by factors of 100 for nickel and 10 for platinum. They examined their surfaces by low-energy electron diffraction and reported that defects of a complex nature were present after bombardment.

Ion bombardment of silver produces disoriented regions[2] and thus increases the number of dislocations at the surface. This effect is similar to the increase in dislocation density due to plastic deformation. A change in the activity of a catalyst by plastic deformation was found by ECKELL[3], according to whom the reaction velocity of the hydrogenation of ethylene increased by a factor of from 600 to 1000 when the polycrystalline nickel catalyst was cold-rolled from 3 to 0·1 mm. On subsequent annealing the effect of cold rolling disappeared. CRATTY and GRANATO[4] considered that these results may be due to the introduction of dislocations by rolling. RIENÄCKER[5] found an increase in the rate of decomposition of formic acid on cold-rolling nickel and also a simultaneous increase in the activation energy. However, these surfaces were probably contaminated and apparently were not cleaned satisfactorily after being rolled.

The purpose of the present study was to investigate the effect of surface damage produced by ion bombardment on the rate of the catalytic decomposition of formic acid at various temperatures. The crystal plates of silver used had (111), (100) and (110) planes, respectively, parallel to their surfaces, and for each of the crystals the catalytic activity was measured as a function of the energy of the bombarding ions.

A preliminary report of this work has already been published.[6]

2. EXPERIMENTAL PROCEDURE

(a) *Preparation of single crystals of predetermined orientation*

The silver single crystals (99·97 per cent purity) were grown from the melt in thin sheets (5 × 1·8 × 0·05 cm) in

* Now at the Institute for the Study of Metals, University of Chicago, U.S.A.

a graphite mould. The mould described previously[7] was modified to accommodate a seed crystal and thereby make possible the growth of a crystal of predetermined orientation.[8]

The seed crystals were prepared using two other types of mould (Fig. 1). Several moulds of type (*b*) were made, each with a different angle. By repeated operations with

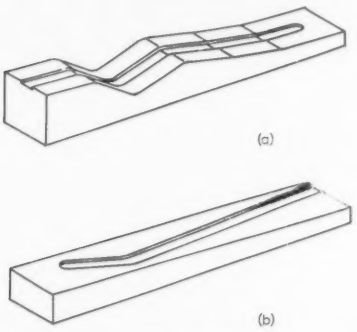

FIG. 1. Graphite moulds for growing thin seed crystals. Close-fitting upper part is not shown. (a) For kinked crystals with sections of different orientations. (b) For changing the direction of growth.

these moulds, using each time a suitable section cut from the previous long crystal, a seed of the required orientation could be grown.

Figure 2 shows the vacuum furnace into which the appropriate mould containing the silver was placed vertically. To remove oxygen from the silver, the tube E was kept evacuated at 10^{-3} mm Hg during the whole period of heating and cooling. The heating of the silver was carried out by induction, the coil being wound more closely over the upper half of the specimen, thereby producing a temperature gradient. The specimen was positioned so that half of the seed crystal remained solid while the other half and the silver above it were melted. The temperature was then slowly decreased over a period of about 15 min by reducing the induction current until the whole specimen solidified. Then the heating was stopped and the mould allowed to cool to room temperature *in vacuo*.

(b) *Surface treatment of single crystals by electropolishing and positive-ion bombardment*

After removing a crystal from the mould, it was chemically polished to a bright finish in hot nitric acid with up to 20 per cent of water added, and then electrolytically polished in a cyanide bath. The electrolyte used was 30 g KCN, 35 g AgCN and 38 g K_2CO_3 in 1 l. of distilled water. It was found advisable to carry out the polishing process in two stages. After approximately 20 min, the polishing was interrupted to remove a solid film which adhered strongly to the surface and largely inhibited further electrolytic polishing. This film was removed by treatment for a short time with hot nitric acid, after which polishing for a few more minutes produced a smooth surface.

The surfaces were then bombarded by positive argon ions in a low-pressure discharge.[2] The specimen surface was set perpendicular to the axis of the discharge tube, which was then evacuated to 10^{-6} mm Hg. The tube was flushed with argon which had passed through a liquid-air trap to remove traces of H_2S from the bladder storing the argon. A steady flow of argon at a low pressure was then established through a leak valve and the discharge started. The discharge was run at an argon pressure of less than 2×10^{-3} mm Hg whatever voltage was applied, so that the mean free path of the ions was high enough to prevent re-deposition of the silver on the

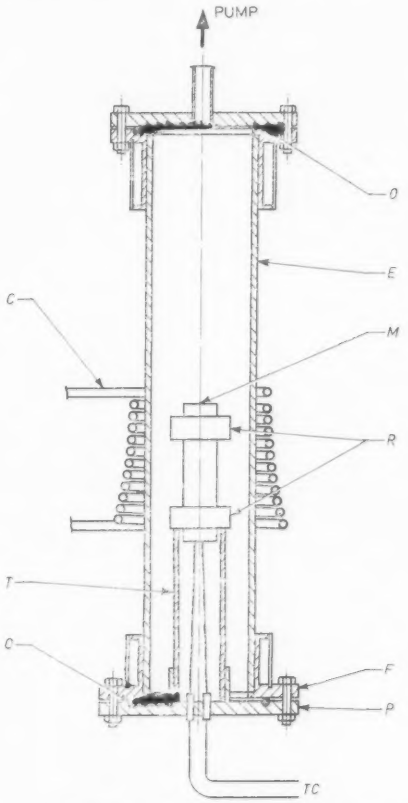

FIG. 2. Vacuum furnace for growing single crystals.

KEY

M Graphite mould held together by graphite rings R.
TC Thermocouple leads.
P, F Metal plates.
O O-ring.
E, T Silica tubes.
C Water-cooled induction coil.

specimen by back scattering. The voltages used varied from 14 to 4000 V. The maximum energy of the bombarding ions, which was less than that to be expected from the voltage applied, was derived in each case from measured ion-energy distributions[9] and the values are indicated in Table 1. Very low discharge currents were used. The energy dissipated was always less than 0·2 W, and the specimen temperature was found to remain below 100°C. The duration of the bombardment was varied between 30 min at 4000 V and 12 hr at 22·5 V to ensure that equilibrium conditions had been reached (see Section 3(d)).

Every surface was cleaned initially by bombardment at a high voltage (between 300 and 4000 V) before being treated at lower ion energies. In all cases after the ion bombardment, and also after being used as catalysts, the surfaces appeared smooth and clean under the microscope. Electron-diffraction patterns of some of these surfaces confirmed that they were clean, but the appearance of spotty rings indicated that structural changes had taken place as a result of the ion bombardment.

In every case the specimen was transferred to the reaction vessel immediately after ion bombardment. It was then annealed *in vacuo* at 250°C for at least 18 hr before rate measurements were begun. One crystal of each orientation was used over the whole range of discharge voltages. However, a few experiments were made on different crystals with the same orientations and under the same bombarding conditions, with comparable results.

Measurement of the reaction rate

The formic acid used in the experiments was prepared from A.R. 98–100 per cent HCOOH by shaking it for two days with anhydrous oxalic acid. It was then distilled at atmospheric pressure through a fractionating column, purified by crystallization, and afterwards distilled *in vacuo* into a storage vessel attached to the apparatus. The dried and purified acid had a melting point of 8·4°C.

The method of investigating the catalytic decomposition of formic acid on silver surfaces was the same as that described previously, a similar flow apparatus being used.[7] The acid decomposed at zero order into CO_2 and H_2 exclusively, but on the glass walls of the apparatus the decomposition occurred by two reactions, forming CO_2, H_2, CO, and H_2O. A McLeod gauge was used to measure the total pressure of the H_2 and CO, and the correction for the decomposition on glass was determined by measurements without the catalyst. Reaction rates on the ion-bombarded silver surfaces were determined in this way at temperatures between 150 and 250°C, and the logarithm of the corrected rate of reaction (ρ) was plotted against $1/T$. A straight line was obtained in each case within the experimental error. The gradient of this line was calculated by the method of least squares and also the intercept at $1/T = 0$, the gradient being proportional to the experimental activation energy E and the intercept the logarithm of the frequency factor A in the Arrhenius equation $\rho = A \exp(-E/RT)$.

3. RESULTS

(a) (111) *surface*

The Arrhenius plot of log ρ against $1/T$ is given in Fig. 3 for applied voltages between 22·5 and 4000 V (maximum ion energies between 15 and 3000 eV). It is seen that within the temperature

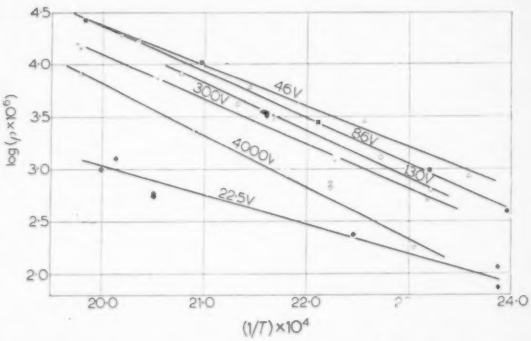

FIG. 3. Arrhenius plots for a (111) surface bombarded with argon ions for various applied voltages. For the corresponding values of maximum ion energy see Table 1.

range used, the lowest values of log ρ are found after bombardment at 22·5 V and the highest values after bombardment at 46 V, the rate changing by a factor of up to 25. On further increasing the voltage, however, the rate decreases. The values of $\log_{10} A$ and E obtained from these plots are given in Table 1. The values of E lie between 12·2 and 22·5 kcal/mole and the corresponding values of $\log_{10} A$ between 2·3 and 7·7. Thus, an increase of about 10 kcal/mole in E is accompanied by an increase in A by a factor of about 10^5. The change in both log A and E is most pronounced in going from a bombarding voltage of 22·5 V to one of 46 V, with a smaller increase after treatment at 86 V. Bombardment of the surface with higher-energy ions (130–4000 V) changes log A and E only slightly.

(b) (110) *surface*

The lowest values of log ρ were found when the surface had been bombarded at 14 V, but the reaction was so slow that a sufficiently accurate rate determination was not possible. The lowest bombarding voltage for which results were plotted (Fig. 4) was 22·5 V. The rate increased continuously with voltage up to 500 V by a factor of up to

100. A slight decrease in the rate was found after bombardment at 4000 V.

The values of $\log_{10} A$ and E are given in Table 1. The values of E lie between 24·1 and 34·5 kcal/mole and those of $\log_{10} A$ between 7·1 and 13·4. These increases occur continuously over the voltage range 22·5–500 V, but the values decrease after bombardment at 4000 V.

which were too low for accurate determinations). At voltages of 46 and 300 V, the rate increased by a factor of 100, but decreased when the voltage was raised to 4000 V. For this orientation the values of log A and E appear to increase continuously as the voltage is increased from 22·5 to 300 V, although the changes in these values are much smaller for this orientation.

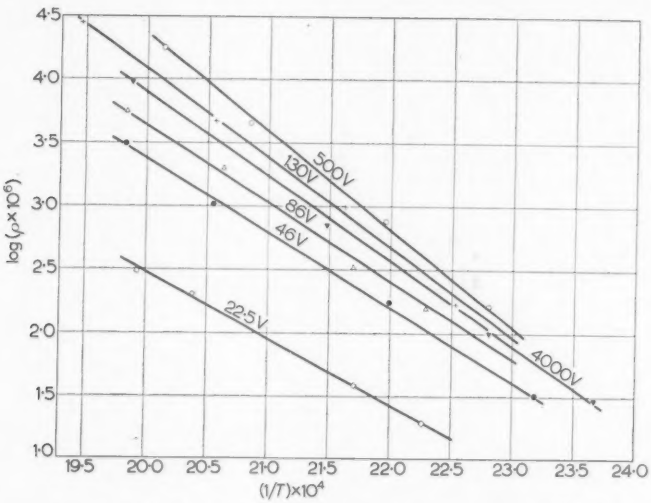

FIG. 4. Arrhenius plots for a (110) surface bombarded with argon ions for various applied voltages.

(c) (100) *surface*

The Arrhenius plots are shown in Fig. 5 and the calculated values of $\log_{10} A$ and E in Table 1. As in the previous two cases, the lowest values of ρ were associated with surfaces bombarded at 22·5 V (argon bombardment at 14 V resulted in rates

(d) *Reproducibility of results*

The time of bombardment for a given voltage was chosen so that an equilibrium state had been reached. For example, after a 30-min bombardment at 4000 V, the Arrhenius plot gave a certain straight line of best fit. Where a different specimen

Table 1. *Effect of bombarding voltage on the catalytic activity of silver crystals of different orientations*

Applied voltage	Max. ion energy (eV)	(111)		(110)		(100)	
		$\log_{10} A$	E (kcal/mole)	$\log_{10} A$	E (kcal/mole)	$\log_{10} A$	E (kcal/mole)
22·5	15	2·3±0·6*	12·2±1·2*	7·1±0·2	24·1±0·5	9·2±0·9	29·9±3·0
46	38	6·1±0·5†	17·6±0·9†	9·1±0·3	26·8±0·7	12·4±0·8	32·5±1·7
86	77	7·3±0·4	20 4±0·8	9·5±1·0	27·1±2·2		
130	118	6·9±0·7	19·9±1·5	12·4±0·6	32·8±1·3		
300	280	6·7±0·9	19·7±1·8			13·2±0·3	34·4±0·6
500	450			13·4±0·4	34·5±0·8		
4000	3000	7·7±1·1	22·5±2·3	11·1±0·3	30·2±0 6	13·0±0·5	35·2±1·1

The ± figures are standard errors and, unless otherwise indicated, were based on four measurements, * on seven measurements and † on five measurements.

with the same orientation and the same bombarding conditions was used, or the same specimen was used and only the bombarding time changed, in nearly every case the Arrhenius plot resulted in a straight line almost coincident with the previous one. A slight change in the gradient was found, corresponding to a change in E of

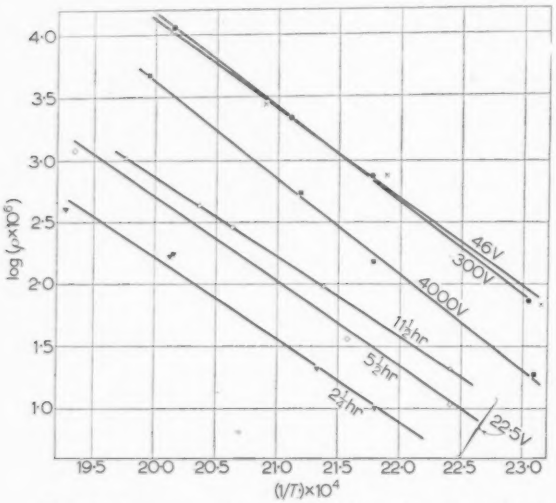

FIG. 5. Arrhenius plots for a (100) surface bombarded with argon ions for various applied voltages and for various times at 22·5 V.

about ± 1 kcal/mole. This reproducibility was found for all three orientations and all bombarding voltages when equilibrium conditions could be reached.

However, for the (110) and the (100) specimens bombarded at 22·5 V, equilibrium conditions were not reached even after 12 hr. For these two specimens after each increase in bombarding time the new Arrhenius plot gave a straight line nearly parallel to the previous one but displaced above it. This behaviour is shown in Fig. 5 for the (100) surface. However, the (111) specimen bombarded at 22·5 V gave the same rates for bombarding times of 3 and 6 hr.

(e) *Relationship between log A and E*

Taking the figures given in Table 1 at face value for all three surfaces after bombardment, an increase in E is always associated with an increase in log A. Fig. 6 shows that a linear relationship exists for each of the three orientations. However,

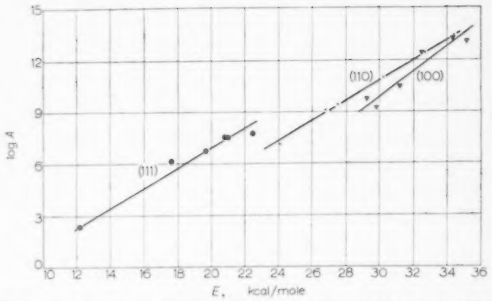

FIG. 6. Log A versus E for (111), (110) and (100) surfaces.

it should be remembered that A and E are not obtained by independent measurements.

4. DISCUSSION

The results show that the catalytic activity of a silver surface can be altered considerably by bombarding it with positive argon ions. With the same crystal, after altering the bombarding energy, systematic changes in A and E were observed which must be associated with some change in the surface produced by the bombardment. The changes in A of several orders of magnitude may imply changes in various factors, including the number of active sites. The surfaces remained smooth, and therefore the surface area is probably not altered appreciably. Assuming that the reaction mechanism remains the same, it seems likely that a change in the number of active sites is the predominant factor. This could be associated with changes in the numbers of dislocations or of point defects such as vacancies, interstitial atoms or argon atoms embedded in the lattice. Changes in the number of point defects cannot be responsible for the change in A, since each crystal was annealed at 250°C *in vacuo* for at least 18 hr before the catalytic measurements were made; after this treatment the concentration of vacancies and interstitial atoms should be negligible,[10] and the concentration of argon atoms should have attained the same value whatever the bombarding conditions had been.[11] However, the possibility that dislocations are responsible for the change in A cannot be eliminated.

Striking evidence has been given that ion bombardment produces disoriented regions[2] bounded by stable arrays of dislocations. This was found by observations on electron-diffraction transmission patterns of single crystals of silver. In our work transmission patterns could not be taken, since the

presence of the holes required for this technique would have made the specimens unsuitable for the rate measurements. However, by reflection electron diffraction, disorientation was detected on some of the crystals used as catalysts. The single crystals used by OGILVIE[2] had orientations close to those used in the present work, and his patterns showed that a change in the structure takes place after bombardment, even with ions of very low energies, with one exception, viz. the case in which a (111) surface is bombarded at 22·5 V. The appearance of extra spots, the arcing of spots and, in some cases, the presence of spotty rings were interpreted as indicating the formation of a surface layer in which small crystalline blocks are rotated through different angles. Thus, ion bombardment gives rise to a greatly increased number of dislocations. It is now proposed that the active sites for the reaction are those where dislocation lines come to the surface.

Furthermore, the transmission diffraction patterns of a crystal[2], when compared with those of HIRSCH *et al.*[12], show that the disorientations introduced by ion bombardment are at least as great as those resulting from cold rolling. Heavy cold work on a polycrystalline aggregate results in an increase in the dislocation density by a factor of about 10^4.[13] This increase is comparable to the maximum increase in A on varying the bombarding conditions for a given crystal. The fact that for the (111) surface (which is obtainable without disorientation) A increases owing to ion bombardment in approximately the same ratio as the dislocation density, strongly suggests that the increase in A is predominantly due to the increase in the number of active sites and not in other factors such as entropy and steric factors.

As shown in Fig. 6, for each crystal an increase in A was always accompanied by an increase in E. Thus, the increase in A by several orders of magnitude on bombardment does not give rise to a similarly large increase in reaction rate, but is, at least partly, compensated.[14] This increase in E with the number of active sites, i.e. with the density of dislocations at the surface, could be due to an interaction between the dislocations. As the new dislocations introduced by bombardment are confined to the boundaries of the small crystalline blocks, their local density is very high and their interaction correspondingly strong. The energy of each site could therefore be lowered, giving an increased value of E associated with the increase in A. It should be emphasized that the presence of dislocations changes not only the geometry of the surface but also the local electronic properties.

To make these ideas more definite, we may note that as different blocks in the surface are rotated through various angles by the ion bombardment, the dislocation density is not the same in all boundaries. Hence, because of the interaction, active sites in different parts of the surface may be characterized by different energies. However, if the interaction between the dislocations, which is responsible for the change in their energy as their number increases, operates only when they are close together, one would predict that the sites in the tilt boundaries would have a range of activation energies distributed fairly closely about a mean. While some of the dislocations intersecting the surface in an undeformed crystal will be incorporated in tilt boundaries after bombardment, a proportion will remain isolated and unaffected.

Thus, we may assume for the sake of simplicity that only two types of site are present in the surface, viz. those with a lower activation energy, E_1, typical of the isolated dislocations, and those with a higher activation energy, E_2, typical of the new dislocations crowded into boundaries. If we then have a concentration c_1 of sites with E_1 and a concentration c_2 of sites with E_2, the observed rate of the reaction should be expressed by:

$$\rho = k\{c_1 \exp(-E_1/RT)+c_2 \exp(-E_2/RT)\},$$

where k may depend on the orientation. The observed values of A and E depend on the relative magnitude of the two terms. If, for a given orientation, we choose for E_1 and E_2 the extreme experimental values of E, we can discuss the significance of the measured A values in terms of the concentrations c_1 and c_2. These E values are: for (111) $E_1 = 12$, $E_2 = 22$; for (110) $E_1 = 24$, $E_2 = 34$; and for (100) $E_1 = 30$, $E_2 = 35$ kcal/mole.

Let us assume that in all cases the concentration c_1 is 10^6 sites/cm^2. For an undeformed crystal, only this one type of site is present in the surface and $c_2 = 0$; then and only then are the observed values of A and E representative of all the sites. Calculations[15] show that if the new

dislocations with activation energy E_2 are introduced in increasing numbers, their effect on the measured values of A and E will be negligible until c_2 has reached $10^{9\cdot3}$ sites/cm^2 for the (111) and (110) surfaces, and $10^{7\cdot5}$ sites/cm^2 for the (100) surface. A further increase in c_2 by a factor of 10 makes the two terms of comparable magnitude and the measured A and E values are composite and larger. When c_2 is greater still ($10^{11\cdot3}$ or $10^{9\cdot5}$ sites/cm^2, respectively), the second term predominates to such an extent that the measured values of A and E are representative only of the higher-energy sites. This analysis shows that, although a substantial amount of deformation may be present in the surface without having any effect on its catalytic activity, heavy deformation should produce increases in the values of A and E provided that this deformation gives rise to a large number of sites of activation energies at or closely distributed around E_2.

It is now possible to associate the change in catalytic properties of the surface with its structure as revealed by electron diffraction.

The (111) *crystal.* Electron diffraction shows that the crystal bombarded at 22·5 V is not deformed, but that there is disorientation at all other voltages. Thus, at 22·5 V, $c_2 = 0$, and the only sites are the 10^6 dislocations/cm^2 with activation energy 12 kcal/mole. The changes in A by a factor of 10^5 and in E of 10 kcal/mole after bombardment at 4000 V can be explained by the introduction of about $10^6 \times 10^5 = 10^{11}$ sites/cm^2, having an activation energy of about 22 kcal/mole. The analysis shows that if the original 10^6 sites of low activation energy remain, their effect is swamped by the 10^{11} new dislocations. It is seen that for this orientation, $k = 10^{2\cdot3}/10^6 = 10^{-3\cdot7}$ (in arbitrary units).

The (110) *crystal.* Electron-diffraction evidence indicates that this surface is disoriented by bombardment at all voltages, even the lowest. Catalysis results show increases in A by a factor of 10^6 and in E of 10 kcal/mole when the voltage is increased. This can be explained if low-voltage bombardment results in a surface containing 10^6 sites/cm^2 with $E_1 = 24$ kcal/mole and up to $10^{9\cdot3}$ sites/cm^2 with $E_2 = 24$ kcal/mole. The latter number of dislocations does not affect the catalytic rate, but should be sufficient to provide the disorientation detected by electron diffraction. With increased bombarding voltage, more dislocations are introduced, and c_2 increases from $10^{9\cdot3}$ to $10^{11\cdot3}$ sites/cm^2 and the higher activation energy is observed. A maximum concentration of 10^{12} sites/cm^2 occurs after bombardment at 500 V. For this orientation $k = 10^{7\cdot1}/10^6 = 10^{1\cdot1}$.

The (100) *crystal.* Arguments similar to those used for the (110) crystal apply. Indeed, additional evidence from a thermally etched crystal (4° from (100)), which gave $E = 30$ kcal/mole and $\log_{10}A = 10$, supports the conclusions that the lowest-voltage bombardment produces a surface whose catalytic behaviour is indistinguishable from that of an annealed crystal. The maximum concentration of dislocations is introduced at the highest voltages, when $c_2 = 10^6 \times 10^4 = 10^{10}$ sites/cm^2. The uncertainty in the values is large, but, at face value, $k = 10^{9\cdot2}/10^6 = 10^{3\cdot2}$.

The variations of k, E_1 and E_2 with orientation are still unexplained, but may be due to an anisotropy of properties associated with a dislocation line intersecting a free surface of differing orientation. However, the values of A and E change together, so that a compensating effect is already present before the number of sites is increased by the bombardment.

5. CONCLUSIONS

1. The large changes in the catalytic activity obtained after bombarding silver surfaces with positive argon ions are most likely due to an increase in the number of dislocation lines intersecting the surfaces.

2. For a given crystal there is a compensating effect (increase of E is always associated with an increase in A) which implies that as the number of dislocations increases, the energy of the sites decreases. This may be due to an interaction between the dislocations.

3. For the same bombarding conditions the values of A and E depend on the orientation of the surface.

Acknowledgements—I wish to thank Mr. E. GILLAM, Dr. G. J. OGILVIE and Mr. J. F. NICHOLAS for their help in discussing the work, and Mr. H. JAEGER and Mr. U. D. MANARIN for their assistance with the experiments.

REFERENCES

1. FARNSWORTH H. E. and WOODCOCK R. F., *Advances in Catalysis* Vol. 9, p. 123. Academic Press, Inc., New York (1957).
2. OGILVIE G. J., *J. Phys. Chem. Solids* **10,** 222 (1959).
3. ECKELL J., *Z. Electrochem.* **39,** 433 (1933).
4. CRATTY L. E. and GRANATO A. V., *J. Chem. Phys.* **26,** 96 (1957).
5. RIENÄCKER G., *Z. Electrochem.* **46,** 369 (1940).
6. SOSNOVSKY H. M. C., OGILVIE G. J. and GILLAM E., *Nature, Lond.* **182,** 523 (1958).
7. SOSNOVSKY H. M. C., *J. Chem. Phys.* **23,** 1486 (1955).
8. GOW K. V. and CHALMERS B., *Brit. J. Appl. Phys.* **2,** 300 (1951).
9. GILLAM E. and OGILVIE G. J., To be published.
10. SEITZ F., *Advances in Phys.* **1,** 43 (1952).
11. LE CLAIRE A. D. and ROWE A. H., *Rev. Métall.* **52,** 94 (1955).
12. HIRSCH P. B., KELLY A. and MENTER J. W., *Proc. Phys. Soc.* B**68,** 1132 (1955).
13. HIRSCH P. B., *Progress in Metal Physics* Vol. 6, p. 236. Pergamon Press, London (1955).
14. CREMER E., *Advances in Catalysis* Vol. 7, p. 75. Academic Press, Inc., New York (1955).
15. NICHOLAS J. F., Private communication.

J. Phys. Chem. Solids Pergamon Press 1959. Vol. 10. pp. 311–313. Printed in Great Britain.

SOME PHYSICAL PROPERTIES OF NEPTUNIUM METAL—I

A DETERMINATION OF THE SPECIFIC HEAT OF α–NEPTUNIUM

J. P. EVANS and P. G. MARDON

Reactor Alloys Section, Metallurgy Division, Atomic Energy Research Establishment, Harwell

(*Received* 29 *December* 1958; *revised* 28 *January* 1959)

Abstract—The specific heat of neptunium over the α-phase range has been determined by a simple calorimetric method. The value of C_p increases from $0{\cdot}031_4$ cal/g at 60°C to $0{\cdot}040_2$ cal/g at 207°C.

In a separate determination, the latent heat of the $\alpha \rightarrow \beta$ transformation was found to be $2{\cdot}0 \pm 0{\cdot}2$ kcal/mole.

1. INTRODUCTION

ONE of the interesting new materials formed when uranium is subjected to neutron irradiation is neptunium 237. This isotope is an α-emitter with a half life of $2{\cdot}5 \times 10^6$ years and forms from uranium 238 by an n, $2n$ reaction. During the extraction of plutonium from irradiated fuel elements at Windscale, the neptunium collected in the waste products. The extraction of a small billet of the metal from this source has been described elsewhere.[1] This material had as its chief impurities 0·34 weight per cent calcium and 0·22 weight per cent uranium.

Neptunium, like plutonium, is highly toxic and must be handled in glove boxes. Thus, when the above-mentioned billet was prepared at the beginning of 1957, a portion of it was made available to the Plutonium Metallurgy Section at A.E.R.E., Harwell, for the determination of as many physical properties as possible and for investigating certain neptunium alloy systems. The results of the investigations into the physical properties are described in the present paper and two subsequent ones.

2. APPARATUS AND EXPERIMENTAL METHOD

Although many of the physical properties could be determined on comparatively small quantities of the metal, for the specific-heat measurements it was decided to use all the available material, 13·9g, which was therefore melted into a small button in an argon-arc furnace. This operated under a pressure of 20 cm of argon, which was gettered for 3 min with molten zirconium prior to melting the sample. The melting loss was < 1 mg/g.

The specific-heat apparatus for use on plutonium and its alloys was not ready at that time,[2] and the only method available was a simple calorimetric one. It had been hoped that a simple form of constant-temperature bath could be constructed by suspending the calorimeter in a tube and surrounding the latter with the vapour of various boiling liquids, but in practice the temperature of the calorimeter was too unstable to give satisfactory results. The apparatus finally adopted is shown in Fig. 1. A small calorimeter formed from silver-soldered nickel strip rested in the bottom of a Dewar vessel. In the top of the latter was fixed a small furnace in which was suspended a copper tray carrying the specimen; the temperature of the specimen was given by a thermocouple resting in the tray and with its hot junction placed in a small hole drilled in the underside of the specimen. The tray could be tilted to release the specimen and a conical-shaped guide prevented it from wedging on the lip of the calorimeter. The temperature of the latter was measured by a second thermocouple mounted in a shallow groove in the wall of the calorimeter; this prevented it from coming into contact with the hot specimen. Both thermocouples were of Chromel/Alumel to give sufficient sensitivity in the measurements.

For each run, 5 cm³ of silicone fluid MS550 were pipetted into the calorimeter. This choice of liquid was based on its low vapour pressure below 200°C and its moderate specific heat, although its thermal transfer characteristics were inferior to

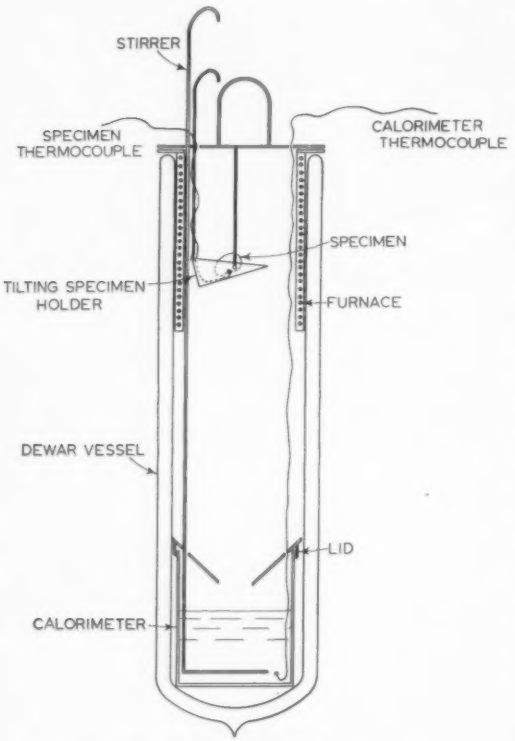

FIG. 1. Cross-section of the apparatus.

those of many more volatile and less viscous liquids. The loaded calorimeter was lowered into the Dewar vessel and the furnace replaced. To reduce heat losses during transfer, the specimen was wrapped in thin aluminium foil before loading into the tray, earlier work on the specific heat of plutonium having shown this measure to be beneficial.[3] After immersion, vigorous stirring ensured relatively rapid heat transfer. For the first series of runs, the furnace was kept at approximately 100°C and very little increase with time in the ambient temperature of the calorimeter occurred. A temperature/time curve for the calorimeter was constructed in the conventional manner, readings of the calorimeter thermocouple being taken at 1-min intervals before immersion and every 20 sec thereafter. To obtain sufficient accuracy, the thermo-electric e.m.f. was measured to 1 μV, the rise in temperature of the calorimeter being equivalent to several hundred μV. The true rise in temperature was then found by the method of equal areas and the fall in temperature of the specimen obtained from a reading of the specimen couple taken immediately before immersion. Ten runs were taken, using an aluminium specimen to determine the water equivalent of the calorimeter, and a similar number of runs on the neptunium. As far as possible, the starting temperatures of the calorimeter and specimen were standardized for all the runs.

Higher-temperature runs were carried out by raising the furnace to 150°C, when it was found that the steady-state temperature of the calorimeter was about 60°C. A fresh series of runs on both aluminium and neptunium was carried out under these new conditions, the starting temperatures again being standardized. In subsequent series of runs, the temperature of the furnace was progressively raised in steps of 40°C. This process was stopped when the furnace temperature reached the $\alpha \rightarrow \beta$ transition temperature of the neptunium. The gap between the starting temperatures of the calorimeter and specimen slowly increased as the starting specimen temperature was raised, and in the highest-temperature runs it reached a value of just over 100°C.

The value of the specific heat of the neptunium obtained from any one series of runs was taken to apply to the mean temperature of the range through which it was cooled; this assumption does not produce a serious error if the specific heat/temperature curve of the metal is approximately linear, as in practice the present results indicate. In calculating the specific heat of the neptunium, a small correction was made for the heat transferred by the aluminium foil; a correction for the self-heating of the neptunium was not necessary, because of the relatively long half-life of $2{\cdot}5 \times 10^6$ years for the isotope tested, Np237.

3. RESULTS

The results for each series of runs for five different temperature ranges are summarized in Table 1.

The water equivalent of the calorimeter

Table 1. Specific heat of neptunium

Specific heat of neptunium (cal/g°C)	Average temperature during run (°C)
0·0314±0·0005	60±1
0·0338±0·0005	102±1
0·0349±0·0004	134±2
0·0370±0·0006	169±2
0·0402±0·0008	207±3

increased from 4·6 g at 60°C to 5·2 g at 207°C. The quoted variations are mean deviations and in plotting the results (Fig. 2), the scatter bands have been drawn on the basis of the total mean deviation for the water-equivalent runs and the neptunium runs at each temperature; the mean deviation in the water-equivalent runs was 1–1½ per cent. Investigators at Windscale[4] have determined a value for the specific heat appropriate to 62°C, which from Fig. 2 is in excellent agreement with the present work.

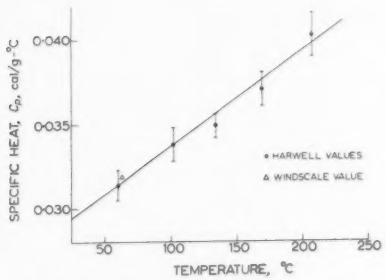

FIG. 2. The specific heat of α-neptunium.

4. DISCUSSION

Owing to the lack of information on the mechanical properties of neptunium, it is not possible to convert the observed c_p values into C_v values; however, if one judges from the case of plutonium, the difference between C_p and C_v is not likely to exceed 1 cal/g-atom. The atomic heat of neptunium calculated from C_p values increases from 7·0 cal/g-atom at 25°C to 9·5 cal/g-atom at 207°C, thus, as in the case of uranium and plutonium, rising rapidly above the classical Dulong–Petit value of 6 cal. This is presumably due to a high electronic specific heat; at first sight the low temperatures at which this phenomenon occurs are surprising when compared with the transition metals or the rare-earth series of elements, but FRIEDEL[5], in a calculation for the case of uranium, has pointed out that the electronic contribution is proportional to the energy of electrons in the neighbourhood of the Fermi surface and also to the molar volume. At similar temperatures, both these factors will lead to much higher electronic specific heats in the actinides than in the transition metals.

Latent heat of the $\alpha \rightarrow \beta$ transition

No attempt was made in the specific-heat determinations to obtain a value for the latent heat of the $\alpha \rightarrow \beta$ neptunium transformation. This was, however, directly determined by HILL in the following manner.

A dilatometer furnace was modified for servo-control, so that the furnace wall was maintained at or near the temperature of the specimen. The specimen had a small heater closely associated with it, and it was found that the heat losses from the specimen region were sufficiently reproducible for a calorimetric calibration of the heater against the latent heat of tin to be possible. Work on a 4-g specimen of neptunium then gave a value of 2·0± ±0·2 kcal/mole for the latent heat of the neptunium transition at 283°C.

REFERENCES

1. NAIRN J. S., COLLINS D. A., MCKAY H. A. C. and MADDOCK A. G., *2nd Internat. Conf. on Peaceful Uses of Atomic Energy (Geneva), Paper* 15/P/1458 (1958).
2. HILL J. D., Unpublished work.
3. MARDON P. G., ROBERTSON J. A. L. and BALL J. G., *Atomic Energy Research Estab. Rep.* No. M/R1181.
4. ELDRED V. W. and CURTIS G. C., *Nature, Lond.* **179,** 910 (1957).
5. FRIEDEL J., *J. Phys. Chem. Solids* **1,** 175 (1956).

J. Phys. Chem. Solids Pergamon Press 1959. Vol. 10. pp. 314–320. Printed in Great Britain.

APPROXIMATE FORMULATION OF THE ORTHOGONALIZED PLANE-WAVE METHOD

E. ANTONČÍK

Institute of Technical Physics, Czechoslovak Academy of Sciences, Prague, Czechoslovakia

(*Received* 19 *January* 1959)

Abstract—An approximate method is derived for calculating the energy band of solids, analogous to the orthogonalized plane-wave method. In this method the exact condition for the orthogonality of the wave functions of valency electrons to the wave functions of the electrons of ions is replaced by a repulsive potential, determined statistically. It is shown by the example of the energy spectrum of diamond that despite the relative simplicity of this method, its results are comparable to those given by other methods. Correlation is also carried out between this method and the Phillips energy-band interpolation scheme.

VOL
10
195

1. INTRODUCTION

THE orthogonalized plane-wave (or OPW) method, originally proposed by HERRING[1] has recently been very successful not only in calculating the energy spectrum of metals but also in particular, that of valency crystals.[2] The basic idea of this method consists in the construction of wave functions of valency electrons in the form of a linear combination of plane waves and the wave functions corresponding to the electron states of ions, so that these functions should be orthogonal to all electron states that are energetically lower. Of course, this process causes considerable complications in the numerical calculations and to a certain extent limits the use of this method when applied to semi-quantitative estimates, such as interpolation,[3] or the solution of the problem of impurity atoms in the crystal,[4] etc.

The solution of these problems in particular led us to try to replace the orthogonalization process by a simpler formulation based on GOMBÁS's paper[5] on the repulsive potential. The simplicity and intuitive character of this approximation will be shown below. On the other hand, there is no doubt that this formulation of the OPW method is only approximate and does not attain the accuracy of the original method. In order to verify the degree of approximation of this new procedure, we calculated the energy spectrum of several materials which had already been calculated by the OPW method. In this paper we calculate the energy levels at some points of the Brillouin zone of diamond and compare it with calculations of the energy spectrum of diamond carried out by the OPW method.

2. OPW METHOD

In the considerations below we shall start from some of the conclusions of the OPW method and shall therefore first briefly repeat the basic assumptions of this method and introduce the necessary notation.†

In solving the Schrödinger equation the OPW method starts out from the variational principle. Let $\mathscr{H}$ denote the Hamiltonian operator of the given system

$$\mathscr{H} = -\Delta + V(r), \tag{1}$$

where Δ is the Laplace operator and $V(\mathbf{r})$ the potential energy of the electron. If ψ_{trial} denotes a suitable normalized wave function containing certain variational parameters, then according to the variational principle the absolute minimum of the integral

$$\int \psi^*_{\text{trial}}\, \mathscr{H}\, \psi_{\text{trial}}\, d\tau$$

due to these parameters is the best approximation (for the given function ψ_{trial}) of the lowest energy eigenvalue of the operator $\mathscr{H}$. If the wave function ψ_{trial} is

† A more detailed discussion of the OPW method can be found in the paper by WOODRUFF.[6]

expanded with respect to a certain system of functions χ_j,

$$\psi_{\text{trial}} = \sum_{j=1}^{n} c_j \chi_j \tag{2}$$

and the coefficients of the expansion c_j are regarded as variational parameters, a system of linear equations is obtained for c_j from the condition that the value of the integral (2) be minimum

$$\sum_{j=1}^{n} [\int \chi^*_i \mathcal{H} \chi_j \, d\tau - E_n \int \chi^*_i \chi_j \, d\tau] c_j = 0. \tag{3}$$

Both c_j and the corresponding value of E_n for a given number n of functions in expansion (2) can be determined from these equations.

The higher-energy states are determined analogously, except that the following condition must be fulfilled:

$$\int \psi_i^* \psi_j \, d\tau = 0 \text{ for } i > j \geqslant 0, \tag{4}$$

i.e. the wave functions of these states must be orthogonal to all wave functions of energetically lower states ($E_i > E_j$). In crystals this condition leads to the requirement that the wave functions of the valency electrons be orthogonal to the wave functions of the electrons of the ions.

In the OPW method one starts out from the assumption that the wave functions of the electrons of ions are described with sufficient accuracy by the wave functions of the tight-binding approximation

$$\psi_{nlp}(\boldsymbol{k}, \boldsymbol{r}) = \frac{1}{\sqrt{(sN)}} \sum_{\nu} b_{nlp}(\boldsymbol{k}, \nu) \exp(i\boldsymbol{k}\boldsymbol{R}_\nu) u_{nl}(\boldsymbol{r} - \boldsymbol{R}_\nu). \tag{5}$$

$\boldsymbol{k}$ is the wave vector, $\boldsymbol{R}_\nu$ the position vector of the nucleus in the ν-th lattice point, N the number of elementary cells in the chosen volume Ω of the crystal, and s the number of atoms in this cell; $b_{nlp}(\boldsymbol{k}, \nu)$ is the phase factor; the index p denotes the dependence of the wave function on the symmetry of the crystal lattice and for a diamond lattice has only two different values. The index ν runs over all lattice points in the crystal. The function u_{nl} is the normalized atomic core wave function; n is the principal quantum number, and l is the angular momentum quantum number. The magnetic quantum number, which for the sake of simplicity does not occur in the notation, has in a coordinate system having its z-axis in the direction of $\boldsymbol{k}$ the value $m = 0$.

The wave functions of the valency electrons are assumed to have the form of plane wave

$$\Omega^{-\frac{1}{2}} \exp(i\boldsymbol{k}\boldsymbol{r}). \tag{6}$$

Since, according to condition (4), the wave functions of valency electrons must be orthogonal to the wave functions of all states of the electrons of the ions, the wave functions of the valency electrons must be written in the form

$$\chi(\boldsymbol{k}, \boldsymbol{r}) = \Omega^{-\frac{1}{2}} \exp(i\boldsymbol{k}\boldsymbol{r}) - \sum_{nlp} B_{nlp}(\boldsymbol{k}) \psi_{nlp}(\boldsymbol{k}, \boldsymbol{r}). \tag{7}$$

The coefficients $B_{nlp}(\boldsymbol{k})$ are determined from condition (4)

$$\int \chi^*(\boldsymbol{k}, \boldsymbol{r}) \psi_{n'l'p'}(\boldsymbol{k}, \boldsymbol{r}) \, d\tau = 0.$$

The wave functions of valency electrons, which are the solution of the corresponding Schrödinger equation, are then written in the form (2), where to the index j of the function χ_j there corresponds the vector $\boldsymbol{k}_j = \boldsymbol{k} + \boldsymbol{K}_j$, where $\boldsymbol{K}_j$ are the vectors of the reciprocal lattice. The energy $E_n(\boldsymbol{k})$ and the corresponding wave function can then be determined by the variational procedure given.

It is obvious from equation (3) that the solution of the secular equations will be relatively complicated, because the functions $\chi(\boldsymbol{k}, \boldsymbol{r})$ are not generally mutually orthogonal.

3. STATISTICAL FORMULATION OF ORTHOGONALITY CONDITION

The approximate expression of the orthogonality condition was first used by HELLMANN[7]. His semi-empirical formulation was later elaborated in detail by GOMBÁS *et al.*[5] from the point of view of statistical theory, and we shall confine ourselves here to stating some of the results.

GOMBÁS dealt with this problem particularly for atoms; he started out from the statistical interpretation of the Pauli principle, according to which valency electrons cannot occur in the electron states of the closed shells of ions. From this assumption GOMBÁS was able to derive essentially two expressions for the repulsive potential, from which we shall use the expression for G_l, which has a number of advantages over the potential F_l originally derived:[5]

$$G_l = -\frac{\pi^2}{4(2l+1)^2} D_l^2 - \frac{1}{2} \frac{1}{r^2} \left[\frac{l^2}{2a_0}\right], \tag{8}$$

where D_l is the radial density of all states with angular momentum quantum number l energetically lower than the state of the valency electron characterized by the same quantum number l.

The solution of the equation

$$\mathcal{H}\psi = E\psi, \tag{9}$$

where condition (4) is simultaneously valid, in

our approximation becomes the solution of the equation

$$(\mathscr{H}+\mathscr{V}_{\text{rep}})\psi = E\psi \tag{10}$$

without any further condition; $\mathscr{V}_{\text{rep}}$ is the operator corresponding to the repulsive potential (8).

It is clear that the wave functions determined in this way and their corresponding energies are only a certain approximation of the exact values. The wave functions can be chosen in a simple form which greatly simplifies the calculations, but, on the other hand, the wave function does not usually contain the correct number of nodes and in the immediate neighbourhood of the nucleus does not approximate the exact function with sufficient accuracy. In many cases, however, this fact has no essential effect on the formulation of the problem.[5] The advantage of determining the energy can be judged to a certain extent from reference (8), where it is clear that the error in determining the energy increases with increasing principal quantum number.

Attention should be drawn here to the work of SZÉPFALUSY[9], who derived an expression for the repulsive potential from the standpoint of wave mechanics. In this sense the use of the repulsive potential is quite analogous to the use of SLATER's exchange potential, approximating exchange effects.

4. THE USE OF THE REPULSIVE POTENTIAL IN THE THEORY OF SOLIDS

The statistically formulated orthogonality condition was used in the form of a repulsive potential in the statistical theory of metals. In a number of papers, GOMBÁS *et al.*[5] have shown the advantage of this conception, which enabled some of the basic constants of metals, e.g. the lattice constants, cohesive energy, etc., to be calculated without great difficulty. Since the advantage of this formulation is expected to be very general, the present author used the repulsive potential in calculating the energy spectrum, both for some monovalent metals,[10] based on HELLMANN's potential, and for homopolar crystals,[11] using expression (8).

Both these papers showed that the approximate replacement of the orthogonality condition by a repulsive potential gives relatively good results, while the simplicity with which the orthogonality condition was respected makes it possible to use a minimum of mathematics. On the other hand, however, the correlation between the symmetry of the wave functions of valency electrons and the electrons of the closed shells of the ions was not sufficiently generally determined in these papers. The aim of the present paper is to solve this problem in a certain approximation.

Let us assume that the wave functions of the electrons of the closed shells of ions are described sufficiently accurately by the wave functions u_{nl}, used in constructing function (5). These wave functions are also used in constructing the repulsive potential in the Hamiltonian operator in equation (10), which for a valency electron of a free atom in the state (n', l') has the usual form[5]

$$\mathscr{V}_{\text{rep}}{}^{l}(\boldsymbol{r})u_{n'l'} = (-G_l)u_{n'l'}\delta_{ll'}, \tag{11}$$

where $\delta_{ll'} = 0$ for $l \neq l'$ and $\delta_{ll'} = 1$. For a certain atom there exists only a certain number $\mathscr{V}^{l}{}_{\text{rep}}$ different from zero and in this case the operator of the repulsive potential of the ion acting on the valency electron can be written as

$$\mathscr{V}^{\text{at}}_{\text{rep}}(\boldsymbol{r}) = \sum_{l} \mathscr{V}^{l}{}_{\text{rep}}(\boldsymbol{r}), \tag{12}$$

where summation is performed over all angular momentum quantum numbers occurring for the given ion. As in paper (11), we shall assume that in the crystal the corresponding term $\mathscr{V}_{\text{rep}}$ in equation (10) is given in the form

$$\mathscr{V}_{\text{rep}}(\boldsymbol{r}) = \sum_{\nu} \mathscr{V}^{\text{at}}_{\text{rep}}(\boldsymbol{r}-\boldsymbol{R}_\nu). \tag{13}$$

Let us now solve equation (10) for a crystal. Since the orthogonality condition is contained in the Schrödinger equation (10) through expression 1(3), the wave functions can be written in the form of linear combinations of the functions (6). These linear combinations must be chosen so as to form the basis for the irreducible representation of the group of the vector $\boldsymbol{k}$. It can be proved[12] that the corresponding functions χ_j in equation (2) can be written in the form

$$\chi_j = \frac{N_j}{\sqrt{(\Omega)}} \sum_{j} a_j \exp(i\boldsymbol{k}_j\boldsymbol{r}), \tag{14}$$

where for the sake of simplicity the summation

index j denotes also the corresponding function χ_j; a_j are the corresponding coefficients determined from group analysis and N_j is the normalizing constant. It now remains to calculate the matrix elements for the solution of equation (3).

Since the functions (14) form an orthonormal system, it is obvious from equation (3) that the energy E occurs only in the diagonal terms. The calculation of the matrix elements $\int \chi_i \mathscr{H} \chi_j \, d\tau$ is described sufficiently in the literature,[6,12] so that it remains only to calculate the terms $\int \chi^*_i \mathscr{V}_{\text{rep}} \chi_j \, d\tau$.

If the functions (13) and (14) are substituted into this expression, we obtain

$$\int \chi_i^* \mathscr{V}_{\text{rep}} \chi_j \, d\tau = \frac{1}{\Omega_0} N_i^* N_j \sum_{l,j} a_i^* a_j \sum_{\nu=1}^{s} \exp[-i(\boldsymbol{k}_i - \boldsymbol{k}_j)\boldsymbol{R}_\nu] \int \exp(-i\boldsymbol{k}_i \boldsymbol{r}) \mathscr{V}^{\text{at}}_{\text{rep}}(\boldsymbol{r}) \exp(i\boldsymbol{k}_j \boldsymbol{r}) \, d\tau \quad (15)$$

where $\Omega_0 = \Omega/N$ is the volume of the elementary cell. In order to calculate the integral in this expression, we use a procedure similar to that of GÁSPÁR in his paper on the statistical theory of aluminium.[13] We expand $\exp(i\boldsymbol{k}_j \boldsymbol{r})$ in series according to the Legendre polynomials P_l and use relation (11), which defines the application of the operator $\mathscr{V}^{\text{at}}_{\text{rep}}$ on the angular part of the wave function u_{nl}. Then:

$$\mathscr{V}^{\text{at}}_{\text{rep}} \exp(i\boldsymbol{k}_j \boldsymbol{r}) = \sum_l (2l+1) i^l [-G_l(r)] j_l(k_j r) P_l(\cos\theta_j), \quad (16)$$

where θ_j is the angle between the vectors $\boldsymbol{k}_j$ and $\boldsymbol{r}$, and summation is only carried out over all the l contained in the expression for $\mathscr{V}^{\text{at}}_{\text{rep}}$. By multiplying expression (16) from the left by the function $\exp(-i\boldsymbol{k}_i \boldsymbol{r})$, we obtain, after a simple calculation,

where θ_{ij} is the angle between the vectors $\boldsymbol{k}_i$ and $\boldsymbol{k}_j$. It can easily be proved that in the limiting case, $\boldsymbol{k}_i = \boldsymbol{k}_j$, $N_i = N_j = a_i = a_j = 1$ and $s = 1$, we get exactly the same expression as equation (14) in GÁSPÁR's paper[13] if the expression F_l is used instead of the repulsive potential G_l.†

5. CALCULATION

The accuracy of this method is verified by the example of the electronic spectrum of diamond, which has recently been studied in great detail particulary by HERMAN[12]. HERMAN determined the energy in the Brillouin zone with great accuracy by the OPW method. Since the present author had only a desk machine at his disposal, it was not possible to carry out the calculations to the same extent as was done by HERMAN. We shall therefore confine ourselves to calculating the energy only in the points Γ, L and X, and the order of the secular equation will not be greater than $n = 6$; it will be seen later that this limitation is quite sufficient for evaluating the accuracy of our method.

So that the comparison of the energies

† GÁSPÁR, in a recent paper,[21] which appeared after the present paper had been prepared for submission, extended this special case also for $\boldsymbol{k}_i \neq \boldsymbol{k}_j$.

$$\int \chi_i^* \mathscr{V}_{\text{rep}} \chi_j \, d\tau = \frac{1}{\Omega_0} N_i^* N_j \sum_{l,j} a_i^* a_j \sum_{\nu=1}^{s} \exp[-i(\boldsymbol{k}_i - \boldsymbol{k}_j)\boldsymbol{R}_\nu] \times$$

$$\times \sum_l 4\pi(2l+1) P_l(\cos\theta_{ij}) \int [-G_l(r)] j_l(k_i r) j_l(k_j r) r^2 \, dr, \quad (17)$$

calculated by means of the exact and approximate orthogonality conditions should be as exact as possible, the author used for the calculation of the matrix elements $\int \chi^*_i \mathscr{H} \chi_j \, d\tau$ the same lattice constant and same Fourier coefficients of the total crystal potential as HERMAN[12].†

The expression G_l must be determined in order to calculate the matrix elements corresponding to the repulsive potential. It is clear from what was stated in Section 4 that only the expression G_0, constructed from the wave function ψ_{1s} of a carbon atom in the $1s^2 2s 3p^3$ state, is none-zero. In order to facilitate the calculation, we assumed ψ_{1s} in the analytical form $\psi_{1s} \approx \exp(-\alpha r)$, the value of the parameter α was chosen, in accordance with TUTIHASI[15] as $\alpha = 5{\cdot}61$. It can be proved that the function G_0 calculated in this way differs only very slightly from the function G_0 determined numerically from JUCYS's values of ψ_{1s} used by HERMAN[12].

The first term in G_0 (8) in expression (17) can be integrated in the limits $(0, \infty)$, since it decreases very rapidly with increasing r. The second term in G_0 in expression (17), however, must be integrated in the limits $(0, R)$, where R is the radius of the elementary sphere, as was done similarly by GOMBÁS in the statistical theory.[16]

The corresponding wave functions χ_j, i.e. the values of the constants N_j and a_j, must be known in order to determine both the repulsive (17) and the Coulomb (and also exchange) parts of the matrix elements. The wave functions χ_j are determined from the requirement that they form the basis for the irreducible representation of the group of the vector $\boldsymbol{k}$. This procedure has been described in sufficiently great detail in many papers[12,17] and will not be repeated here. We merely point out, however, that in contrast to HERMAN[12], the elementary cell, as in reference (11) contained eight atoms and the origin of the co-ordinate system was chosen in one lattice point. An example of the wave functions at the point Γ in this co-ordinate system is given in reference (11).

The solution of the secular equation corresponding to system (3) was carried out numerically. The results of these calculations are given in Fig. 1, where the values of the energy (in Ry units) at the points Γ, Γ_2', $X_1^{(1)}$, $X_1^{(2)}$, $L_1^{(1)}$, $L_1^{(2)}$ and L_2' are plotted as a function of the order of the secular equation n. On the right-hand side of the figure HERMAN's final values from Table 1 in reference (3) are given. The other states, where orthogonalization is not necessary, are not given in the figure, since they are practically the same as HERMAN's values[12].

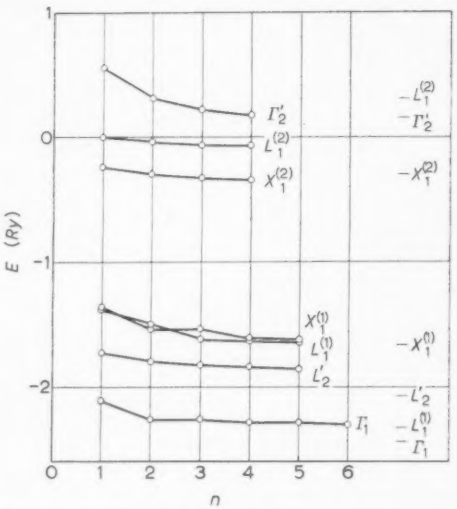

FIG. 1. o—o Convergence of the energy eigenvalues; n is the order of the secular equation. — HERMAN's final results (after Table 1 of reference (3)).

6. DISCUSSION

It is clear that when using the repulsive potential we cannot attain such a degree of accuracy as in the OPW method, either in determining the characteristic values of the energy or of the wave functions. While the error introduced by using the repulsive potential can be at least approximately estimated with atoms,[8] this estimate is practically impossible in the case of solids. In any case it is clear that the errors in determining

† With the exception of the Fourier coefficients V_h^c (in HERMAN's notation), for which $h = (2, 2, 2), (6, 2, 2)$ &c.; like some other investigators, e.g. CASELLA,[13] we put for them $V_h^c = 0$. Since the Fourier coefficients for these values of h are very small compared with the others, the changes in energies are quite insignificant and practically negligible compared with HERMAN's calculations.

the energy not only will not be smaller than those for atoms, but will be even larger. This is due, on the one hand, to the character of the function G_l and, on the other, to the symmetry of the wave functions in the crystal.

The repulsive potential G_l was derived for atoms where the wave functions of the valency electrons decrease exponentially with increasing r. While this is of no special significance for the first term of the function G_l (8) with the second term, (which follows from the statistical formulation of the problem) the contributions for large values of r are considerably limited when integrating in the limits $(0, \infty)$. With solids, however, we should obtain an infinite contribution for $k_l = k_j = 0$, and we therefore put $G_l = 0$ for $r > R$. This limitation, of course, increases the estimate of the error in comparison with free atoms.[8]* A further complication arises if we consider a crystal lattice with a basis, as is the case, for example, with diamond. It is clear from the derivation of the operator $\mathscr{V}_{\text{rep}}$[13] that this operator is the same for both values of the parity index p. This approximation is the source of further inaccuracy, particularly with states with $l = 0$, where the term $1/2r^2$ in the expression for G_l plays an important part. Since, however, it is very difficult to estimate all these errors, it will be very illuminating to compare our calculations with those of HERMAN[12].

Fig. 1 shows the course of the energy of the different states for increasing n (i.e. for the number $(n-1)$ of variable parameters c_j in expansion (2)). Unfortunately, the author did not have HERMAN's equivalent values at his disposal, so that only the final values according to Table 1 in PHILLIPS's paper[3] are given in Fig. 1 for purposes of comparison. It follows from comparing these values that for the states Γ_1, Γ_2', $X_1^{(1)}$ and $X_1^{(2)}$ the agreement is quite satisfactory, and it can be expected that for a larger number of functions in expansion (2) the difference in the corresponding values would not exceed 0·15 Ry. The situation at the point L is quite different. Here not only do the energies for the different states $L_1^{(1)}$ and $L_1^{(2)}$ differ greatly, but so does also the order of the different states compared with HERMAN's results. This is probably due to a mistake made by HERMAN in constructing the factored secular determinants for these representations, as has been pointed out by PHILLIPS[3]. HERMAN's later paper, concerning the electron structure of germanium,[2,18] is however very interesting. Here not only is the order of the states at the point L exactly the same as in our calculations, but also the course of the energies exhibits approximately the character of the band structure of "an empty lattice", as in our own case. The energy in the [100] direction in diamond has the same character in HERMAN's calculations, but in the [111] direction the values of the energy of the state $L_1^{(1)}$ (−2·33 Ry) differ very little from the energy of the state Γ_1 (−2·44 Ry), which is quite unusual. It is interesting that this anomaly is not exhibited either by the band structure of hypothetical carbon metal[14] or by the band spectrum of diamond, calculated by MORITA[19] by means of the tight-binding method; however, the latter is not conclusive, since according to SLATER and KOSTER[20], it probably contains a numerical error.

It is also very interesting to compare our method with the energy-band interpolation scheme of PHILLIPS[3]. Without going into detail, which will be discussed in a later paper, it is obvious at first glance that our method not only enables the physical interpretation of PHILLIPS's method to be made, but also explains some of its deficiencies and points out the way in which they can be eliminated. This is, in particular, the problem of the orthogonalization of the p and d states, which appear in diamond. PHILLIPS tries to approximate as well as possible the energy spectrum in the neighbourhood of the band of forbidden energy values, where the wave functions of most of the states need not be orthogonalized to the wave functions of the electrons of the ions in the conception of the OPW method. Since, however, according to our method the effective potential of the p and s states in diamond differ greatly, PHILLIPS's method can be expected to give a bad approximation in cases where the wave functions of the valency electrons must be orthogonalized according to the OPW method. This actually occurs, as can be seen from Table

* The term $1/2r^2$ would obviously vanish when consistently deriving the repulsive potential for solids; in our approximation, however, when we start out from an analogy with free atoms, it cannot be neglected, since this would lead to erroneous values of the energies.

1 in reference (3). A detailed analysis of this problem, particularly in connection with references (10) and (11), will be carried out in a later paper, where attention will also be paid to the problem of the convergence of the different energy values (with PHILLIPS this is the problem of the "truncation" of the secular equation). We shall merely state here that in most cases the ratio of the absolute values of the non-diagonal and diagonal terms decreases with growing number n of the functions in expansion (2), so that a further increase in the order of the secular equation has no substantial effect, as is seen, for example, in Fig. 1. Since the repulsive potential may have a different form from that used by us, it is to be expected that by a suitable choice of repulsive potential (in PHILLIPS's method, choice of the matrix elements) very good convergence can be obtained for a relatively small number n of functions in expansion (2).

In conclusion we should like to emphasize that the aim of this paper was not to derive a definite expression for the repulsive potential in solids, but merely to point out the usefulness of this conception. In order to solve this problem similar calculations and comparisons will have to be carried out with other materials, particularly metals and semiconductors, and even ionic crystals; some calculations have already been performed and are gradually being published in the *Czechoslovak Journal of Physics*. The main purpose of the present paper was to solve the problem of the energy spectrum in such a way as to permit the simplest possible solution of some of the problems dealt with by the author, such as the problem of impurity atoms in a crystal,[4] the problem of impact ionization in semiconductors, etc. Work on these problems is continuing and will be published later.

Acknowledgements—The author is indebted to Dr. F. HERMAN and Dr. J. TAUC for information concerning the thesis,[3] which enabled the two methods to be compared, and to Dr. J PHILLIPS for a preprint of his paper. He also thanks K. TRNKOVÁ and J. GREIFOVÁ for carrying out the numerical calculations.

REFERENCES

1. HERRING C., *Phys. Rev.* **57,** 1169 (1940).
2. See e.g. the comprehensive paper by HERMAN F., *Rev. Mod. Phys.* **30,** 102 (1958).
3. PHILLIPS J. C. (in the press).
4. HERRING C., *Photoconductivity Conference*, Atlantic City, 1954 (Ed. R. G. BRECKENRIDGE, B. R. RUSSELL and E. E. HAHN). John Wiley and Sons, New York (1956).
5. GOMBÁS P., *Handbuch der Physik* Vol. 36, Part 2. Springer, Berlin (1956).
6. WOODRUFF T. O., *Solid State Physics* (Ed. F. SEITZ and D. TURNBULL) Vol. 4, p. 367. Academic Press, Inc., New York (1957).
7. HELLMANN H., *Acta Phys.-chim. U.R.S.S.* **1,** 913 (1935); **4,** 225 (1936); **5,** 23 (1936).
8. ANTONČÍK E., *Czech. J. Phys.* **7,** 118 (1957).
9. SZÉPFALUSY P., *Acta Phys. Hungar.* **5,** 325 (1955); **6,** 273 (1956).
10. ANTONČÍK E., *Czech. J. Phys.* **4,** 439 (1954).
11. ANTONČÍK E., *Czech. J. Phys.* (in the press).
12. HERMAN F., Thesis, Columbia University (1953).
13. GÁSPÁR R., *Acta Phys. Hungar.* **2,** 31 (1952).
14. CASELLA R. G., *Phys. Rev.* **109,** 54 (1958).
15. TUTIHASI S., *J. Phys. Soc. Japan* **3,** 135 (1948).
16. GOMBÁS P., *Acta Phys. Hungar.* **1,** 301 (1952).
17. See e.g. KOSTER G. F., *Solid State Physics* (Ed. F. SEITZ and D. TURNBULL) Vol. **5,** p. 174. Academic Press, Inc., New York (1957).
18. HERMAN F., *Physica s'Grav.* **20,** 801 (1954).
19. MORITA A., *Sci. Rep. Tôhoku Univ.* **33,** 92 (1949).
20. SLATER J. C. and KOSTER G. F., *Phys. Rev.* **94,** 1498 (1954).
21. GÁSPÁR R., *Acta Phys. Hungar.* **9,** 79 (1958).

J. Phys. Chem. Solids Pergamon Press 1959. Vol. 10. pp. 321–325. Printed in Great Britain.

INVESTIGATION OF THE INTERACTION OF ALKYL IODIDE VAPOURS WITH A CARBON SURFACE BY KINETIC AND ISOTOPIC METHODS

I. KENDE, L. GUCZI, and D. GÁL*

Isotope Laboratory, Research Institute for Soil Science and Agrochemistry, Hungarian Academy of Sciences, Budapest

(*Received* 15 *December* 1958)

Abstract—The rate of desorption of ethyl, propyl and butyl iodides adsorbed by active carbon was examined at various temperatures. From the desorption curves obtained, the kinetic equation of desorption, the activation energies of desorption and the corresponding partition functions were determined.

1. INTRODUCTION

SURFACE phenomena occurring during adsorption have been studied by a number of authors. Many indirect methods, and recently a few direct methods using isotopes, have been reported in the literature.[1–5]

The present experiments relate to the interaction of adsorbent and adsorbate at low pressures. Carbon was used as the adsorbent, while ethyl, propyl and butyl iodides and ethyl iodide labelled with ^{131}I were the adsorbates.

Another aim of the investigations was to detect any effects that appear with increasing numbers of CH_2 groups and to show in this way the effect of changes in the alkyl radical on the interaction between the vapour molecules and the carbon surface.

2. EXPERIMENTAL METHOD

Half-gramme samples of activated carbon were used as adsorbent, being regenerated by heating for 2 hr at 350°C under conditions of continuous pumping.

The alkyl iodides used as adsorbates were prepared by the conventional chemical methods and purified to secure analytical grade. Ethyl iodide labelled with ^{131}I was produced by a heterogeneous isotope-exchange reaction.[6]

Measurements were carried out in the glass apparatus shown in Fig. 1. Prior to the tests, the system was evacuated to 10^{-4}–10^{-5} mm Hg by means of a mechanical pump and a mercury diffusion pump (3). The pressure in the system was measured by a McLeod gauge (5). The freezing flask (6) removed residual traces of active vapours. Vessels (8) and (9) contained the alkyl iodides to be examined, the gamma radiation from the active compound in vessel (8) being absorbed by a lead shield of adequate thickness (18). Changes in pressure were followed with a mercury manometer (17) and a differential manometer filled with apiezon oil (16). Pressure measurements are given throughout the experiments in millimetres of apiezon oil (the ratio of mm Hg to mm apiezon oil being 1 : 18). Tube (13) was used to measure the activity. The external jacket contains the vapour to be tested and the central tube is a thin-walled "Aquadag" Geiger–Müller counter. The latter was attached to a counting rate-meter which indicated the activity of the desorbed vapour. In order to find the self-absorption factor, the curve of activity versus pressure was determined. The measurements showed that deviations from the linear correlation occur only at values of $p > 300$ mm;

* Present address: Central Isotope Laboratory, University of Szeged, Szeged, Hungary.

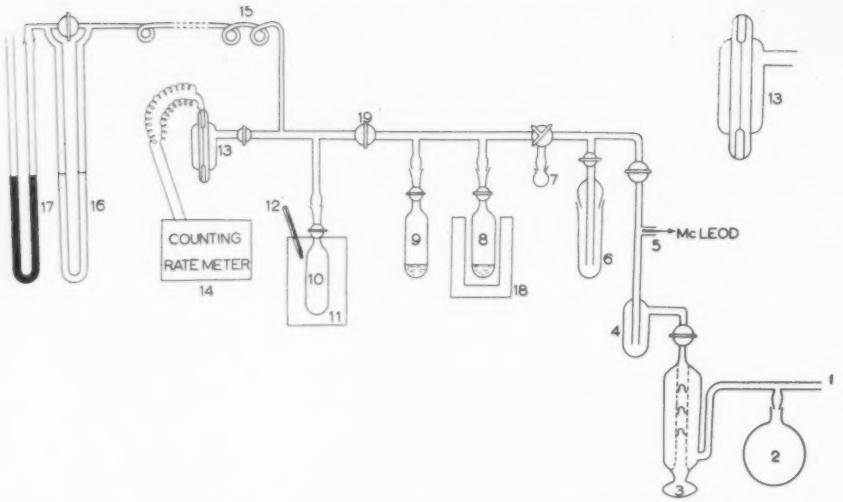

FIG. 1. Apparatus for measuring rates of desorption and isotope concentration of desorbed vapours.

thus the correction for self-absorption was negligible in the majority of experiments.

3. EXPERIMENTAL RESULTS

In the course of the kinetic measurements, the changes of desorption rate with time were plotted for various temperatures. It is to be noted that the measurements were carried out over the initial portion of the adsorption isotherm, at pressures below saturation. At the end of adsorption, the apparatus (excluding the adsorption vessel) was evacuated, and then the adsorption vessel was pumped out for 30 sec. The rate curves for the desorption of ethyl, propyl and butyl iodides at 60°C are presented in Fig. 2.

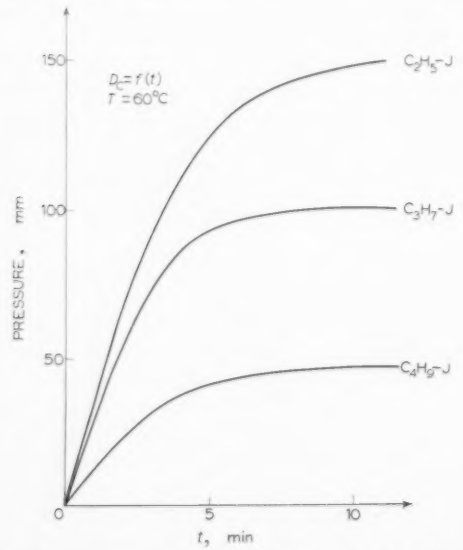

FIG. 2. Desorption curves for ethyl, propyl and butyl iodides at 60°C.

In the case of ethyl and propyl iodides the best approximation to the desorption curves is given by an equation of the type:

$$\frac{D}{D_\infty} = 1 - e^{-kt}, \qquad (1)$$

where D is the quantity desorbed at time t, and D_∞ the maximum amount desorbed. After transformation we get the following equation, and plotting it in this form, the results are shown in Fig. 3:

$$\log\left(1 - \frac{D}{D_\infty}\right) = -k't. \qquad (2)$$

A straight line is obtained in the case of ethyl and propyl iodides, some deviation from linearity occurring with butyl iodide. This behaviour of butyl iodide was already observable in determining activation energies. Kinetic functions of the type $D/D_\infty = 1 - e^{-kt}$ indicate, according to the

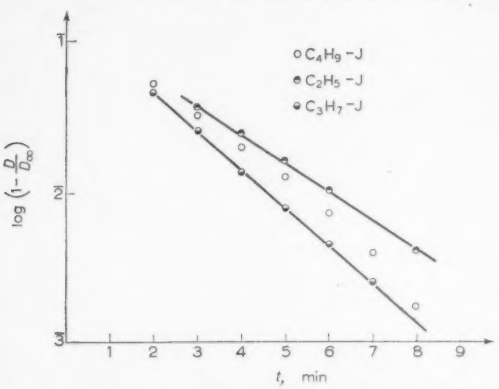

FIG. 3. Experimental data calculated by equation (2).

statistical calculations of ROGINSKY[2], that a rearrangement may take place at the surface, a fact apparently confirmed by experimental data given later on. Initial rates are presented in Table 1.

Table 1. *Initial rates*

Compound	w_0(sec^{-1})
C_2H_5I	1·07
C_3H_7I	0·993
C_4H_9I	0·558

The partition functions obtained from the experimental data[6] by graphical differentiation are shown in Fig. 4.

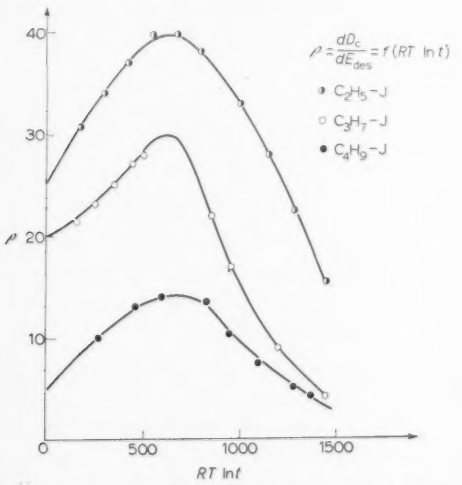

FIG. 4. Partition functions of ethyl, propyl and butyl iodides at 60°C.

It can be seen that the magnitude of the maximum depends on the number of CH_2 groups, whilst the position of the maximum is independent of this number. Thus, the bulk of the desorbed substance is liberated, in the case of all three compounds, from sites possessing almost equal desorption energies. In order to determine activation energies, the kinetic curves for the three compounds were determined at 40°, 60° and 100°C. Values of activation energies calculated from the Arrhenius equation are given in Table 2.

Table 2. *Activation rates calculated from the Arrhenius equation*

Compound	E(cal/mole)
C_2H_5I	7·420
C_3H_7I	6·100
C_4H_9I	6·400

It can be seen that the behaviour of butyl iodide is exceptional in this case too.

Although surface phenomena can be elucidated to a certain extent by kinetic methods, the use of the so-called differential isotope method is suitable for the thorough investigation of processes taking place on surfaces. It is known that the changes in the values of the heat of adsorption with the degree of surface coverage can be interpreted in two different ways: it can be assumed that an interaction occurs between adsorbed molecules or that the surface consists of discrete adsorption sites which are heterogeneous in respect of their adsorption energies.[2–4] In order to decide whether a surface is homogeneous or heterogeneous, the method used by KEIER and ROGINSKY[8] and by EMMETT[9] has recently been widely applied. In this method, the inactive and the labelled (active) forms of a compound are adsorbed in a definite order, and then, on desorption, the isotopic composition of desorbed vapours is measured. From these data, conclusions are drawn with regard to the heterogeneity of the surface.

In the present investigation the following method was used. First, a known quantity of labelled ethyl iodide of known specific activity was admitted, then, after removing non-adsorbed

Table 3. Experimental desorption data

T (°C)	Pressure of desorbed portions of gas (mm apiezon)	Total activity of desorbed vapours (impulses/min)	Specific activity of desorbed portion, $S = A/p$ (impulses/min mm)	Reduced specific activity, S/S_0
60	41	0·582	14·2	0·72
75	37·5	1·051	12·51	0·63
96	51·5	1·524	9·18	0·465
100	17	1·790	15·65	0·79
104	17·5	2·135	19·71	0·997
110	42	2·644	12·11	0·61
115	14	2·741	6·83	0·35
117	23·5	3·038	12·63	0·64
125	18	3·415	20·95	1·06
130	15·5	3·661	16·07	0·81
148	10·5	3·754	8·86	0·45
155	12	3·921	13·92	0·705
160	15·5	4·227	19·73	1·00
220	20	4·453	11·3	0·57

vapours, a known amount of inactive ethyl iodide was adsorbed by the surface. Then desorption data were obtained by measuring the pressures and isotope concentrations of the desorbed gases while the temperature was gradually raised. (Adsorption data are as follows: specific activity of the first adsorbed ethyl iodide was $A/p = 19{\cdot}75$ impulses/min mm, the ratio of active to inactive ethyl iodide was 1·76. The temperature in both cases was 26°C.) The experimental desorption data are summarized in Table 3.

The variations in activity shown in Table 3 may be interpreted by assuming that desorption and rearrangement take place at similar rates. During the initial period of desorption, molecules are liberated first at sites of lower energy. Then, molecules in the proximity of these sites begin to migrate to the vacant sites. This process results in changes of specific activity in a manner determined by the sequence of adsorption. The data obtained can be interpreted by assuming that these processes take place repeatedly at several "centres".

To study the interactions of molecules in the vapour phase with molecules adsorbed on the surface, experiments were carried out by adsorbing labelled ethyl iodide almost to saturation, removing excess vapours by pumping and then passing inactive ethyl iodide over the adsorbed phase. In other tests, propyl iodide vapours were equilibrated with the labelled ethyl iodide bound by the surface. The isotope concentrations of the vapour phase measured in both experiments are shown in Fig. 5, where the abscissa represents time and the ordinate values of A/A_f. (A is the value of *activity* measured, whilst A_f is the *specific activity* of adsorbed ethyl iodide.)

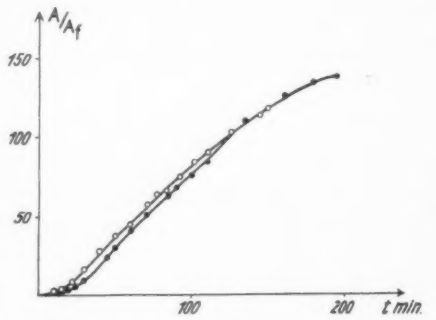

FIG. 5. Time-dependence of the exchange between adsorbed molecules and molecules in the vapour phase at 20°C.

It can be seen from Fig. 5 that both curves run fairly close to each other. Accordingly the assumption is justified that molecules are exchanged instead of iodine atoms, since in the reverse case, marked differences would appear in the exchange rates of ethyl iodide and propyl iodide. This is in

accordance with our assumptions with regard to the migration of molecules. This assumption is supported by the data of MARTIN and SUTTON, who did not find any significant exchange between ethyl and propyl iodides.[10]

Acknowledgements—Thanks are due to Professor JÁNOS DI GLERIA for his support.

REFERENCES

1. MOLINARI E., *Z. phys. Chem. (Frankfurt)* **6,** 1 (1956).
2. ROGINSKY S. Z., *Adsorption and Catalysis on Heterogeneous Surfaces*. Academic Press, Moscow (1948). (In Russian.)
3. KUMMER J. T. and EMMETT P. H., *J. Amer. Chem. Soc.* **73,** 2886 (1956).
4. EISCHENS R. P., *J. Amer. Chem. Soc.* **74,** 6167 (1952).
5. KEIER N. P. and ROGINSKY S. Z., *Dokl. Akad. Nauk. S.S.S.R.* **57,** 157 (1947).
6. GUCZI L., KENDE I., and GÁL D., *J. Phys. Chem. Solids* **10,** 326 (1959).
7. DUTKA F. and GÁL D., *Int. J. Appl. Rad. Isot.* **5,** 106 (1959).
8. KEIER N. P. and ROGINSKY S. Z., *Izv. Akad. Nauk. S.S.S.R., Otdel. Khim. Nauk* 27 (1950).
9. EMMETT P. H. and KUMMER J. T., *J. Chim. Phys.* **47,** 67 (1950).
10. MARTIN G. R. and SUTTON H. C., *Trans. Faraday Soc.* **48,** 812 (1952).

OL.
10
959

J. Phys. Chem. Solids Pergamon Press 1959. Vol. 10. pp. 326–332. Printed in Great Britain.

USE OF THE DIFFERENTIAL ISOTOPE METHOD FOR STUDYING THE INTERACTION BETWEEN VAPOURS OF ALKYL IODIDE AND SURFACE OF RED PHOSPHORUS

L. GUCZI, I. KENDE, and D. GÁL*

Isotope Laboratory, Research Institute for Soil Science and Agrochemistry, Hungarian Academy of Sciences, Budapest

(*Received* 15 *December* 1958)

Abstract—The kinetic curves of the desorption of ethyl, *n*-propyl and *n*-butyl iodides on red phosphorus at 40, 60 and 100°C were determined. From these and from the rate-of-desorption curves the partition functions were obtained, giving desorption energies and activation energies for the desorption processes.

Making use of a radioactive iodine isotope, the differential isotope method was applied to studies of the interaction between alkyl iodides and the surface of red phosphorus.

The experimental results seem to indicate that the surface of red phosphorus is heterogeneous, and that, in addition to adsorption, certain chemisorption processes also take place, leading to cleavage of the C–I bond in the molecules of alkyl iodides.

1. INTRODUCTION

CATALYSTS are becoming increasingly important in organic chemical reactions, and consequently an increasing number of investigations are being devoted to elucidating the mechanism of heterogeneous catalysis, in particular to studying the surface properties, the structure, and the elementary processes—such as exchange, diffusion, desorption and chemisorption—taking place on the surface of the catalysts. These processes are markedly influenced by the degree of heterogeneity of the surface. Numerous authors have evolved methods for the study of surface heterogeneity. KEIER and ROGINSKY[1,2] applied the so-called differential isotope method, using H_2 and D_2 isotopes, to the examination of carbon surfaces. KUMMER and EMMETT and also EISCHENS and his co-workers[3–5] determined the number of centres of different energy on the surface of "ferrum reductum" by examining the rate of the exchange process between ^{12}CO and ^{14}CO. The technique of KUMMER and EMMETT was rather similar to that of KEIER and ROGINSKY. CHARLWOOD[6] determined the heterogeneity of surfaces by diffusion measurements.

Although the processes taking place on surfaces depend to a great extent on the structure and on the surface-energy conditions, the radicals participating in the elementary reactions occurring on the surface also play a significant role. Therefore, the present experiments were designed to examine, with the use of ethyl, *n*-propyl and *n*-butyl iodides as typical compounds, the effect of the increase in the number of carbon atoms in alkyl radicals on the processes taking place on the surface of red phosphorus.

The reason for choosing these particular substances was that organic iodides are produced by the reaction of alcohols with elementary iodine in the presence of red phsophorus as catalyst. In this reaction phosphorus tri-iodide presumably acts as an intermediate, a fact not yet definitely proved. It appeared to be of interest to discover, by means of desorption measurements, whether other processes besides physical adsorption—possibly chemisorption—occur when alkyl iodides are adsorbed by red phosphorus. In the present investigations, alkyl iodides labelled with ^{131}I radio-

* Present address : Central Isotope Laboratory, University of Szeged, Szeged, Hungary.

active isotope were used in conjunction with the differential isotope method.

2. EXPERIMENTAL METHODS

Inactive ethyl, *n*-propyl and *n*-butyl iodides were prepared in accordance with VOGEL's[7] instructions and purified as directed. The products were repeatedly distilled, and the fractions from the prescribed temperature intervals were used in the tests. In isotope experiments, alkyl iodides labelled with ^{131}I isotope* were used, ^{131}I being introduced into the inactive molecule by the technique of heterogeneous exchange, i.e. the solution of $K^{131}I$ was evaporated to dryness in a 25-ml flask with a ground-glass stopper, then inactive alkyl iodide was added, and the mixture was allowed to stand at 60°C for 24–36 hr, during which time the majority of the ^{131}I atoms entered the organic molecules. The alkyl iodide was then distilled. In a series of experiments, a solution of $K^{131}I$ of 2-Mc activity was used, from which alkyl iodide of approximately 200-μc/ml activity was prepared.

The red phosphorus was prepared by purifying the commercial product in the way described by VOGEL[7]. Five-g portions of the completely dried substance were weighed into the reaction vessel.

The apparatus was described in an earlier paper.[8] As desorption experiments were carried out at temperatures of 40, 60 and 100°C, respectively, the complete desorption vessel was placed in a Höppler ultrathermostat. Higher temperatures were produced by a controllable electric furnace. Red phosphorus was, prior to the experiments, regenerated by heating the reaction vessel to 350°C and holding it at this temperature for 1 hr under conditions of continuous pumping.

When the regeneration of the phosphorus was complete, the apparatus, including also the space over the adsorbent, was evacuated to 10^{-5} mm Hg. Then a weighed amount of alkyl iodide was adsorbed at 26°C, and the apparatus was again evacuated to 5×10^{-4}–10^{-5} mm Hg. During pumping the tap of the adsorption vessel was opened for $\frac{1}{2}$ min. This time was found to be satisfactory for removing non-adsorbed gas from the adsorption vessel. Subsequently, the desorption process was measured.

* Carrier-free ^{131}I in the form of KI was supplied by the Committee for the Application of Isotopes of the Hungarian Atomic Energy Commission.

3. EXPERIMENTAL RESULTS

Desorption curves of ethyl, *n*-propyl and *n*-butyl iodide were determined at 60°C. The ordinate in Fig. 1 shows the quantities desorbed in units p_x/p_∞, where p_x is the pressure of gas desorbed in time t and p_∞ the equilibrium pressure. The abscissa indicates the time.

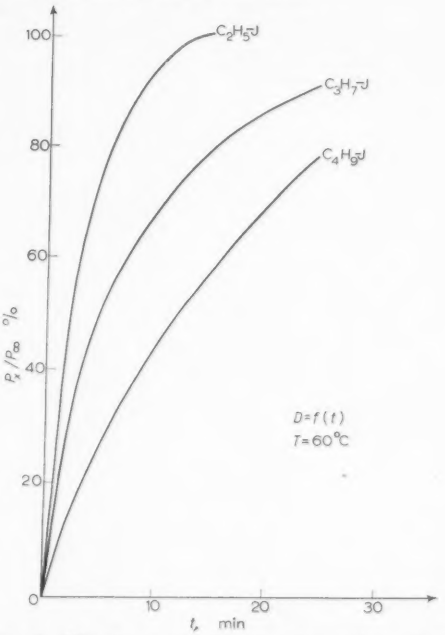

FIG. 1. Kinetic curves for the desorption of ethyl, *n*-propyl and *n*-butyl iodides at 60°C, plotted against time.

Quantities desorbed increased for each substance with rise in temperature. As Fig. 1 does not include values of time corresponding to the equilibrium pressure, these are summarized in Table 1.

Table 1.

Compound	$t_{p\infty}$(min)		
	40°C	60°C	100°C
C_2H_5I	20	15	10
C_3H_7I	60	40	30
C_4H_9I	100	50	30

The rate curves for all three compounds at 60°C are shown in Fig. 2. These were obtained by the graphical differentiation of the curves of Fig. 1. Rate curves intersect each other, in accordance with the fact that the rates of desorption of various

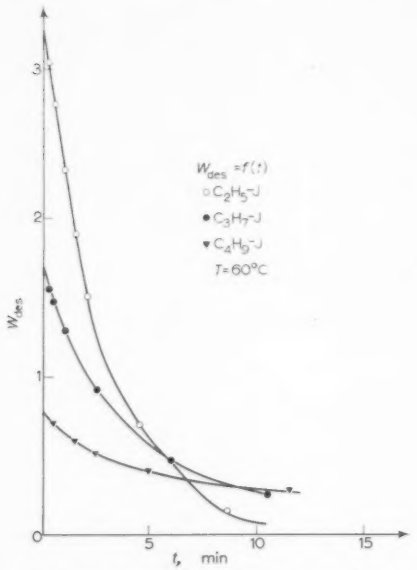

FIG. 2. Rate curves for ethyl, *n*-propyl and *n*-butyl iodides at 60°C, plotted against time.

substances are identical at given moments. As the initial sections of the desorption curves are unreliable because of experimental difficulties, values of w_0 (the initial rate) were established by extrapolation.

Values of w_0 for the three compounds at the temperatures given are shown in Table 2.

Table 2.

Compound	w_0(min^{-1})		
	40°C	60°C	100°C
C_2H_5I	1·81	3·23	11·05
C_3H_7I	1·00	1·70	3·00
C_4H_9I	0·46	0·82	1·90

According to the theory of ROGINSKY[9], the activation energy of the desorption process on a heterogeneous surface can be expressed by the formula

$$E_{des.} = RT \ln t/\tau_0, \qquad (1)$$

where $E_{des.}$ is the activation energy of desorption, t the time in min, and τ_0 is a constant.

For the case of desorption on a heterogeneous surface, the value of $RT \ln t$ depends only on the degree of coverage of the surface, i.e. $E_{des.}$ has a constant value for any given surface coverage. Thus, for two temperatures T_1 and T_2 and a given coverage:

$$\Delta E = (RT_1 \ln t_1/\tau_0 - RT_2 \ln t_2/\tau_0)_{D\text{-const.}} = 0$$

where D is the quantity desorbed. From this, by rearrangement,

$$(RT_1 \ln t_1 - RT_2 \ln t_2)_{D\text{-const.}} = R(T_1 - T_2)\ln \tau_0 \quad (2)$$

This is the "law of constant shift", the validity of which is at the same time a precondition for the applicability of the theory. That is the reason why the desorption of butyl iodide at 40, 60 and 100°C was plotted against values of $RT \ln t$ (see Fig. 3).

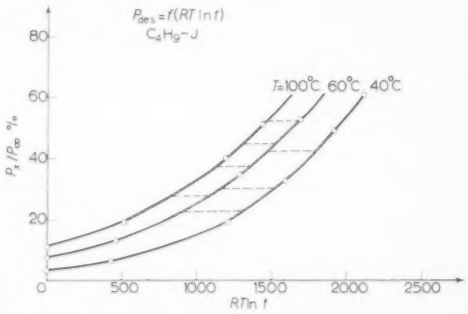

FIG. 3. Desorption curve for *n*-butyl iodide at 40, 60 and 100°C, plotted against values of $RT \ln t$.

The length of the dotted horizontal lines between the curves in Fig. 3 can be considered constant within the limits of experimental error.

The function $D = f(t)$ can be described in the case of all three alkyl iodides by equations of the type

$$D^n = a \ln t + C \qquad (3)$$

The constant n was determined by differentiation of equation (3):

$$w = \frac{dD}{dt} = \frac{1}{n}(a \ln t + C)^{(1/n)-1} \cdot \frac{a}{t} \qquad (4)$$

On multiplying by t, introducing logarithmic values, and substituting b for a/n, we obtain:

$$\log(wt) = \log b + (1-n)\log D. \qquad (5)$$

Plotting values of $\log(wt)$ against $\log D$, where D is the quantity desorbed designated by us as p_x/p_∞, the value of n can be calculated from the

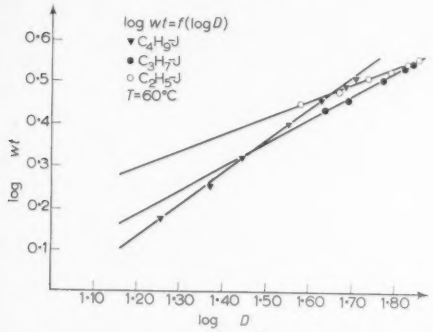

FIG. 4. Function log (wt) for ethyl, n-propyl and n-butyl iodides, plotted against log D.

slope of the line obtained (Fig. 4). Values of n obtained in this way are summarized in Table 3.

Table 3.

Compound	n
C_2H_5I	2/3
C_3H_7I	2/5
C_4H_9I	1/5

Subsequently, the partition functions according to energies were determined for the three alkyl iodides. This function was derived as follows:

$$\rho(E) \equiv \frac{dD}{dE} = \frac{t}{RT}\cdot\frac{dD}{dT} = \frac{dD}{RT\,d\ln t} \qquad (6)$$

For this purpose, it was necessary to plot the desorbed quantities against $E = RT\ln t$ (Fig. 5), whilst the graphical differentiation of the function $D = f(E)$ yielded directly the function $\rho(E)$ (Fig. 6). The partition function expresses the probabilities of the occurrence of sites of a given energy in the desorption process. The partition function

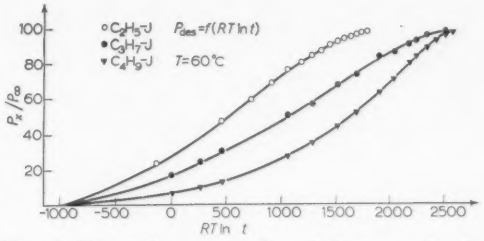

FIG. 5. Desorption curves for ethyl, n-propyl and n-butyl iodide at 60°C, plotted against values of energy.

in the case of the kinetic equation (3) is given by an equation of the form[10]

$$\rho(E) = H\cdot E^k \qquad (7)$$

The corresponding values for k are shown in Table 4.

Table 4.

Compound	k
C_2H_5I	4
C_3H_7I	3/2
C_4H_9I	1/2

It appears from Fig. 6 that the maximum of the function $\rho(E)$ is displaced towards higher energies

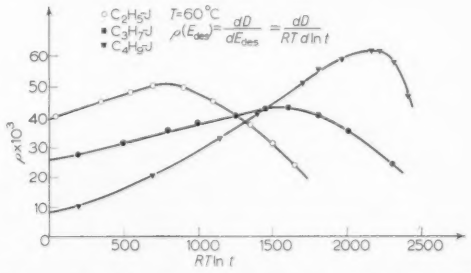

FIG. 6. Partition functions $\rho(E)$ of ethyl, n-propyl and n-butyl iodides at 60°C, plotted against energies.

with increasing number of carbon atoms, in accordance with the values of the activation energy calculated from the Arrhenius equation (see discussion below).

Activation energies of desorption were determined (1) by the Arrhenius equation and (2) by the method described by ROGINSKY.

(1) In order to determine the activation energies of desorption, the kinetic curves of desorption

were determined at 40, 60 and 100°C for each of the three iodides. Fig. 7 presents the desorption curves of butyl iodide at 40, 60 and 100°C, the quantities desorbed in units of p_x/p_∞ being plotted on the ordinate and the time on the abscissa. From

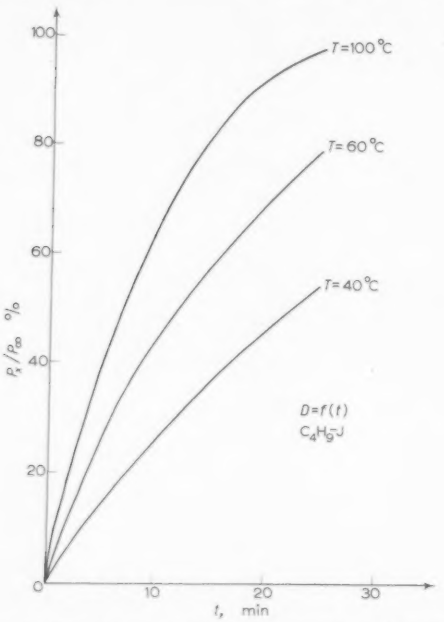

FIG. 7. Kinetic curve for the desorption of *n*-butyl iodide at 40, 60 and 100°C, plotted against time.

these curves, the function $w = f(t)$ was obtained by graphical differentiation, the results being summarized in Table 2.

In accordance with the Arrhenius equation

$$w = Ae^{-E/RT}$$

values of log w_0 were plotted against $1/T$ (Fig. 8) and the activation energies were calculated from the slopes of the lines (Table 5).

Table 5.

Compound	$E_{des.}$, calc.	
	Arrhenius, $t = 0$ min.	Roginsky, $t = 0$ min.
C_2H_5I	3960	4200
C_3H_7I	4340	4620
C_4H_9I	4560	4940

(2) The function $D = f(RT \ln t)$ was established for each of the three iodides at 40, 60 and 100°C. Then, at an arbitrary value D, which was identical at the three temperatures examined, the

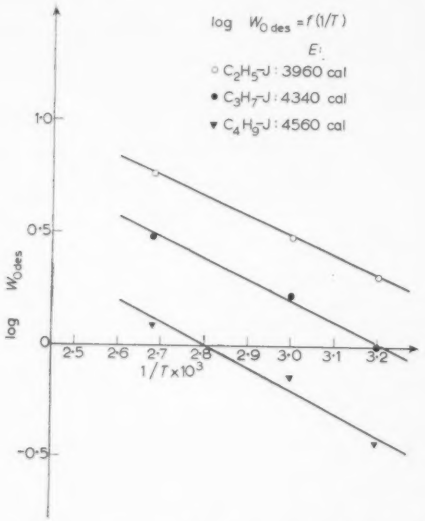

FIG. 8. Values of log w for ethyl, *n*-propyl and *n*-butyl iodides, plotted against values of $1/T$.

values of ln τ_0 were calculated for each of the substances from the differences between the curves

$$\ln \tau_0 = \frac{(RT_1 \ln t_1 - RT_2 \ln t_2)_{D=\text{const.}}}{R(T_1 - T_2)} \qquad (8)$$

The results were substituted into equation (1) and values of the activation energies were determined at time $t = 1$ min (Table 5).

Although the equations so far discussed describe in a quantitative manner the processes taking place on the surface of red phosphorus, no conclusions can be drawn from them with regard to the heterogeneity of the surface. Only the application of the differential isotope method appeared to be promising. This method, described by us in detail elsewhere,[8] has been used several times for studies of surfaces and surface reactions.

Desorption was examined in the temperature interval 60–370°C. In connection with our experimental technique it must be noted that the active gases were frozen, before leaving the apparatus, by a carbon dioxide–acetone mixture.

Experimental results are shown in Figs. 9–11, values $S/\bar{S}$ of specific activity being plotted against pressure. $\bar{S}$ is here the average specific activity of the total adsorbed gases $\left(\frac{\text{impulses/min}}{\text{Hg mm}_{\text{active+inactive}}}\right)$, i.e. the value which would be obtained in the case of a homogeneous surface at desorption. Values of S, i.e. the real specific activity of the desorbed gas, were calculated by dividing the differences in the activities of portions of gas desorbed consecutively, by the differences of the pressure values corresponding to them.

(1) Fig. 9 shows the activities of desorbed ethyl iodide, when active ethyl iodide has previously been adsorbed. It can be seen that at 60°C, at low pressures, the desorbed gas is of higher specific activity than was the gas originally adsorbed. At pressures greater than 6 mm Hg, no changes appeared in the specific activity of the desorbed gas.

(2) In Fig. 10 (corresponding to case 2), the curve of activity values has a shape similar to that of the previous one, except that it starts at a higher value of $S/\bar{S}$. In the pressure range 7–14 mm Hg, the specific activity was approximately constant.

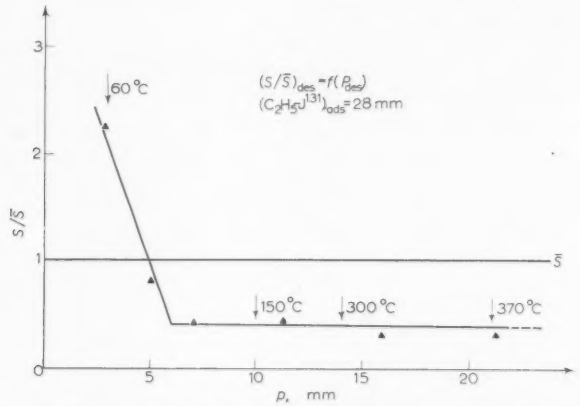

FIG. 9. Changes in the specific activity of ethyl iodide, plotted against pressure.

Three series of experiments were carried out independently of each other:

(1) Only active gas was adsorbed.

(2) First an inactive, then an active gas was adsorbed.

(3) First an active, then an inactive gas was adsorbed.

The expected values of specific activity were measured only at about 20 mm Hg.

(3) In our third series of experiments (Fig. 11), with active-gas adsorption followed by inactive-gas adsorption, the curve $S/\bar{S}$ did not reach the line $\bar{S}$. At first, an abrupt decrease was observed which, after a sharp break, became a slow decrease.

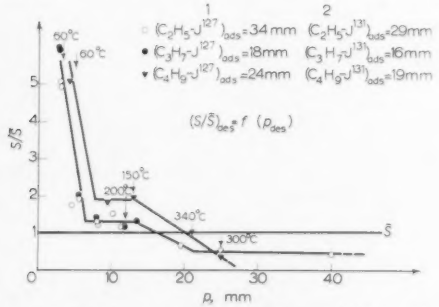

FIG. 10. Changes in the specific activities of ethyl, *n*-propyl and *n*-butyl iodide, plotted against pressure.

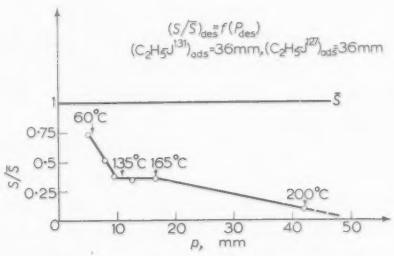

FIG. 11. Changes in the specific activity of ethyl iodide plotted against pressure.

Table 6.

Compound	$\Delta E_{hom.}$, calc.	$\Delta E_{P_{des.}}$, calc.	$w_0/w_{0eth.}$, hom.	$w_0/w_0P_{des.}$
C_2H_5I	0	0	1	1
C_3H_7I	390	420	0·48	0·51
C_4H_9I	750	740	0·31	0·27

4. DISCUSSION

The experimental results were interpreted as follows. There are at least three different energy levels on the surface of red phosphorus. In the experiment inactive–active gas, the lowest energy level is occupied by the molecules of the substance adsorbed first, i.e. inactive gas, which, however, also populate to a certain extent the levels of medium energy. This second energy level is completely filled up by the molecules labelled with ^{131}I, which are adsorbed next. Some residual labelled molecules populate the third energy level.

The alkyl iodide molecules desorbed at first at 60°C formed probably a poly-iodine complex. The labelled iodine atom presumably originates from the medium energy level as the energy liberated there is sufficient to break the bond C–I. The residual alkyl radical is probably linked to phosphorus.

The active–inactive experiments also support these assumptions. In this case the surface was occupied by the molecules just as in the inactive–active experiment, only with the order reversed. The curve $S/\bar{S}$ (Fig. 11) runs completely below the line $\bar{S}$, and only a fraction of the total activity applied is recovered. At the end of the desorption process (above 300°C), the gas contained no labelled atoms, indicating that the majority of the iodine atoms were bound by phosphorus.

It is interesting to compare the present results with those obtained in an earlier investigation,[8] where the desorption of the same compounds on active carbon was studied. These can be summarized as follows.

In the case of active carbon the adsorption and desorption processes proved to be reversible. On considering the differences in the activation energies of desorption or in the kinetic parameters obtained with increasing numbers of carbon atoms, no monotonic changes in the reactivities could be inferred. Neither the results of kinetic measurements nor the data yielded by the differential isotope method indicated the breakdown of the C–I bond.

By contrast, with red phosphorus as adsorbent, the equations describing desorption and the partition function $\rho(E)$ are quite different for each adsorbate. In the case of red phosphorus, a chemical reaction takes place on the surface, connected with the breakdown of the C–I bond and with the formation of new compounds. It is of interest to compare the results observed in the case of red phosphorus with those obtained at the exchange reactions of alkyl iodides in a homogeneous phase (Table 6, columns 1 and 3[11]).

Both the values ΔE and $w_0/w_{0eth.}$ are in fair agreement, thus confirming that chemical processes are dominant on the surface of red phosphorus.

Acknowledgements—Thanks are expressed to Professor JÁNOS DI GLÉRIA for supporting the present experiments.

REFERENCES

1. KEIER N. P. and ROGINSKY S. Z., *Dokl. Akad. Nauk. S.S.S.R.* **57,** 157 (1947).
2. KEIER N. P. and ROGINSKY S. Z., *Zh. Fiz. Khim.* **23,** 897 (1949).
3. KUMMER J. T. and EMMETT P. H., *J. Amer. Chem. Soc.* **73,** 2886 (1951).
4. EISCHENS R. P., *J. Amer. Chem. Soc.* **74,** 6167 (1952).
5. WEBB A. N. and EISCHENS R. P., *J. Amer. Chem. Soc.* **77,** 4710 (1955).
6. CHARLWOOD P. A., *J. Phys. Chem.* **57,** 125 (1953).
7. VOGEL A. I., *Practical Organic Chemistry* p. 285. Longmans, Green and Co., London (1956).
8. KENDE I., GUCZI L., and GÁL D., *J. Phys. Chem. Solids* **10,** 321 (1959).
9. ROGINSKY S. Z., *Problems of Kinetics and Catalysis* Vol. 7, p. 412 Moscow (1949).
10. ROGINSKY S. Z., *Adsorption and Catalysis on Heterogeneous Surfaces* p. 129. Academic Press, Moscow (1948). (In Russian.)
11. DUTKA F. and GÁL D., *Int. J. Appl. Rad. Isot.* **5,** 106 (1959).

Photoconductivity in indium sulfide powders and crystals

(*Received* 11 *December* 1958; *revised* 27 *January* 1959)

PHOTOCONDUCTIVITY measurements have been made on powders and single crystals of β-In_2S_3. According to HAHN and KLINGER[1], this material has a spinel-like structure with eight of the seventy-two possible cation sites in three unit cells being vacant. A defect structure of some type is found for several of the Group III–Group VI compounds; measurements on gallium compounds will be reported at a future date.

Three methods were used for the preparation of β-In_2S_3: (1) α-In_2S_3 may be precipitated from $InCl_3$ solution with H_2S.[2] After washing and drying, it is heated in H_2S which helps to remove any chloride, converts any oxide present to sulfide and converts the α-In_2S_3 to β-In_2S_3. (2) β-In_2S_3 is formed when In_2O_3 is heated in H_2S.[1] (3) Direct combination of the elements followed by heating in H_2S can also be used. Method (2) was used for most of the materials described in this report, except where otherwise noted.

In_2S_3 can be made to have high dark conductivity either by incorporation of halogen donors, as from $CdCl_2$ or NH_4Cl, or by heating the pure material in nitrogen to temperatures above 800°C. The latter method results in considerable sintering and hence was not often used. Photosensitive powders were prepared in three ways: (1) Heating In_2S_3 with $CdCl_2$ and Mn (100 p.p.m.) in nitrogen, (2) making In_2S_3 : Mn conducting by heating in nitrogen, followed by heating in H_2S to reduce the dark conductivity and (3) annealing In_2S_3:Cl in arsenic vapor. All three powders had about the same sensitivity, showing a light-to-dark current ratio of about 100 at 3 ft-candles and 6×10^3 V/cm; thus these powders are only about 10^{-2} to 10^{-3} times as sensitive as standard CdS and CdSe powders. Spectral-response curves for the In_2S_3:Cl:Mn and In_2S_3:Cl:As powders are given in Fig. 1.

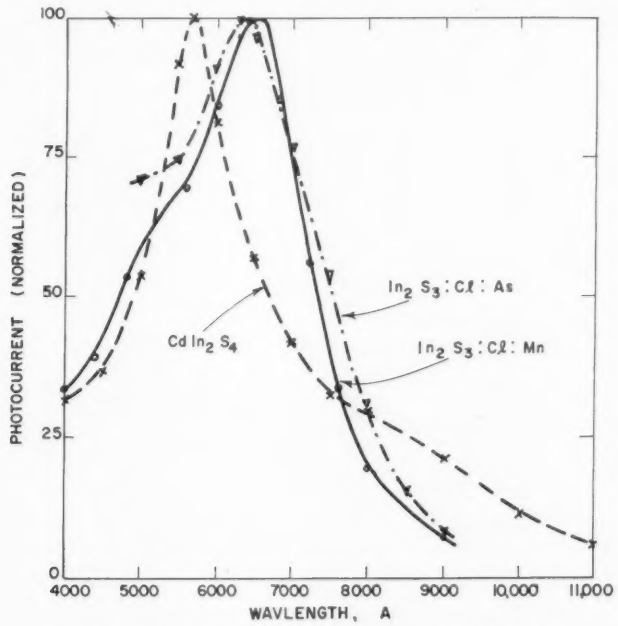

FIG. 1. Spectral response for photoconductivity at room temperature in In_2S_3:Cl:Mn, In_2S_3:Cl:As and $CdIn_2S_4$ powders.

The compound $CdIn_2S_4$ was prepared by heating CdS and In_2S_3. The resulting powder had about the same photosensitivity as In_2S_3, but the maximum response indicates a band gap of 2·18 eV for $CdIn_2S_4$, as compared to a band gap of 1·97 eV for In_2S_3. The spectral response for $CdIn_2S_4$ is also indicated in Fig. 1.

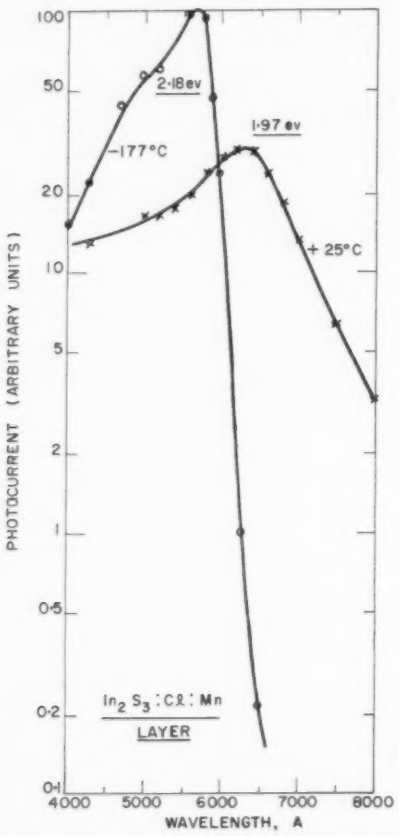

FIG. 2. Spectral response for photoconductivity in In_2S_3:Cl:Mn layer at −177 and at 25°C.

Fig. 2 shows the spectral response of an In_2S_3:Cl:Mn layer at low temperature compared to the room-temperature curve. The temperature-dependence of the response maximum indicates that the band gap of In_2S_3 can be expressed over this temperature range as: $E_G(\text{eV}) = 2{\cdot}28 - -10{\cdot}4 \times 10^{-4}\, T(°\text{K})$.

Conducting In_2S_3:Cl was prepared by method (3), using NH_4Cl. Subsequent annealing in atmospheres of various impurities revealed that the conductivity could be reduced by sulphur or elements from Group V, such as arsenic, but that elements from Groups I and II which would be expected to act as acceptors, such as copper, silver and cadmium, either did not affect the dark conductivity or actually increased it. Lead also increased the dark conductivity. These impurities had the same effect on samples of In_2S_3 made conducting by heating in nitrogen as on insulating samples prepared with prior heating in H_2S. Annealing of In_2S_3:Cl:Ag in arsenic reduced the dark conductivity. These results suggest that the elements from Groups I, II and IV are behaving as donor impurities.

Crystals of In_2S_3 were obtained by heating In_2S_3 powder in an evacuated sealed silica capsule for 6 days at 1000°C. These crystals showed only low sensitivity at room temperature, but at liquid-nitrogen temperature the sensitivity was within an

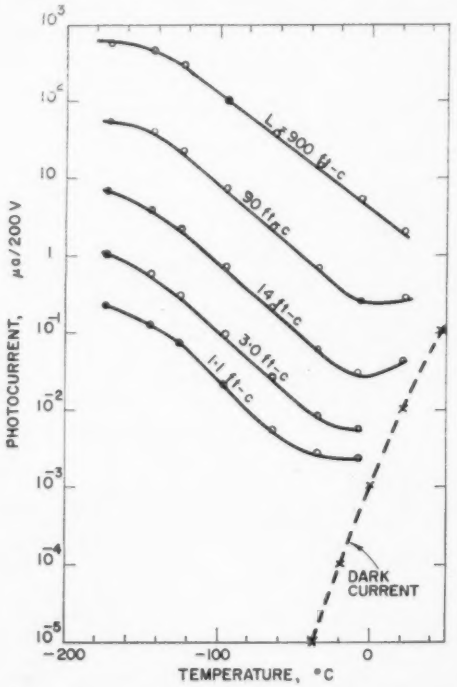

FIG. 3. Photocurrent as a function of temperature for In_2S_3 crystal, measured at several excitation intensities; also dark current for same crystal as function of temperature. Light intensity of 100 corresponds to 900 ft-candles.

order of magnitude of that of photosensitive CdS or CdSe crystals. The temperature-dependence of the photocurrent for several light levels is shown in Fig. 3, together with the temperature-dependence of the dark current. Instead of thermal quenching of photoconductivity occurring rapidly over a narrow range of temperatures, as in CdS or CdSe,[3] the photocurrent decreases almost exponentially with temperature over a wide temperature range. Using the analysis of temperature quenching presented in a previous publication,[3] it can be shown that the onset of quenching corresponds to an activation energy of about 0·1 eV, whereas the termination of quenching corresponds to an energy of about 0·8 eV. This behavior is similar to that reported for ZnSe crystals with Group V acceptors,[4] and for certain CdS and CdSe crystals with high acceptor concentrations.[5] An effectively continuous distribution of sensitizing levels is indicated in these materials.

RCA Laboratories RICHARD H. BUBE
Princeton, N.J. WILLIAM H. MCCARROLL

VOL. 10 1959

REFERENCES

1. HAHN H. and KLINGER W., *Z. anorg. Chem.* **260,** 97 (1949).
2. STUBBS M. F., SCHUFLE J. A., THOMPSON A. J. and DUNCAN J. M., *J. Amer. Chem. Soc.* **74,** 1441 (1952).
3. BUBE R. H., *J. Phys. Chem. Solids* **1,** 234 (1957).
4. BUBE R. H. and LIND E. L., *Phys. Rev.* **110,** 1040 (1958).
5. BUBE R. H., *J. Chem. Phys.* **30,** 266 (1959).

The diffusion coefficient of zinc in indium antimonide

(*Received* 24 *February* 1959)

THE diffusion coefficient D has been measured for zinc in InSb by the p–n junction method developed by FULLER[1]. This involved diffusing zinc (an acceptor) from the vapour phase into two differently doped n-type samples of InSb under identical conditions; by measuring the depths of the p–n junctions, two points on the complementary error function distribution of the diffusant are obtained, and D may be calculated. It is assumed that the boundary condition at the surface is one of constant concentration of zinc. The n-type specimens were cut from tellurium-doped single-crystal material, and had carrier concentrations ranging from 3×10^{16} to 2×10^{18} cm^{-3}, as determined by Hall-constant measurements at 77°K; by using heavily doped material, the effect of rapidly diffusing acceptors of lower solubility was minimized (HULME, to be published). The specimens were etched and mechanically ground, one surface being subsequently polished to a mirror finish with Linde fine abrasive type A-5175; they were then re-etched in dilute "Analar" HCl, washed in doubly distilled water, and finally sealed off with several mg of etched "spectrographically" pure zinc, under $\sim10^{-5}$ mm Hg pressure, in ~11-cm lengths of quartz tubing, 5 mm in internal diameter, which had previously been cleaned with "Analar" acids and washed with doubly distilled water. The diffusion process was performed in a furnace, the temperature of which was controlled to ±2°C by a platinum resistance thermometer. The specimen was arranged to be close to the thermometer and also to a calibrated Chromel/Alumel thermocouple, used in conjunction with a potentiometer to measure its temperature; the zinc was arranged to be in a region of the furnace about 15°C colder than the specimen. Annealing times ranged from 1 to 240 hr; when the allotted time had elapsed, the specimen was removed from the furnace and allowed to cool in its tube to room temperature. A technique closely similar to that of BOND and SMITS[2] was used to obtain the depths of the p–n junctions. Bevels ($\sim2°$) were polished across the previously polished surfaces of the specimens; the p–n junctions were then located by thermoelectric probing at 77°K,* and their positions were marked with the sharp tungsten point used for probing. The depths were then measured interferometrically, or, in the case of depths greater than $\sim25\mu$, by using the calibrated fine-focus adjustment of a microscope fitted with a 4-mm metallurgical objective (depth of focus $\sim1\mu$); the measured depths ranged from 5 to 81μ.

In calculating the diffusion coefficients it was assumed that the concentration C of diffused zinc was of the form

$$C = C_0 \operatorname{erfc}\xi,$$

* At this temperature the correction associated with the concentration of intrinsic carriers is negligibly small; it is not small at 290°K (see WEISS[3]).

where

$$\xi = x/\{2(Dt)^{\frac{1}{2}}\},$$

x being the distance below the surface and t the time. The assumption that the surface concentration of zinc, C_0, is constant ought to be valid, the vapour pressure of zinc being between 1 and 10^{-2} mm Hg (in the temperature range involved); even if this assumption is not strictly valid, the effect on the diffusant distribution is not large (see SMITS[4]), and the values of D derived should not be greatly in error. An approximate calculation shows that the other assumption involved—that there is no loss of tellurium from the specimen surface—will be valid provided that the tellurium is not absorbed into the quartz at the temperatures used. For values of $\xi > 2$, the approximate method of FULLER[1] was used to calculate the values of D.

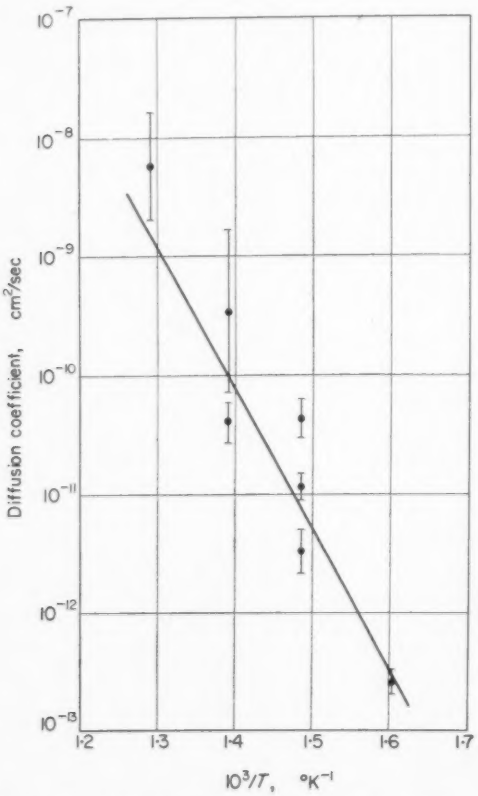

FIG. 1. The diffusion coefficient of zinc in indium antimonide determined by the p–n junction depth method.

$$D = 1{\cdot}6\times10^{6}\exp\{-(53{,}000\pm6{,}000)/RT\}$$

For $\xi \ll 2$, a graphical method suggested by Dr. P. N. BUTCHER of this laboratory was used; this involved the sliding of a log–log plot of erfc ξ_1/erfc ξ_2 against ξ_1/ξ_2 over a log–log plot of erfc ξ against ξ, ξ_1 and ξ_2 being the values of ξ appropriate to the two junction depths. For one pair of specimens a result was not obtained because the junction depths were too small to measure, for another pair because the zinc alloyed into the specimen surfaces, and in the case of a third pair the junction depth was anomalously greater in the more heavily doped specimen.

The results obtained are shown in Fig. 1; the expected linear relationship between log D and $1/T$ appears to be satisfied. The scatter of the experimental points is accounted for by the errors in determining carrier concentrations and junction depths. The calculated surface concentrations ranged from 4×10^{17} to 8×10^{19} per cm^3, but, because of the unreliability of determinations of C_0 by this method, no correlation with source or specimen temperature was obtained. The equation of the line in the figure, obtained by a weighted least-squares method, is $D = 1{\cdot}6\times10^{6}\exp[(-53{,}000\pm\pm6{,}000)/RT]$ cm^2/sec with R in cal/deg. mol. The activation energy for zinc diffusion, 53 ± 6 kcal/mole (or $2{\cdot}3\pm0{\cdot}3$ eV), thus appears to be close to those for self-diffusion, -42 ± 6 and 45 ± 8 kcal/mole for indium and antimony, respectively, as determined by EISEN and BIRCHENALL[5], although much lower values, 6·5 and 17·5 kcal/mole, respectively, were obtained by BOLTAKS and KULIKOV.[6]* Our results suggest that the measurements of EISEN and BIRCHENALL[5] are the more reliable—the activation energies for self- and impurity-diffusion are generally close to one another if the impurity is substitutional; it is usually assumed that zinc in InSb is located substitutionally on indium sites.

* In both cases the self-diffusion coefficients were measured by means of radioactive isotopes. Perhaps the explanation for the enormous discrepancies between the two results is due to one group carrying out the diffusion annealing under conditions in which there was a continuous loss of antimony by evaporation from the specimens. In our experiments the quartz tubes used to contain the specimens were short enough to prevent their temperature anywhere dropping low enough for antimony to condense; a rough calculation shows that unless antimony were absorbed into the quartz at this temperature, losses would be negligible.

Acknowledgements—The authors would like to thank their colleagues for useful discussions, also Miss J. M. WRIGHT and Dr. J. B. MULLIN, who were involved in the preparation of the tellurium-doped single-crystal specimens of InSb. We also acknowledge the permission of the Controller of Her Britannic Majesty's Stationery Office to publish this letter.

Royal Radar Establishment, K. F. HULME
Great Malvern, Worcs. JANET E. KEMP

REFERENCES

1. FULLER C. S., *Phys. Rev.* **86,** 136 (1952).
2. BOND W. L. and SMITS F. M., *Bell Syst. Tech. J.* **35,** 1209 (1956).
3. WEISS H., *Z. Naturforsch.* **11a,** 131 (1956).
4. SMITS F. M., *Proc. Inst. Radio Engrs.* **46,** 1049 (1958).
5. EISEN F. E. and BIRCHENALL C. E., *Acta Met.* **5,** 265 (1957).
6. BOLTAKS B. I. and KULIKOV G. S., *Zh. Tekh. Fiz.* **27,** 82 (1957).

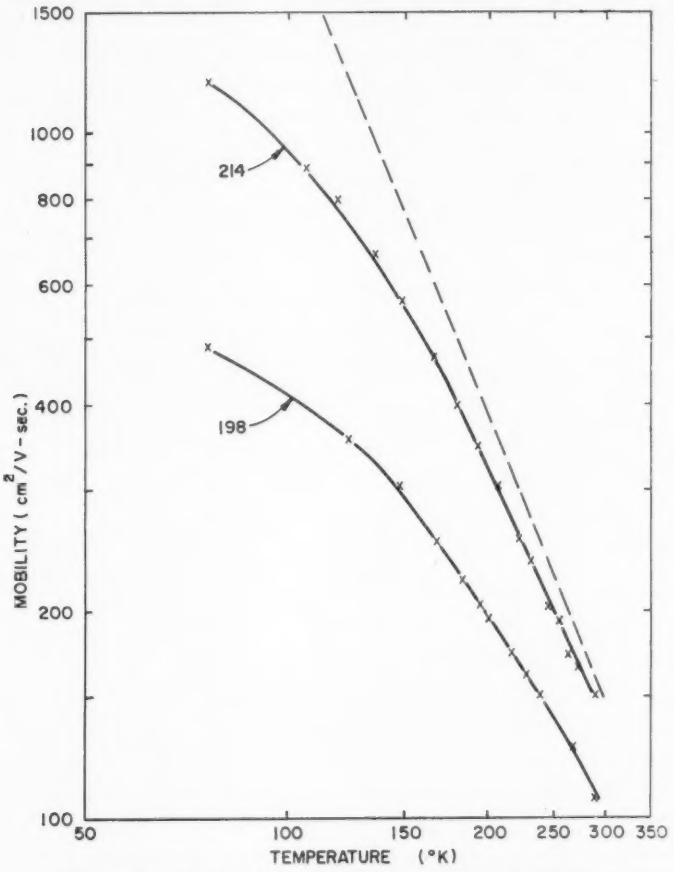

FIG. 1. The Hall mobility of *p*-type InP crystals as a function of temperature. The dashed curve is the lattice mobility calculated from the 214 curve, assuming $m^* = 0{\cdot}2\ m_0$.

Electrical properties of *p*-type InP†

(*Received* 20 *February* 1959)

BECAUSE of the recent availability of InP with impurity concentrations of 10^{16} cm^{-3} and less,[1] it has become possible to produce crystals of relatively pure *p*-type InP and to investigate their properties. Fig. 1 is a plot of the temperature-dependence of the measured Hall mobilities of two samples prepared by doping with cadmium. It is important to note that the mobility of the purer

† Supported in part by the U.S. Air Force.

specimen was 150 cm²/V-sec at 290°K and rose to 1200 cm²/V-sec at 77°K. This is to be compared with the previous published value[2] of 60 cm²/V-sec at room temperature, for a specimen heavily doped with zinc.

Both crystals showed appreciable deionization between 290 and 77°K. Table 1 summarizes their properties, as deduced from the observations. The net impurity concentration, $N_A - N_D$, was taken from the behavior of the Hall coefficient in the vicinity of room temperature. The ionization energy given in the last column was calculated from Hall-coefficient measurements at low temperature (see Fig. 2), and may be an underestimate because of incomplete deionization in the temperature range observed. The donor concentration may be estimated from the low-temperature behavior, if the effective mass of the holes is known.

An effective mass value of $0{\cdot}4\ m_0$ is calculated from the measured larger ionization energy (sample 214) and the assumed hydrogenic-type expression for the ionization energy:

$$E_i = \left(\frac{m^*}{m_0}\right) \times K^{-2} \times (13{\cdot}6\ \text{eV}),$$

where K is the high-frequency dielectric constant, whose value is taken as[3] 10·8. Such a value for the effective mass may not be reliable; it is assumed that the bound hole orbits are hydrogenic in character, and that the complicated nature of the band and its degeneracy have a negligible effect on the ionization energy. The high-frequency dielectric constant is used because the energy of the electron in its ground state is a little larger than the *Reststrahlen* energy[4] of 0·041 eV. Theoretically it is difficult to predict which value of the dielectric constant in the range 10·8–15·0[4] (the "static" value) is appropriate. The static value leads to an effective mass of $0{\cdot}8\ m_0$. Estimates of this kind from the ionization energies of column-III elements in germanium yield values, however, in rather poor agreement with the experimentally determined effective mass values.[5]

One may also estimate the effective mass from the observations of intrinsic carrier concentration made by FOLBERTH and WEISS[2], which gave $(m_n^* m_p^*)^{\frac{1}{2}} = 0{\cdot}23\ m_0$. The intrinsic concentrations of electrons used by FOLBERTH and WEISS were in the range $1\text{–}8 \times 10^{16}$ cm^{-3}; for these concentrations the available evidence[4,6] indicates that most of the electrons should be in a conduction band with an effective mass value[1,7] of about $0{\cdot}05\ m_0$. This leads to a value of m_p^* of about m_0, which would yield even larger values for the compensating concentration of donors, N_D, than those given in the third column of Table 1.

Table 1. Properties of p-type InP crystals

Crystal	Net concentration $N_A - N_D$ (cm^{-3})	Compensating donor concentrations† $N_D^{(1)}$ (using $m^* = 0{\cdot}8\ m_0$) (10^{17} cm^{-3})	$N_D^{(2)}$ (using $m^* = 0{\cdot}8\ m_0$) (10^{17} cm^{-3})	$N_D^{(1)}$ (using $m^* = 0{\cdot}4\ m_0$) (10^{17} cm^{-3})	$N_D^{(2)}$ (using $m^* = 0{\cdot}4\ m_0$) (10^{17} cm^{-3})	$N_D^{(1)}$ (using $m^* = 0{\cdot}2\ m_0$) (10^{17} cm^{-3})	$N_D^{(2)}$ (using $m^* = 0{\cdot}2\ m_0$) (10^{17} cm^{-3})	Ionization energy (eV)
198	$8{\cdot}5 \times 10^{17}$	33	$< 1{\cdot}1$	11·5	$< 1{\cdot}8$	4·1	< 3	0·026
214	3×10^{16}	2·6	$< 0{\cdot}25$	0·92	$< 0{\cdot}4$	0·32	$< 0{\cdot}6$	0·047

† $N_D^{(1)}$ is the donor concentration deduced from low-temperature Hall measurements.
$N_D^{(2)}$ is the limit on the donor concentration deduced from the fit of impurity mobility to data.

Another more indirect estimate of the effective mass comes from an analysis of the mobilities measured. It was assumed that the mobility was due to a combination[8] of impurity scattering and lattice scattering, with the impurity scattering calculated from the BROOKS–HERRING expression.[5,9] Effective masses of 0·8, 0·4 and $0{\cdot}2\ m_0$ and a dielectric constant of 15 were assumed, and the compensation was varied to give at least as large a calculated impurity mobility as the measured value at 80°K. The maximum concentrations arrived at in this fashion are given in Table 1. For $m^* = 0{\cdot}8$ and $0{\cdot}4\ m_0$, these estimates are considerably lower than those calculated from the low-temperature Hall measurements. Better agreement is possible for

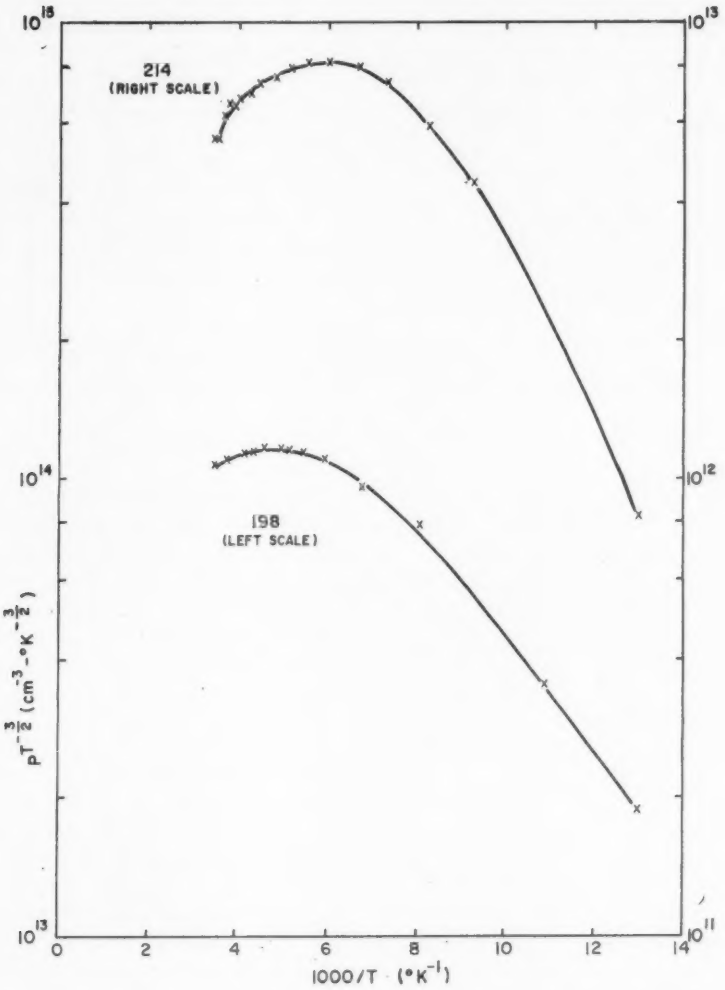

FIG. 2. The product of hole concentration and (temperature)$^{-\frac{3}{2}}$ as a function of $1/T$. The slope at low temperatures was used to estimate the ionization energy.

the values of N_D with an effective mass for the holes of the order of $0{\cdot}2\ m_0$.

The lattice mobility may be obtained by subtracting the calculated impurity mobilities from the measured values for the two crystals. The dotted curve in Fig. 1 gives the result of this procedure for crystal 214, using $m^* = 0{\cdot}2\ m_0$. For crystal 198, such a procedure results in a lattice mobility somewhat lower in value. The lattice mobility calculated for 214 varies as $T^{-2{\cdot}4}$, with a value of 160 cm^2/V-sec at 290°K. The electron lattice mobility at this temperature is 5000 cm^2/V-sec[1] (or 6600 cm^2/V-sec, as extrapolated by REID and WILLARDSON[10]), giving a ratio b of

electron to hole mobility of ~ 30 (or ~ 40). Even the larger value would still place the point plotted by FOLBERTH[11] in his Fig. 2, where b is given as a function of the relative polarization in the III–V compounds, far off a curve which indicates a simple functional relationship between these two variables.

Acknowledgements—It is a pleasure to acknowledge the assistance of B. SEABURY and R. R. VANNOZZI in the carrying out of the experiments described above.

R.C.A. Laboratories M. GLICKSMAN
Princeton, N.J. K. WEISER*

REFERENCES

1. GLICKSMAN M. and WEISER K., *J. Electrochem. Soc.* **105,** 728 (1958).
2. FOLBERTH O. G. and WEISS H., *Z. Naturforsch.* **10a,** 615 (1955).
3. OSWALD F. and SCHADE R., *Z. Naturforsch.* **9a,** 611 (1954).
4. NEWMAN R., *Phys. Rev.* **111,** 1518 (1958).
5. BROOKS H., *Advances in Electronics and Electron Physics*, Vol. 7, p. 87. Academic Press, New York (1955).
6. GLICKSMAN M., *Bull. Amer. Phys. Soc.* **3,** 120 (1958); *J. Phys. Chem. Solids* **8,** 511 (1959).
7. REYNOLDS W. N., LILBURNE M. T. and DELL R. M., *Proc. Phys. Soc.* **71,** 416 (1958).
8. CONWELL E. M., *Proc. Inst. Radio Engrs.* **40,** 1327 (1952).
9. BROOKS H., *Phys. Rev.* **83,** 879 (1951).
   HERRING C., Unpublished work.
10. REID F. J. and WILLARDSON R. K., *J. Electronics and Control*, **5,** 54 (1958).
11. FOLBERTH O. G., *Z. Naturforsch.* **13a,** 856 (1958).

On the boron–nitrogen donor–acceptor bond

(*Received* 25 *February* 1959)

IN this note, a comparison of various B–N bonds with each other and with C–C bonds is considered. On the basis of published experimental results, it is shown that a coherent picture may be obtained. In particular, it is pointed out that the B–N bond in the recently prepared cubic boron nitride[1] may be considered the ideal tetrahedral covalent bond with which the donor–acceptor bonds should be compared. This criterion suggests that at least one donor–acceptor compound, $H_2MeN–BF_3$, has a B–N bond which, within experimental error, is a tetrahedral covalent bond. It follows that other reported donor–acceptor B–N bonds are then either stronger or weaker than a tetrahedral covalent bond, depending on the groups or atoms bonded to the boron and nitrogen.

To date, there are only five donor-acceptor compounds involving the B–N bond, for which the structures have been accurately determined and reported. These are three amine–boron trifluorides and methyl cyanide–boron trifluoride, determined by HOARD and coworkers,[2] and pyridine–boron trifluoride, determined by ZVONKOVA[3].

ZVONKOVA points out[3] that when a fourth bond is formed from boron to nitrogen, one should not expect electron transfer from nitrogen to boron, because nitrogen is more electronegative than boron. That appreciable electron transfer does not take place is experimentally established by the measured electron densities of not only the pyridine–boron trifluoride, but also of the amine–boron trifluorides and the methyl cyanide–boron trifluoride. Because the SCHOMAKER and STEVENSON rule[4] works so well in predicting the B–F distances in these compounds, it would be expected that it should also correctly predict the B–N distance. If the difference in electronegativity of boron and nitrogen were to play a role, the resulting reduction of the B–N distance would be about 0·09 Å. No such reduction has been observed. In pyridine–boron trifluoride, it is probable that the B–N distance is shortened to 1·53 Å, mainly because of the character of the other nitrogen bonds.

When the structure of $H_2MeN–BF_3$ was determined, the nature of the donor–acceptor B–N bond was not clear. However, the length, 1·57 Å, of the B–N bond in this compound led to the observation[5] that the difference, 0·12 Å, between the C–C bond lengths in graphite and diamond, added to the B–N bond length, 1·45 Å, in graphitic BN would give a B–N distance of 1·57 Å in a BN which might crystallize in the SiC form related to the diamond. This, in fact, is exactly the B–N bond length in cubic BN.[1] On the basis of this relationship, one may consider the B–N bond in

* Now at the I.B.M. Research Center, Poughkeepsie, N.Y.

cubic BN as the ideal tetrahedral covalent B–N bond. It is noteworthy also that there is a close analogy between the pairs B-trichloroborazole[6] ($d_{B-N} = 1{\cdot}41$ Å)–benzene ($d_{C-C} = 1{\cdot}39$ Å) and graphitic BN[7] ($d_{B-N} = 1{\cdot}45$ Å)–graphite ($d_{C-C} = 1{\cdot}42$ Å).

We see from the above that the differences between lengths of the B–N linkage in the three-ligand covalent and donor–acceptor forms are not really surprisingly large (see references (3), (8), (9)). One may compare the B–N donor–acceptor bond with the B–N bond in cubic BN, just as one may compare the C–C bond in ethane with that in diamond. In the latter case, both have very nearly the same length and energy. In considering the former comparison, we see that in $H_2MeN{-}BF_3$, the B–N bond length is the same as that in cubic BN and therefore should be considered a single bond. It would then follow that: the B–N bonds in $Me_3N{-}BF_3$ (1·585 Å) and $H_3N{-}BF_3$ (1·60 Å) are somewhat longer (weaker) than single bonds; the B–N bond in $MeCN{-}BF_3$[2] (1·64 Å) is significantly longer (weaker) than a single bond; and as one might expect, the B–N bond (1·53 Å) in $H_5C_5N{-}BF_3$ is significantly shorter (stronger) than a single bond.

The change in bond energy with change in length appears to be somewhat greater for the B–N[9] than for the C–C linkages.[10] In the case of C–C bonds, the change appears to be approximately 2–3 kcal/mole/0·01 Å. (This is in agreement with GLOCKLER's[10] more exact empirical relations between energies and lengths of C–C bonds.) For the B–N bonds, the change is approximately 4 kcal/mole/0·01 Å.

Although the exact relationship between bond energy and length is undoubtedly complicated, if the B–N bond has exactly the same length in two different compounds or crystals, it should have very nearly the same bond energy. Thus the B–N bond in $H_2MeN{-}BF_3$, of length 1·57 Å, should have very nearly the same energy as that in cubic BN. If the estimates of the B–N bond energies[9] of $H_3N{-}BF_3$ and $Me_3N{-}BF_3$ are approximately correct, the energy for the bond of 1·57 Å length is about 35 kcal/mole. This is considerably lower than that, 84·9 kcal/mole, of the analogous C–C bond of 1·54 Å length. On the other hand, from the B–N bond energy of B-trichloroborazole,[8, 9] 85 ± 5 kcal/mole, one may estimate the energy of the B–N bond in graphitic BN to be about 75 ± 10 kcal/mole, again a considerably lower value than that, 111·1 kcal/mole, for the C–C bond in graphite.

It should be noted that the above reasoning predicts that the heat of sublimation of cubic BN into single atoms should be less than half that of diamond.

Acknowledgements—The presentation of the ideas in this note has profited from discussion with Dr. A. D. LIEHR. The author wishes also to thank Mrs. A. WERNER for translating ref. (3) from the Russian.

Bell Telephone Laboratories S. GELLER
Murray Hill, N.J.

REFERENCES

1. WENTORF R. A., Jr., *J. Chem. Phys.* **26,** 956 (1957).
2. HOARD J. L., GELLER S. and OWEN T. B., *Acta Cryst., Camb.* **4,** 405 (1951).
3. ZVONKOVA Z. V., *Kristallografiia* **1,** 73 (1956).
4. SCHOMAKER V. and STEVENSON D. P., *J. Amer. Chem. Soc.* **63,** 37 (1941).
5. GELLER S. and HOARD J. L., *Acta Cryst., Camb.* **3,** 121 (1950).
6. COURSEN D. L. and HOARD J. L., *J. Amer. Chem. Soc.* **74,** 1742 (1952).
7. PEASE R. S., *Acta Cryst., Camb.* **5,** 356 (1952).
8. VAN ARTSDALEN E. R. and DWORKIN A. S., *J. Amer. Chem. Soc.* **74,** 3401 (1952).
9. SKINNER H. A. and SMITH N. B., *J. Chem. Soc.* 4025 (1953).
10. GLOCKLER G., *J. Phys. Chem.* **61,** 31 (1957).

The thermal conductivity of silver antimony telluride

(*Received* 4 *March* 1959)

As part of a survey of the properties of ternary compound semiconductors, the thermal conductivity of silver antimony telluride[4], $AgSbTe_2$, was determined.

The compound was prepared directly from the elements in an evacuated quartz ampule by heating to 700°C, mixing the resulting liquid by agitation, and then cooling at 5°C/min. The product was a macrocrystalline ingot with grains up to 5 mm in length and with an electrical resistivity of $5{\cdot}3 \times 10^{-3}$ Ω-cm. Thermoelectric measurements

showed it to be a p-type, non-degenerate semiconductor. X-ray powder diffraction patterns showed a single-phase face-centered cubic structure with $a = 6{\cdot}076$ Å, in agreement with that given by WERNICK *et al.*[4]

The thermal conductivity at 300°K was determined by the standard method of placing cylindrical specimens between a heater and a heat sink.[1] Measurements were made of the thermal gradients associated with known heat flows. The experimental results for four specimens of the same diameter, but with differing lengths, are shown in

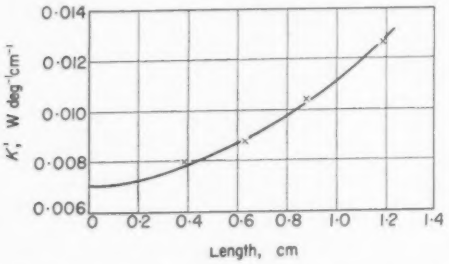

FIG. 1. Variation of apparent thermal conductivity, K', with length of cylindrical specimen.

Fig. 1. The variation of the apparent thermal conductivity results from radiation losses from the heater and from the surface of the specimen. If the thermal resistance of the heater–specimen interface is assumed to be negligible compared with the thermal resistance of the specimen, then it can be shown that the apparent thermal conductivity should follow a parabola when plotted against the length of the specimen. The experimental data can be well represented by:

$$10^3K' = 7{\cdot}06 + 0{\cdot}87l + 3{\cdot}30l^2.$$

In this expression the first term is the true thermal conductivity, while the second and third terms represent radiation losses from the heater and from the specimen, respectively. The total thermal conductivity of the solid is thus 0·0071 W deg^{-1}cm^{-1}. The electronic component of the thermal conductivity was estimated from the electrical resistivity to be 0·0008 W deg^{-1}cm^{-1}, assuming a Boltzmann distribution and thermal scattering of the carriers.[2] The ambipolar component[3] was considered to be negligible in view of the high carrier concentration. Thus the lattice thermal conductivity of silver antimony telluride is 0·0063 W deg^{-1}cm^{-1} with an estimated error of ±10 per cent.

This value of lattice thermal conductivity is smaller than is generally found for crystalline solids, and considerably smaller than for most known semiconductors. The temperature-dependence of the thermal conductivity is being investigated.

Acknowledgement—The X-ray examination was made by Dr. J. G. WHITE.

RCA Laboratories E. F. HOCKINGS
Princeton, N.J.

VOL
10
195

REFERENCES

1. LEES C. H., *Phil. Trans.* **208,** 381 (1908).
2. WILSON A. H., *The Theory of Metals* p. 200. Cambridge University Press (1953).
3. PRICE P. J., *Phys. Rev.* **95,** 596 (1954).
4. WERNICK J. H., GELLER S., and BENSON K. E., *J. Phys. Chem. Solids,* **4,** 154 (1958).

Superconductivity of AuBe

(*Received* 27 *February* 1959; *revised* 19 *March* 1959)

NEITHER gold nor beryllium in its usual modifications is a superconductor. However, it was reported recently that thin films of beryllium deposited at low temperatures are superconducting.[1] This is consistent with the hypothesis that the divalent elements may or may not be superconducting.

Two superconducting gold compounds are known, Au_2Bi[2] and Nb_3Au.[3] The number of gold valence electrons involved is one for the Au_2Bi and eleven for the Nb_3Au. This is understandable when one considers that bismuth and niobium are on opposite sides in the Periodic System with respect to gold.

In an earlier investigation[4] we had checked the gold-rich portion of the gold–beryllium system without, however, finding any superconducting compounds. This we believe was due to the fact that counting gold as having either one or eleven valence electrons would have caused in both cases

the average concentration of valence electrons per atom to fall outside the superconducting range. In order to get into it, we have now made the compound AuBe by fusing together the elements in a quartz tube.

This compound has the cubic FeSi-type structure ($B20$),[5] and becomes superconducting at 2·64°K. Thus it supports the belief that the number of gold valence electrons varies, according to whether the element forming the compound is to the right or to the left of gold in the Periodic System. In AuBe it would have to be counted as eleven.

Acknowledgement—I want to thank Mrs. V. B. COMPTON for the X-ray work.

Bell Telephone Laboratories B. T. MATTHIAS
Murray Hill, N.J.

REFERENCES

1. LAZAREV B. G., SUDOVTSOV A. I. and SMIRNOV A. P., *Zhur. Eksper. Teor. Fiz.* **33,** 1059 (1957).
2. DE HAAS W. J., VON AUBEL E. and VOOGD J., *Proc. K. Akad. Amsterdam* **32,** 226 (1929); *Comm. Phys. Lab. Univ. Leiden* No. 197a (1929).
3. WOOD E. A. and MATTHIAS B. T., *Acta Cryst., Camb.* **9,** 534 (1956).
4. MATTHIAS B. T., *Phys. Rev.* **92,** 874 (1953).
5. CULLITY B. D., *Trans. Amer. Inst. Min. (Metall) Engrs.* **171,** 396 (1947).

The effect of pressure on the absorption edge of $BaTiO_3$ and TiO_2

Received 2 *March* 1959; *revised* 26 *March* 1959

THE effect of pressure has been measured on the absorption edge of $BaTiO_3$ and TiO_2 (rutile). The $BaTiO_3$ crystals were obtained from J. H. NIELSEN, of Bell Telephone Laboratories, and E. C. STEWART, of Harshaw Chemical Company. The TiO_2 crystals were from the Linde Company. The experimental techniques have been previously described.[1] The shifts were measured for an absorption coefficient $\alpha \cong 75$, in a region where the absorption was considerably larger than the reflection for the usual sample thickness (0·004–0·010 in). The shape of the edge was independent of pressure as far as could be determined from our measurements. The results are shown in Fig. 1.

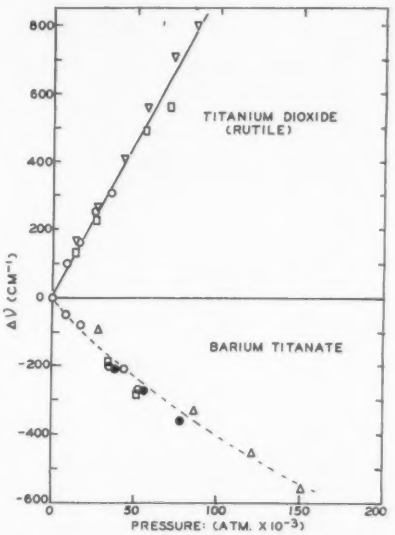

FIG. 1. Shift of barium titanate and titanium dioxide (rutile) with pressure. ($\nu_0 = 23{,}800$ cm^{-1} for barium titanate and 24,200 cm^{-1} for titanium dioxide.)

The different symbols refer to different runs. The points shown were taken with increasing pressure, but check points were measured with decreasing pressure on each run, and the shifts were reversible. There is a small but definite red shift in $BaTiO_3$ and a blue shift in TiO_2. The atmospheric edge is at nearly the same place in both crystals and probably corresponds to O^{--} to Ti^{4+} charge transfer. In each case the Ti is surrounded by 6 O^{--} ions, but the TiO_2 is much more symmetrical than the $BaTiO_3$. The nearest-neighbor O–Ti distances are shown below:

Compound	No. of bonds	Length (Å)	Ref.
$BaTio_3$	1	1·869	(2)
	1	2·167	
	4	1·999	
TiO_2	2	1·988	(3)
	4	1·944	

*This work was supported in part by U.S. Atomic Energy Commission Contract AT(11–1)–67, Chemical Engineering Project 5.

The average Ti–O bond length is 0·05 Å greater in $BaTiO_3$ than in TiO_2, a fact which may contribute to the difference in the shift. The much lower degree of symmetry of $BaTiO_3$ quite possibly allows energy bands forbidden by symmetry considerations in TiO_2.

Acknowledgements—The authors wish to thank F. SEITZ for helpful suggestions, and J. H. NIELSEN, E. C. STEWART and the Linde Company for crystal samples. H. L. SUCHAN wishes to acknowledge financial assistance from a Standard Oil Company (Ohio) Fellowship. A. S. BALCHAN wishes to acknowledge financial support from a Pittsburgh Consolidation Coal Company Fellowship.

Department of Chemistry
and Chemical Engineering
University of Illinois
Urbana, Ill.

H. L. SUCHAN
A. S. BALCHAN
H. G. DRICKAMER

REFERENCES

1. FITCH R. A., SLYKHOUSE T. E. and DRICKAMER H. G., *J. Opt. Soc. Amer.* **47**, 1015 (1957).
2. MEGAW H. D., *Ferro-Electricity in Crystals*. Methuen and Co., London (1957).
3. BAUER W. H., *Acta Cryst., Camb.* **9**, 515 (1956).

VOL
10
195

T. S. Moss: **Optical Properties of Semiconductors, a Semiconductor Monograph.** General editor C. A. Hogarth. Butterworths Scientific Publications, London, and Academic Press, New York, 1959. 279 pp., 74 figs., 50*s*.

In the preface to this book, Dr. Moss refers to the present widespread research effort on semiconductors, and to the need for books reviewing the subject. He concludes that there is a genuine requirement for specialized treatments covering in detailed fashion only a small fraction of the field. Few people will quibble with this, the stated aim of the present volume, especially since great care has been taken to make the book as up-to-date as possible. Published in the early months of 1959, the book nevertheless includes many of the important results of the International Semiconductor Conference held at Rochester in August 1958. It is said to be "primarily intended for the experimental physicist engaged in active research or development, and for the honors student who wishes to increase his specialized knowledge. . .". While the book will undoubtedly be useful to the former worker in providing a quick review of the salient physical phenomena and equations that describe optical properties, and in affording an up-to-date account of current optical work in the different semiconductors, it is doubtful if the honors student will find it an adequate pedagogical treatment. This is no real criticism of Dr. Moss' presentation, as the two aims of the book are somewhat antithetical.

The first forty per cent of the book discusses absorption and emission processes, interrelation of optical constants, internal photo effects, and so on. The first chapter reviews the theory of the optical properties of conducting media, and is likely to serve a most useful purpose in collecting in a few pages those formulae an active worker has found useful. Similar considerations apply to the second chapter which discusses dispersion theory. It is perhaps a pity that the approximation of representing the dispersion properties of semiconductors such as germanium and silicon by a single oscillator frequency is pressed as far as it is; while the classical model has considerable value in its place, its use for semiconductors whose band structure is beginning to be reasonably well known is questionable.

The third chapter discusses absorption processes in semiconductors and is, in general, succinct and adequate. However, in the section on direct and indirect optical transitions different formulae for apparently the same absorption process are presented, without critical appraisal, and the reader is left to make his choice. Dr. Moss would have performed a real service in disentangling the confusion of formulae in the literature. Most of the rest of the chapter which discusses features of absorption edges, the dependence of the edge position on pressure, temperature, magnetic field and impurities, is compact and well done. For this reviewer, however, the addition of a section describing an empirical relation between refractive index and energy gap, n^4E_g = constant, seemed unfortunate. While it is quite true that, in general, materials of small energy gap will have high refractive index, there is no theoretical justification for this particular functional relationship. The energy gap is determined by the eigenvalues for specific states in the valence and conduction bands, while the refractive index depends on the energies of all the states in these two bands. Thus the energy gap in germanium is set at 0·65 eV by 111 conduction band minima and (000) valence band maxima, while the main contribution to the refractive index comes from states separated by about twice this energy. It is interesting to note that the relation fails to correlate the pressure dependence of the energy gap and refractive index in silicon for just this reason: the energy gap decreases because of a rather special behavior of the silicon conduction band minima, while the refractive index also decreases because the overall tendency is for the conduction and valence band states to *separate* with applied pressure.

The fourth chapter deals with photoelectric effects, and treats the p.e.m. effect in particular in considerable detail. The fifth treats magneto-optical effects, perhaps in somewhat cursory fashion, and the sixth discusses recombination radiation and the emissivity of thermal radiation. As the reader delves deeper into the book, the wealth of references and cross-references becomes impressive, and one's earlier quibbles on some aspects of the treatment seem much less significant. The remainder of the book discusses the

optical properties of practically all of the well-known semiconductors in succinct and readable fashion. It is here that what would appear to be the major contribution of the book is made. For the new worker in any of these semiconducting elements and compounds, a ready source of predigested facts and references is invaluable. Dr. Moss has provided this, and more: in many cases he has given critical discussion and comparison of data, in an authoritative way. He himself is very clearly in continuous close touch with much of the experimental work and all of the literature. For this report and compendium of information he deserves our sincere thanks.

WILLIAM PAUL

Growth and Perfection of Crystals. Edited by R. H. DOREMUS, B. W. ROBERTS, and DAVID TURNBULL. John Wiley and Sons, New York. Chapman and Hall, London, 1958. 608 pp., $12.50.

CONFERENCES attended by large numbers of scientists may enable the participants to meet, but the useful discussions are held outside the conference rooms. In fact, if those attending have to be counted in thousands instead of in hundreds, there is little chance of meeting others with similar interests and the main activity seems to be to parade the veterans of science to the younger generation. Profitable and frank discussions can only be held in a restricted circle and therefore conferences arranged as working committees of specialists have recently come into favour. The volume under review is the report of such a meeting.

The conference on recent research in crystal morphology, whiskers and polymer crystallization was held at Cooperstown, New York, on August 27–29, 1958. It was sponsored jointly by the U.S. Air Force Office of Scientific Research, Air Research and Development Command, and the General Electric Research Laboratory, the same combination that had sponsored and organized the successful and so enjoyable Lake Placid Conference in 1956. The success of the conference at Cooperstown was clearly due to the same causes: careful selection of the participants (63, thirteen of whom came from outside U.S.A.) who were invited by the Committee, careful planning of the programme leaving sufficient time for discussion, and careful preparation of the papers.

The conference report starts with an invited lecture by F. C. FRANK, who takes crystal morphology as the central connecting subject to which all other subjects of the conference are related. He points out that if we had appreciated WILLARD GIBBS' work earlier and known all the scientific literature, we would have realized that the shape of crystals is mostly dictated by the kinetics of their growth and not by conditions of thermodynamic equilibrium and that discrete centres of growth are necessary in the crystal faces for a polyhedral crystal to result. He then draws attention to the effect of impurities on crystal growth; obviously, impurities may poison the surface and change the rate of adsorption. This results in "bunching", i.e. in growth steps of many thousand Burgers vectors in height such as they were observed on quartz crystals by MIERS with the naked eye over 50 years ago. The same principle is also applied to the growth of whiskers. But all these points are discussed later in detail, and FRANK in his introductory lecture just presents some of the highlights.

The subjects of the conference were discussed under five headings, each section starting with one invited review paper (two in the section on crystallization of polymers).

The first section, on growth of whiskers, contains an outstanding review of 85 pages by NABARRO and JACKSON. It traces the knowledge of the existence of whiskers back for centuries and collects all information, experimental and theoretical, on whisker growth from vapour and melt, within solids, from solution, by chemical decomposition and electrolysis, and under mechanical stress. The critical evaluation of the present state of the theory given for each of these methods of growth is of particular value.

It is, of course, quite impossible in a review even to name the thirty-five shorter papers of more specialized character. This should not be taken to mean that their value is not considerable or not appreciated, but rather that this wealth of recent results and ideas has to be absorbed by the interested reader—and everyone taking this volume to hand will become an interested reader—and cannot be prepared for him in a short space.

The second section deals with properties of whiskers and crystal imperfections. The review is

given by S. S. BRENNER and deals competently with elastic and plastic behaviour, electrical, magnetic and surface properties, dekinking and phase changes. The two first sections on growth and properties of whiskers take up almost half of the whole volume. Quite rightly so, since a collection of our knowledge about whiskers is most welcome and important and not available elsewhere in such completeness.

Growth of crystals of the solvent phase is the subject of the third section to which BRUCE CHALMERS has written the review. He is mainly concerned with crystal growth from the melt and precedes his discussion of the mechanism of crystal growth by comments on the structure of liquid metals and of the liquid-solid interface. He then discusses the origin of cellular interfaces and dendritic growth and finally points out how crystal imperfections may result from the process of solidification. All these subjects are discussed in more detail in the papers of this section; however, special attention should be drawn to the descriptions of methods of growing dislocation-free crystals of silicon and germanium of up to 50 g and over 2 cm in diameter (W. C. DASH) and of preparing single crystalline discs of silver chloride (about $\frac{1}{3}$ mm thick and 25 mm in diameter) with a very low dislocation density (J. W. MITCHELL).

CABRERA and VERMILYEA have written the review for the section dealing with the growth of crystals from solution. They emphasize the importance of the manner in which steps moving over a growing surface interact with each other and draw attention to the great effect impurities may have on the step heights and the rate of growth. Such effects have been suspected earlier but with the papers in this section we have the beginnings of quantitative treatments.

The final section is devoted to the crystallization of polymers, and of the two invited review papers; that by L. MANDELKERN (National Bureau of Standards) deals with the kinetics and that by A. KELLER (University of Bristol) with the morphology. According to the preface of the book, one of the main purposes of holding the conference was to "promote useful exchange of views between scientists studying polymer crystallization and those investigating the crystallization of simpler molecules" and this purpose seems to have been achieved, though the exchange appears to have benefited primarily those interested in polymers.

The volume has been well produced by the photo-offset printing process and some of the full-page photographs are most artistic and exciting. The editors have to be congratulated on their effort in bringing out such a volume of just over 600 pages within 6 months of the conference. They have refrained from imposing uniformity of word usage and conventions on the authors and thereby left untouched the individuality of the authors. This lack of interference is particularly marked in the discussions which come very much to life on reading and where, knowing the speakers, one can almost hear their intonation and certainly feel the atmosphere of the meeting. This volume is an important scientific document and most enjoyable to read, and though its price will prevent many individuals from buying, it is a must for all those interested in the physics and chemistry of solids.

W. BOAS

BOOKS RECEIVED

GEORGE SHORTLEY and DUDLEY WILLIAMS. *Principles of College Physics*, (a rigorous and integrated treatment of basic classical and modern physics,) 898 pp. (Prentice-Hall Inc., New York, 1959) $9.00.

E. J. CABLE, R. W. GETCHELL, W. H. KADESCH and W. J. POPPY. *The Physical Sciences*, (from atoms to galaxies—an exciting, lucid and integrated explanation of the fundamentals of astronomy, chemistry, physics, geology and meteorology,) 553 pp. (Prentice-Hall Inc., New York, 1959) $6.95.

ERRATA

B. N. BROCKHOUSE, *J. Phys. Chem. Solids* **8,** 400 (1959).

The discussion on p. 421 should have read as follows:

H. BROOKS (Harvard): If you interpret the two larger HAYNES phonons in silicon as two-phonon processes, where are the other two phonons that should show up in the HAYNES experiment?

B. N. BROCKHOUSE (Atomic Energy of Canada Limited): I am not an expert on group theory but it seems to me to be possible that some lines may be *almost* forbidden by reason of symmetry selection rules which might hold fully if the minimum were located at the zone boundary (point X) instead of near it on line Δ.

G. J. WOLGA and M. W. P. STRANDBERG, *J. Phys. Chem. Solids* **9,** 309 (1959).

In Fig. 1 delete $\eta_-(m = 9{\cdot}5$; add $\eta_-(m = -9{\cdot}5)$ by plotting $\eta_-(m = -9{\cdot}5) = -1{\cdot}4152 + 4{\cdot}5\theta$.

Proceedings of 1958 *International Conference on Semiconductors.*

Because of an error in the binding procedure two plates were omitted from some copies of the above. For the convenience of subscribers they are reproduced in this issue:

G. FEHER, *J. Phys. Chem. Solids* **8,** 486–489 (1959). Fig. 2 should be inserted between pages 486 and 487.

G. W. LUDWIG, H. H. WOODBURY and R. O. CARLSON, *J. Phys. Chem. Solids* **8,** 490–492 (1959). Fig. 2 should be inserted between pages 490 and 491.

VOL.
10
1959

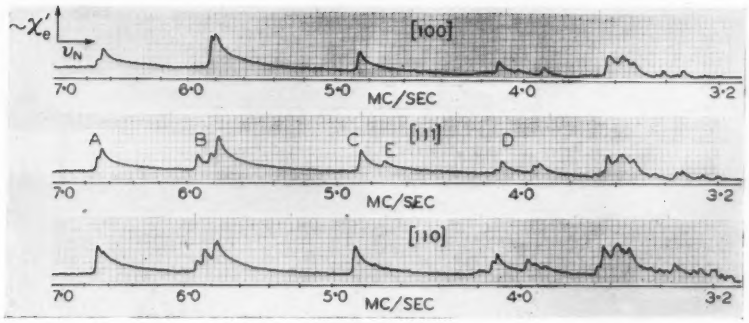

FIG. 2. Part of the ENDOR signal from arsenic doped silicon (8×10^{16} As/cm^3, $T = 1{\cdot}2°$, $\nu_e \approx 9000$ Mc/s). The lines represent the h.f. interaction of the donor electron with the Si^{29} nuclei at different lattice points.

VOL
10
195

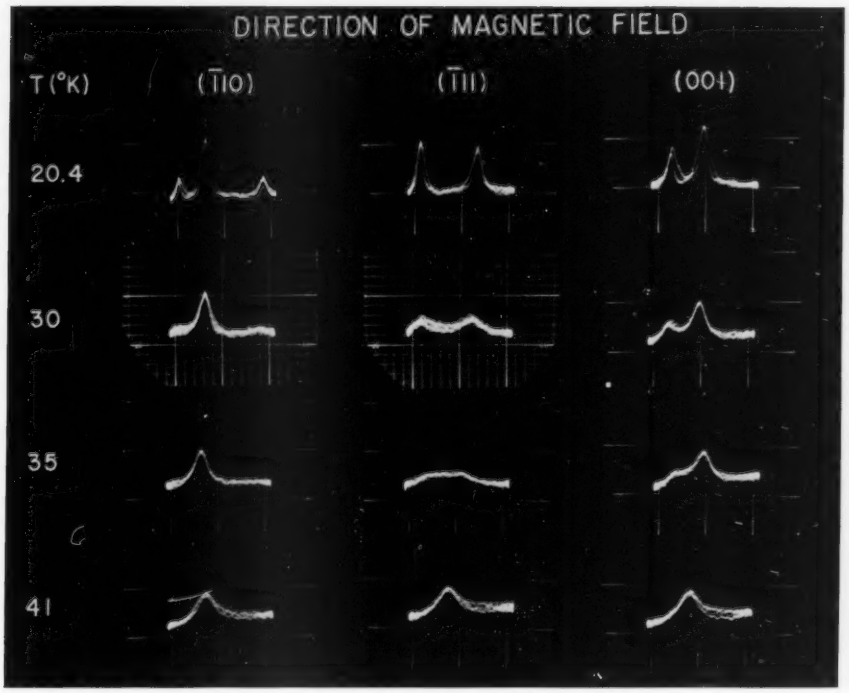

FIG. 2. Photographs of an oscilloscope display of the Ni^{-} spectrum as seen in absorption, showing the broadening and merging of the lines as the temperature is raised above 20·4°K.

facing page 491]